PETROGENESIS OF COLOMBIAN ARC VOLCANOES:

A REGIONAL STUDY

by

DAVID EDWARD CAVELL

A thesis submitted to the University of Birmingham for the degree of

DOCTOR OF PHILOSOPHY

Department of Earth Sciences

School of Geography, Earth and Environmental Sciences

College of Life and Environmental Sciences

University of Birmingham

October 2020

Abstract:

The petrogenesis of intermediate silica magmas in continental arc settings remains heavily debated. Contention focuses on the importance of slab components (subducted sediments and altered oceanic crust) compared to processes within the overlying plate to imparting the distinctive geochemical signature of intermediate arc lavas. The Colombian Andes are an understudied region compared to other continental arc settings. The region has several compelling features, including a moderate crustal thickness for continental arcs and geochemically well characterised mid and lower crustal basement. This study utilises high quality geochemistry of major and trace elements and isotopes as petrogenetic tracers of the different components and processes within the Colombian Volcanic Arc, demonstrating that mantle derived melts undergo magma mixing and assimilation processes during ascent through the crust, promoting a diversity of geochemical signatures mainly dependent on pathway through the crust and assimilation of specific crustal components. A developing idea is that crustal thickness may act as a control on some arc parameters, and it is clear that magmatism is strongly controlled by crustal features from previous orogenic events, allowing for primitive compositions to be emplaced in contrast to highly fractionated compositions.

Dedicated to my family for making the years on this possible.

And to Mum for everything else.

And

For the women and men of the Colombian Geological Survey.

Para el mujeres y el hombres del Servicio Geológico Colombiano.

“Geology is the study of pressure and time. That's all it takes, really.

Pressure, and time.

That and a big goddamn poster.”

- Ellis Boyd 'Red' Redding, The Shawshank Redemption.

Acknowledgments

This work owes much to the contribution of others, and would not of been possible without an army of dedicated, helpful and patient people.

My Father and my sister Louisa, who gave their unwavering support not just to me doing the PhD, but for making sure I was pursuing what I really wanted and needed. I could not have done this without you. Dad is especially thanked for the day to day support he gave me, even when I was busy and a bit too pre-occupied with life and work. You are the best Dad and always look out for me. My thanks to Louisa for reminding me that families are there to support each other through thick and thin, and for advice on writing: Sometimes shorter and simpler is better. I also want to thank my partner Gemma. You coming into my life was like colour coming into the world. Love, care and understanding are what you need when doing a PhD and you provided these in spades.

Dr Alan Hastie and Dr Seb Watt are thanked for their saintly patience and keeping the faith in a sometimes wayward student. We got there in the end. I count myself extremely fortunate to have had Alan as a supervisor. Rarely do the qualities of a down to earth approachable attitude, a sharp scientific mind and the drive to seek the answers to intractable scientific problems meet in one person. Your reassuring manner and smile made it easier, even in the tough moments. I know I wasn't an easy student but you were a brilliant supervisor despite this - You kept the faith even when I didn't. Thank you. Seb Watt asked some of the tough questions on this project (which I spent a lot of time trying to answer) and without these this thesis

would be immeasurably poorer. You proved to me the value of vigilant skepticism and a focus on what's in front of you, things I will carry with me in the rest of my research and life. You were also a kind and patient face in doctoral meetings who I knew wanted to see this through to success.

There is a third member of the supervisory team at Birmingham who sadly won't be on any of the papers - Gretchel Coldicott. Gretchel looked after me at Birmingham providing a caring presence but also the best admin support we could ask for. This was complimented by Aruna Mistry, who's wry wit and down to earth approach was the perfect antidote to dealing with university bureaucracy. Many projects would die an early death without support from people like Gretchel and Aruna.

When I say "us" in this acknowledgement, the other half of that "us" is Dr Daniel Cox. Fieldwork bonds people, and after spending three months in Latin America and over four years in research together, through good and bad, I can say I now have a brother for life. His easy smile, no nonsense attitude, good humour and intellect (amongst a hundred other good qualities) made the journey here all the easier. His influence and good ideas are a thread running through this thesis. Thank you, I hope this partnership continues for the rest of our lives.

Alastair Hodgetts for having my back in school rep matters and for being a good sounding board on all things volcanology and monogenetic related. I think everyone all can see that you will go very, very far in earth science and outpace us all one day. Dr Emma Dunne and Dr Ben Harvey are also thanked for their continual advice, kind

words and making sure the coffee was always flowing. I would not have gotten this far without both of you behind me.

The postgraduate community in Birmingham deserves a special mention too, for being a welcome and non-judgemental group that really look after you. I feel lucky to have been part of it. In no particular order are the ensemble of other PGRs/postdocs who kept me going during the project: Dr Gael “Papa Francais” Lymer, Jack Richardson, “Little” Emma Hansen, Murray Hoggett, Lisa Schnetz, Dr Derren Cresswell, Juan Pablo Castañeda, Dr Dan “Cashback” Cashmore, Amy Jones, Dr Simiao Sun, Anya Lawrence, Jonathan Hall, Nicola Kirby, Dr Rosemary Dartnell, And of course the staff outside my supervisors who in little and large ways helped me along: Dr James Wheeley, Dr Carl Stevenson, Dr Paul Anderson, Dr Sarah Greene, and the whole department.

None of this would be possible without the help, advice and expertise of those who assisted us in Latin America. Your kindness and generosity for total strangers overwhelmed me. Dr Hugo Fernando Murcia, Camilo Pinzón, Pablo Osorio and Alvaro Botero are thanked for tremendous efforts in the Northern Volcanic Province of Colombia. Hugo made us feel very welcome during the time in Manizales and he and the group at Caldas went above and beyond to provide us further material in the area, vastly improving the dataset for the region and the project itself. Professor Alvaro Nivia, the first Colombian point of contact we had, provided good advice in the planning stages, opened his home to us and even provided an unforgettable night of salsa in Cali. The man has moves! Professor Jose Trujillo Duque of EAFIT University and Professor Marion Weber of the Universidad Nacional (Medellin) are also

thanked for their kindness and great assistance in Colombia. Jose is a brilliant geologist who utterly saved my bacon in Central Colombia by having the foresight to provide samples from areas too dangerous for us to visit. This provided us a good sample set for the Patia-Cauca belt and modern arc in the region. Marion, a fellow Leicester alumni, made me feel like one of the team from the moment I stepped off the plane in Colombia.

This project gave me the chance to work alongside the Servicio Geologico Colombiano and visit their volcanic observatories. I was left with a lasting admiration for their work and that of the Colombian geological community at large. Dr Gloria Patricia Cortes was a friendly face at the Manizales Observatory and again in Southern Colombia. Dan and I were truly touched by her gift of a Ruiz sample marked up to commemorate the anniversary of the 1985 eruption and Armero tragedy. We were profoundly moved by the work of the survey in light of this. Finally the staff of the Pasto observatory are thanked, particularly Dr Diego Gomez and (colleagues) for their herculean efforts getting our samples out of the country. There would be no project without your help!

Analyses can’t happen without the laboratories and those running them. The practical help and advice offered by staff at UoB, Cardiff University, NIGL and SUERC was invaluable. Dr Andy Rees was a welcome source of advice and care in the first half of the project and even after leaving for greener pastures kept up an interest - I wish you could have stayed! Special mention to Anthony Oldroyd at Cardiff, for absolutely stellar work throughout, from samples shipment to thin sections - There would be no project without you Tony! Dr Ian MacDonald is thanked

for patience and sound advice on methodology whilst I prepared and asked him to run an unreasonably large number of analyses. Your ICP work gave us the foundation. Dr Xianhong is also thanked for day to day advice in the ICP lab at Cardiff. The staff at the National Isotope Geosciences Facility, British Geological Survey are also thanked, with special mention to Dr Ian Millar, a friendly face and fellow Antarctic geology aficionado, for his support as well as Dr Nicola Atkinson and Doris Wagner for running me through the columns at NIGL. Dr Simon Tapster is also thanked for useful conversations on oceanic plateaus at NIGL which focused my mind going into the final year of the project. At SUERC, Dr Dan Barfod and Dr Darren Mark are thanked for solid advice on applications to facilities and for hosting me. Dan gave me an excellent crash course in Ar-Ar geochronology and helped me not be too bewildered by the “black magic” of dating. Nicole Doran is also thanked for administrative support.

Support was also provided by Geological Research on the Isthmus of Panama (GRIP) also at Cardiff University. Dr David Buchs is thanked first and foremost for helping me find my feet in Panama and get the expedition off to a good start - but I would also like to thank him for his patience and help on the Panama side of my project. It took time, but we got there. Dr Joanna Brims, Jian Wang, Dr Andrew Kerr and Dr Henry Coombs of GRIP and Cardiff University are also thanked for help and advice throughout the project. I also gratefully acknowledge and pay respect to the indigenous communities of Panama and Colombia as the traditional owners of the land on which this research was conducted, and the Embará for help and assistance in Panama. This work was completed as part of a NERC/CENTA studentship, and we acknowledge their contribution.

Contents:

List of Figures:

Project Overview

Continent volcanic arcs, located where oceanic plates sink into the mantle beneath a continent, are formed by dehydration and sometimes melting of the subducting plate, and the fluid-fluxed melting of the mantle wedge, leading to magmas which rise up through the mantle and continental crust. These arcs are primary sites of chemical transfer from Earth's surface to interior and where materials can be taken to the deep mantle or returned to crust and surface. As such, they are important sites of crustal formation, volatile exchange and a locus for ore deposit formation. This thesis is a study of the Colombian continental arc, assessing the processes and components which formed the Colombian arc through petrography, major and trace element geochemistry and radiogenic isotope geochemistry.

1 Introduction

Chapter 1 presents a short summary of current ideas and controversies regarding the subduction zone volcanism, in particular continental arcs. An outline of petrogenesis of intermediate magmas is given by both processes within the overlying plate (intra-crustal) and processes external to this (extra-crustal) within the mantle and the downgoing plate. The Colombian arc from the Miocene onwards is presented as good locality for studying these processes, and an outline of the geology, tectonics and volcanism of the study area is given. The aims and specific objectives of the study are given.

2 Andesite Petrogenesis Models

A detailed summary of the processes and components involved in subduction zones and continental arc volcanism is given, including a historical literature review. Particular focus is then given to arguments around the petrogenesis of intermediate magmas and the hypotheses arising from these, based on processes within the crust of the overlying plate and processes outside of it. The paradigm of a specific of magma type, adakites, is outlined along with brief discussion of the link between arc magmatism and continental crust generation.

3 Geological History of the Northern Andes of Colombia

The third chapter presents a summary of the terranes and tectonics of the Colombian Andes, along with a geological history of the region including major orogenic and magmatic episodes. The evolution of the Caribbean Plate is briefly discussed. Focus is given to basement terranes and major structural/tectonic features which relate or may have influenced the Miocene to recent volcanism in Colombia. Hypotheses regarding the nature of the subducting slab segments beneath Colombia are also outlined.

4 Analytical methods

A brief discussion of analytical techniques (ICP-OES, ICP-MS for major and trace elements, respectively and Sr, Nd, Hf isotopes by column chemistry) is given. The precision and accuracy of the geochemical data is discussed in detail.

5 The Northern Volcanic Province of Colombia

A complete multi-centre major and trace element and isotopic study of the Northern Volcanic Province of Colombia (NVP) is presented, along with comparable data from other recent studies. This is used to assess the models of intermediate magma petrogenesis through modelling of assimilation, fractional crystallisation and magma mixing processes.

6 Controls on Colombian Magmatism: An arc scale perspective

Major, trace element and isotopic analyses from the selected Central and Southern segments of the modern Colombian arc, along with Miocene-Pliocene arc remnants, are presented. These are compared and contrasted to previous analyses of the Colombian arc and compared with findings on the NVP outlined in Chapter 5, allowing for the petrogenesis of the whole arc to be discussed in detail. Fractional crystallisation and assimilation processes are modelled using trace elements and isotopes, and the influence of slab derived components is discussed in detail. The petrogenesis of the Miocene arc front is briefly discussed.

7 Conclusions and avenues for further work

A synthesis on the petrogenesis of samples in this study and the Colombian arc at large is presented. The limitations of this study's dataset are discussed. Recommendations for further geochemical studies are outlined, including those for more detailed geochronology.

1 Introduction

1.1 Background: Subduction, Intermediate Magmas and the Andesite Problem:

Subduction zones, where oceanic lithosphere descends into the Earth's interior, are known as a major site of chemical exchange between the planet's deep and near surface environments, and a major focus of subaerial volcanism (Gill, 1981; Tatsumi and Eggins, 1995; Elliott, 2003; Tatsumi and Kogiso, 1997, 2003).

Current research on subduction focuses on a general model whereby the downgoing slab, composed of igneous oceanic crust, and overlying sediments, gradually progresses through a sequence of metamorphic dehydration reactions with increasing depth. These reactions release aqueous fluids from the slab into the overlying mantle wedge (Gill, 2010; Arturo-Gomez et al. 2013). The effect of these fluids is to lower the solidus temperature of the mantle wedge peridotite and precipitate melting, producing basaltic melts. These fluids also impart chemical signatures of the subducting slab to these melts (e.g.: Tatsumi and Eggins, 1995; Elliott, 1997; Bebout, 2014).

Continental volcanic arcs are produced when the lithospheric plate overlying the subducting slab is composed of continental and/or thickened accreted oceanic material (Ducea et al. 2015). The magmatic products of continental arcs are generally more silicic and incompatible-element enriched than their oceanic arc counterparts (e.g.: Tatsumi and Eggins, 1995; Tatsumi and Kogiso, 2003; Ducea et al. 2015). Though the continental crust overall can be composed of a wide range of

lithologies, its bulk composition is generally recognised as intermediate or “andesitic” (e.g.: Taylor and McLennan, 1985; Rudnick and Gao, 2014). Continental volcanic arcs are recognised as the primary sites where crust of intermediate and silicic composition is produced by magmatic processes today (e.g.: Taylor and McLennan, 1985; Clift et al. 2009; Rudnick and Gao, 2014; Roberts et al. 2014). This has fed into the paradigm that continental arc systems can inform our understanding of continental genesis (e.g.: Taylor and McLennan, 1995; Rudnick, 1995; Martin et al. 2005; Reubi and Blundy, 2009; Moyen and Martin, 2012; Condie, 2014).

The mechanisms of generating intermediate (52 to 66 wt.% SiO_2) magmas (La Bas et al. 1986; Best, 2002) remain debated in the earth sciences (e.g.: Tatsumi, 2012; Arturo-Gomez et al. 2013; Kelemen et al. 2014). This has led to the so called “andesite problem” in literature, whereby two major families of models have developed to explain the formation (or petrogenesis) of intermediate magmas in continental arcs (Figure 1).

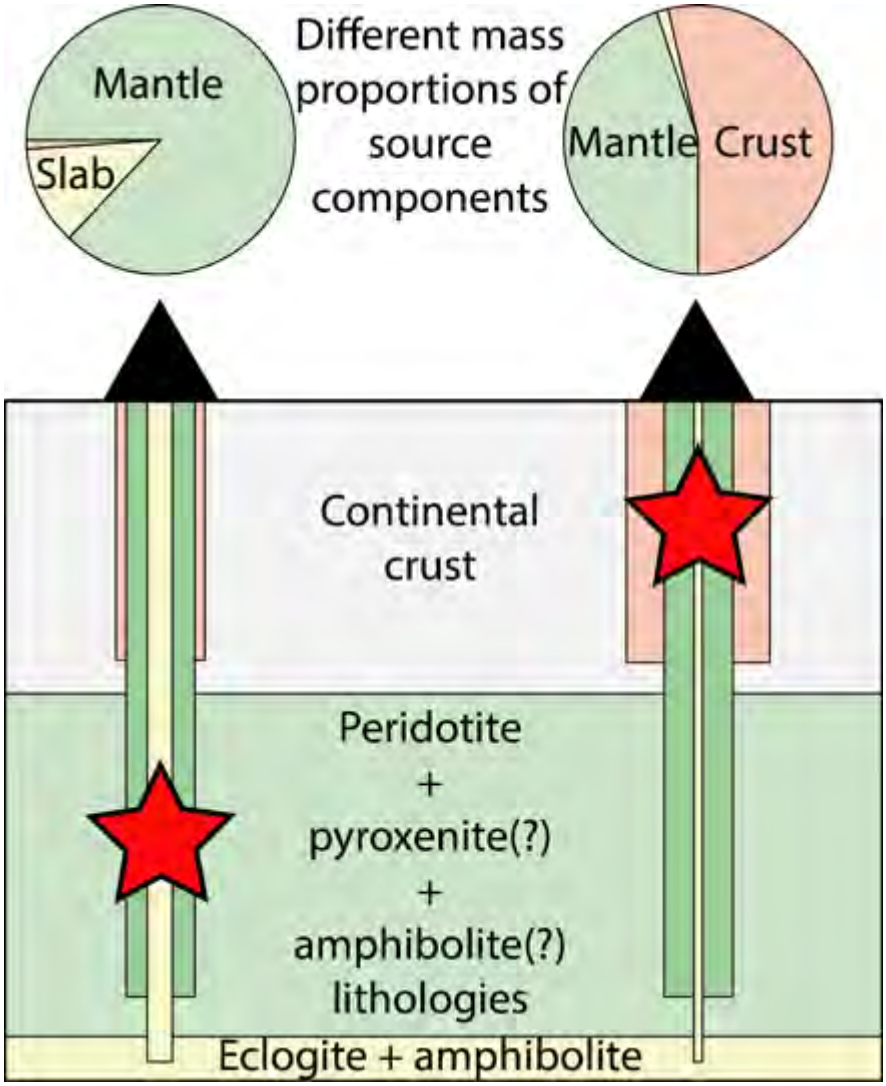

Figure 1.1: Schematic diagram of the two contrasting principal locations of andesite petrogenesis. Left: formation of andesite by hybridisation of slab and mantle components in the mantle wedge; right: parental arc basalts evolve to form andesites in the crust of the overlying plate. Mass proportions may vary within models. Adapted from Gómez-Tuena et al. (2014).

One group of models emphasises the role of “extra-crustal” processes involving primary melts of slab material (oceanic crust and sediments) and mantle wedge components (Gómez-Tuena et al. 2014). Early models of subduction proposed melting of the oceanic crust as the underlying cause of andesite production (e.g.: Ringwood and Green, 1966; Brophy and Marsh, 1986). However, flux melting of the

mantle wedge caused by slab dehydration later became a more dominant paradigm (e.g.: Ringwood, 1974; 1975; Tatsumi et al. 1983; 1984; Tatsumi, 1989; Tatsumi and Eggins, 1995). Despite this, a role for melts of slab components has been a running theme through subduction research (e.g.: Wyllie and Sekine, 1982; Sakayuma and Nesbitt, 1986), leading to new avenues of research on arc lavas such as “adakites”, thought to be derived from melts of subducted oceanic crust (Defant and Drummond, 1990). Such melting of the altered oceanic crust (and to a lesser extent the sedimentary component) of the slab was thought to require anomalously hot conditions (i.e.: Peacock et al. 1994) restricted to young (<25 Ma), hot arc settings (Defant and Drummond, 1990) or those with unusual features such as slab windows or flat subduction (e.g.: Thorkelson, 1996; Gutscher et al. 2000). However, more recent thermal modelling, which includes variable upper mantle viscosity and subduction induced corner flow, indicate that the uppermost part of the subducting oceanic crust may be warm enough to induce partial melting of slab components across a wide range of current subduction conditions (e.g: Abers et al. 2006; Syracuse et al. 2010; Castro et al. 2010; van Keken et al. 2011). As a result, some subduction zone models have focused on partial slab melts as a possible mechanism for producing at least a portion of intermediate magmas. However, sufficient temperatures may not be reached at the slab-mantle interface to accomplish melting and some models propose the formation of thermochemical slab plumes - mixtures of partially molten sediment and basalt derived from the slab mixed with hydrous mantle material - more commonly known as “slab diapirs” (Gerya et al. 2004; Castro et al. 2010; Behn et al. 2011; Marshall and Schumacher 2011) which could rise into parts of the mantle wedge sufficiently hot to induce melting and underplate the base of the overlying arc crust (Hacker et al. 2011). Some experimental studies have proposed

slab diapirs may be more common in arcs than previously thought (e.g.: Hermann and Spandler, 2008; Klimm et al. 2008; Plank et al. 2009; Behn et al. 2011) and these models have been applied to explain the products of the Colombian volcanic arc (Errazuriz-Henao et al. 2019).

The above outlined models may produce a portion of the intermediate composition melts observed in arcs, or the starting compositions for more evolved melts. Alongside this, flux melting of mantle wedge peridotite above the dehydrating slab and decompression melting (e.g.: Jaramillo et al. 2019) also produces basaltic melts that then ascend to the lower crustal boundary. These then undergo “intra-crustal” processes such as fractional crystallisation (FC), assimilation fractional crystallisation (AFC) and/or mixing, assimilation, storage and homogenisation (MASH) within the overlying plate (e.g.: Hildreth and Moorbath, 1988; Feeley et al. 1993; Annen et al. 2006; Macpherson et al. 2006; Solano et al. 2010), producing more evolved intermediate to silicic magmas. Factors such as thickness of the overlying plate, residence times of magmas within the crust and through flow and influx of mafic magmas and mixing could all play a key role in this scenario (e.g.: Chiaradia et al. 2009; Chiaradia, 2014; Farner and Lee, 2017). Such mechanisms can also produce melts with similar chemical properties to adakites derived by melting of subducted oceanic crust, but without the need for slab melting (e.g.: Macpherson et al. 2006; Castillo, 2012; Ribiero et al. 2016), including in the Colombian arc (Laeger et al. 2013). These can include fractional crystallisation of magmas beneath the arc crust (Macpherson et al. 2006) as well as fractional crystallisation of hydrous magmas within the crust (Richards and Kerrich, 2007). In summary, there are likely to be a broad range of processes at work in continental arcs which generate intermediate

magmas. A regional study of the Colombian volcanic arc, which generates a range of compositions from basalts through to dacites, and has geochemically and isotopically distinct components such as exotic accreted terranes and unusual subducting sediment compositions, would be an excellent site to study and better constrain these processes.

1.1.1 The Colombian Volcanic Arc:

The Northern Volcanic Zone (NVZ) of the Andes, composed of Plio-Pleistocene (~3

Ma) to recent volcanic edifices, stretches across Colombia and Ecuador between ~5°N and 2°S (e.g.: Gómez et al. 2015; Bloch et al. 2017) and consists of over 125 volcanoes (Marín-Cerón et al. 2019). These are generated by subduction of segments of the Nazca plate with varying steepness of subduction as recorded by seismic tomography (Chiarabba et al. 2015) and shear wave anisotropy (Idarraga-Garcia et al. 2016). The structure of the overlying plate was early recognised as a major control on the position of volcanism (e.g.: Hall and Wood, 1985), resulting in three discrete arc segments concentrated along faults and separated by amagmatic regions. This has been refined by subsequent studies, which emphasise the role of crustal scale structures, and particularly palaeo-sutures as conduits for volcanism (e.g.: Cediel et al. 2003; Droux and Delaloye, 1996; Marín-Cerón et al. 2010; 2019) across three geographically divided Northern, Central and Southern segments of the NVZ (Stern, 2004) which are used within this study (Figure 1.2).

The northernmost of these is a ~140 km long province (Figure 1.2) which includes some of Colombia's most dangerous (and newly discovered) polygenetic volcanoes as well as three known fields of monogenetic volcanoes (Melson et al., 1990; Thouret et al., 1990; Toro Toro et al., 2008; Borrero et al., 2009; Laeger et al., 2013; Londoño, 2016; Monsalve et al., 2017a; Murcia et al., 2017; Pinzón et al., 2018; Osorio et al., 2018). This volcanically active area is sometimes referred to as the San Diego-Cerro Machin Volcano-Tectonic Province (SCVTP) (e.g.: Murcia et al. 2018) or alternatively, the Northern Volcanic Province (NVP) (Errazuriz-Henao et al. 2019). Herein, we use the second term.

The Central and Southern segments of the Colombian arc are more loosely defined in literature, and sometimes grouped together in regional studies as the "Southwestern" volcanic arc (i.e.: Marín-Cerón et al. 2010; 2019). As well as structural considerations (Hall and Wood, 1985), segregation on geochemical characteristics has been attempted. This is based on either assimilation and contamination of different basement lithologies (Droux and Delaloye, 1996) or due to arc front (Southern; Galeras and Azufral) and rear-arc (Central; Doña Juana and Puracé-Coconucos) position above the slab (Marín-Cerón et al. 2010). Overall, the Central and Southern segments defined in Figure 1.2 conform to these geochemical patterns, though the processes underlying these trends are still debated (Marín-Cerón et al. 2019). The northernmost of these "Southwestern" edifices, Nevado del Huila, is included in the NVP in some studies (c.f.: Marín-Cerón et al. 2019).

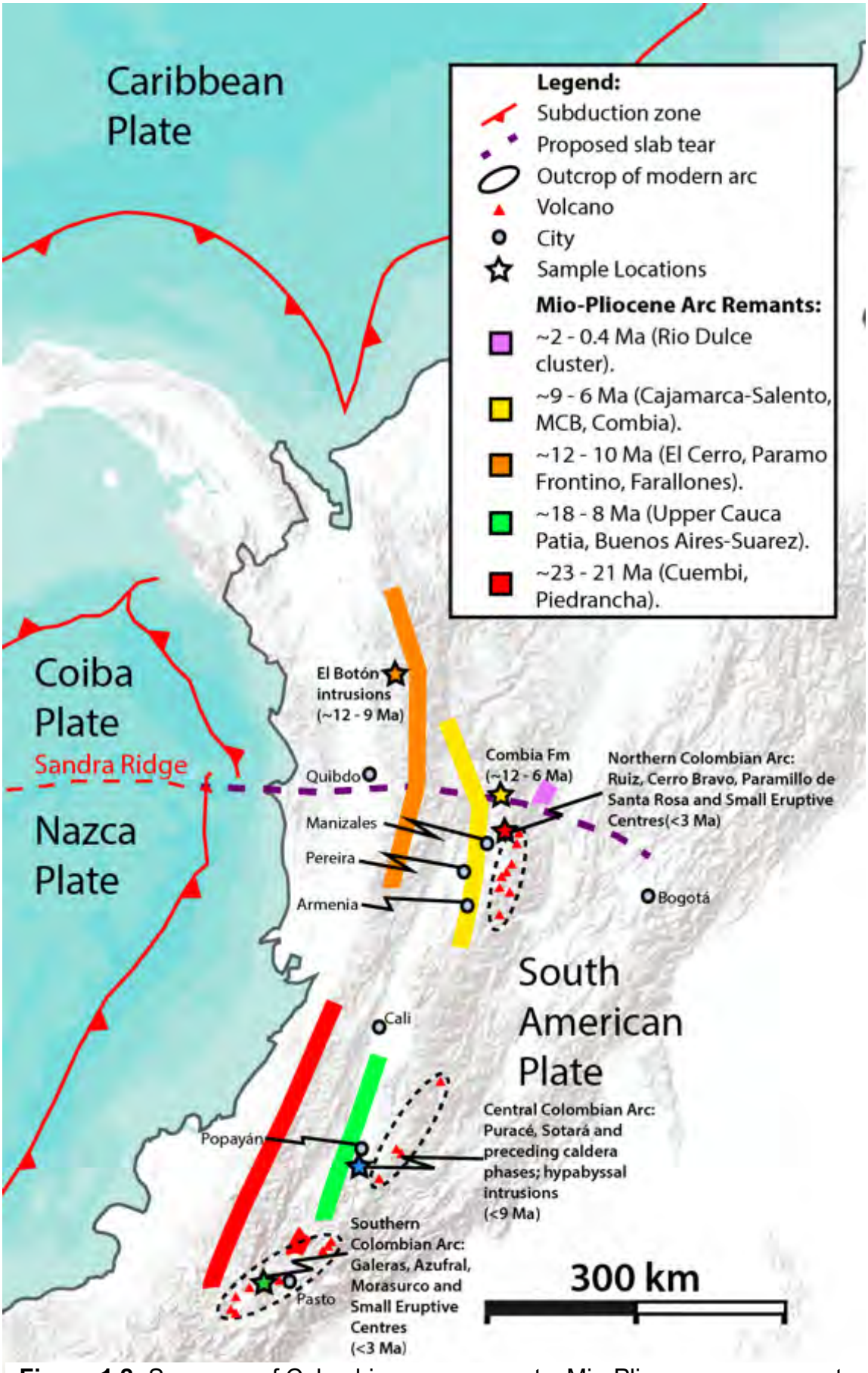

Figure 1.2: Summary of Colombian arc segments, Mio-Pliocene arc remnants and sample locations. Adapted after Laeger et al. (2013); Leal-Mejía et al. (2019).

Continental magmatism along the western margin of Colombia has persisted for hundreds of millions of years (e.g.: Leal-Mejía et al. 2019 and references therein). The most recent period of this arc magmatism began ~23 Ma at the end of the Oligocene (Leal-Mejía et al. 2019), and volcanic and plutonic remnants of this are preserved across Colombia (e.g.: Zapata and Rodriguez, 2011; Gil-Rodriguez, 2014; Mesa-García, 2015; Toro et al. 2016; Jaramillo et al. 2019). The distribution and chemistry of these remnants can offer clues to the development of subduction and magmatism since the Miocene (Wagner et al. 2017) leading into the development of the modern arc system.

Notable in the literature is the increasing reporting of adakite-like geochemical signatures in the modern arc (Toro et al. 2008; Borrero et al. 2009; Monsalve et al. 2009; Laeger et al. 2013; Martinez et al. 2014; Osorio et al. 2018) and the Miocene-Pliocene arc remnants (Gil-Rodriguez, 2014; Toro et al. 2016; Jaramillo et al. 2019). Key to this study will be identifying the processes which formed the intermediate magmas of the Colombian arc, including these unusual compositions, initially implied by Defant and Drummond (1990) to indicate deep melting of basalt, and whether the components present in the slab, in the overlying crust or within the mantle wedge played a prominent role in their formation (Castillo, 2012).

1.2 Overall Aims:

This thesis aims to characterise the products of Colombian volcanic arc on a regional scale, and identify the processes responsible for producing the arc and intermediate magmatism in this region in recent geological time. In particular, whether

components of the overlying crust or of the subducting slab had greatest influence across the region. This will be accomplished with a new dataset of major and trace elements and Sr, Nd and Hf isotopes representing an important contribution to research on the Colombian volcanic arc. This follows the recent publication of extensive mapping, petrological and geochemical analysis of the active volcanic complexes of the arc by the Colombian Geological Survey (e.g.: Pulgarín et al. 2010; Martinez et al. 2014; Monsalve et al. 2017b; Pardo et al. 2019) along with recent research on the geochemistry of the arc from the early Miocene (e.g.: Gil-Rodriguez, 2014; Jaramillo et al. 2019) to the most geologically recent and active edifices (e.g.: Marin-Ceron et al. 2010; Laeger et al. 2013; Monsalve et al. 2017a; Murcia et al. 2017; Botero et al. 2018b; Pinzon et al. 2018; Errazuriz-Henao et al. 2019).

Although the volume of high-quality geochemical data has improved, a detailed study of the Northern Volcanic Province (NVP) of the Colombian arc has been lacking (Errazuriz-Henao et al. 2019). Most studies to date have either focused on a single edifice or monogenetic field (e.g.: Toro et al. 2008; Pinzon et al. 2017; Osorio et al. 2018) or featured a comparison of two edifices (Errazuriz-Henao et al. 2019), or have attempted to extrapolate the petrogenesis of other parts of the Colombian arc northwards to the NVP (Marin-Ceron et al. 2019).

The work here therefore represents the first detailed study using high quality trace element and radiogenic isotopic analyses of multiple edifices within the NVP. This is combined with earlier datasets to construct a tectonomagmatic history for the province as a whole. This is used to test the numerous models proposed to explain the geochemistry of monogenetic fields and polygenetic edifices of the NVP, explain

compositional evolution through time and produce a general model of petrogenesis for the province (Chapter 5).

Additionally, further geochemical and isotopic data has been produced for Central and Southern segments of the Colombian arc. Previous studies of these segments have focused either on single edifices (e.g.: Calvache and Williams, 1997; Pulgarín et al. 2010; Duque-Trujillo et al. 2010) or on regional studies of several edifices of both Central and Southern segments (Droux and Delaloye, 1996; Marín-Cerón et al. 2010). The geochemical and radiogenic isotopic data presented in this study compares data for the Central and Southern segments as one group, as has been done in previous regional studies of the southwest Colombian arc (Chapter 6).

A small number of analyses from Miocene-Pliocene hypabyssal intrusions also form part of this study, related to precursors of the current arc. These are examined alongside larger scale geochemical studies of these arc remnants (e.g.: Zapata and Rodriguez, 2011; Rodriguez and Zapata, 2012; Gil-Rodriguez, 2014; Toro et al. 2012; Leal-Mejía et al. 2019) to discuss the development of the Colombian arc from the Miocene onwards (Chapter 6).

1.2.1 Specific objectives:

1) Undertake a regional field study of the Colombian arc to collect samples for analysis.
2) Obtain new major and trace element and radiogenic isotope analyses of multiple edifices across the Colombian arc.
3) Assess the existing published data and combine with the new data here in order to provide a detailed and unified model of the development and petrogenesis of the Northern Volcanic Province (NVP) province.
4) Utilise the model from (2) alongside data for edifices across the rest of the Colombian arc to better constrain the petrogenesis of the Colombian arc as a whole.
5) Construct a synthesis model (as far as possible) from the evolution of Colombian arc volcanism covering the Miocene, the inception of the current arc edifices to the modern active volcanic systems.
6) Compare the above findings with those of continental arc systems globally, and how findings in Colombia better constrain our understanding of intermediate magma petrogenesis in continental arcs.

2 Andesite Petrogenesis Models

2.1 Overview:

Subduction zones are sites of first order exchange between earth's surface and interior, through mass transfer of materials into the mantle through subduction, and resulting magmatism producing up to ~2.5 - 3.5 km^3/year of new arc crust (Clift et al., 2009). Subduction zone magmas across all convergent margins possess a common range of geochemical features distinct from other tectonic environments, including an enrichment in Large Ion Lithophile elements (LILE - e.g.: Cs, Rb, K, Ba, Pb, Sr) and mostly mantle like High Field Strength element (HFSE - e.g.: Ta, Nb, Zr, Ti) concentrations (e.g.: Hawkesworth et al. 1993; Elliott, 2003; Tatsumi and Kogiso, 2003; Spandler and Pirard, 2013; Turner and Langmuir, 2015 a,b). This reflects an overall enrichment in incompatible and volatile elements in the arc magmas (especially H_2O) across a range of silica contents (Ducea et al. 2015; Bebout, 2014; Turner and Langmuir, 2015b), which implys a unifying geological process across all subduction zones (Spandler and Pirard, 2013; Ducea et al. 2015). However, thin crusted, intra-oceanic arcs are dominated by high volumes of mafic outputs, whilst continental arc systems generate predominantly silicic igneous rocks (e.g.: Taira et al. 1998; Rudnick and Gao, 2003, 2014; Ducea et al. 2015). Understanding the relative enrichments of LILE and HFSE can shed light on the underlying processes in subduction zones, as well as the genesis of continental crust (e.g.: Gill, 1981; Thorpe, 1982).

Initial models of subduction zone volcanism posited a role for partial melting of the subducting slab (metamorphosed at sub-arc depths to eclogite) as the source of

evolved arc magmas (e.g.: Green and Ringwood, 1968). Due to compositional differences between experimental melts of subducting oceanic crust and the products of arcs, and the high temperatures needed to accomplish basalt melting (Peacock et al. 1996), this idea was quickly overturned in favour of dehydration of subduction components (e.g.: altered oceanic crust and overlying sediment) as they underwent metamorphic reactions descending into the mantle wedge (e.g.: Wyllie, 1973; Ringwood, 1974; Gill, 1981). This dehydration contributes fluids and soluble elements to the overlying mantle wedge, causing melting of the wedge peridotite whilst imparting a geochemical signature of the subducting components (e.g.: Coats, 1962; Kushiro, 1973; Ringwood, 1974; Perfit et al. 1980; Kay, 1980). Dehydration of the slab causing melting in the overlying mantle wedge remains the accepted general model underlying subduction zone magmatism (Figure 2.1), but the specific processes involved remain enigmatic.

The mostly intermediate composition of continental arcs creates a paradox - If the bulk of magmas at continental margins are derived from melting of mantle peridotite, producing melts dominantly basaltic in composition, then why are the majority of their products more evolved in composition? Clearly a further petrological process is required within the crust to produce intermediate and evolved magmas (e.g.: Rudnick, 1995; Petford and Atherton, 1996; Gomez-Tuena et al. 2014; Skora and Blundy, 2010; Tang et al. 2019). Variations in arc magma geochemistry could arise from a number of processes such as depth of melting within the wedge (Plank and Langmuir, 1988), the proportion and type of subduction inputs (e.g.: Stern, 1991; Plank and Langmuir, 1998; Goss and Kay, 2006) and inputs by mixing, assimilation, storage and homogenisation (MASH) processes (Hildreth and Moorbath, 1988) and

by mixing between pre-existing components in the crust with mantle derived melts (Lee et al. 2006; Annen et al. 2006).

Models of intermediate magma petrogenesis have developed around intermediate magmas forming through processes within the overlying plate and chemical distinctiveness gained there (Tang et al. 2019), as well as slab derived signatures Turner and Langmuir, 2015a,b). Although slab, mantle and overlying crust all play a role (Figure 2.1) there is some debate as to the predominant process in arcs (e.g.: Arturo-Gomez et al. 2014). Herein, we refer to this dichotomy as between “intra-crustal” and “extra-crustal” mechanisms.

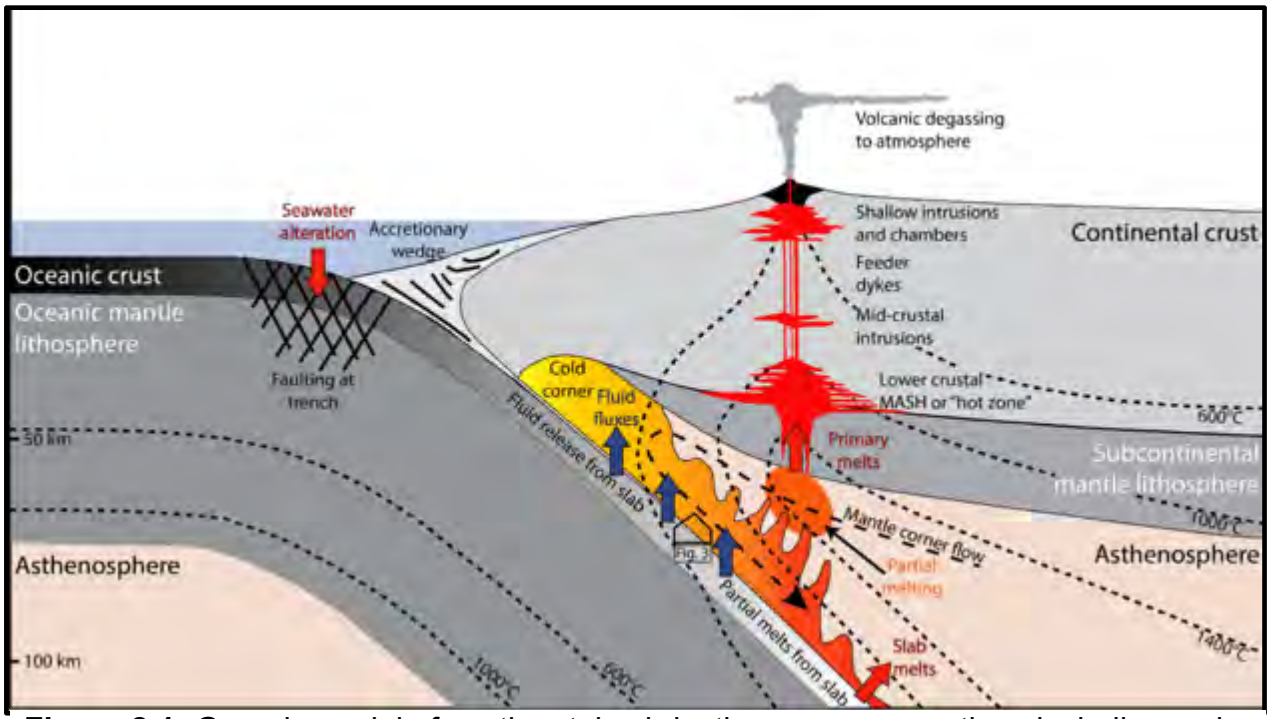

Figure 2.1: Generic model of continental subduction zone magmatism, including major melt areas and fluxes. Adapted after Zellmer et al. (2015) and Bebout (2014).

2.2 Current Models of Intermediate Magma Petrogenesis:

2.2.1 Intra-Crustal Processes:

The predominance of intermediate magmatism at thicker crusted continental arcs compared to thinner crusted intra-oceanic arcs has led many to point to an association between processes within the thick crust of the overlying plate and intermediate and silicic magmatism (e.g.: Eichelberger, 1978; DePaolo, 1981; Gill, 1981; Leeman, 1983; Hildreth and Moorbath, 1988; Feeley et al. 1993; Reubi and Blundy, 2009; Farner and Lee, 2017). This idea is supported by compilations of global arc geochemistry, which show good correlations with crustal thickness globally (i.e.: Turner and Langmuir, 2015a), leading to some geochemical parameters being used as proxies for crustal thickness (e.g.: Profeta et al. 2015; Chiaradia, 2015; Lieu and Stern, 2019).

Most models invoking a predominant role for the overlying crust involve an initial input of a basaltic melt from the mantle wedge into the lower crust, followed by differentiation within and/or assimilation of the crust of the overlying plate to produce more evolved compositions (e.g.: Gill, 1981; DePaola, 1981; Hildreth and Moorbath, 1988; Plank and Langmuir, 1988; Annen et al. 2006). The simplest process involved in these basalt input models is fractionation of primitive magmas within the crust or uppermost mantle (e.g.: Gill, 1981; Müntener et al. 2001; Grove et al. 2003). Such models of fractional crystallisation through a series of magma chambers have been applied to continental arc stratovolcanoes (e.g: Vatin-Perignon, 1990). However, most models assume at least some assimilation of crustal components alongside fractional crystallization, as assimilation of the diverse range of lithologies in the

continental crust would help explain the great compositional diversity observed in continental arc magmas (Spandler and Pirard, 2013; Ducea et al. 2015).

The idea of fractional crystallisation alongside contamination and assimilation of wallrock (DePaola, 1981) was developed into the MASH model of Hildreth and Moorbath (1988), which proposed that new magmas could be modified in the crust by intrusion and incomplete crystallisation of mantle derived basalt melts, which provide heat and volatiles necessary to melt and assimilate crustal materials (Annen and Sparks, 2001). This model is attractive in continental arc systems as the combination of assimilation and repeated flux of basalt from the mantle in a focused region would naturally lead to a diverse range of magma compositions. Such models have been especially influential in the Andes (i.e.: Hildreth and Moorbath, 1988; Feeley et al. 1993; Mamani et al. 2010), and in arcs with the thickest crust (up to 70 km) such as the Central Andes of Peru and northern Chile, which are likely geochemically and isotopically distinct from most other arcs due to efficient assimilation of crustal material at high depths and pressures (Turner and Langmuir, 2015a).

Assimilation of crustal materials, especially of mafic lower crust (e.g.: Atherton and Petford, 1993; Wolf and Wyllie, 1994; Rapp and Watson, 1995) can be explained by the widely accepted paradigm of “hot zones” in the lower arc crust (Annen et al. 2006). Similar to the influential MASH model, this proposes that mantle melts, ponding as sills at or near the mantle-crust boundary, begin to crystallise and fractionate under high pressure in the lower crust, whilst mixing with other melts in the lower crust (Figures 2.1 and 2.2). The melt then ascends upwards, leaving behind depleted mafic to ultramafic cumulates (e.g.: Ducea et al. 2015). The mantle

melts themselves promote this process through input of heat and volatiles. In this way, the isotopic and trace element diversity within arc magmas will be strongly influenced by the lower crust (Hildreth and Moorbath, 1988; Annen et al. 2006).

Assimilation of mid- and upper-crustal components, such as the pre-existing framework of metamorphic or sedimentary rocks as well as previous intrusions, could also provide an important reservoir of enriched incompatible element and isotopic compositions for arc magmas (Ducea et al. 2015). Assimilation processes could be less efficient at shallow depths due to the cooler temperatures of the lithosphere and more silicic, volatile poor melts produced after crystal fractionation. Shallow assimilation may be further hindered by lack of consistent input of heat and volatiles from mantle melts as compared the lower crust (e.g: Dufek and Bergantz, 2005; Jagoutz and Schmidt, 2013). However, this could be compensated for by the composition of the country rock, especially if it is hydrous or contains hydrous phases. Furthermore, such components could also be delivered to the lower crustal depths by crustal thickening when the arc is under compression (Ducea, 2001).

Repeated flux melting of basalts from the mantle beneath the arc front could form a mafic underplate beneath continental arc systems within which magma chambers could be hosted and maintained over long periods of time (e.g.: Schmitz, 1994; Petford and Atherton, 1996). Thickening of arc crust in this manner requires long lived arc volcanism in a relatively restricted area. As most arcs occur as narrow (25 - 150 km), arc parallel features at ~100 - 125 km above the subducting slab (Tatsumi and Eggins, 1995; Stern, 2002; Grove et al. 2012) a long lived subduction zone and associated magmatic system such as that observed along the western margin of

South America (e.g.: Grunder and Klemetti, 2008) would see a significant flux of basalt through its plumbing systems. However, extensive thickening of arc crust, or shallow dipping of the slab beneath thick arcs, can limit convection through the mantle wedge and lead to migration or cessation of the arc front (Ducea et al. 2015; Wagner et al. 2017).

The primary sources of data on these arc roots come from exposed sections through exhumed arcs (e.g.: De Paoli et al. 2009; Hacker et al. 2011; Jagoutz and Behn, 2013) and xenoliths from the mantle and lower crust (e.g.: Ducea and Saleeby, 1998; Rodriguez-Vargas et al. 2005). Lower crustal xenoliths are typically cumulates of moderate to high-Mg# garnet pyroxenites, amphibolites, granulites and gabbros (Müntener et al. 2001; Rodriguez-Vargas et al. 2005; Lee et al. 2006; Jagoutz, 2014), reflective of the predominance of clinopyroxene with variable amphibole and garnet in the lower crust (Smith, 2014; Ducea et al. 2015). The garnet and clinopyroxene bearing components of these arc roots are on average denser than average mantle peridotite (Hacker et al. 2003). Mantle xenoliths are typically garnet clinopyroxene, websterite and garnet peridotite (e.g.: Weber et al. 2002; Saleeby et al. 2003).

These arc roots could be the primary location for the formation of intermediate and evolved magmas, especially those with a geochemical signature (e.g.: high Sr/Y, La/Yb and Dy/Yb) indicating derivation from a residue containing garnet and/or amphibole (Macpherson et al. 2006; Davidson et al. 2007) in the deep crust of continental arcs. This signature is due to retention of HREE elements within garnet and amphibole. This would leave behind dense residues of mafic cumulates at the base of the crust (e.g.: Lee et al. 2006; Clarke et al. 2013; Tang et al. 2019). These

cumulate residues are either unrecorded in the lower crust/upper mantle (e.g.: Takahashi et al. 2007; Pirard et al. 2013), or due to their high density and inherent instability after significant melt extraction, they periodically delaminate from the base of the crust and founder into the mantle (e.g.: Kay and Kay, 1993; Saleeby et al. 2003; Zandt et al. 2004; Kelemen et al. 2014; Bloch et al. 2017). This could occur as large-scale drip events (Kay and Kay, 1993) or as drop off and entrainment of smaller scale pieces of lower crustal residue in the mantle (e.g.: Currie et al. 2015; Bloch et al. 2017). There is some geophysical (e.g.: Zandt et al. 2004; Jones et al. 2014) and geochemical (Bloch et al. 2017) evidence of such bodies descending into the mantle wedge and being convectively removed by corner flow (Ducea and Saleeby, 1998), which would prevent blockage of convective flow in the mantle wedge in long lived, thickened arcs where this process is hypothesised (DeCelles et al. 2009; Ducea et al.2015). This process provides us a viable mechanism by which continental arcs could achieve their intermediate to silicic compositions.

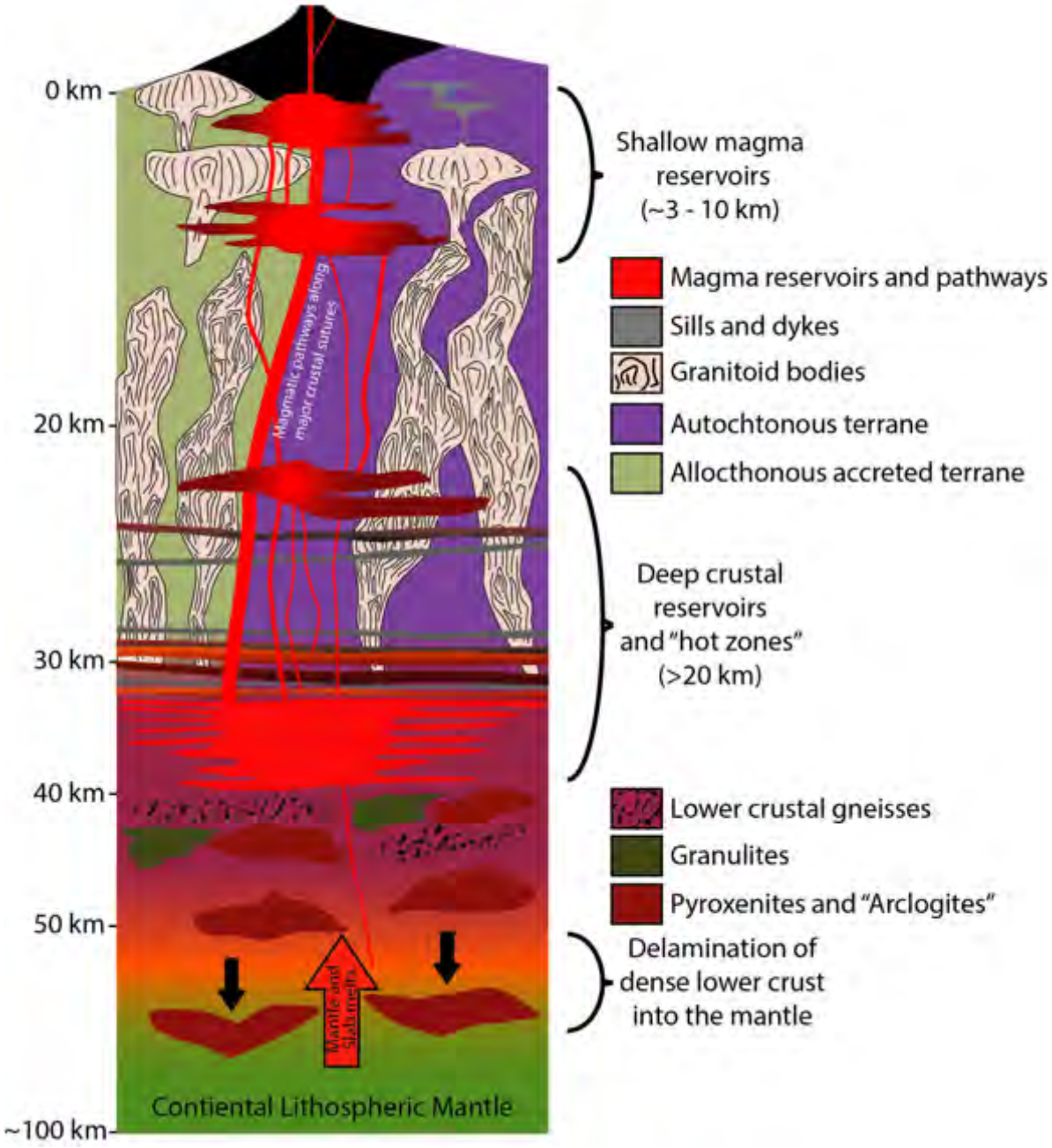

Figure 2.2: Synoptic vertical cross-section through a continental arc built along moderately thick crust with magmatism focused along a crustal suture both features common to the northern Andes. Adapted after Annen et al. (2006); Ducea et al. (2015); Blanco et al. (2017); Murcia et al. (2017) and Bloch et al. (2017).

2.2.2 Extra-Crustal Processes:

It has long been recognised that the geochemistry of arc magmas is strongly influenced by slab components in the form of subducting oceanic lithosphere and sediments (Plank and Langmuir, 1993; Spandler and Pirard, 2013; Bebout, 2014). Along with intra-crustal processes, the geochemical variation in continental arc rocks could be caused by differences in type and volume of subduction components or eroded of fore-arc crust (e.g.: Plank and Langmuir, 1993; Goss and Kay, 2006; Turner and Langmuir, 2015b). Oceanic lithosphere will experience hydrothermal alteration by seawater prior to subduction, altering some of its trace element and isotopic characteristics (Elliott, 2003), producing an altered oceanic crust (AOC). Overlying this are subducting sediments, which can vary in composition between arcs (e.g.: Errazuriz-Henao et al. 2019). If the margin is erosive, crust abraded from the upper plate may be entrained and subducted with the slab (e.g.: Goss and Kay, 2006; Tonarini et al. 2011).

Metasomatism of the mantle wedge, whereby chemical components are leached from or imparted to the mantle wedge by a fluid, is central to the genesis of arc magmas in subduction zones (e.g.: Gill, 1981). This transfer is classically thought to occur through breakdown of hydrous minerals and release of aqueous fluids as the slab descends. The relatively consistent heights of volcanic fronts above the Wadati-Benioff zone (~90 - 160 km) has been seen as indicative that these dehydration reactions are more pressure than temperature dependent (e.g.: Tatsumi, 1989; Tatsumi and Eggins, 1995).

Experimental studies show that dehydration of the slab occurs as continuous metamorphic reactions as the slab descends and dehydrates, continuously expelling aqueous fluids (Schmidt and Poli, 1998; Kerrick and Connolly, 2001). Early release of fluids into the fore-arc of the mantle wedge will hydrate the peridotite, forming serpentinite or amphibole peridotite (Tatsumi and Eggins, 1995) The hydrous serpentinite and amphibole will be dragged deeper into the mantle wedge (>100 km) by convective corner flow, dehydrating and adding to the volatile flux to the wedge (Tatsumi, 1986; Schmidt and Poli, 1998; Rüpke et al. 2004). The breakdown of pargasite and phlogopite occurs in sequence (e.g.: phlogopite at greater depths than pargasite). This is important as thermal modelling of hydrous mineral stabilities (Hacker, 2008; van Keken et al. 2011) indicates that, in most arc systems, relatively little water is released from the AOC and sediment components directly beneath the volcanic front (~90 - 160 km). Therefore, the majority of water involved in fluxing the mantle derives from breakdown of minerals such as antigorite and chlorite in serpentinites down-dragged to sub-arc depths (~90 - 160 km) from the fore-arc mantle wedge (Ulmer and Trommsdorff, 1995; Fumagalli and Poli, 2005). At deeper levels, more water is released from phases such as phengite in K-rich sediments and metabasalts or lawsonite in the subducting oceanic crust of cold slabs to depths >150 km (Schmidt and Poli, 1998; Hermann et al., 2006; Hacker, 2008).

Partial melts of subducted components, primarily sediments may play a small (Elliott et al. 1997) or large role (e.g.: Gertisser and Keller, 2003) in the production of arc magmas. Partial melting of igneous components of the slab is seen as relatively rare (e.g.: Defant and Drummond, 1990; Peacock et al., 1994). Conversely, experimental studies demonstrate lower melting temperatures of pelagic sediments, especially in

hydrous conditions. Such sediment melt, along with fluids derived from AOC, could effectively account for some isotopic and trace element characteristics of arc magmas (Elliott, 2003).

There are however debates as to whether the signature derived from subducting sediments and imparted to arc magmas is derived from aqueous fluids or melts (e.g.: Stolper and Newman, 1994; Johnson and Plank, 1999) and such a dichotomy between melts of subducted components may also be misplaced, and “supercritical” fluids could mimic compositions attributed to both melts and aqueous fluids at a wider array of temperatures and pressures up to ~160 km (Kessel et al., 2005; Hermann et al., 2006).

A simplistic model of the interface (Figure 3a) imagines the preservation of distinct lithological domains of AOC, sediments and mantle wedge, with fluid pathways from slab components out into the mantle wedge (Bebout et al. 2007; Bebout, 2014). The way in which slab fluids and melts travel through the mantle wedge is key here. We can think of the interactions between fluids and/or melts and the mantle wedge as a ratio between fluid or melt and peridotite, in order to assess the relative proportions of each involved. A low ratio of fluids/melt to rock would mean that fluids or melts had interacted with large areas of the mantle. This could be achieved by melts or fluids percolating through the mantle wedge porously, interacting on a grain scale; or by being channeled through narrow pathways such as veins through the mantle (e.g.: Spandler and Hermann, 2006). A high melt/fluid:rock ratio would imply interaction of fluids or melts with only a small areas of the mantle, which could be due to high flow rates of fluids/melts limiting time to interact with peridotite, or by armouring of the

edges of conduits for flow (such as veins) by previous flow or melt events, restricting interaction of new fluid or melt with peridotite (Spandler and Pirard, 2013).

Alternatively, flow of fluids and melts upwards through the wedge could be restricted to discreet pathways, such as a network of veins. Evidence for this has been observed in mantle xenoliths (Arai et al. 2003; Kepezhinskas et al. 1995) and some ophiolite exposures (e.g.: Berly et al. 2006). This channeled flow (such as through veins) has modelled timescales faster than porous infiltration, and is consistent with the rapid transfer of material from slab to crust, but fluids and melts coming off the slab would largely avoid interaction with hydrous mineral phases such as phlogopite or pargasite in the mantle wedge (Spandler and Pirard, 2013). This more limited interaction with mantle materials proposed by channelled flow models would make sense for high-silica compositions thought to be derived from direct melting of subducting slab eclogite with little geochemical evidence for mantle wedge interaction (Martin et al. 2005; Moyen, 2009). There is no consensus as to whether porous or channelled flow prevails, though a number of these mechanisms likely operate at different times or contemporaneously within subduction zones (Manning, 2004).

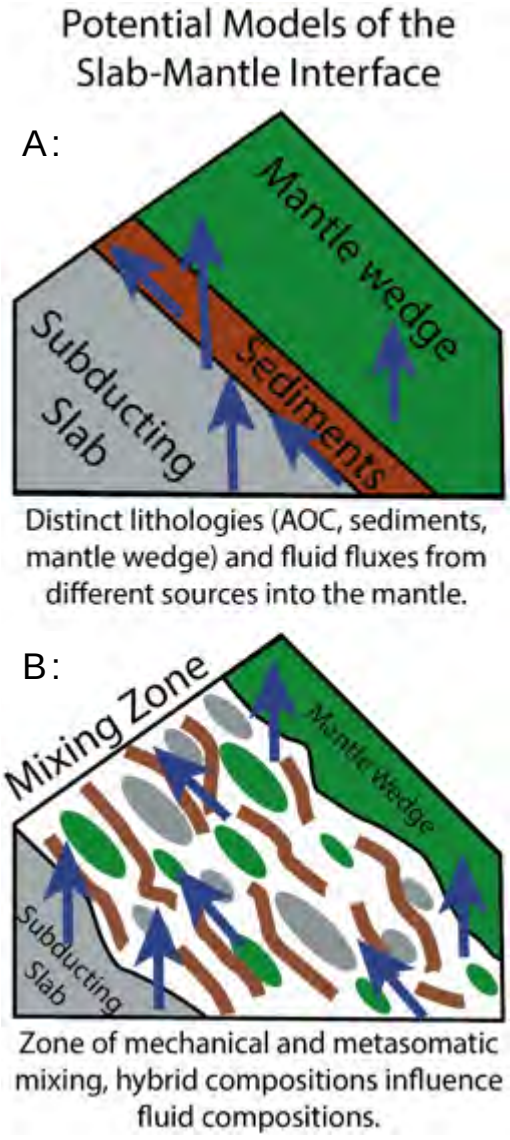

Figure 2.3: Proposed models of the slab-mantle interface. Adapted after Bebout (2014).

Whilst the interior of the slab remains cold, the top of the slab is rapidly heated as it descends into the mantle (Syracuse and Abers, 2006; Syracuse et al. 2010). This could facilitate mixing in a “subduction channel” (Figure 3b) of slab lithologies and hydrated mantle wedge (e.g.: Gerya et al. 2002), as evidenced by exposures of slab-mantle interfaces (e.g.: Mori et al. 2014). Mixing of slab metasediments, AOC and mantle materials in such a mélange environment could also account for silicic enrichments in arc magmas (e.g.: Castro et al. 2010).

Movement of slab components through the mantle wedge has also been hypothesised as a mechanical mixture of slab and mantle wedge components can extrude and rise into the overlying mantle wedge beneath the volcanic arc in the form of slab diapirs (e.g: Behn et al., 2011; Gerya and Yuen, 2003; Hacker et al. 2011; Marschall and Schumacher, 2012). This rising mélange diapir material can either undergo fluid-present partial melting within the mantle wedge after detaching from the slab, driven by the heat of the surrounding mantle wedge and/or influx of slab derived fluids (Marshall and Schumacher, 2012) or relaminate to the base of the arc crust (Hacker et al. 2011). Partial melting of these diapirs in the relatively high temperature core of the mantle wedge has been proposed as a possible source for intermediate arc magmas (Gerya & Yuan, 2003; Behn et al. 2011; Errazuriz-Henao et al. 2019). However, such a process is more likely to form melts with S-type granite compositions rather than the intermediate magmas erupted at most volcanic arcs. Additionally, incorporation of the altered oceanic crust component would also be difficult in such a model (Elliott, 2003; Spandler and Pirard 2013), and upwelling of slab diapirs of metasediments would also be orders of magnitude slower in their passage through the mantle than slab derived aqueous fluids (Behn et al. 2011; Hack and Thompson, 2011). Upwelling sedimentary diapirs are also likely to interact with aqueous fluids rising separately from the slab, as well as hydrous melts of wedge peridotite (Spandler and Pirard, 2013) which could partially melt these diapirs or more simply transfer their sediment and mélange signature to these rapidly rising slab fluids.

2.3 Adakites and High-Mg# andesites:

Some of the main problems with differentiating intra- and extra-crustal petrogenesis models are highlighted by the study of intermediate arc rocks known as adakites. The term “adakite" was first coined by Defant and Drummond (1990), after previously described magnesian andesites from Adak Island in the western Aleutian arc with distinct geochemical characteristics (e.g.: 56–59 wt.% SiO2; 5 wt.% MgO; Ni =150 ppm; high Sr contents and La/Yb ratios compared to other arc lavas (Castillo, 2012; Kay, 1978)). The original definition denotes adakites as volcanic rocks and their intrusive equivalents (e.g.: tonalites and granodiorites) with this particular geochemical signature (Defant and Drummond, 1990; Defant et al., 1992). These geochemical characteristics are also similar to those of high-Mg# andesites (whole rock Mg# >50 - Kelemen et al. 2014). However, as no specific Mg# for adakite has been defined, and many high-Mg# andesites are reported with Sr/Y <50 and La/Yb <9 (Kelemen et al. 2014), these are not synonymous groups, though high-Mg# andesites may be parental to adakites (e.g.: Yogodzinski and Kelemen, 1998).

“Crucially however, the term adakite was given a genetic definition as well as a geochemical/petrological one, with Defant and Drummond (1990) concluding that the most likely source of adakites is by partial melting of the young (<25 Ma) altered oceanic crust of the subducting slab. However, a major trend in the adakite literature has been away from the age of the subducting slab (<25 Ma) as a key prerequisite for adakite formation (Castillo, 2012) and towards alternative explanations. These allow for old (>25 Ma), cold slab/oceanic lithosphere to be abnormally heated and include highly oblique subduction, shallow subduction (Bourdon et al., 2003), opening

of slab windows (Yogodzinski et al., 2001) and ridge subduction (Martin et al., 2014). Though slab melts can certainly form adakites, not all adakites are slab melts (Castillo, 2012). This has further been elucidated on with the proposal of fractional crystallisation origins for adakites, which could occur by fractionation of basaltic mantle derived magmas at high pressures within the stability field of garnet (Macpherson et al. 2006). Additional evidence shows that many of the commonly applied adakite parameters (e.g: La/Yb and Sr/Y ratios) can be successfully reproduced by crystal fractionation of mantle derived magmas within the crust as well as interaction with that crust during their ascent to the surface (Richards and Kerrich, 2007; Moyen, 2009).

Though adakite, along with synonymous terms such as “adakitic” and “adaktite-like”, has been used freely in the Colombian arc literature (and will be used in this context), the use of the term adakite is restricted herein, to stop confusion about petrogenetic interpretations arising from petrological names used (c.f.: Castillo, 2012; Kelemen et al. 2014). Here, adakite is simply thought of as part of a spectrum of lavas produced by arcs, alongside terms such as high-Mg# andesites. However, the presence of these rock types in the Colombian arc, and in arcs globally, could point to a more common role for melts in the slab and/or lower sections of continental arcs as means for delivering compositional diversity (Castillo, 2012).

2.4 Synthesis:

This study offers the opportunity to use new geochemical and isotopic data for the Colombian arc within the framework of modern subduction zone models (i.e: Annen

et al. 2006; Spandler and Pirard, 2013; Turner and Langmuir, 2015a,b). This is critical to help resolve competing ideas proposed for the Colombian arc based on more localised datasets, invoking intra-crustal models such as mixing and assimilation within the continental crust (e.g.: Laeger et al. 2013; Gil-Rodriguez, 2014), or by slab fusion (Monsalve et al. 2009; Errazuriz-Henao et al. 2019) or depth of melting within the mantle wedge (Marín-Cerón et al. 2010), or a composite of these models (e.g.: Marín-Cerón et al. 2019).

3 Geological History of the Northern Andes of Colombia

3.1 Introduction:

The history of the Northern Andes is one of terrane accretion paired with magmatism. The Northern Andes in Colombia are physiographically divided into three mountain ranges: The Western, Central and Eastern Cordilleras, separated by the Cauca and Magdalena river valleys (Figure 3.1) (e.g.: Villágomez et al. 2011; Boschman et al. 2014; Weber et al. 2015; Naranjo et al. 2018). Each of the Cordilleras is made up of terranes with a distinct geological make-up, recording a continual cycle of terrane collision and accretion in the Northern Andes (e.g.: Ramos, 2009). Both the autochthonous and allochthonous terranes of Colombia have been classified by a variety of names in the literature (e.g.: Cediel et al. 2003; Ramos, 2009; Restrepo et al. 2011; Villagómez et al. 2011), but for simplicity in this chapter the classifications of Cediel et al. (2003; 2018) and Leal-Mejía et al. (2018) are used. This is partly because of the temporal divide between these terranes, with older terranes related to pre-Northern Andean Orogeny events (largely autochthonous, continental terranes), and those accreted terranes of Aptian age and younger related to the Northern Andean Orogeny, which lasted from the late Cretaceous to the Palaeogene with magmatism and exhumation recorded into the Neogene (Cediel, 2011; Cediel et al. 2018; Leal-Mejia et al. 2018). Additionally, the Northern Andes of Colombia have hosted four temporally and spatially distinct periods of magmatism during the Phanerozoic (Leal-Mejía et al. 2018): Palaeozoic to mid-Triassic; latest Triassic to Jurassic; Cretaceous to Eocene and latest Oligocene to Plio-Pleistocene (Cediel,

2018; Leal-Mejía et al. 2018). This final Neogene phase of volcanism leads into the modern, Plio-Pleistocene volcanic arc of Colombia (e.g.: Leal-Mejía et al. 2018; Marin-Cerón et al. 2018) but is treated separate from the modern arc volcanism in regional studies. The record of magmatism from the Cretaceous onwards is an expression of the Northern Andean Orogeny (Cediel et al. 2003; Cediel et al. 2018) and therefore critical to understanding the geotectonic evolution of the Northern Andes in the Cenozoic.

Figure 3.1: Location of major physiographic features of Colombia, including cordilleras and and massifs and the separating intermontane valleys. The volcanic is concentrated along the Central Cordillera. The Cauca-Patia valley also represents a major crustal boundary. The Northern Andes are the site of collision between the Caribbean, Pacific and South American plates, as well as deatached blocks (Panama and Coiba), creating a complex tectonic interaction in the region.

3.2 Terranes and Magmatic Events of the Northern Andes:

3.2.1 Continental Terranes and Intrusions:

East of the Cordilleran ranges, the inland basins of Colombia are dominated by rocks of the Precambrian Guiana Shield (Figure 3.2), part of the cratonic interior of NW South America. The deformed and metamorphosed character of the Shield today is due largely to continental collision during the Grenville orogeny (~1.3 - 0.9 Ga) and assembly of Rodinia (e.g.: Fuck et al. 2008; Kroonenberg, 2019). This was the first of many accretion events in which the Guiana Shield has acted as a backstop to accretion along the margin of NW South America (e.g.: Cediel et al. 2003; Cediel, 2019). Formation and accretion of an arc along the margin is recorded in the Garzon Massif (Jimenez-Mejia et al. 2006), with a calk-alkaline arc developing ~1.2 - 1.1 Ga (Kroonenberg, 2019), followed by accretion to the Guiana Shield and granulite facies metamorphism during The Grenville orogeny ~1 Ga (Restrepo-Pace et al. 1997; Cediel, 2019; Figure 3.8). Further north and west, in the Central Tectonic Realm (CTR), the Chicamocha terrane (Figure 3.3) records Mesoproterozoic (~1.54 - 1.50 Ga) formation of within-plate granitoids and oceanic island arc rocks (Cuadros et al. 2014), with accretion to Guiana Shield also taking place during the Grenville orogeny ~1 Ga (Restrepo-Pace and Cediel, 2010; Cediel, 2019).

Northeastern Colombia to the boundary with the Caribbean plate is dominated by the Maracaibo Subplate (MSP), a wedge-shaped segment of the Guiana Shield overlain by later Palaeozoic sequences and including Triassic-Jurassic ensialic extensional basins, and holocrystalline granitoids of early Palaeozoic to latest Triassic-Jurassic age (Cediel, 2019; Leal-Mejia et al. 2019). The MSP began migrating northwards

along bounding fault systems in the Late Cretaceous, causing significant deformation and physiographic uplift as it interacted with the Caribbean plate (Cediel, 2019). Short-lived (<10 Ma) and punctuated magmatism of adakitic character is recorded in the early Cenozoic by the Santa Marta batholith (Figure 3.4) and related granitoids (e.g.: Cardona et al. 2014; Duque-Trujillo et al. 2018). This is likely related to the forced underthrusting and subduction of the Caribbean plate beneath the MSP as it migrated northwards (Duque-Trujillo et al. 2018).

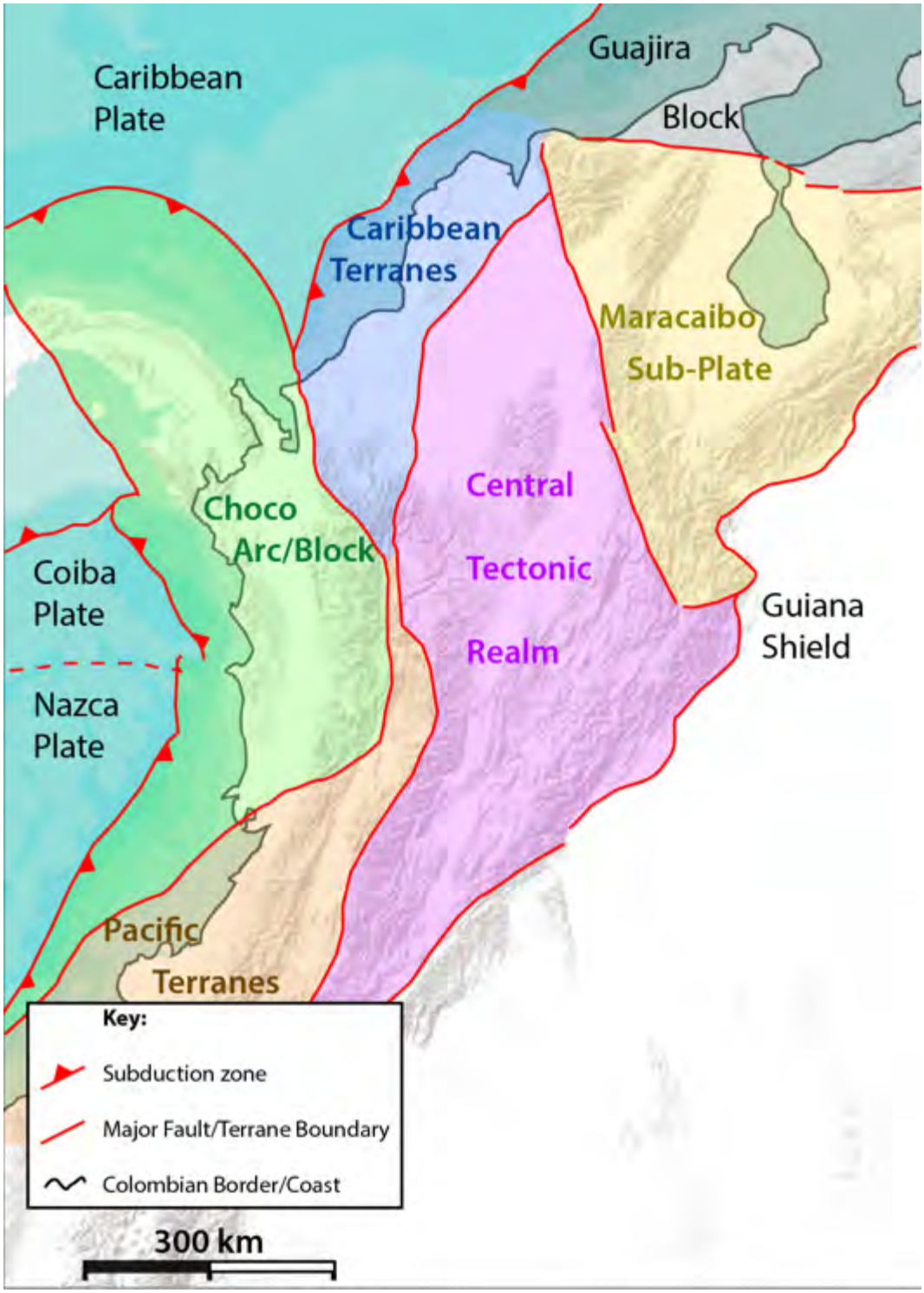

Figure 3.2: Major Terrane Assemblages of the northwestern South America. Adapted after Cediel et al. (2003); Cediel (2019) and Leal-Mejía et al. (2019).

The terranes of the Central Tectonic Realm (CTR) accreted to the Guiana Shield form much of the underlying basement of the Central Cordillera (Gomez et al. 2017). West of the Chicamocha terrane lies the Neoproterozoic to early Palaeozoic (Cediel and Cáceres, 2000; Spikings et al. 2015) Valdivia-Cajamarca Terrane (CA-VA) (Figure 3.3). This is composed of amphibolitic, graphitic and semi-pelitic schists and marbles metamorphosed to greenschist through to epidote amphibolite facies (e.g.: Cediel and Cáceres, 2000; Cediel et al. 2003; Cediel, 2011). Geochemical and geological characteristics suggest the CA-VA represents peri-cratonic island arc and accretionary prism accreted along the western edge of the Chicamocha Terrane during the Ordovician (Restrepo-Pace, 1992; (Cediel et al. 2003; Gomez et al. 2015; Cediel, 2018; Leal-Mejía et al. 2018). The suture between the CA-VA and the Chicamocha Terrane is the Palestina fault, which has since been reactivated by the later Northern Andean Orogeny and provides a vector for magmatism in the modern volcanic arc (Cediel and Cáceres, 2000). Despite their accreted origin, the terranes of the CTR are considered autochthonous parts of the Northern Andes of Colombia due to later accretion events to the west, recorded by the terranes of the Western Tectonic Realm (WTR).

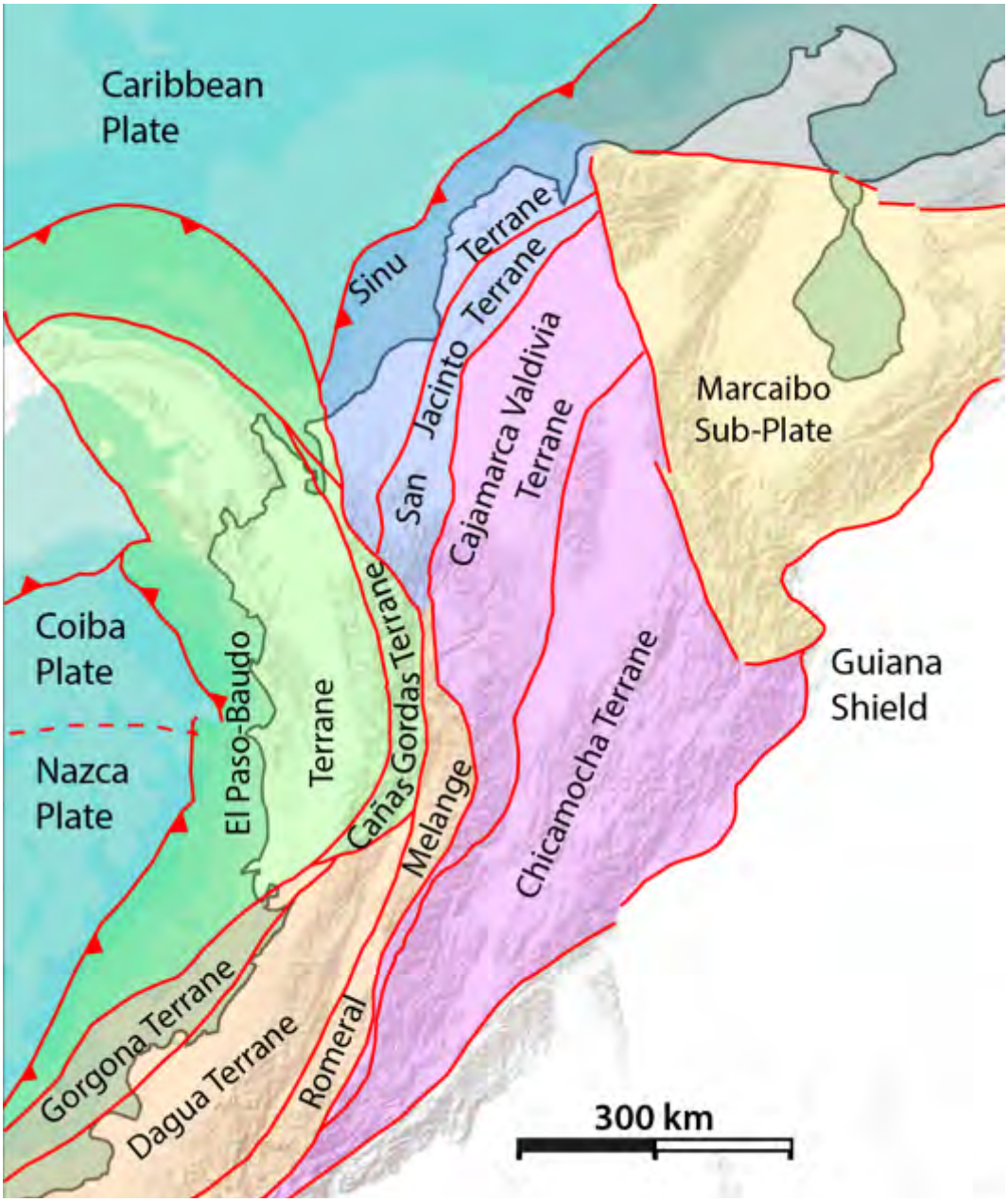

Figure 3.3: Terranes of northwestern South America. Adapted after Leal-Mejía et al. (2019).

Superimposed upon the terranes of the CTR are a succession of magmatic arc segments of Jurassic to Pleistocene age (Figure 3.4), and the Plio-Pleisticene to recent volcanic arc (Leal-Mejía et al. 2019; Marín-Cerón et al. 2019). Tectonic reconstructions for NW South America suggest initiation of an E- to NE-facing, dextral-oblique subduction zone beneath the western margin of Colombia, initiating ~100 Ma, related to subduction of proto-Caribbean crust beneath South America

(e.g.: Cediel et al. 2003; Kennan and Pindell, 2009; Wright and Wyld, 2011; Spikings et al. 2015; Weber et al. 2015) or alternatively a west-facing Farallon subduction system which reversed polarity later due to collision of the Caribbean Oceanic Plateau (Neill et al. 2013). This subduction zone generated the metaluminous, calc-alkaline continental arc granitoids of the Antioquian Batholith and satellite plutons, beginning ~96 Ma, which intrude the Cajamarca-Valdivia Terrane. The Antioquian Batholith and its satellite plutons are notable for their high volume but limited extent (Figure 3.4), which has been attributed to a dextral, transpressive regime of emplacement (Aspen et al. 1987; Pindell and Kennan, 2001; Cediel et al. 2003) as opposed to the orthogonal subduction generating the more Cretaceous arcs (Figure 3.4) in other parts of the Andes (Leal-Mejía et al. 2018). Granitoid magmatism in the Antioquian Batholith ceases at ~72 Ma, followed by a 10 Ma hiatus before granitoid magmatism resumes in the CTR, after ~10 Ma of magmatic hiatus. This next phase of continental arc magmatism is recorded by ~62 - 52 Ma granitoids including the Providencia, Sonsón, Manizales, El Hastillo, El Bosque and in the Central Cordillera (Figure 3.4). These plutons represent a limited volume of magmatism following the initial collision of Farallon and/or Caribbean-Colombian Oceanic Plateau (CCOP)/Caribbean Large Igneous Province (CLIP) lithosphere along the Colombian margin (Figure 3.8). These plutons are post-collisional granitoids, hypothesised to have formed after cessation of subduction by delamination of the lower crust, upwelling asthenosphere and resultant anatexis of the crust (Leal-Mejía et al. 2018), with U-Pb zircon ages that illustrate a progressive southward migration of the arc axis from the Providencia suite into the Central Cordillera south of the Antioquian Batholith (Leal-Mejía et al. 2018). Geochemical and isotopic results distinguish these granitoids from other groups in Colombia, especially in terms of their Sr, Nd and Hf

isotopes which indicate crustal contamination and/or anatexis. Hf isotope data for the El Hastillo stock and El Bosque batholith (Bustamante et al. 2017) suggest a moderate degree of crustal contamination, and the El Bosque batholith itself contains inherited Permian-aged zircons which gives direct evidence of contamination by the Cajamarca-Valvidia Terrane in the generation of this granitoid (Bustamante et al. 2017; Leal-Mejía et al. 2018). Additionally, the “adakite-like” character of the ~62 Ma Providencia suite has been noted (Leal-Mejía, 2011; Bustamante et al. 2017) and contrasted to the medium Sr/Y vs. Y ratios observed in the El Hastillo Stock, Sonsón and El Bosque Batholiths (Leal-Mejía, 2011; Bustamante et al. 2017; Leal-Mejía et al. 2018). The petrogenesis of these adakitic signatures has been ascribed to magmatic differentiation at the base of a thick lower crust of convergent or subducting CCOP/CLIP lithosphere, with an increasing degree of crustal contamination as magmatism progresses southwards (Leal-Mejía et al. 2018). However, similar geochemical and isotopic trends could be the result of delamination of subducted oceanic lithosphere and asthenospheric upwelling following terrane collision (Leal-Mejía, 2011). This Paleocene-Eocene magmatism lasted only for ~10 Ma, shutting down ~52 Ma, likely caused by collision and accretion of the buoyant oceanic crust along the Pacific margin of Colombia (Cediel et al. 2003; Kerr and Tarney, 2005).

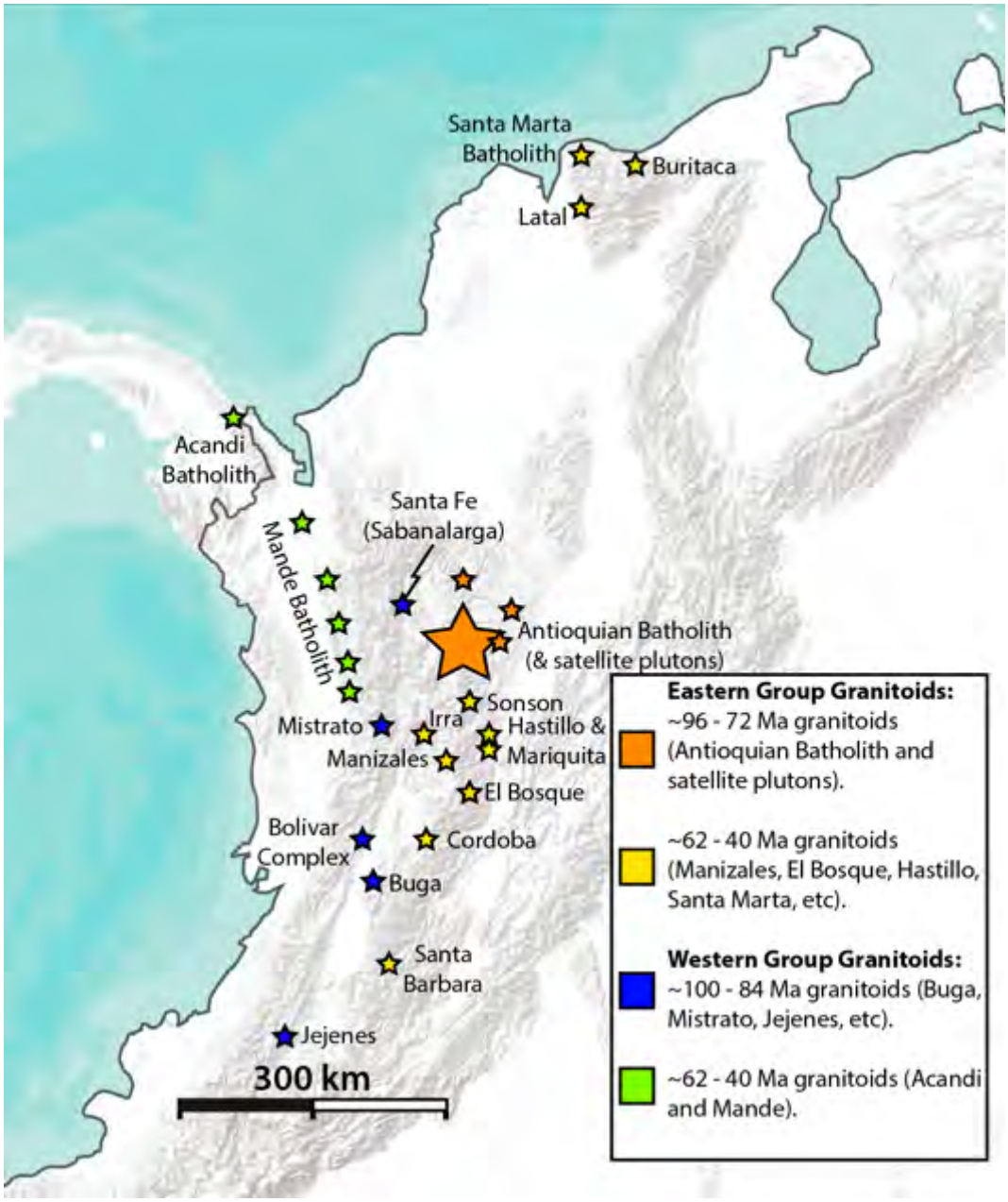

Figure 3.4: Major Late Cretaceous to Oligocene granitoid bodies of Colombia. Eastern groups are those emplaced in the Central Tectonic Realm and other autochtnous terranes. Western group granitoids are emplaced in Western Tectonic Realm terranes. The ~97 – 72 Ma granitoids are dominated by the Antioquian batholith (large orange star), a very large, multi-stage, late Cretaceous batholith. Adapted after Leal-Mejía et al. (2019).

3.2.2 Oceanic Terranes and Intrusions:

The oceanic (and largely allochthonous) crust of the Western Tectonic Realm (WTR) is composed of three main terrane assemblages; the Pacific and Caribbean terrane assemblages and the Chocó Block/Arc (Figure 3.2). The northernmost of these is the Caribbean Terrane Assemblage (CAT), composed of the San Jacinto and Sinú terranes. The basement of both terranes comprises mafic and ultramafic oceanic rocks, which could be a fragment of the Caribbean-Colombian Oceanic Plateau (CCOP)/Caribbean Large Igneous Province (CLIP) (i.e.: Kerr et al. 1997; Sinton et al. 1998); N-MORB tholeiitic basalts and fragments of a Coniacian to Campanian (~86.3 - 72.1 Ma) age island arc (Cansona and Finca Veija Formations) with interspersed with sediments (Cediel, 2019; Leal-Mejía et al. 2019). Palaeomagnetic data suggests an allochthonous Pacific origin for these volcanic sequences, south and west of their current position (Cediel, 2019). These volcanics are unconformably overlain by a thick sequence of marine and terrestrial sediments Palaeocene to Miocene sediments. This terrane accreted to the Central Tectonic Realm in the Eocene along the San Jacinto Fault (Cediel and Cáceres, 2000). Located outboard of the San Jacinto Terrane is the Sinú Terrane, emplaced along the margin of the San Jacinto Terrane in the Miocene (Leal-Mejía et al. 2018). The volcanic basement of the Sinú terrane is overlain by turbidite sequences of Oligocene age and younger.

The Pacific Terrane Assemblage (PAT) forming the basement of southwestern Colombia, is composed of three distinct terranes. The first of these is the Romeral Melange, the terrane bounding the autochthonous CTR terranes to the east along the Romeral Fault System (RFS). This is a regional scale tectonic melange (Cediel and

Cáceres, 2000) composed of intensely deformed and fragmented blocks of Palaeozoic, Jurassic and Cretaceous arc volcanic rocks, ophiolite, meta-sediments, layered mafic and ultramafic complexes, eclogite, blueschists, amphibolite and carbonaceous schists (Cediel et al. 2003; Leal-Mejía et al. 2018). The terrane was formed along the western edge of the CTR within a transtensional basin at the Pacific margin of Colombia during the early Cretaceous (Nivia et al. 2006), though there is dispute over whether it is allochthonous or autochthonous in nature, studies suggest the presence of both elements formed in a continental margin basin (I.e.: Nivia et al. 2006) and in an allochthonous, intra-oceanic setting (Cediel et al. 2003). The melange underlies most of the Cauca-Patia valley, including the physiographic depression north and south of the city of Pasto which hosts some of the Plio-Pleisticene to recent volcanic arc (e.g.: Calvache and Williams, 1997; Duque-Trujillo et al. 2009). West of the Romeral Terrane is the Dagua Terrane, occasionally referred to in literature as the “Dagua-Piñon Terrane” (e.g.: Cediel, 2019; Marin-Cerón et al. 2018). This is composed of volcanic basement of the Diabasico Group, overlain by the sediments of the Dagua Group. The Diabasico Group is a volcanic and hypabyssal basement of mafic and ultramafic rocks of E- and N-MORB affinity (Kerr et al. 1997; Sinton et al. 1998). The overlying flyschoid siliciclastic sediments including greywacke, cherts, marls and siltstones compose the Dagua Group. Though this terrane has been described in literature variously as an ophiolite, accreted oceanic crust or aseismic ridge (Nivia, 1996 and references therein) it is most commonly interpreted as part of the CCOP (I.e.: Kerr et al. 1997; Sinton et al. 1998). The oceanic sediments of the Dagua terrane have mid- to late-Cretaceous biostratigraphic ages (Etayo-Serna and Rodríguez 1985), in line with the oceanic plateau rocks of the Diabasico Group which have reported mid-Cretaceous Ar-Ar

ages (~91 - 89 Ma - Kerr et al. 1997; Sinton et al. 1998). Approach and collision of the Dagua terrane began in the late-Cretaceous along the Cauca fault/suture which separates this terrane from the Romeral Melange to the east. Furthest west of the PAT terranes is the Gorgona Terrane, located mostly offshore on southwest margin of Colombia, bounded to the west by the Colombian trench (Leal-Mejía et al. 2019). Similar to the basement of the Dagua Terrane this is accreted oceanic plateau (Kerr and Tarney, 2005), or potentially an aseismic ridge (McGeary and Ben-Abraham, 1989). The terrane is composed of a peridotite-gabbro complex, massive basaltic and spinifex-textured komatiitic lava flows and pillow lavas (McGeary and Ben-Avraham, 1989; Cediel, 2019; Leal-Mejía et al. 2018). Palaeomagnetic data shows no clear correlation with other accreted CCOP terranes (Estrada, 1995) and a location of origin further south and west than those terranes, which would be consistent with a separate “Gorgona” oceanic plateau (e.g.: Kerr and Tarney, 2005). Radiometric ages for this terrane place it at ~87 - 83 Ma (Sinton et al. 1998), later than ages for CCOP recorded in the Dagua terrane. Accretion of the Gorgona terrane along the western margin of the Dagua terrane also occurred later, taking place prior to the Eocene (Cediel et al. 2003; Kerr and Tarney, 2005) or prior to the Miocene (McGeary and Ben-Abraham, 1989). Later strike-slip movement along the Gorgona Terranes eastern boundary, the Buenaventura fault zone/suture, may have led to fragmentation of the terrane (Cediel, 2019). The PAT also hosts a number of granitoid intrusions in a NNW-orientated, curvilinear arc segment stretching ~600 km (Figure 3.4) including the Buriticá, Santa Fé (Sananalarga), Mistrató, Buga and Jejénes granitoids along with associated intrusive suites (Leal-Mejía et al. 2018). These occur along the tectonised front of the Romeral Melange, where the WTR contacts the continental terrains of the CTR (Gomez et al. 2015; Leal-Mejía et al.

2018). Geological, geochemical and isotopic data for these granitoids characterise them as a primitive calcic to calc-alkaline arc system, generated within an intra-oceanic setting, emplaced within the Dagua and Cañas Gordas terrane assemblages of the Western Tectonic Realm, prior to the accretion of these terranes to the continental margin. An adakitic character (i.e.: Santa Fé and Buga) has been noted for some of the plutons of this arc segment, related to subduction initiation beneath the incoming CCOP terranes (Leal-Mejía et al. 2019).

The final component of the WTR is the Panamá-Chocó terrane assemblage (CHO), which straddles NW Colombia and eastern Panama, and hosts segments of the Panama double arc (Leal-Mejía et al. 2018). CHO basement is composed of Campanian to Eocene oceanic plutonic rocks of mafic to intermediate composition with volcanic arc compositions. In Colombia, this assemblage can be divided into two terranes: The Cañas Gordas Terrane and the El Paso-Baudó Terrane. The Cañas Gordas Terrane is a mixture of volcanic basement (the Barroso Formation) overlain by fine grain sediments (Penderisco Formation). The basement of the Barroso Formation is a made up of massive porphyritic amygdaloidal basalt and andesite flows of tholeiitic to calc-alkaline composition alongside agglomerates and tuffs (Rodriguez and Arango, 2013). The overlying Penderisco Formation is made up of thin beds of chert, greywacke, mudstone, siltstone and marls. Biostratigraphy of some mapped areas of the Barroso Formation provide a Barremian to middle Aptian age (~125 - 113 Ma) (González, 2001 and referees therein), but there is dispute over whether the Barroso Formation is part of the CCOP plateau assemblages (Weber et al. 2015) or if it represents the accreted Farallon plate onto which the plateau assemblages were constructed (Nerlich et al. 2014). Current consensus favours an

oceanic plateau origin (Buchs et al. 2018). The Cañas Gordas Terrane is intruded by the ~100 - 90 Ma Santa Fé batholith and Buriticá tonalite at its eastern margin, and was accreted to the continental margin (Central Tectonic Realm) in the late Cretaceous to Paleocene (Leal-Mejía et al. 2018). Composed of late Cretaceous to Paleogene tholeiitic basalts of E-MORB and N-MORB affinity (e.g.: Kerr et al. 1997) overlain by pyroclastic deposits, cherts and turbidites (Leal-Mejía et al. 2018), the Cañas Gordas has a similar composition, including late Cretaceous CCOP, and likely a similar origin to the later accreted Pacific Terranes further south. The El Paso-Baudó Terrane is thought to have formed along the trailing edge of the Caribbean plate. Collision of this terrane with the Cañas Gordas Terrane occurred in the mid-Miocene (Montes et al. 2012). This terrane hosts Alaskan-type zoned ultramafic complexes (e.g.: Alto Condoto) intruded in the early Miocene (Tistl et al. 1994) the remnants of the Mandé-Acandí arc, emplaced ~60 - 42 Ma (Leal-Mejía, 2011; Montes et al. 2012). These granitoids of the Mandé-Acandí arc and their preserved coeval volcanic footprint represent the development of an intra-oceanic arc sequence emplaced within CCOP crust, as represented by the El Paso-Baudó Terrane (Montes et al. 2012; Cediel, 2018). This Paleogene arc is associated with a SW-facing intra-oceanic subduction zone within the Farallon plate at the trailing edge of the CCOP plateau (e.g.: Aspden et al. 1987; Kennan and Pindell, 2009; Wright and Wyld, 2011; Montes et al. 2012; Nerlich et al. 2014; Weber et al. 2015), coeval with the intra-oceanic arc recorded in Central America as the Middle American Arc (i.e.: Buchs et al. 2010; Wright and Wyld, 2011). The earliest recorded ages of this magmatism are in the Panamanian parts of this segment (i.e.: Acandí; Figure 3.4), placing magmatism there ~62 - 59 Ma (Wegner et al. 2011; Montes et al. 2012), compared to U-Pb crystallisation ages in the Colombian parts of the Mandé Batholith of 50 Ma

(Montes et al. 2015) to 43 Ma (Leal-Mejía et al. 2018), younging southwards. This age progression has been attributed to the onset of dextral-oblique transpression of the approaching CCOP crust of the Caribbean Plate with NW South America, with final docking of the Caribbean Plate likely occurring ~54 Ma (e.g.: Kennan and Pindell, 2009; Nerlich et al. 2014) and cessation of Mandé-Acandí arc magmatism soon afterwards.

This cessation in subduction-related granitoid magmatism lasted for ~30 Ma throughout Central Colombia (Leal-Mejía et al. 2018) noted by a conspicuous absence of plutonic or magmatic evidence or 50 - 20 Ma detrital zircon populations in the Colombian Andes (e.g.: Horton et al. 2015). It has been speculated that magmatism did occur during this period of hiatus but has since been erased by subsequent uplift and erosion during the Northern Andean orogeny.

3.2.3 Emplacement and Evolution of the Caribbean Plate:

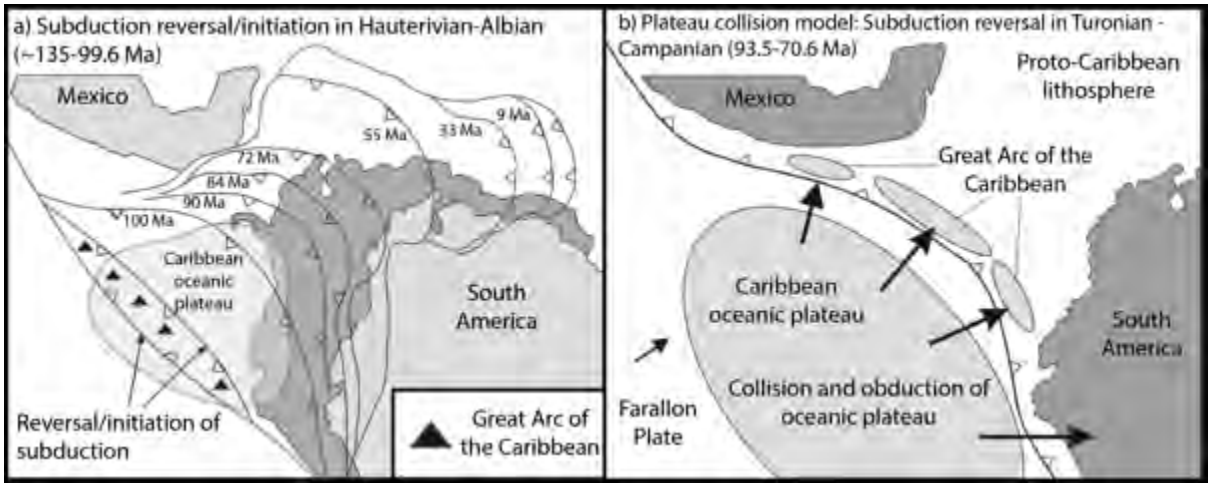

Figure 3.5: Primary models regarding emplacement of the Caribbean Large Igneous Province/Caribbean-Colombian Oceanic Plateau (CLIP/CCOP) between the Americas. Adapted after Hastie et al. (2013).

An integral part of the magmatism and terrane accretion presented above is the involvement of the Caribbean-Colombian Oceanic Plateau (CCOP) which today forms the bulk of the Caribbean plate between the Americas (e.g.: Boschmann et al. 2014; Nerlich et al. 2014). A number of models have been proposed to explain the emplacement of a Pacific origin oceanic plateau between the Americas, in front of the current Central American volcanic arc (e.g: Burke, 1988; Kerr et al., 1999, 2003; Pindell et al., 2006; Pindell & Kennan, 2009; Neill et al. 2011). During the Cretaceous an extensive island-arc system was located between North and South America (e.g.: Kerr et al., 2003; Pindell et al., 2006). Fragments of this arc are preserved today in the Greater Antilles, Netherland Antilles and the Aves Ridge (e.g.: Pindell and Kennan, 2009; Neill et al., 2011). The main controversy between Pacific origin models is the mechanism by which the CCOP was accommodated between the Americas and when this occurred. This requires either a reversal in subduction polarity of this inter-American arc or initiation of another SW-facing subduction zone, and causal mechanisms to initiate this subduction (Figure 3.5).

One group of models suggests a subduction initiation/reversal in the Early Cretaceous (e.g.: Pindell et al. 2006; 2011; Pindell and Kennan, 2009). In this case, rifting between North and South America in the Early Cretaceous formed the ocean crust of the proto-Caribbean plate. This was bounded between the Americas by a NW-dipping subduction zone or alternatively an “inter-American transform”, a large transform fault (Pindell et al. 2011). Subduction was either initiated or experienced a polarity reversal from NE to SW as a result of accelerated of Atlantic seafloor spreading (Kennan and Pindell, 2009) during the Early Cretaceous (Albian-Aptian - 125 - 99.6 Ma). In such scenarios, later eruption of the oceanic plateau (~91 - 89 Ma

- Kerr et al. 1997) could be then be accommodated by subduction of the proto-Caribbean lithosphere beneath the Farallon plate (onto which the CCOP is emplaced), or a “slab gap” resultant from a spreading ridge in the subducted proto-Caribbean lithosphere, through which an ascending mantle plume, and therefore the CCOP could erupt.

A new SW-facing subduction zone (e.g.: Pindell et al. 2005) requires the NE subducting Farallon slab to be broken off to accommodate the newly subducting proto-Caribbean lithosphere, with breakoff facilitated by subduction of back-arc basin spreading ridges (Neill et al. 2011; Hastie et al. 2013). However older, mechanically strong (e.g.: Hall et al., 2003; Stern, 2004) Farallon lithosphere would be difficult to break off during Hauterivian-Albian time when, in a scenario where accelerated Atlantic seafloor spreading was the cause of polarity reversal (e.g.: Pindell et al. 2005), compression would be focused on the proto-Caribbean slab rather than the Farallon lithosphere (Hastie et al. 2013).

This thesis favours another group of models which suggest that polarity reversal of the subduction zone was triggered by collision with the CCOP (e.g.: Hastie et al. 2013) in the Late Cretaceous (Turonian-Campanian - 93.5 - 70.6 Ma) (e.g.: Duncan and Hargreaves, 1984; Burke, 1988; Kerr et al. 1999, 2003; Neill et al. 2011; Hastie et al. 2013) as the thick, more buoyant oceanic plateau is unable to subduct and can choke an active subduction zone (Hastie et al. 2013). This is in line with modern examples of plateau driven polarity reversal, such as the collision of the Ontong Java Plateau (OJP) with the North Solomon Trench System (Petterson et al., 1999; Smith et al., 2009). By far the most convincing line of evidence in favour of a later Turonian-

Campanian polarity reversal is the Caribbean crust itself. Models advocating a Hauterivian-Albian polarity reversal propose an Aptian age CCOP based on geochronology from CCOP units in Curaçao (Wright and Wyld, 2011) and Ecuador (Lapierre et al., 2000). In Ecuador, this CCOP attributed San Juan unit has been shown to be distinct from other COP units (Kerr et al., 2003) and later U-Pb geochronology by Vallejo et al. (2006) of this unit produced an age of 87.10 ± 1.66 Ma, consistent with other CCOP ages. This calls into question any Aptian phase for CCOP volcanism (Hastie et al, 2013). The latest Hauterivian-Albian initiation/reversal models have argued that the subduction of proto-Caribbean crust, along with its spreading ridge, could have led to the formation of a “slab gap”, through which a mantle plume could have been accommodated, as opposed to direct derivation from an extremely distal location in the Pacific realm such as the Galapagos hotspot (e.g.: Pindell et al., 2011). Alternatively, earlier break off of the slab could have also accommodated a plume. This has been challenged by Hastie and Kerr (2010) who point out that any ascending plume entering through a slab gap would have been contaminated by slab derived fluids, and no such plateau rocks with arc signatures have been observed in the circum-Caribbean region (e.g.: Kerr et al., 2003). This absence of evidence could however be the result of lack of these signatures in present exposure, and future investigation of sites such as the Aves Ridge and Dutch Antilles may counter this assertion (Neill et al. 2011). This model allows for obduction of oceanic plateau material to NW South America, as described above and observed in Colombia (e.g.: Kerr et al., 1997; Kerr and Tarney, 2005) and Ecuador (Vallejo et al., 2006) as the CCOP skirted the edge of the continent.

Tectonic reconstructions show that the CCOP terranes of the Western Tectonic Realm had largely been emplaced in the near shore of South America by the late Oligocene to early Miocene (e.g.: Cediel et al. 2003; Kennan and Pindell, 2009; Cediel, 2018). The Panamá-Chocó terrane assemblage (CHO), including the Mandé-Acandí batholith, was located at the trailing edge of the Caribbean plate to the west of the continent by this time (e.g.: Farris et al. 2011). As previously discussed, the Mandé-Acandí batholith is interpreted in tectonic reconstructions as an expression of a volcanic front, co-linear with the Middle American arc (Figure 3.5), formed by NE-subduction of Farallon crust beneath the trailing edge of the Caribbean plate during the mid-Cretaceous to Paleogene (e.g.: Aspden et al. 1987; Cediel et al. 2003; Kerr et al. 2003; Kennan and Pindell, 2009; Farris et al. 2011; Wright and Wyld, 2011; Montes et al. 2012; Weber et al. 2015; Figure 3.8). Convergence between the Chocó Block and the Colombian margin probably began in the late Oligocene (e.g.: Duque-Caro, 1990; Cediel et al. 2003; Leal-Mejía et al. 2018), possibly ~23 - 25 Ma (Farris et al. 2011). It is important to note the lack of any major granitoids associated with the convergence of the Chocó block and NW South America (i.e.: Gomez et al. 2015). This has been interpreted as due to the lack of a significant subduction zone between these incoming terranes and the NW margin of South America (Leal-Mejía et al. 2018) and the underthrusting of thick, buoyant CCOP lithosphere beneath the South American margin, as suggested by numerous plate reconstructions and geophysical studies, forming an amagmatic zone (e.g.: van der Hilst and Mann, 1994; Cediel et al. 2003; Kerr et al. 2003; Farris et al. 2011; Idarraga-Garcia et al. 2016; Leal-Mejía et al. 2018) which could persist as an impediment on subduction zone volcanism north of ~5 ºN to this day.

3.3 Latest Oligocene to Plio-Pleistocene Magmatism:

By the end of the Oligocene, the triple junction between the Farallon, South American and Caribbean plates was located in the near-shore of the Colombian Pacific margin, along the southwestern most margin of the Panamá-Chocó terrane assemblage. East facing subduction of the Farallon plate beneath the Pacific margin of Colombia is evident from ~24 Ma (Leal-Mejía, 2011). The magmatic evidence for this subduction zone are a series of geographically and temporally distinct volcano-magmatic arc segments emplaced within the Central Tectonic Realm, Maracaibo sub-plate and parts of the Western Tectonic Realm (Figure 3.6). As all these terranes had been emplaced on the continental margin by the time of initiation of latest Oligocene magmatism, the arc segments themselves are considered autochthonous (Leal-Mejía et al. 2018). NE-SW trending faults (e.g.: Garrapatas; Uramita) marking the southern margin of the Chocó Block terranes (and therefore the trailing edge of the Caribbean plate) were also present as crustal scale weaknesses by this time (Duque-Caro, 1990; Cediel et al. 2003; Montes et al. 2012). The western plate motion of South America resulted in near-orthogonal convergence between the Farallon plate and the Colombian Pacific margin (Lonsdale, 2005). At ~23 Ma the Farallon plate is split along an E-W fracture near the boundary between the Middle American and South American arcs, forming the Nazca and Cocos plates (Lonsdale, 2005). In the mid-Miocene, rifting within the Nazca plate resulted in the formation of the Sandra Ridge, which now divides the younger crust of the Coiba sub-plate (~14 - 9 Ma) from the slightly older crust (~18 - 14 Ma) of the rest of the Nazca plate (Figure 3.7) as far south as the Malpelo Ridge (Lonsdale, 2005).

Following the short-lived magmatism in the Eocene-Oligocene and proposed magmatic hiatus, a renewed pulse of magmatism throughout the Neogene is documented (Figure 3.6). This was likely due to dextral compression, transform faulting and plate reorganisation along the Pacific Margin of Colombia (e.g.: Cediel et al. 2003; Kennan and Pindell, 2009; Cediel, 2019; Leal-Mejía et al. 2019). Granitoid magmatism first reappears ~24 Ma hosted in CCOP related rocks of the Dagua Terrane in the south-western Colombian Andes (Echeverri et al. 2015), well to the south of the proposed trailing edge of the Caribbean plate during the late Oligocene (e.g.: Kennan and Pindell, 2009; Hastie and Kerr, 2010; Montes et al. 2012). Intriguingly, rather than forming one continuous arc segment or a succession of them (as with previous Cretaceous-Eocene episodes), the Oligocene to Plio-Pleistocene granitoids of Colombia form a complex collage of arc segments spread over the Western and Central Cordilleras, Cauca and Patia valleys and elsewhere (e.g.: Gomez et al. 2015), with ages for these granitoids (Figure 3.6) describing a complex migration of arc segments in space and time (Cediel et al. 2003; Leal-Mejía, 2011; Wagner et al. 2017; Leal-Mejía et al. 2018). This complexity in the spatial distribution and genesis of Oligocene to Plio-Pleistocene granitoids could be due to complex collision between South America and the trailing edge of the Caribbean plate in the late Oligocene-Miocene, resulting in the accretion of the El Paso-Baudó Terrane and/or the evolution of the Farallon (Nazca-Cocos) plate system along the Colombian Pacific margin (Leal-Mejía et al. 2018).

A possibly continuous period of arc magmatism since the Late Oligocene can be observed, with a major peak in activity after the Middle Miocene, followed by development of a Late Oligocene to Early Miocene arc, which migrated eastwards in

the Middle Miocene (Bayona et al., 2011; Echeverri et al., 2015). This is linked to a major increase in crustal deformation, crustal thickening and magmatic activity in the arc, which could have been caused by shallowing of subduction of the Nazca plate in the Miocene (Echeverri et al., 2015; Wegner et al. 2017). Following this, an eastward progressing series of continental arcs is identified, beginning with a Late Miocene sub-belt along the axis of the Western Cordillera, including small tonalite, monzonite and diorite stocks (Figures 3.6 and 3.8). This was followed by a late Miocene to Pliocene sub-belt in the Cauca valley composed of explosive andesite volcanism, followed by andesite and dacite plugs and alkali basalt dykes. Finally, the modern volcanic arc in the northern Andes, of Plio-Plesitocene to Quaternary age occurs along the axis of the Central Cordillera (e.g.: Toussaint and Restrepo, 1982) and into the Western Cordillera in southernmost Colombia (Droux and Delaloye, 1996).

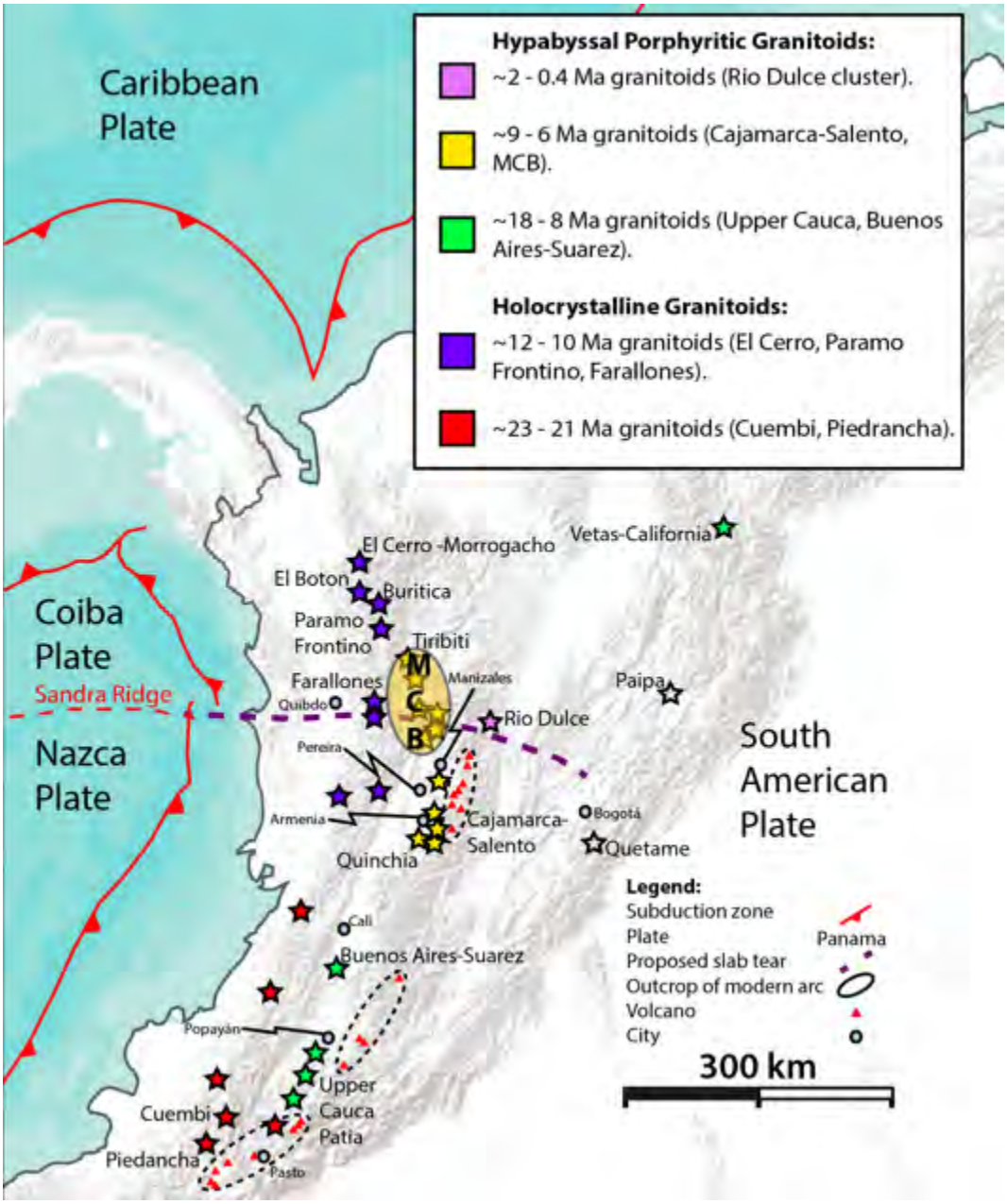

Figure 3.6: Latest Oligocene to Quaternary arc remnants, recorded by hypabyssal granitoids and occasional volcanic sequences. Active Plio-Pleistocene to recent volcanic arc is also shown. Adapted after Laeger et al. (2013) and Leal-Mejía et al. (2019).

A plethora of models on Miocene to recent subduction beneath continental Colombia based on distribution of volcanic activity; magnetic, gravity and seismic surveys and tomographic imaging have been presented (e.g.: Pennington, 1981; van der Hilst and Mann, 1994; Taboada et al. 2000; Zarifi et al. 2007; Vargas and Mann, 2013; Bissig et al. 2014; Chiarabba et al. 2015; Wegner et al. 2017). All of these studies agree that data shows E-SE subduction of a segmented Nazca plate of Miocene age (Figure 3.7). Geophysical data and tomographic imaging (e.g.: Pennington, 1981; van der Hilst and Mann, 1994; Taboada et al. 2000; Zarifi et al. 2007; Vargas and Mann, 2013; Chiarabba et al. 2015) have additionally shown evidence of an E-W discontinuity or tear in the oceanic slab subducting beneath Colombia (Figure 3.7). This feature has been dubbed the “Caldas Tear” (Vargas and Mann, 2013). The Caldas Tear lies between 4.8ºN and 5.2ºN, coincident with features outboard of the Colombian margin such as the Sandra rift (Vargas and Mann, 2013) and the Coiba transform fault (Chiarabba et al. 2015), as well as inboard features such as the southern end of the Serrania de Baudó (Taboada et al. 2000), Uramita suture (Cediel et al. 2003) and Villamaria-Termales Fault (Vargas and Mann, 2013). A difference in the geometry of the subducting slab north and south of the Caldas Tear (Figure 3.7) has been noted by several authors (e.g.: Pennington, 1981; van der Hilst and Mann, 1994; Taboada et al. 2000; Cediel et al. 2003; Zarifi et al. 2007; Vargas and Mann, 2013; Bissig et al. 2014; Chiarabba et al. 2015). There is consensus that south of ~5ºN, the Nazca plate is subducting steeply beneath Colombia at ~30-40º steepening to >50º beneath the Eastern Cordillera (Leal-Mejía et al. 2018). This southern segment of “normally” dipping subducting slab is responsible for the volcanism of the Colombian section of the Northern Volcanic Zone of the Andes. A variety of models have been presented on the geometry of subduction north of ~5ºN. Beneath the

Eastern Cordillera, tomographic imaging and seismic data implies a dipping slab associated with a cluster of intermediate depth (~150 km) seismic activity known as the Bucaramanga seismic nest (Pennington, 1981). This slab has been interpreted by some authors as the shallowly subducting down-slab segment of CCOP terranes observed at surface in the Chocó Block (e.g.: Pennington, 1981; Taboada et al. 2000; Zarifi et al. 2007; Vargas and Mann, 2013; Bissig et al. 2014). A flat, buoyant slab subducting beneath Colombia north of ~5ºN has been used to explain the abrupt cessation of magmatic activity north of this and is often presented as an amagmatic zone. However, a lack of seismic activity up-slab of the Bucaramanga seismic nest has led to speculation that the slab segment north of ~5ºN has detached from the slab subducting at surface (i.e.: Taboada et al. 2000; Vargas and Mann, 2013). The northernmost segment of the Nazca plate, the Coiba microplate is subducting beneath Colombia between 5ºN and 8ºN (e.g.: Aspden et al. 1987; van der Hilst and Mann, 1994; Taboada et al. 2000; Cediel et al. 2003; Lonsdale, 2005; Vargas and Mann, 2013; Chiarabba et al. 2015). The Coiba microplane could contain buoyant features (see van der Hilst and Mann, 1994; Chiarabba et al. 2015) which would cause it to subduct at lower angle when compared to the normally subducting segment of the Nazca plate south of the Sandra Ridge/Caldas Tear. This would also explain the lack of magmatic activity north of ~5ºN (van der Hilst and Mann, 1994; Chiarabba et al. 2015). There is a major departure in respective models here: Whilst some authors (e.g.: Taboada et al. 2000; Vargas and Mann, 2013) suggest that CCOP lithosphere is underthrusting beneath the Colombia margin north of ~5ºN, other authors (e.g.: Cediel et al. 2003; Farris et al. 2011; Chiarabba et al. 2015) propose that a fragment of the Nazca plate (Coiba microplate), not the Caribbean plate is subducting beneath NW South America, and instead suggest that the

Caribbean plate is underthrusting beneath the Western Caribbean margin of Colombia (i.e.: Bissig et al. 2014). The majority of studies have focused in on geophysical datasets and the lack or presence of volcanism, with little attention being paid to the distribution and age of volcanism itself over latest Oligocene to Plio-Pleistocene period itself (c.f.: Wegner et al. 2017; Leal-Mejía et al. 2018). The eastward migration of both Coiba and Nazca subduction has been attributed to a shallowing of the angle of subducting slab in both instances caused by subduction of younger and therefore more buoyant lithosphere and/or buoyant features such as the aseismic Sandra Ridge (Lonsdale, 2005; Chiarabba et al. 2015). Leal-Mejía et al. (2018) interprets Neogene granitoid magmatism observed in the Cauca-Patia valley, Western and Central cordilleras to be the result of subduction of segments of the Nazca plate from the late Oligocene onwards. The Caldas Tear, separating the Coiba microplate from the rest of the Nazca plate, has led to differences in the rate and style of subduction and in the distribution of volcanism north and south of ~5ºN (Cediel et al. 2003; Leal-Mejía et al. 2018). Leal-Mejía et al. (2018) argues against the idea of any of the Neogene suites being the result of subduction of Farallon/CCOP lithosphere per se. Fault reactivation and the presence of paleo-sutures from docked terranes have also likely played a significant role in the distribution of Colombian arc volcanism.

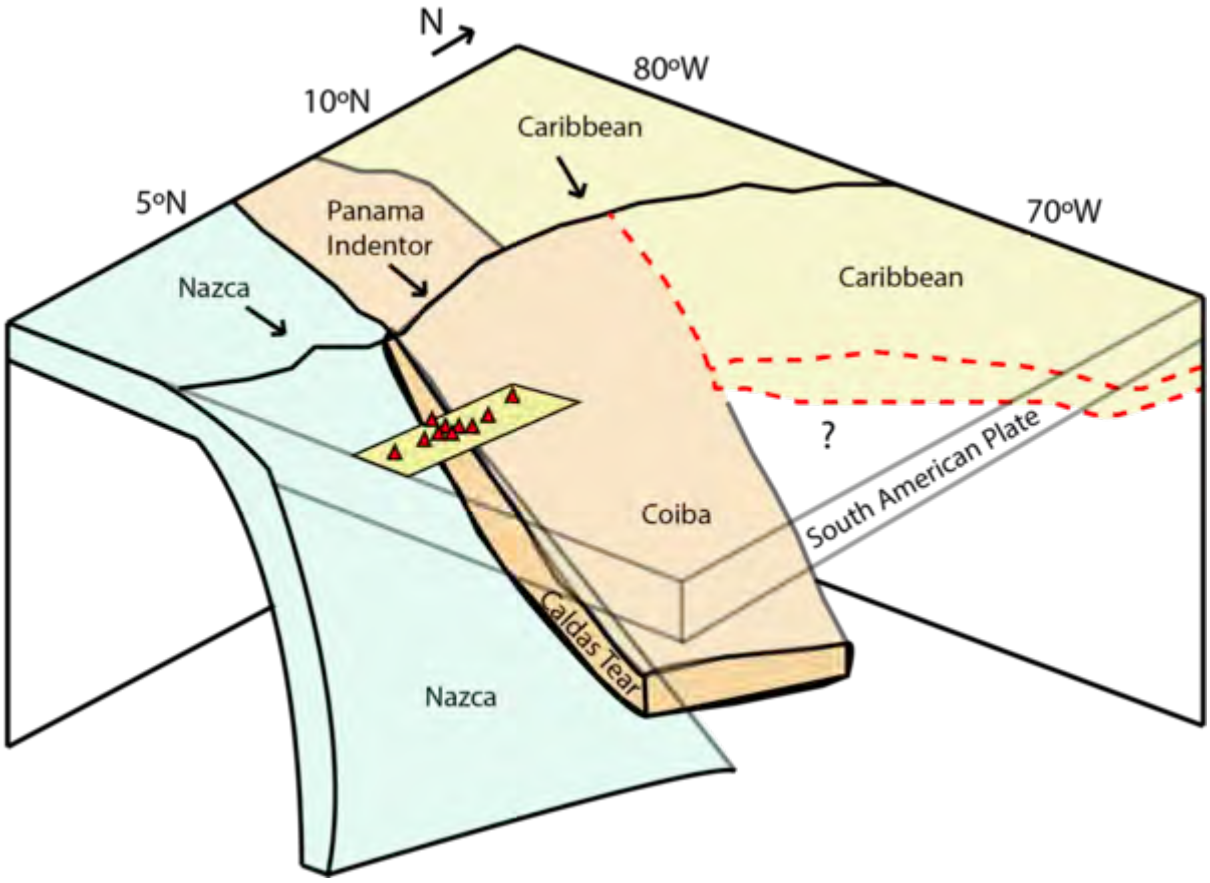

Figure 3.7: Box model illustrating one possible tectonic scenario beneath the Northern Andes. Here, a slab tear derived from the subducting Sandra Ridge (the Caldas Tear) has separated the more steeply subducting Nazca plate from a more shallowly subducting Coiba plate north of ~5°N. Position of volcanoes of the northernmost segment of the active Colombia arc are shown, south of this tear. Adapted after Bissig et al. (2014).

In summary, the events leading up to and during the Northern Andean Orogeny (Figure 3.8) and the inception of the modern arc can be summarised as follows:

- Migration of the South American plate to the north and west, relative to a stationary Caribbean plate in the Eocene. This migration results in tectonic stacking and buckling along the Colombian-Caribbean margin and uplift of the San Jacinto and Sinú terranes, but not significant magmatism. NW movement of South America continues into the mid-Miocene, closing the Middle American Seaway, accretion of Panama/Choco block terranes and uplift along the northwest Colombian margin.

- Breakup of the Farallon plate ~23 Ma due to the divergent pull of the plate from subduction beneath both Central and South America (Lonsdale, 2005) results in the development of the Cocos and Nazca plates. Rifting within the Nazca plate ~20 - 9 Ma further gives rise to the Coiba microplate north of the E-W striking Sandra Ridge, separate from the rest of the Nazca plate. Subduction of these Nazca plate segments leads to granitoid magmatism along the Pacific margin of Colombia beginning with the ~23 - 21 Ma Piedrancha-Cuembí arc segment in SW Colombia. Shallowing of the angle of subduction in the Nazca plate south of the Sandra Ridge led to eastward migration of the arc axis, forming the Upper Cauca-Patia suite ~18 - 9 Ma. Migration of the arc axis continued northwards and eastwards from the Miocene onwards until the formation of the modern Northern Volcanic Zone in Central and Southern Colombia.

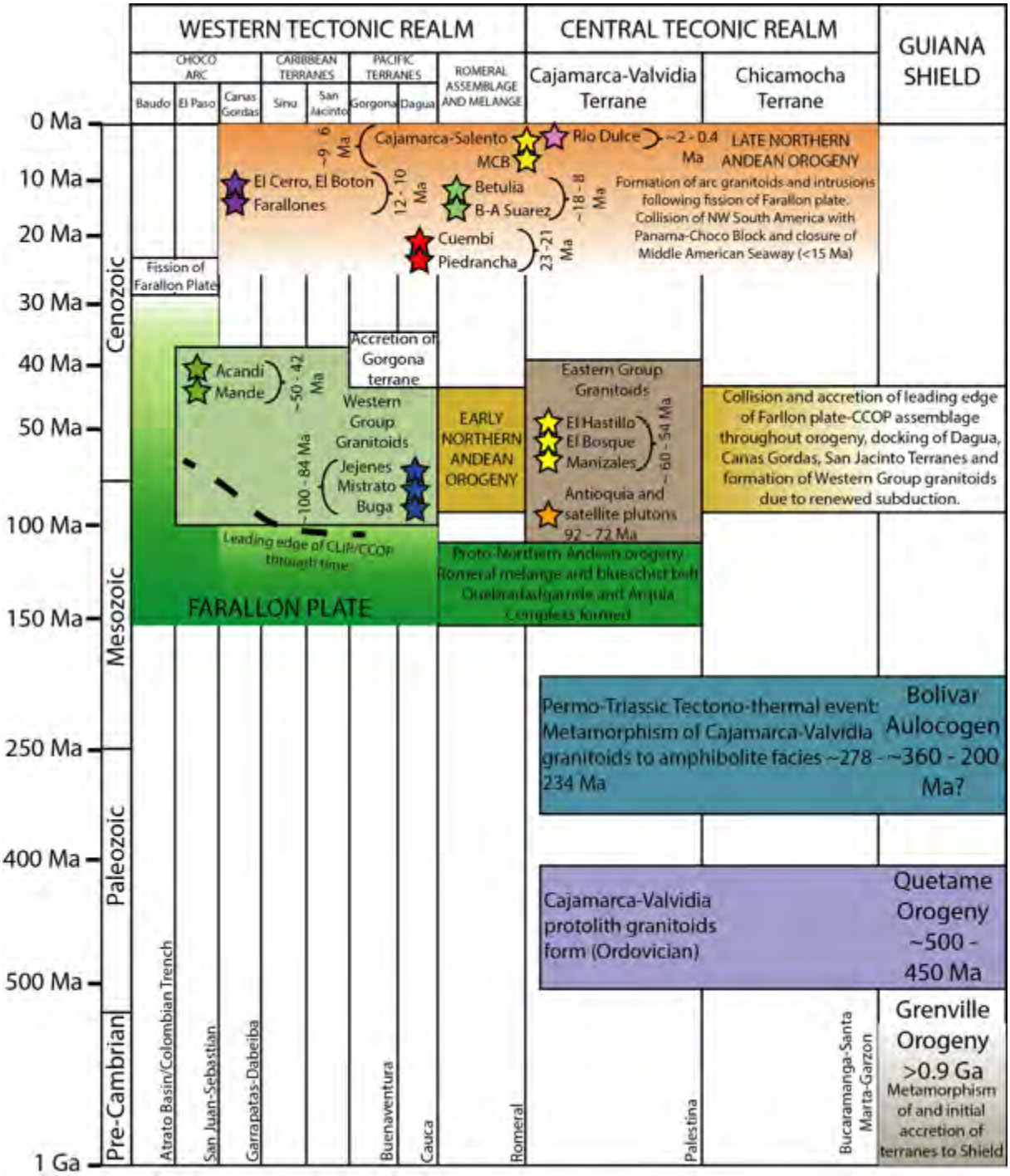

Figure 3.8: Time-space diagram of major tectonic, magmatic and orogenic events of concern in Colombia, corresponding their occurrence across specific terranes (as labelled at the top of the diagram) and divided by specific faults and crustal sutures (labelled at the base of the diagram). Major batholiths and intrusions are named and highlighted as stars, with colours and names corresponding to those used on previous map figures. Adapted after Leal-Mejía et al. (2018) and references therein.

4 Analytical methods

Outlined below are the analytical techniques and preparatory techniques used to obtain whole rock major and trace element analyses as well as Sr, Nd and Hf radiogenic isotope analyses during the current project. Additional detail on these methods can be found in **Appendix B**, and raw data from analyses in **Appendix C.**

4.1 Inductively Coupled Plasma-Optical Emission Spectrometry and Inductively Coupled Plasma-Mass Spectrometry (ICP-OES and ICP-MS:

4.1.1 Sample preparation for ICP-OES and ICP-MS:

4.1.1.1 Preparation of rock powders:

All samples were prepared at facilities at Cardiff University, U.K. Whole rock samples were inspected for alteration and any alteration surfaces removed by rock saws. During sawing, small pieces of unaltered rock approximately 76 x 26 x 10 mm were cut from each sample from which thin sections could be made. Rocks were further cut into small pieces to be placed into a metal jaw crusher. Each sample was run through a clean jaw crusher at least twice to ensure any large fragments had been crushed prior to the milling stage. Though every effort was made to minimise contamination, limited metal contamination may have been introduced by use of the jaw crusher, though the amount of sample crushed compared to that analysed should have eliminated such contamination. Jaw crushed material was then milled to powder

in an agate planetary ball mill, with any excess jaw crushed material archived and labelled. A uniform running time and revolutions per minute (rpm) of 30 minutes at 275 rpm were adopted for milling, with an extra run of 10 - 15 minutes at 275 rpm adopted if samples were found to still contain crystals or coarse fragments. Efforts were taken at each stage to avoid contamination through cleaning of the workspace and equipment between sample runs.

4.1.1.2 Loss on ignition (LOI):

Volatile contents of samples were measured by loss on ignition (LOI) whereby a portion of the sample were weighed before and after baking at high temperature (~900°C) to determine mass loss of H_2O, CO_2 and other common volatile compounds. Approximately 2 - 3g of each sample were weighed out into clean, pre-weighed crucibles which had also been pre-dried at ~150°C to drive off remnant volatiles. Sample masses were recorded prior to the sample bearing crucibles being placed in batches in a Vecstar furnace at 900°C for ~2 hours. This allowed sample volatiles to be “burned off” and mass loss to be determined by reweighing the crucibles and sample. All possible steps were taken to avoid contamination and especially introduction of volatiles during this process. Physical handling of crucibles was avoided as far as possible, and tongs were used when transferring crucibles to and from the furnace. Sample powders were placed in airtight storage bags and housed within desiccators during and after the procedure up to preparation for ICP-MS and ICP-OES analysis. Full details of loss on ignition procedures used can be found in **Appendix B**. LOI values for samples can be found in **Appendix C**.

4.1.1.3 Preparation of sample solutions for ICP-OES and ICP-MS analysis:

Prepared rock powders for this study, along with a selection of prepared international standard reference material (ISRM) samples available at Cardiff, underwent fusion and dissolution to solution in preparation for ICP-OES and ICP-MS analysis. Preparation and analysis of Colombian samples was made in two separate runs at Cardiff University in September 2017 and June 2019, respectively. Fusion was undertaken by mixing 0.1 ± 0.001g of sample and 0.6 ± 0.001g of lithium borate flux into clean platinum crucibles, thoroughly mixing the two components with a clean spatula and adding 5 - 6 drops of lithium iodide wetting agent to the mixture. Crucibles were then mounted, three at a time into a Claisse Fluxy fusion machine, which rotated and heated the samples for 9 minutes to produce a glass. This was then deposited by the fusion machine into labelled teflon beakers, each containing a magnetic stirring bar in a mix of 30 ml of deionised water and 20 ml of 10% nitric acid. Crucibles were inspected for any remnant sample glass, which was removed and the crucible placed in the respective teflon beaker to remove any further sample material. Teflon beakers were placed on to ~80°C hotplates for 10 - 15 minutes or until sample glass was completely dissolved. Crucibles were removed and rinsed in deionised water, which was then added to the respective teflon beaker with any remaining sample. The sample solutions were then transferred to 100 ml Nalgene flasks. A 1 ml rhenium spike of prepared 100 ppm Rh stock solution was added to each flask, and all were made up to 100 ml with deionised water. All equipment (crucibles, sample beakers, Nalgene flasks, spatulas, etc) was thoroughly cleaned before and after use. The June 2019 sample run was performed on a newer Claisse

Fluxy fusion machine. Further discussion on all the sample preparation methods outlined above can be found in **Appendix B**.

4.1.2 Analysis of major and trace elements by ICP-OES and ICP-MS:

4.1.2.1 ICP-OES analysis:

Inductively coupled plasma optical emission spectrometry (ICP-OES) analysis was used to analyse major element oxides and a selection of trace elements (Sc, V, Cr, Co, Ni, Cu, Zn, Sr, Y, Zr, Ba) for all samples and ISRMs. In ICP-OES, samples are introduced as an aerosol by a nebuliser into an inductively coupled plasma, usually fuelled by argon, at ~10,000 K (Hou et al. 2016). This plasma volitalises and disassociates the sample aerosol into atoms, ions, dissociated molecular fragments and unvolatilised particles (Rollinson, 1993) which emit photos to return to their ground state (Hou et al. 2016). The wavelength of these photons can be used to identify the elements from which they originated, and as the number of photons is proportional to the element concentration of the sample (Hou et al. 2016) these wavelengths can be measured in a spectrometer to identify elements and proportions can be measured to determine their abundance. This information is then converted to an electric signal, amplified and sent to a computer where correlations and corrections can be made (Hou et al. 2016).

4.1.2.2 ICP-MS analysis:

An ICP similar to that described above is also used in mass spectrometry (MS) techniques to produce ions, which are directed toward a mass spectrometer. This is kept in a separate chamber at high vacuum, and linked to the ICP by two conical apertures, the sample cone and skimmer. These apertures deflect away uncharged particles but allow the passage of ions. The ions are focused by a lens beyond the skimmer to the mass spectrometer (Jarvis, 2014). The mass spectrometer separates the ions according to their mass-to-charge ratio (m/z), producing a spectrum of lighter and heavier ions (Rollinson, 1993). Separate elemental mass number peaks are derived from analysis of these ions, whilst ion detectors account for the proportion of ions per element (Jarvis, 2014). This information is then amplified and transferred digitally to a computer for correction and correlation.

Further details on ICP-OES and ICP-MS methods can be found in **Appendix B**.

4.2 Sr, Nd, Hf radiogenic isotopes:

4.2.1 Sample preparation for analysis of Sr, Nd, Hf radiogenic isotopes:

4.2.1.1 Sample Leaching:

A subset of samples was prepared from archive of sample powders prepared at Cardiff University for analysis of Sr, Nd and Hf isotopes. This subset was prepared for mass spectrometer analysis at the NERC Isotope Geosciences Laboratory (NIGL), Nottingham.

Sample powders were first leached in multiple stages, with 0.2 ± 0.0200g of each sample weighed out into 15 ml Savillex teflon beakers. Samples were then leached in 5 ml of 6M HCl at 60°C for 2 hours. Leachate was discarded, samples washed in MilliQ H2O. Samples were then centrifuged twice, dried and reweighed. The next leaching phase involved 1 - 2 mls of 2x quartz-distilled 16M HNO3 and 5-6 mls of 29M HF, in which samples were left overnight on hotplates at ~140°C. Once dried, 1-2 mls of HNO3 was added and samples left overnight. At this stage 20 mls of 2x quartz-distilled HCl was added to convert samples to chloride form. Lastly, samples were dissolved in ~2 ml of 1M HCl + 0.1M HF and transferred to a centrifuge prior to column chemistry.

4.2.1.2 Column Chemistry:

The next stage was chemical separation of sample solutions by column chemistry, to produce three fractions; of bulk high field strength elements (HFSE: Ti, Hf, Zr), bulk rare-earth elements (REE) and a fraction containing Sr, Ca and Rb. Columns were first prepared by washing through with 20 ml of 6M HCl, 10 ml of H2O and 20 ml of 6M HCl. Columns were then conditioned with 10 ml of 1M HCl + 0.1M HF. The primary columns themselves are made up of 2 ml of Eichrom AG50 x 8 cation exchange resin in 10 ml Biorad Poly-Prep columns. Samples were pipetted from centrifuge tubes on to columns in ~1.5 mls of 1M HCl + 0.1M HF. Another 5 - 10 mls of 1M HCl + 0.1M HF was then added which immediately eluted high field strength elements, which were collected and evaporated to dryness ready for analysis of Hf isotopes. The addition of 25 mls of 1.5M HCl eluted the fraction containing Sr and matrix elements (Ca, Rb) which was collected and evaporated to dryness. The REE fraction was eluted in 10 mls of 6M HCl, collected and evaporated to dryness.

The fraction of Sr and matrix elements were dried down and taken up in ~2 mls of 2.5M HCl. Solutions were transferred to quartz-glass columns with a 4 mls of AG50x8 cation exchange resin. Matrix elements were removed by washing columns with 48 mls of calibrated 2.5M HCl. Final Sr fraction was collected in 12 mls of 2.5M HCl and evaporated to dryness. The REE fractions were initially dissolved in 200 microlitres of 0.2M HCl. These solutions were then transferred to 10ml Biorad Poly-Prep columns with 2 mls of EICHROM LN-SPEC ion exchange resin to remove Sm and Nd. Columns were flushed with 14 mls of 0.2 HCl to remove La, Ce, Pr and the final Nd fraction was eluted in in 3 mls of 0.3M HCl.

Hf separation follows the procedure of Münker et al. (2001), adapted by NIGL. The HFSE fractions were dissolved in ~2 mls of 6M HCl and then placed on to 10 ml Biorad Poly-Prep columns packed with 1 ml of EICHROM LN-SPEC ion exchange resin. 10 - 20 mls of 6M HCl is used to elute matrix elements. The columns are then washed through with 2 mls of milliQ water to remove HCl, which could combine with peroxide in later stages to elute all HFSE. Several washes of 10 ml solutions of citric acid, nitric acid and peroxide were then run through the columns to help identify and remove traces of Ti. A 5 ml solution of peroxide-free citric and nitric acid was run through the columns to remove peroxide before a wash of 50-80 ml of 6M HCl + 0.06M HF was added. The Hf fraction was collected by 10 mls of 6M HCL + 0.2M HCl.

Additional details on preparation of samples at NIGL and column chemistry methods used can be found in **Appendix B**.

4.2.2 Analysis of Sr, Nd, Hf radiogenic isotopes:

4.2.2.1 Sample Analysis:

Analysis of samples for Sr, Nd and Hf isotopes were undertaken at NIGL in two runs, N833, performed in September 2019, N836, performed in January 2020. In both cases the following procedure was followed. Sr fractions were loaded onto outgassed single Re filaments using a TaO activator solution and analysed by a Thermo-Electron Triton mass spectrometer in multi-dynamic mode. Nd fractions were loaded onto one side of an outgassed Re filament assembly using dilute HCl, and analysed

in a Thermo Scientific Triton mass spectrometer in multi-dynamic mode. Hf fractions were first dissolved in 1 ml of 2% HNO3 + 0.1M HF. Samples were then loaded and analysed in a Nu Plasma HR mass spectrometer in static multi-collection mode. Full details of sample analysis for Sr, Nd and Hf isotopes can be found in **Appendix B** and raw data in **Appendix D**.

4.3 Assessment of data:

Data can be assessed based on precision and accuracy. Precision, or reproducibility, is the amount of statistical variation in replicate analyses from an average or mean value. The greater the number of determinations of a particular quantity in a sample, the smaller the precision and more reliable the average (Best, 2002). Accuracy is a determination of how close a measurement is to a “true” known value, usually determined by comparing a measurement of an international standard reference materials (ISRM) within a set of analyses to known and precisely measured analyses of that standard (e.g.: Govindaraju, 1989).

4.3.1 ICP-OES and ICP-MS data:

4.3.1.1 Accuracy of data:

A first run of analyses were performed at Cardiff University in 2017. This consisted of Colombian samples obtained by the author in 2016 (DC16), samples obtained by Dr David Buchs in 2015 (DB15) and samples donated by EAFIT University, Medellín, Colombia to the project (PKSW, SESW, JLSW, LHSW). Analysed alongside these

were a subset of samples from the Scotia arc (DR and SS samples) analysed from powders used in the author's Masters project at the University of Leicester. These were used to help assess the reproducibility of the data by comparing back to pre-existing XRF analyses of these samples performed at Leicester (XRF analyses of these samples performed at Leicester are included in **Appendix C**). ISRMs JA2, JB1a and JG1a were also included in this run.

Major and trace elements of analysed ISRMs fell within 5-10% of reference values for the majority of elements analysed, and r^2 values of >0.995 were reported across all analysed elements in both ICP-OES and ICP-MS (Figure 1). Scrutiny of the data revealed that in JB1a and JA2 the largest outlier was Pb, which was recognised as unreliably measured during analysis by ICP-MS due to mass interferences. If Pb is excluded from analyses of JA2 and JB1a during this run, r^2 values improve to >0.998. However, ICP-MS analyses of JG1a remain just below this due to poorer replication of metallic elements Cr, Ni, Cu and Zn, which vary by more than 25% compared to certified values. Inspection of ICP-OES values for these elements shows similar results.

The second run of ICP-OES and ICP-MS analyses performed at Cardiff University in 2019 consisted of samples obtained by Dr Hugo Fernando Murcia of Caldas University, Manizales, Colombia in 2018 (UB-) in collaboration with the author. Alongside these were run four ISRMs (JB1a, JA2, MRG1 and SDO1). Two duplicate analyses of UB samples were also performed and, as the run of ICP-OES and ICP-MS was performed alongside a set of solutions from another PhD project, MRG1 was

analysed twice during this run, providing both an ISRM standard and a duplicate analysis.

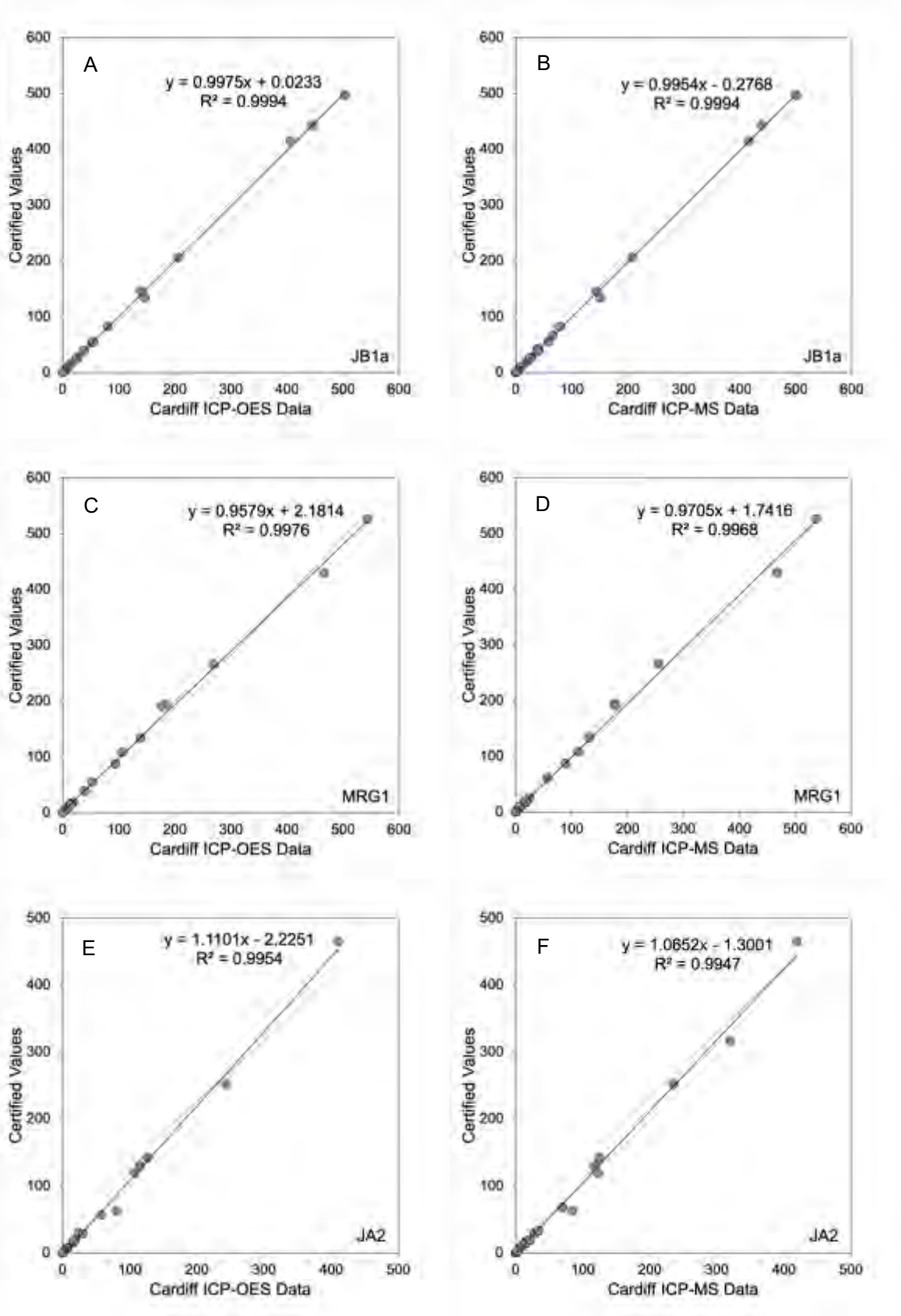

Figure 4.1: Comparison of ISRMs (JA2, JB1a, JG1a) analysed by ICP-OES (A, C, E) and ICP-MS (B, D, F) at Cardiff University in 2017 to certified values.

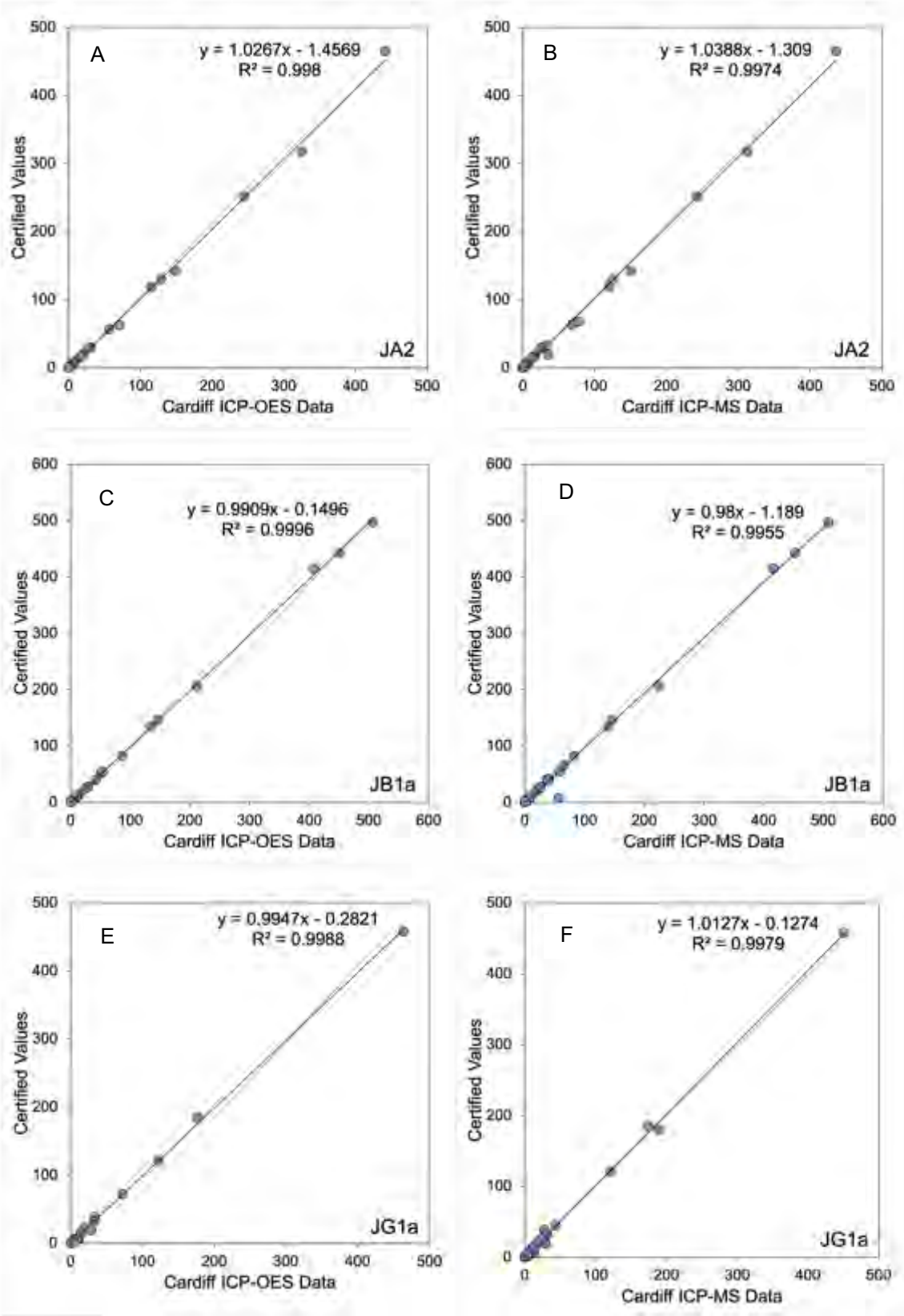
A
y = 1.0267x - 1.4569
R² = 0.998
JA2
Certified Values
Cardiff ICP-OES Data
B
y = 1.0388x - 1.309
R² = 0.9974
JA2
Certified Values
Cardiff ICP-MS Data
C
y = 0.9909x - 0.1496
R² = 0.9996
JB1a
Certified Values
Cardiff ICP-OES Data
D
y = 0.98x - 1.189
R² = 0.9955
JB1a
Certified Values
Cardiff ICP-MS Data
E
y = 0.9947x - 0.2821
R² = 0.9988
JG1a
Certified Values
Cardiff ICP-OES Data
F
y = 1.0127x - 0.1274
R² = 0.9979
JG1a
Certified Values
Cardiff ICP-MS Data

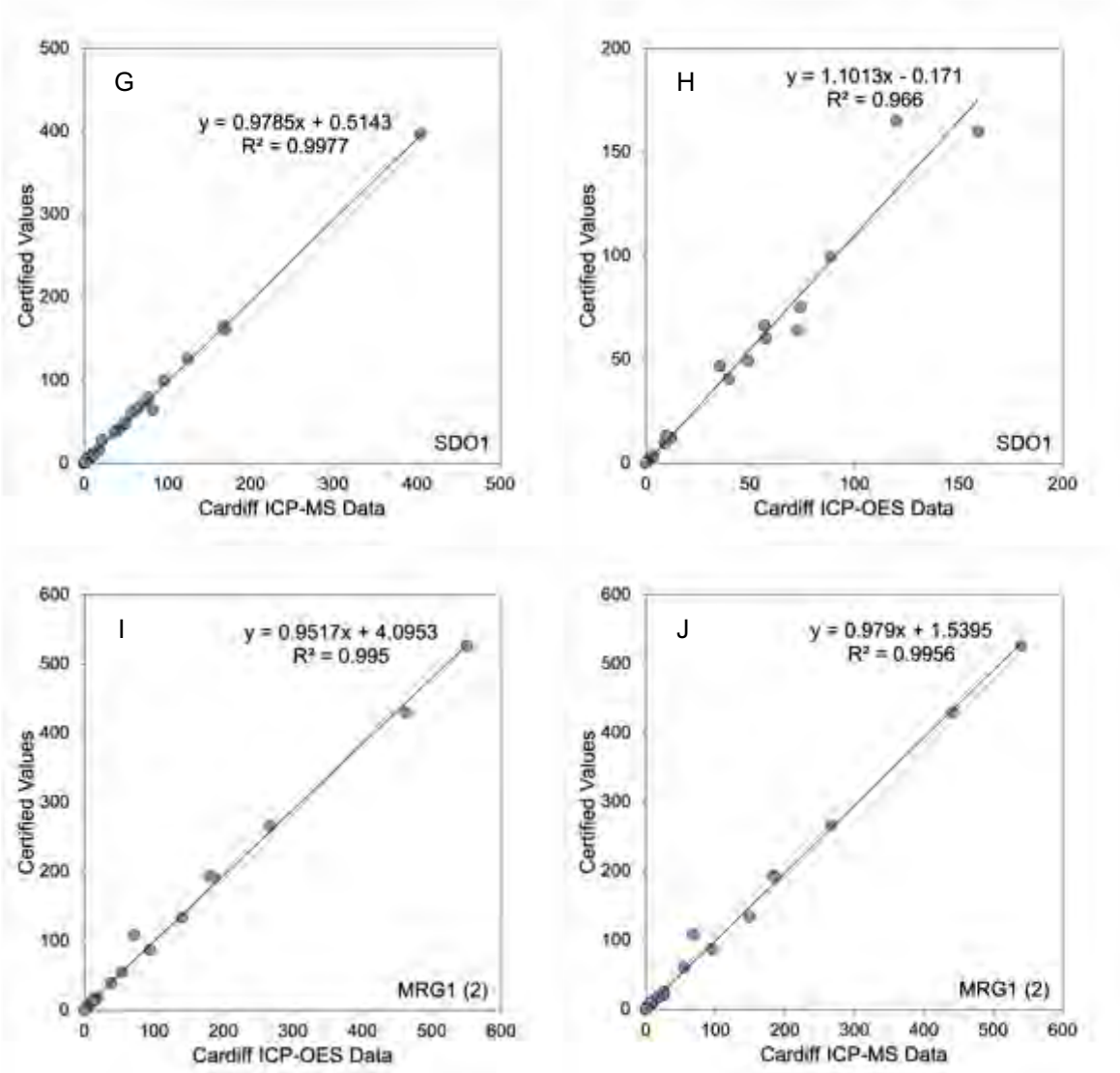

Figure 4.2 (above): Comparison of ISRMs (JB1a, MRG1, JA2, SDO1) analysed by ICP-OES (A, C, E, G, I) and ICP-MS (B, D, F, H, J) at Cardiff University in 2019 to certified values. Note that MRG1 was analysed a twice, this second analysis is recorded as MRG1 (2), and compared to ISRM values in Figure 2 I and F.

Comparison of certified values of ISRM and analyses from ICP-OES and ICP-MS performed at Cardiff in 2019 reveal that JB1a, MRG1 and MRG1 (2) all return r^2 value >0.995 for comparisons of ICP-OES and ICP-MS values compared to certified values (Figure 2). SDO1 returns an r^2 value of 0.966 for ICP-OES data. This is due to >10% difference between analysis and certified values for Sc, Cr, Co, Ni, Zn and Zr. JA2 also returns r^2 values >0.994 for comparisons of ICP-OES and ICP-MS to certified ISRM values. The accuracy of other elements seems good and consistently shows <5% difference for the vast majority of elements analysed. Full raw analyses and values for ISRM standards used can be found in **Appendix C**.

4.3.1.2 Precision/Reproducibility of data:

Data reproducibility was tested during the 2017 ICP-MS and ICP-OES run at Cardiff by re-analysing major and trace elements of samples from the Scotia arc previously analysed by X-ray fluorescence (XRF) at the University of Leicester. These repeat analyses consisted of samples from Saunders island (SS18.15) and seamounts Orca (DR166.4, DR166.7) and Fin (DR167.1, DR167.4).

Samples DR 166.7 and DR 167.1 have overall r^2 values of >0.995 when Leicester XRF data is compared to both ICP-OES and ICP-MS analyses (Figure 3). Sample DR166.4 has slightly lower r^2 values of >0.98 compared to Cardiff ICP data, whilst sample SS18.15 and sample DR167.4 return r^2 values of >0.90 and only >0.5 respectively (see Figure 3). In the case of the later sample, DR167.4 this is largely down to a large discrepancy in Cr values obtained at Leicester compared to those

obtained at Cardiff by both ICP-OES and ICP-MS, and simple removal of Cr increases the r^2 values returned when compared to ICP analyses to >0.9975. Much of the remaining variance between Leicester and Cardiff analyses appears to be from metallic elements, namely from trace element analyses of V, Cr, Co, Ni and Cu. This suggests that some metal contamination may have been introduced during analysis at Leicester or Cardiff or possibly both. Checking of ISRM analyses has shown that there is some variance in these elements between analysed and certified values. This leads us to the conclusion that the analysis of some elements, such as Cr, at Leicester are less accurate than those reported by ICP-OES and ICP-MS than those at Cardiff, but due to the discrepancies observed in JG1a and other standards, analyses of V, Cr, Co, Ni and Cu are treated with caution.

Sample SS18.15 shows by far the greatest variance in major and trace elements of all re-analysed Scotia samples. This is also the only sample amongst the re-analysed Scotia material taken from pre-existing archive material and not processed from hard rock material at Leicester. As this sample was recorded as prepared using a tungsten carbide mill (as opposed to an agate ball mill), this could have introduced contamination, and indeed SS18.15 shows significant variance in Co, Nb and Mo which are likely derived from contamination by a tungsten carbide source (Sertek et al. 2014). However, this does not explain variation in other elements particular to this sample. Prior to analysis at the University of Leicester, sample SS18.15 was collected and crushed as part of project work with the British Antarctic Survey, Cambridge and stored for ~20 years, and a further two years prior to analysis at Cardiff, during which time contaminants could have been introduced to the material.

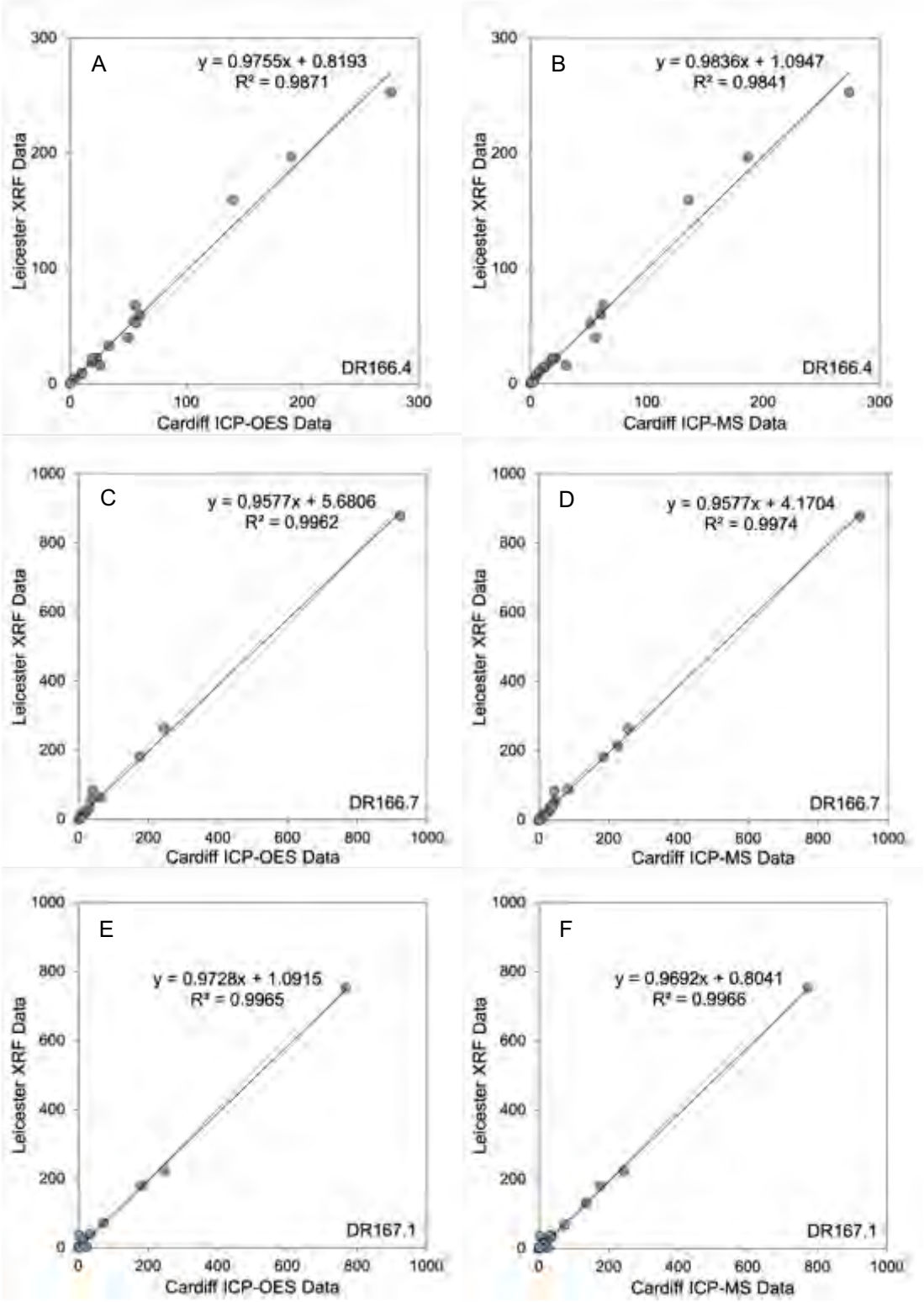
A
y = 0.9755x + 0.8193
R² = 0.9871
DR166.4
Leicester XRF Data
Cardiff ICP-OES Data
B
y = 0.9836x + 1.0947
R² = 0.9841
DR166.4
Leicester XRF Data
Cardiff ICP-MS Data
C
y = 0.9577x + 5.6806
R² = 0.9962
DR166.7
Leicester XRF Data
Cardiff ICP-OES Data
D
y = 0.9577x + 4.1704
R² = 0.9974
DR166.7
Leicester XRF Data
Cardiff ICP-MS Data
E
y = 0.9728x + 1.0915
R² = 0.9965
DR167.1
Leicester XRF Data
Cardiff ICP-OES Data
F
y = 0.9692x + 0.8041
R² = 0.9966
DR167.1
Leicester XRF Data
Cardiff ICP-MS Data

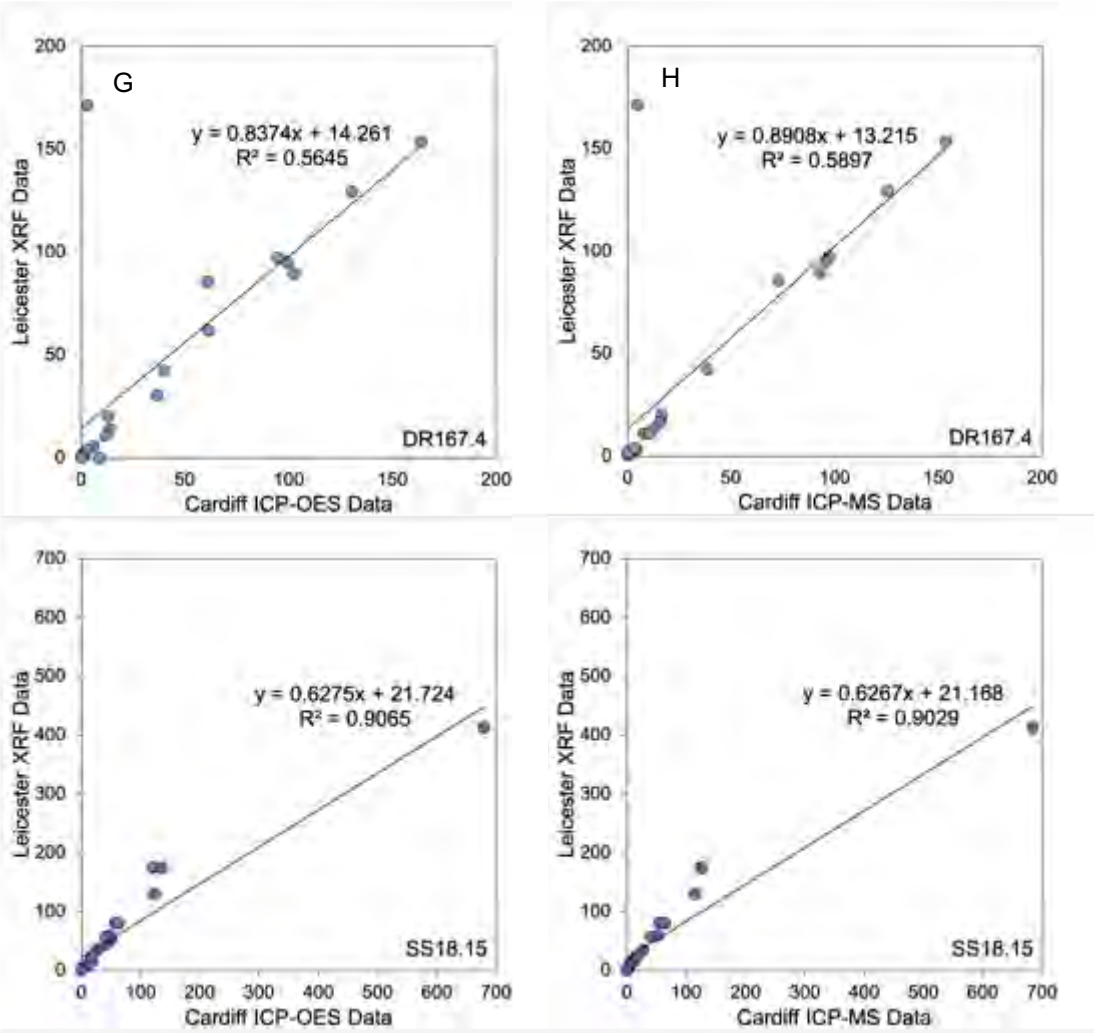

Figure 4.3 (above): Comparison of analyses of rocks from the Scotia arc analysed at Cardiff University by ICP-OES (A, C, E, G, I) and ICP-MS (B, D, F, H, J) to previous XRF analyses obtained at the University of Leicester in 2015.

In the 2019 ICP-OES and ICP-MS run at Cardiff, samples UB-05 and UB-13 were run twice to create replicate analyses to examine reproducibility (analyses UB-05-D and UB-13-D, respectively). Comparison of ICP-OES and ICP-MS analyses of these samples (Figure 4) reveals r^2 values of >0.9995.

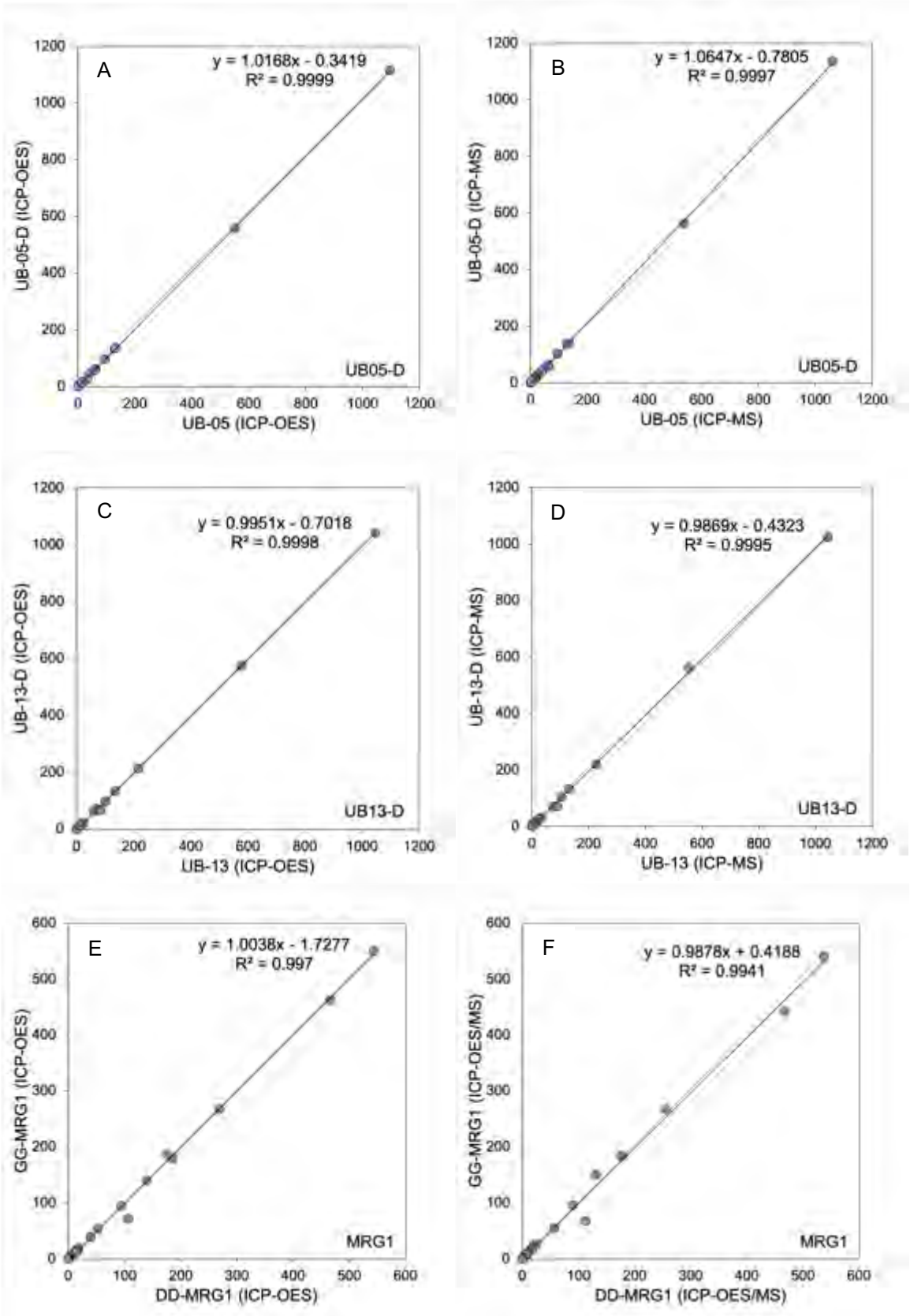

Figure 4.4: Duplicate analyses of two UB (UB-05 and UB-13) samples performed on ICP-OES (A, C) and ICP-MS (B, D) at Cardiff University in 2019. An additional duplicate is provided by two analyses of the ISRM MRG1 by ICP-OES (Figure 4 E) and ICP-MS (Figure 4 F) during the same analytical run.

4.3.1.3 LOI and oxide totals:

Sample collection in this study was performed in low latitude regions, where tropical weathering can have a significant impact on the character of outcrop. Tropical weathering alters rocks at a greater rate than that seen in temperate climates, due to higher available water in humid conditions promoting production of silicic acids (Summerfield, 1997). The volcanoes of the Colombian arc are topographically prominent (>4,500 metres) but the majority of their accessible outcrop, especially of older sequences, lies at significantly lower altitudes with large amounts of tropical vegetation and high rainfall (e.g.: Lescinsky, 1990; Pardo et al. 2019). Many of these volcanic complexes are also sites of active hydrothermal systems producing acid waters and extensive hydrothermal alteration in outcrop (e.g.: Forero et al. 2011; Williams et al. 2017; Pardo et al. 2019). These factors combine to alter primary minerals to secondary alteration products, such as clays.

Whilst great care was taken in the field to ensure samples were relatively unaltered, and any altered fragments were removed, some analysed samples may have had significant alteration. Petrography and geochemistry of samples are used to constrain this, but loss on ignition also provides us a useful tool to identify the more altered samples in this study. Figure 5 shows a plot of LOI against calculated total oxides. All samples but one (DB15-081) fall within 1.5% of a 100% total. The majority of LOI values fall within ±2.5 wt.%, though a small number of DC16 and DB15 samples, along with one Scotia analysis (DR166.7) and one EAFIT sample (LHSW-18F) fall outside of this. DR samples of Scotia are submarine dredge collections, which could explain high LOI in some instances.

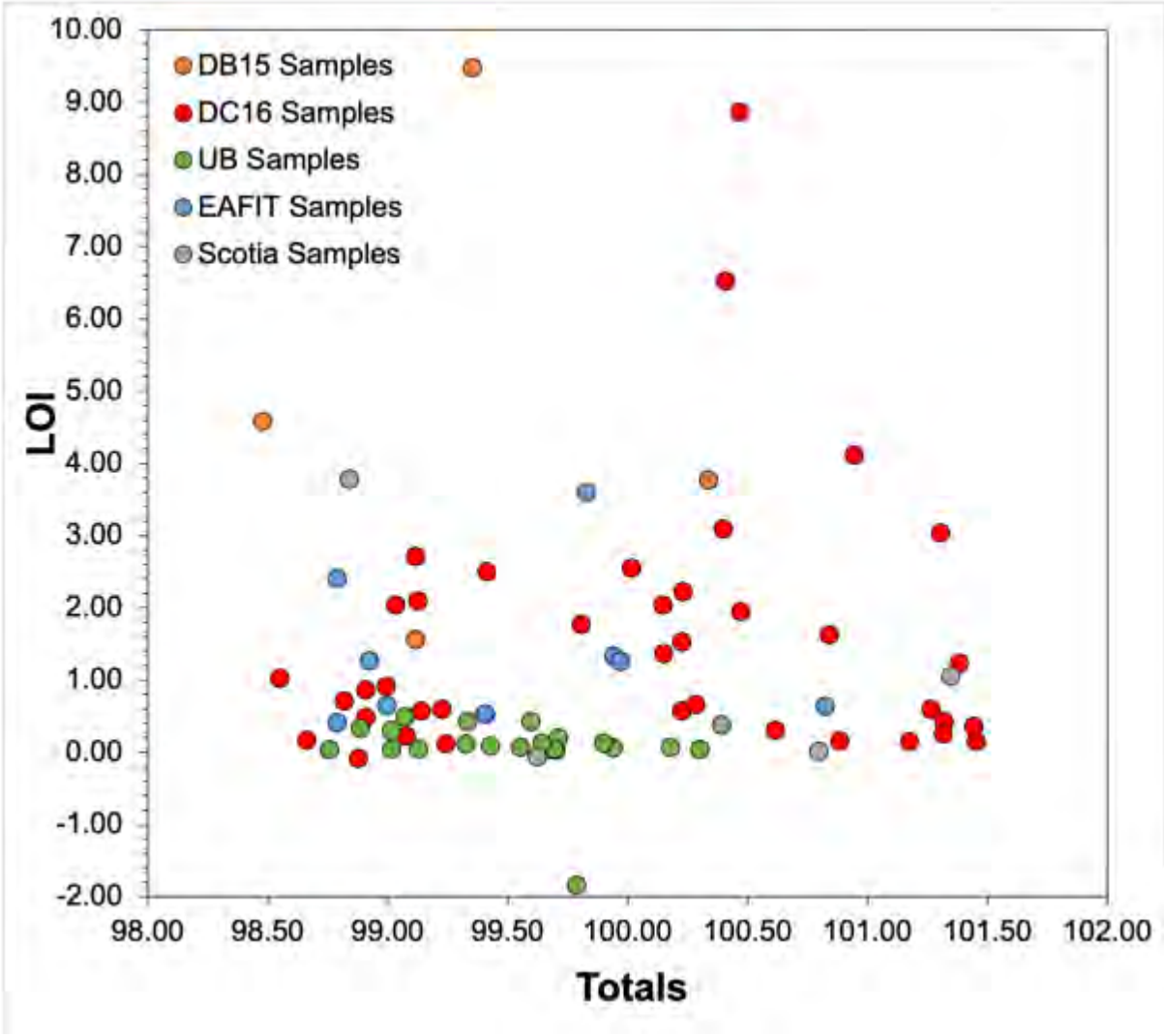

Figure 4.5: Plot of Loss on ignition (LOI) values for samples versus recorded oxide totals. All samples but one fall within ±1.5% of a 100% total, whilst the majority of samples have LOI values <2.5 wt.%. A minority of DB15 and DC16 samples fall well outside this range, potentially due to alteration or possibly introduction of moisture during analytical preparation.

There appears also to be a correlation between oldest lava sequences of the volcanic complexes (e.g.: Duque-Trujillo et al. 2010; Martinez et al. 2014) and higher LOI. This also appears to be the case for some of the older intrusions (DB15 samples) collected, and for some basement rocks (i.e.: DB15-087). This correlation between high LOI and older parts of complexes or intrusions is likely down to greater

degrees of both weathering with age and extensive hydrothermal alteration (Forero et al. 2011), which is also evident in petrography (see **Appendix A**). All new analyses in this study are recalculated to anhydrous total compositions for geochemical scrutiny. For comparative data from other studies this is done wherever possible from the available data. Raw analyses of all data are available in **Appendix C and D**.

5 The Northern Volcanic Province of Colombia

5.1 Setting of the Samples:

The Northern Volcanic Province (NVP) of Colombia (Errázuriz-Henao et al. 2019) is the northernmost active segment of the Northern Volcanic Zone (NVZ) of the Andes (Bourdon et al. 2003; Marín-Cerón et al. 2019) and is located along the Central Cordillera of Colombia (Figures 5.1a and 5.1b). The known extent of the NVP stretches from the newly discovered edifices of the Semana Monogenetic Field in the north to the Pijao Monogenetic Field in the south (Figure 5.1b) (Martínez et al. 2014; Monsalve et al. 2017a; Murcia et al. 2019). The samples in this study are derived from the polygenetic volcanoes Cerro Bravo (CBV), Nevado del Ruiz (NRV) and Paramillo de Santa Rosa (PSR) as well as the monogenetic domes and lava flows of the Villamaria-Termales Monogenetic Field (VMTVF), located between CBV and NRV (Figures 5.1b & 5.1c).

The NVP shows abundant evidence of historic activity (e.g.: Lescinsky, 1990; Murcia et al. 2010; Pinzon et al. 2018) and is heavily monitored by the Servicio Geologico Colombiano (e.g.: Londoño, 2016; Martínez et al. 2014; Pulgarin et al. 2017). Nevado del Ruiz, Cerro Bravo and Paramillo de Santa Rosa have had multiple eruptive episodes in the Holocene and historic time (e.g.: Thouret et al. 1990; Lescinsky, 1990a; Martínez et al. 2014; Monsalve et al. 2017b; Pinzon et al. 2018).
The NVP overall is considered in a state of unrest, based on monitoring of gas emissions and seismic events (Londoño, 2016).

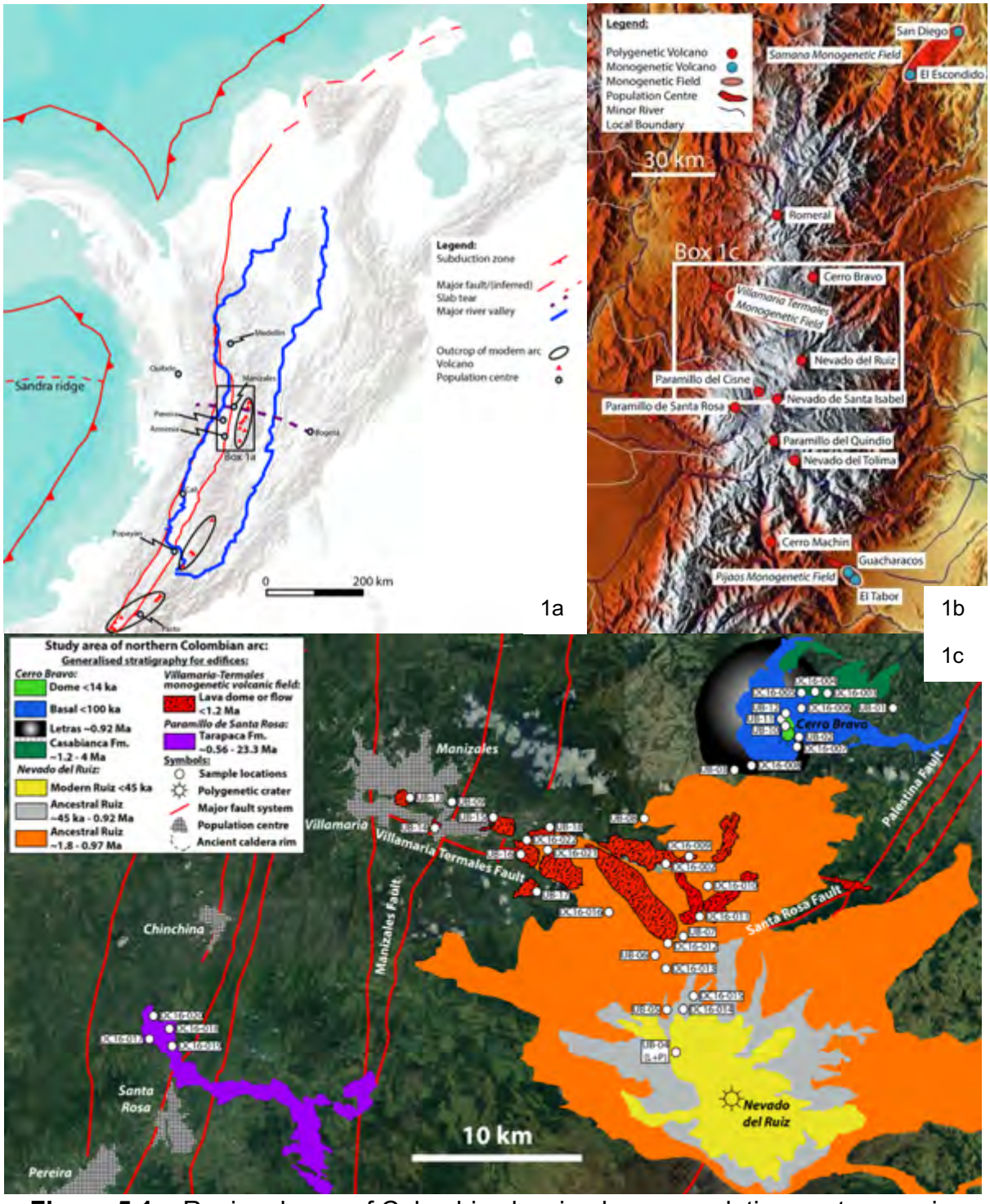

Figure 5.1a: Regional map of Colombia showing large population centres, major terrane bounding faults and location of active volcanoes and segments of the Colombian arc. Figure 1b: Location of polygenetic and monogenetic volcanoes and fields within the Colombian Northern Volcanic Province (NVP). Figure 1c: Detailed map ofstudy regional, including regional geology and mapped extent of products of Nevado del Ruiz, Cerro Bravo and Ancestral Paramillo de Santa Rosa.

The basement of the NVP consists of terranes of the Central and Western Tectonic Realms, intruded by Cretaceous, Paleogene, Eocene and Miocene plutonic bodies and stocks (Gomez et al. 2015; Murcia et al. 2018 and references therein). The majority of the basement beneath Cerro Bravo, the VMTVF, Nevado del Ruiz and the proximal deposits of Paramillo de Santa Rosa (Figure 1c) consists of late Palaeozoic and Mesozoic units, intruded by Eocene plutonic bodies (Cochrane et al. 2014). The most predominant of these is the Paleozoic to early Mesozoic Cajamarca-Valvidia Complex, composed of amphibolitic, graphitic and semi-pelitic schists and marbles of greenschist to epidote amphibolite facies (e.g.: Cediel and Cáceres, 2000; Cediel et al. 2003; Cediel, 2011; Leal-Mejía et al. 2019). This forms the majority of the basement of the Central Cordillera west of the Palestina Fault where it bounds the Mesoproterozoic Chicamocha Terrane (Murcia et al. 2018; Leal-Mejía et al. 2019). The Palestina Fault itself is interpreted as the primary conduit for magmatism along the NVP (e.g.: Cediel and Cáceres, 2000; Martínez at al. 2014). In faulted contact west of the Cajamarca-Valvidia Complex along the edge of what is today the Central Cordillera are a series of terranes including oceanic arc, oceanic plateau, ophiolite and epiclastic basinal sediment sequences that were accreted to the continental margin in the late Mesozoic (Villagomez et al. 2011; Villagomez and Spikings, 2013; Cochrane et al. 2014a;b; Marín-Cerón et al., 2019) as part of the Romeral Melange. This includes the late Cretaceous volcanic and metasedimentary rocks of the Quebradagrande Complex; consisting of gabbros, diorites, basalts, andesites and tuffs of unmetamorphosed to greenschist facies. The origin of Quebradagrande complex is debated (e.g.: González, 1980; Nivia et al. 2006), but is mostly likely related to an accreted late Cretaceous island arc (Toussaint and Restrepo, 1994).

Cerro Bravo (based on Lescinsky, 1990 and Pinzon et al. 2018)	**Villamaria-Termales Monogentic Volcanic Field** (based on Osorio et al. 2018a,b; Murcia et al. 2018)		**Nevado del Ruiz** (after Martinez et al. 2014)	**Paramillo de Santa Rosa** (after Monsalve et al. 2017b)
Cerro Bravo Dome <14 ka to Present	**Post-Glacial Group:** Lusitania Lavas, *La Laguna Dome, Santana Dome (Martinez et al. 2014)*, El Plato Dome, Santa Luis Dome Post glacial; <0.045 ± 0.010 Ma.		**Second Eruptive Period (SER)** <0.045(?) Ma to Present	**Modern Paramillo de Santa Rosa** 0.26 Ma to Present
Basal Cerro Bravo <50 ± 50 ka**	**Ancestral Group 2:** Gallinazo Dome, Amazonas Dome, Victoria Dome, La Negra Dome, La Oliva Dome, Sabinas Dome. Between ~1.8 Ma and 0.045 ± 0.010 Ma from glacial evidence.	**Inter-Ruiz linked:** *La Esperanza Fissure (Martinez et al. 2014) ~<0.2 - 0.045 Ma based on relationship to INTER-Ruiz products and glacial evidence.*	**Intermediate Eruptive Period (INTER)** <0.2(?) Ma* to ~0.045(?) Ma	
Quebrada Seca Caldera 0.92 ± 0.06 Ma*			**First Eruptive Period (PER)** <0,97 Ma* to ~0.2 Ma?*	**PSRV First Eruptive Period** ~0.5 to 0.26 Ma
		Ancestral Group 1: Sancancio Dome dated 1.2 ± 0.08 Ma**; Tesorito Dome dated 1.2 ± 0.2 Ma**	**PRE-Ruiz Eruptive Period (PRE)** Maximum and Minimum ages: 1.8 ± 0.1 Ma to 0.97 ± 0.05 Ma*	**PRE-Paramillo de Santa Rosa** 2.3 - 0.56 Ma

Basement: Mio-Pleistocene Volcano-sedimentary formations (i.e.: Casabianca Fm) (Borrero & Naranjo, 1990); Quebradagrande and Cajamarca-Valavidia Complexes

*ages after Thouret et al. 1990
**ages after Thouret et al. 1985

Figure 5.2: Comparative stratigraphy of Cerro Bravo, Nevado del Ruiz, Paramillo de Santa Rosa and the VMTVF.

The two major plutonic bodies, the Manizales Stock and El Bosque Batholith, underly the study area. These are Eocene post-collisional granitoids related to a limited (>10 Ma) phase of magmatism (Bustamante et al. 2017; Leal-Mejia et al. 2018). These granitoids contain zircons inherited from Cajamarca-Valvidia Complex, and isotopic evidence suggests a moderate degree of crustal contamination in their formation (Bustamante et al. 2017). They have “adakite-like” high Sr/Y ratios, leading speculation that these granitoids are the result of either post-collisional delamination of the lower crust following the end of Cretaceous subduction, or a brief resumption

of subduction by Caribbean Large Igneous Province (CLIP) or Farallon lithosphere along the Colombian Pacific margin (Leal-Mejia et al. 2018). Minor Oligo-Miocene plutonic stocks are recorded in the vicinity of the NVP (Gomez et al. 2015; Bissig et al. 2017; Marin-Ceron et al. 2019; Figure 1c). These basement terranes and intrusions are overlain by a collage of Miocene to Pleistocene sedimentary, volcanoclastic and volcanic sequences (Martínez et al. 2014; Pulgarin et al. 2017; Murcia et al. 2018 and references therein) derived from the current arc edifices and preceding Miocene arc segments (e.g.: Borrero and Naranjo et al. 1990; Martínez et al. 2014; Pulgarin et al. 2017; Leal-Mejia et al. 2019; Marín-Cerón et al. 2019). These basement lithologies are represented in this study by samples UB-01 (Cajamarca-Valvidia Complex); UB-08 and DC16-022 (Manizales Stock) and UB-09 (Quebradagrande Complex).

5.1.1 Nevado del Ruiz (NRV) and the Villamaria Termales Monogenetic Volcanic Field (VMTVF):

Nevado del Ruiz is by far the best studied and characterised edifice in the NVP (e.g.: Martínez et al. 2014), especially following the November 1985 eruption, which created a lahar that destroyed the town of Armero, causing >23,000 deaths. Study of Ruiz has included geochemical characterisation of the eruptive products (e.g.: Vatin-Perignon et al. 1990; Melson et al. 1990; Sigurdsson et al. 1990) and detailed stratigraphic mapping (e.g.: Thouret et al. 1985; 1990; Borrero et al. 2009; Martinez et al. 2014).

Recent work has updated this stratigraphy and outlined four eruptive periods for NRV (Martinez et al. 2014; Figure 5.3). These are the **Ancestral Ruiz Eruptive Period**, which includes largely effusive eruptive products (mainly extensive lava flows) deposited over basement and topped by an unconformity marked by the appearance of volcanic avalanche deposits (Martínez et al. 2014); K/Ar ages for this period are between ~1.8 and 0.97 Ma (Thouret et al. 1990). Overlying these are deposits of the **First Ruiz Eruptive Period**, which proceeded initially with an effusive constructive phase followed by a later, caldera forming destructive phase of activity. Known K/Ar ages for this eruptive period are ~0.2 Ma (Thouret et al. 1990). This is overlain unconformably by the deposits of the **Intermediate Ruiz Eruptive Period**, composed of lava domes. La Esperanza monogenetic dome and flow is included in this eruptive period (Martínez et al. 2014; Figure 1c). Lastly, the **Second Ruiz Eruptive Period** comprises the deposits erupted since around the end of the last glacial maximum to the present day. In the study of Martínez et al (2014), this period also incorporates the monogenetic domes and flows of La Laguna and Santana (Figure 1c). In this study, Ruiz samples are divided into groups related to the above outlined Eruptive Periods (after Martinez et al. 2014). Ancestral Ruiz samples are those sampled from the mapped extent of the First Ruiz Eruptive Period (~1.8 to 0.97 Ma) whilst the Antique Ruiz samples are sampled from a combination of the Second and Intermediate Ruiz eruptive periods (~0.97 to 0.2 Ma), with the exception of La Laguna and Santana domes, which are part of the VMTVF (Figures 5.1c and 5.3).

The Villamaria-Termales Monogenetic Field consists of 14 distinct domes and flows, situated between Cerro Bravo and Nevado del Ruiz. It was not until recently that these were recognised and classed as a distinct volcanic field (Osorio et al. 2018a,b;

Murcia et al. 2018), having previously been considered products of Ancestral NRV volcanism (I.e.: Borrero et al. 2009; Toro et al. 2010; Martínez et al. 2014). The field was first characterised as a whole by the studies of Osorio et al. (2018a, b) who identified monogenetic volcanoes aligned along the Villamaria-Termales Fault (Figures 1c and Figure 4).

The domes and flows of the Villamaria-Termales Volcanic Field (VMTVF) have been linked to the activity of Nevado del Ruiz due to their proximity as well as petrological and geochemical similarity to some eruptive periods (e.g.: Toro et al. 2008; Borrero et al. 2009; Martínez et al. 2014). Previous studies of the area have mapped the domes and flows of the VMTVF as part of Nevado del Ruiz (e.g.: Thouret et al. 1985; 1990). However, there are notable differences in the petrological and geochemical characteristics of the VMTVF and products of Nevado del Ruiz (e.g.: Borrero et al. 2009; Toro et al. 2010; Martinez et al. 2014).

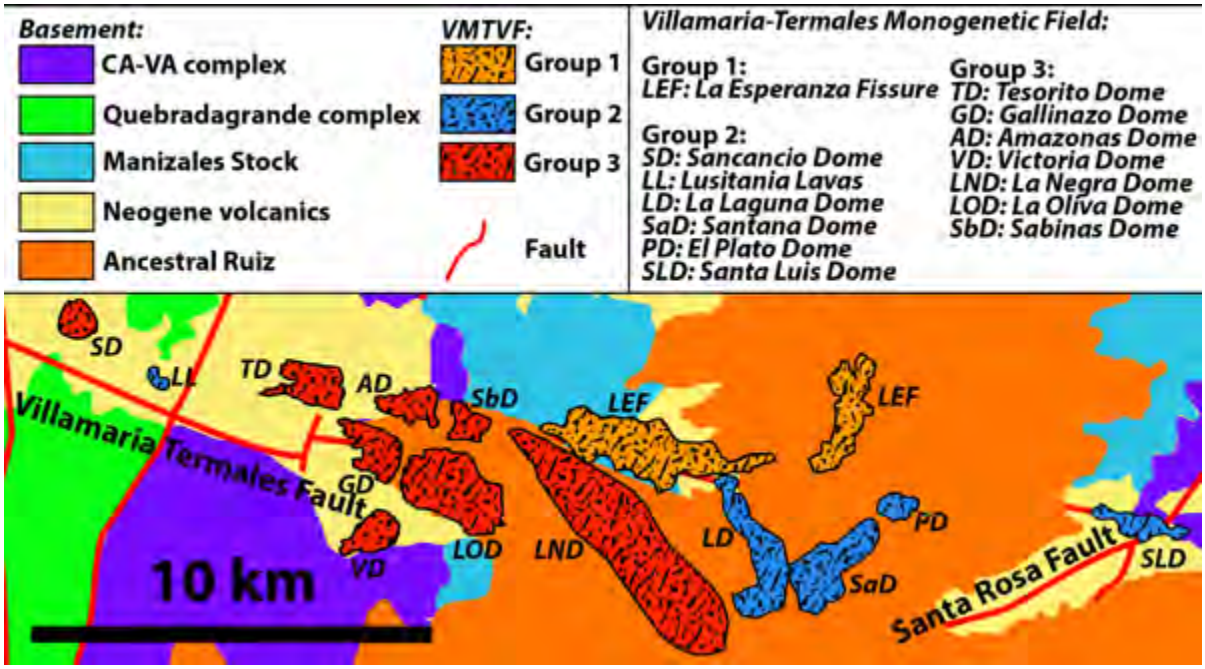

Figure 5.3: Inset map of the Villamaria-Termales Monogenetic Field (VMTVF), including underlying geology (as per Figure 1c). These are colour grouped, with Ancestral (i.e: pre-glaciation) domes and flows in red; young post-glaciation domes marked in purple, with known or approximate ages. Adapted after Osorio et al. (2018).

The VMTVF can be subdivided into two age groups based on dating, stratigraphic, palaeomagnetic and geomorphological relationships. The only absolute ages for the field so far are recorded for Sancancio and Tesorito domes, in the west of the field (Figure 5.3) dated at 1.2 ± 0.08 Ma and 1.2 ± 0.2 Ma by K/Ar, respectively (Thouret et al., 1985). These belong to a larger “Ancestral Group” (Figure 5.1c and Figure 5.2) which pre-dates glacial action in the area (~45,000 years) and also includes Gallinazo, Amazonas, La Negra, La Oliva, Sabinas and possibly Victoria dome. However, Victoria dome has not been previously analysed or well-studied and the analyses here will be the first assessment of this edifice in the context of the VMTVF. A further subgroup of this is the La Esperanza fissure, which contrasts the rest of the field in composition, being by far the most mafic in composition and with its relationship to glacial geomorphology and the products of NRV providing a tighter age bracket ~0.2 - 0.045 Ma (Martínez et al. 2014; Osorio et al. 2017a).

A second, Post-Glacial group has been identified by its relationship to products of NRV and glacial landforms. This consists of the domes La Laguna, Santana, El Plato, San Luis and the Lusitania lavas (Osorio et al. 2018a). All of these are located to the east of the field, with exception to the Lusitania lavas, which are in the far west (Figure 5.3).

5.1.2 Cerro Bravo (CBV):

Cerro Bravo is located ~25 km east of Manizales along the axis of the Central Cordillera (Figure 5.1c) and represents one of the northernmost polygenetic edifices of the NVP (Murcia et al. 2018), with the exception of the poorly studied Romeral volcano and monogenetic fields further north (Figure 5.1b).

The CBV has produced numerous Holocene fall and flow deposits erupted <6.2 ka which mantle much of the area surrounding the volcano (Lescinsky, 1990). The edifice itself overlies older sequences from a previous caldera edifice, and is composed of steep sided lava sequences which are dated by K/Ar to ~50 ± 50 ka (Thouret et al. 1990). This is capped by a large intercrater lava dome, dated at ~14 ka, giving the current CBV edifice an eruptive history of <100 ka (Lescinsky, 1990; Pinzon et al. 2018).

The longer history and stratigraphy of Cerro Bravo is far less well characterised than the neighbouring volcanoes. The oldest age for volcanic products in the area of CBV is 0.92 ± 0.06 Ma (Thouret et al. 1990) which is attributed to the Quebrada Seca Caldera which can be thought of as “Ancestral” phase for Cerro Bravo, comparable to that of Nevado del Ruiz, whose activity preceded the formation of the modern CBV edifice (Thouret et al. 1988; Lescinsky, 1990). This earliest phase of eruption is however poorly sampled, being characterised by only a small number of geochemical analyses. No detailed mapping of this caldera phase has been undertaken; nevertheless, the current edifice sits within a ~3km semi-circular caldera structure to the southwest, hypothesised to be a crater/caldera wall (Lescinsky, 1990; Figure 5.1c

and Figure 5.2). The age obtained by Thouret et al. (1990) comes from the Letras Volcano-Tectonic Depression, to the west and south of this structure (Lescinsky, 1990). Critically, the known ages of eruptive products of Quebrada Seca and Cerro Bravo imply an evolution through time from south to north (Pinzon et al., 2017) which could link the early Cerro Bravo activity to some of the early products of the VMTVF.

5.1.3 Paramillo de Santa Rosa (SRV):

Paramillo de Santa Rosa is located ~10 km off the axis of the main volcanic arc and is the furthest west of the NVP edifices (Figure 5.1b). Based on recent mapping and fieldwork (Pulgarin et al. 2017) Paramillo de Santa Rosa (SRV) can be divided into two distinct eruptive phases. These are the PRE-Paramillo de Santa Rosa (PRE-PSR), lasting from 2.3 to 0.56 Ma; and the second, current edifice of Paramillo de Santa Rosa (PSR), whose eruptive record lasts from 0.56 Ma to the Holocene (Monsalve et al. 2017b). For brevity, “SRV” herein refers to discussion of the activity of Paramillo de Santa Rosa throughout its two phases of eruptive history; specific discussion of activity in each phase will be referred to as PRE-Paramillo de Santa Rosa (PRE-PSR) and Paramillo de Santa Rosa (PSR), respectively.

PRE-PSR volcanism was initially effusive, followed by more explosive eruptive behaviour after ~0.56 Ma (Pulgarin et al. 2017). The initial products of this volcanism were mostly andesitic lava flows. The samples analysed in this study are from this earliest phase of activity, dated by K/Ar to 2.3 ± 0.1 Ma (Thouret et al. 1990). Later activity was predominantly destructive with gravitational collapse events creating

significant deposits on the west flank of the volcano (Monsalve et al. 2017b; Murcia et al. 2017).

5.2 Characterisation of the Samples:

5.2.1 Petrography of the samples:

5.2.1.1 Overview:

Petrographically, the rocks of the NVP are typical of intermediate volcanic rocks, with the dominant common phenocryst phases being plagioclase and clinopyroxene, with variable small quantities of olivine, amphibole, biotite and quartz reported in the polygenetic and monogenetic volcanoes across the province (e.g.: Laeger et al. 2013; Murcia et al. 2018; Marín-Cerón et al. 2019; Errázuriz-Henao et al. 2019). Extended petrographic descriptions of all samples in this study can be found in **Appendix A**.

5.2.1.2 Nevado del Ruiz (NRV):

Twelve samples were collected from Nevado del Ruiz during this study. The petrography of Ruiz has been studied in detail previously and is reasonably consistent across all mapped eruptive phases (Martínez et al. 2014), further detailed in **Appendix A**. Petrographically, products of NRV are dominantly porphyritic, two-pyroxene andesites and amphibole andesites (e.g.: Martínez et al. 2014). The major porphyritic phases are plagioclase, pyroxenes, amphibole or occasionally biotite, alongside groundmass phases of plagioclase, clinopyroxene, orthopyroxene,

amphibole, opaques and biotite. The groundmass is consistently 65 – 85% of the samples. Disequilibrium textures such as reaction rims, glass and matrix inclusions in phenocryst phases, intergrowth of pyroxenes and corrosive edges are ubiquitous. However, there is variance in the proportion of accessory phases between different age segments of Ruiz. In particular, amphibole contents equal to clinopyroxene content is observed for some Ruiz Ancestral samples, whilst pyroxene and especially clinopyroxene is more prevalent in subsequent eruptive phases. The only exception is in the modern Ruiz eruptive period, where amphibole content has a similar abundance to clinopyroxene in some flows. Plagioclase appears as a phenocryst or microphenocryst in all sections, usually identifiable by characteristic polysynthetic twinning and with sieve textures and oscillatory zoning of phenocrysts.

For example, UB-06 (Figure 5.5) has a microcrystalline to cryptocrystalline matrix largely composed of plagioclase and pyroxene microlites and opaques. The dominant phenocryst phases are euhedral to subhedral plagioclase, clinopyroxene and orthopyroxene. The pyroxenes show corroded edges and also form glomercrysts (Figure 5.5). Biotite and amphibole also occur as minor accessory phases (<5%), along with opaques in larger proportions. This is representative of petrography previously described for this area of Ancestral Ruiz, where relatively unaltered (Martinez et al. 2014). The Ancestral Ruiz phase is also represented by samples DC16-012 and DC16-021, though these present a greater degree of alteration than UB-06 (Figures 5.6 and 5.7). DC16-012 (Figure 5.6) has plagioclase, amphibole, pyroxene and biotite phenocryst, with amphibole in equivalent proportions to pyroxene. This is consistent with flows in the northern sectors of Ancestral Ruiz with a greater proportion of amphibole compared to other flows (Martinez et al. 2014). DC16-021 displays sericite alteration in plagioclase, and epidote alteration to

pyroxene. Main phenocryst phases are euhedral zoned plagioclase, pyroxene (predominantly clinopyroxene) along with lesser amounts of amphibole and biotite. Groundmass is altered to clays but where relict crystals are present appears dominated by a micro- to cryptocrystalline texture of plagioclase, pyroxenes and opaque minerals.

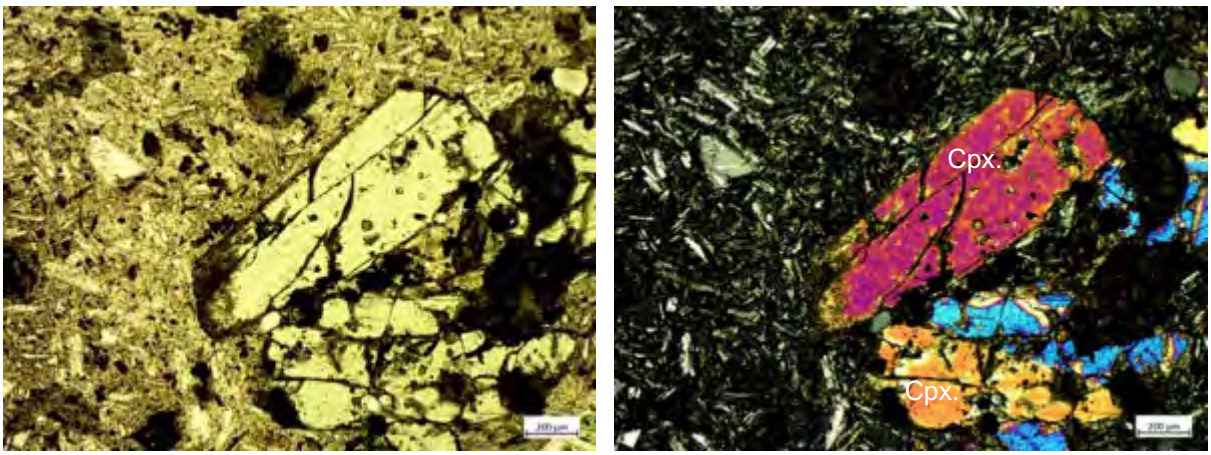

Figure 5.5: Thin section images in plane polarised light (PPL) and cross polarised light (XPL) for UB-06, from lava flows related to the Ancestral phase of Nevado del Ruiz. Large euhedral (clino- and ortho-)pyroxene phenocrysts representative of those in section; some occurrences of pyroxene as glomerocrysts. Groundmass consists of small (<0.5 mm) laths of (plagioclase) feldspar and pyroxene, and other constituent minerals. Plagioclase laths exhibit a tracytic flow texture in some cases.

The younger phases of Nevado del Ruiz (Antique and Modern) show only small variations from the Ancestral phase. In general, lava flows are porphyritic with plagioclase and pyroxenes as the major phenocryst phases. Clinopyroxene (augite) is more predominant than orthopyroxene. Amphibole and/or biotite can occur as accessory phases in groundmass and as phenocrysts. Groundmass is micro- to cryptocrystalline and consists of microcrysts reflective of main phenocryst phases. Disequilibrium textures (e.g.: sieve and honeycomb textures in plagioclase, intergrowth textures of pyroxenes and reaction coronas) are common.

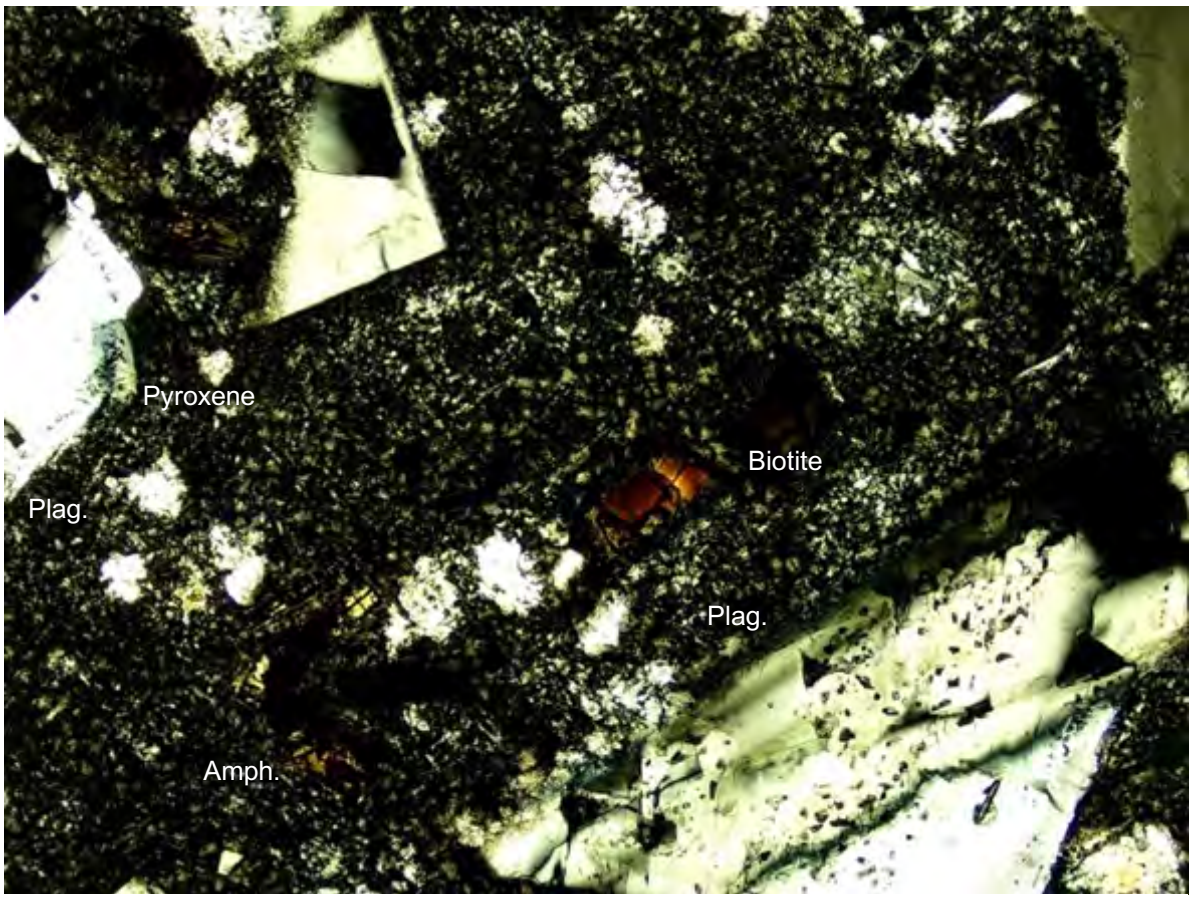

Figure 5.6: Thin section capture of DC16-012, altered material collected from lava flows of the Ancestral phase of Nevado del Ruiz, in plane polorised (left) and cross polarised (right) light. Note the preservation of biotite (centre of section), pyroxenes and large laths of feldspar amongst altered glassy groundmass. Field of view 5mm.

5.2.1.3 Villamaria-Termales Monogenetic Volcanic Field (VMTVF):

Nine samples were collected from the domes and flows of the Villamaria-Termales Monogentic Voclanic Field (VMTVF) for this study. Previous studies have established that the VMTVF has a ubiquitous mineralogy of plagioclase and pyroxene, with differing proportions of amphibole, olivine ± quartz (Osorio et al. 2018b). In this study, the VMTVF is divided into three groups, based on largely on geochemistry and age (Figure 5.3).

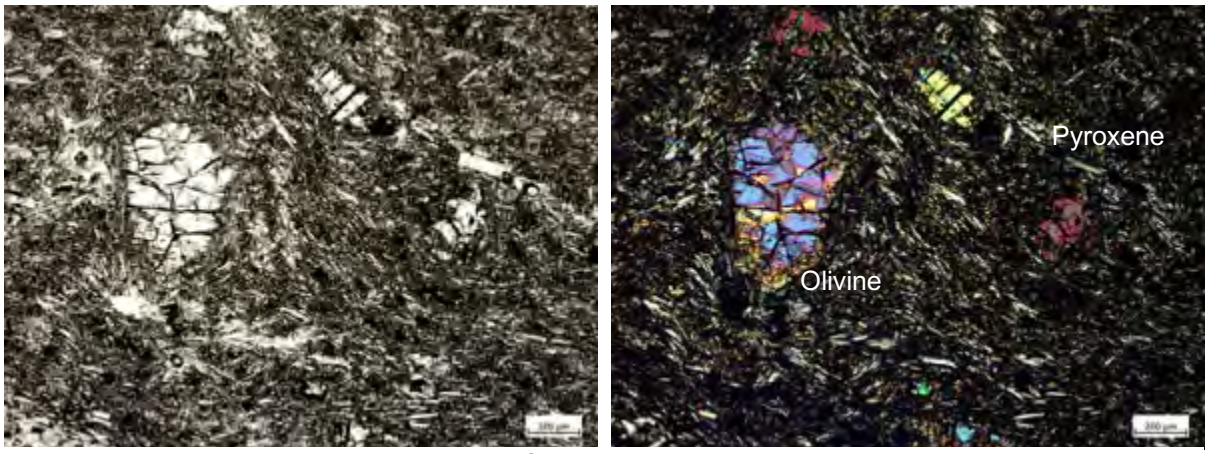

Figure 5.7: Thin section captures for La Esperanza Fissure, showing the typical tracytic flow texture defined by small plagioclase laths in a groundmass of olivine and pyroxene microphenocrysts. Larger phenocrysts in La Esperanza samples sparse and predominantly olivine followed by orthopyroxene.

Group 1 is composed of samples from La Esperanza fissure (Figure 5.7). These rocks are composed largely of microcrystalline groundmass of olivine, pyroxene and plagioclase with the later defining a trachytic texture, Olivine is the only major phenocryst phase.

Groups 2 and 3 are mineralogically diverse, consisting of plagioclase and pyroxene as ubiquitous phases, but also olivine (in the case of Santana and La Negra domes), amphibole, quartz (Gallinazo dome) and potassium feldspar (La Laguna and El Plato domes) (Osorio et al. 2018b). One previous study does report an olivine-bearing sample from Amazonas, but this is attributed to missampling (Osorio et al. 2018b).

In this study, the Group 3 domes of Gallinazo and Victoria are studied petrographically. Gallinazo is sampled in UB-16 (Figure 5.8) and is a porphyritic rock with phenocrysts of euhedral plagioclase (with disequilibrium textures), euhedral quartz and pyroxene (orthopyroxene and clinopyroxene) along with microphenocrysts

of amphibole with opaque reaction rims. Groundmass is crypto- to microcrystalline with some devitrified glass.

In comparison, Victoria dome (UB-17) is made up of phenocryst phases of euhedral pyroxene, subhedral plagioclase with disequilibrium textures and subhedral amphibole microphenocrysts (Figure 5.9). Groundmass is which is micro- to cryptocrystalline, composed of microliths of plagioclase and pyroxene. Reaction rims are observed on pyroxene and especially amphibole phenocrysts. Clinopyroxene also appears as anhedral inclusions within large plagioclase phenocrysts.

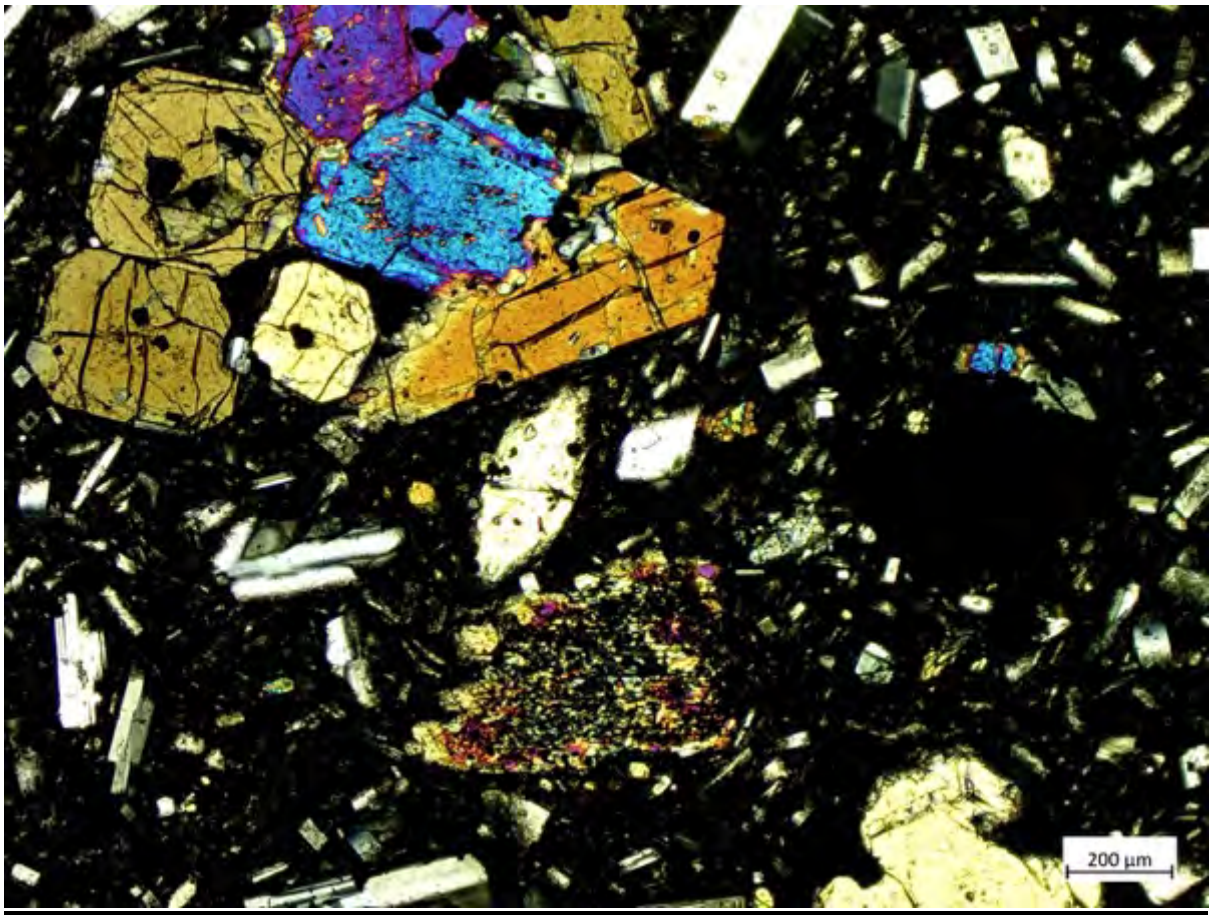

Figure 5.8: Cross polarised light image of sample UB-16 Gallinazo Dome, part of the Group 3 of the VMTVF. Here a pyroxene and amphibole glomerocryst Minor phenocrysts of plagioclase and quartz predominate in section alongside hornblende and amphibole in an aphanitic groundmass.

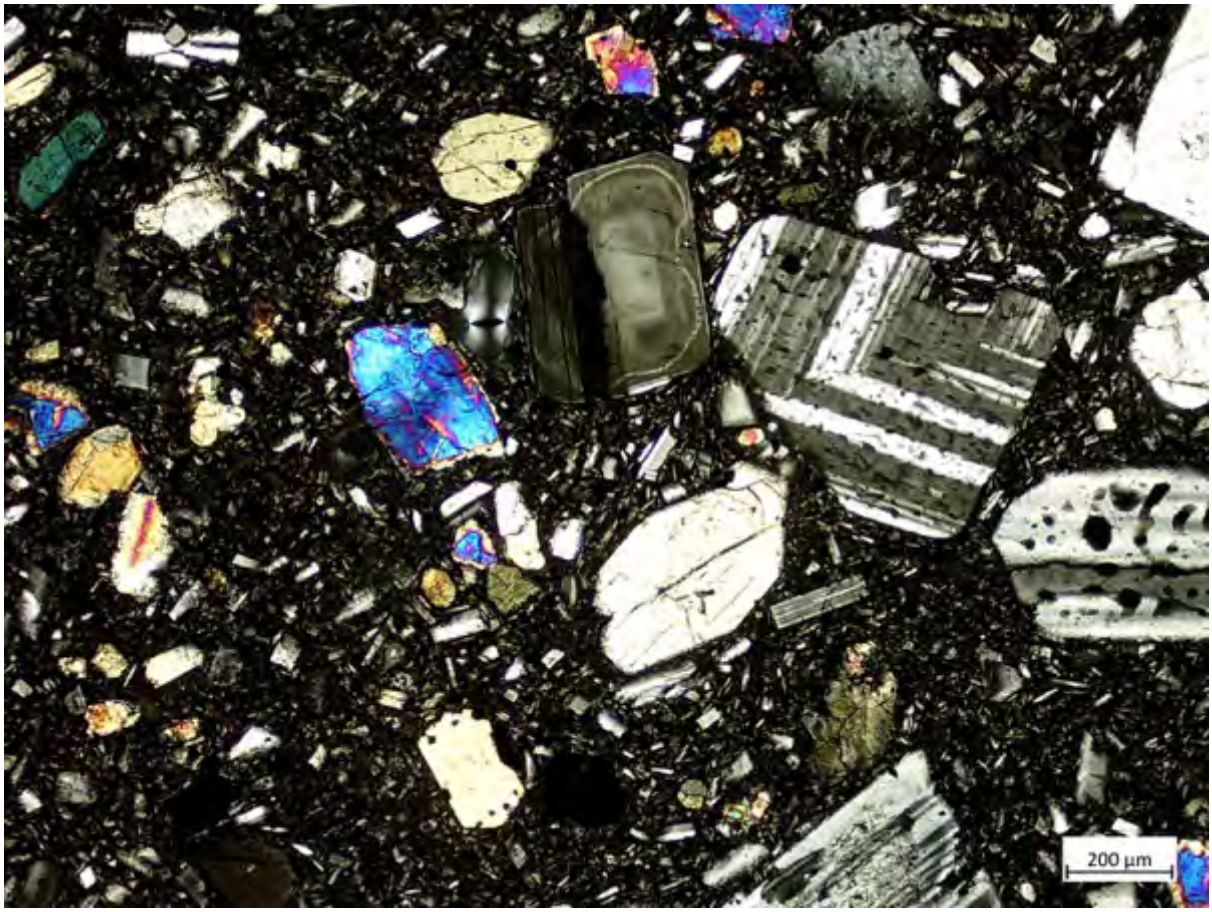

Figure 5.9: Thin section capture of Victoria dome in cross polarised light. The largest phenocryst phase is plagioclase, showing sieve textures and oscillatory zoning.

5.2.1.4 Cerro Bravo (CBV):

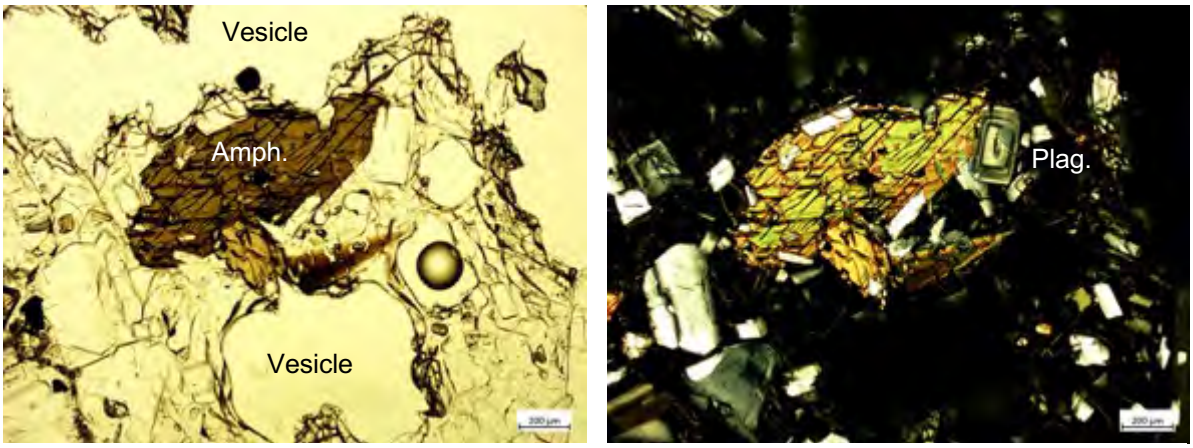

Figure 5.10: Thin section captures for DC16-006, from the lava flows of the basal modern Cerro Bravo. Large euhedral amphibole phenocryst with abundant, euhedral zoned plagioclase (~1-3 mm along long axis) in cryptocrystalline to aphanitic groundmass. Large vesicules (>6 mm) abundant in section.

Eleven samples related to Cerro Bravo were collected in this study. Petrologically the most recent dome of Cerro Bravo has a mineral assemblage of plagioclase, amphibole, orthopyroxene, clinopyroxene, oxyhornblende ± apatite and opaques, both as inclusions within phenocrysts and as microliths in the groundmass (Pinzon et al. 2018). The limited previous study of the basal areas of the current Cerro Bravo edifice suggests phenocryst phases are predominantly plagioclase, amphibole, orthopyroxene, and titanomagnetite (Lescinsky, 1990). Clinopyroxene (augite) and biotite is also reported in as accessory minerals (Lescinsky, 1990). These basal lava sequences of the current Cerro Bravo edifice are sampled in DC16-006, which has phenocrysts of euhedral plagioclase, euhedral to subhedral amphibole, euhedral (but rare) biotite and orthopyroxene and microphenocrysts of pyroxenes and opaque minerals. Groundmass is glassy with microcrystalline phases as described. Sample itself is highly vesicular (>50% vesicles).

The petrography of Letras sample (UB-03) in contrast is far more groundmass dominated (Figure 5.11). This sample has phenocrysts of plagioclase, hornblende

and clinopyroxene with the pyroxene more predominant (and preferentially altered), though all these are phases are in general smaller and more poorly formed than in younger Cerro Bravo samples (Figure 5.11). Pyroxene phenocrysts also appear to have been preferentially removed from sample by some process. The trachytic groundmass texture is reminiscent of the textures exhibited by VMTVF Group 1 sample, DC16-002, as both are dominated by a trachytic groundmass texture defined by small laths of feldspar (c.f.: Figure 8).

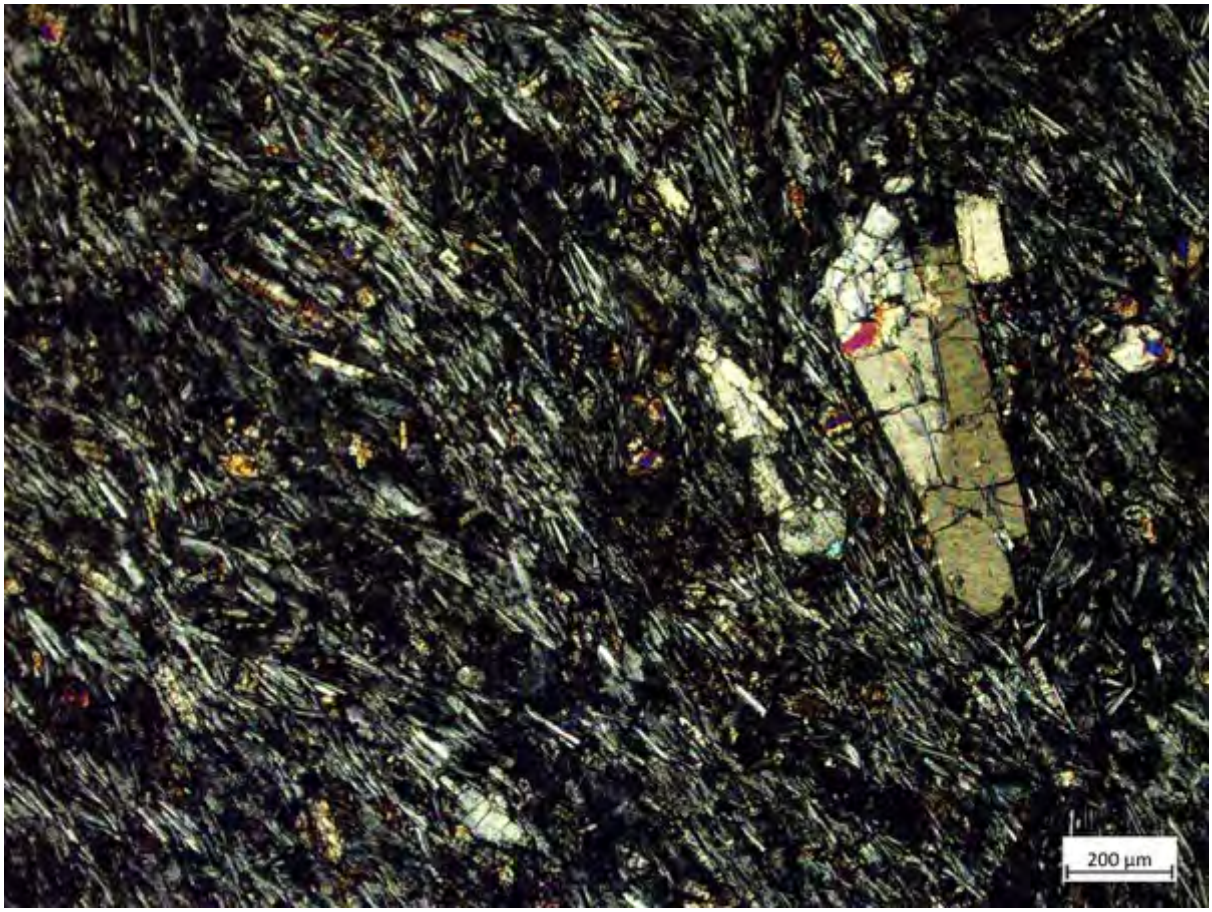

Figure 5.11: Thin section capture of UB-03 in cross polarised light (XPL). Note the tracytic texture in groundmass dominated by plagioclase microliths. Pyroxenes are the only major phenocryst phase present.

5.2.1.4 Paramillo de Santa Rosa (PSR):

Four samples were collected from flows of Paramillo de Santa Rosa. Petrographically, products of the SRV overall have a narrow mineralogical composition of orthopyroxene and two-pyroxene andesite, with occasional clinopyroxene andesites (Pulgarin et al. 2017). The oldest phase, sampled by this study, is the Tarapaca Formation. This has a reported assemblage of plagioclase, orthopyroxene, clinopyroxene, opaques, with accessory amphibole ± apatite and are classified as orthopyroxene andesites (Pulgarin et al. 2017). DC16-019 has a composition close to this, with phenocrysts of plagioclase, orthopyroxene, amphibole with reaction rims (and some pseudomorphs) and microphenocrysts of clinopyroxene and plagioclase. The groundmass is microcrystalline and dominated by plagioclase microliths which in places do form a trachytic flow texture (Figure 5.12). Pulgarin et al. (2017) also identified three geographically distinct textural groups have been identified within the Tarapaca Formation, based mainly on textural variations in the matrix. DC16-019 closely matches samples described from the western sector of the Tarapacá Formation (and occurs in a similar location), with microcrystalline matrix with skeletal plagioclase; a possible flow (trachytic) texture and a higher content of amphibole crystals. A greater proportion of vitreous inclusions in plagioclase compared to the rest of the Tarapaca Formation is also reported (Pulgarin et al. 2017; **Appendix A**).

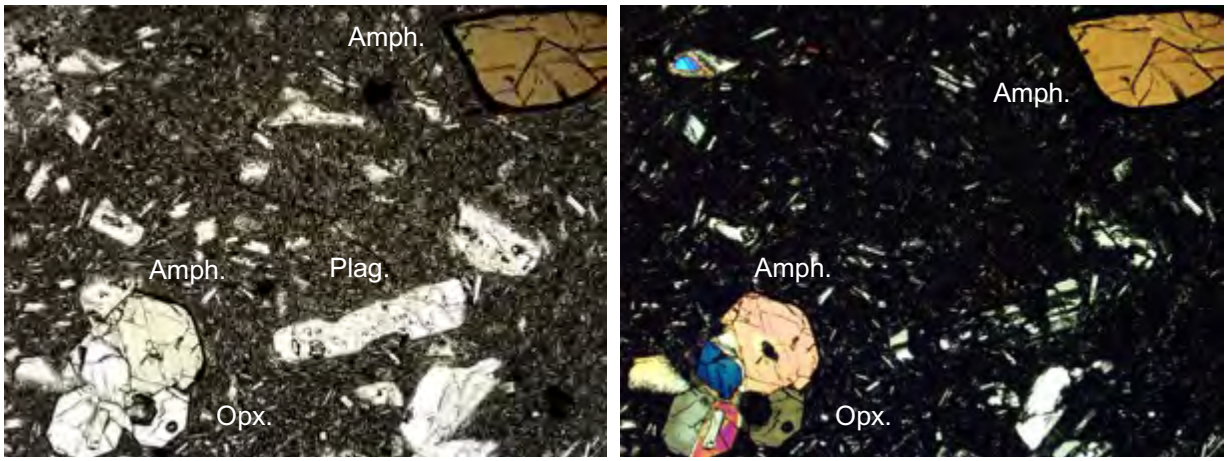

Figure 5.12: Thin section captures for DC16-019, from the Tarapaca Formation the earliest eruptive stage of Paramillo de Santa Rosa in PPL and XPL. This phase of activity is characterised by a cryptocrystalline to microphenocrystic groundmass of plagioclase, pyroxenes and opaques. Larger (~0.3-0.5 mm) subhedral to anhedral laths of plagioclase are also present in section. Orthopyroxene is the dominant phenocryst, also sometimes occurring as glomerocrysts. Amphibole phenocrysts are present with a reaction rim of oxides.

5.2.2 Geochemistry of the Samples:

5.2.2.1 Overview:

The Forty samples were collected from the Northern Volcanic Province, including basement, were analysed for major and trace elements and grouped by edifice and formation as outlined above. In this chapter, these analyses are used to investigate the comparative role of crustal contaminants, including sampled basement, in the petrogenesis of the Northern Volcanic Province alongside inputs from the subducting slab and mantle.

5.2.2.2 Major Elements:

For samples collected in the Northern Volcanic Province, SiO_2 ranges between 53 and 71 wt.% and the data forms a sub-alkaline fractional crystallisation trend (Figure 5.13). A subgroup composed of some Nevado del Ruiz and VMTVF samples can be identified by elevated total alkalis and particularly elevated K_2O contents (Fig. 5.14), which are further investigated below. This elevated K_2O is similar to that previously identified at Nevado del Ruiz (Martinez et al. 2014) and Nevado del Santa Isabel (Errazuriz-Henao et al. 2019) (Figure 5.14). VMTVF samples are subdivided based on their relative ages, petrography and previously published geochemistry in line with findings from Osorio et al. (2018) and Botero-Gomez et al. (2018).

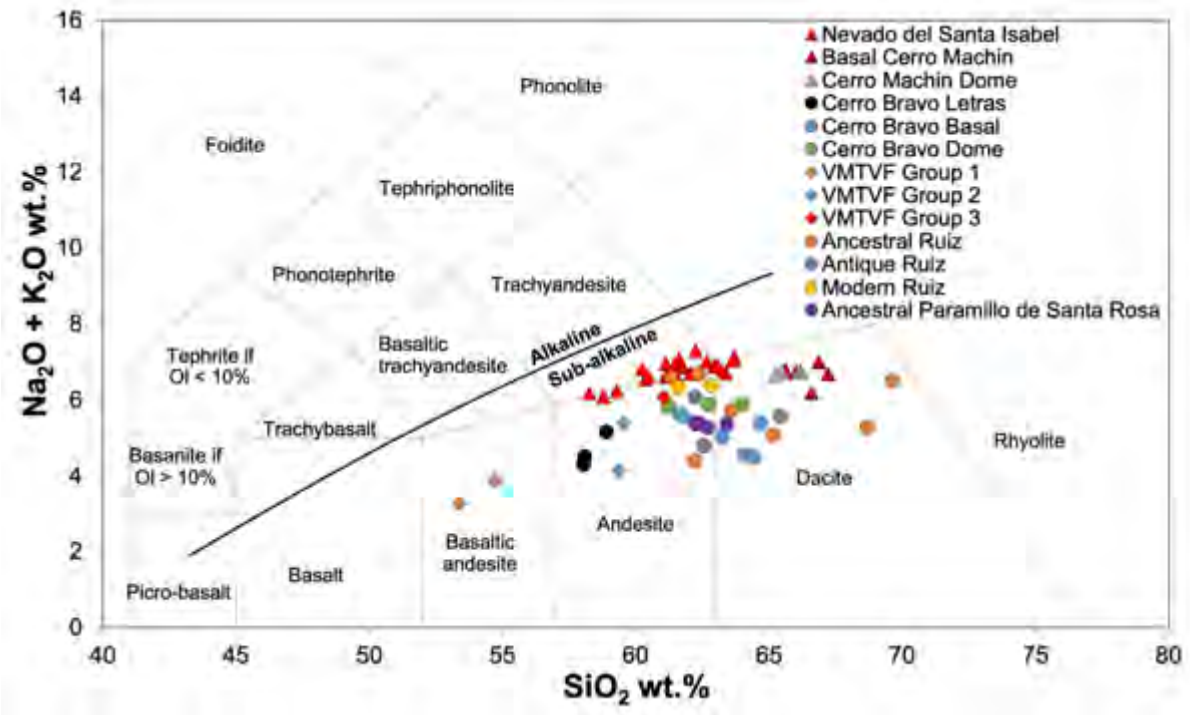

Figure 5.13: Total alkali silica plot of samples analysed in this study. Data from two other NVP edifices, Nevado del Santa Isabel and Cerro Machin (Laeger et al. 2013 and Errazuriz-Henao et al. 2019) are also shown. Fields after Le Bas et al. (1986) and alkaline/sub-alkaline line after Irvine and Barager (1971).

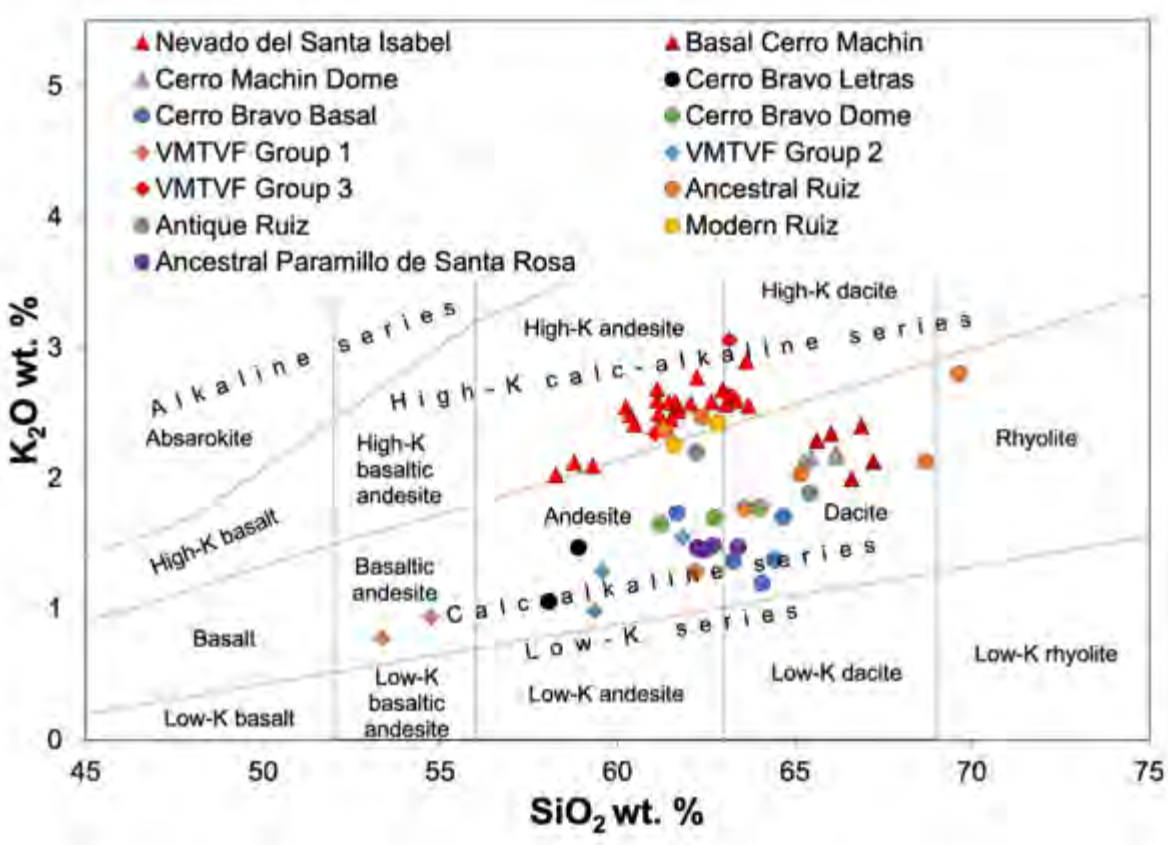

Figure 5.14: K_2O versus SiO_2 plot with fields after Ewart (1982). Alongside data for NVP edifices in this study, data from two other NVP edifices, Nevado del Santa Isabel and Cerro Machin (Laeger et al. 2013 and Errazuriz-Henao et al. 2019) are also shown.

The NVP groups can be classified as predominantly calc-alkaline on both K_2O-SiO_2 Alkalis (K2O) and Pearce trace element diagrams, (Figures 5.14 and 5.15). Most notable is the concentration of samples with higher total alkalis and MgO contents, which includes the groups with moderate to high K_2O, including Cerro Bravo Dome, VMTVF Group 3, Modern Ruiz and a subset of older Ruiz samples.

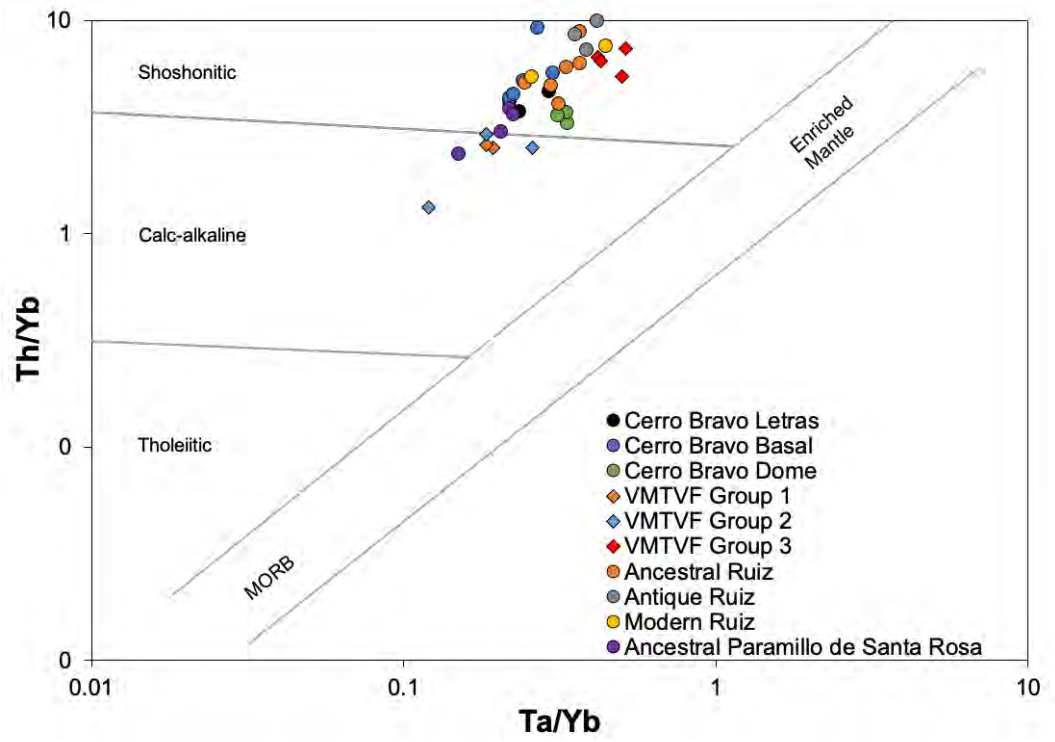

Figure 5.15: Th/Yb versus Ta/Yb plot (after Pearce, 1983), to distinguish between MORB and mantle compositions and Th enriched arc magma compositions.

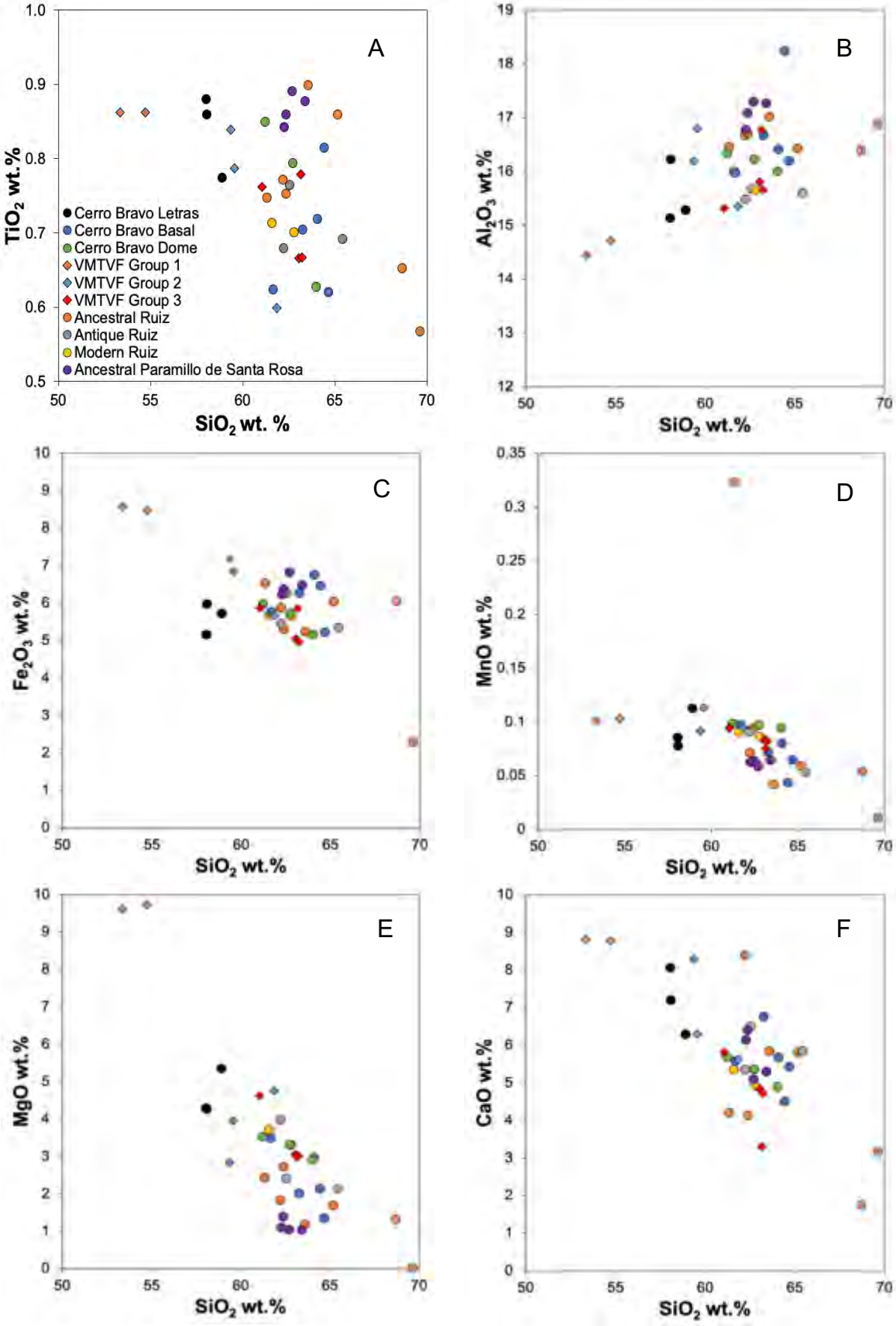

Figure 5.16 (above and continued overleaf): Bivariate plots of major element analyses for samples in this study. Legend is as for Figures 5.13 and 5.14.

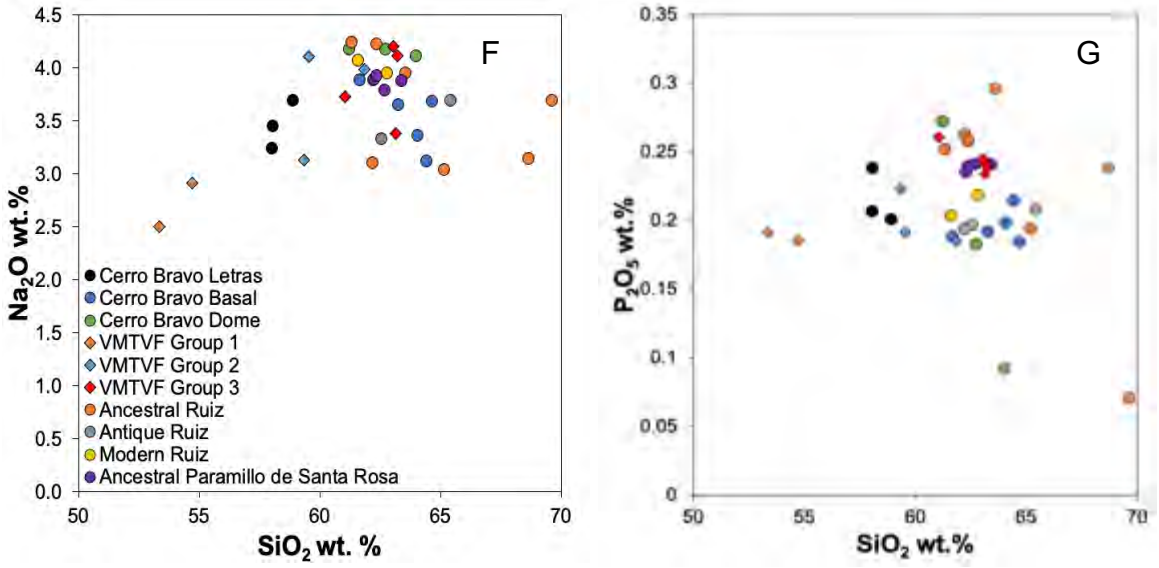

Figure 5.16 (above and overleaf): Bivariate plots of major element analyses for samples in this study. Legend is as for Figures 5.13 and 5.14.

Bivariate plots of the major elements show a mix of linear to slightly inflected liquid lines of descent. For example, TiO_2 appears to show an inflection in all groups at >60 wt.%, but a subset of Ancestral Ruiz (DC16-013 and DC16-016) and Paramillo de Santa Rosa samples do not follow this trend (Figure 5.16A). Analyses of most other groups have values which broadly correlate with increasing SiO_2, though they do not fall along a single liquid line of descent, which is not unexpected for data from multiple edifices. Al_2O_3 values lie between 14 – 17 wt.% showing a broadly positive trend, with the exception of one Cerro Bravo Basal sample (Al_2O_3 >18). Fe_2O_3 shows a consistent negative correlation with silica, but with some separation of groups between around 60 – 63 wt.% SiO_2. VMTVF, Nevado del Ruiz and Cerro Bravo Dome groups have generally lower Fe_2O_3 compared to Basal Cerro Bravo and Paramillo de Santa Rosa samples (Figure 5.16C). MnO has one elevated outlier from the Ruiz Ancestral dataset (UB-06), but otherwise has a negative correlation. Notably, Cerro Bravo Dome, VMTVF Group 3 and Nevado del Ruiz samples (with the exception of DC16-012 and DC16-016) have slightly elevated MnO contents compared to silica than Paramillo de Santa Rosa and to a lesser extent, Basal Cerro

Bravo (Figure 5.16D). MgO shows a negative correlation with silica across all groups (Figure 5.16E). Paramillo de Santa Rosa, in agreement with data from literature (Monsalve et al. 2017b), Basal Cerro Bravo and some Ancestral Ruiz samples have the lowest MgO at comparable silica contents. CaO shows a relatively tight negative correlation for Cerro Bravo Dome, VMTVF Group 3 and Modern Ruiz samples of lower CaO for a given silica than Paramillo de Santa Rosa and Basal Cerro Bravo samples, though some overlap is evident (Figure 5.16F). Na_2O is elevated in analyses of Cerro Bravo Dome, Modern Ruiz and Paramillo de Santa Rosa compared to other groups (Figure 5.16G). Lastly, P_2O_5 shows a very weak trend with silica across all groups (Figure 5.16H). Contents are elevated in VMTVF Group 3, Paramillo de Santa Rosa and some Ancestral Ruiz samples (with the exception of DC16-012 and DC16-013).

Overall, the products of the Northern Volcanic Province are compositionally dominated by calc-alkaline medium- to high-K_2O, intermediate-silicic composition basaltic andesite to dacites. Major element Harker diagrams point to an evolution with increasing silica in composition throughout the province, with some groups and samples (especially Cerro Bravo Dome, VMTVF Group 3 and a subset of Nevado del Ruiz analyses) being distinguished by elevated alkali contents. This is consistent with trends previously identified in literature (i.e: Laeger et al. 2013; Martínez et al. 2014; Errazuriz-Henao et al. 2019), and in line with general major element trends for continental arc systems globally.

5.2.2.3 Trace Elements:

Bivariate plots of trace elements (Figure 5.18) allow us to further characterise and distinguish between groups. Sc (Figure 5.18a) is analysed by ICP-OES and shows a broadly linear negative correlation across all groups, though with some scatter in Basal Cerro Bravo and Ancestral Ruiz samples.

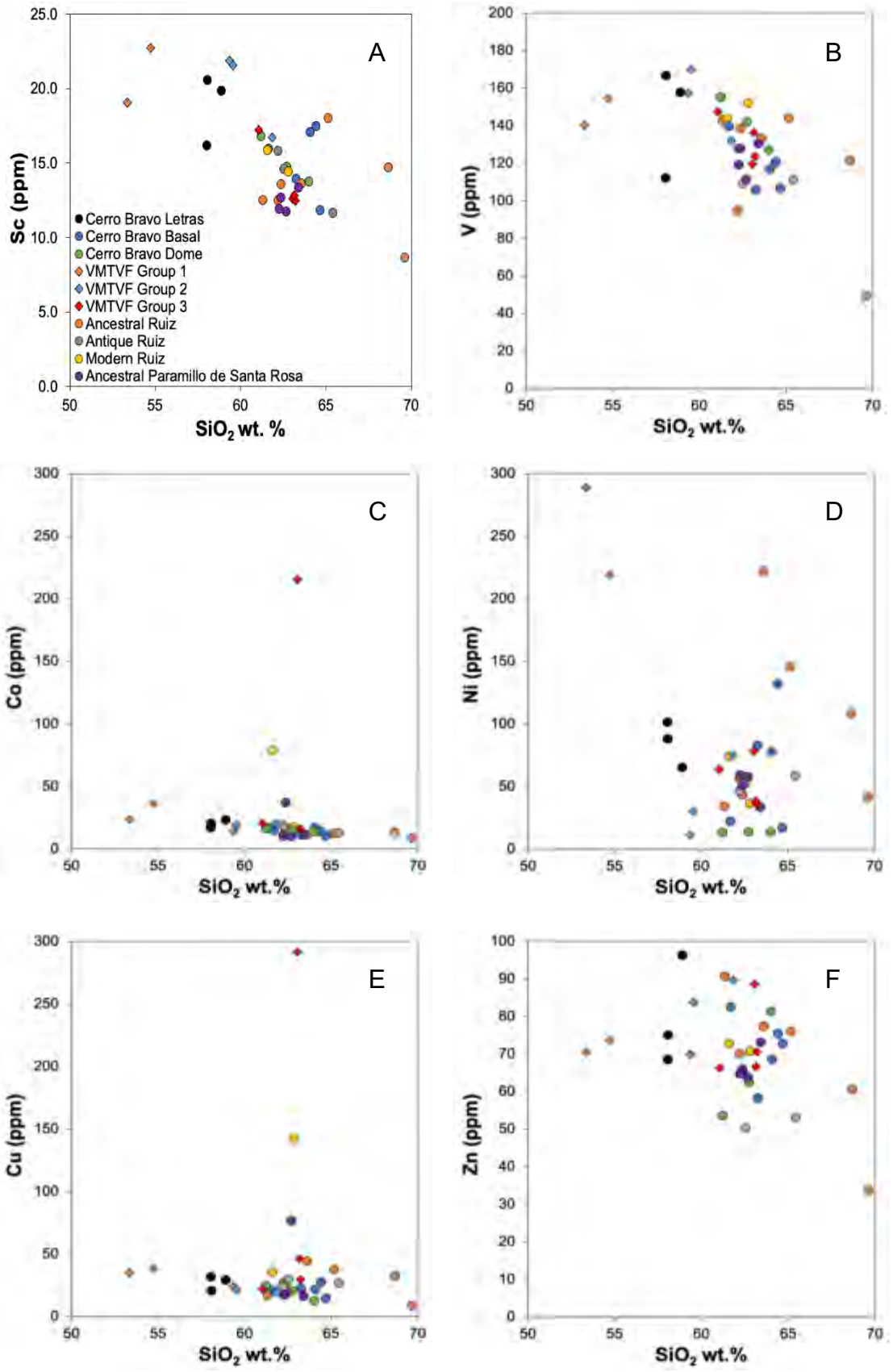

Figure 5.17 (above and overleaf): Bivariate plots of select trace elements analysed by ICP-MS and ICP-OES.

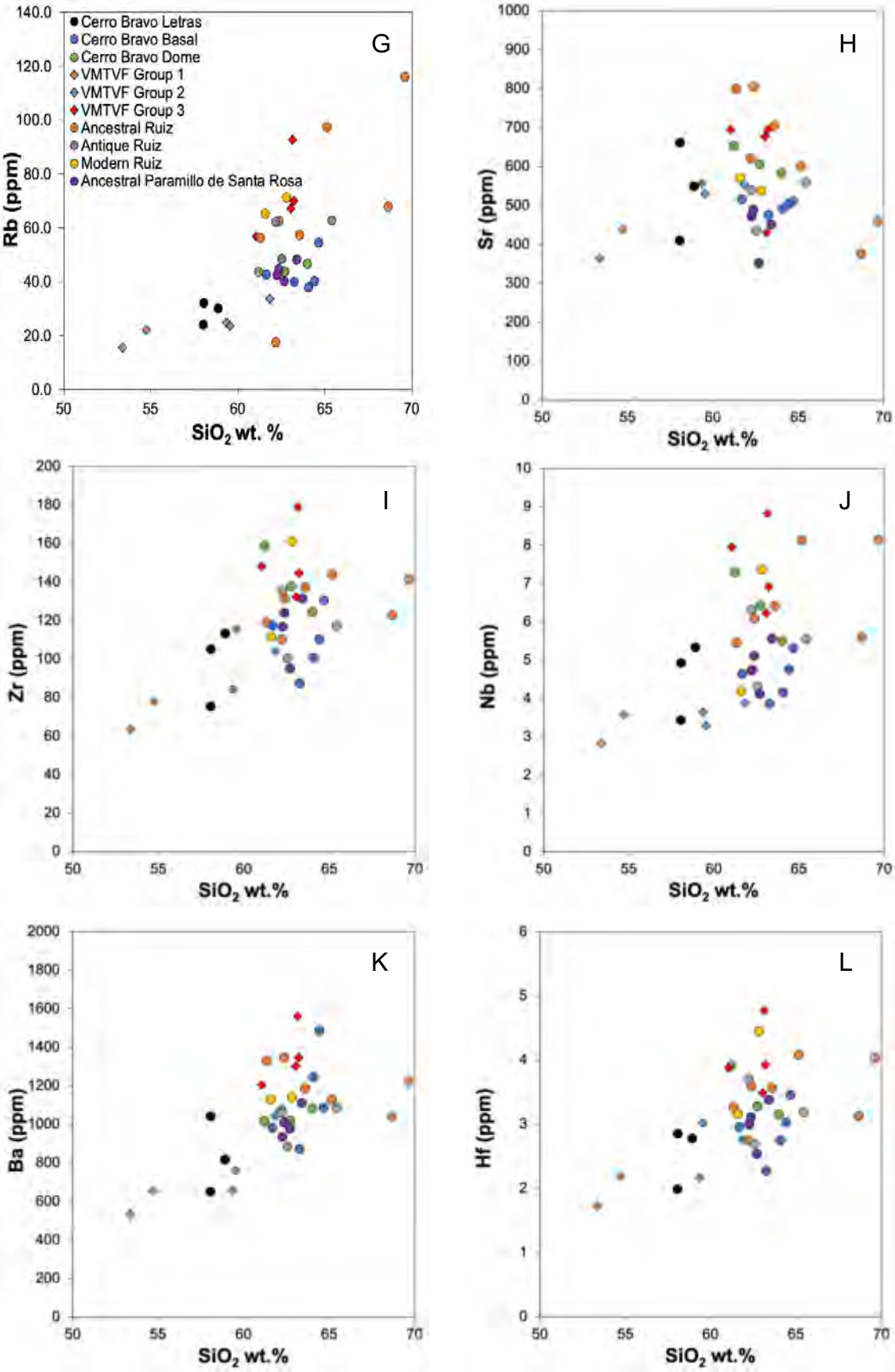

Figure 5.17 (above and overleaf): Bivariate plots of select trace elements analysed by ICP-MS and ICP-OES.

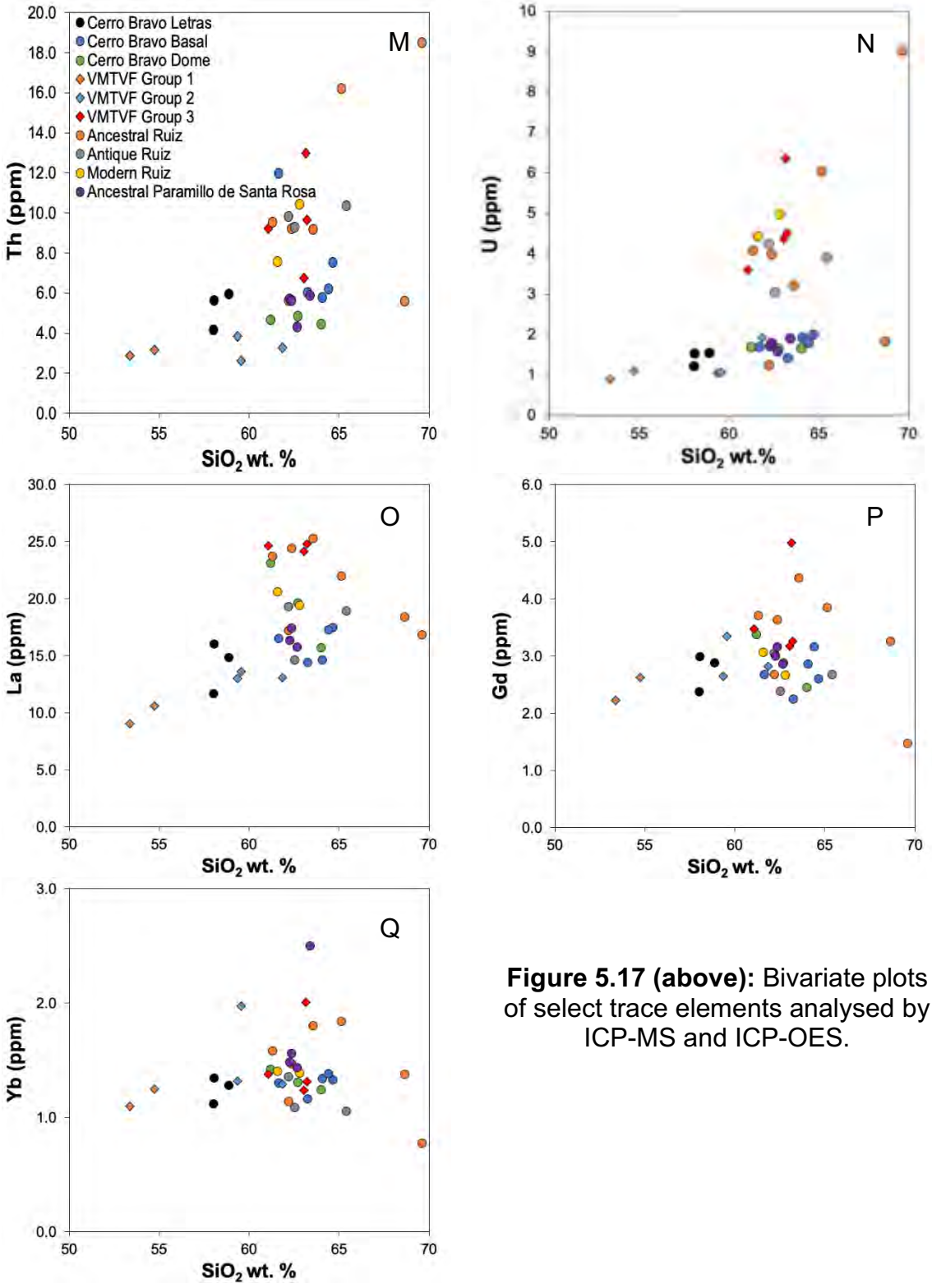

Figure 5.17 (above): Bivariate plots of select trace elements analysed by ICP-MS and ICP-OES.

The transition elements (i.e.: Cr, Ni, Co, V, Cu and Zn) in general show a negative correlation with silica. Vanadium has a strong general negative correlation with increasing silica, with a possible inflection ~58 – 59 wt.% SiO_2 and ~155 – 170 ppm V, best defined by the Cerro Bravo, Letras (with the exception of DC16-005) and

VMTVF Group 2 samples (Figure 5.17B). There are some noticeable outliers in other elements, primarily in Co and Cu, where one of the outliers consists of UB-15, a VMTVF Group 3 sample (Co >200 ppm) as well as a Modern Ruiz sample (UB-04-L) with Co >37 ppm and Paramillo de Santa Rosa sample (DC16-020) with a smaller Co content (Figure 5.17C). These samples also have elevated Cu concentrations (Figure 5.17E). The remainder of the data falls on a decreasing trend with increasing silica which correlates well for Co across all groups (Figure 5.17C), but only fairly well for Cu, due to elevated Cu contents in some Ancestral Ruiz and VMTVF Group 3 analyses (Figure 5.17E). Correlation is poorest in Ni, with a wide spread of values for Ancestral Ruiz and Basal Cerro Bravo samples. Cerro Bravo Dome shows the lowest Ni (>30 ppm) across a range of silica compositions and some Basal Cerro Bravo samples (UB-02; DC16-003) and VMTVF Group 2 (DC16-011; UB-14) also fall within this range. This is similar to low Ni values reported in Cerro Machin analyses (Laeger et al. 2013; Errazuriz-Henao et al. 2019). Anomalously high Ni at high silica is recorded in some Ancestral Ruiz (DC16-013; DC16-016) and Basal Cerro Bravo (DC16-007) samples. Zn has a wide spread of values and a very rough negative correlation with increasing silica, very similar to analyses from previous studies and other NVP edifices such as Nevado del Santa Isabel analyses (Errazuriz-Henao et al. 2019). A group of high Zn (>80 ppm) samples at SiO_2 <63 wt% define a separate trend, consisting of Cerro Bravo Letras (UB-03), Basal (DC16-007), VMTVF (UB-13, -14, -15) and Ancestral Ruiz (UB-06) samples.

Large Ion Lithophile Elements (LILE - Rb, Sr, Ba, Th and U) show two separate trends, consisting of Nevado del Ruiz analyses of all ages and VMTVF Group 3, which have elevated contents across all of these elements and a second less LILE-

enriched trend in most other groups (Figure 5.17). There are exceptions to this, such as the elevated Sr in Cerro Bravo Dome samples (Figure 5.17H) and individual samples of Group 3 VMTVF and Ancestral Ruiz (Figures 5.17G and 5.17H), which are likely due to the predominance of plagioclase crystallization in these samples. One Cerro Bravo basal analysis also shows elevated Th contents distinct from the rest of the group (Figure 5.17M).

High Field Strength Elements (HFSE – Zr, Nb, Hf) do show elevated contents for Nevado del Ruiz and VMTVF Group 3 analyses, and to a lesser extent, Cerro Bravo Dome samples show elevated Zr and Hf (Figure 5.17I and 5.17L). There is a significant overlap between these groups of Hf at ~60 – 65 wt.% SiO_2 (Figure 5.17L). Trends across both LILE and HFSE within the NVP could be more reflective of relative mobility of elements as LILE compared to the usually immobile HFSE such as Th. Compatibility of elements in crystal phases likely also plays a role in segregating these groups (Green, 1995). This could also point to VMTVF Group 3, a subdet of Ruiz samples and possibly Cerro Bravo suites being related, and not cogenetic with other groups which are more depleted in these elements. Overall, Harker diagrams repeatedly show two separate geochemical trends which are not simply segregated by edifice or geographical position. These consist of the VMTVF Group 3, Nevado del Ruiz and samples from Cerro Bravo Dome in some cases, which have elevated alkalis and incompatible elements, and are here grouped together as a high-K_2O group. The remaining sample groups form a low-K_2O group. The rare earth elements (REE) show an inflection at ~62 wt.% SiO_2 with the high K2O group notable for its depletion in middle and heavy REE (Figure 5.17O – Q).

Further scrutiny on these trace element variations can be gained using normalised multi-element plots for each respective edifice analysed in this study (Cerro Bravo, the VMTVF, Nevado del Ruiz and Paramillo de Santa Rosa (Figures 5.19, 5.20, 5.21 and 5.22). Normalisation to N-MORB allows us to compare relative enrichments and depletions in the arc lavas of the NVP compared to each other and compared with MORB and constrain processes other than those of normal upper mantle partial melting (Elliott, 2003).

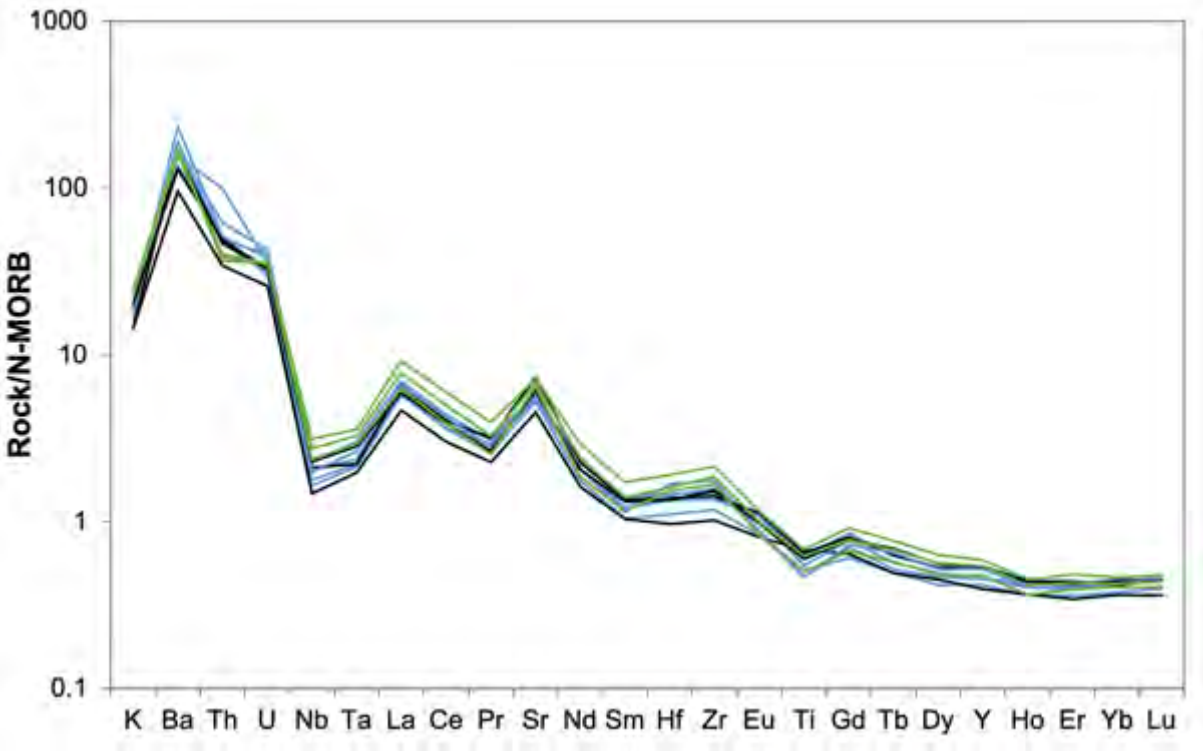

Figure 5.18: Multi-element plot of analyses for Cerro Bravo Letras (black), Cerro Bravo Basal (blue) and Cerro Bravo Dome (green). Normalised to N-MORB values from Sun and McDonough (1989).

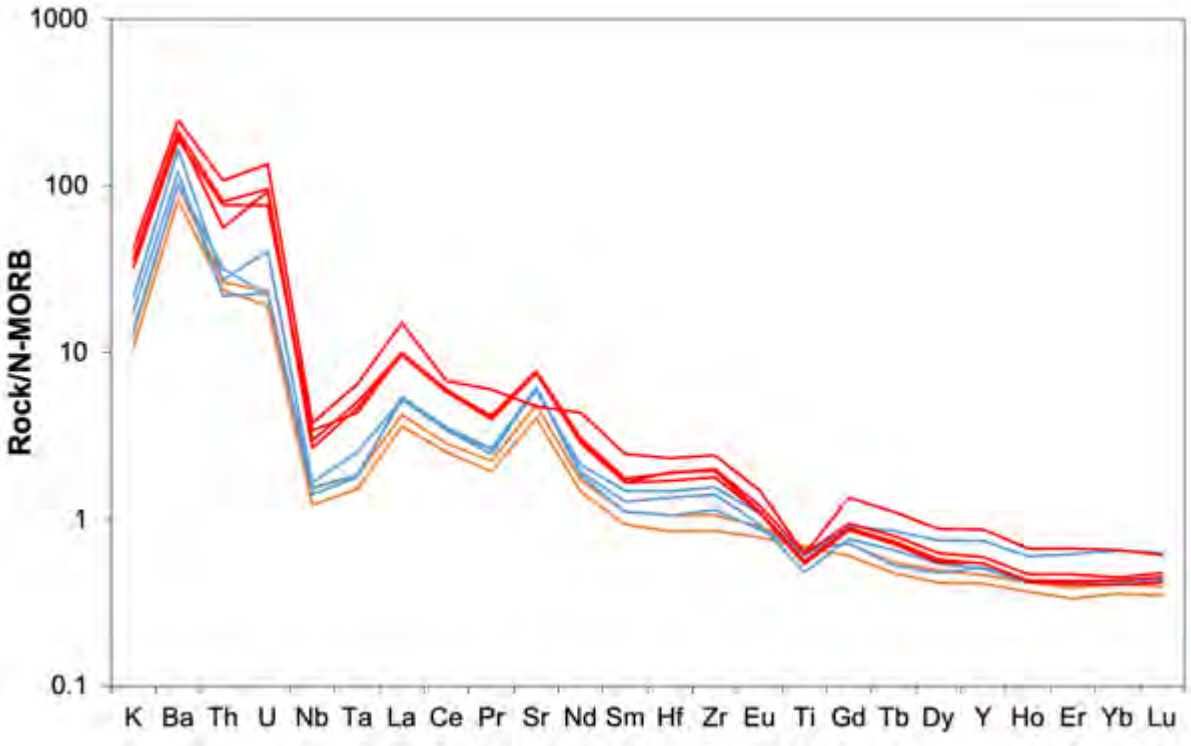

Figure 5.19: Multi-element plot of analyses for the VMTVF analysed in this study, including VMTVF Group 1 (orange), VMTVF Group 2 (blue) and VMTVF Group 3 (red). Normalised to N-MORB values from Sun and McDonough (1989).

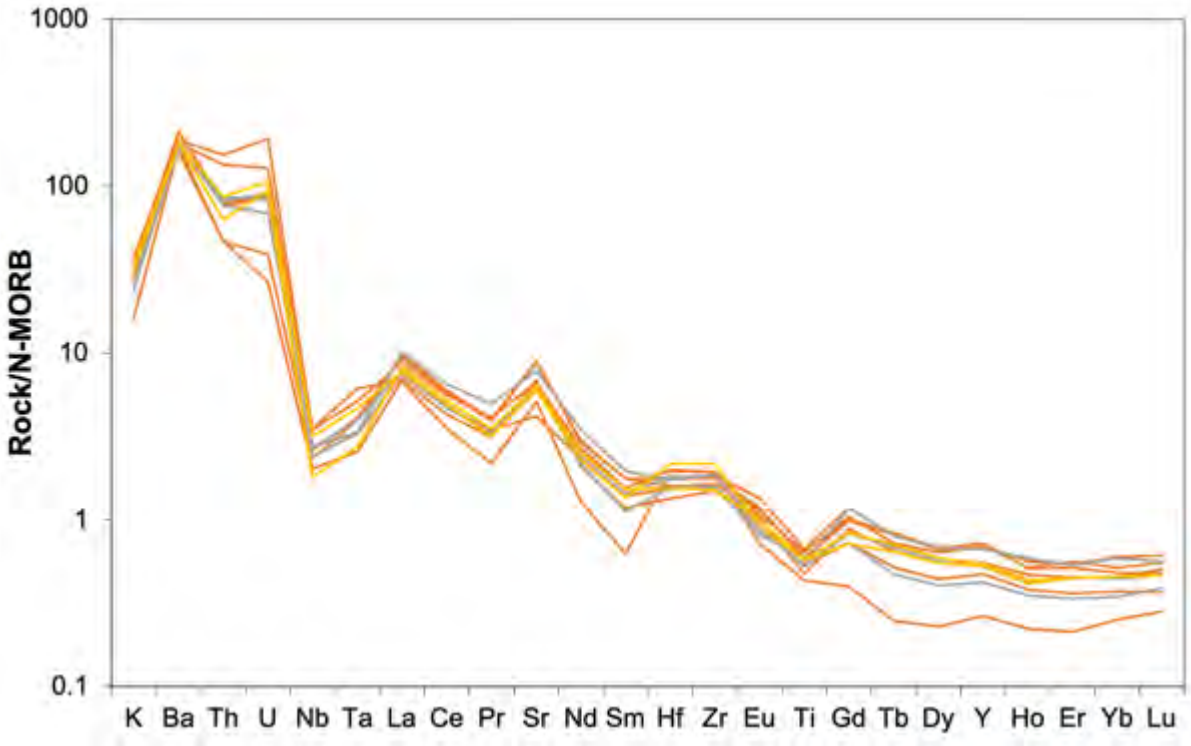

Figure 5.20: Multi-element plot of analyses for Nevado del Ruiz, with Ruiz Ancestral (orange), Ruiz Antique (grey) and Ruiz Modern (yellow). Normalised to N-MORB values from Sun and McDonough (1989).

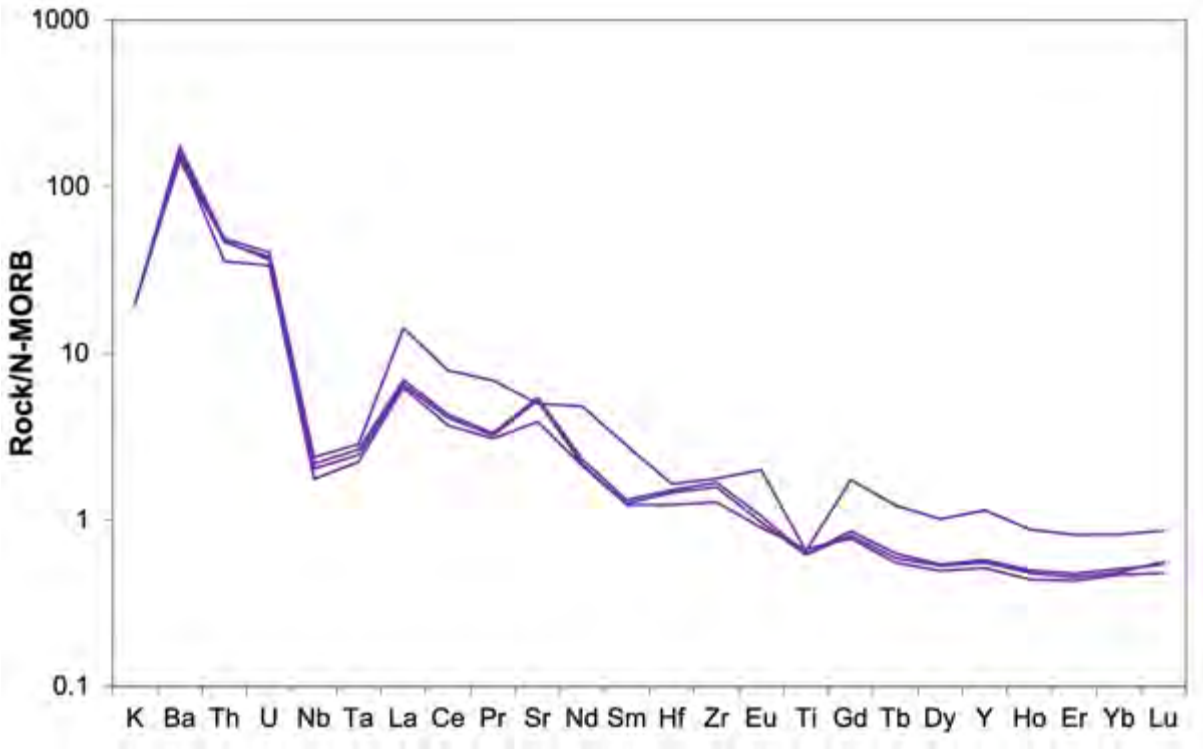

Figure 5.21: Multi-element plot of analyses for Paramillo de Santa Rosa from this study. Normalised to N-MORB values from Sun and McDonough (1989).

The analyses in general are typical of those for continental volcanic arcs, with a noticeable relative depletion in Nb, Ta and Ti, enrichment in LILE (K, Th and Sr) and sub-horizontal REE patterns.

The first noticeable trend for Cerro Bravo (Figure 5.18) is an enrichment in the majority of elements (with the exception of Ba, Th and U) for Cerro Bravo Dome samples compared to older components of Cerro Bravo. A depleted pattern relative to MORB across more compatible elements, along with a negligible negative Ti anomaly, is observed for one sample of Cerro Bravo Letras (DC16-005). Beside this however, Cerro Bravo is remarkably consistent in composition across all ages.

VMTVF analyses (Figure 5.19) show a noticeable difference between the more enriched Group 3, which is more enriched in almost all elements (except Ti)

compared to the other groups. In comparison, Group 1 is most depleted in composition, and similar to Group 2. One Group 3 sample, from Amazonas dome (UB-18) has higher REE values and a negligible Sr anomaly, in contrast to all other samples of the VMTVF (Figure 5.19). There is also an elevated REE pattern in one VMTVF Group 2 sample, from the Lusitania Lavas (UB-14).

Analyses of Nevado del Ruiz (Figure 5.20) reveal a variety of compositions for the Ancestral Ruiz group, though the majority of these appear to be enriched in incompatible elements. The exceptions to this are DC16-012, which has far more depleted Ti, REE and Y than all other samples of Nevado del Ruiz. DC16-010 also has a more depleted composition compared to other Ruiz Ancestral samples in all elements. Modern Ruiz seems to form an intermediate composition between the depleted composition of these samples and the more enriched Antique and Ancestral Ruiz analyses, with the exception of Hf and Zr, which are enriched in one Modern Ruiz sample (UB-04-P).

Paramillo de Santa Rosa has comparable Nb, Ta and Ti anomalies to Cerro Bravo but somewhat lower than high-K_2O Nevado del Ruiz and the VMTVF values. This might be suggestive of a weaker subduction signature for Paramillo de Santa Rosa, however Ba/Nb values have a comparable range (138 – 312) across the NVP, with Paramillo de Santa Rosa in the mid-range of these values. There is a significant difference in composition between DC16-018 which has much more elevated concentrations in compatible elements (La onwards), with the exception of Sr than all other analyses.

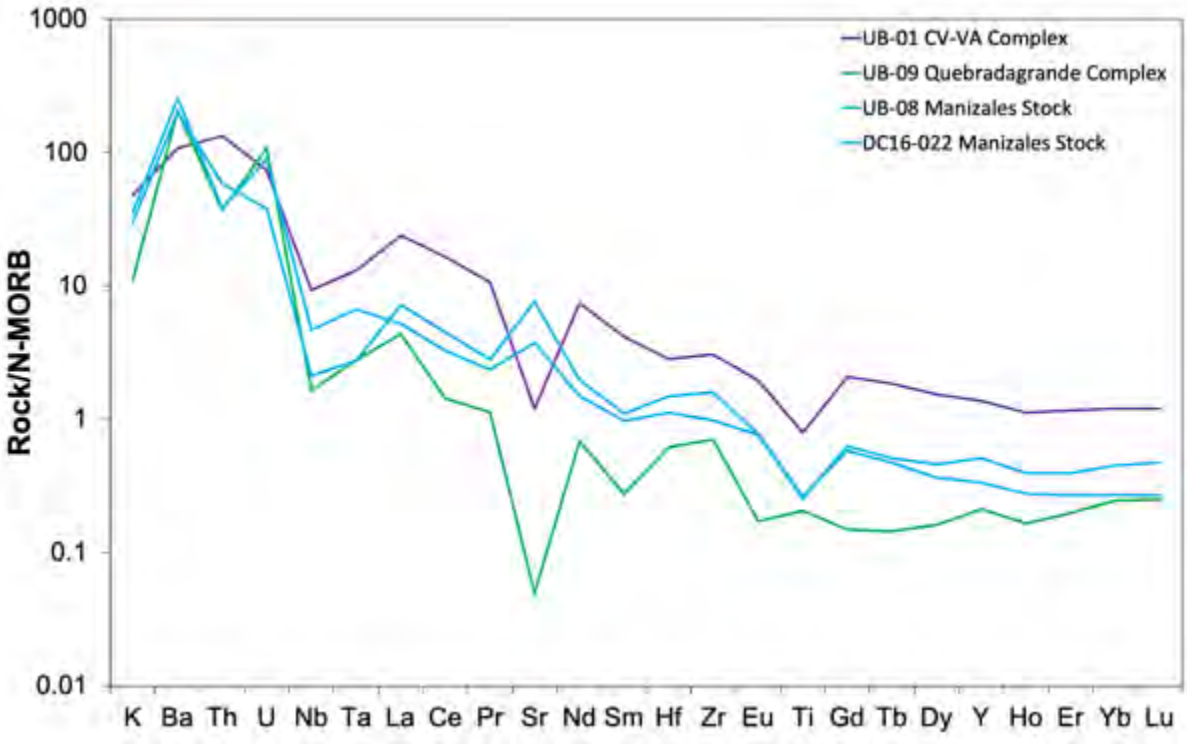

Figure 5.22: Multi-element plot of sampled basement of the Northern Volcanic Province (NVP), consisting of the Cajamarca-Valvidia complex (UB-01), Quebradagrande complex (UB-09) and Manizales stock (DC16-022 and UB-08). Normalised to N-MORB values from Sun and McDonough (1989).

The basement of the NVP is assessed using multi-element plots (Figure 5.23) to best compare to our volcanic samples. Basement in this case is N-MORB normalised to allow for direct comparison to the trends seen in the NVP and because the basement is dominantly of subduction origin (as in the Manizales stock) or oceanic origin (Quebradagrande complex). The Cajamarca-Valvidia (CV-VA) complex is the most enriched, typical of the autochthonous continental crust, whilst the Quebradagrande complex has compositions closer to MORB, though with depletions reminiscent of subduction (such as Nb and Ta), consistent with this being of intra-oceanic arc affinity.

REE patterns can also shed light on differences between the edifices of the NVP. Analyses of Cerro Bravo are remarkably consistent (Figure 5.23), but overall, more

recent analyses of Cerro Bravo appear more enriched, particularly in light (L)REE and slightly so in heavy (H)REE.

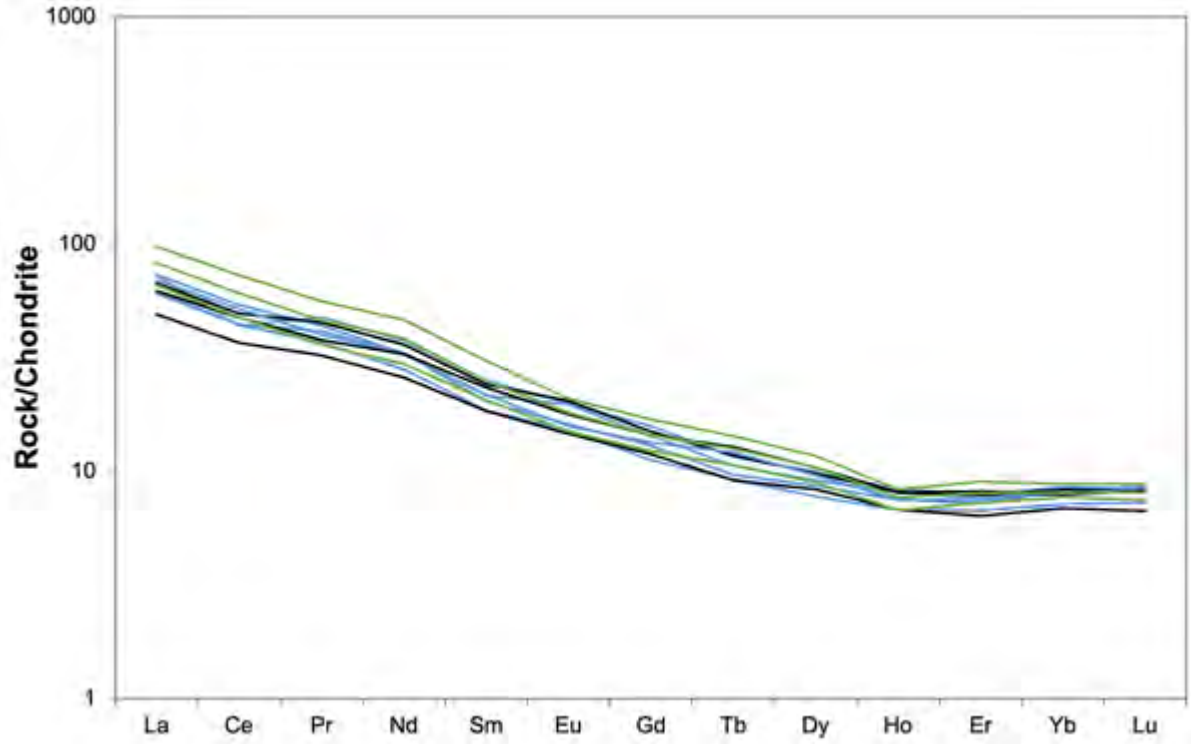

Figure 5.23: Rare earth element pattern for analysed samples from Cerro Bravo, including Cerro Bravo Letras (black), Cerro Bravo Basal (blue) and Cerro Bravo Dome (green). Chondrite normalised using values from Sun and McDonough (1995).

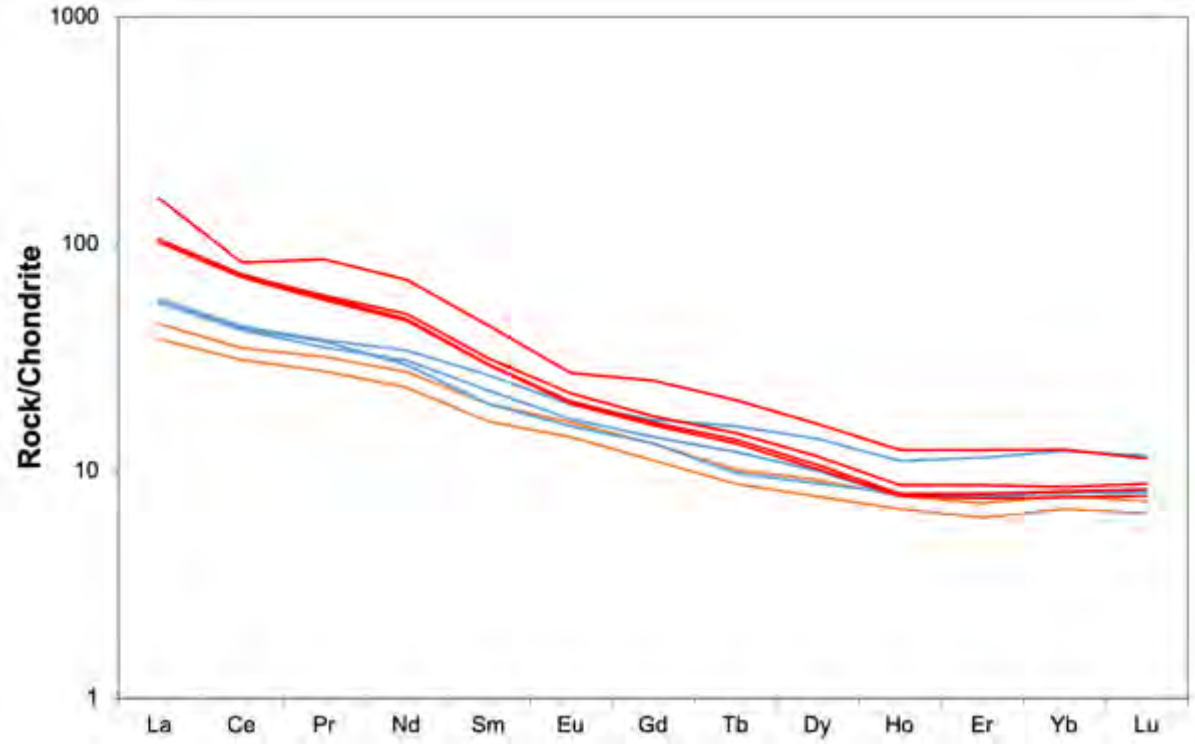

Figure 5.24: Rare earth element pattern for analysed samples from the VMTVF, including Group 1 (orange), Group 2 (blue) and Group 3 (red). Chondrite normalised using values from Sun and McDonough (1995).

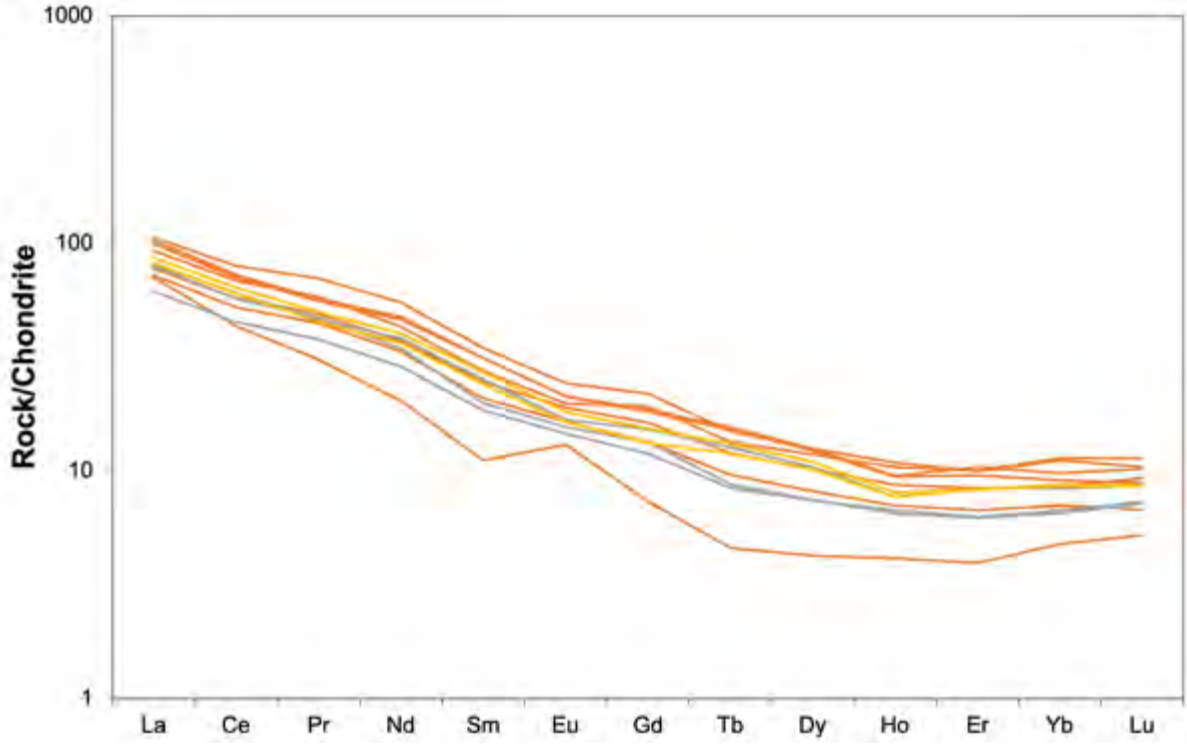

Figure 5.25: Rare earth element pattern for analysed samples from Nevado del Ruiz, including Ancestral Ruiz (orange), Antique Ruiz (grey) and Modern Ruiz (yellow). Chondrite normalised using values from Sun and McDonough (1995).

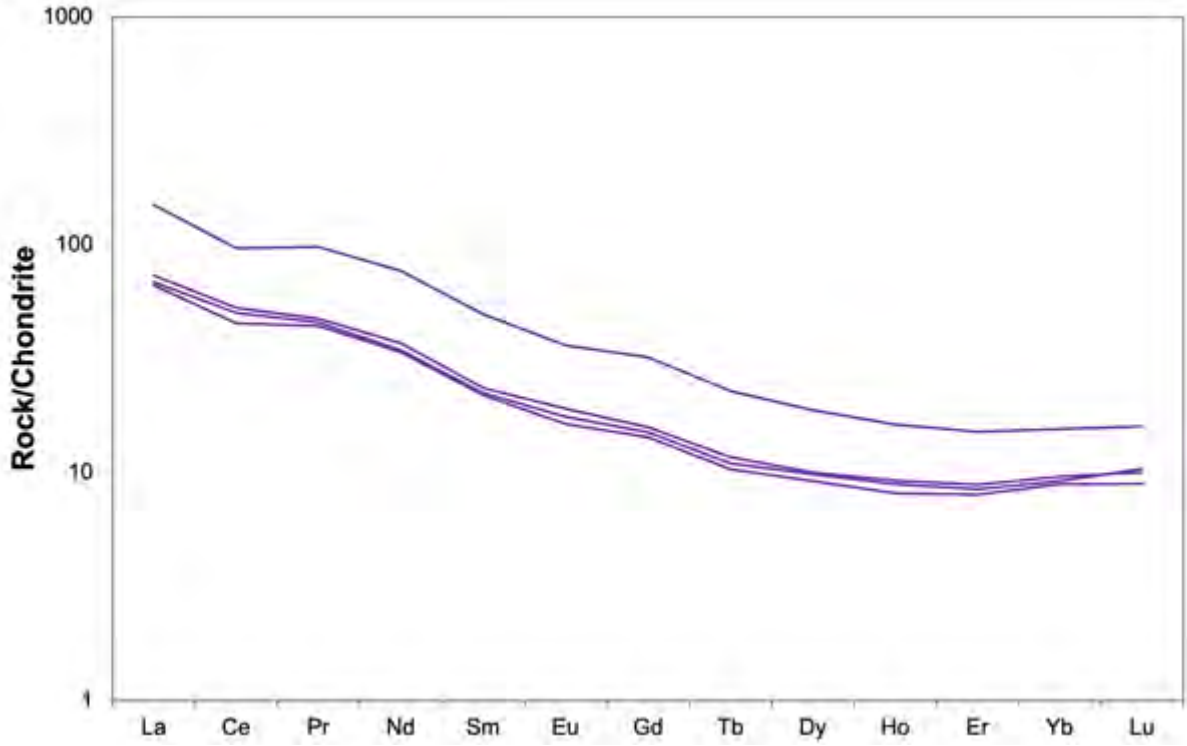

Figure 5.26: Rare earth element pattern for analysed samples from Paramillo de Santa Rosa. Chondrite normalised using values from Sun and McDonough (1995).

REE patterns of the VMTVF (Figure 5.24) show significant differences between groups, with VMTVF Group 3 significantly more LREE enriched and therefore displaying a steeper REE pattern than other groups. There are not significant differences between HREE abundances between groups. VMTVF Group 1 is the most depleted in REE overall.

Though overlapping in some cases, Nevado del Ruiz groups can be distinguished by REE patterns (Figure 5.25). Ancestral Ruiz analyses, with the exceptions of DC16-010 and DC16-012, are more REE enriched overall than Antique and Modern Ruiz samples. Ruiz samples are also similar in LREE enrichment and steepness to VMTVF Group 3 samples (Figure 5.24).

Lastly, Paramillo de Santa Rosa is similar in LREE enrichment to Cerro Bravo analyses and is less enriched than samples from Ruiz and the VMTVF. The only exception to this is sample DC16-018, which is anomalously enriched in REEs (Figure 5.26).

5.2.3.4 Radiogenic isotopic analyses:

Sr, Nd and Hf isotope analyses are obtained for a subset of Cerro Bravo, VMTVF, Nevado del Ruiz and Paramillo de Santa Rosa samples, as well as sampled basement from the Cajamarca-Valvidia complex, Quebradagrande complex and Manizales stock. Comparable data is available for the basement (e.g.: Cochrane et al. 2014; Bustamante et al. 2017) and the NVP (James and Murcia, 1984; Laeger et

al. 2013; Errazuriz-Henao et al. 2019), but this study represents the first radiogenic isotopic analysis of Cerro Bravo, the VMTVF and Paramillo de Santa Rosa.

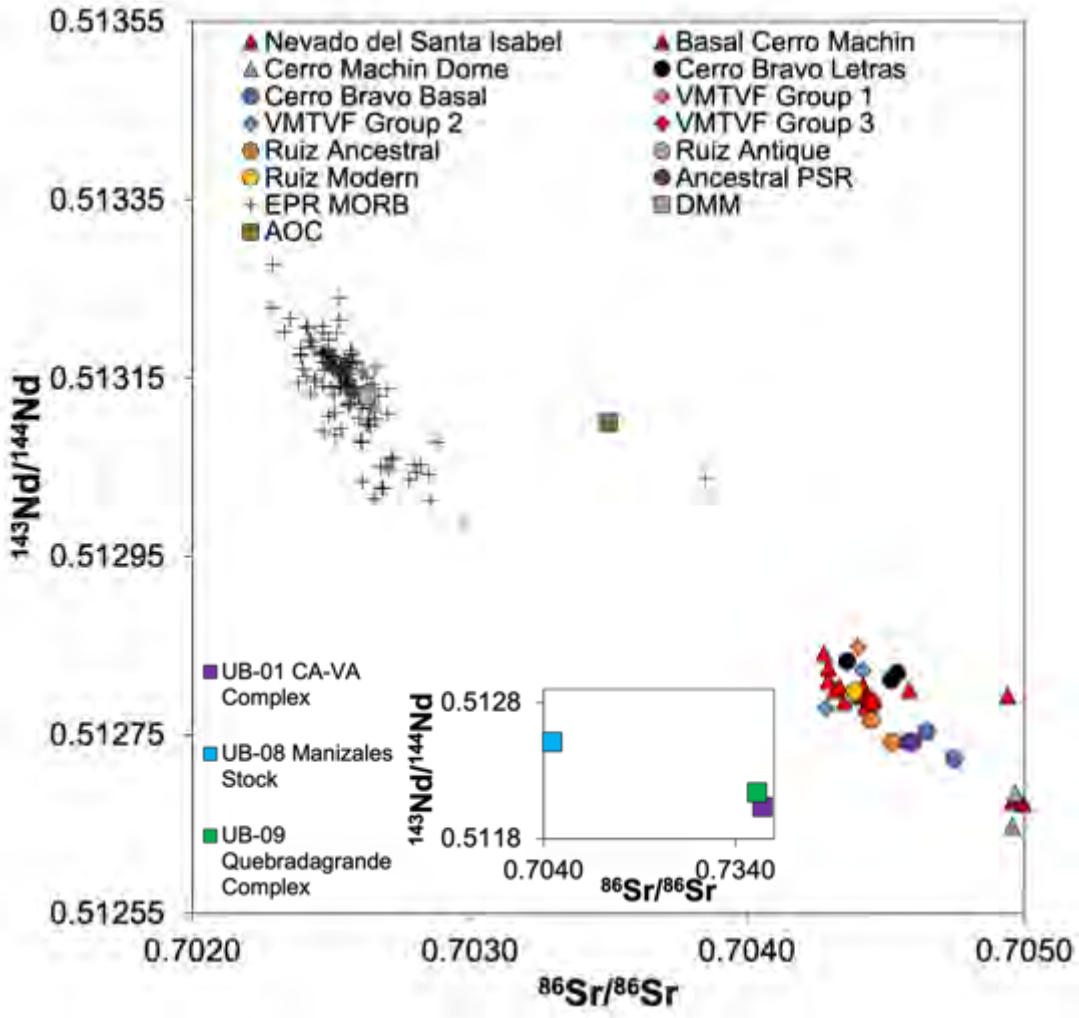

Figure 5.27: $^{143}Nd/^{144}Nd$ versus $^{87}Sr/^{86}Sr$ plot for NVP edifice data analysed and inset for basement samples analysed. Data from two other NVP edifices, Nevado del Santa Isabel and Cerro Machin (Laeger et al. 2013 and Errazuriz-Henao et al. 2019) are also shown. Data for mid-ocean ridge basalts from the East Pacific Rise (EPR MORB), average depleted MORB mantle (DMM) and average altered oceanic crust are also included (data from Gale et al. (2013), Workman and Hart (2005) and Patino et al. (2000) respectively.

Radiogenic Sr and Nd isotopes correlate well, showing a general negative correlation to lower $^{143}Nd/^{144}Nd$ values of 0.51285 and 0.51270, and higher $^{87}Sr/^{86}Sr$ compositions between 0.7042 and 0.7048. This compares well to existing analyses available for Nevado del Ruiz (James and Murcia, 1984), which have $^{87}Sr/^{86}Sr$ compositions of 0.70429 – 0.70445 and $^{143}Nd/^{144}Nd$ of 0.512765 - 0.512842, and

close to isotopic values recently obtained for Nevado del Santa Isabel (Errazuriz-Henao et al. 2019) which have ranges of 0.704278 – 0.704939 and 0.512782 – 0.512841, but contrasts values from Cerro Machin that trend towards basement values (Laeger et al. 2013) (Figure 5.27).

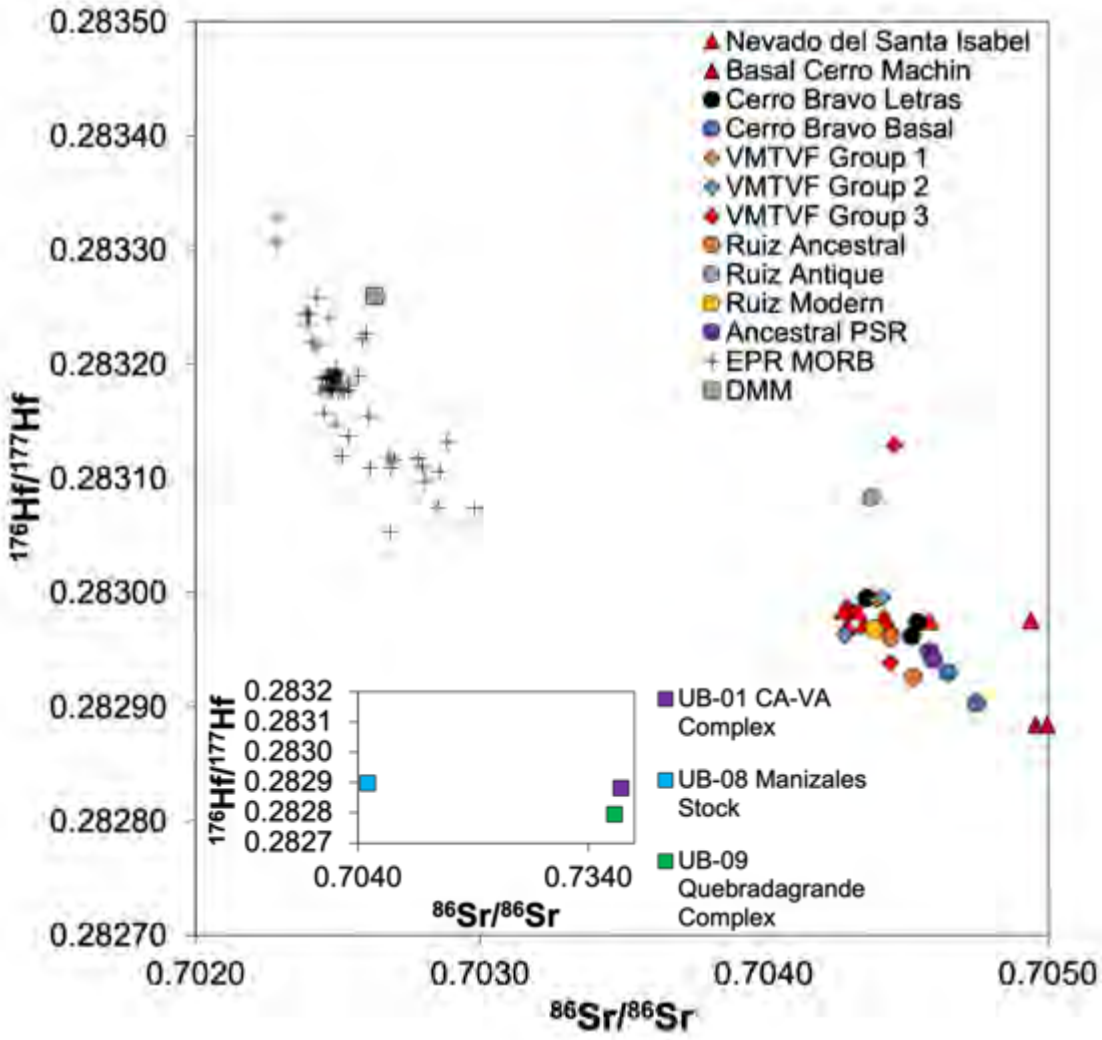

Figure 5.28: $^{176}Hf/^{177}Hf$ versus $^{87}Sr/^{86}Sr$ plot for NVP edifice data analysed and inset for basement samples analysed. Data from two other NVP edifices, Nevado del Santa Isabel and Cerro Machin (Laeger et al. 2013 and Errazuriz-Henao et al. 2019) are also shown. Data for mid-ocean ridge basalts from the East Pacific Rise (EPR MORB) and average depleted MORB mantle (DMM) are also included (data from Gale et al. (2013) and Workman and Hart (2005), respectively.

Hf isotopes also show similar decreasing trends towards crustal sources such as basement compositions (Figure 5.28). However, two samples, from Antique Ruiz (UB-05) and VMTVF Group 3 (UB-15) have greatly elevated Hf concentrations offset

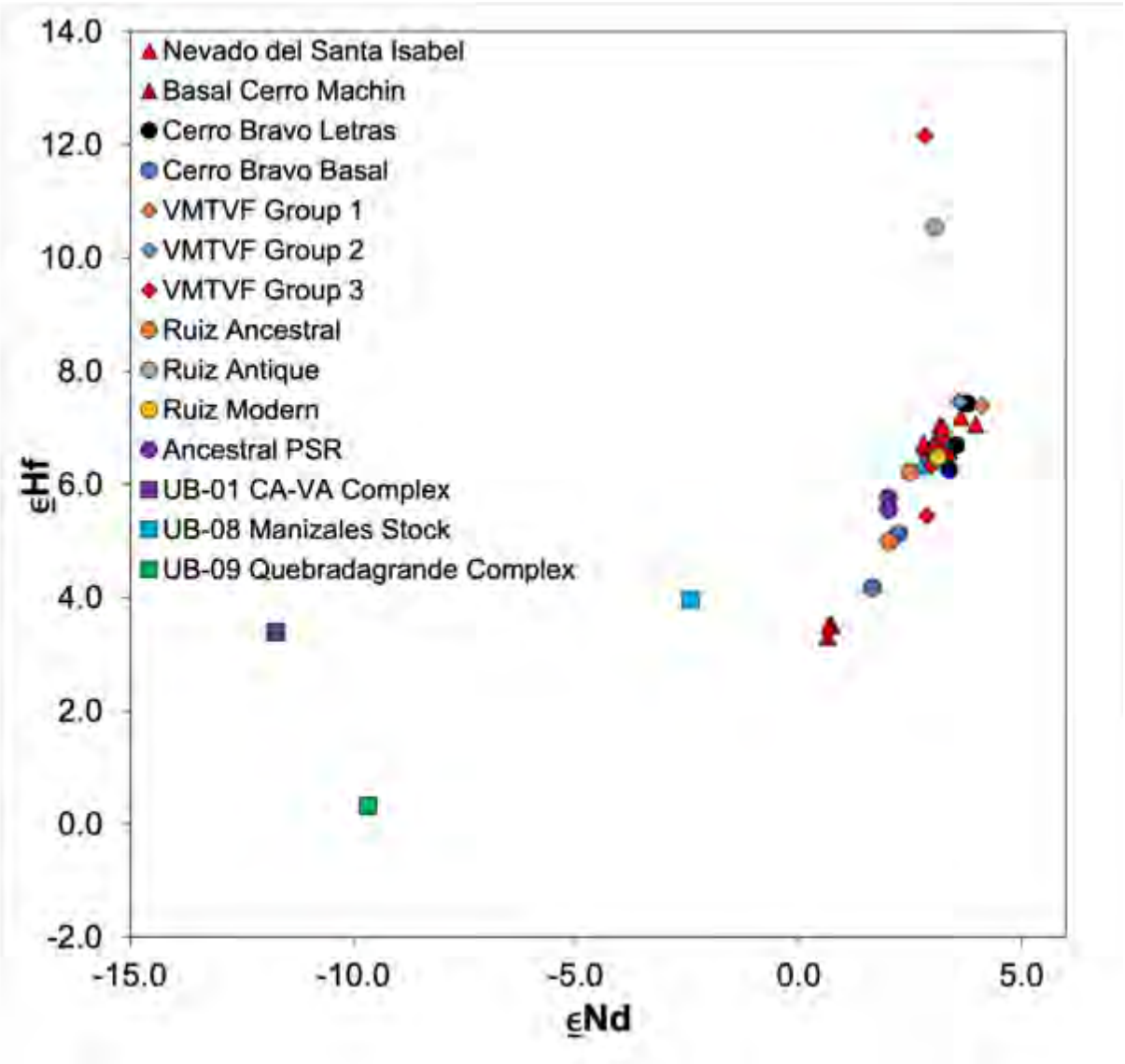

Figure 5.29: Epsilon Nd versus Hf plot of NVP analyses in this study and analysed basement. All but two samples follow an array trending towards lower values and basement compositions. Data from two other NVP edifices, Nevado del Santa Isabel and Cerro Machin (Laeger et al. 2013 and Errazuriz-Henao et al. 2019) are also shown.

from other NVP analyses. Hf isotope data exists for the NVP but is limited to analyses of Nevado del Santa Isabel and Cerro Machin (Figure 5.1b; Figure 5.28) have $^{176}Hf/^{177}Hf$ ranges of 0.282972 – 0.282988 and 0.282879 – 0.282885, respectively. This distinguishes Cerro Machin from other edifices of the NVP as having the lowest (most enriched) Hf and Nd isotopic values and highest Sr. Analyses of Basal Cerro Bravo also approach these values. Overall, isotopic data show a trend towards compositions similar to those of plutons such as the Manizales

stock and basement, with the Cerro Bravo Letras being and VMTVF having the highest $^{143}Nd/^{144}Nd$ and $^{176}Hf/^{177}Hf$ values whilst Ruiz and VMTVF Group 3 have lower values (reflected in Epsilon plots – Figure 5.29). As samples are very young (<3 Ma) age corrections are unnecessary for epsilon values given above.

The two values decoupled form the mantle array formed by the majority of samples in Figure 5.29 (which are from VMTVF Group 3 and Antique Ruiz, respectively) could be the result of fragments of ancient South American sub-continental lithospheric mantle (SCLM) within their mantle source. SCLM is to have known to be highly variable Hf isotope ratios which are decoupled from the mantle array, due to lack of mixing with the convecting mantle (Neill et al. 2012). Therefore, small amounts of ancient SCLM could be present in the mantle beneath the Colombian arc as evidenced by these samples and pointing to a slightly heterogenous source for Colombian arc magmas.

5.2.2.5 Ar/Ar geochronology:

Four samples from the NVP, two from the VMTVF (UB-16 and UB-17) and one each of the oldest phases of Cerro Bravo (UB-03) and Nevado del Ruiz (UB-06) were selected and prepared for Ar/Ar geochronology. The purpose of the VMTVF dates was to provide the first radiometric ages for Gallinazo and Victoria domes of the VMTVF, which are some of the most evolved and geochemically distinct samples. Gallinazo dome has been identified as having an “adakite-like” tendency and is part of the high K_2O geochemical group. Victoria dome was chosen as its composition has petrological and geochemical characteristics which overlap with both Group 2

and Group 3 of the VMTVF, and radiometric dating could help better constrain the petrogenesis of Victoria within the context of the VMTVF. Moreover, neither dome has previously been dated by absolute geochronology methods. The underlying basis for the volcanic stratigraphy in this area are a small number of K/Ar ages obtained across a wide area of the Northern Volcanic Province (e.g.: Thouret et al. 1990). As well as improvements in geochronology as outlined above, mapping of known volcanic structures and sampling of the area has advanced significantly since these ages were obtained, and therefore more up to date geochronology of these newly identified structures (such as the VMTVF) and mapped flows of the larger edifices is vital to improve the existing volcanic stratigraphy and hypothesised relations of these structures.

Previous geochronology work on all edifices has relied on the K/Ar technique (e.g.: Thouret et al. 1985; 1990), and $^{40}Ar/^{39}Ar$ step heating techniques offer an improvement on K/Ar analyses. As samples can be step heated in a furnace, or by a laser, individual aliquots to be released and analysed in a mass spectrometer, and an age calculated for each individual heat step. These calculated ages are then plotted against ^{39}Ar to create an age spectrum plot and a plateau age can be calculated from the individual step (Mattey, 1997). This not only improves precision, but excesses and losses of Ar may also be identified. Alteration of rocks may induce an excess of Ar which would produce an erroneously old K/Ar age, which can be identified by old apparent ages in low and high temperature heating steps (Mattey, 1997). Alternatively, post-crystallisation loss of Ar would produce erroneously young K-Ar ages, and young apparent step ages in the low temperature steps. In this way, complex age spectra produced by step heating can shed light on inheritance or loss

of Ar which would produce erroneous K/Ar results. Additionally, step heating can shed light on petrogenetic processes as different minerals with different closure temperatures are heated and analysed in each step (Mattey, 1997).

However, though preparation of samples was completed in good time, and samples were sent for irradiation, analysis of the samples has not yet been performed. This is due to continued delays at the analytical facility, the Scottish Universities Environmental Research Centre (SUERC). Despite the author's best efforts to expedite the dates and obtain regular updates from SUERC, analyses had still not been performed prior to the outbreak of the COVID-19 pandemic. SUERC facilities were closed in light of the pandemic and government restrictions being introduced in March 2020. SUERC staff have informed the author that the soonest analyses can be completed over Summer-Autumn 2020 if restrictions are lifted by then. However, given these circumstances, Ar/Ar geochronology of Colombian samples could not be included in this thesis prior to submission. The author has contextualised the samples in question as far as possible based on known stratigraphy, location, geochemistry and existing geochronology of related units to provide relative age estimates where possible.

5.2.2.6 Outliers in the Dataset:

A number of samples recur as outliers in the dataset across all groups and are therefore treated with caution during interpretation, especially in elements where they show greatest variance from their group. These include Basal Cerro Bravo sample DC16-004 and DC16-007 which have elevated trace element compositions,

particularly in ferromagnesian elements. VMTVF Group 3 sample UB-18 which has anomalously high REE values is also included here. Ancestral Ruiz Samples DC16-010 and DC16-012 have fluctuations away from their group in multiple elements and are perhaps the most altered samples (based on petrography and field notes) of the Ruiz dataset. Lastly, Paramillo de Santa Rosa sample DC16-018, has elevated trace and REE elements.

5.2.2.7 Summary:

Two broadly distinct geochemical groups emerge within the NVP analyses of this study. Major and trace element bivariate diagrams show that VMTVF Group 3 and the majority of analyses of Nevado del Ruiz of all ages have lower concentrations of TiO_2, CaO, and higher concentrations of K_2O, Na_2O, Ta, U, and a greater enrichment in incompatible elements overall compared at equivalent silica contents compared to samples from other NVP in this study. However, analyses of Cerro Bravo Dome also show some geochemical similarities to this sub-group, in elevated contents of Nb, Zr and Hf. Isotopic values for edifices vary along an array similar in composition to previous studies.

5.3 Petrogenesis of the Northern Volcanic Province of Colombia:

5.3.1 Overview:

The majority of studies of the NVP have so far focused on only a single edifice or volcanic field (e.g.: Laeger et al. 2013; Martinez et al. 2014; Botero-Gomez et al.

2017; Monsalve et al. 2017a,b; Pinzon et al. 2018) or comparison of two edifices as potential end members (i.e.: Errazuriz-Henao et al. 2019). As such, this work presents a unique opportunity to bring together new and existing petrological and geochemical data to assess the regional petrogenesis of the NVP. Previous work has proposed several explanations for geochemical variance observed in the arc varying from simple fractional crystallisation of a relatively enriched mantle derived basalt with little to no crustal contamination (e.g., Vatin-Perignon et al. 1990), assimilation fractional crystallisation (AFC) of a mantle derived melt (e.g., James and Murcia, 1984) or high degrees of intra-crustal mixing and melting/assimilation of lower crustal lithologies at the base of the crust (Laeger et al. 2013). The presence of compositions which have been called “adakite-like” in the area has also led to proposals invoking direct melting of subducting ocean crust at a slab tear (Martinez et al. 2014) though these are more accurately magnesian andesites, defined here by the high-K_2O subgroups and by Cerro Machin. Recent work has also proposed a role for melting of subducting sediments to produce these enriched compositions (Errazuriz-Henao et al. 2019). This controversy in the studies of the province so far as to whether the products of the NVP are mainly influenced by variable slab and mantle inputs (e.g.: Vatin-Perignon et al. 1990; Errazuriz-Henao et al. 2019) or by mixing, assimilation and fractionation of melts in the crust of the overlying plate (e.g.: James and Murcia, 1984; Laeger et al. 2013) or a combination of the these two end member processes is a key question in this study.

In addition to data from this study, it is useful to compare the petrography as well as the geochemistry from studies of other NVP edifices not sampled by previous studies (Laeger et al. 2013; Errazuriz-Henao et al. 2019), namely Nevado del Santa Isabel

(NSI), Cerro Machin (CM) (Figure 1b), which can provide further insight into the petrogenesis of the NVP.

Petrologically and geochemically these two edifices are distinct. NSI has a mineral assemblage similar to that of Nevado del Ruiz and parts of the VMTVF, dominated by plagioclase + clinopyroxene + orthopyroxene, with variable minor phases of olivine, biotite and amphibole (Errazuriz-Henao et al. 2019). Plagioclase dominantly occurs as small laths within the matrix and displays a trachytic texture. However, phenocrysts of plagioclase are also reported, which show disequilibrium features including corroded rims, complex zoning, mineral overgrowths and sieve textures (Errazuriz-Henao et al. 2019). Geochemically, Nevado del Santa Isabel is similar in character to its close neighbour Nevado del Ruiz, with similar major element abundances including elevated K_2O, and an enrichment in incompatible elements similar to that observed at Nevado del Ruiz in this study.

In contrast, samples of Cerro Machin in general have a plagioclase + amphibole + biotite ± minor olivine, quartz and pyroxene mineral assemblage. Plagioclase is present as both phenocryst phases (up to 4mm) with complex zoning and as aggregates in the matrix. Medium grained (0.5 – 2 mm) crystals of biotite and amphibole occur as single crystals and as glomeroporphyritic aggregates (Errazuriz-Henao et al. 2019). The most recent feature of Cerro Machin is an inter-crater dome of dacite composition (Cerro Machin Dome). This dome has a phenocryst assemblage of plagioclase + amphibole + quartz + biotite with accessory apatite, olivine and Fe-Ti oxides (Laeger et al. 2013). Both plagioclase and amphibole phenocrysts are subdivided by Laeger et al. (2013) into distinct groups. Plagioclase

phenocrysts form three groups consisting of a) Resorbed cores with strongly zoned overgrowth rims; b) Phenocrysts with continuous oscillatory zoning and c) Euhedral phenocrysts lacking zoning with anhedral resorbed outer rims. Amphiboles occur as phenocrysts of either olive-green to brown or deep brown colour, with the former (Type I) sometimes occurring as inclusions in plagioclase and latter always having a small reaction rim (Type II) (amphibole type classification after Laeger et al. 2013). Accessory phases occur in the matrix and as inclusions within plagioclase, amphibole and biotite phenocrysts. Olivine is observed as a rare phenocryst (xenocryst) and overgrown by amphibole and clinopyroxene (Laeger et al. 2013). Geochemically, Cerro Machin is one of the most evolved volcanoes in the province, capped by a dacite dome. Although on major element Harker diagrams it can define a high silica end member for our low-K_2O subgroup (Figure 5.14, its trace element compositions are distinct compared to those in the rest of the NVP (e.g.: having the most depleted HREE's).

As shown above, there are clear petrological, geochemical and isotopic differences observed in the individual volcanic centres of the NVP. On the basis of these differences, the NVP sampled in this study and by previous work can be divided into two broadly distinct groups. The first group (NVPG1) consists of high-K_2O, high-Mg# (Mg# = (Mg/[Mg+Fe] x 100)) (Figure 5.30) rocks, consisting of VMTVF Group 3, a subset of Nevado del Ruiz samples and, less consistently, the Cerro Bravo Dome samples. These have higher modal proportions of amphibole and clinopyroxene compared to orthopyroxene. Quartz is also observed in some of the more evolved rocks of this group (e.g.: UB-16). NVPG1 also tend to be more enriched in incompatible elements, HFSE and LREE. The only exception to this is the Cerro

Bravo Dome, which is less abundant in some HFSE (Nb, Zr) and Sr. NVPG1 is also consistent with the majority of Nevado del Ruiz analyses in literature (Martinez et al. 2014), and with analyses of Nevado del Santa Isabel (Errazuriz-Henao et al. 2019).

The remainder of NVP analyses (NVPG2) in this study consists of samples with medium-K_2O and low-Mg# including Paramillo de Santa Rosa, Letras and Basal stages of Cerro Bravo and VMTVF Groups 1 and 2. Ancestral and Antique Ruiz samples show affinity to both groups. Larger geochemical studies of Galeras have also identified this disparity, with a small minority of samples of Ancestral Ruiz trends identified as showing similar trends to the NVPG2 group here (Martinez et al. 2014). In our case, most Ancestral Ruiz samples correspond to this trend (Figures 5.14 and 5.31) NVPG2 has a diverse petrography, varying from primitive, mafic olivine and pyroxene compositions (VMTVF Group 1) up to far more evolved compositions containing biotite. These have a lower K_2O and overall silica and tend to be less enriched in incompatible elements and LREE compared to the NVPG1 group. The most evolved members of this group are the andesites and dacites of Cerro Machin volcano, though the magmatic rocks of this edifice have some geochemical features more common to the NVPG1 group, with a strongly elevated Mg# and enrichment in LREE compared to HREE. Examining these two groups, we can start to unpick the petrogenesis of the NVP.

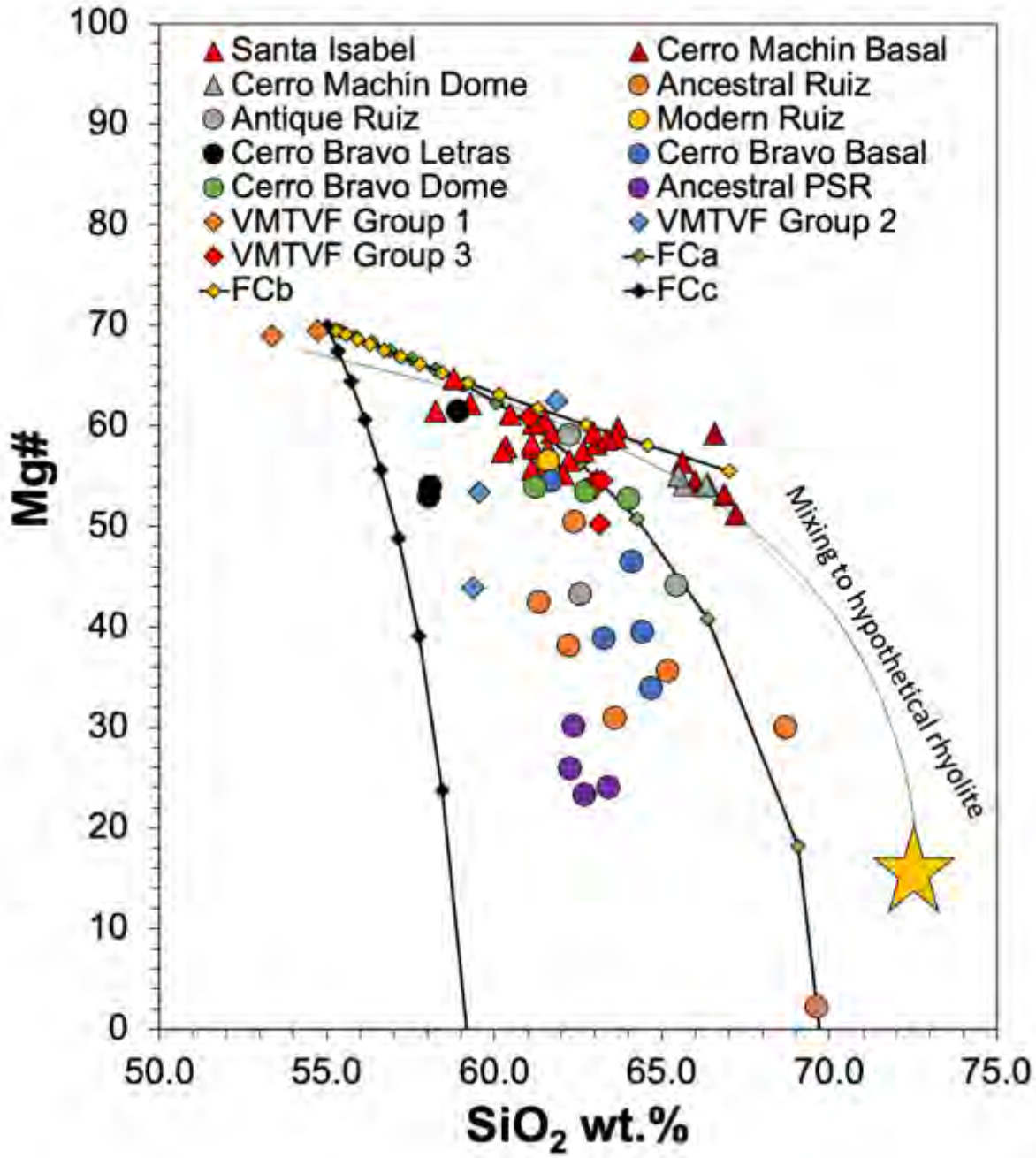

Figure 5.30: Mg# versus SiO_2 for Northern Volcanic Province samples in this study. Note that Cerro Bravo Dome, VMTVF Group 3 and a subset of Ruiz samples form a high-Mg# group along with Nevado del Santa Isabel and Cerro Machin analyses. Also shown are a hypothetical mixing line between a basalt and rhyolite (after Errazuriz-Henao et al. 2019 and modelled FC trends (discussion in text).

5.3.2 Intra-Crustal Processes:

5.3.2.1 Fractional Crystallisation:

Magmatic differentiation by fractional crystallisation of melts in the crust of the overlying plate has played an obvious role in the evolution of NVP volcanism. The magmas form trends away from primitive basalt compositions with ferromagnesian concentrations far lower than mantle derived melts, and crystallisation of mineral phases at significantly lower temperatures (e.g.: biotite, quartz). The simplest explanation for this is fractional crystallisation of magmas as they ascend through the crust, as phases are gradually crystallised out of the magma as it ascends and cools and changes composition (Bezard et al. 2015). This is clearly evidenced by the fractionation trends with increasing silica observed on Harker diagrams (Figure 5.14, 5.15, 5.16) with trends in agreement with work from previous studies (e.g.: Martinez et al. 2014; Errazuriz-Henao et al. 2019). For these trends to be consistent with fractional crystallisation within a closed system, inflections within major and trace element Harker diagrams would be expected, as different mineral phases crystallise and begin to alter the composition of the melt (e.g.: Al_2O_3 and Sr being sequestered into plagioclase), which is observed in Cerro Bravo Dome samples. However, fractional crystallisation of olivine and pyroxene could reduce the Mg# contents of magmas even at low SiO_2 (Kelemen, 1995). Such a decrease in Mg# with increasing silica is therefore suggestive of fractional crystallisation processes, as shown for NVPG2 group rocks (Figure 5.30) and could be due to early crystallisation of pyroxene. However, the high-Mg# maintained by NVPG1 suggests that a simple closed system where the fractional crystallisation is the only driver, as has been

suggested previously for Nevado del Ruiz (Vatin-Perignon et al. 1990) is not the case, especially for NVPG1 groups. Rather, fractional crystallisation, though a dominant process within the NVP, is supplemented by assimilation or mixing of a crustal component or magma which could maintain the high-Mg# observed. As stated previously, this high-Mg# can be interpreted as greater interaction with primitive mantle melts (or mixing between this and a high silica end member, as suggested by the hypothetical mixing line in Figure 5.30).

However, modelling suggests that both NVPG1 and NVPG2 groups could be equally if not more plausibly explained by fractional crystallisation trends, with variations arising due to differences in the fractionating assemblage. Figure 5.30 shows three modelled fractional crystallisation trends. The starting composition for these models is a basaltic andesite composition adapted from Bucholz et al. (2014) and broadly and similar in major element composition to La Esperanza basalts. These simple fractional crystallisation trends are modelled using the equation:

$$C_l = C_0 F^{(D-1)}$$

Where C_l is the concentration in the liquid, C_0 is the initial concentration before fractional crystallisation, D is the bulk partition coefficient of the fractionating assemblage and F is the proportion of melt remaining. Trend FCa consists of a fractionating assemblage of plagioclase, hornblende, biotite and magnetite in proportions 30:54:10:6, with fractional crystallisation of such an assemblage successfully replicating Cerro Bravo Dome, VMTVF Group 3 and the majority of Nevado del Ruiz analyses. Additionally, slightly increasing the abundance of

hornblende respective to plagioclase in this modelling allows the trend to pass through Basal Cerro Bravo compositions with lower Mg# and silica (trend not shown). Therefore, fractional crystallisation of a primitive magma in such an assemblage offers a plausible mechanism for NVPG2. Modelling trend FCb (Figure 5.30), consisting of a fractionating assemblage of plagioclase, hornblende and biotite in proportions 48:48:4 successfully models the high-Mg# trend of Cerro Machin, Nevado del Santa Isabel and NVPG1. There is significant overlap between this trend and FCa, due to the similarity in fractionating assemblage and shared source. The major difference between these two models is likely later stage crystallisation of biotite in FCa, as observed at Cerro Bravo, compared to a lack of biotite in FCb, where high degrees of FC successfully reproduce Cerro Machin compositions. Lastly, given a possible role for garnet in the petrogenesis of the NVP (e.g.: Laeger et al. 2013), an assemblage including garnet was modelled as trend FCc (Figure 5.30) This comprises clinopyroxene, garnet and hornblende in proportions 45:25:15, and as shown is unsuccessful in modelling the observed trends. Therefore, elevations in trace element ratios involving medium or heavy rare earth elements (M/HREE) are more likely to be driven by amphibole and clinopyroxene than garnet fractionation.

Direct surveying such as seismic tomography (Vargas et al. 2017) as well as indirect methods such as thermobaraometry (Laeger et al. 2013; Pinzon et al. 2017) have identified shallow magma chambers (<5 km) beneath the edifices of the NVP, which are probably major sites of fractional crystallisation within the NVP. This would facilitate degassing of the magmas, and explains the formation of small plagioclase microliths and secondary phenocrysts observed throughout the province. These likely

crystallised at a relatively late stage in the life of the magmas (e.g.: Laeger et al. 2013; Pinzon et al. 2018) after significant loss of volatiles at shallow depths, as high melt H2O contents and higher pressures retard plagioclase nucleation (Hattori and Sato, 1996). The common feature of a trachyitic texture defined by plagioclase microlites in groundmass throughout the province (i.e.: Pulgarin et al. 2017; Osorio et al. 2017a; Errazuriz-Henao et al. 2019) suggesting a late growth of plagioclase during shallow cooling and eruption of lava flows and domes. This can be coupled with other evidence of shallow processes, such as amphibole and pyroxene geothermobarometry conducted at Cerro Machin (Laeger et al. 2013) and Cerro Bravo (Pinzon et al. 2018) which indicates crystallisation of amphiboles and pyroxenes in mid- to lower-crustal magma chambers (5 – 20 km) prior to plagioclase nucleation in shallow, near surface chambers. Both studies suggest that the magmas were fed by a deeper source, possibly directly from mantle derived melts (Laeger et al. 2013), but also from a system in the deep crust at ~20 – 30 km, where initial fractional crystallisation across the NVP could be taking place (i.e.: Murcia et al. 2017). This is further evidenced by a large low velocity anomaly beneath the province located at this depth (Londoño, 2016). This evidence of a well-developed magmatic plumbing system beneath the NVP furthers the idea of fractional crystallisation being a first order control on the compositional variation in NVP magmas, along with secondary processes such as magma mixing and assimilation alongside fractional crystallisation. Additionally, prolonged residence in more developed magmatic systems, and decreasing fractions of melt following crystallisation could have heightened incompatible element concentrations as observed in the NVPG1 subgroup.

5.3.2.2 Magma Mixing:

Mixing of magmas has previously been suggested as a key factor in the compositions of the NVP volcanoes (i.e.: Gourgaud and Thouret, 1990; Laeger et al. 2013). Evidence for mixing of mafic/felsic components was observed in the field, related to light and dark banding and flow textures within outcrop related to Paramillo de Santa Rosa. The abundance of disequilibrium textures observed in NVP lavas overall also suggests magmatic systems where mafic and felsic components are mixed (i.e.: sieve textures and oscillatory zoning of feldspars; Fe-Ti oxide rims to amphiboles and biotite). Such disequilibrium features at both outcrop and at the microscopic level are consistent with mechanical mixing and mingling of magmas with contrasting compositions (e.g.: Gourgaud and Thouret, 1990; Vatin-Perignon et al. 1990). Bulk rock compositions with elevated Cr can also indicate mixing of a mafic input from a mantle wedge derived magma, which will be enriched in Ni and Cr (in line with high-Mg#), with a more felsic magma (or other enriched component) already resident in the crust (Streck et al. 2007). Cr across the NVP is slightly elevated (>34 ppm), even in evolved samples (Figure 5.32) and those lacking olivine, perhaps indicating the prevalence of mixing processes across the province. However, as shown in Figure 5.31, fractional crystallisation offers a more plausible mechanism for generating the compositions observed, though field and petrographic evidence suggests a small role for mixing.

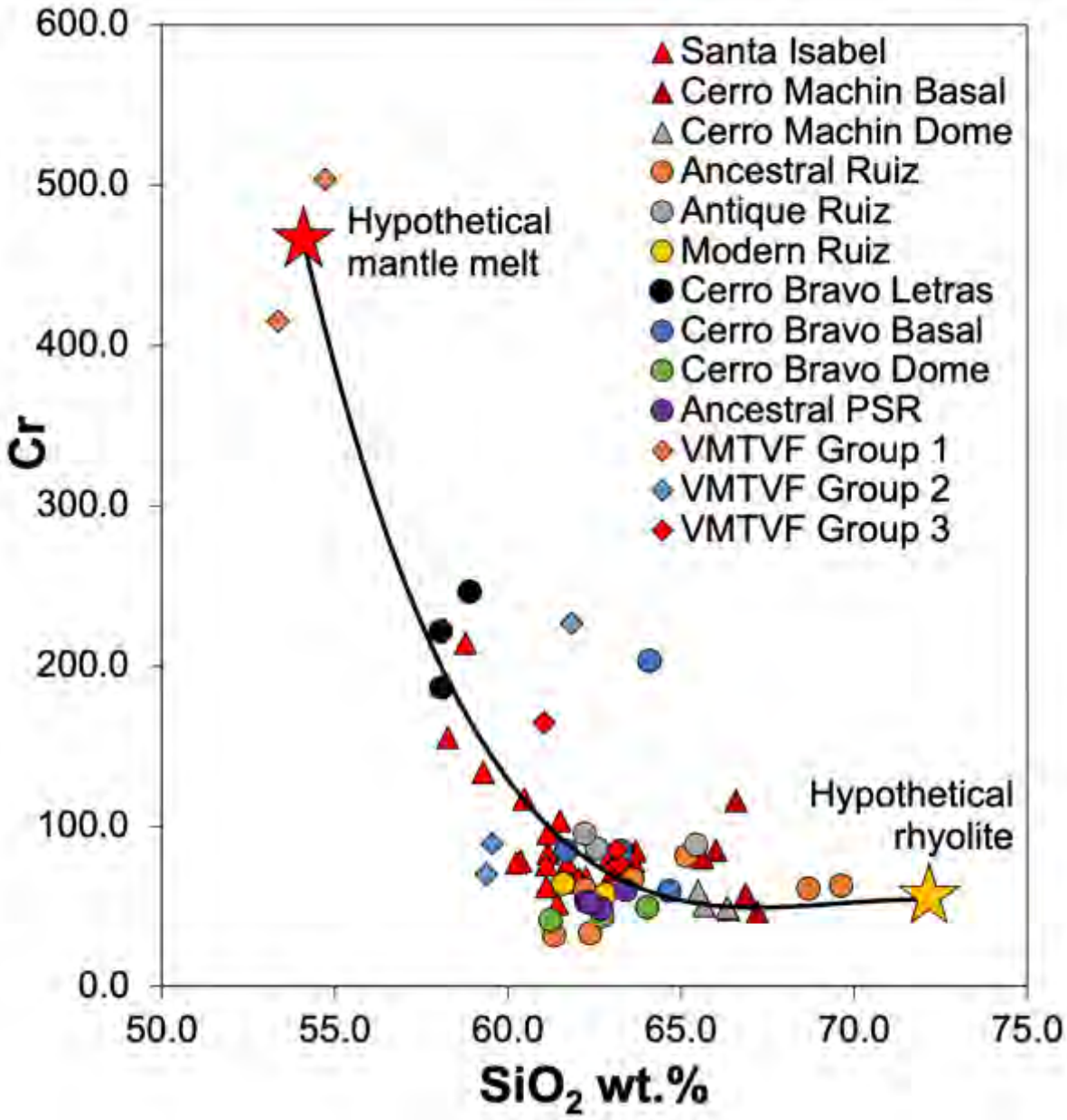

Figure 5.31: Cr versus SiO2 for NVP edifices. VMTVF Group 1 have ferromagnesian contents similar to mantle values and could represent parental compositions to the NVP. A hypothetical rhyolite composition is also shown as a potential, hypothetical, mixing end member. Note also the depletion of Cerro Bravo Dome and the majority of Cerro Machin analyses compared to VMTVF Group 3.

5.3.2.3 Assimilation and Fractional Crystallisation:

Alongside mixing of magmas within the crust, a high flux magmatic system with a continual input of mantle derived mafic melts could introduce enough heat and volatiles into the system to begin melting wallrock components (Hildreth and Moorbath, 1988; Annen et al. 2006). This would affect the composition of the ascending magmas and potentially provide a source for incompatible element enrichments and more radiogenic isotope compositions.

As noted above, the diversity of arc magmas is mainly acquired by processes occurring during transport of magma through the crust of the overlying plate (Turner and Langmuir, 2015a), evidenced by pervasive mixing textures observed in arc magmas globally (e.g.: Eichelberger et al. 2006), correlations with crustal thickness in the Andes (e.g.: Hildreth and Moorbath, 1988; Feeley et al. 1993) and chemical systematics (e.g.: Reubi et al. 2011; Laeger et al. 2013). Crustal thickness could be important here, as the boundary between the lower crust and the mantle acts as a density filter for magmas ascending from the wedge, allowing them to pond at depth in this area and begin to differentiate (e.g. Muntener et al., 2001; Annen & Sparks, 2002). Therefore, a deep crustal component consisting of pyroxenites, amphibolites and garnet bearing rocks may also contribute to the compositions seen in the NVP rocks, in addition to any mixing processes or contamination by components within the upper crust. A number of workers have identified correlations between crustal thickness and specific trace element parameters such as Sr/Y and La/Yb (e.g.: Chiaradia, 2015). In the NVP (Figure 5.32), this is manifest in depletion in medium and heavy rare earth elements (e.g.: La/Yb, Dy/Yb, Gd/Yb) and elements such as Y

(Sr/Y, Ce/Y) probably related to the compatibility of these elements in minerals such as garnet and amphibole which are stable at high pressures within the crust (Macpherson et al. 2006; Ribiero et al. 2016).

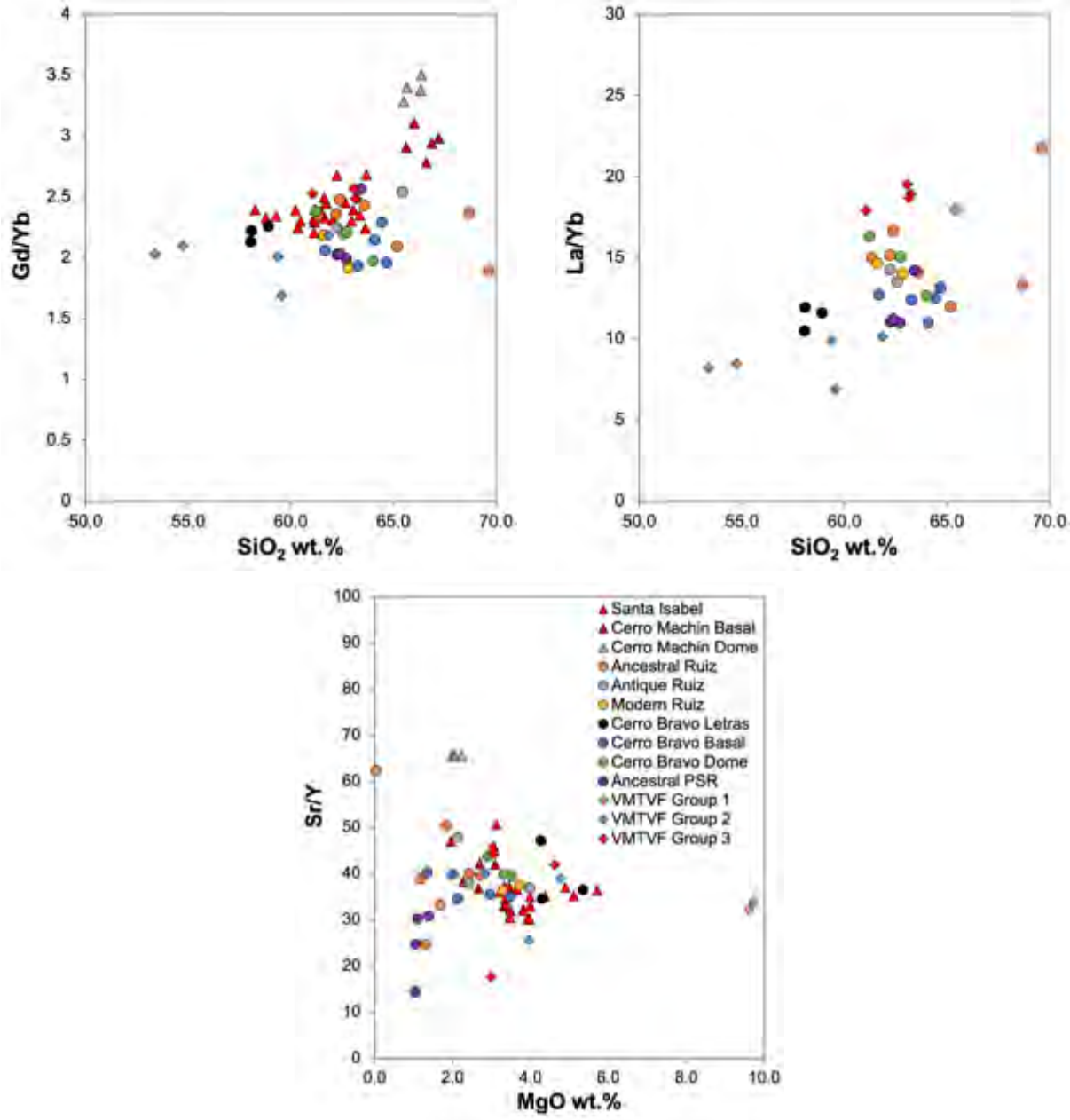

Figure 5.32: Ratios of Gd/Yb, La/Yb over silica and Sr/Y over MgO (after Chiaradia, 2015). Note the elevation of high-Mg# subgroup ratios and especially VMTVF Group 3 (in La/Yb space) and Cerro Machin in Sr/Y and Gd/Yb space.

Geophysical surveys have shown that the crust beneath the NVP is some of the thickest in Colombia, varying from ~45 km up to ~52 km thick beneath Cerro Machin (Poveda et al. 2015). This thicker crust below Cerro Machin would explain the more depleted HREE and Y trends seen in Figure 5.34. and points to a greater role for amphibole alongside clinopyroxene (and possibly small amounts of garnet for the dacites of Cerro Machin Dome) as fractionating phases at depth. Similarly, elevated ratios recorded by the NVPG1 subgroups suggest a dominant role for amphibole fractionation, which is modelled in Figure 5.30. Global compilations of continental arcs have shown that ratios such as La/Yb and Gd/Yb only begin to increase after crustal thickness exceeds ~43 km which corresponds to ~1.2 GPa (Farner and Lee, 2017) which is also where experimental studies indicate stability of amphibole and garnet stability in hydrous mafic systems (e.g.: Alonso-Perez et al., 2008). Evidence for the magmas in this study ascending through a crustal region in the garnet stability field is given by the presence of lower crustal derived garnet bearing xenoliths (Weber et al. 2002; Rodriguez-Vargas et al. 2005) in southwest Colombia, as well as the presence of garnet bearing magmatic rocks in this region of Colombia (e.g.: Jaramillo et al. 2019). However, amphibole seems a more likely candidate given the lower Dy/Yb and La/Yb ratios (Figures 5.34 and 5.34) shown by NVP rocks, as well as the predominance of amphibole phenocrysts and pyroxene glomerocrysts observed in these rocks in thin section, perhaps indicative of a source rich in these minerals (e.g.: Smith, 2014). This would still accord with a lower crustal origin, evidenced by samples of amphibole bearing xenoliths with Lu-Hf ages of <5 Ma, coeval with volcanism (Bloch et al. 2017).

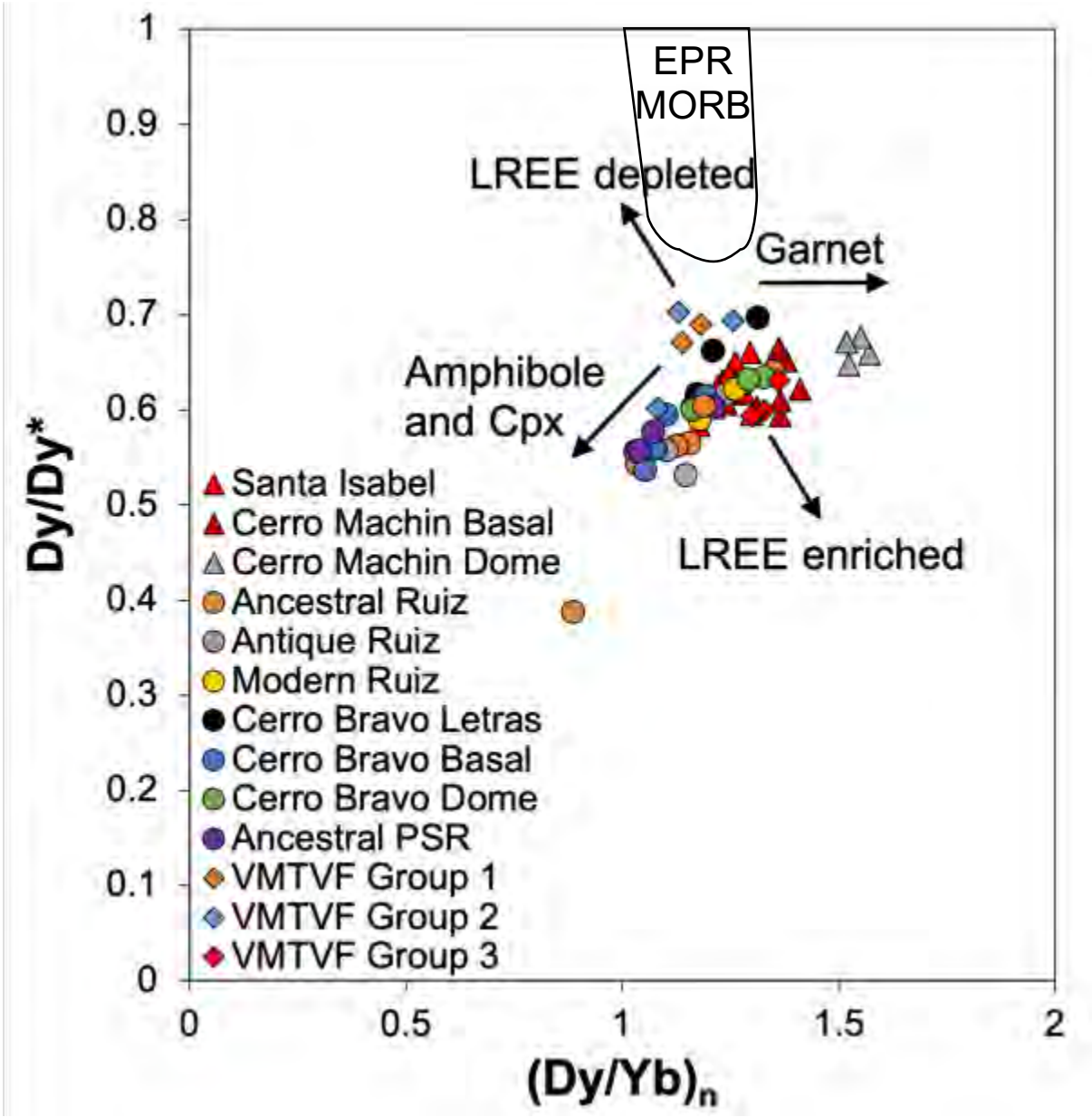

Figure 5.33: Dy/Dy* versus chondrite normalised Dy/Yb, used as a proxy for REE curvature and depletion/enrichment. Note the LREE depletion of most primitive parts of NVP (VMTVF Groups 1 and 2, Cerro Bravo Letras) and tendency of high-Mg# subgroups towards garnet influence. [$Dy/Dy^* = (Dy_N / La_N^{4/13} Yb_N^{9/13})$] modified after Davidson et al. (2013). Normalisation values from Sun and McDonough (1995). Field for East Pacific Rise (EPR) MORB based on data from Gale et al. (2013).

The term “adakite” has been applied haphazardly to some rocks within the NVP in past studies (e.g.: Toro et al. 2008; Borrero et al. 2009), with elevated Sr/Y and La/Yb ratios used as justification for applying the term (Martinez et al. 2014) and this leading to speculation as to whether elevated Sr/Y and La/Yb (as displayed in our

NVPG1 subgroup) rocks are the result of partial melting of subducted and/or lower crust (e.g.: Martinez et al. 2014). Examination of the NVP shows they do not meet many of the defined adakite parameters, which are typically defined by more evolved major element compositions typical of intermediate to silicic rocks (e.g.: SiO_2 >56 wt.%, Na_2O >3 wt.%). Al_2O_3 is also typically high (>15 wt.% at 70 wt.% SiO_2) due to partial melting of eclogite or amphibolite facies at high pressures (Castillo, 2012). Low ferromagnesian element concentrations are used as indicators partial melting of eclogite as opposed to the peridotite mantle (Castillo, 2012) which our samples lack, and though samples here do show elevated concentrations of Sr (>500 ppm), indicative of the lack of residual plagioclase in the source region (Castillo, 2012) along with characteristic low Y and Yb contents, perhaps indicative of amphibole in the source, leading to elevated Sr/Y and La/Yb ratios (Figure 5.32), these signatures are not nearly enriched enough to be true adakites. In addition, melting of oceanic crust would produce isotopic values akin to MORB (e.g.: $^{87}Sr/^{86}Sr$ <0.704) which are not observed in NVP lavas (Figure 5.27). NVP samples also show elevated Ba/La ratios (>50) which are uncharacteristic of MORB melting (Castillo, 2012). Therefore, samples with elevated Sr/Y and La/Yb ratios within the NVP are not adakites (Defant and Drummond, 1990) derived from partial melting of a mafic source. Additionally, though Sr/Y and La/Yb commonly correlate, though they can be decoupled in some circumstances, such as during fractionation of arc magmas in the presence of either amphibole (e.g.: Davidson et al. 2007) or garnet (e.g.: Alonso-Perez et al. 2009). Furthermore, modelling of mineral fractionation and melting trends by Moyen (2009) shows that though amphibole fractionation will increase both ratios, it will have a greater effect on Sr/Y values than La/Yb, which appears to be the case for NVP compositions (Figure 5.32).

For Cerro Machin, whilst the textural diversity observed in these rocks could have formed by mixing in mid- and shallow-crustal chambers, isotopic and trace element data indicate addition of another more radiogenic component, such as lower and mid-crustal material (Laeger et al. 2013). This is a model which could be applied to other NVP samples, as Sr/Nd is ~30 – 40 across the province, suggesting assimilation of a plagioclase rich source or oceanic crust lithology, for example the Quebradagrande Complex or mid- or lower-crustal gabbro (Woodhead, 1988). Lower crustal compositions typically have low abundances of highly incompatible elements (Rudnick and Fountain, 1995), precipitating the need for a larger slab flux to contribute these or a crustal assimilant enriched in incompatible elements. This could only be overcome if a very large degree of crystal fractionation (>65%) of the lower crustal source occurred (e.g.: Schiano et al. 2010). This degree of fractionation would require large volumes of mafic cumulate, and in any case there are good but only small correlations between fractionation indices and isotope values (e.g.: SiO_2, Sr, MgO, Eu/Eu*) indicative of a limited role for AFC processes in the petrogenesis of all NVP rocks, and especially Cerro Machin (Figure 5.34).

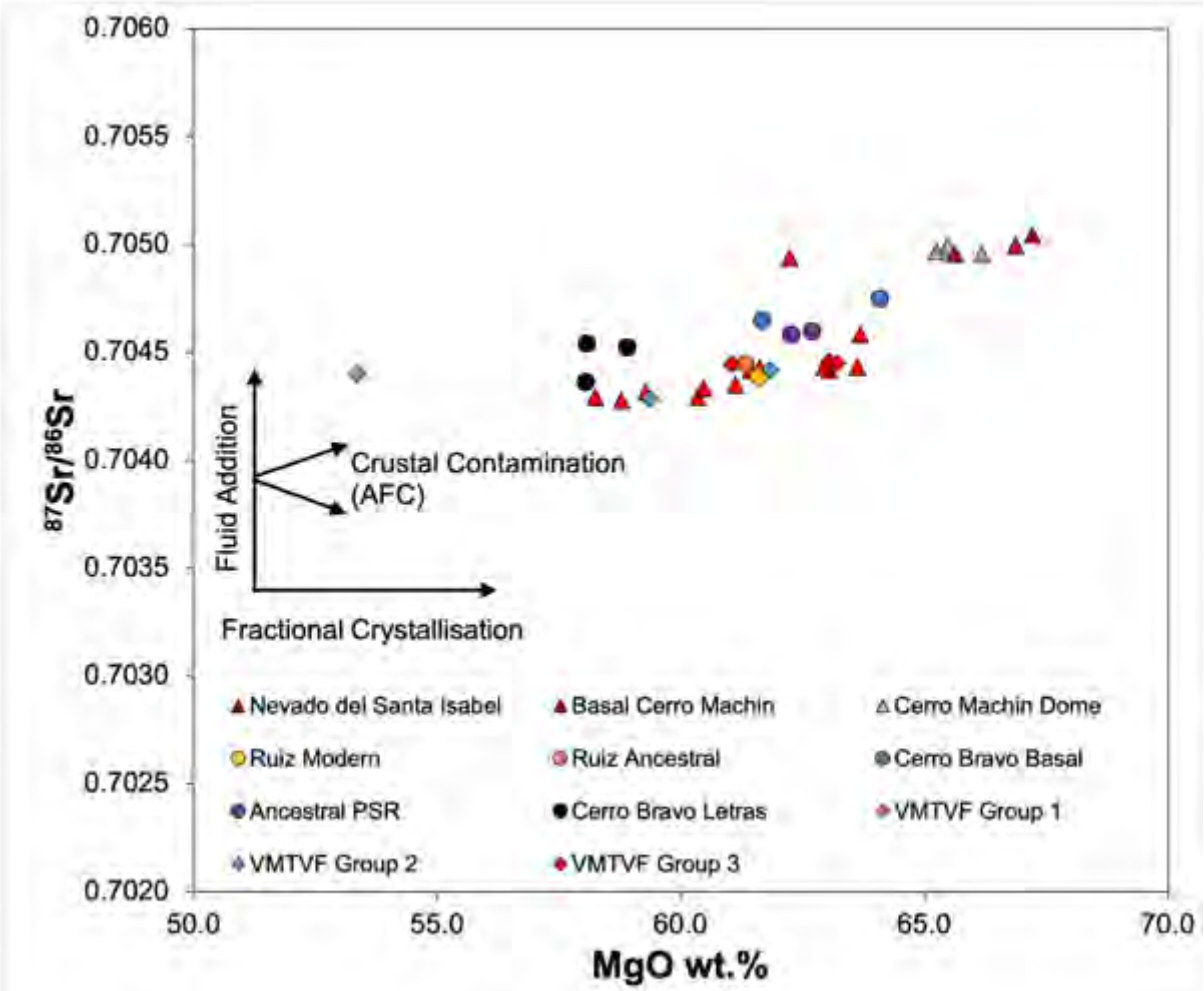

Figure 5.34: Plot of $^{87}Sr/^{86}Sr$ over MgO, used here as an index of fractionation. Not the shallow positive correlation indicating a limited amount of assimilation alongside fractional crystallisation for all NVP groups, with Cerro Machin and one Santa Isabel sample defining the most radiogenic compositions. These trends are reflected in other plots of isotopes versus fractionation indices (e.g.: Sr, SiO_2, Eu/Eu*).

5.3.2.4 Assimilation of shallow plutonic rocks:

A notable feature of the area underlying the NVP, and exposed in the vicinity of Cerro Bravo, Nevado del Ruiz and the VMTVF is the Manizales Stock, a large Eocene plutonic body of granodiorite and tonalite composition. This, along with the El Bosque Batholith of similar composition and age further south, underly the majority of the NVP as far south as Cerro Machin (Gonzalez-Garcia et al. 2015). Recent work on the geochemistry of the VMTVF (Osorio et al. 2018b) suggests that some features of NVPG1 identified here, such as an incompatible element enrichment, could be gained by assimilation of this Eocene plutonic material as wallrock in shallow magma chambers feeding these systems.

Alternatively, there is the possibility of assimilation occurring in the lower crust, as part of assimilation processes there already implied, by melting of metamorphic lithologies such as gneisses, represented by xenoliths obtained from SW Colombia. A selection of these samples (XC-1, GNS-3, GNS-5) do exhibit compositions of trace elements which are more enriched as end member compositions than almost anything else in the basement of the NVP (Figure 5.35), and if assimilated could provide an alternative enriched end member source to the Eocene basement. However, data from other lower crustal xenoliths reveals a higher proportion of granulite and pyroxenites with far more depleted compositions (Figure 5.35), and modelling of the bulk lower crustal composition based on these xenoliths suggests it acts as an end member depleted in incompatible elements, complementary to the enriched end member provided by the Eocene stock.

To test this hypothesis, we can use trace element and isotopic data of the Manizales Stock collected in this study (as well as other Eocene plutonic bodies of the Central Cordillera with similar ages and compositions) to model if shallow assimilation of any of these bodies could have produced the compositions observed.

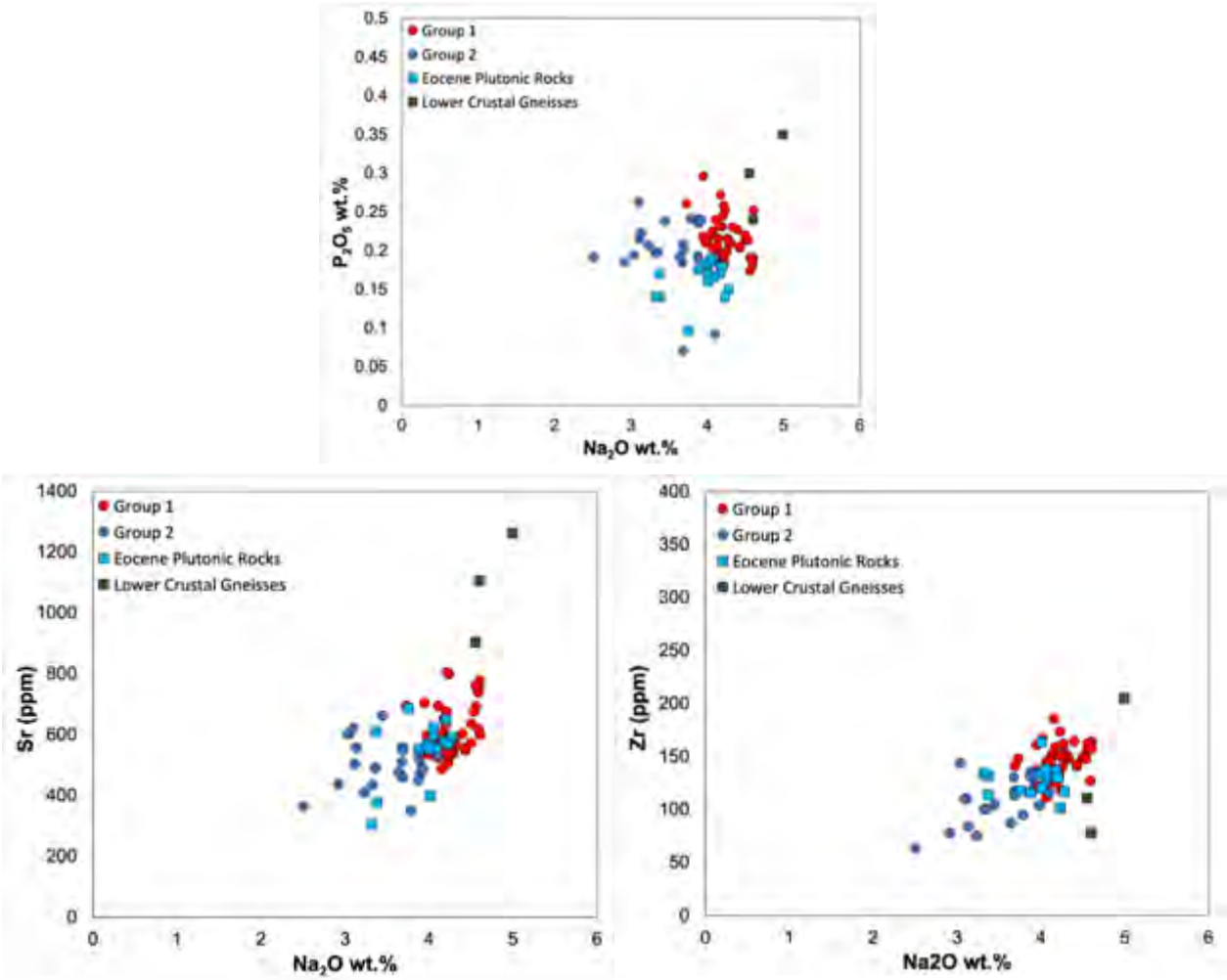

Figure 5.35: Comparison of NVP groups to Eocene plutonic bodies such as the Manizales Stock and El Bosque Batholith which form their upper crustal basement and lower crustal gneisses sampled by xenoliths. NVP samples overlap with Eocene stock compositions but high-Mg# NVP subgroups tend to have equivalent or greater enrichment in incompatible elements compared to Eocene basement, closer to those of LCC gneisses.

Trace element modelling of a selection of elements of varying compatibility (La, Nb, Sm) against Yttrium is used to assess mixing, assimilation and fractional crystallisation trends modelled between the most primitive sample of the NVP collected within this study, from the La Esperanza flow of the VMTVF. Based on petrography and geochemistry (olivine phenocrysts, high Mg# and ferromagnesian contents close to mantle values) this is interpreted as a mantle derived melt which has undergone little fractionation in the crust and could perhaps be parental to other NVP compositions (c.f.: Murcia et al. 2019). Simple mixing, assimilation fractional crystallisation (AFC) and fractional crystallisation (FC) trends are calculated using this composition and that of sample UB-08, collected from outcrop of the Manizales Stock (Figure 5.36). Fractional crystallisation trends are calculated using the following equation:

$$C_l = C_o F^{(D-1)}$$

Where C_l is the concentration of the trace element in the resultant magma, C_o is the initial concentration of the trace element prior to fractionation, F is the proportion of melt remaining and D is the bulk partition coefficient. Assimilation fractional crystallisation (AFC) trends are plotted using the following equation:

$$C_l = C_o [F^{-z} + (r/r-1)\, C_w/zC_o\, (1-F^{-z})]$$

In which r is the assimilation/fractionation ratio, here set at 0.7 and C_w is the element concentration in the assimilant. The remaining parameters are as for the fractional crystallisation equation given above. Finally, simple mixing between components is calculated using the following equation:

$$C_l = C_oX + C_A (1\text{-}X)$$

In the above case C_A defines the concentration of the element in the wallrock assimilant And X defines the mixing proportion. The crystallising mineral assemblage used in this modelling is from Woodhead (1988) consisting of plagioclase + clinopyroxene + magnetite + olivine in proportions 60:25:10:5 to approximate a gabbroic assemblage. Partition coefficients are from McKenzie and O'Nions (1991) and Bedard (2006). For the AFC models, the assimilation/fractionation ratio is set to 0.7 in all cases. Tick marks represent 10% reductions in the fraction of melt remaining from the initial magma. These trends reveal that both mixing with, and AFC of small volumes of a Manizales Stock composition could partially replicate some of the NVP compositions observed (Figure 5.36). In particular, it shows that the high-Mg# NVPG1 samples may simply result from a greater degree of assimilation fractional crystallisation compared to the low-Mg# NVPG2 groups, whilst Ancestral Ruiz samples may be related to simple mixing processes between mafic and evolved magmas (Figure 5.36).

This can be further explored by modelling of end-member simple mixing and AFC trends using radiogenic isotope compositions (Figure 5.37). Simple mixing trends are calculated using the following equation:

$$rC_M = rC_AC_AX + rC_BC_B(1 – X) / C_AX + C_B(1 – X)$$

Where rC_M is the isotope ratio value of the mixture, rC_A and rC_B are the isotopic ratios of components A and B, respectively, C_A and C_B are the corresponding Hf and Nd values of these components, and X is the mass fraction of component A in the mixture (Hastie et al. 2015). Assimilation fractional crystallisation trends are calculated using the following equation:

$$rC_i = r/r\text{-}1\ C_W/z\ (1 - F^{-Z})iC_W + C_0F^{-Z}\ iC_0 / r/r\text{-}1\ C_W/z\ (1 - F^{-Z}) + C_0F^{-Z}$$

In this case, Z is the result of the equation:

$$Z = r + D_0 - 1 / r - 1$$

In the above equations rC_i is the isotope ratio value of the magma, iC_W is the isotope ratio of the wallrock assimilant, iC_0 is the isotope ratio value of the original magma, r is the assimilation/fractionation ratio (set at 0.7 in all cases), F is the fraction of melt remaining, C_0 and C_W are respectively the element concentrations in the initial magma and the wallrock assimilant and D_0 is the bulk partition coefficient. D_0 in this case is calculated using a fractionation assemblage after Woodhead (1988) consisting of plagioclase + clinopyroxene + magnetite + olivine in proportions 60:25:10:5, with partition coefficients from McKenzie and O'Nions (1991) and Bédard (2006).

As with trace elements, mixing and AFC trends involving the Manizales Stock and average compositions for Eocene plutonic bodies (Hastillo Stock and El Bosque Batholith) do follow a trend in isotope space initially close to that for NVP samples, but trend towards much lower Nd isotope compositions at equivalent Hf isotope values to some of the group. AFC and simple mixing trends of primitive NVP compositions and Eocene Stock cannot replicate the trends observed in NVP data. This suggests that although a small amount of assimilation and/or mixing may influence compositions of trace elements, another either another crustal component is involved, or there is a different mantle source for the NVPG1 and NVPG2 groups. Also plotted on Figure 5.37 are simple mixing and assimilation fractional crystallisation trends between average lower continental crust (LCC) after Marin-Ceron et al. (2010), sediment components (after Errazuriz-Henao et al. 2019) and shallow assimilants. This shows that some of the more primitive NVP compositions may be generated by a mixture of assimilants, including LCC and, perhaps Eocene Stock underlying the NVP, particularly the Manizales Stock or El Bosque Batholith (or another shallow assimilant), and that AFC of LCC and shallow crustal components, with some input from sediment components, can convincingly demonstrate the whole range of NVP isotopic compositions.

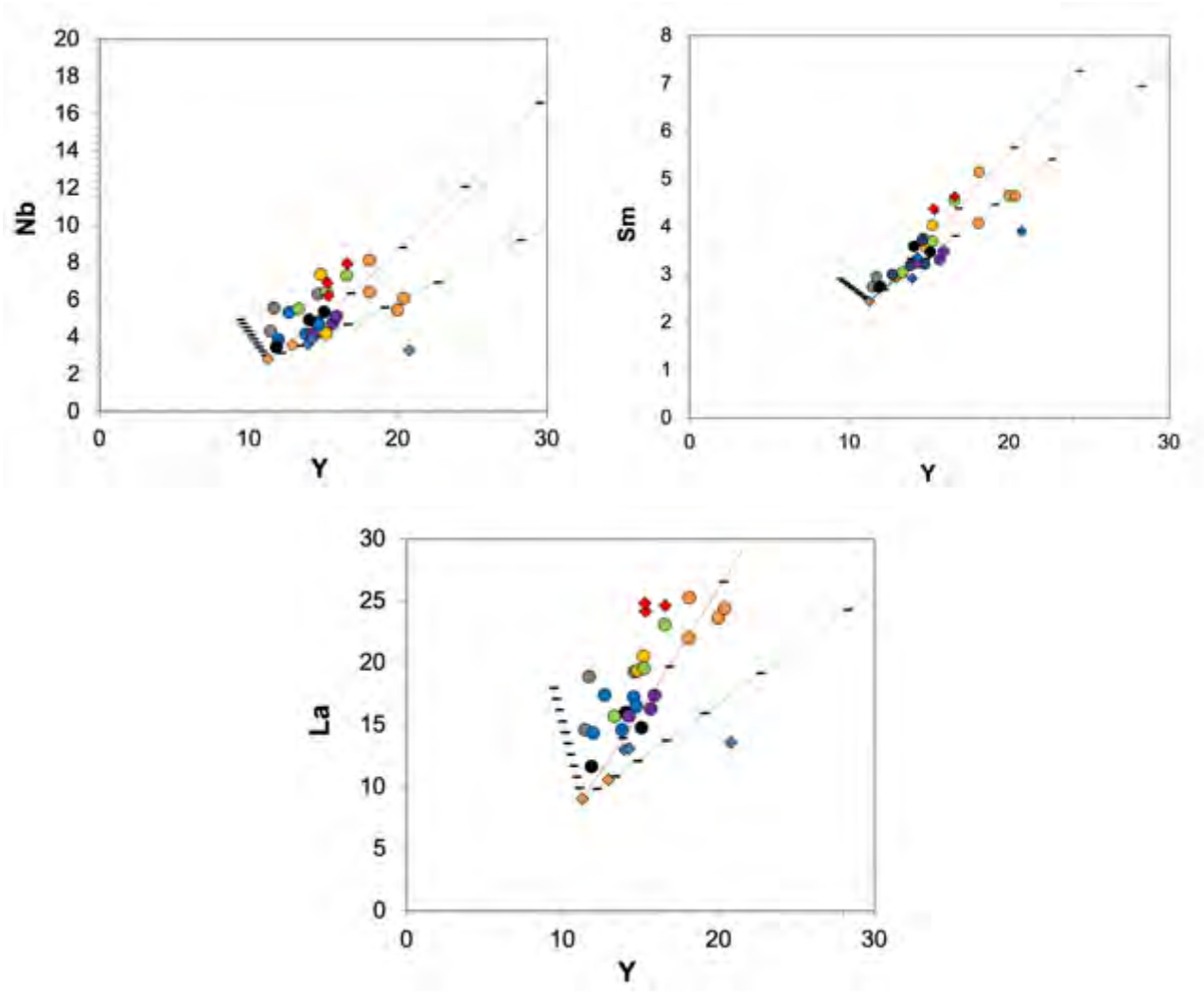

Figure 5.36: Trace element modelling of fractional crystallisation (blue line), assimilation fractional crystallisation (red line) and simple mixing (green line) for NVP groups, using the most primitive analysed sample and UB-08 Manizales Stock compositions as mixing/assimilation end members. Tick marks represent 10% fractions in the amount of melt remaining.

Average sediment compositions of hemipelagic and carbonate sediments entering the Colombian trench (after Errazuriz-Henao et al. 2019) are also included, as mixing between these and an LCC derived components provides similar, though less convincing trends for NVP petrogenesis (Figure 5.37). Clearly, a slab and mantle wedge influence on primary magmas of the NVP is inferred by the proximity of NVP compositions to MORB and depleted MORB mantle (DMM) compositions in isotopic space (Figure 5.37) compared to more isotopically enriched parts of the Andes where large degrees of fractionation and crustal contamination overprint this signature (e.g.:

Hildreth and Moorbath, 1988). However, slab and mantle derived enrichments are difficult to unpicking using the trace element and isotopic data presented here (e.g.: using X/La and X/Nb plots). These contributions are further explored in Chapter 6.

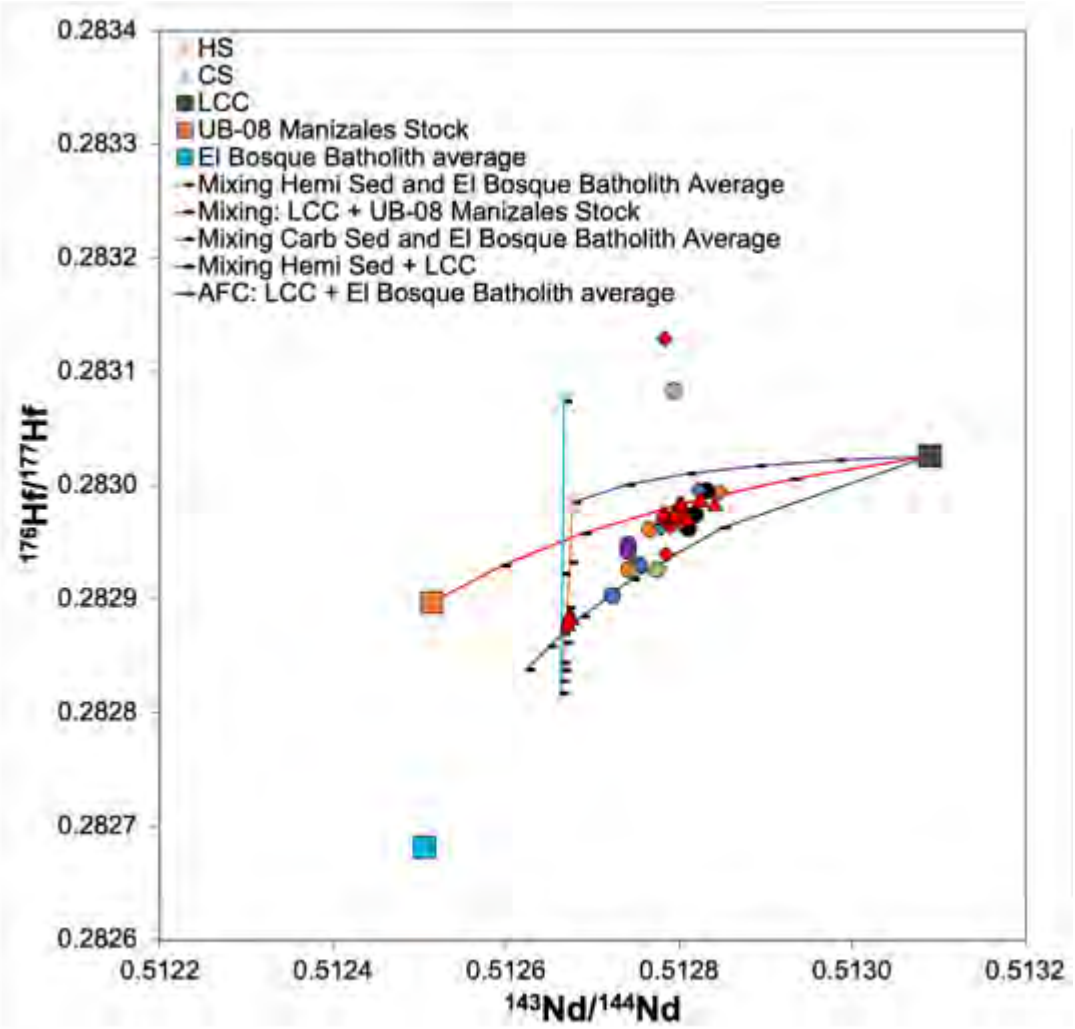

Figure 5.37: Radiogenic Hf and Nd plot with modelled AFC and simple mixing trends using La Esperanza, Manizales Stock and average lower continental crust (after Marin-Ceron et al. 2010) compositions. Tick marks represent 10% fractions in the amount of melt remaining.

5.3.3 Conclusions:

The relatively homogenous isotopic compositions of the NVP, follow an array leading away from MORB and depleted mantle compositions towards more radiogenic values (Figures 5.28 and 5.29), suggesting that the magmas which produced the NVP are derived from partial melting a depleted mantle wedge contaminated with slab components, in line with previous findings (Marin-Ceron et al. 2018). The major standout in the NVP are analyses of Cerro Machin, which are the most radiogenic, possibly indicative of a greater degree of crustal assimilation at greater depths and possibly with longer residence times in the crust.

These mantle derived melts ascend into the overlying crust where clinopyroxene + amphibole (and possibly garnet in some areas) are stable, in the mid- to lower-crust. This provides a plausible mechanism to explain the moderately elevated La/Yb, Sr/Y observed in some samples of the NVP. Within the lower crust, limited assimilation of crust and mixing with previously emplaced magmas can occur (Annen et al. 2006; Laeger et al. 2013). Additionally, modelling indicates that Eocene plutonic rocks underlying the NVP may also be assimilated in the mid- and shallow crust, and lower crustal compositions and Eocene basement could act as end member components which mix with mantle derived melts to form NVP compositions (Figure 5.38) and assimilation of this alongside fractional crystallisation of amphibole, plagioclase and biotite in shallow magma chambers is reasonable (Figure 5.31). Accompanying calc-alkaline magmas lacking elevated incompatible element, La/Yb and Sr/Y signatures can be explained by shorter residence times of these melts within the lower- and mid-crustal parts of the system, and possibly lower magma fluxes through these systems,

both leading to lower degrees of fractionation and assimilation. A tentative correlation between fractionation and age is also observed, especially at Cerro Bravo, which could point to less well-developed magmatic systems early in the history of the NVP and particularly edifices such as the early Letras Cerro Bravo and Paramillo de Santa Rosa, or perhaps less prolonged storage of magmas within these systems. An alternative explanation, particularly for the VMTVF, is a fast ascent mechanism (the Villamaria-Termales fault) allowing for less fractionated melts (such as La Esperanza and the Post-Glacial Group) to reach the surface. This contrasts to the more evolved and fractionated character of the Ancestral Group, which likely ascended through a more developed magmatic system linked to the early plumbing system of Nevado del Ruiz.

6 Controls on Colombian Magmatism: An arc scale perspective.

6.1 Introduction:

Now we turn our attention to the wider picture of arc magmatism in Colombia, both spatially and temporally. Chapter 5 dealt with the Northern Volcanic Province (NVP), the northernmost segment of the volcanic arc in Colombia. This chapter examines volcanism in the southwest of Colombia, from south of the NVP to the Ecuadorian border (Figure 6.1). The petrogenetic models invoked in the NVP can be applied to the rest of the modern Colombian arc in the southwest of the country. Additionally, we can use analyses of Miocene Colombian magmatism sampled in this study to assess the development of the arc temporally and consistently with the conclusions drawn from the NVP.

Volcanism in southwestern Colombia can be subdivided geographically into two arc segments (Hall and Wood, 1984; Stern, 2004) alongside the NVP detailed in Chapter 5. The underlying cause of the uneven distribution of volcanism in Colombia is debated, but thought to be due to underlying structural features of the Northern Andes such as the Romeral fault system and Cauca faults (Marin-Ceron et al. 2018), indicating an intrinsic link between overlying plate structure and volcanism across Colombia. For the purposes of this study, we subdivide the Pliocene to Quaternary arc south of the NVP into two distinct segments (Figure 6.1), the Central Colombian arc (represented here by samples of Purace and Sotara volcanoes, along with Nevado del Huila and the Coconucos chain volcanoes) and the Southern Colombian

arc (sampled from Morasurco, Galeras, Bordoncillo and Azufral volcanoes, but also including Doña Juana volcano and volcanoes south of Azufral to the Ecuadorian border – Figure 6.1). This southern segment also extends south to include a number of polygenetic and monogenetic edifices near the Ecuadorian border.

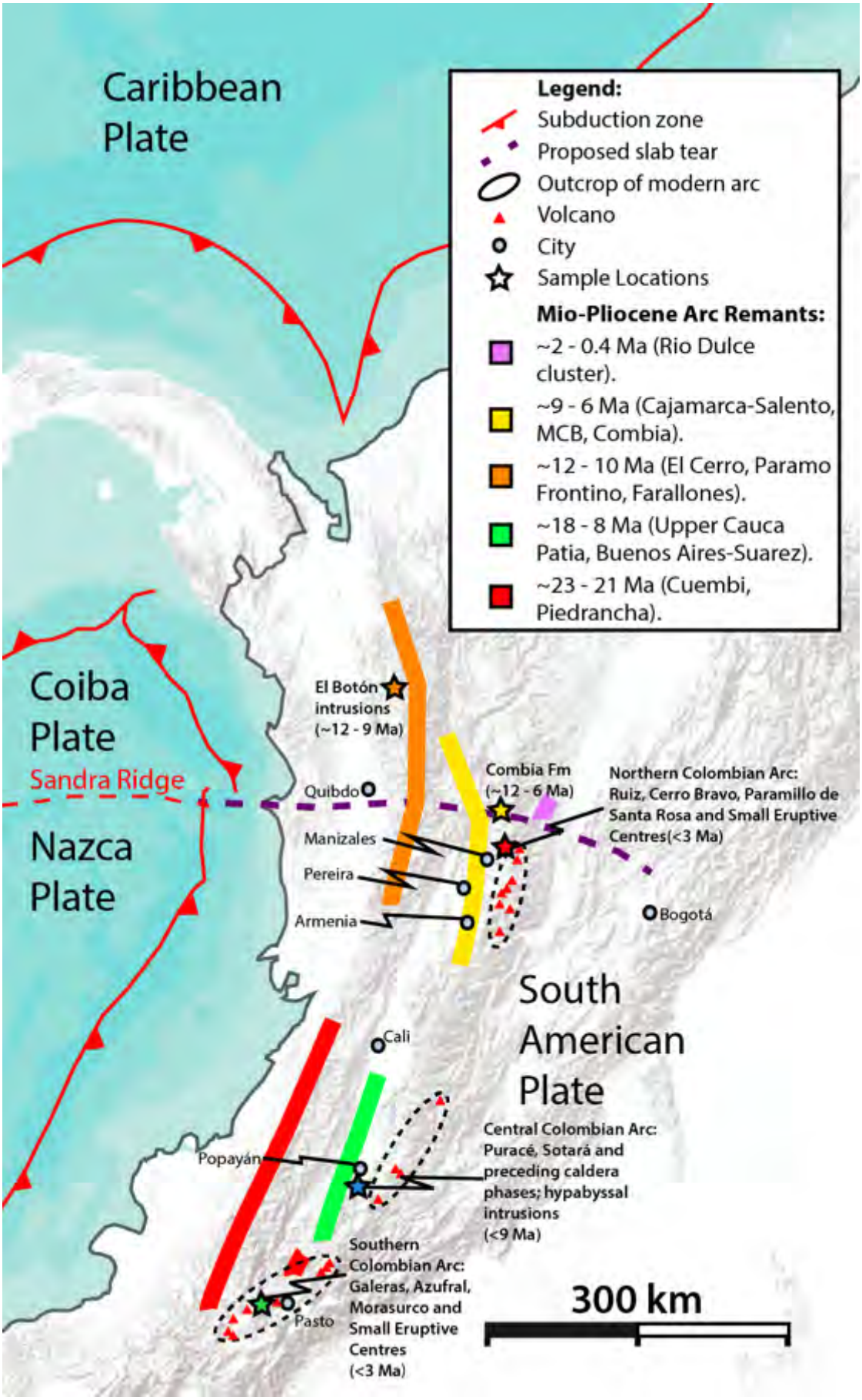

Figure 6.1: Synoptic overview map of the modern Colombian arc and previous arc segments, including sample locations in this study. Adapted after Leal-Mejia et al. (2018) and Marin-Ceron et al. (2018).

Geochemical studies of the Colombian arc have also detailed compositional differences between these two groups (e.g.: Droux and Delaloye, 1996; Marín-Cerón et al. 2010). This has mainly been ascribed to either differences in the basement andslab components and/or slab depth beneath the respective segments of the arc (Figure 6.2) thought to give rise to differing trace element and isotopic differences between the two provinces (Marin-Ceron et al. 2010). As with the NVP, the volcanoes throughout southwestern Colombia formed as a result of steep subduction of the young Nazca plate (~14 Ma, Hardy, 1991) beneath South America.

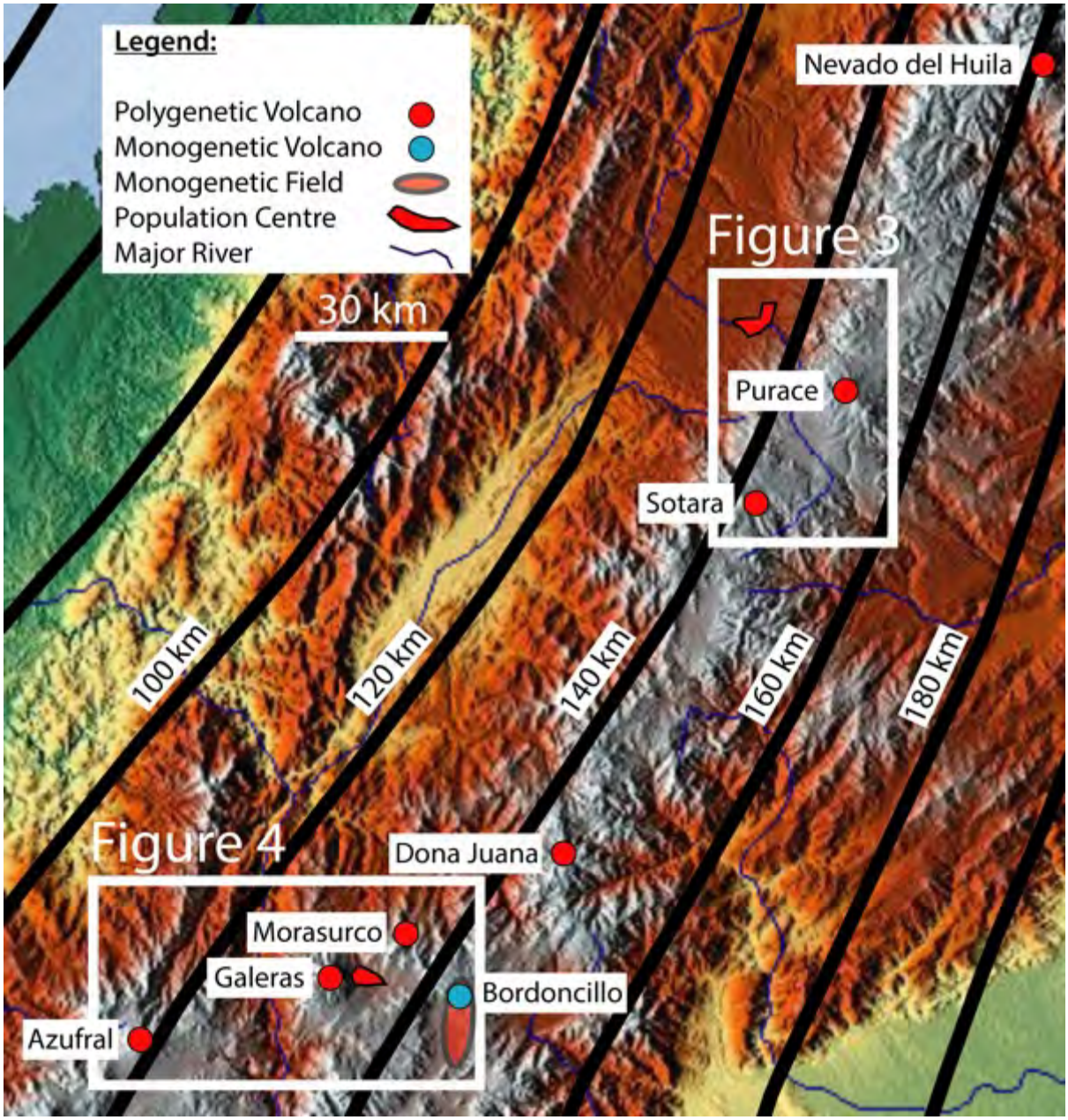

Figure 6.2: Map of the Central and Southern Colombian arc segments, with insets for detailed map figures of each region (see Figures 6.3 and 6.4, below). Slab depth contours and calculated depth to the Wadati-Benioff zone beneath volcanoes from Slab2 (Hayes et al. 2018).

6.2 The Central Colombian Arc:

The Central Colombian Arc consists of the volcanoes Purace and Sotara within this study. The primary basement in the area consists of shales of the Cajamarca-Valvidia Complex, the oldest formation (255 – 236 Ma by U-Pb geochronology (Cochrane et al. (2014a)) in the region, along with accreted volcanic sequences of the Quebradagrande Complex (Maya and González, 1995), and is therefore generally similar to the basement observed in the NVP but without Eocene granitoids. The basement is covered by a number of later volcanic deposits and numerous Oligocene to Pliocene age intrusions related to previous arc segments in the Cauca-Patia valley to the west (Figure 6.3). The current physiographical profile of the area is made up of thick layers of volcanic rocks and related deposits (Lopez, 2009). These deposits are mostly Pliocene to Quaternary in age and have been classified as the Popayán and Coconucos Formations (Torres et al., 1992; Monsalve and Pulgarin, 1995; Torres et al., 1999 and Monsalve, 2000), though the extent and character of these deposits is poorly mapped in many places (Figure 6.3). Volcanism related to the current arc is thought to have begun in the area ~2.8 Ma (Torres et al., 2010) marking the base of the Popayán Formation (Lopez, 2009). This conforms to the maximum age observed in all provinces of the modern Colombian arc (e.g.: Marin-Ceron et al. 2018). The Popayán Formation extends over a wide area surrounding the volcanoes of the Central Colombian arc and includes a large >200 km^2 area of ignimbrite deposits, as well as associated lavas and fall deposits (Torres et al., 1992). This magmatism is likely related to a large Caldera structure >3 km in diameter known as Chargaton, which underlies the current Purace-Coconucos volcanic chain (Figure 6.3). The deposits of Purace are mapped as part of the

Coconucos Formation though their exact extent and relationship to the underlying (or perhaps partly coeval) Popayán Formation require further investigation (Lopez, 2009). Two samples in this study related to the Popayán Formation and the early activity of the Purace edifice were sampled (PKSW-16A and PKSW-16B). All samples in this study were collected by staff and students from EAFIT University and donated to this study by Professor Jose Duque-Trujillo as part of a collaboration with the author. Figure 6.3 shows the parts of the Coconucos Formation related to Purace volcano. Two samples were collected from the Paletara (SESW-55B) and San Francisco (SESW-106A) members of the Coconucos Formation (Monsalve, 2000). The Coconucos has been dated by K/Ar to 2.9 Ma (Ramirez, 1982) making it in part coeval to the Popayán Formation (Torres et al. 1999).

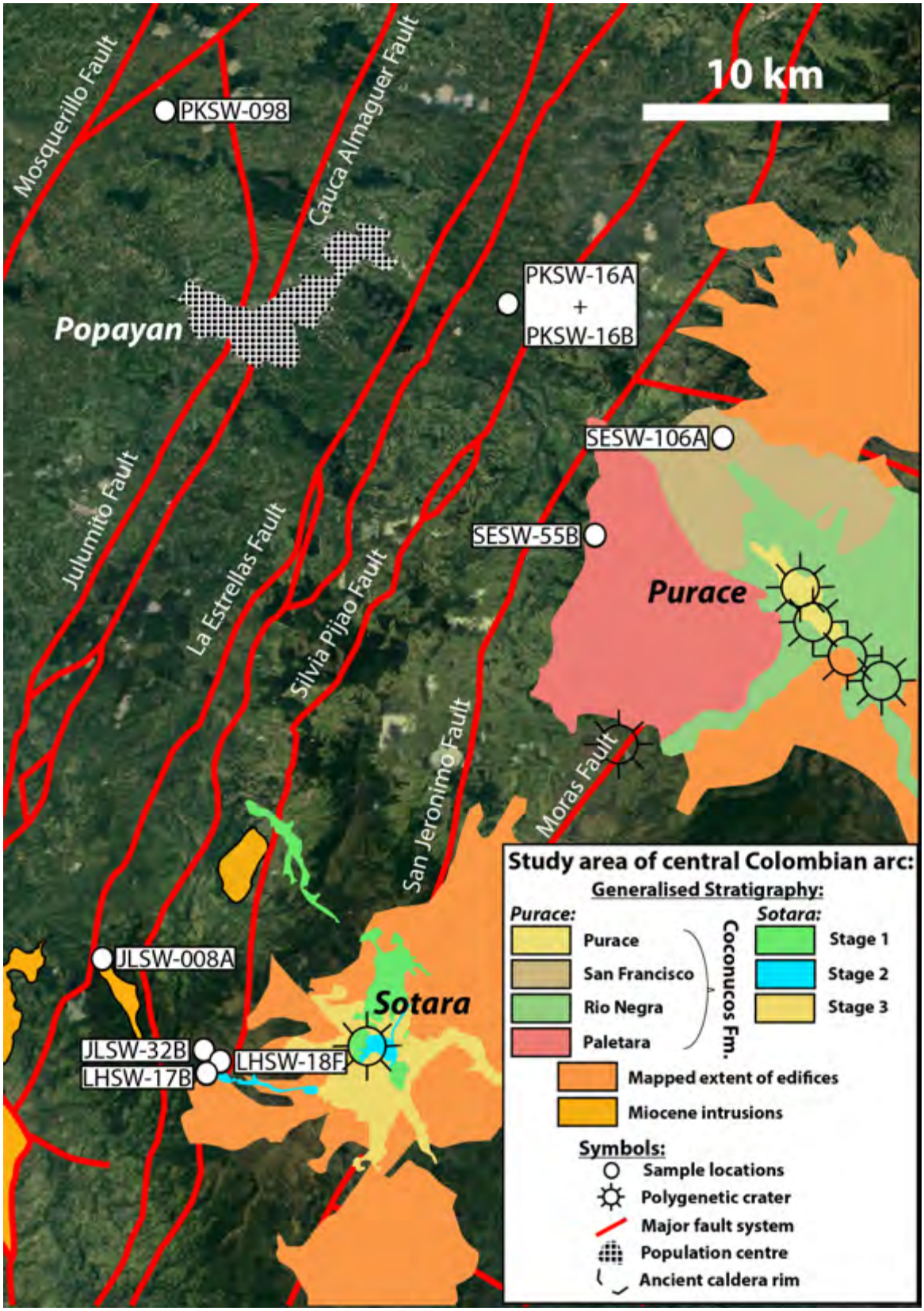

Figure 6.3: Synoptic map of volcanoes sampled in the Central Colombian arc segment, including their individual formations and mapped extents. An approximate stratigraphy is provided in the legend for each edifice. Major crustal faults and marked in red. Adapted from Gomez et al. 2015; Pulgarin et al. 2009 and Lopez, 2009.

Further south lies Sotará volcano, which along with Purace, is an active edifice monitored by the Colombian Geological Survey. However, it has no record of eruptions in historical time and its activity is primarily fumarolic (Pulgarin et al. 2009). The modern edifice of the volcano is part of wider complex (Figure 6.3) which includes the remnants of an older stratovolcano (Pre-Sotará) which formed a caldera in which the current edifice now sits (Pulgarin et al. 2009). Samples in this study are obtained from pre-Sotara and more recent deposits along the rim of the old caldera structure (JLSW-32B, LHSW-17B, LHSW-18F).

6.3: The Southern Colombian Arc:

The southern Colombian arc is represented by samples in this study from the volcanoes Morasurco, Galeras, Bordoncillo and Azufral (Figure 6.4). The basement of this region is slightly different compared to that of the other volcanic arc segments, as it straddles the Romeral Fault System which divides the allocthonous terranes of the Central Tectonic Realm from the accreted, allocthonous oceanic Western Tectonic Realm (Cediel et al. 2003; Leal-Mejia et al. 2018). In fact, Galeras is emplaced directly above the Romeral Fault System, which likely acts as the primary conduit for magmatism to the volcanoes of the Southern Colombian arc segment (Marin-Ceron et al. 2018). The main basement underlying these volcanoes is the accreted Cretaecous and younger terranes, which is covered by thick tertiary volcaniclastic sequences (Duque-Trujillo et al. 2016) produced by the activity of volcanic arcs predating the modern one (Leal-Majia et al. 2018; Marin-Ceron et al. 2018).

The northernmost of the volcanoes studied in this area is Morasurco, an eroded and ancient edifice which is no longer active and displays no historic activity (Duque-Trujillo, 2010). Only a handful of studies have been performed on Morasurco, but these provide an excellent, absolutely dated stratigraphy and mapped extent of the edifice (i.e.: Duque-Trujillo et al. 2010). From Ar/Ar geochronology, we know that Morasurco is the oldest edifice in this province, with initial activity ~2 Ma, developing rapidly into a broad and laterally extensive series of lava flows and pyroclastic deposits (Figure 6.4). This study has sampled the lava flows of Cerro Morasurco (DC16-023 and DC16-027), Loma la Cocha (DC16-025), the latest forming Daza lava dome (DC16-026) and an unmapped lava flow adjacent too and likely related to early activity of Morasurco (DC16-024).

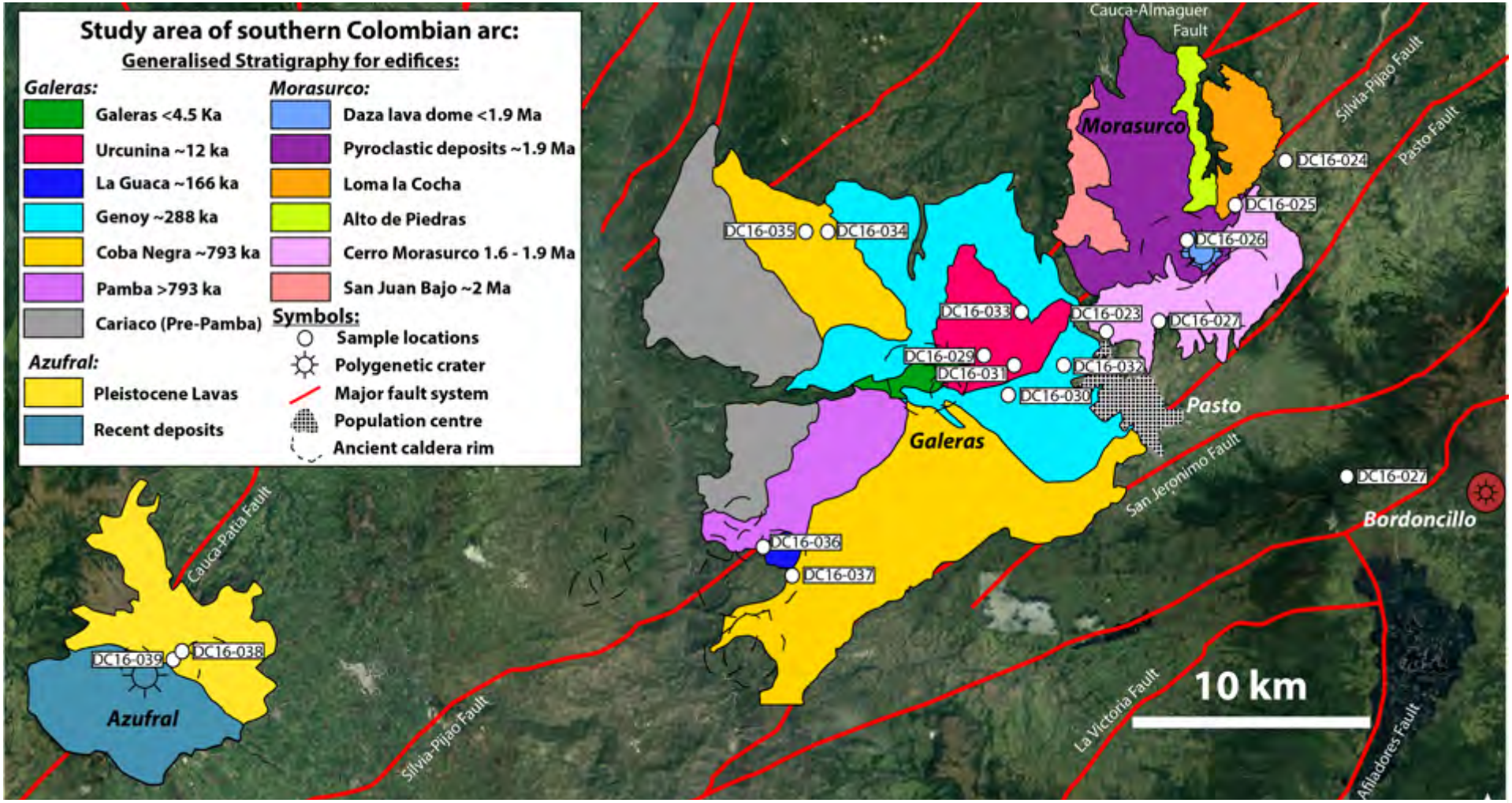

Figure 6.4: Synoptic map of volcanoes sampled in the Southern Colombian arc segment, including their individual formations and mapped extents. Ages and approximate stratigraphy are provided in the legend for each edifice. Major crustal faults and marked in red. Adapted after Gomez et al. (2015), Duque-Trujillo and Calvache (2016), Bechon and Monsalve (1991).

To the southwest of Morasurco lies Galeras volcano, which has been the subject of intense study, including extensive mapping, geochemistry, geochronology and, due to its active nature and historic eruptive record, extensive monitoring (e.g.: Calvache et al. 1997; Duque-Trujillo and Calvache, 2016). The history of the complex prior to the current Galeras edifice is divided into five stages (Figure 6.4). The most ancient of these is the Cariaco stage, which has been glacially eroded, suggesting it was a topographic high during the Pleistocene (Calvache et al. 1997). This was followed by the Pamba stage and then the most voluminous of the deposits, the Coba Negra eruptive stage at ~793 ka (Calvache et al. 1997). Following the Coba Negra eruptions, a small monogenetic cinder cone, La Guaca, formed to the southwest of the current edifice. This is dated at ~166 ± 34 ka (Calvache et al. 1997). The following eruptive stage, Jenoy, was a more explosive caldera forming event producing pyroclastic sequences and is dated to ~40 ka (Calvache et al. 1997). Much of the edifice as it appears today is made up of the penultimate stage, Urcunina (~12 ka) which is made up of lava flows and pyroclastic deposits. The modern Galeras volcano is located in the collapse scar leftover from the Urcunina edifice (Duque-Trujillo and Calvache, 2016). Samples were obtained from across the formations of Galeras, including Coba Negra (DC16-034, -035, -037), Jenoy (DC16-030, -032), La Guaca (DC16-036) and Urcunina (DC16-029, -031, -033).

One sample was obtained from Bordoncillo, an inactive monogenetic edifice located southeast of Galeras. This volcano is hypothesised to be part of a small monogenetic field extending further south, mapped based on geomorphology by the Geological Survey (Gomez et al. 2015). However, this edifice is poorly characterised and almost unmapped and doubt has been cast on whether it is an edifice in itself or part of the

Tertiary volcanic deposits mantling much of the area (Robertson et al. 2002). Sample (DC16-028) was collected, along with another sample from La Guaca, to provide a possible comparison to analyses from monogenetic edifices sampled in the NVP (VMTVF).

The southernmost volcano of the Colombian arc sampled by this study was Azufral, which despite being sampled and geochemically analysed as part of other regional studies (e.g.: Marin-Ceron et al. 2010), is poorly characterised and the subject of only a handful of studies (Bechon and Monsalve, 1991; Williams et al. 2017). The southern half of the edifice is dominated by pyroclastic flow deposits (Bechon and Monsalve, 1991) and a number of domes of evolved (dacite to rhyodacite) compositions. The basal parts of Azufral are represented by andesite lava flows, dated by K/Ar to 0.58 ± 0.03 Ma (Bechon and Monsalve, 1991). These flows are sampled as part of this study (DC16-038 and DC16-039). Unfortunately, only two samples are collected in this instance due to limited time on the volcano (<1 day) and restrictions on access to volcano.

6.4: Miocene Arc remnants:

A subset of samples was also collected related to the volcanic-plutonic successions preceding the modern Colombian arc (Figure 6.1) which are preserved as isolated volcanic and volcanoclastic sequences to the west of the modern volcanic arc. These remnants are west of the modern arc, in the Cauca-Patia valley and Western Cordillera (Figure 6.1; Figure 6.5A+B). As with the modern volcanic arc the magmatism which produced Miocene volcanism these is related to subduction of the

Nazca plate beneath South America from the latest Oligocene onwards (Leal-Mejia et al. 2018; Marin-Ceron et al. 2018). As outlined in Chapter 3, there is debate surrounding the configuration of subduction during this time, and whether the character and distribution of magmatism was affected by episodes of extension and trans-tension (Jaramillo et al. 2019) as well as periods of flat subduction (Wagner et al. 2017). Study of a subset of Miocene magmatic material, and comparison with the basal series we have sampled from multiple contemporary arc volcanoes may help us understand the development of the Colombian arc into its modern configuration.

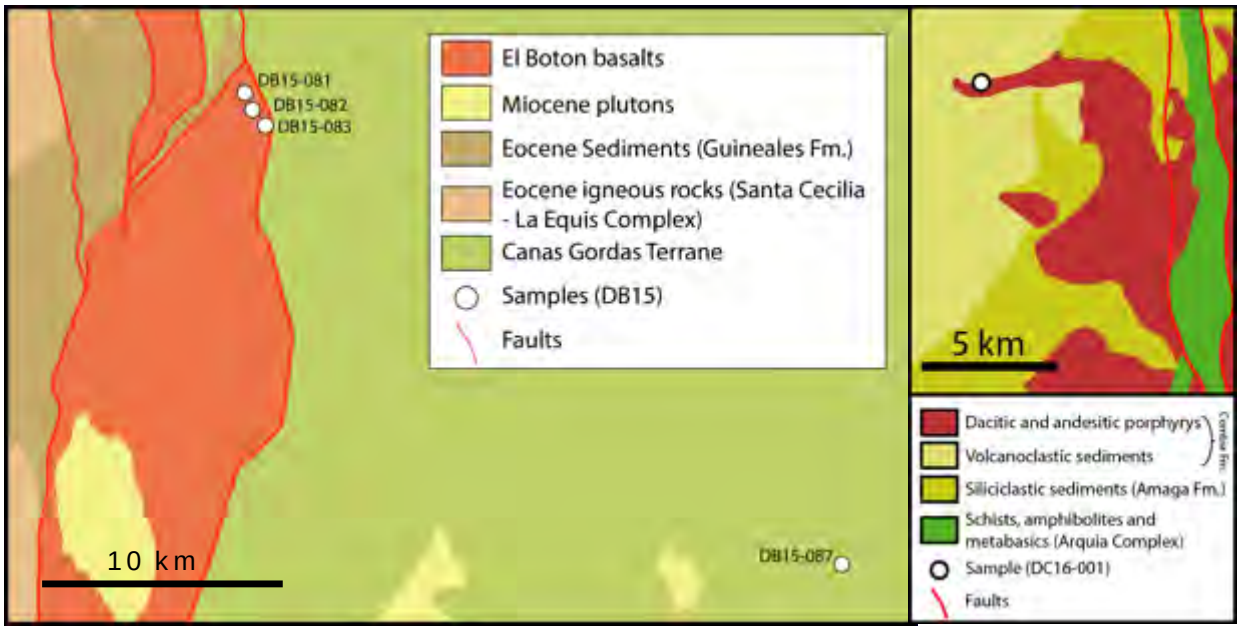

Figure 6.5: A: Simplified geological map of the El Boton Basalts outcrop and surrounding areas, including sample locations. **B:** Simplified geological map of the Combia Formation and surrounding geology closest to sample DC16-001. Adapted after Zapata and Rodriguez (2012), Gomez et al. (2015) and Jaramillo et al. (2019). Locations of these sample sites within Colombia is shown on Figure 6.1.

The Miocene samples collected fall into three groups. The first of these are the El Boton basalts (Figure 6.1 and 6.5A). These are the furthest west deposits collected in this study (collected and donated by Dr David Buchs of Cardiff University) and lie above the accreted oceanic Cañas Gordas terrane in the Western Tectonic Realm

(Cediel, 2018). Also included in these samples is a rock of the basement (DB16-087) related to the accreted Cretaceous Barroso arc, and to be used for comparison and as a possible crustal assimilant. The remaining samples are related to basalts and related intrusive bodies which outcrop on the western flank of the Western Cordillera, formed between 9 – 12 Ma, dated by Ar/Ar and K/Ar (Zapata and Rodriguez, 2012). These are generally shoshonitic and alkaline in character and are hypothesised to be some of the earliest products of Nazca subduction in northern Colombia, related to dry magmatism and extensional pull apart basins (Zapata and Rodriguez, 2012; Jaramillo et al. 2019).

The second group of Miocene rocks consists of a single sample (DC16-001) related to the Combia Formation, located ~40 km east of the El Boton basalts. The Combia formation is made up of basalts, andesites, pyroclastic rocks, porphyritic andesitic-dacitic domes, and dacitic to andesitic porphyries (Toro et al. 2016; Jaramillo et al. 2019). These have a highly heterogenous composition, varying from tholeiitic basalts to lavas and porphyries with adakite-like compositions (Toro et al. 2016; Jaramillo et al. 2019). These rocks have been dated by U/Pb to between 8.5 and 5.2 Ma, and are hypothesised to represent a short-lived episode of magmatism in pull apart basins, related to localised crustal thinning under transtension (Jaramillo et al. 2019), and are underlain by deformed sediments of the Amaga Formation. The sample collected in this study is of a porphyry (Figure 6.5B), which in this region have adakite-like compositions and elevated trace metal compositions (e.g.: Cu). The Combia Formation forms part of a wider array of Miocene arc remnants in this region (Figure 6.1), which include garnet bearing deposits and magmatic ore deposits (e.g.: Bissig et al. 2017).

The final group of Miocene samples consists of two hypabyssal intrusions from the Cauca-Patia valley west of Purace and Sotara volcanoes (Figure 6.3). One of these is an undated hypabyssal intrusion located ~40 km west of the modern arc (PKSW-098) and an intrusion just west of Sotara volcano (JLSW-008a), and possibly related to the earlier pre-Sotara edifice. However, these samples are based on existing mapping part of the Miocene (~18 – 8 Ma) arc remnant located throughout the Cauca-Patia valley (Figure 6.1).

6.5: Characterisation of the Samples:

6.5.1 Petrography:

6.5.1.2 Overview:

Overall, the samples collected from the modern arc system in southwest Colombia are porphyritic, holocrystalline andesites, containing phenocrysts of plagioclase, orthopyroxene, clinopyroxene with varying amounts of amphibole and biotite as the main phases. Microphenocryst and groundmass phases are commonly plagioclase and pyroxene dominated, with accessories of Fe-Ti oxides as minor components. In some more mafic samples olivine is also observed as a phenocryst phase. Disequilibrium features are common, including strong sieve textures and oscillatory zoning to plagioclase crystals and in particular phenocrysts, as well as reaction rims to amphiboles and pyroxenes. Alteration or complete replacement of minerals, especially of biotite where it occurs and minor glassy components of the groundmass is also observed.

The Miocene arc remnants are compositionally diverse, but with the exception of El Boton basalt samples (represented petrographically by DB15-082) they contain more evolved mineral phases, particularly biotite and quartz, in far greater proportions than the modern Colombian arc rocks studied. The phenocrysts of these and all other phases are also much larger than those of the modern arc rocks, with plagioclase mega-phenocrysts recorded in the Central Colombian intrusions of >7 mm, and other phenocryst phases >5 mm, typical of hypabyssal intrusive rocks. Alteration is also more pervasive in these rocks, with replacement of plagioclase by sericite and biotite by chlorite common.

6.5.1.3 Central Colombian segment:

6.5.1.3.1 Purace:

Located northwest of Purace volcano (Figure 6.3) are two samples attributable to the pre-Purace edifice (and the Popayán Formation), PKSW-16A and PKSW-16B. These rocks are dominantly composed of cryptocrystalline/glassy groundmass in a similar proportions to the largest phenocryst phase, plagioclase. Groundmass and plagioclase phenocrysts alone make up roughly 70 – 80% of both samples. Plagioclase phenocrysts are euhedral to subhedral tabular laths of 1 – 4 mm (Figure 6.6) whilst other euhedral to subhedral orthopyroxene and clinopyroxene of 0.5 – 3 mm (Figure 6.7) and small phenocrysts (<0.5 – 2 mm) of opaques, Fe-Ti oxides are also observed. Plagioclase shows clear twinning and disequilibrium textures of sieving and oscillatory zoning. Small inclusions of oxides (<0.5 mm) occur in orthopyroxene phenocrysts, and glomerocrysts composed of clinopyroxene and

opaques are observed in PKSW-16A. Groundmass of both samples is crypto- to microcrystalline, though only plagioclase is identifiable.

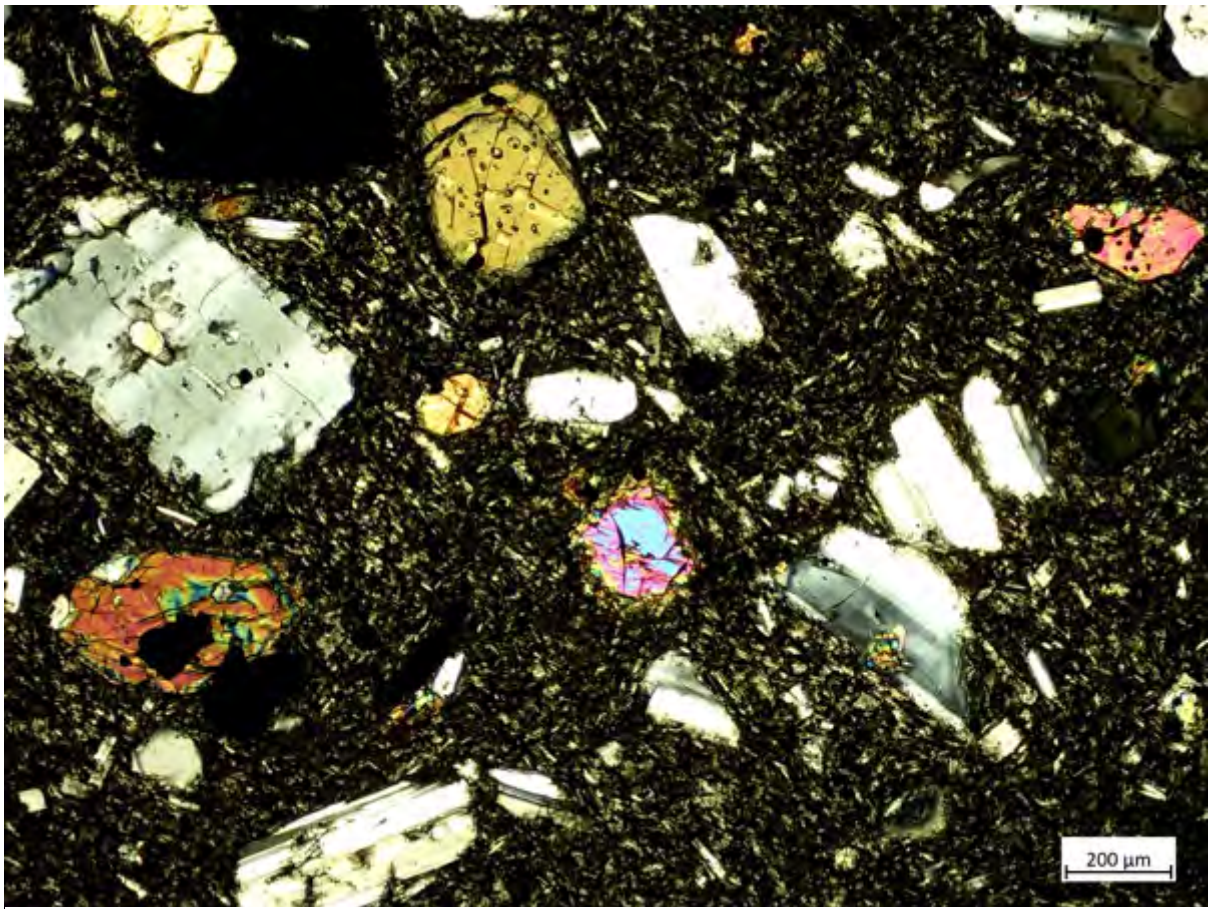

Figure 6.6: Cross polarised light (XPL) image of PKSW-16A, showing subhedral plagioclase and pyroxenes in a microcrystalline groundmass.

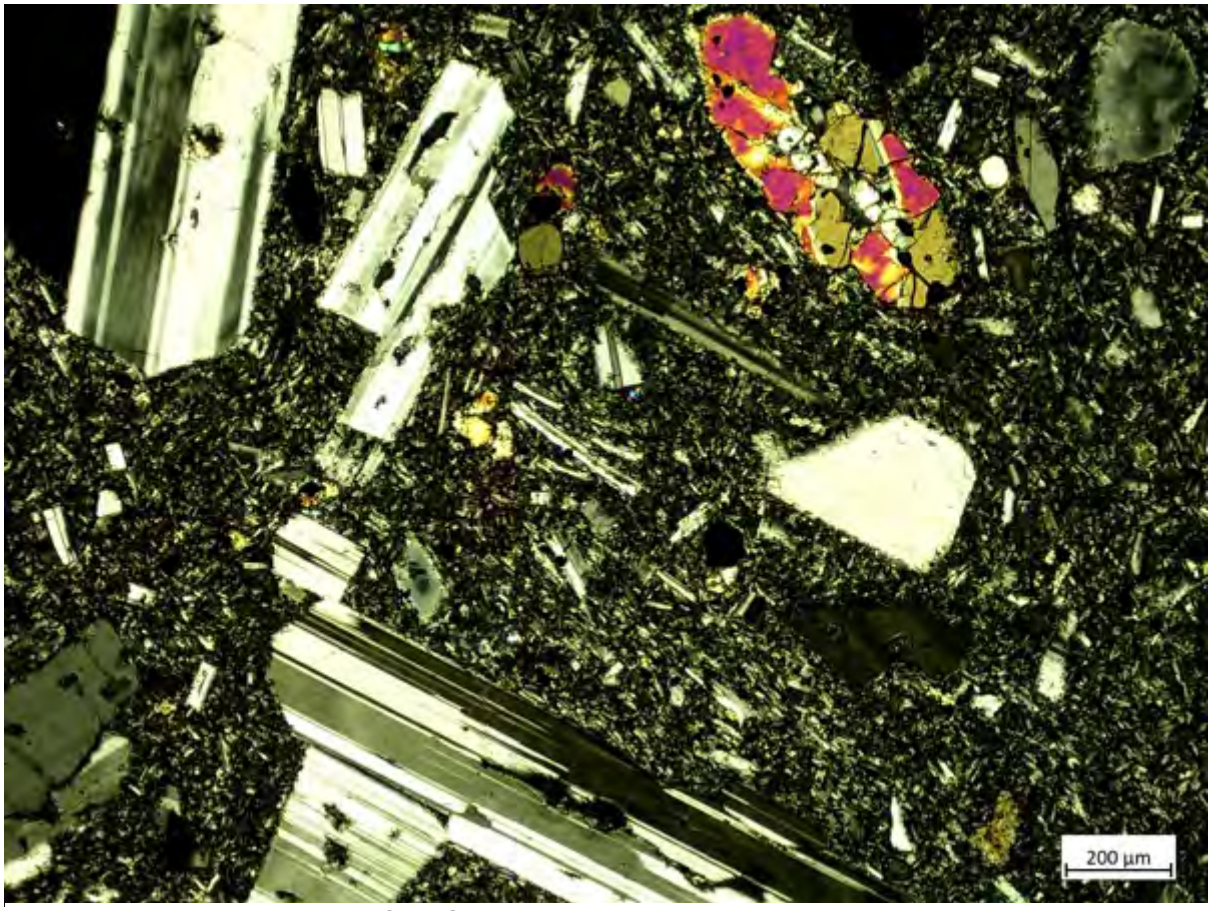

Figure 6.7: XPL image of PKSW-16B, showing euhedral to subhedral plagioclase and clinopyroxene in a microcrystalline groundmass.

More proximal to the modern Purace edifice, and attributed to the Coconucos Formation of Purace deposits are samples SESW-55B and SESW-106A. These are also plagioclase and pyroxene dominated. Primary phenocryst phases in both rocks are euhedral to subhedral plagioclase phenocrysts of up to 1 – 3 mm with disequilibrium textures and subhedral orthopyroxene and clinopyroxene phenocrysts of <2 mm. Groundmass of SESW-55B is largely composed of microcrystalline laths of plagioclase and pyroxenes, whilst the groundmass of SESW-106A is more glassy, making up a higher proportion of the sample than single phenocryst phases. Plagioclase microphenocrysts in both samples lack disequilibrium textures, perhaps representing two generations of crystallisation with the larger crystals in disequilibrium. Small inclusions of opaques (<0.5 mm) are entrained within

plagioclase and pyroxene phenocrysts in SESW-55B (Figure 6.8). Groundmass is composed of plagioclase and pyroxenes. Glomerocrysts of pyroxene are observed in PKSW-106A.

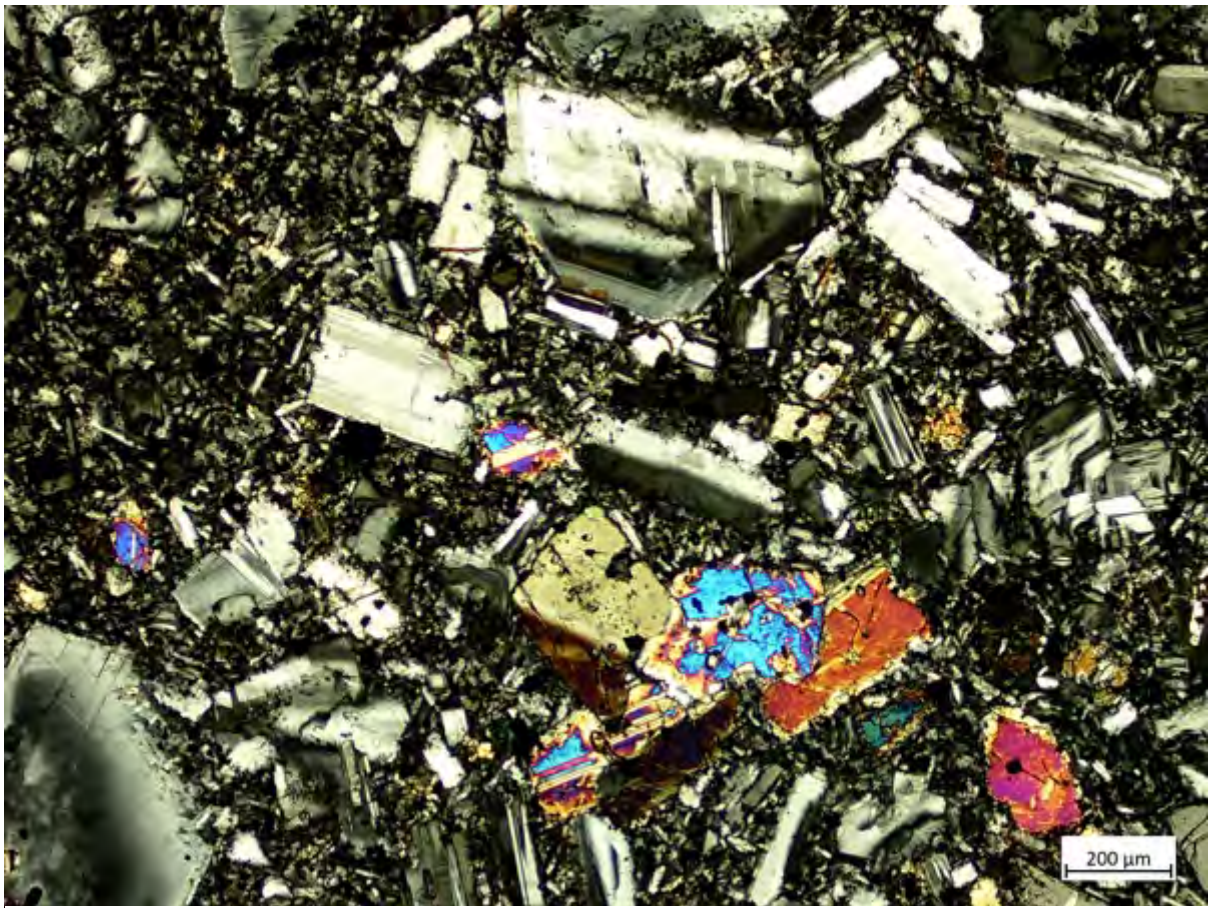

Figure 6.8: XPL image of SESW-55B, showing euhedral plagioclase and subhedral ortho- and clinopyroxenes in a microcrystalline groundmass. Note the opaque mineral inclusions within pyroxene phenocrysts.

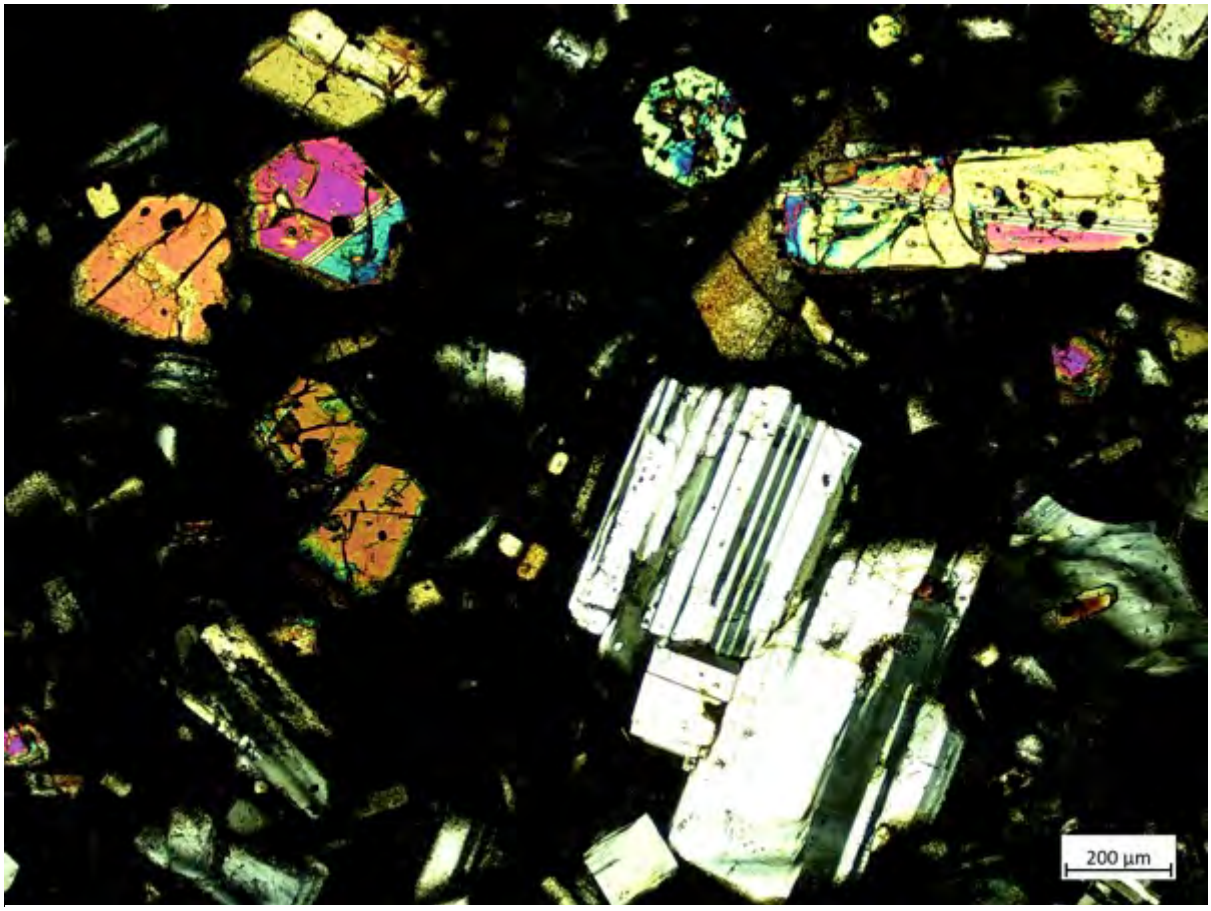

Figure 6.9: XPL image of SESW-106A, showing plagioclase and pyroxenes in a cryptocrystalline and partially altered groundmass.

6.5.1.3.2 Sotara:

Sotara samples (JLSW-032B, LHSW-17B and LHSW-18F) are located to west of the current edifice and are related to the pre-Sotara deposits of older caldera and dome forming sequences in that area (Figure 6.3). All of these samples are porphyritic and hypocrystalline, and have a large or dominant groundmass component, which is either glassy and aphanitic or in the case of JLSW-32B, largely altered to amorphous silica. Main phases are euhedral to anhedral plagioclase crystals 2 – 5 mm, alongside phenocrysts of minor pyroxene and opaque minerals in the case of -32B, and larger (<1 – 3 mm) crystals of biotite, amphibole and pyroxene in the case of -17B and -18F. Plagioclase phenocrysts in all these samples exhibit carlsbad

twinning and oscillatory zoning textures. 17B also contains large, subhedral biotite phenocrysts up to 3 m and smaller (<1 mm), subhedral phenocrysts and microphenocrysts of amphibole and pyroxene, which display opaque altered rims, indicative of disequilibrium and alteration to oxides. 18F has minor phenocrysts and microphenocrysts of orthopyroxene ~1 – 1.5 mm. Subhedral plagioclase is also seen as inclusions and poikilitic to amphibole phenocrysts, possibly suggesting two generations of plagioclase crystallisation. Again, the phenocrysts of plagioclase display carlsbad and also albite but lack sieve textures, which are present in other Purace samples. Microliths of plagioclase, amphibole and pyroxene visible in the groundmass of 18F.

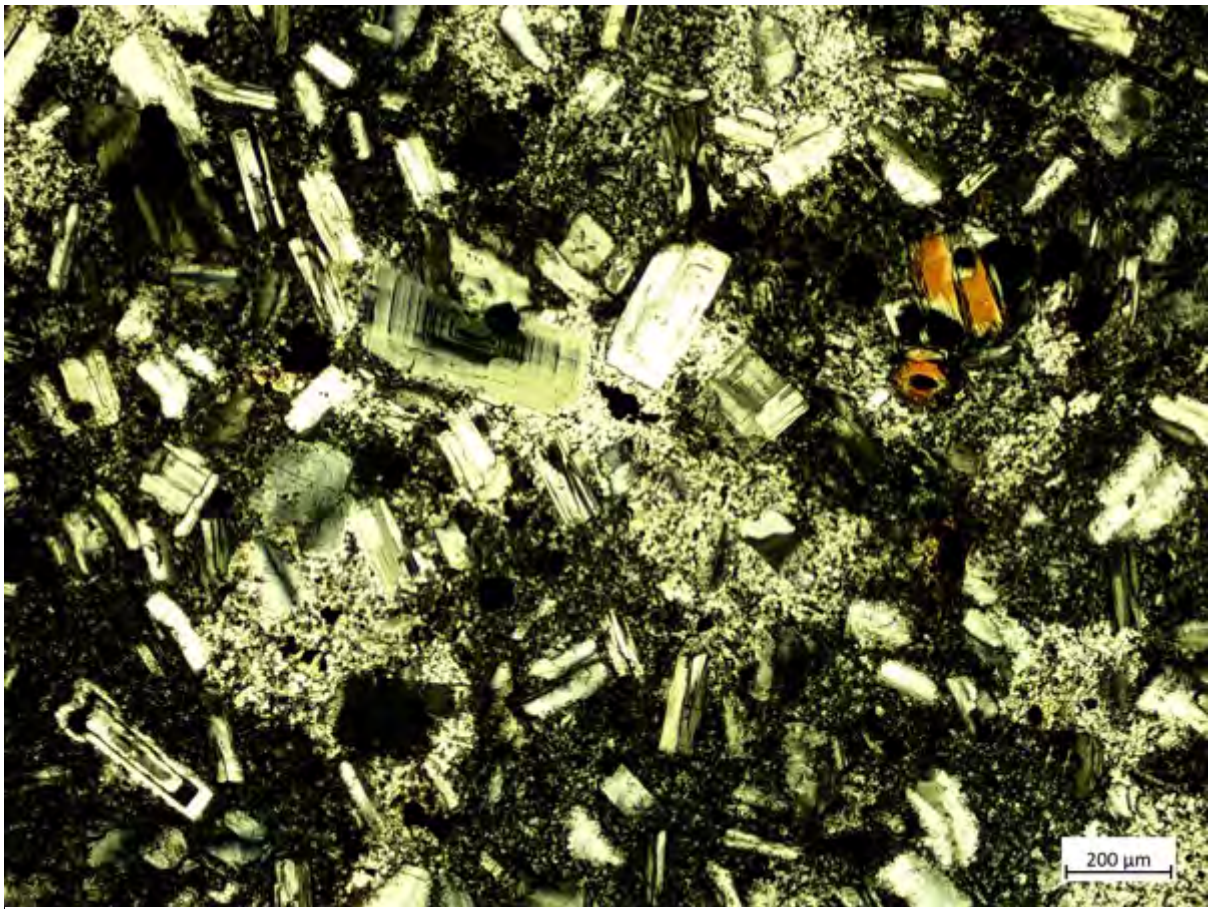

Figure 6.10: XPL image of JLSW-32B, showing strongly zoned plagioclase phenocrysts dominant within an altered groundmass.

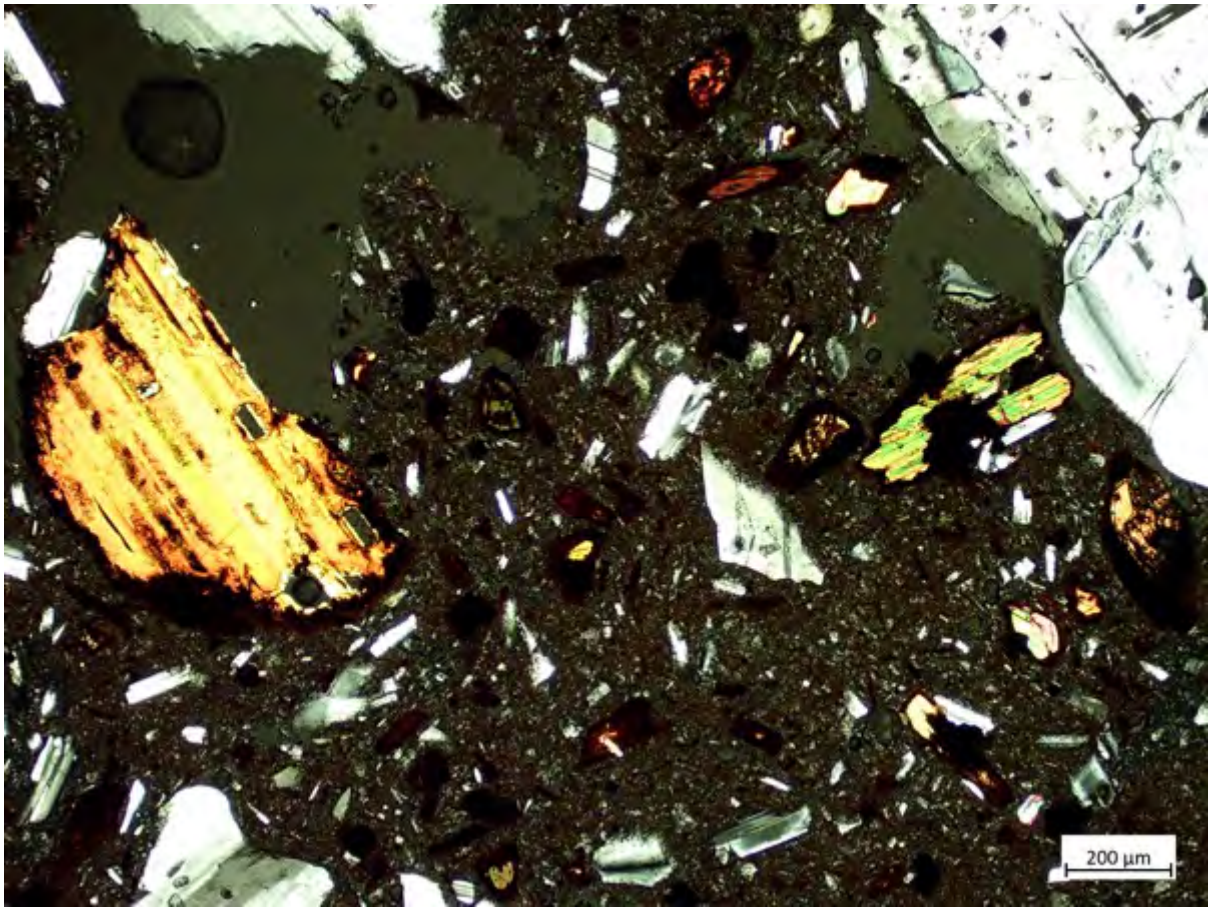

Figure 6.11: XPL image of LHSW-17B, with biotite and plagioclase phenocrysts and microphenocrysts in a cryptocrystalline to microcrystalline groundmass.

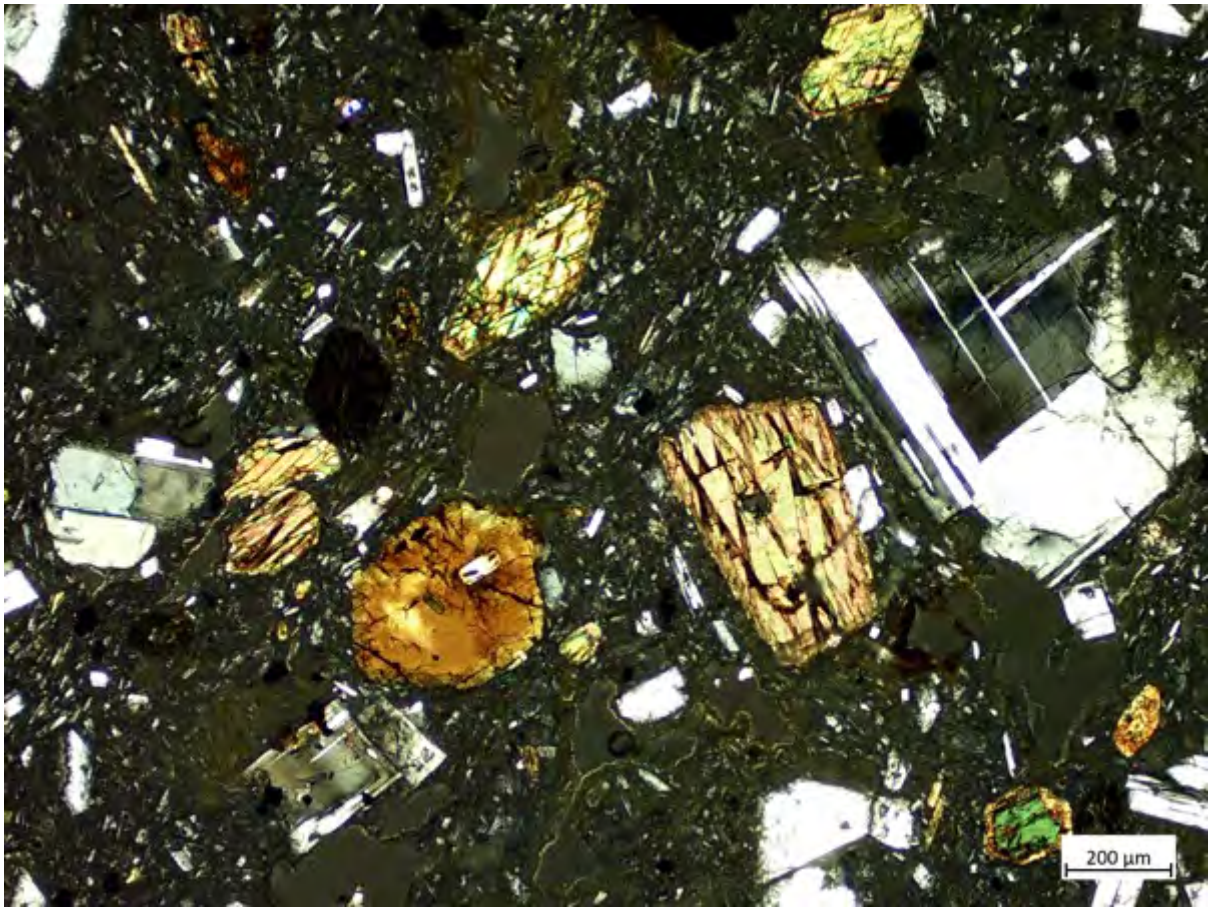

Figure 6.12: XPL image of LHSW-18F, showing euhedral amphibole phenocrysts plagioclase and pyroxenes in a microcrystalline groundmass.

6.5.1.2 Southern Colombian segment:

6.5.1.2.1 Morasurco:

DC16-024 is a porphyritic rock with plagioclase and clinopyroxene and orthopyroxene pheonocrysts (all of which are 1 – 3 mm). Smaller anhedral crystals (<1 mm) of opaque minerals and Fe-Ti oxides are also observed. Plagioclase phenocrysts exhibit albite and carlsbad twinning and strongly developed oscillatory zoning textures in the largest phenocrysts. Pyroxenes are form glomoerocrysts with

opaques in section (Figure 6.13). Plagioclase microliths define a trachytic flow texture in the groundmass which is otherwise aphanitic.

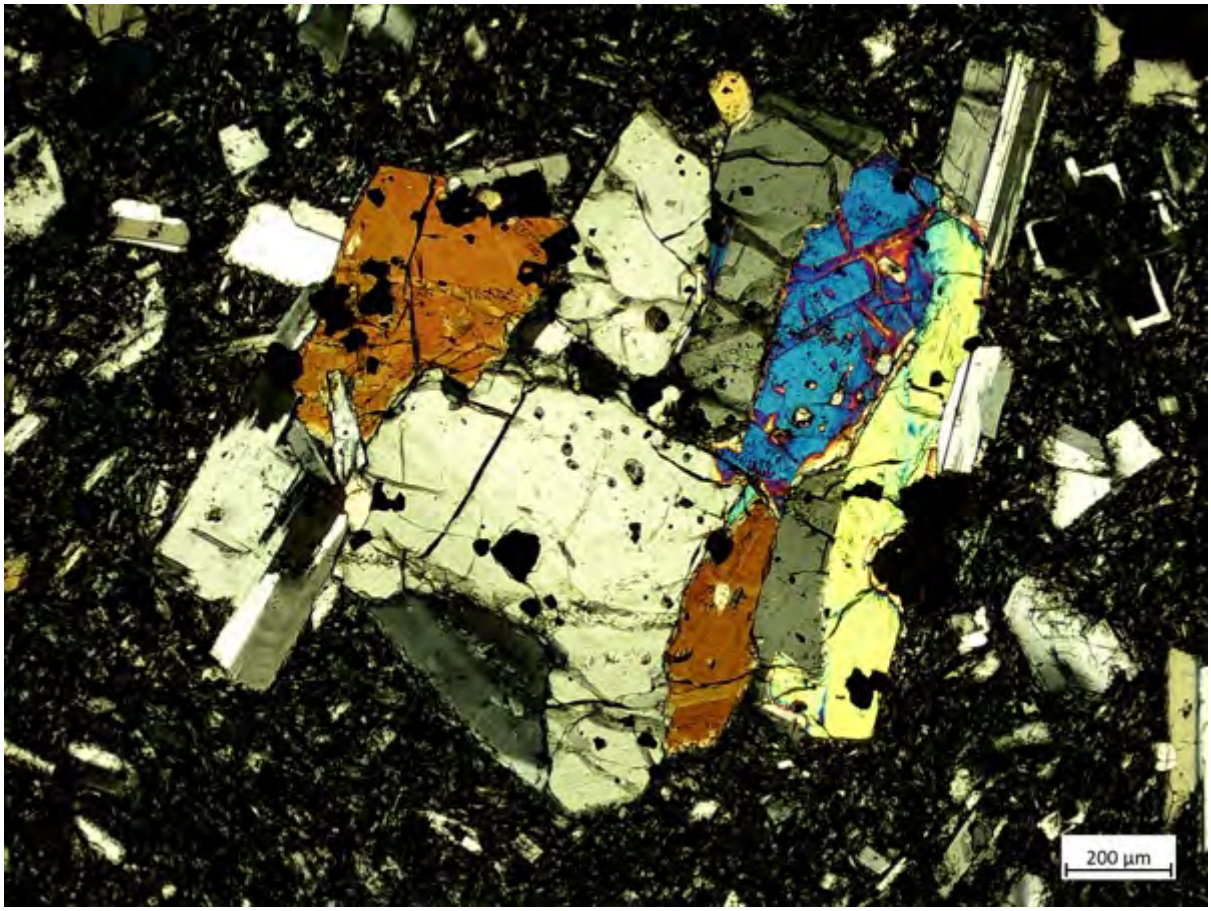

Figure 6.13: Cross polarised image of a pyroxene glomerocryst within DC16-024.

6.5.1.2.2 Bordoncillo:

DC16-028 is a heavily altered sample dominated by an overprint of sericitic and clay alteration across groundmass and all phenocryst phases, though crystals and original textures are preserved. This is a porphyritic, hypocrystalline rock with phenocryst phases of euhedral to subhedral plagioclase (up to 4 mm) and smaller euhedral crystals of pyroxene and opaque minerals. Where unaltered, plagioclase shows well defined twinning and oscillatory zoning textures. The groundmass is composed of

plagioclase microliths along with minor opaques and pyroxene, but is otherwise aphanitic.

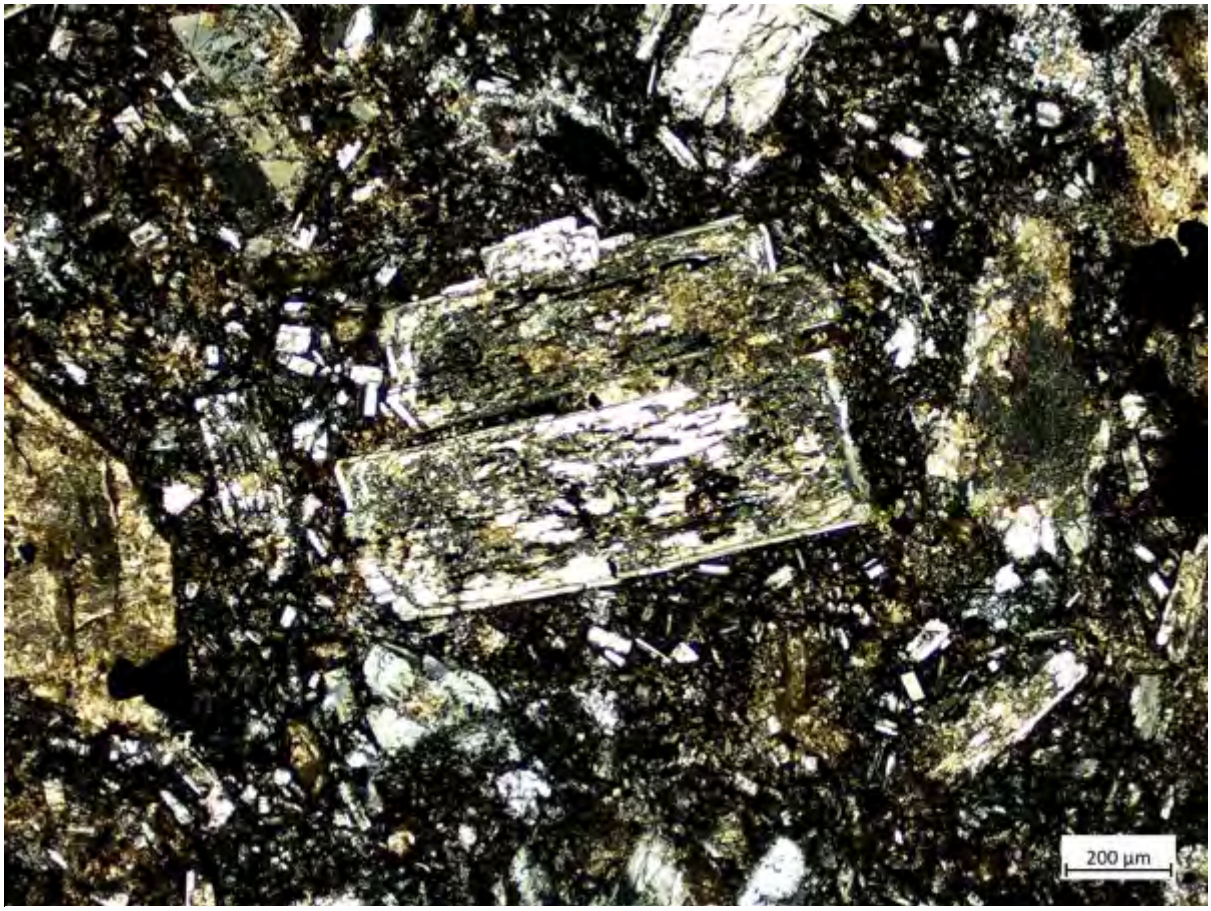

Figure 6.14: XPL image of the altered Bordoncillo sample, DC16-028, showing altered euhedral plagioclase and pyroxenes phenocrysts.

6.5.1.2.3 Galeras:

Galeras petrography is here represented by samples DC16-034 (Figure 6.15) and DC16-037 from the Coba Negra eruptive phase. The later of these samples was collected in close proximity to La Guaca cinder cone. Both of the samples are porphyritic rocks dominated by plagioclase phenocrysts, to the extent that DC16-037 is composed almost entirely of phenocrysts and microphenocrysts of this phase. The

only other major phases are small opaque minerals and minor occurrences of pyroxene with reaction rims. In DC16-034 plagioclase is less abundant, but still the largest (1 – 3 mm) and dominant phenocryst phase, present as subhedral laths. The other dominant phenocryst phases are clinopyroxene and orthopyroxene, which are present as subhedral, rounded laths of 1 – 2 mm. Orthopyroxenes are generally of similar size and lesser abundance than clinopyroxenes. Opaque minerals of <1 mm occur throughout both sections, and also as attachments to or inclusions within pyroxenes in DC16-034. Disequilibrium textures including sieve textures and some oscillatory zoning are abundant in plagioclase crystals >2 mm in both samples, along with albite twinning. Groundmasses are microcrystalline and plagioclase microlith dominated, with a minor trachytic texture defined by these microliths in DC17-037.

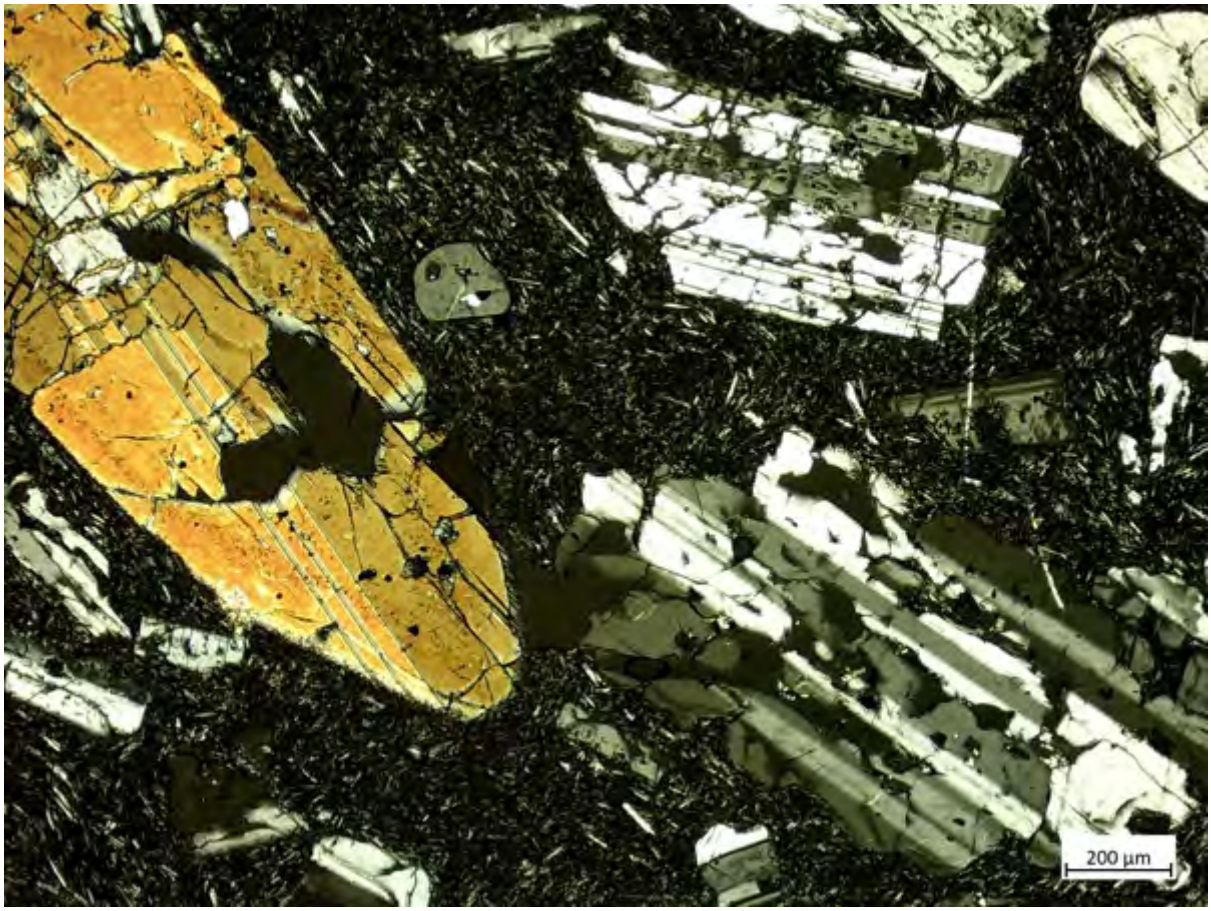

Figure 6.15: Cross polarised light capture of DC16-034, showing large subhedral plagioclase and pyroxenes phenocrysts, the former with prominent sieve textures.

6.5.1.2.4 Azufral:

The basal lava flows of Azufral volcano are here represented by DC16-039. This is a holocrystalline porphyritic rock with phenocrysts of plagioclase of 1 – 3 mm, orthopyroxene and clinopyroxene between <1 – 2 mm and opaque accessory minerals. In one case (possibly as a xenocryst of an Fe-Ti phase) these are up to 3 mm, but far more commonly are present as <1 mm phases. The groundmass is made up of plagioclase and pyroxenes.

6.5.1.3 Miocene Arc remnants:

6.5.1.3.1 El Botón basalts:

The basalts of El Botón from the Western Cordillera of Colombia (Figure 6.5A) are represented petrographically here by DB15-082 (Figure 6.17). This has a phaneritic character of interlocking euhedral plagioclase and clinopyroxene phenocrysts (1 – 2 mm). Opaque and oxide phases are anhedral and of <0.1 to 1 mm. Plagioclase can be up to megacryst scale (<0.5 cm) but is commonly much smaller and commonly shows twinning. In rare instances, amphibole is also observed. Groundmass consists of microcrystalline euhedral to subhedral clinopyroxene and plagioclase. Alteration of interstitial areas and some over print of minerals (to chlorite and to palagonite) is observed.

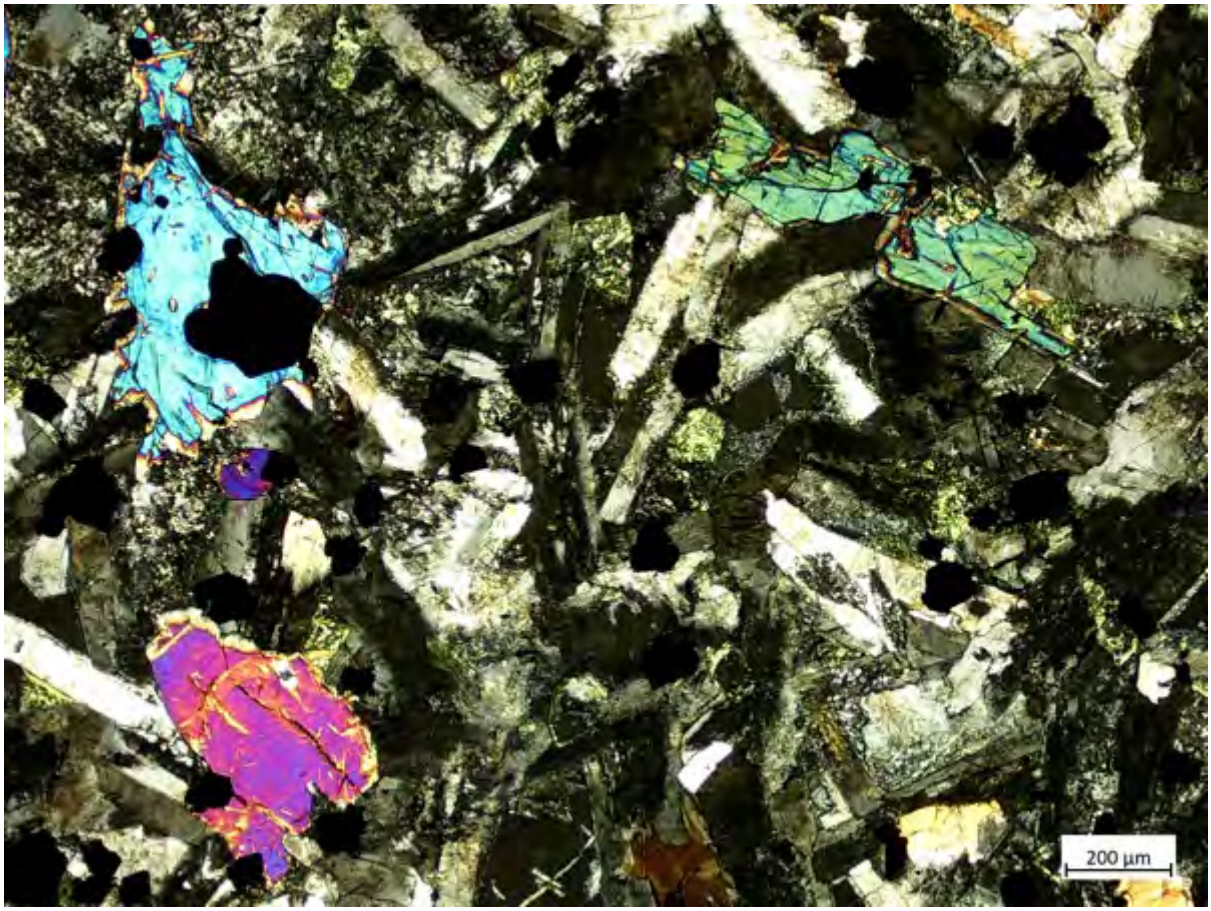

Figure 6.16: Cross polarised light (XPL) image of DB15-082, showing altered subhedral plagioclase and pyroxenes.

6.5.1.3.2 Combia Formation:

The Miocene rocks of the Combia Formation are represented here by DC16-001. This sample is heavily altered and has a pervasive overprint of sericite and secondary mineral alteration throughout all mineral phases, leaving relict crystals and pseudomorphs in some cases. Phenocrysts are plagioclase (1 – 2 mm), with some altered crystals up to ~5 mm, as well as amphibole (~1 mm) and euhedral biotite (0.5 – 1 mm). Opaque minerals can vary up to phenocryst phases, and some of these may be altered oxides of previous phenocryst phases. However, one large (0.5 – 1 mm) crystal appears to be garnet, which has also been reported in other parts of the

Combia Formation and Miocene volcanic sequences (Bissig et al. 2017; Jaramillo et al. 2019). Groundmass is highly altered to sericite and chlorite but made up of <1 mm plagioclase laths and cryptocrystalline phases.

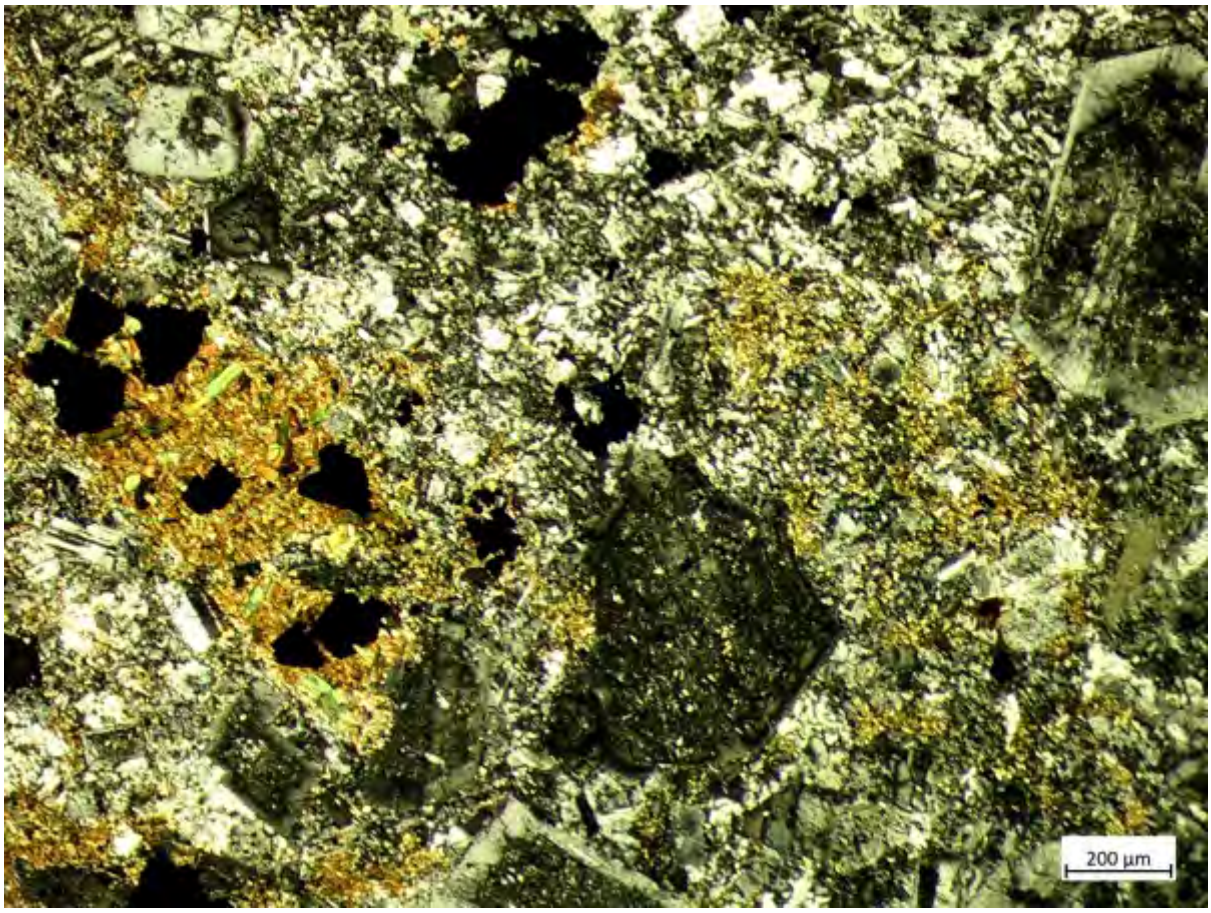

Figure 6.17: XPL image of DC16-001, showing pervasively altered character of sample as well as garnet (large black crystal, lower centre of section).

6.5.1.3.3 Central Colombian intrusions:

Two samples from hypabyssal intrusions located close to the outcrop of the modern, Central Colombian arc segment were also analysed. These are PKSW-098, located in the Cauca-Patia valley west of Purace volcano, and JLSW-008A, located close to the deposits of Sotara and pre-Sotara volcano described above (Figure 6.3)

PKSW-098 is porphyritic with phenocrysts of anhedral quartz (>5 mm), zoned and twinned plagioclase (5 – 7 mm) and biotite (2 – 3 mm). One occurrence of subhedral and broken (likely xenocrystic) garnet is also observed in the section, surrounded by a strong reaction corona texture. Alteration is pervasive, with plagioclase altered to sericite and almost all biotite is altered to chlorite. Apatite and zircon are rarely minor phases (<0.5 mm). Some voids in section are also observed, which are likely due to removal of phases by alteration and secondary processes, as evidenced by phenocryst alteration. The groundmass consists of small laths of equigranular plagioclase along with alteration products of calcite and sericite of <0.2 mm.

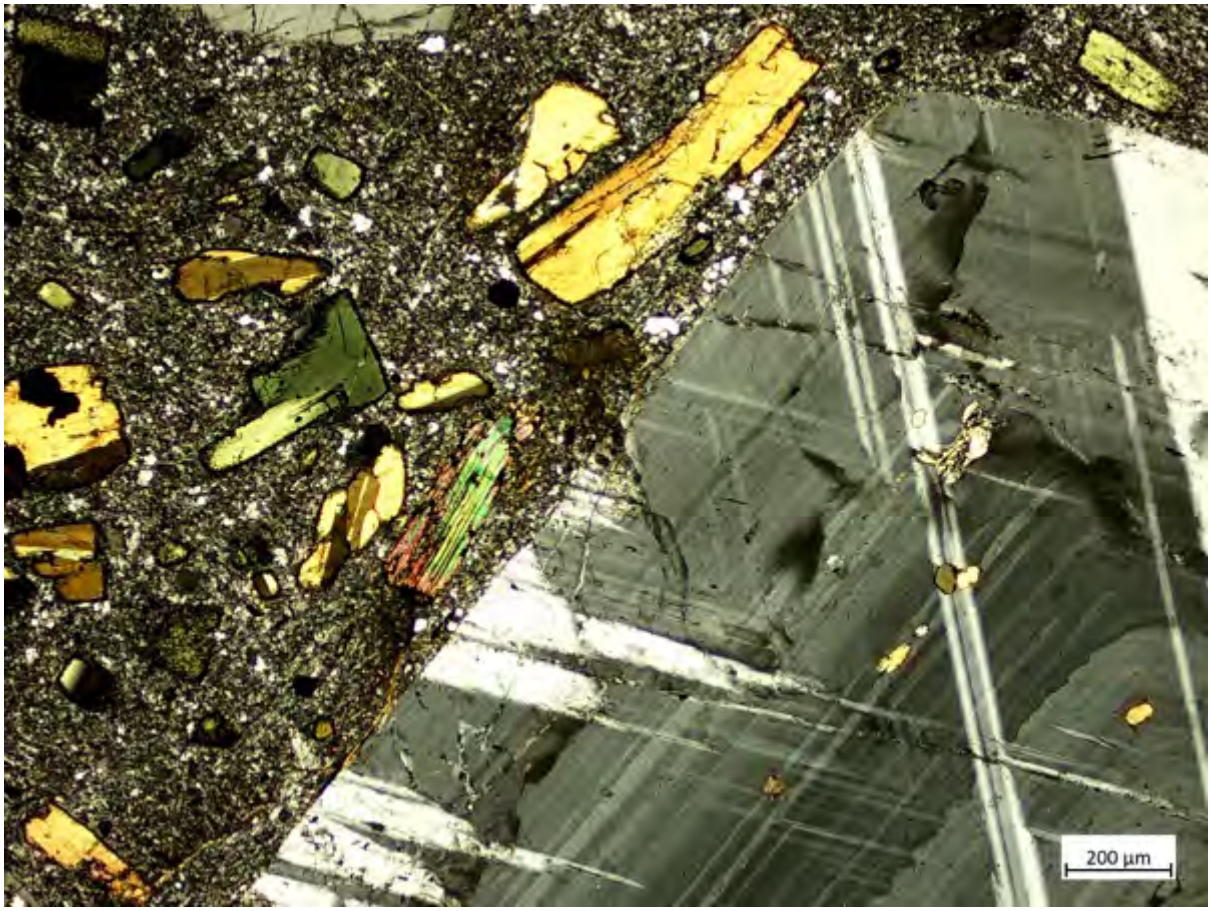

Figure 6.18: Cross polarised light (XPL) image of JLSW-008A, showing very large and zoned plagioclase phenocrysts and biotite in a microcrystalline groundmass.

JLSW-008A contrasts in character with -098, with large phenocrysts of twinned, euhedral to subhedral plagioclase >7 mm with oscillatory zoning (Figure 6.18), euhedral amphibole ~3 mm, euhedral to subhedral biotite ~1 – 2 mm with reaction rims and quartz microphenocrysts of <1 mm. Plagioclase and amphibole phenocrysts commonly contain inclusions of amphibole (in the former case), melt and opaque minerals. Groundmass is crypto- to microcrystalline, composed of plagioclase and quartz.

6.5.1.3.4 Western Tectonic Realm Basement:

The basement underlying the westernmost samples of this study, in particular those samples overlying the Cañas Gordas terrane, is here represented by DB15-087. This is a holocrystalline porphyritic rock with phenocrysts of plagioclase in an interlocking texture of phenocrysts and microphenocrysts >1 mm. Groundmass is composed of interstitial plagioclase, clinopyroxene and minor opaque phases, all of which <1 mm, and altered to chlorite and sausserite (for plagioclase). Anhedral calcite is also observed, possibly as infill of vesicles.

6.6 Geochemistry of the Samples:

6.6.1 Overview:

This part of the study consists of major and trace element analyses of 9 samples of the Central Colombian arc segment, 17 samples from the Southern Colombian arc segment and 6 samples of Miocene arc segments preceding the modern volcanic arc, including three samples of the El Boton basalts and one of the Combia Formation (Figures 6.5 A+B) as well as two intrusions from Central Colombia. A subset of these samples was also analysed for Sr, Nd and Hf radiogenic isotopes.

6.6.2 Major Elements:

Samples across the southwestern segments of the modern Colombian arc mostly cluster as basaltic andesites to dacites on a total alkali silica (TAS) plot (Figure 6.19) Samples from the Southernmost segment of the Colombian arc occupy a range of compositions from basaltic andesite to dacite, whilst analyses of the Central segment of the arc form a narrower trend of andesite compositions, with the exception one analysis with a rhyolite composition (JLSW-32B) which can likely be attributed to silica replacement within the sample as noted in Section 6.5. The Miocene arc rocks from the Combia Formation and Central Colombia fall along a similar trend to the modern arc, but with more evolved andesite to dacite compositions. The El Botón basalts (which is a published name, after Rodriguez and Zapata, 2012, and not an

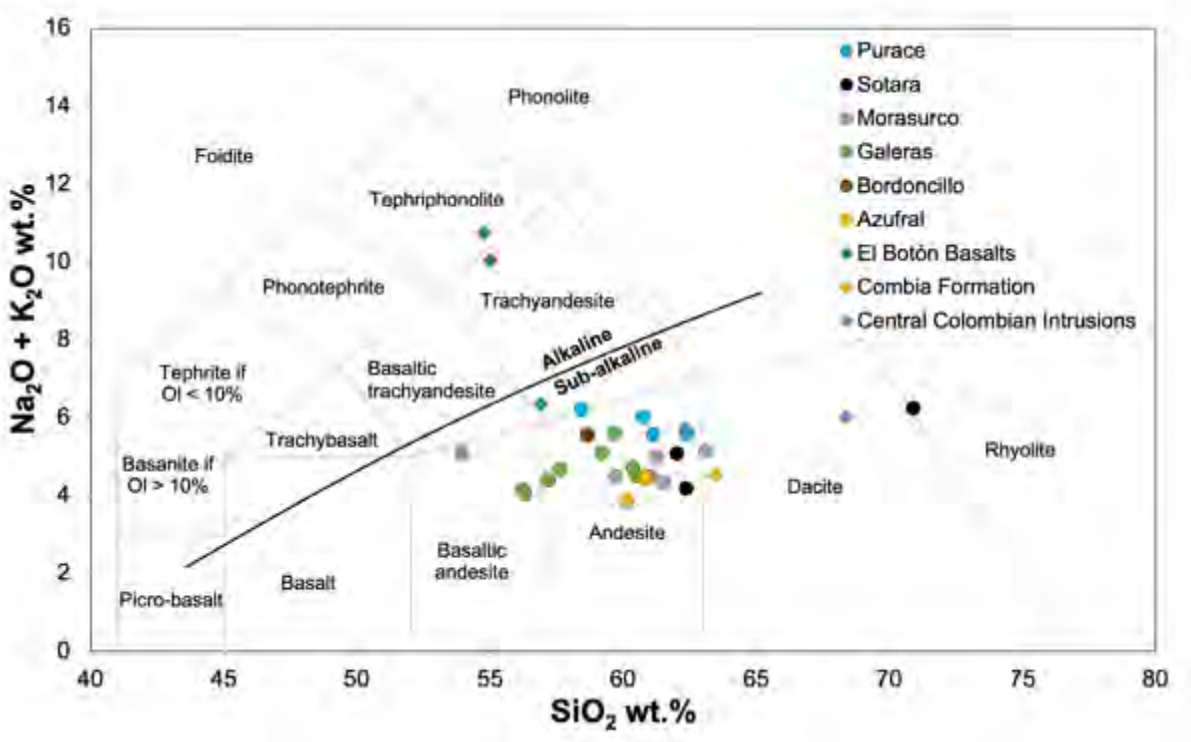

Figure 6.19: Total alkali silica plot for samples from the modern Central and Southern Colombian arc segments, along with Miocene arc remnants. Fields after Le Bas et al. (1986).

accurate geochemical label) are far richer in total alkalis compared to all other analyses, and plot as alkaline trachyandesites and tephriphonolites.

Central Colombian arc data range between dominantly high-K calc-alkaline compositions for Purace, especially the SESW samples compared to lower K_2O trends for other Purace samples and Sotara, with the exception of sample JLSW-32B. The Southern Colombian arc data plots as a low-K_2O trend with the exception of Bordoncillo, which plots within the high-K calc-alkaline field. There also appears to be a trend moving up silica and alkalis from Galeras to Azufral through to Morasurco compositions, possibly following similar evolution trends. Miocene arc segments are again divided between compositions similar to those of the modern arc but more evolved, represented by the Combia Formation and Central Colombian intrusions

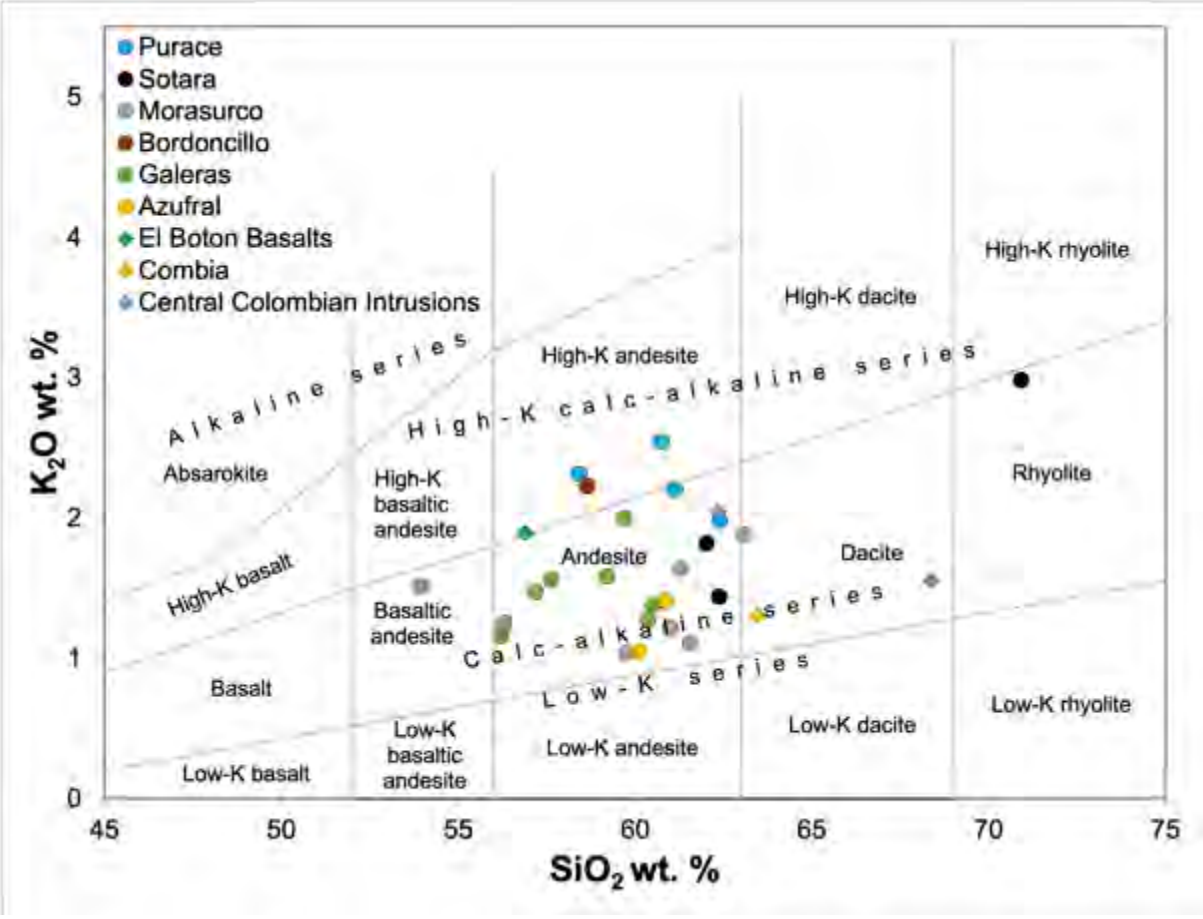

Figure 6.20: K_2O versus SiO_2 Harker diagram for samples from the Central and Southern segments of the modern Colombian arc and Miocene arc remnants. Fields after Ewart (1982).

with lower K_2O, and higher K_2O compositions represented by the El Boton basalts (two samples of which plot off the diagram with compositions highly alkali compositions >6 wt.%).

All modern Colombian arc analyses can be classified as calc-alkaline, falling closer to and along the boundary with tholeiitic compositions (Figure 6.20). Southern Colombian volcanic rocks are less enriched in alkalis compared to Central Colombian data. At the extreme end of the trends towards high silica and alkali contents on is Sotara sample JLSW-32B (Figure 6.20).

Bivariate plots of other major elements (Figure 6.21) show a number of different trends. TiO_2 shows a linear trend for the modern arc samples overall, with slightly elevated TiO_2 contents at similar silica compositions for Purace and Morasurco compared to other samples. The Miocene Colombia samples for El Boton off tren of other samples with low TiO_2 but overall the trend seems to be one broad liquid line of descent (Figure 6.21A). The Al_2O_3 contents also follow a generally linear trend with increasing silica, although Galeras samples show a larger variety of Al_2O_3 values compared to other groups (Figure 6.21B). Fe_2O_3 follows a generally linear trend with silica, with Central Colombian samples showing a more mafic character than Southern Colombian samples. El Boton basalts show a lower Fe content than the modern arc at a given silica, whilst the Combia samples shows a higher range Fe content at a given silica (Figure 6.21C).

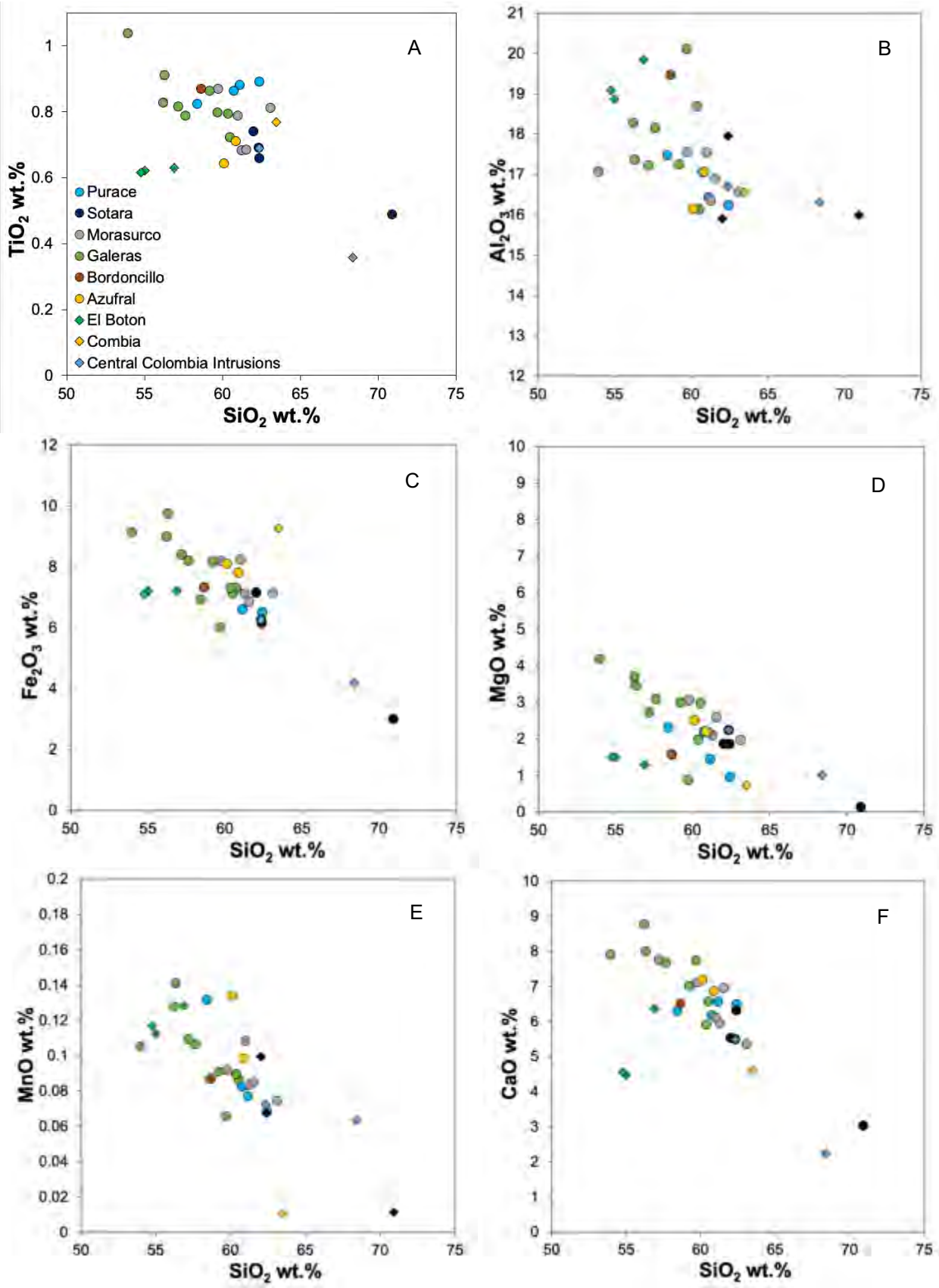

Figure 6.21 (above and overleaf): Harker bivariate diagrams of major elements against silica for the Central and Southern segments of the modern Colombian arc alongside Miocene arc remnant samples collected in this study.

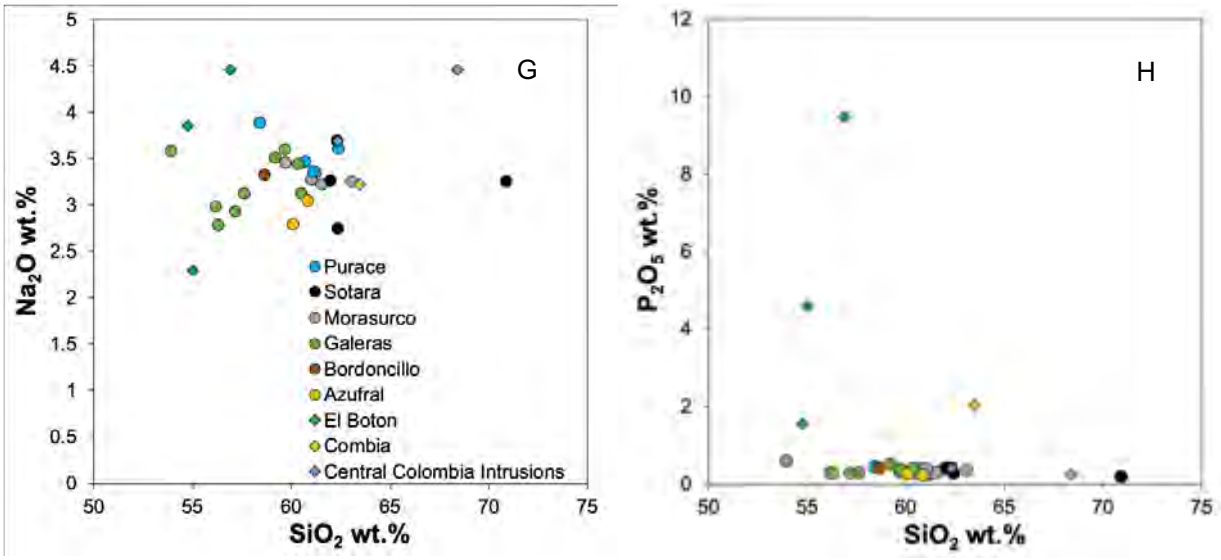

Figure 6.21: Harker bivariate diagrams of major elements against silica for the Central and Southern segments of the modern Colombian arc alongside Miocene arc remnant samples collected in this study.

All samples plot in an array of decreasing MnO with increasing silica, though Galeras and El Boton basalts have lower values at a given silica compared to other samples (Figure 6.21E). The Combia Formation sample also plots off the main array and has a very low MnO compared to other samples of a similar silica content. MgO values of all samples analysed are <5 wt.% and also follow a generally linear negative correlation with increasing silica, although El Boton basalt analyses have lower MgO at a given silica compared to other samples (Figure 6.21F). This trend is similar to that observed in CaO values, which also, with the exception of El Boton basalt analyses, follow a negative trend with increasing silica (Figure 6.21G). Contents of Na_2O for all analysed samples vary between 2 – 5 wt.%, with El Boton basalt samples showing the greatest range in Na_2O. There appears to be an inflection in the analyses of Southern Colombian samples at ~60 wt.% SiO_2 (Figure 6.21H). Purace and Central Colombian intrusions show the most elevated contents at SiO_2 values

>60 wt.%. El Boton basalts stand out from other groups in their extremely elevated P_2O_5 contents, which along with the Combia Formation sample are >0.5 wt.%. All other analyses plot on as a general negative correlation with increasing silica, although Galeras does show some lower values at a given silica than other groups (Figure 6.21I). Overall, the modern Colombian arc and Miocene arc remnant samples follow a trend of decreasing broad trend major element components with increasing silica content, although El Boton basalts and the Combia Formation sample do plot off this trend for some elements. There are also notable differences between major element analyses of the Central and Southern Colombian arc compared to the NVP (Chapter 5), such as a lower abundance of P_2O_5 at a given silica in the NVP compared to the rest of the Colombian arc.

6.6.3 Trace Elements:

Bivariate plots of selected trace elements (Figure 6.22) can also geochemically distinguish the groups presented here. Scandium falls along a negative correlation trend with increasing silica amongst all groups (Figure 6.22A). El Boton basalts are an exception to this, with notably lower Sc compared to other groups. Vanadium follows a more regular downward trend of decreasing V with silica across all groups, this is true also for Co (although this also has more depleted values for El Boton basalts - Figure 6.22B+C). Ni values are highest in a subset of Galeras samples (DC16-031, -032, -033 and -036) with contents >100 ppm. The Combia Formation sample also has elevated Ni (Figure 6.22D).

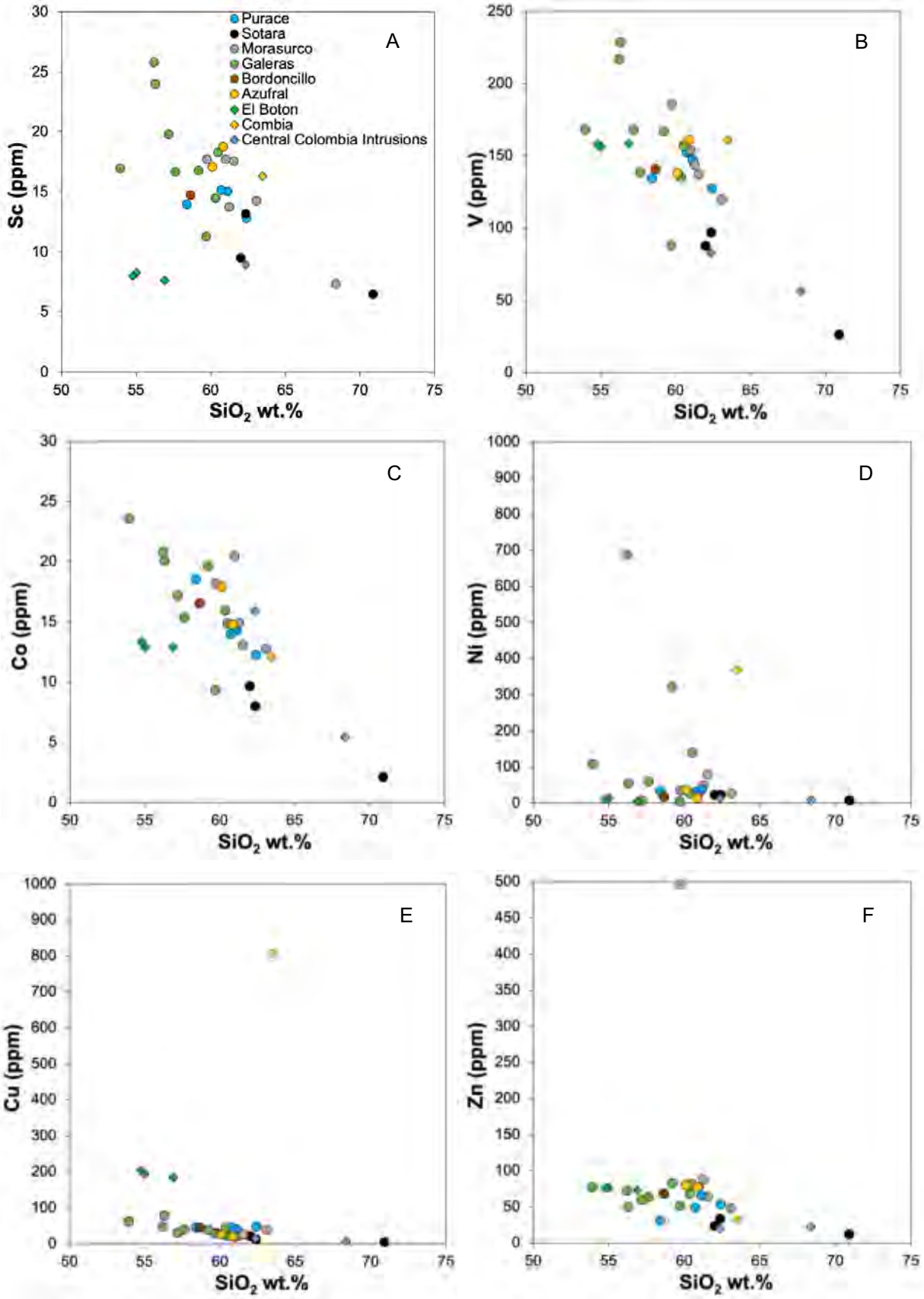

Figure 6.22 (above and overleaf): Harker bivariate diagrams of trace elements against silica for the Central and Southern segments of the modern Colombian arc alongside Miocene arc remnant samples collected in this study.

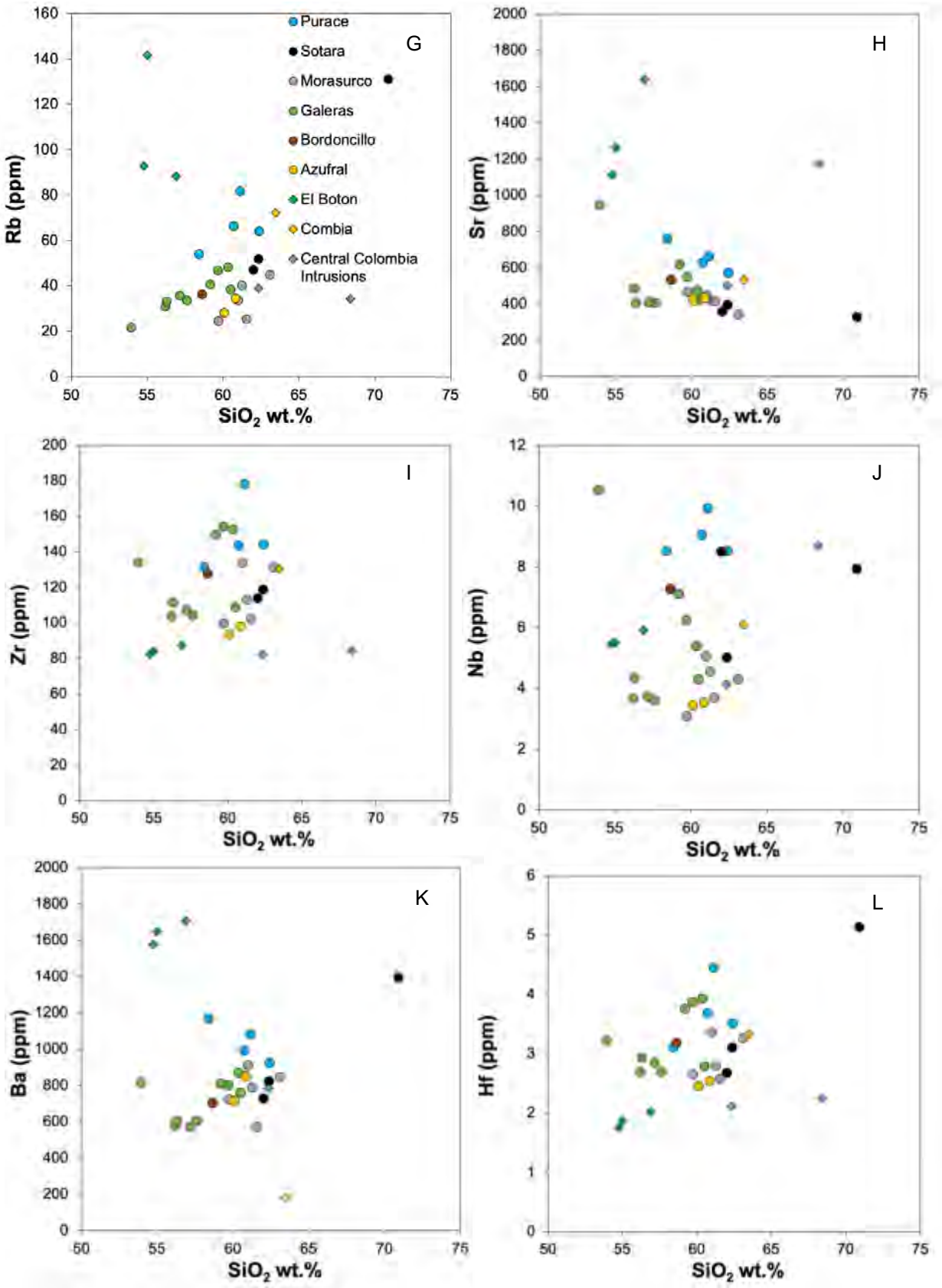

Figure 6.22 (above and overleaf): Harker bivariate diagrams of trace elements against silica for the Central and Southern segments of the modern Colombian arc alongside Miocene arc remnant samples collected in this study.

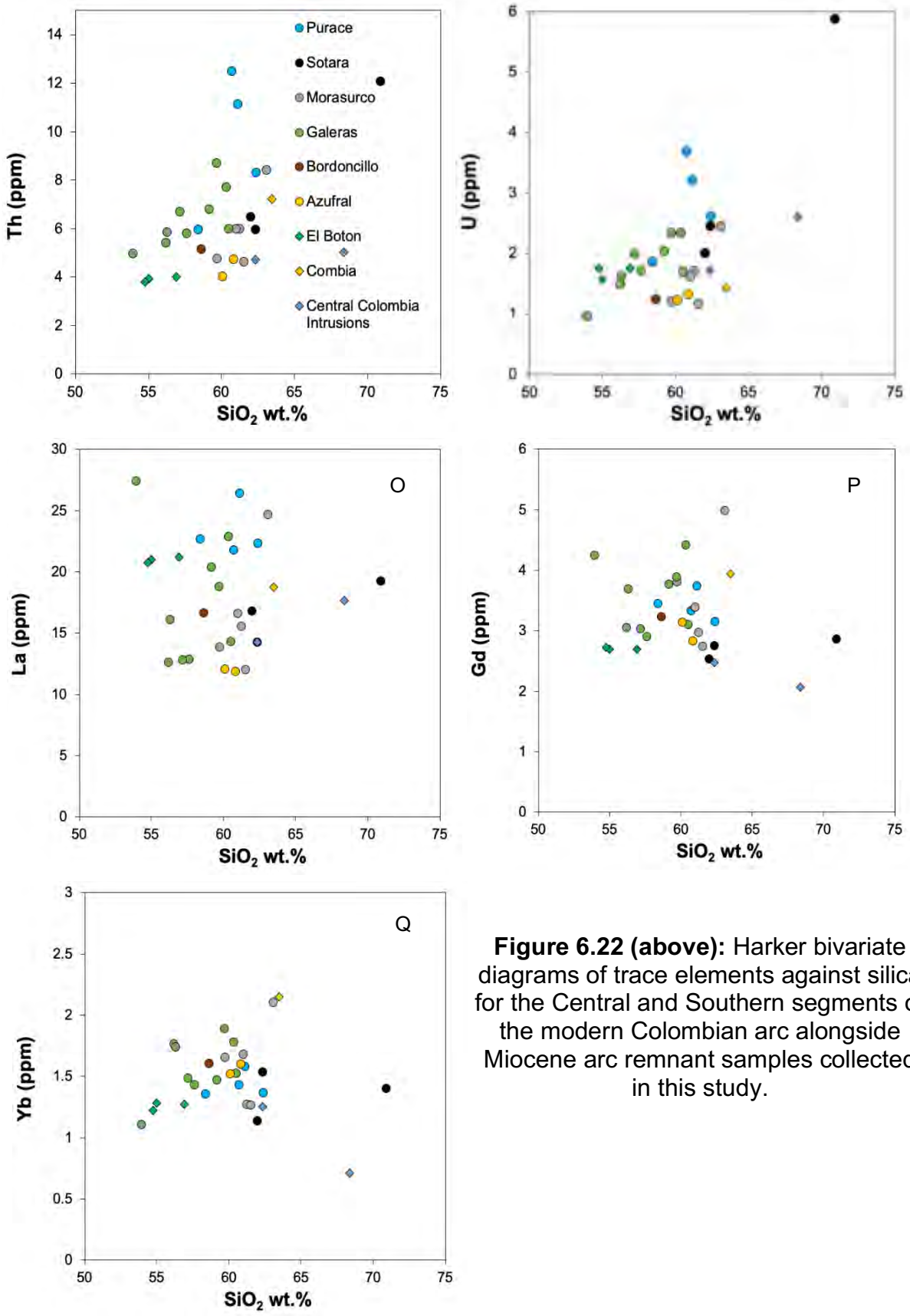

Figure 6.22 (above): Harker bivariate diagrams of trace elements against silica for the Central and Southern segments of the modern Colombian arc alongside Miocene arc remnant samples collected in this study.

Contents of Cu are elevated in El Boton basalts and extremely elevated in the Combia Formation sample, but follow a general decreasing trend with increasing silica content for all other groups. There is a similar negative trend with increasing silica in Zn values, but with slightly elevated Zn contents in Azufral and Morasurco samples compared to other groups (Figure 6.22E+F). Central Colombian analyses of Purace and Sotara have the highest Rb values of the modern arc groups presented, though some Galeras samples have similar values to those of Sotara. The highest Rb values overall belong to El Boton basalts and the Combia Formation sample, whilst analyses of Central Colombian intrusions are noticeably lower (Figure 6.22G). El Boton basalts are also the most elevated in Sr of all groups, the remainder of the groups follow a similar trend to other trace elements of decreasing Sr content with increasing silica. There are; however, outliers along this trend, most notably elevated contents in one Central Colombian intrusion (PKSW-098). Central Colombian intrusions, Combia Formation and Purace samples also fall a slightly elevated group compared to the trend of Southern Colombian arc samples. A subset of the Galeras samples (DC16-029, -030, -031 and -035) also exhibit slightly lower Sr values than other Southern Colombian samples at a given silica (Figure 6.22H). Zr values are lowest for El Boton basalt and the Central Colombian intrusions. The highest values are those of Purace, along with a subset of Galeras samples, though these have a wide range of values and other groups in general show little correlation with silica other than a rough correlation within groups of increasing values with increasing silica, with Zr between 90 – 180 ppm (Figure 6.22I). There is a notable difference in Nb contents for Central Colombian analyses mostly ≥8 ppm. The exception to this is JLSW-008A. All Southern Colombian samples, except for DC16-036, have values <8 ppm, along with El Boton basalts and Combia Formation samples. Ba contents

increase along a positive trend with increasing silica for most sample groups. The exceptions to this are Purace samples, which have the highest Ba overall and show a negative trend with increasing silica along with the El Boton basalts. The Combia Formation sample also has a notably low Ba. Hf values are lowest (<2.5 ppm) in the Miocene groups of the El Boton basalts and Central Colombian intrusions, with the exception of the Combia Formation sample, which has a similar value to the modern Colombian arc groups, which range between ~2 – 5 ppm. Th and U show relatively similar values, with Purace showing the most elevated values. One sample from Sotara (JLSW-32B) plots at high silica and high values in both Th and U, distinct from all other groups. Overall values for Miocene intrusions are similar for those for the modern arc. No clear trend across groups in defined for either Th or U, though Galeras samples do plot in weak positive correlation with increasing silica. Finally, light, medium and heavy rare earth elements (Figure 6.22O, P, Q, respectively) show a positive correlation with silica up to around 60 wt.% before levelling out or in the case of Yb in more evolved samples, dropping.

Relative depletions and enrichments between edifices and N-MORB can be observed using N-MORB normalised multi-element diagrams (Figures 6.23 – 6.28).

Figure 6.23: Multi-element plot of analyses from Purace. Normalised to N-MORB values from Sun and McDonough (1989).

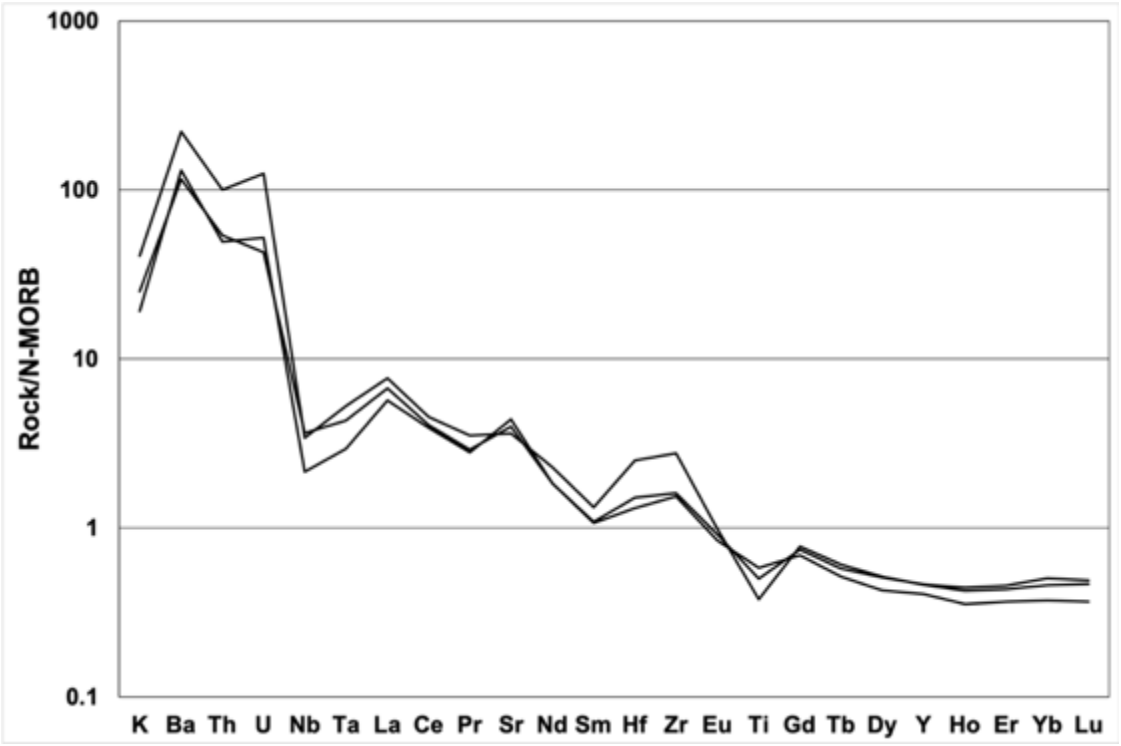

Figure 6.24: Multi-element plot of analyses from Sotara. Normalised to N-MORB values from Sun and McDonough (1989).

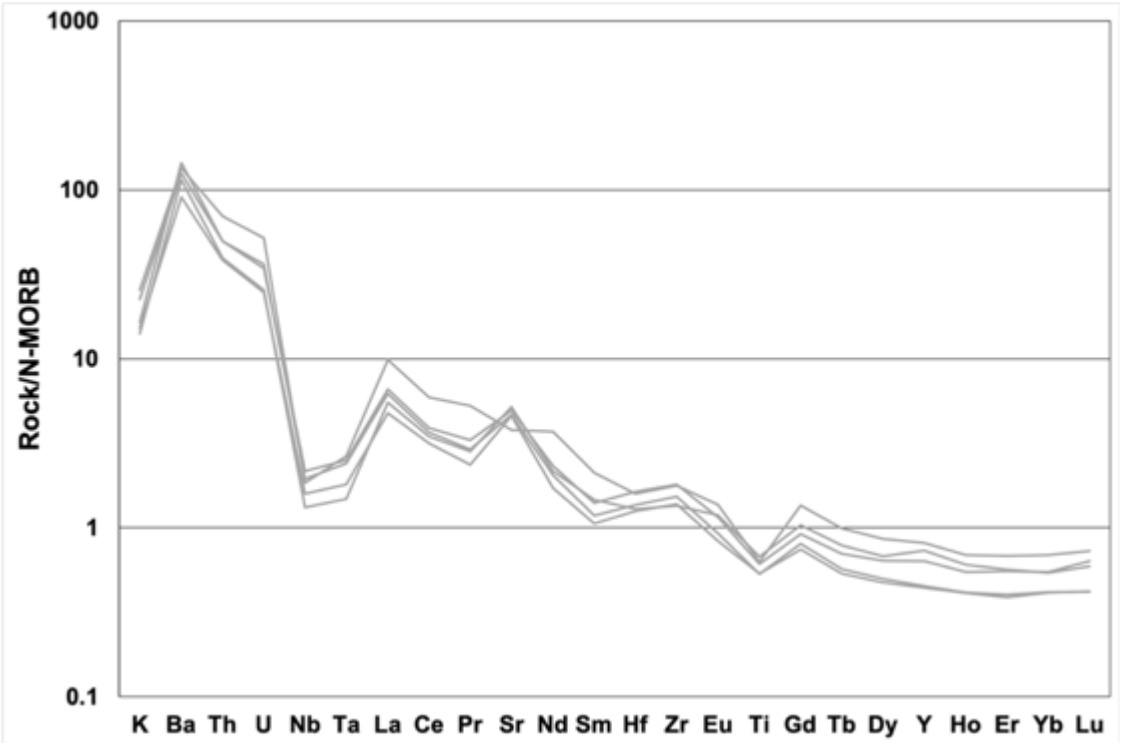

Figure 6.25: Multi-element plot of analyses from Morasurco. Normalised to N-MORB values from Sun and McDonough (1989).

Figure 6.26: Multi-element plot of analyses from Galeras. Normalised to N-MORB values from Sun and McDonough (1989).

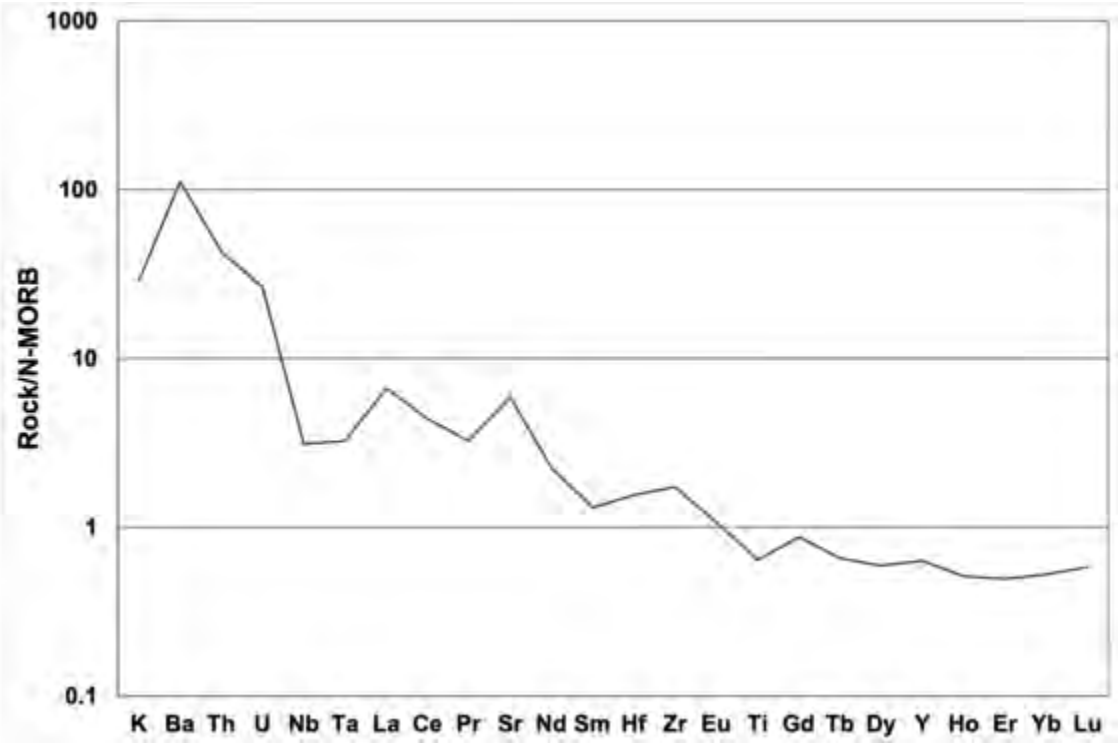

Figure 6.27: Multi-element plot of analysis from Bordoncillo. Normalised to N-MORB values from Sun and McDonough (1989).

Figure 6.28: Multi-element plot of analyses from Azufral. Normalised to N-MORB values from Sun and McDonough (1989).

Multi-element analyses for both Central and Southern segments of the Colombian arc have features typical of those for continental volcanic arcs, with relative depletions in Nb, Ta and Ti, enrichment in LILE (K, Ba, Th and Sr) and sub-horizontal REE patterns.

In general, Central Colombian analyses, and in particular Purace, show a greater overall enrichment in incompatible elements and lower relative depletions in Nb, Ta and Ti compared to other southwestern Colombian edifices (Figure 6.23). Analyses of Sotara differ from Purace in their less pronounced Ta depletion and slightly lower light (L)REE abundances. One Sotara sample (JLSW-32B) does show more elevated incompatible element abundances and highly elevated Zr and Hf, though as previously noted this sample has some secondary replacement minerals such as amorphous silica, and these differences may be reflective of these rather than the initial mineralogy. This sample overall shows significant differences to other samples across multiple elements, likely as a consequence of alteration. However, both edifices do show relative Hf and Zr enrichments.

The edifices of the Southern Colombian arc have broadly similar multi-element plots. Depletions across the diagram are far closer to N-MORB values than the majority of the Colombian arc dataset overall, though there are outliers to this. In the case of Morasurco (Figure 6.25), one analysis (DC16-025) does stand out with higher incompatible element abundances overall, but lack of a positive Sr anomaly. One Galeras sample (DC16-036) also has a heavy (H)REE depletion unlike that observed in the rest of the southwestern arc (Figure 6.26). This is the sample from La Guaca cinder cone, which is notably different in composition compared to other Galeras

samples and has the highest overall incompatible element enrichments, and lower depletions in Nb and Ta. La Guaca overall has a pattern much closer to that of Purace and even some NVP analyses. Though lacking the HREE depletion of La Guaca, the single analysis of Bordoncillo (Figure 6.27) does also show a less notable depletion in Nb and Ta compared to other southern Colombian analyses, but overall correlates well to other analyses. Azufral analyses (Figure 6.28) appear to be the least enriched in almost all elements, though one Morasurco sample (DC16-024) does have a greater Nb-Ta depletion and both samples show the lowest LREE and Ti abundances of the southern edifices. Hf and Zr are slightly enriched, but not to the same extent as the Central Colombian segment reported here.

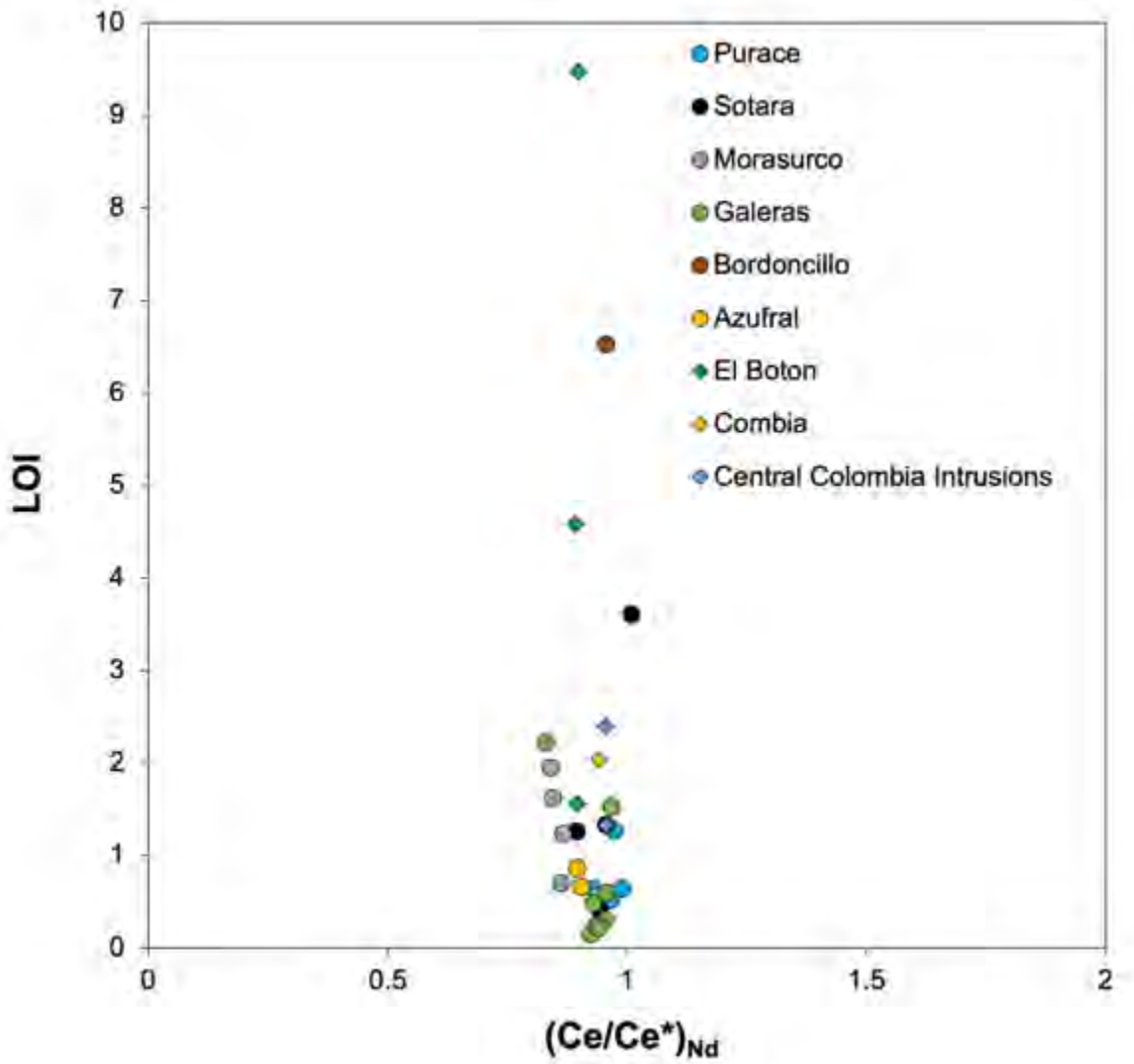

Figure 6.29: Loss on ignition (LOI) versus $(Ce/Ce^*)_{Nd}$ used to quantify the Ce anomalies of SW Colombian and Miocene samples (after Hastie et al. 2013). Morarurco samples appear to have the largest negative Ce anomalies of modern arc samples. Miocene subgroups overall have more elevated LOI than most modern arc samples, with the exception of JLSW-32B (Sotara) and the analysis of Bordoncillo. $(Ce/Ce^*)_{Nd}$ calculated as $Ce_{CN}/(La_{CN}^{2/3} \times Nd_{CN}^{1/3})$. Chondrie normalisation values taken from Sun and McDonough (1995).

Both the Miocene arc segments and basement of the Western Cordillera in northern Colombia can also be assessed using multi-element plots. The northern Miocene arc remnants show broadly similar trends, though the Combia Formation sample is more enriched in compatible elements compared to El Boton basalts. Both show prominent negative Ce and positive La anomalies, perhaps produced by alteration and the

preferential fluid mobility of LREE (Holm et al. 2016). Quantification of these Ce anomalies as a function of alteration can also be made using an LOI – $(Ce/Ce^*)_{Nd}$ diagram (Figure 6.29), which show no strong correlation between LOI and negative Ce anomalies, but do show that El Boton samples have some of the most elevated LOI contents. The Combia Formation sample also has a less pronounced Ta anomaly than El Boton samples, which are also more incompatible element enriched (Figure 6.30).

The Central Colombian intrusions each show distinct patterns, though both are marked by typical subduction zone signatures, such as an Nb, Ta and Ti anomaly, a Sr enrichment and an overall enrichment in incompatible elements. JLSW-008A is broadly similar to the El Boton basalt analyses in incompatible element enrichment,

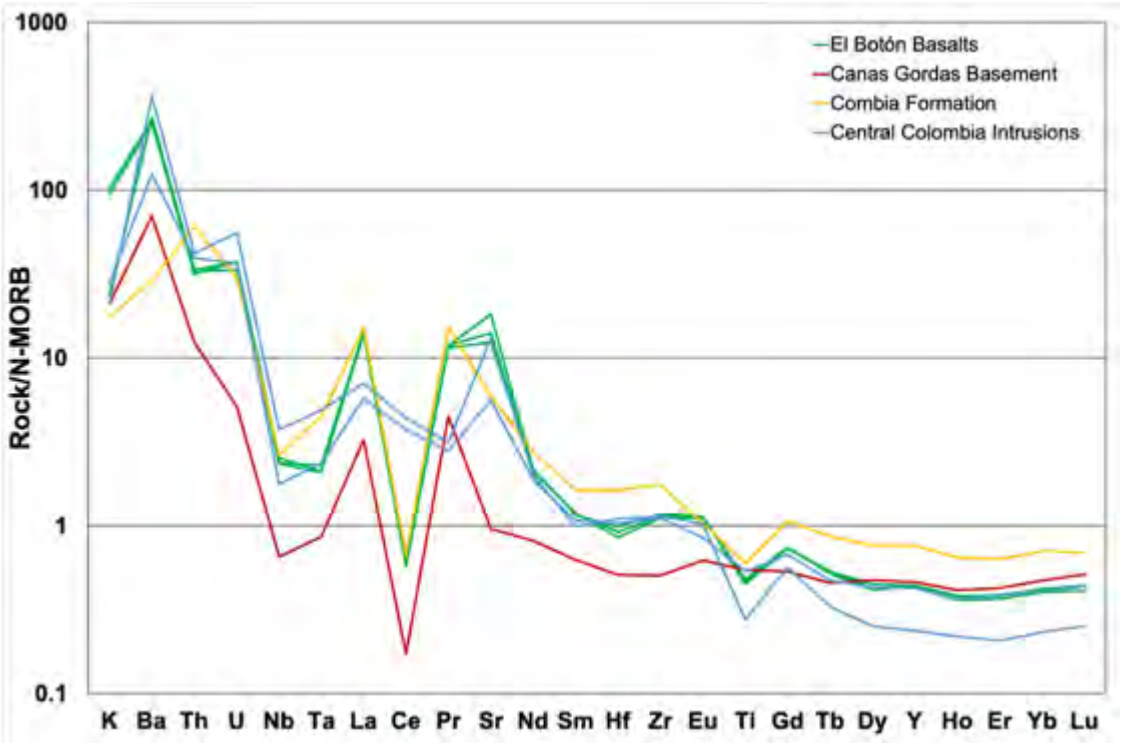

Figure 6.30: Multi-element plot of analyses of Miocene arc remnants sampled in this study from the El Boton basalts and Combia Formation in northern Colombia and intrusions from the Cauca-Patia valley west of the Central Colombian volcanoes. Basement of the Western Cordillera is represented here by part of the Cañas Gordas formation. Normalised to N-MORB values from Sun and McDonough (1989).

strong Nb-Ta and Ti depletions, and sub-horizontal medium to heavy REE (MREE – HREE) patterns. In contrast, PKSW-098 shows a strong depletion in Ti and MREE to HREE elements. The overall element enrichment is similar to the Combia Formation analysis and, in general, the enriched compositions of the Central Colombian arc and NVP.

The basement of the Western Cordillera sampled here is part of the Barroso Formation, which is part of a Cretaceous intra-oceanic arc formed outboard of Colombia and later accreted to the continent (Leal-Mejia et al. 2018), and its composition reflects this with a lower proportion of incompatible elements compared to other the continental arc signatures presented here. Alteration is also present as represented by La and Ce anomalies in common with Miocene analyses.

Further insight on the differences in the modern Colombian arc and between that and the Miocene arc remnants can be explored with chondrite normalised REE patterns (Figures 6.31 – 6.38).

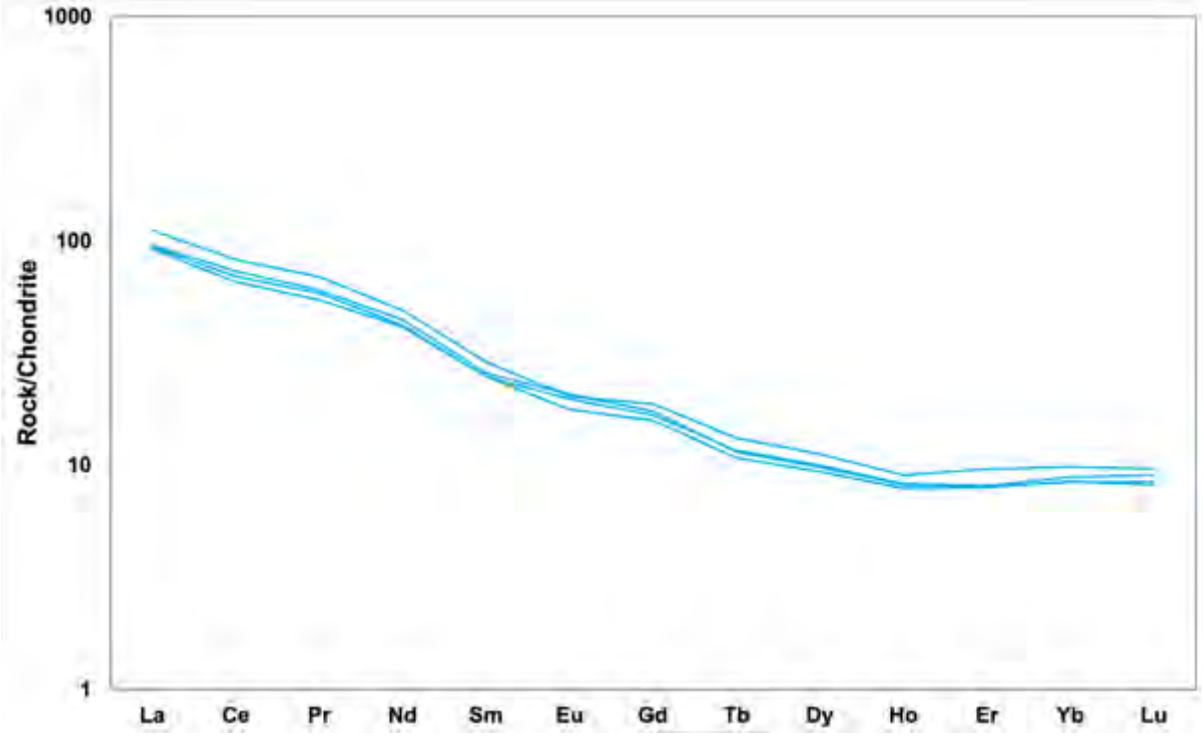

Figure 6.31: Rare earth element pattern for analysed samples from Purace. Chondrite normalised using values from Sun and McDonough (1995).

Analyses of Central Colombian edifices Purace and Sotara show more LREE enrichment compared to Southern Colombian analyses, especially in the case of Purace (Figure 6.31). Overall, the abundance of REE across all of southwestern Colombia has a remarkably similar range, and concave M-HREE patterns, though Purace has the highest abundance of REE amongst the southwestern edifices (Figure 6.31). The only exception to this is the La Guaca sample, which has a depleted HREE pattern, which has a Gd/Yb ratio of 3.84 (Figure 6.36). Overall, the Southern Colombian arc segment has a lesser enrichment in LREE compared to the Central Colombian arc segments.

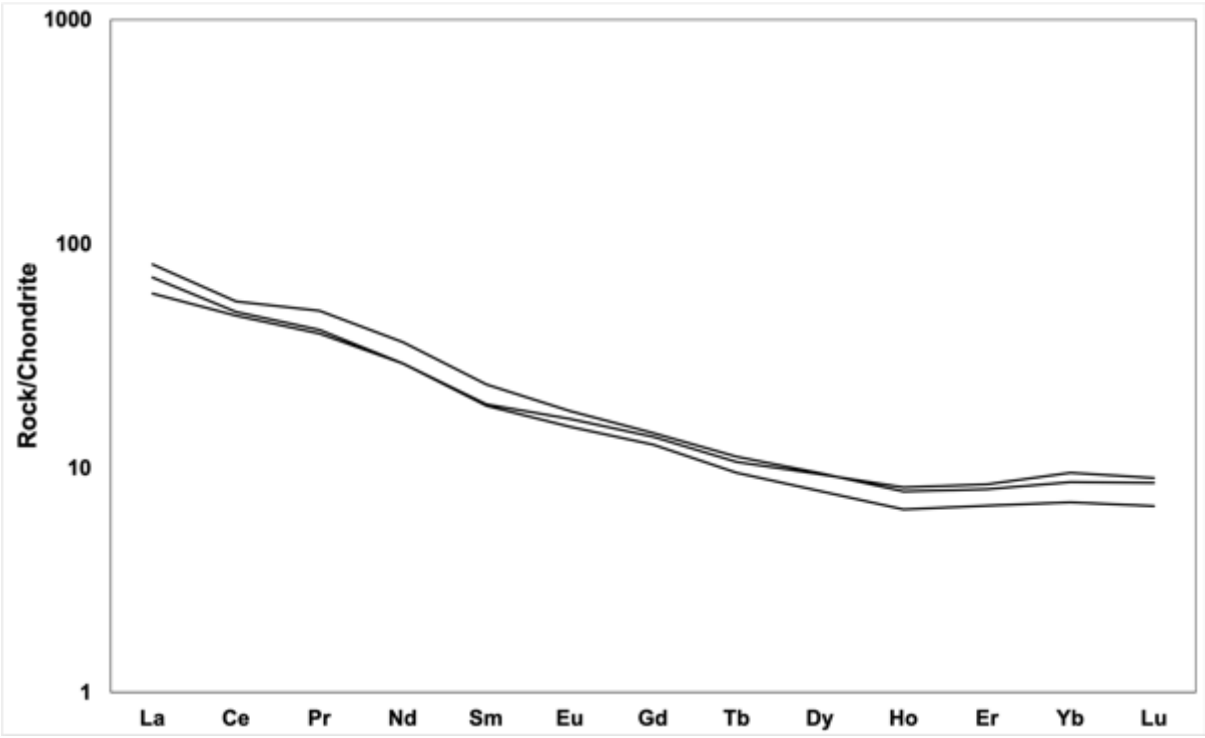

Figure 6.32: Rare earth element pattern for analysed samples from Sotara. Chondrite normalised using values from Sun and McDonough (1995).

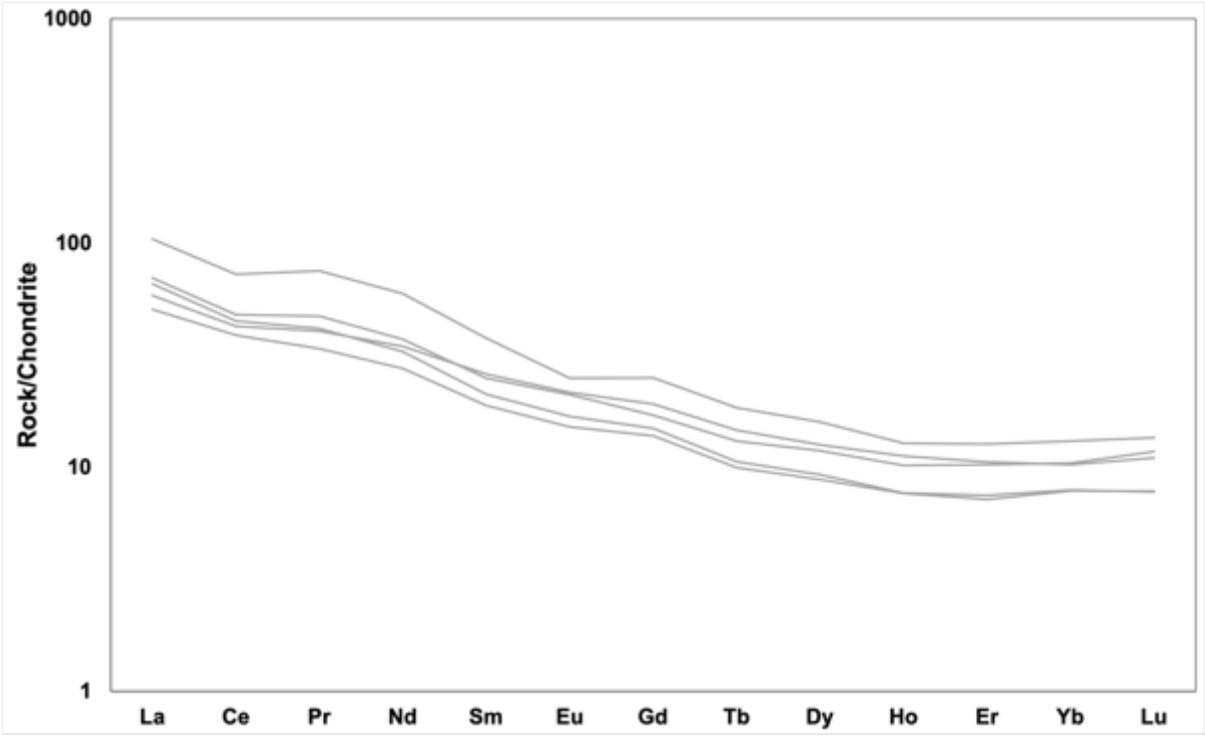

Figure 6.33: Rare earth element pattern for analysed samples from Morasurco. Chondrite normalised using values from Sun and McDonough (1995).

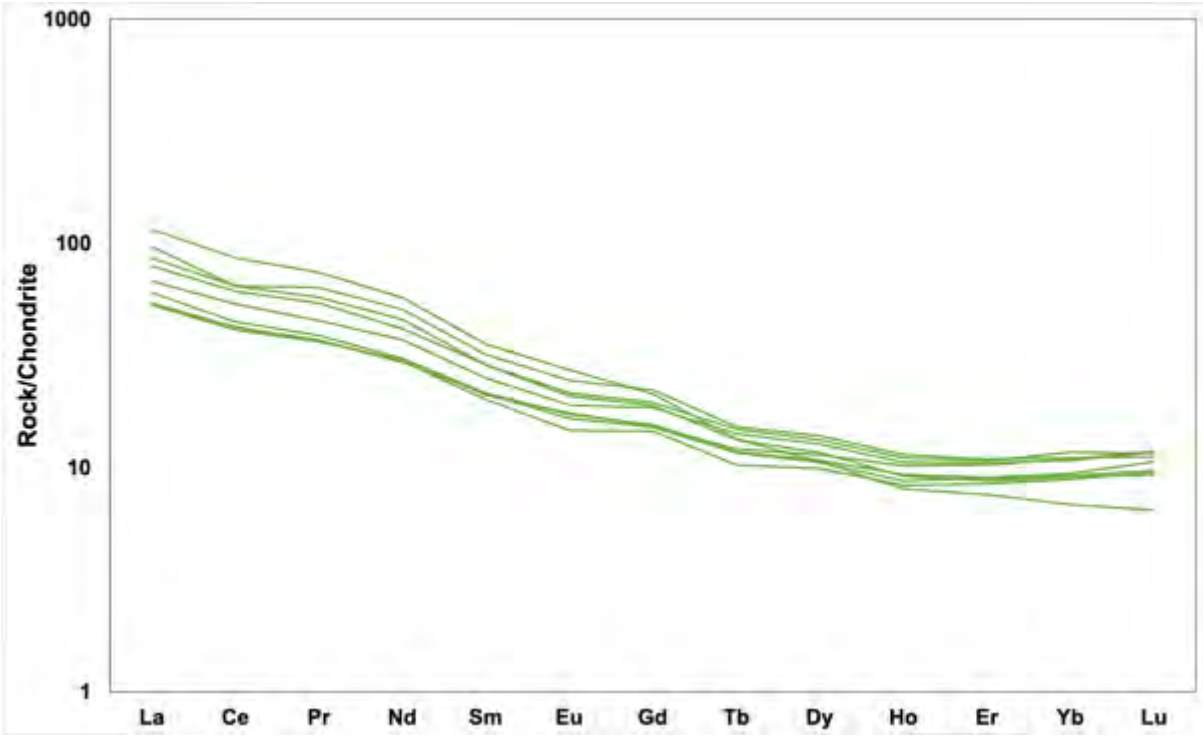

Figure 6.34: Rare earth element pattern for analysed samples from Galeras. Chondrite normalised using values from Sun and McDonough (1995).

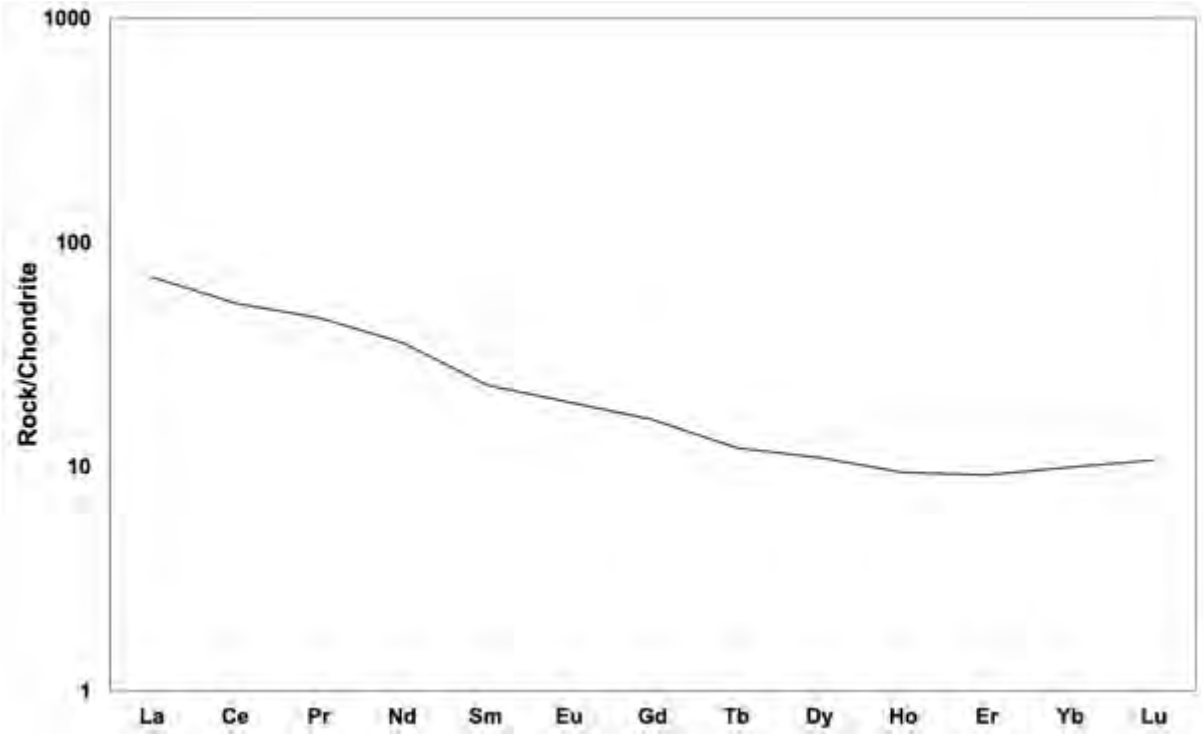

Figure 6.35: Rare earth element pattern for analysed samples from Bordoncillo. Chondrite normalised using values from Sun and McDonough (1995).

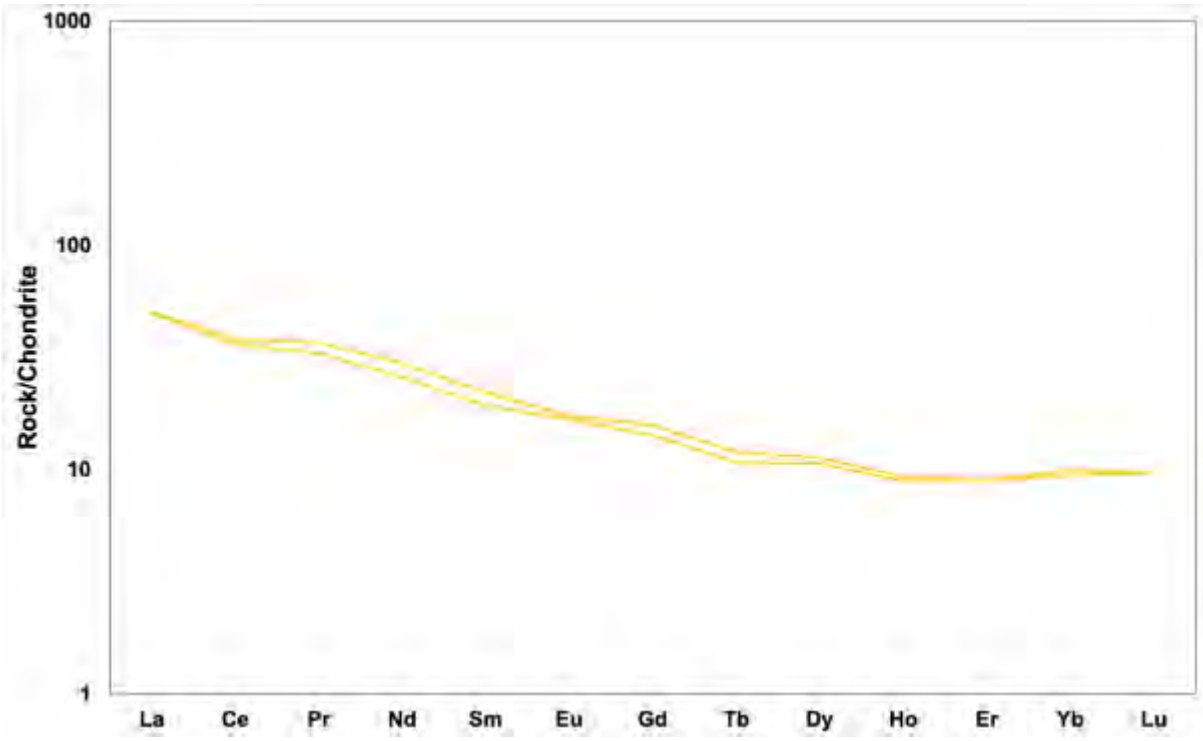

Figure 6.36: Rare earth element pattern for analysed samples from Azufral. Chondrite normalised using values from Sun and McDonough (1995).

In agreement with observations from multi-element diagrams, Azufral has the lowest abundance in REE overall amongst Southern edifices and the lowest enrichment in light rare earth elements (LREE). Other than this and the La Guaca analysis (Figure 6.34), samples show a remarkably similar range of REE concentrations.

Analyses of Miocene arc remnants show significant differences in REE analyses (Figure 6.37). The Combia Formation analysis shows enrichment in HREE compared to other analyses. The range of LREE contents is similar between all Miocene remnant analyses presented here. El Boton and Central Colombian analysis JLSW-008A have similar REE patterns and depletion in HREE, whereas PKSW-098 is far more HREE depletion compared to all other analyses (Figure 6.37).

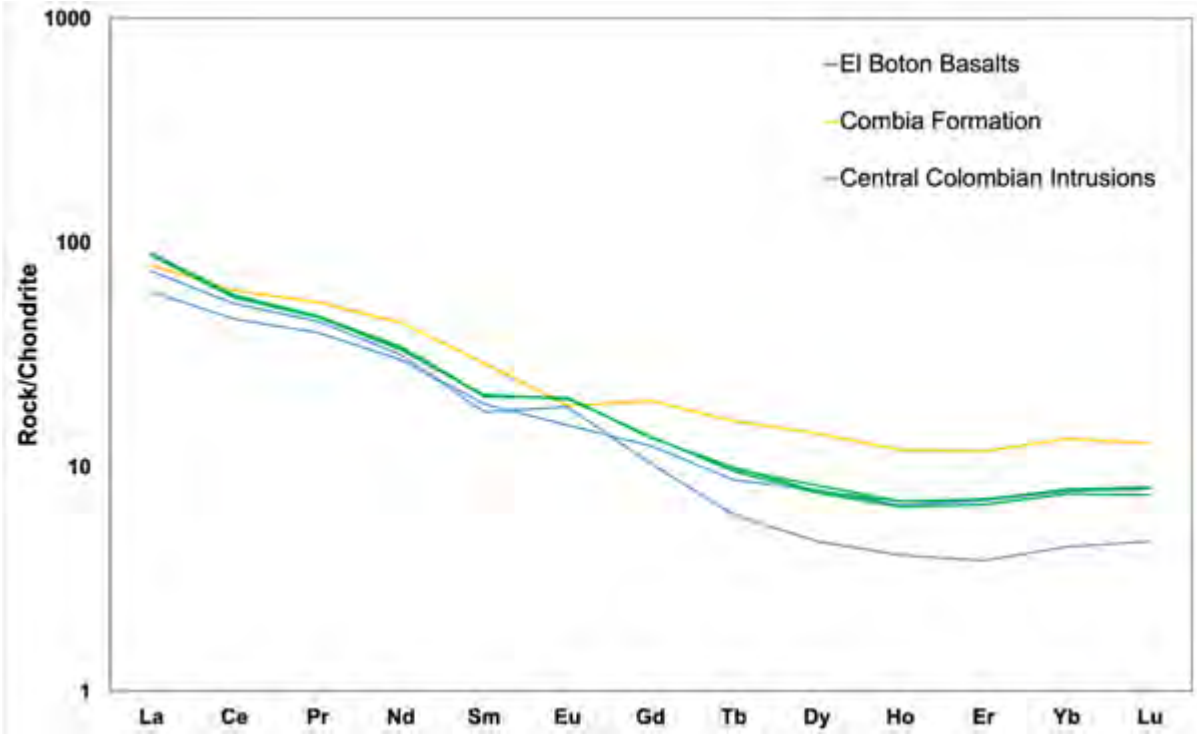

Figure 6.37: Rare earth element pattern for analysed samples from Miocene arc remnants sampled in this study, including El Boton basalts (green), Combia Formation (yellow) and Central Colombian intrusions (blue). Chondrite normalised using values from Sun and McDonough (1995).

6.6.4 Radiogenic isotope analyses:

Sr, Nd and Hf radiogenic isotope analyses have been obtained for a subset of samples from the Central and Southern Colombian arc segments and the Miocene arc remnants sampled in this study (Figures 6.38 and 6.39). Also, samples in this study include the first radiogenic isotope analyses of Morasurco volcano. In general, radiogenic Sr and Nd isotopes correlate well, following a negative correlation to lower $^{143}Nd/^{144}Nd$ values and higher $^{87}Sr/^{86}Sr$ compositions. Modern Colombian arc analyses range between 0.704 and 0.7045 $^{87}Sr/^{86}Sr$ and 0.51295 and 0.51275 $^{143}Nd/^{144}Nd$, in line with pre-existing isotope compositions reported for southwestern Colombia (e.g.: Marin-Ceron et al. 2010). Miocene arc remnants show a wide range

of compositions, with El Boton basalts plotting closest to MORB and DMM values and the Combia Formation plotting

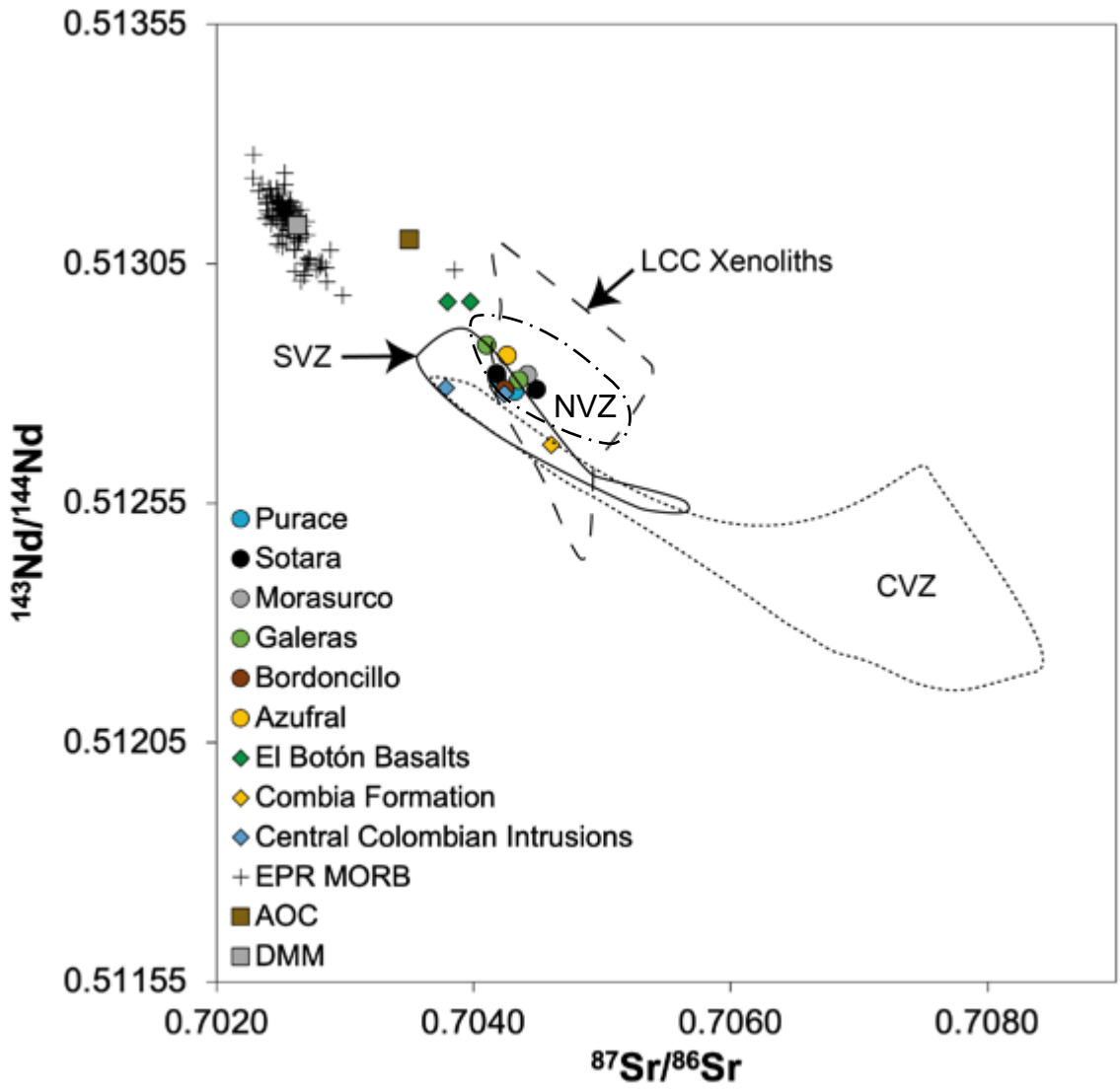

Figure 6.38: $^{143}Nd/^{144}Nd$ versus $^{87}Sr/^{86}Sr$ plot for Central and Southern Colombian edifices and Miocene arc remnants sampled in this study, alongside a field for Colombian lower crustal xenoliths (Rodriguez-Vargas et al. 2005). Data for mid-ocean ridge basalts from the East Pacific Rise (EPR MORB), average depleted MORB mantle (DMM) and average altered oceanic crust are also included (data from Gale et al. (2013), Workman and Hart (2005) and Patino et al. (2000) respectively) as well as fields for the Northern, Central and Southern Volcanic Zones of the Andes (NVZ, CVZ and SVZ, respectively). SVZ data from Jacques et al. (2013) and Hickey-Vargas et al. (2016). CVZ data from Hildreth and Moorbath (1988), Feeley and Davidson (1994), Delacour et al. (2007), Hora et al. (2007), Sørenson and Holm (2008) and Mamani et al. (2008; 2010). NVZ data from Marin-Ceron et al. (2010) and Errazuriz-Henao et al. (2019).

with more radiogenic Sr and Nd compositions. Central Colombian intrusions also have distinct isotope compositions, with PKSW-098 offset from the other samples at less radiogenic Sr at similar Nd values (Figure 6.38). In contrast, JLSW-008A has a composition similar to modern Central and Southern Colombian arc segments.

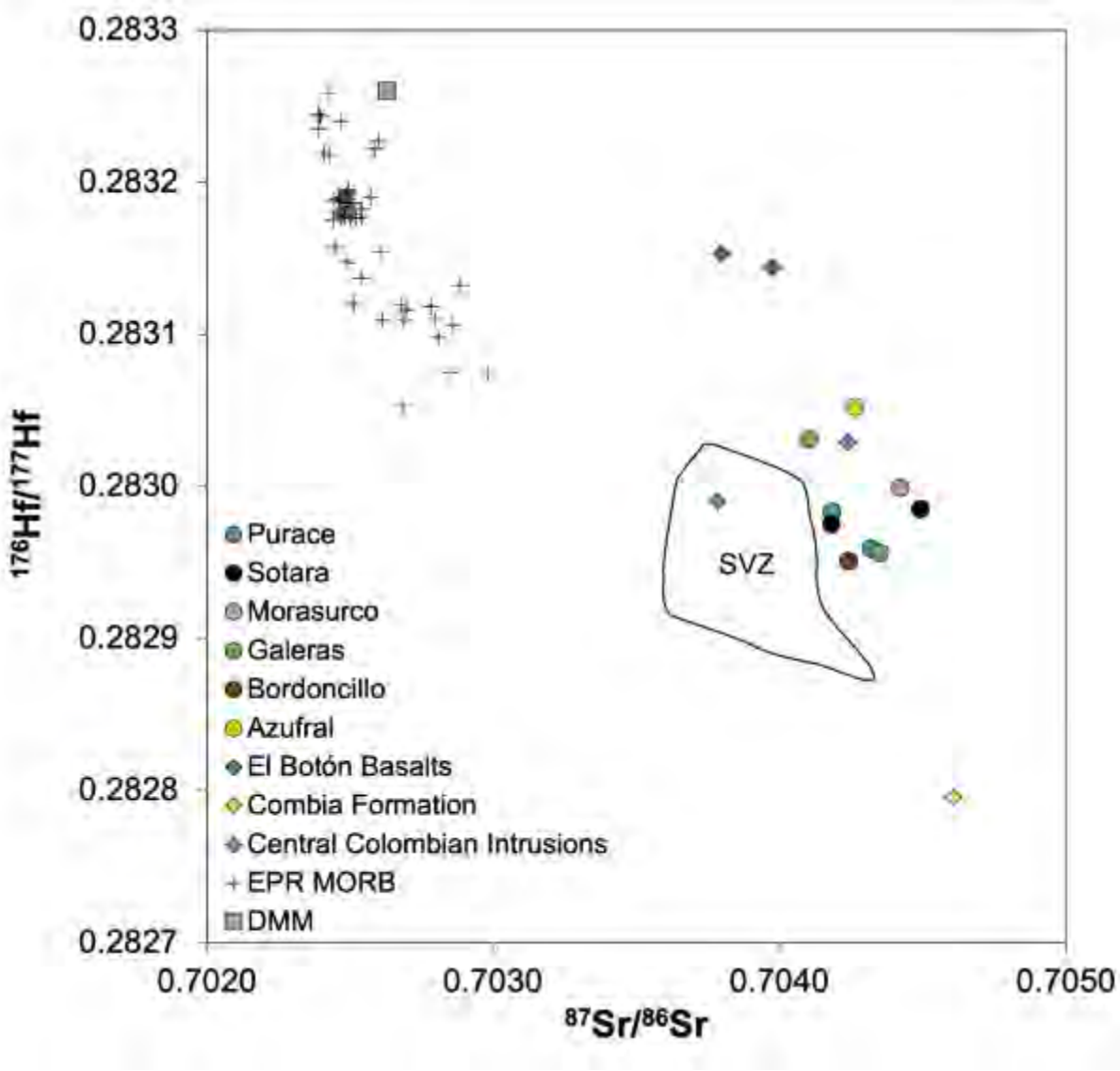

Figure 6.39: $^{176}Hf/^{177}Hf$ versus $^{87}Sr/^{86}Sr$ plot for Central and Southern Colombian edifices and Miocene arc remnants sampled in this study. Data for mid-ocean ridge basalts from the East Pacific Rise (EPR MORB) and average depleted MORB mantle (DMM) are also included (data from Gale et al. (2013) and Workman and Hart (2005) respectively) as well as a field for the Southern Volcanic Zone of the Andes (SVZ data from Jacques et al. (2013) and Hickey-Vargas et al. (2016)).

$^{176}Hf/^{177}Hf$ trends reflect those in Sr and Nd isotopes, with El Boton compositions being the least radiogenic and Combia Formation analyses the most radiogenic. PKSW-098 is again offset from the other samples towards less radiogenic Sr compositions at similar Hf values (Figure 6.39). The Central and Southern arc segments plot as an array between MORB and more radiogenic compositions, which also includes JLSW-008A.

The correlation of isotopes and samples analysed on a spectrum of compositions close to MORB and DMM compositions towards more radiogenic $^{176}Hf/^{177}Hf$ and $^{143}Nd/^{144}Nd$ compositions is further shown on Figure 6.40. This also demonstrates that although southwestern Colombian samples fall on a trend away from MORB and DMM compositions, this is not consistent with a trend towards local basement such as the Cajamarca-Valvidia complex or Quebradagrande complex as sampled in this study (Figure 6.40). Additionally, the SW Colombian segments sampled here have a strong overlap (though some samples are slightly less radiogenic than) the Southern Volcanic Province of the Andes.

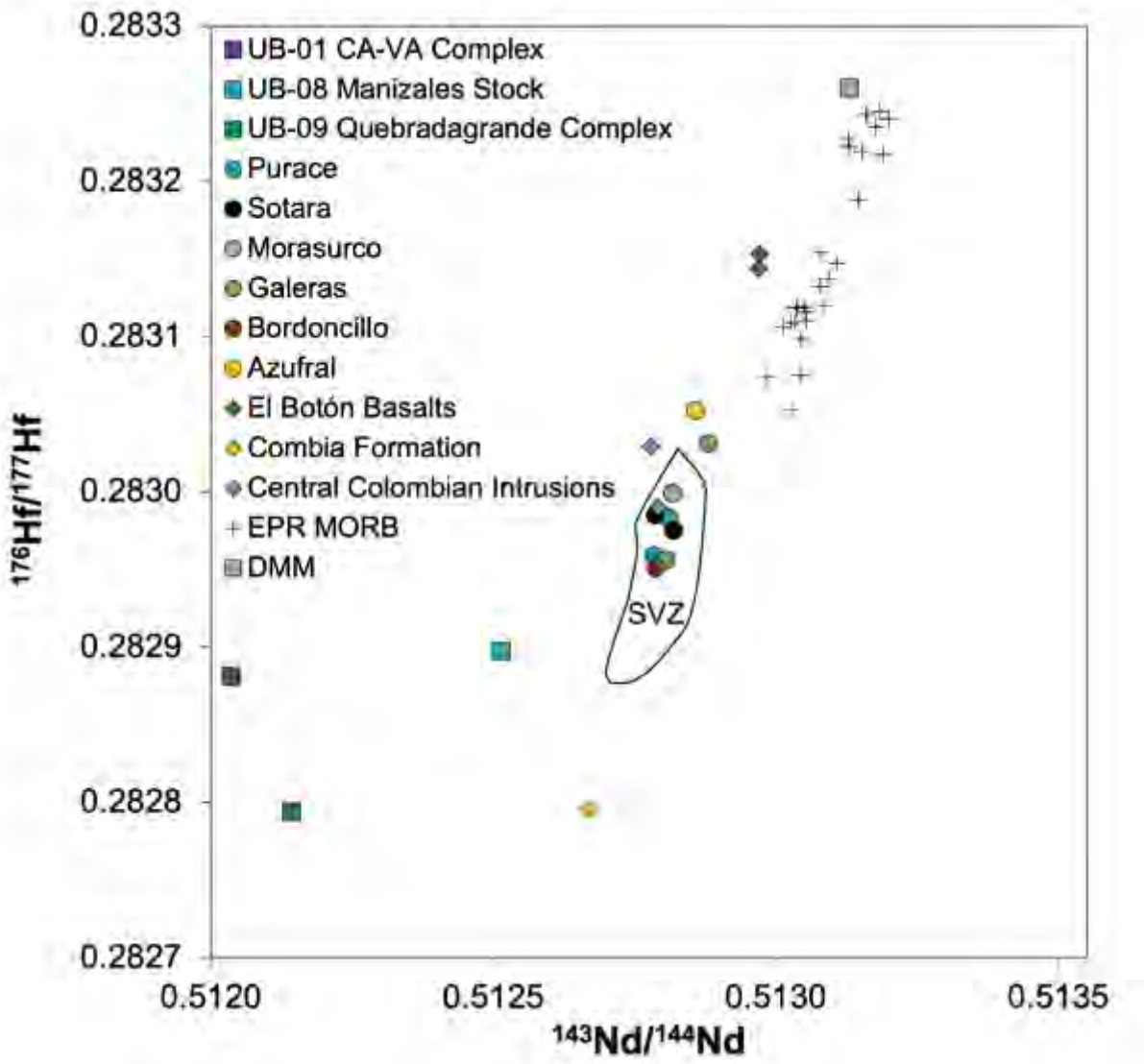

Figure 6.40: $^{176}Hf/^{177}Hf$ versus $^{143}Nd/^{144}Nd$ plot for Central and Southern Colombian edifices and Miocene arc remnants sampled in this study. Data for mid-ocean ridge basalts from the East Pacific Rise (EPR MORB) and average depleted MORB mantle (DMM) are also included (data from Gale et al. (2013) and Workman and Hart (2005) respectively) as well as a field for the Southern Volcanic Zone of the Andes (SVZ data from Jacques et al. (2013) and Hickey-Vargas et al. (2016)).

6.6.5 Ar/Ar geochronology:

As discussed in Chapter 5, a subset of four samples were selected and prepared for Ar/Ar geochronology, two from the Central Colombian arc, of Purace (PKSW-16B and SESW-106A) as well as two samples from the Central Colombian intrusions

(PKSW-098 and JLSW-008A). The purpose of these dates was twofold. Firstly, although there are radiometric dates for the lavas in Central Colombia related to the Popayan and Coconucos Formations, previous studies of Purace have repeatedly suggested that further geochronology is needed to better constrain the age and extent of these formations (e.g.: Lopez, 2009). Ar-Ar geochronology of PKSW-16B and SESW-106A would allow for a better understanding of the proximal and distal deposits of these formations and their relationship to Purace.

The significant geochemical differences between the two Central Colombian intrusions (PKSW-098 and JLSW-008A), imply that PKSW-098 has a distinct petrogenesis compared to JLSW-008A and the modern Central Colombian arc. Ar-Ar geochronology would help to verify whether there is also a matching age difference between these samples, and if the compositional similarity between JLSW-008A and the modern arc is due to a common petrogenesis. Previous work on Central Colombian intrusions has outlined that they are predominantly Miocene in age, but have a wide range of ages and compositions (Jerez, 2010; Gil-Rodriguez, 2014). Geochronology would help to place PKSW-098 within these intrusions. Additionally, as detailed in Chapter 5, step heated Ar-Ar geochronology would offer a distinct advantage over previous K/Ar geochronology performed in the area (Mattey, 1997).

However, though preparation of samples were prepared along with the four samples for the NVP in good time, and samples were sent for irradiation, analysis of the samples has not yet been performed due to continued delays at the analytical facility, the Scottish Universities Environmental Research Centre (SUERC) and the ongoing COVID-19 pandemic as previously discussed.

6.6.6 Outliers in the Dataset:

The main recurring outliers in the dataset are JLSW-32B, which is likely due to the replacement of much of the matrix of the rock with amorphous silica, though compositions of most trace elements and isotopic values. are still consistent with other analyses from the Central Colombian arc. The composition of La Guaca is also distinct from analyses of Galeras and other Colombian arc samples, especially in HREE depletion, which will be further investigated.

6.6.7 Summary:

Analyses of the Central and Southern Colombian arc rocks show similar trends (i.e: relative HFSE depletion and LILE enrichment compared to MORB) compared to other Andean arc segments. The Central Colombian arc, especially Purace does show some characteristics (e.g.: greater incompatible element enrichment and higher LREE) similar to those observed in the NVP, and distinct from other southwestern edifices. Modern Colombian arc segment analyses follow an array between depleted mantle compositions and more radiogenic compositions in isotopic space. Analyses of Miocene arc segments show greatly different trends, with El Boton basalts showing compositions closer to DMM and MORB than all other analyses, whilst the Combia Formation is far more radiogenic. Though only limited conclusions can be drawn from this Miocene data, distinct petrogenetic processes may have contributed to these rocks that did not play a role in the modern Colombian arc.

6.7 Petrogenesis and Development of the Colombian arc:

6.7.1 Overview and current understanding of SW Colombian magmatism:

Only a handful of studies have attempted to investigate the regional geochemistry of the Colombian arc as a whole (e.g.: Droux and Delaloye, 1996; Marin-Ceron et al. 2010). In this section geochemical observations from the Central and Southern Colombian arc segments are combined with previous discussion of the NVP to evaluate the primary chemical inputs to subduction across the whole arc. The subset of Miocene arc data collected and analysed here is also used to hypothesise on the development of the subduction system prior to modern arc magmatism.

Previous work on southwest Colombian magmatism has focused on the inputs from the crust (Droux and Delaloye, 1996) and the addition of variable fluid mobile components from the slab (Marin-Ceron et al. 2010). In their analyses, Droux and Delaloye (1996) identified Central Colombian arc rocks as having lavas with high TiO_2 and K_2O, high Ce/Yb ratios and LREE enrichment as well as low HREE content and low Ba/La ratios. In the Southern Colombian arc segment, the inverse was observed, with lower K_2O, TiO_2, Ce/Yb and less depleted REE and higher Ba/La ratios (Droux and Delaloye, 1996). These trends are interpreted to signify differences in crustal inputs and magmatic processes between the two regions. The elevated incompatible element concentrations in the Central Colombian arc were interpreted as due to assimilation of the siliceous metamorphic basement (Cajamarca-Valvidia terrane), whilst the Cretaceous basement beneath the Southern Colombian arc segment could not cause similar incompatible element enrichment. Further minor

compositional variation between the volcanoes was attributed to magma mixing and fractional crystallisation in shallow magma chambers (Droux and Delaloye, 1996). However, more recent models have proposed these geochemical differences between the southwestern Colombian arc segments are derived from varying proportions of slab derived components, namely **a**ltered **o**ceanic **c**rust (AOC), hemipelagic sediments (HS) and carbonate sediments (CS). These slab components combine with mantle wedge material to form a spectrum of primary compositions at the source of arc magmas within the wedge (Rodriguez-Vargas et al. 2005). To form the intermediate magmas observed in southwestern Colombia, it has been suggested that these magmas combine with a radiogenic Pb enriched end member, interpreted as the lower continental crust (LCC) (Marin-Ceron et al. 2010; 2018). This is reinforced by the strong similarity in isotopic compositions between lower continental crust and Colombian arc lavas (Rodriguez-Vargas et al. 2005; Figure 6.40). Within this model, the differences between arc segments first noted by Droux and Delaloye (1996) are attributed to differences in the depth of the slab beneath the arc segments, with the Southern Colombian arc segment representing shallower volcanic front compositions with primary arc magmas with higher Ba/Nb, lower $^{206}Pb/^{204}Pb$ and greater $^{176}Hf/^{177}Hf$, $^{143}Nd/^{144}Nd$ and $^{87}Sr/^{86}Sr$ compositions. A carbonate sediment (CS) component is frequently invoked to explain these isotopic and particularly Pb and Hf isotope compositions of some magmas, as addition of a less radiogenic carbonate sediment component would lower the Pb and Hf isotope values of primary lavas and their derivatives (Marin-Ceron et al. 2010; 2018).

6.7.2 Miocene arc remnants and their relationship to the modern arc:

It is clear from results presented here and from previous work (e.g.: Zapata and Rodriguez, 2012; Gil-Rodriguez, 2014; Toro et al. 2016; Leal-Mejia et al. 2018; Marin-Ceron et al. 2018; Jaramillo et al. 2019) that Miocene volcanic and plutonic rocks located to the west of the modern arc segments are products of subduction of the Nazca plate beneath Colombia. However, the clear geochemical and isotopic differences between these rocks and the modern Colombian arc segments demonstrates that additional petrogenetic processes may have been at play during the Miocene. These could include tectonic complexities and/or changes in the angle and obliquity of subduction between the Miocene and today (Wagner et al. 2017; Jaramillo et al. 2019). However, the small size and wide geographical spread of Miocene data obtained, limit exploration of these hypotheses. Miocene samples are contextualised as far as possible below.

6.7.3 Crustal influences on Colombian arc segments:

Previous work on the volcanoes of southwestern Colombia highlights a possible role for AFC in the petrogenesis of Galeras volcano (James and Murcia, 1984) and Purace (Droux and Delaloye, 1996). Regional studies initially suggested that the oceanic plate and mantle composition were consistent across southwestern Colombia (Pennington, 1981) and, therefore, any geochemical variation between volcanoes in the area was the consequence of interaction of magmas with the basement beneath the volcanoes (Lopez-Escobar et al. 1993; Droux and Delaloye, 1996). The volcanoes of the Central sector of the Colombian arc traverse the

allochthonous terranes of the Cajamarca-Valvidia terrane and the accreted mélange of the Romeral Terrane (Gomez et al. 2015; Marin-Ceron et al. 2018), whilst the Southern segment of the Colombian arc has accreted Romeral and Dagua terranes of the Western Tectonic Realm as basement, and volcanic edifices lie above faults which bound these terranes (Figure 6.4), and likely act as vectors for magmatism (Marin-Ceron et al. 2019). If assimilation of basement does indeed play a major role in the Central and Southern Colombian arc sectors, there should be a noticeable difference in geochemical difference between segments in line with this.

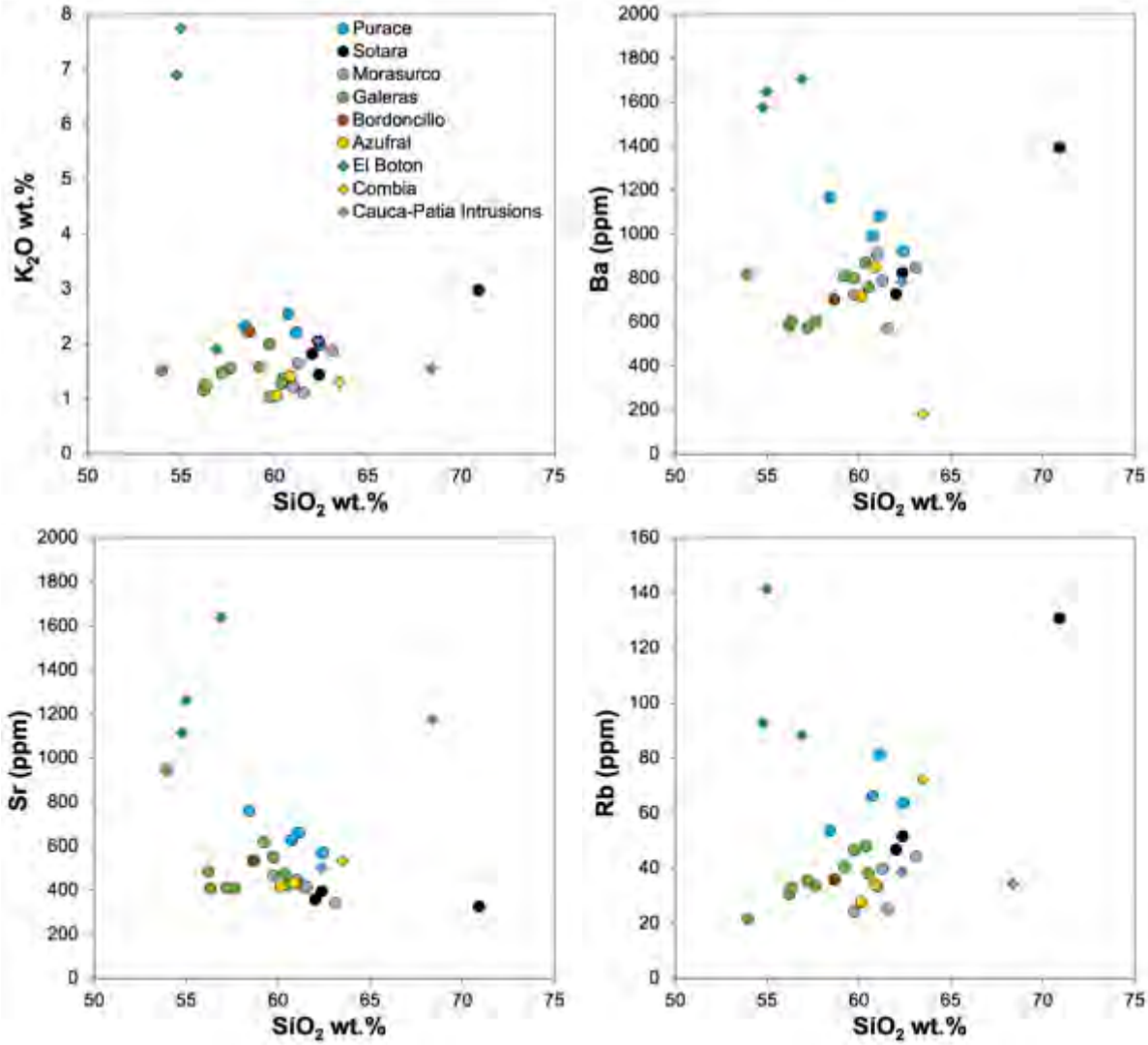

Figure 6.41: Data from select incompatible elements (Ba, Rb and Sr) for southwestern Colombia edfices, Miocene arc rocks and Northern Volcanic Province edifices. These show that Purace has comparable enrichments in these elements to the NVPG1 group outlined in Chapter 5.

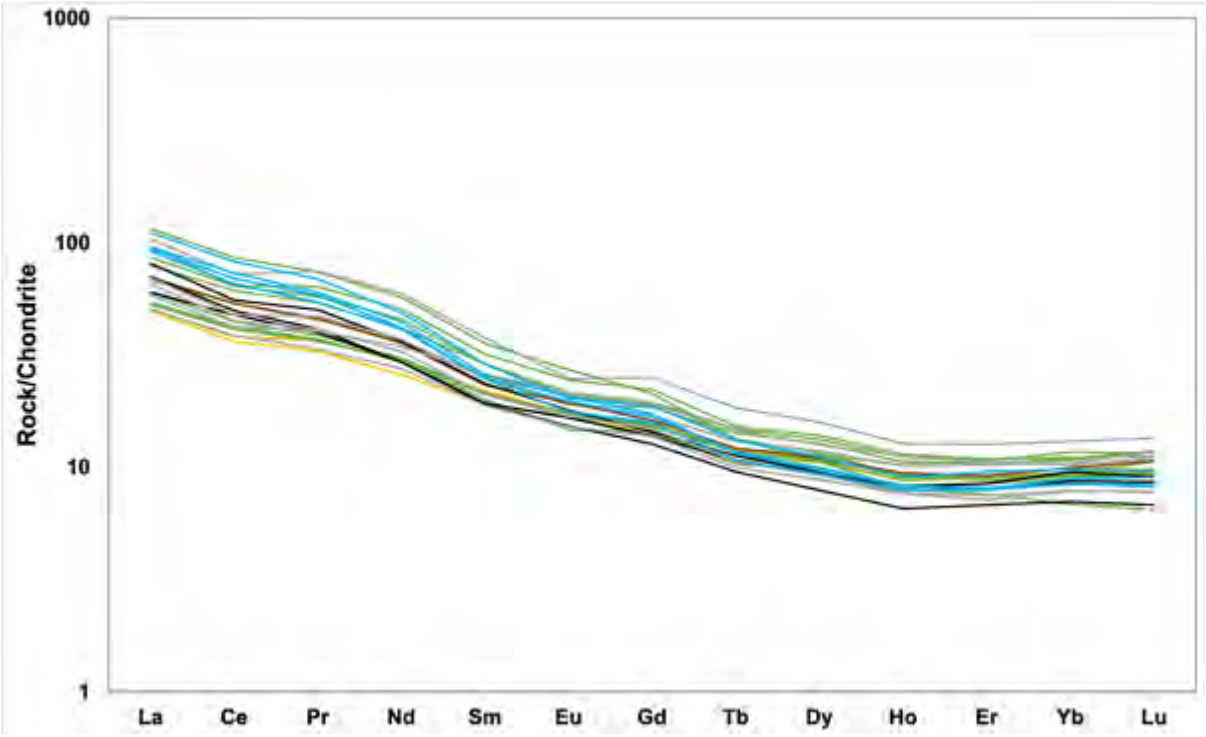

Figure 6.42: Combined REE plot of Central and Southern Colombian (excluding Miocene) analyses demonstrating enrichment in LREE for Purace compared to other groups but comparable LREE contents, with the exception of La Guaca, which has slightly depleted HREE contents.

K_2O is most elevated in Purace (Figure 6.20), though one Galeras (DC16-037) and Bordoncillo sample also show comparable elevations. The remainder of Central and Southern Colombian samples have lower K_2O values, following a typical medium-K calc-alkaline trend similar to that of the low-K_2O group outlined in Chapter 5. The only exception to this is Sotara sample JLSW-32B, which has anomalously high K_2O compared to the rest of Sotara, above even Purace – though the enrichments in this sample are likely the result of alteration and not considered further here. These trends are largely reflected in Ba, Rb and Sr and LREE contents (Figure 6.41 and 6.42), with Purace having the greatest enrichment in Ba, Rb and a high Sr trend

(Figure 6.41). Such enrichments are similar to the NVPG1 enriched group outlined in Chapter 5 and illustrate that some processes within the petrogenesis of Purace must be enriching it in incompatible elements.

The Miocene arc remnants show a range of K_2O and incompatible element compositions, which are most elevated in El Boton basalt samples (Figure 6.41). The Central Colombian intrusions differ significantly, with JLSW-008A having K_2O >2 wt.%, equivalent to Purace values, whilst PKSW-098 has a K_2O value of ~1.5 wt.%, similar to that of most of the Southern Colombian samples. The Combia Formation sample has comparable K_2O to the Southern Colombian arc samples, but similar, elevated Rb values to Purace samples. The Combia Formation sample and El Boton basalts have comparable values of Rb (and one sample of the El Boton (DB15-081) has Rb ~140 ppm) and Sr is most elevated in El Boton basalt samples (1113 – 1638 ppm) and PKSW-098 (1173 ppm) and JLSW-008A, though the latter is closest to elevated modern arc values (Figure 6.41). El Boton basalts and PKSW-098 are selectively enriched in these elements over other Miocene samples.

Incompatible element and LREE enrichments could reflect greater degrees of assimilation of an enriched crustal source beneath Purace compared to other volcanoes. Previous work had suggested this for volcanoes of the Central Colombian segment due assimilation of their underlying Cajamarca-Valvidia basement (Droux and Delaloye, 1996). However, the lack of similar enrichment at Sotara volcano, which lies on the same basement and is similar in composition to Southern Colombian arc analyses, argues against this hypothesis.

Rather, the process may be tied to fractionation and assimilation processes at different depths. Samples from the Central and Southern modern arc segments form an array on trace element diagrams of HREE and Y ratios (e.g.: Ce/Y, Sr/Y, La/Yb) (Figure 6.43). When plotted alongside data from the NVP, these ratios show that

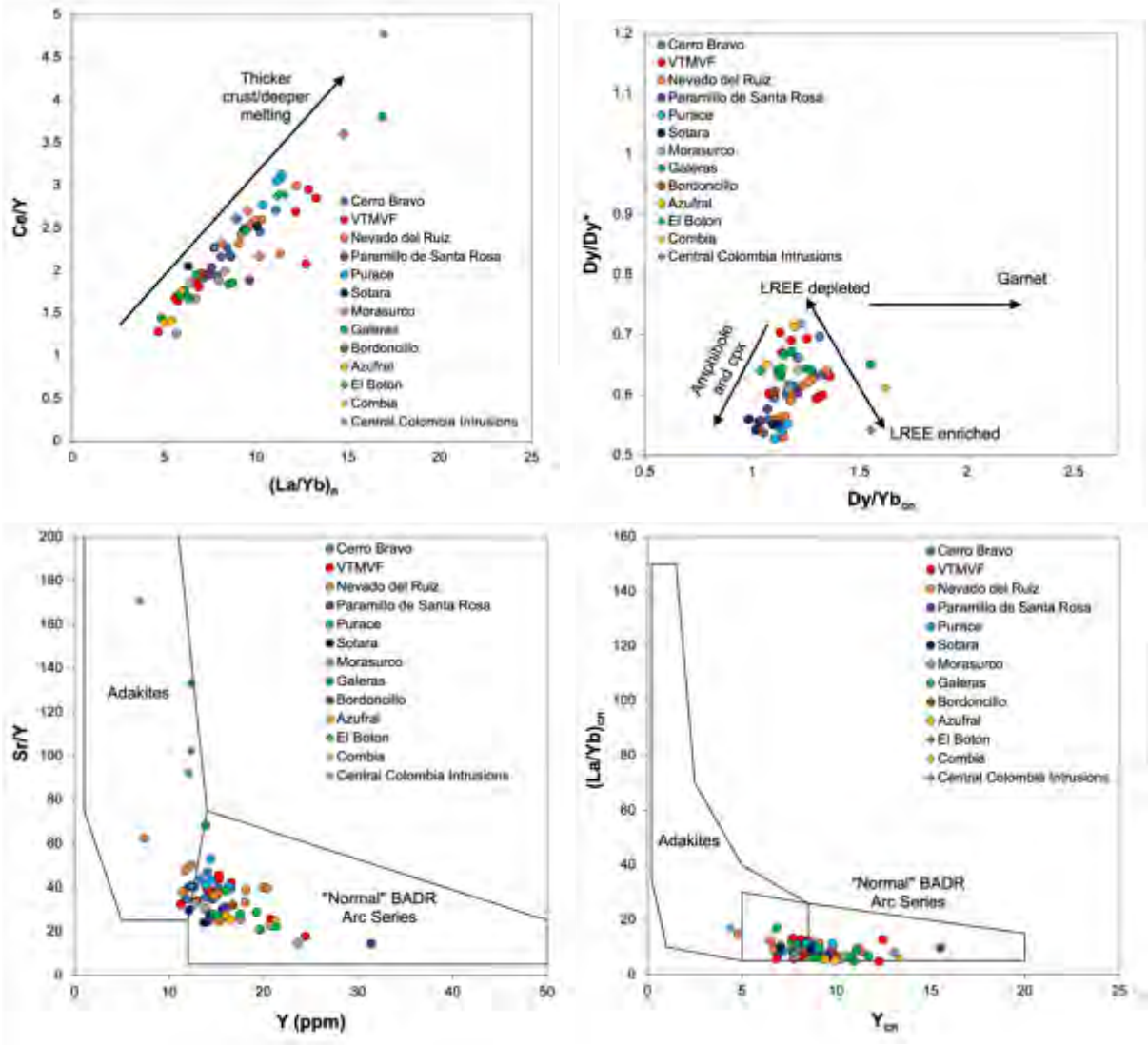

Figure 6.43: Trace element ratios used to segregate fractionating assemblages from different pressures (plagioclase, amphibole, garnet) and sometimes linked to crustal thickness, including Dy/Yb, Ce/Y, Sr/Y and $(La/Yb)_{cn}$. Chondrite normalization after Sun and McDonough (1989). Fields for normal arc and adakites from Hansen et al. (2002).

Purace commonly plots alongside the enriched NVPG1 samples (here shown by edifice, but consistently enriched in incompatibles and displaying high HREE and Y ratios), which reflects differences in the fractionating assemblage and may also

reflect a deeper source for the melts feeding some NVP edifices and Purace. The major exception to this is one sample from the Southern Colombia segment (Figure 6.43) from the La Guaca cinder cone of Galeras. Although this has a very mafic composition (53 wt.% SiO_2), it consistently plots with high values on HREE and Y trace element diagrams. This contrasts with primitive compositions of La Esperanza in the NVP, which plots at the lower end of these diagrams and has ferromagnesian contents similar to mantle derived melts. Therefore, La Guaca is best interpreted not as a primitive, mantle derived melt as La Esperanza is for the NVP, but rather as a melt which has undergone fractionation in the deepest parts of the Galeras plumbing system (where amphibole is stable) and little to no further fractionation in shallow parts of the system. This was likely facilitated by the crustal scale Silvia-Pijao fault which lies beneath La Guaca and likely facilitated rapid ascent of melt from a deep chamber (Figure 6.4).

This contrasts with the remainder of Southern Colombian arc samples, which plot at the lower end of HREE and Y ratio diagrams along with the low-K_2O NVPG2 samples of the NVP. This suggests a predominance of shallow level processes in the petrogenesis of southern Colombian arc lavas and NVPG2 lavas (Figure 6.43).

This could additionally be linked to the amount of assimilation of crust beneath these arc segments. Figure 6.46 shows K/Rb, used an index of assimilation against Rb (after Davidson et al. 1987) and $^{87}Sr/^{86}Sr$. These diagrams show that in principle, assimilation is a process affecting the majority of volcanic rocks analysed, but crucially, Purace (along with the NVP) show greater degrees of assimilation compared to edifices of the Central and Southern Colombian arc. However, the

restricted isotopic range displayed by Central and Southern Colombian modern arc samples (Figures 6.38, 6.39 and 6.40) suggests that the assimilation component was similar across the province, and therefore cannot be driven by the isotopically distinct shallow basement as suggested by Droux and Delaloye (1996), or Eocene plutonic rocks as implied in the NVP, as these are lacking elsewhere.

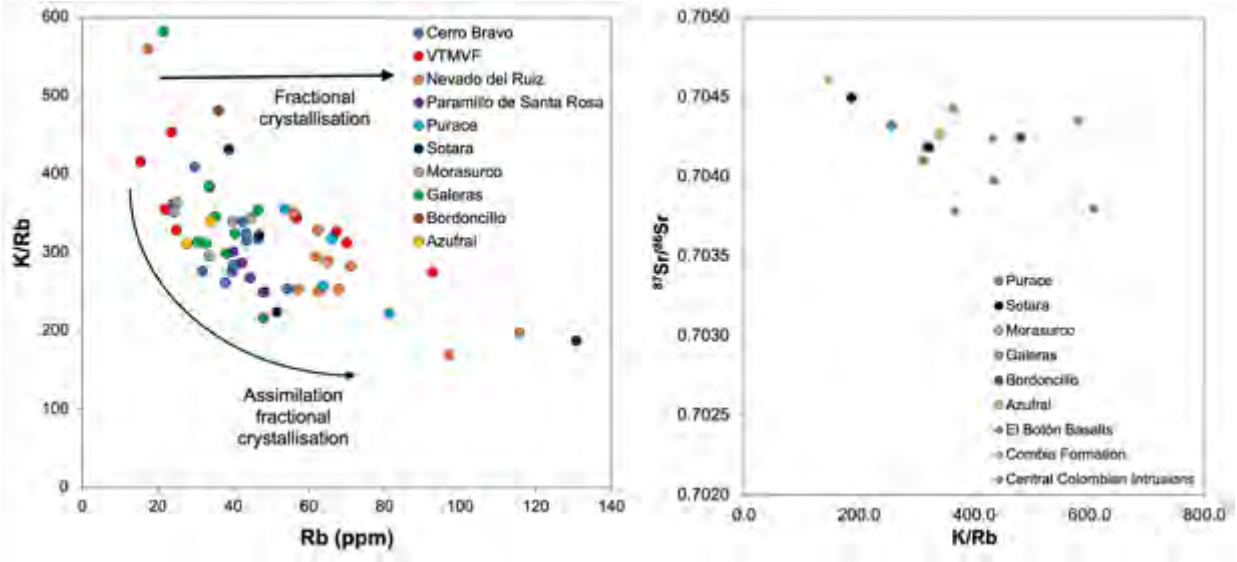

Figure 6.44: Plots, of K/Rb, used as an assimilation index, over Rb and radiogenic Sr (which shows only Southern Colombian and Miocene analyses).

The most likely candidate for variable assimilation whilst maintaining relatively narrow isotopic compositions is the lower continental crust, as sampled by the Mercaderes xenoliths (Weber et al. 2002; Rodriguez-Vargas et al. 2005), parts of which have a very similar isotopic composition to the whole Colombian arc.

6.7.3.1 Fractional crystallisation modelling:

Fractional crystallisation processes have also been shown to successfully reproduce many of the geochemical parameters (such as La/Yb and Sr/Y ratios, as shown in Figure 6.43) associated with adakites (e.g.: Macpherson et al. 2006; Richards and Kerrich, 2007; Moyen, 2009) and these can be successfully modelled in line with trace element and isotopic modelling produced in Chapter 5. In this case, the basaltic andesite from La Guaca cinder cone is utilised as a starting composition for the modelled fractional crystallisation trends (Figure 6.45). As previously, these simple fractional crystallisation trends are modelled using the equation:

$$C_l = C_0 F^{(D-1)}$$

Where C_l is the concentration in the liquid, C_0 is the initial concentration before fractional crystallisation, D is the bulk partition coefficient of the fractionating assemblage and F is the proportion of melt remaining. Trend FCd consists of a fractionating assemblage of plagioclase, clinopyroxene and magnetite in proportions 50:45:5. A second trend (FCe) is plotted with the same fractionating assemblage but with proportions 63:33:5. These two trends show that fractional crystallisation of a magma with such assemblages can successfully account for the compositions in the Central and Southern segments of the Colombian arc (Figure 6.45). Trend FCd offers a good fit for samples at the lower end of Mg# and silica compositions such as Bordoncillo and possibly Purace compositions could be accounted for with more plagioclase.

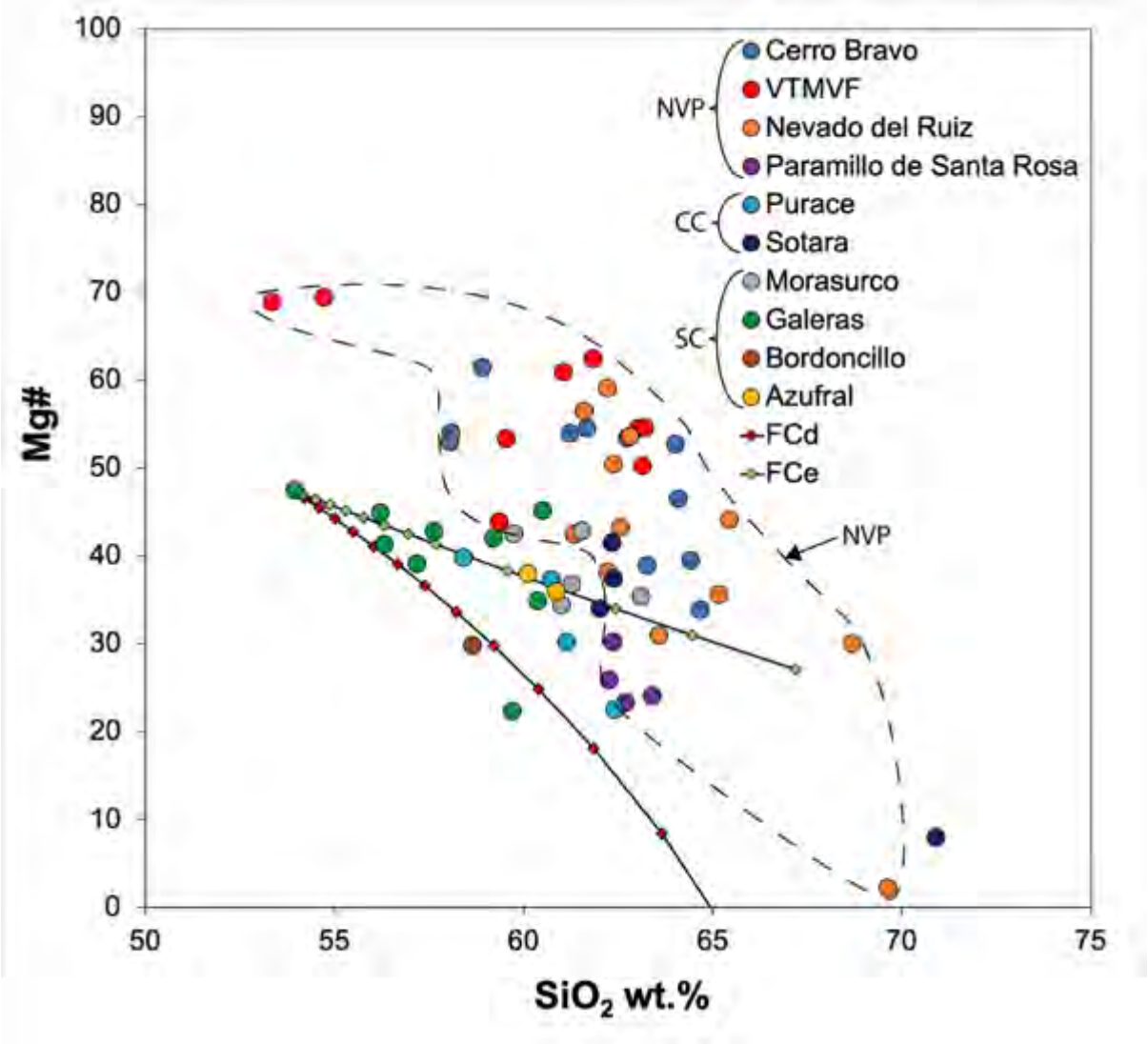

Figure 6.45: Mg# versus SiO2 showing modelled fractional crystallisation trends from La Guaca composition for the Central (CC) and Southern (SC) Colombian arc edifices. Northern Volcanic Province (NVP) edifice data is plotted for comparison along with an outline field.

This is reflected in trend FCe that, with a near equant plagioclase and clinopyroxene assemblage, successfully trends through the majority of Southern and Central Colombian analyses as a simple fractional crystallisation trend. Again, the exception to this is Purace, which is best modelled by the assimilation fractional crystallisation trends involving higher pressure assemblages shown in Chapter 5.

6.7.3.2: Influence of slab and mantle components:

Subduction zone volcanism is commonly related to the breakdown of minerals with components of the slab (subducting sediments and AOC) as they subduct, generating a water-rich flux that causes melting in the core of the mantle wedge. The nature of this interaction is debated in terms of both transport of the flux as well as whether this takes the form of an aqueous fluid, sediment melt or supercritical fluid (see Spandler and Pirard, 2013 for a review).

Assimilation and later fractionation processes within the crust may overprint slab and mantle derived signatures. However, at least some of the elevated K_2O and related incompatible element trends and enrichments will be the result of variations in slab inputs and proportion of mantle melting. Depth to the slab and the K-h relationship (Dickinson, 1975) may play a role, as we would expect aqueous fluid compositions (represented by K_2O and ratios such as Ba/La) to become less pronounced with increasing depth to the slab, as the transition from aqueous fluids to supercritical fluids or melts is made. Elements such as Th may be more mobile in supercritical fluids and melts (e.g.: Kessel et al. 2005). In the case of K_2O, enrichment in slab derived aqueous fluids is due to high solubility of K_2O in fluids at high pressure, to the extent that a few wt.% H_2O will entirely dissociate phengite within subducting components, and all K_2O will be dissolved in the mobile slab-derived phase (Kessel et al. 2005). Therefore, one possible explanation for enriched compositions of incompatible elements may be the addition of higher modal proportions or more enriched slab derived components by aqueous fluids.

Ba/La can be used as a proxy for transfer of elements by aqueous fluids from the slab, again due to their greater solubility in hydrous fluids (e.g.: Elliott, 2003; Goss et al. 2013; Holm et al. 2014). For all modern arc groups except Azufral, Ba/La is between 29 – 57 (Figure 6.46). Purace shows a decreasing trend with silica (not shown) in a mid to upper range of these values (41 – 51). Sotara values, other than JLSW-32B fall within the same general range as other sample groups. Galeras, with the exception of DC16-033 (Ba/La = 53), and Bordoncillo have Ba/La <48. In comparison, East Pacific Rise MORB has Ba/La values consistently <10, and all groups show the characteristic enrichment in Th of continental arcs affected by crustal contamination and/or enrichment by subduction components compared to MORB basalts (e.g.: Pearce, 1983, Figure 5.15). Other than a trend of decreasing with increasing silica for Purace and Morasurco, no trends correlating with silica can be found for other groups, possibly indicative that Ba/La is not being substantially affected by subsequent AFC processes. However, with the exception of Azufral, NVP analyses do generally occupy a higher Ba/La range than Southern and Central Colombian arc analyses (Figure 6.46), though the arc as a whole has a similar range of Ba/La values, indicating that although aqueous fluid input is similar across the arc, some of the incompatible element enrichment could be due to a larger slab fluid component into the NVP.

El Boton basalts have the highest Ba/La (>70) other than Central Colombian intrusion sample PKSW-098 (Ba/La = 128) for Miocene samples. JLSW-008A contrasts with Ba/La values similar to normal arc segments. Combia Formation sample has the lowest Ba/La (9). However, discussion and inclusion of Miocene

samples is restricted in this section as the nature and angle of the slab beneath the Colombian arc segments is debated (e.g.: Wagner et al. 2017).

Ba/La is plotted against Th/La in Figure 6.46, as a proxy of greater contribution of sediments (supplied by supercritical fluids or melts) or contaminants over aqueous fluid contributions. This illustrates that Galeras, Purace and a subset of NVP analyses, are enriched in Th/La, implying the possibility that the enrichments described above could be related to different subduction inputs (Marin-Ceron et al. 2010; Errazuriz-Henao et al. 2019). However, ratios such as Th/La may also be skewed by fractionation processes within the continental crust which would fractionate Th and La as well as crystallisation of accessory phases in silicic magmas (Plank, 2005). Therefore, Th ratio diagrams used here exclude samples with >63 wt.% SiO_2.

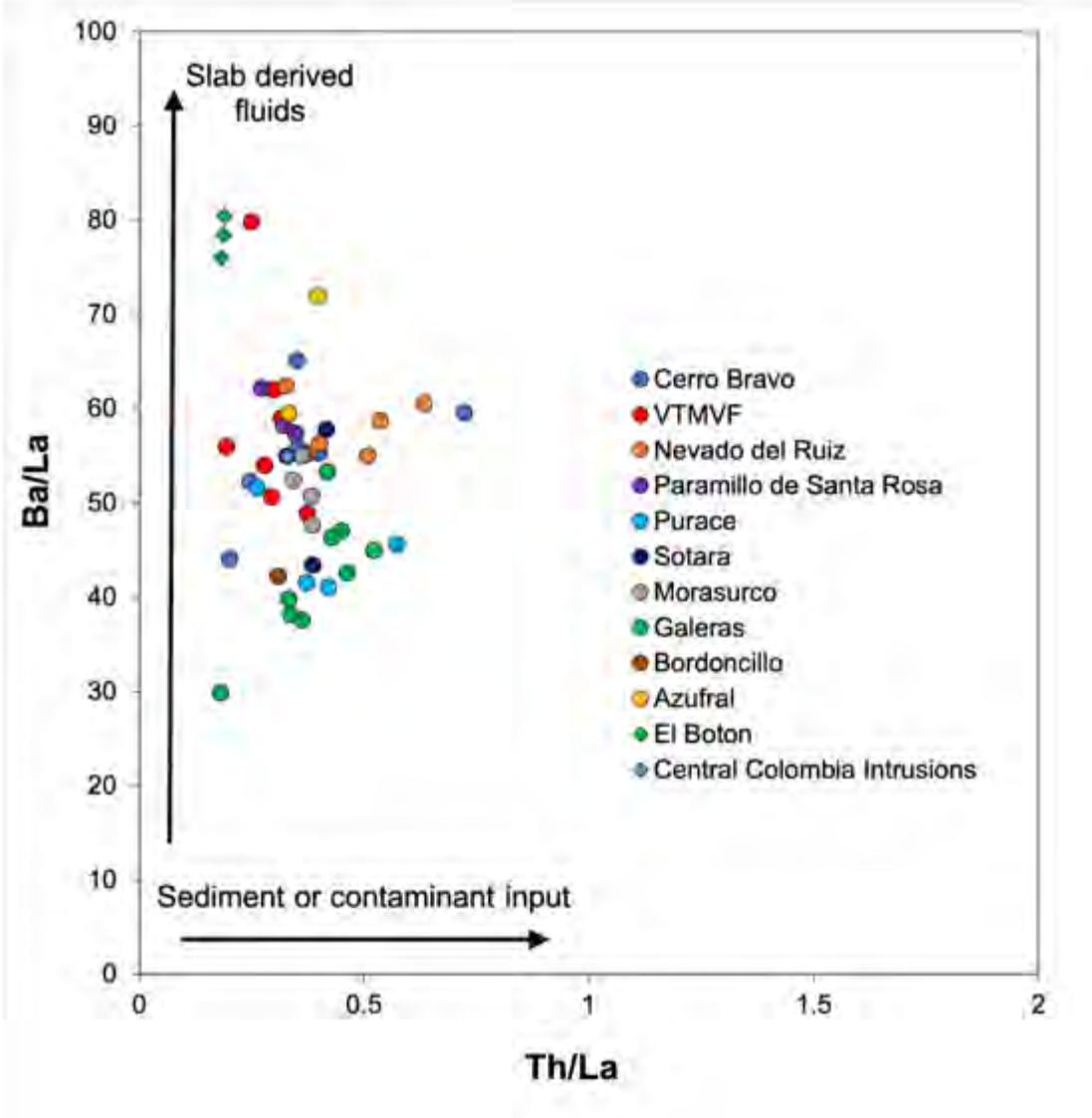

Figure 6.46: Ba/La versus Th/La for data from all Colombian modern arc edifices sampled and Miocene data. Note the offset of Purace, Sotara and the NVPG1 samples to right of diagram, due to greater addition of sediment or contamination. Samples with >63 wt.% SiO_2 have been excluded.

To further investigate whether Ba/La is an accurate proxy of slab fluids and is not affected by later assimilation of local basement, Ba/La is plotted against $^{143}Nd/^{144}Nd$ (Figure 6.47). This shows that modern Colombian arc data for all edifices form a cluster but no clear trend towards any local basement other than a minor trend of NVP data towards Eocene plutonic basement (furthering arguments for some

assimilation of this material made in Chapter 5). Rather, Colombian arc analyses overall form a trend perpendicular to any trend between MORB and other local basement (e.g.: Cajamarca-Valvidia and Quebradagrande complexes) and more consistent with a mix between subducting sediments and lower continental crust, as represented by the lower crustal xenoliths in Figure 6.47. Ba/La is therefore interpreted here as representing a reliable proxy of slab fluids for the Colombian arc. Additionally, we can examine relation of such ratios to slab depth, not affected by assimilation or fractionation processes. Figure 6.48 shows plots of Ba/La and Th/La against slab depth. There is a weak correlation between decreasing Ba/La and increasing Th/La, as we would expect if aqueous fluid input was being superseded by supercritical fluids and/or melts at greater depths. This is not, however, consistent across the arc, especially in the case of Th/La, with Nevado del Ruiz showing highly elevated ratios compared to edifices with a much deeper source, and no consistent increase in Th/La down slab overall. Therefore, although Ba/La does appear to have a relationship to slab depth as expected, Th/La must be partly controlled by at least one other process, such as the presence of accessory phases in the subducting sediments which fractionate Th and La.

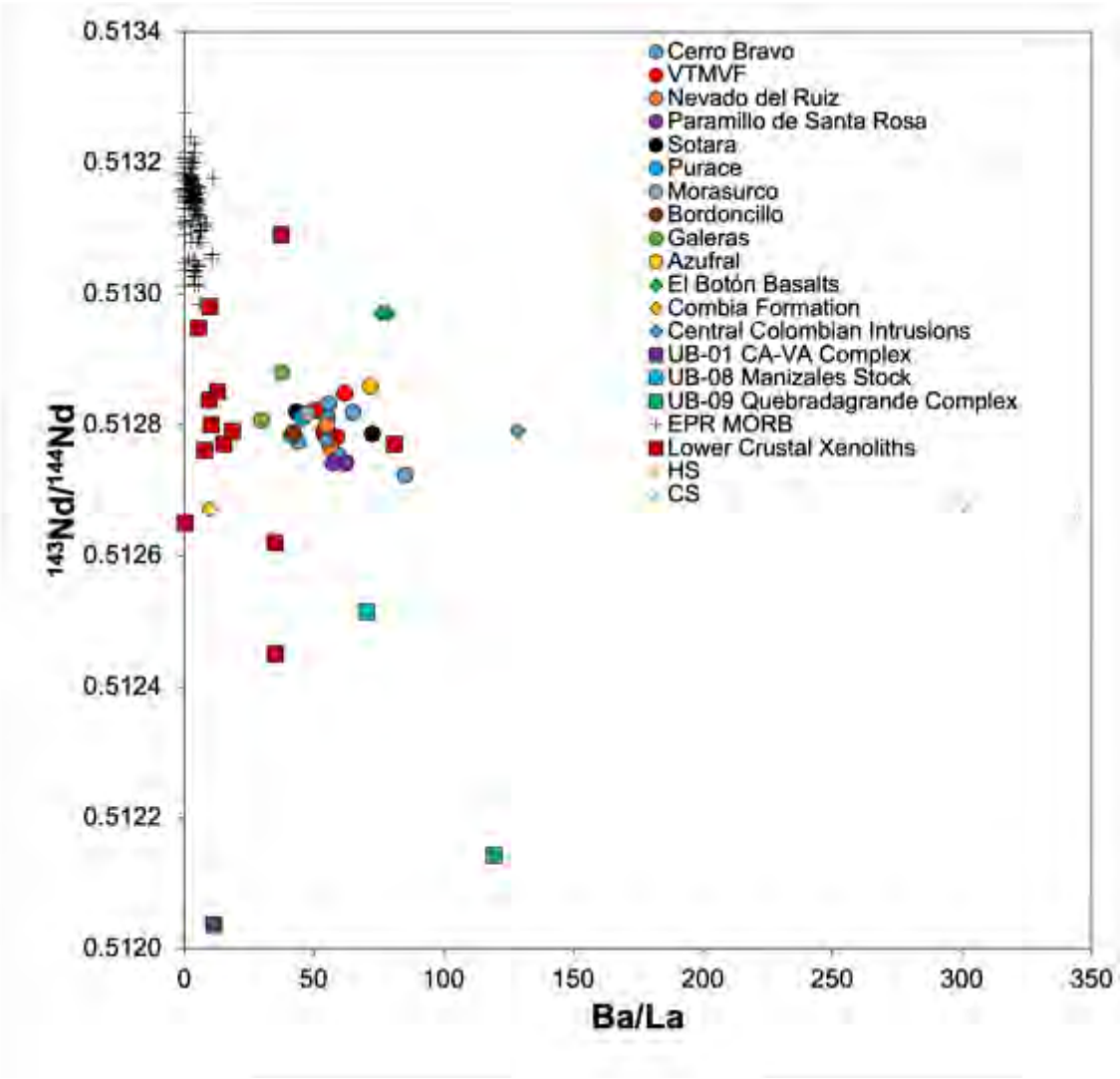

Figure 6.47: $^{143}Nd/^{144}Nd$ versus Ba/La plot for all Colombian modern arc edifices and Miocene data. Also included for comparison are analyses of regional basement in this study. East Pacific Rise MORB values are from Gale et al. (2013), lower crustal xenolith data from Weber et al. (2002) and Rodriguez-Vargas et al. (2005) and averages for subducting hemipelagic sediments (HS) and carbonate sediments (CS) are taken from Errazuriz-Henao et al. (2019).

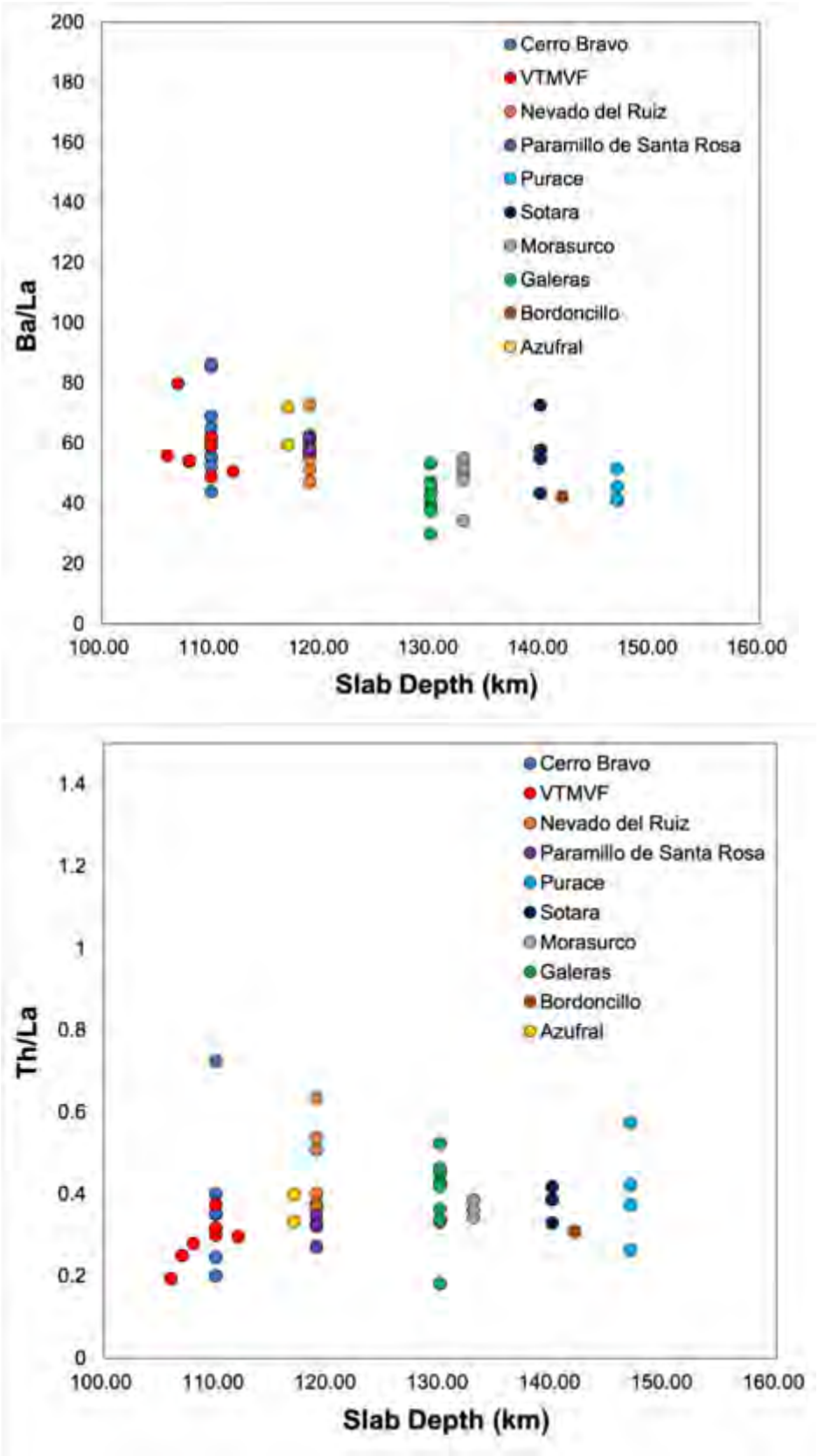

Figure 6.48: Plots of Ba/La and Th/La against slab depth (as calculated using Slab2 model after Hayes et al. 2018), indicating some correlations between slab and element enrichments and depletions in the arc. Samples with >63 wt.% SiO2 have been excluded from the Th/La plot.

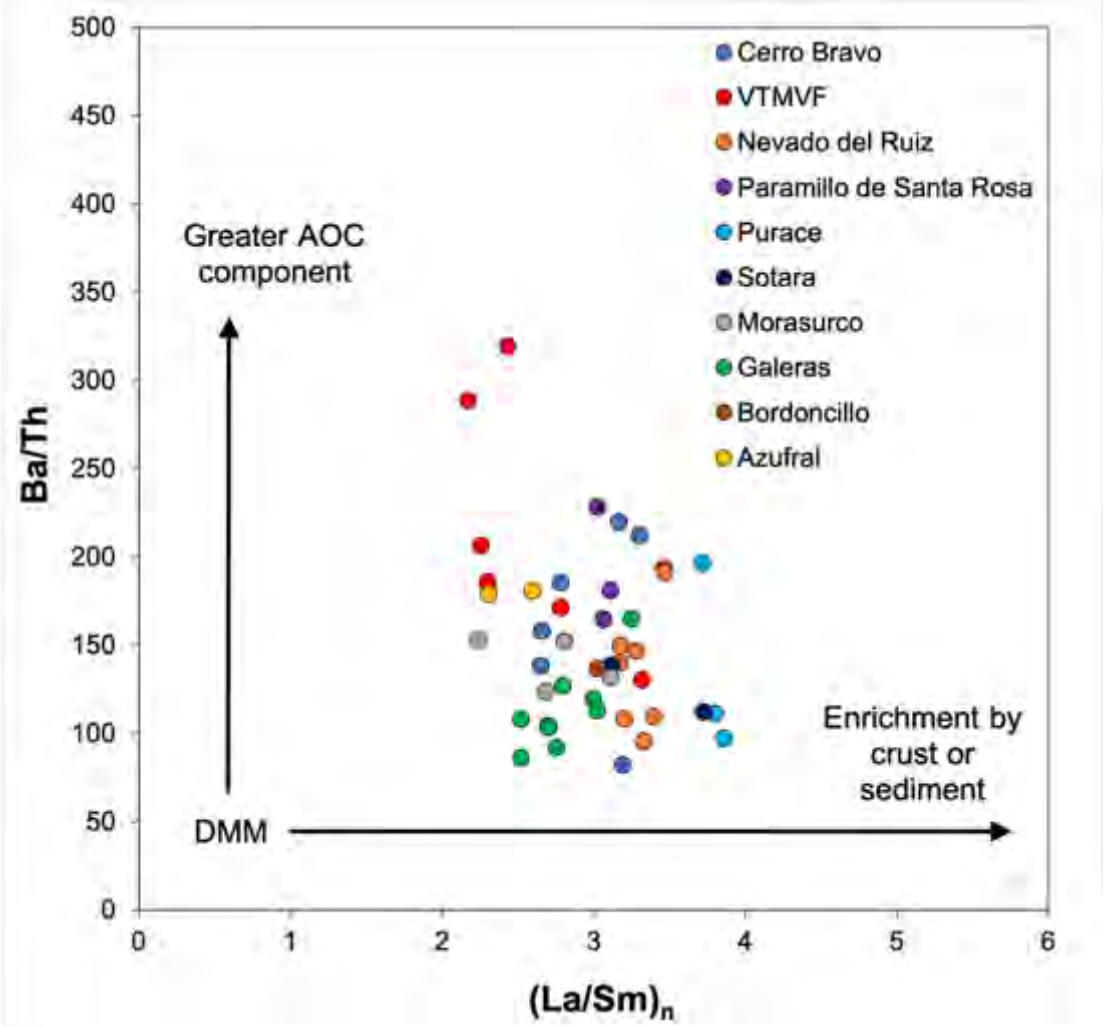

Figure 6.49: Plot of Ba/Th, used as a proxy for fluid from the altered oceanic crust, versus enrichment (after Elliott, 2003). Note the relatively enrichment in La/Sm in Purace and NVP samples compared to the rest of the arc, and slightly lower Ba/Th. Normalisation after Sun and McDonough (1989). Samples with >63 wt.% SiO2 have been excluded.

We can also examine more conservative elements such as Sm, which is less fluid mobile than the LILE and LREE (Holm et al. 2016), and therefore a good tool for examining evaluating fluid-borne enrichments from the slab (e.g.: Ba). Sm is also less enriched in crustal rocks compared to incompatible REEs and Th. Also, reductions in Ba/Th would be suggestive of a smaller aqueous component entering the mantle (Holm et al. 2016). However, these trace element ratios can also be affected by fractionation during mantle melting.

In the case of the Colombian arc, samples from the NVPG2 generally have greater Ba/Th compared to the Central and Southern Colombian arc edifices, whilst NVPG1 and Purace has higher $(La/Sm)_n$ at lower Ba/Th (Figure 6.49). This could indicate the predominance of a flux from subducted sediment compared to that from altered oceanic crust (AOC) for NVPG1 and Purace compared to the rest of the Colombian arc. However, the relatively modest Ba/Th elevations overall do indicate that AOC is the lesser component in slab flux overall, and the elevated (La/Sm)n ratios indicate that the source of Colombian arc magmas is primarily a mixture of the depleted MORB mantle (DMM) of the mantle wedge mixed with a slab flux derived from subducting sediments. The potential effects of amphibole fractionation, which would increase (La/Sm)n also need to be accounted for.

Although there is clear role for a slab flux, the sediments adding to this slab flux have not yet been further constrained. Colombian trench sediments consist of hemipelagic and carbonate sediment components (Marin-Ceron et al. 2010; Errazuriz-Henao et al. 2019). For altered arc rocks which may have experience subtropical weathering, a Th/La – $(Ce/Ce^*)_{Nd}$ plot (Figure 6.50) can be utilised to identify the sediment components involved (Hastie et al. 2009; 2013), including volcanic and continental detritus and slow sedimentation rate clays (SSC). SSC's can be divided into two categories based on the Ce anomalies of their components. Hydrogenous Fe-Mn rich oxides in SSC sediments (SCC-HD) have positive Ce anomalies ($(Ce/Ce^*)_{Nd} > 1$) due to their preferential removal of Ce^{4+} from the water column (Elderfield and Greaves, 1982). This in turn depletes seawater in Ce^{4+} leading to negative Ce anomalies ($(Ce/Ce^*)_{Nd} < 1$) which are inherited by other SSC sediments such as fish debris and hydrothermal sediments, or SSC-FH (Hastie et al. 2013).

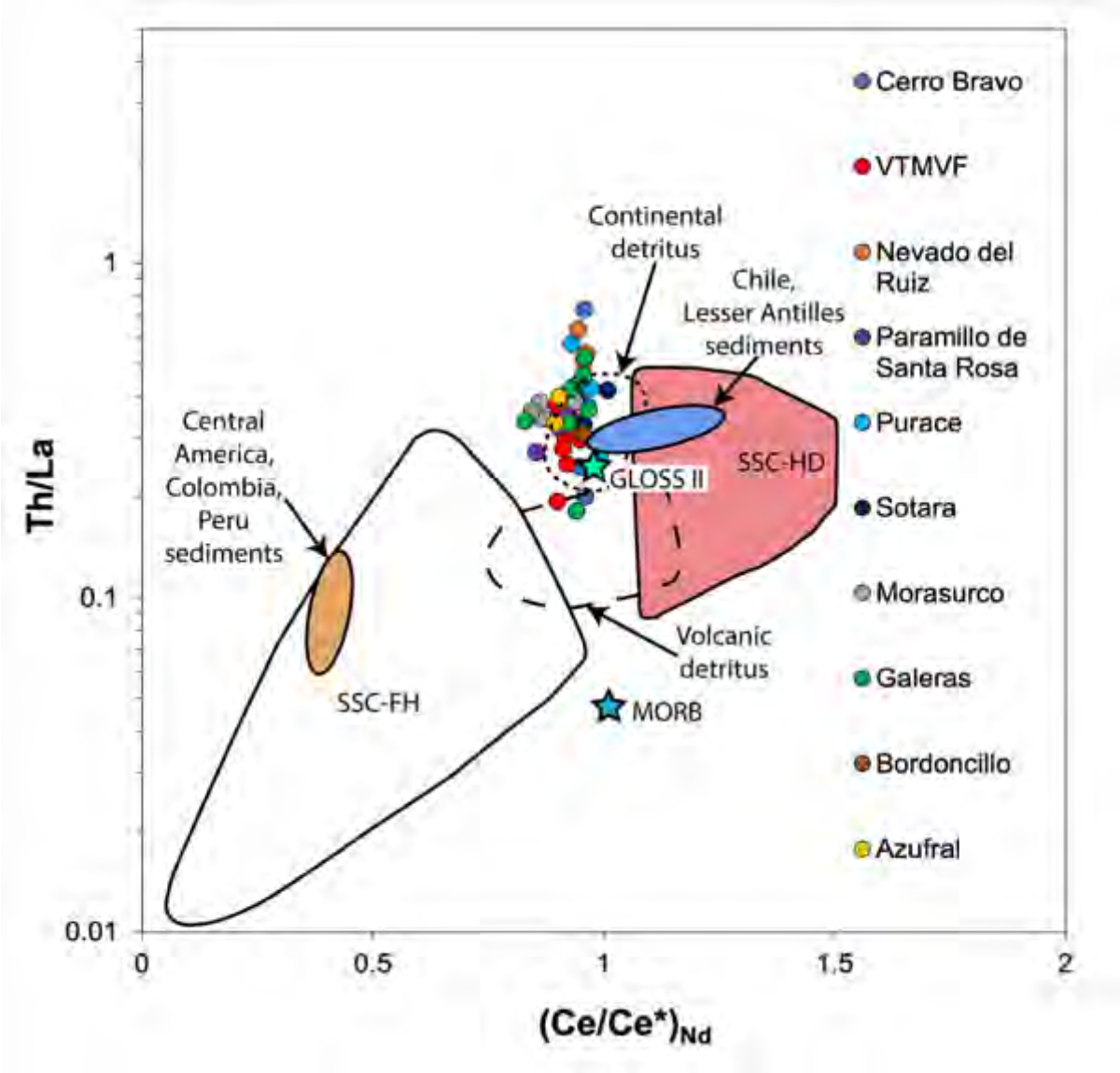

Figure 6.50: Th/La – $(Ce/Ce^*)_{Nd}$ plot to illustrate fractionation of Th and La and Ce anomaly in Colombian lavas. Fields adapted after Hastie et al. (2013) and references therein. GLOSS II value from Plank (2014). Samples with >63 wt.% SiO2 have been excluded.

Modern Colombian arc samples show a slightly negative Ce anomalies at high Th/La values. Samples also plot as a near vertical array in a Th/La – $(Ce/Ce^*)_{Nd}$ space (Figure 6.50). This would be consistent with mixing between a high Th/La source and a MORB-like source.

Accessory minerals (especially apatite and zircon) acts as controls on the budget and fractionation of Th and LREE during fractionation processes (e.g.: Sawka and Chappell, 1988). These two accessory phases are most common in the lower continental crust (e.g.: Wendlandt et al. 1993), with apatite being the more abundant accessory phase and the one which favours La over Th (Rudnick and Presper, 1990; Bea et al. 1994; Plank, 2005), leading to partitioning of La and Th in the presence of apatite. Other common residual phases (e.g.: pyroxene, plagioclase, amphibole and garnet) will also partition Th over La, which will accentuate this effect in the lower crust (Plank, 2005). There is strong evidence of the presence of amphibole and clinopyroxene in the source of Colombian arc magmas as shown by the Dy/Dy* diagram in Figure 6.43. Furthermore, fractional crystallisation modelling (Figure 6.47) also implies a predominant role for plagioclase and clinopyroxene in the petrogenesis of Colombian arc rocks. Therefore, mantle derived mafic magmas could enter the lower crust and begin to crystallise, leaving low-Th/La residues and producing magmas with slightly elevated Th/La (Plank, 2005). Further crystal fractionation in the crust may increase the Th/La of these resultant magmas. This would be consistent with processing and fractionation of magmas beginning in a lower crustal setting as proposed here.

Alternatively, the small number of volcanic arcs with high Th/La values similar to those observed in some Colombian arc are also those where either apatite rich sediments or carbonate sediments are subducting (Plank, 2005). The majority of trench sediments globally have bulk compositions with <3.5 wt.% CaO and <10% calcium carbonate (Plank, 2005). This contrasts with Colombian trench sediments also have much higher CaO and calcium carbonate contents in both their

hemipelagic (~33% $CaCO_3$ and 11.6 wt.% CaO) and carbonate (~80% $CaCO_3$ and 38.7 wt.% CaO) components. As such, Ca-rich sediment accessory phases, such as apatite and allanite would increase the Th/La ratio (Plank, 2005). However, if elevated Th/La compositions at the Colombian arc are produced by slab flux from apatite rich sediments, we would also expect those sediments to be enriched in P_2O_5 by an order of magnitude compared to global averages, but this is not the case for subducting hemipelagic or carbonate sediments at the Colombian trench, which have P_2O_5 of 0.13 – 0.15 wt.% (Errazuriz-Henao et al. 2019). Instead, Th/La enrichment could also be driven by subduction of carbonate rich sediments (Plank, 2005), which would also explain the negative Ce anomalies and trend towards Colombian sediment values and SSC-FH field shown by the Colombian arc in Figure 6.50.

6.7.3.3: Conclusions:

In summary, the geochemistry of the Central and Southern segments of the modern Colombian can be explained in large part by variable fractionation processes and limited assimilation fractional crystallisation processes, especially in the lower crust. Geochemical variability between the arc segments and individual edifices (for example Purace and Sotara) can largely be attributed to fractionation and the extent of this assimilation, both of which are related to the residence time of magmas within the crustal system and where within that system (i.e.: lower, middle or upper crust) that residence time was longest. Crustal thickness could be a predominant factor here, as the evolved, high-K2O compositions of Purace are most similar to those of the NVP, and geophysical data suggests that the crust is thickest beneath Purace and the NVP (Poveda et al. 2015) compared to Southern Colombia. However, the

presence of primitive magmas sampled across the arc, such as La Guaca and La Esperanza, also suggests that crustal scale faults may selectively “tap” magma chambers, allowing less evolved compositions to the surface whilst other magmas experience a significantly longer journey through a complex plumbing system. These magmas undergo the greatest degrees of fractionation and assimilation, and their geochemistry reflects this. Variations in the type and nature (fluid or melt) of subduction input also play a role in the geochemical trends observed, but this cannot be consistently explained by a simple slab depth/melt relationship within this dataset or unpicked from later crustal derived signatures. Additionally, if a slab melt component was involved, we would expect to see adakites (sensu stricto) which are not observed, meaning the slab flux across the Colombian arc was most likely delivered by an aqueous fluid. In short, the variable enrichment of incompatible elements between edifices was delivered by variable slab-fluxes composed of pelagic and carbonate dominated sediments and enhanced in some cases by later assimilation and fractionation within the crust.

Analyses of Miocene samples in this study are perhaps too disparate to draw firm conclusions. However, some preliminary conclusions can be drawn regarding each suite. JLSW-008A does share common features with Sotara volcanics sampled, suggesting a common petrogenesis or at least petrogenesis in a similar, preceding system. In contrast, PKSW-098 differs isotopically from other samples and shows significant enrichment in incompatible elements, HREE and Y as well as MORB like (e.g.: ~0.704 $^{87}Sr/^{86}Sr$) compositions, perhaps pointing to an origin by deep partial melting. The El Boton basalts show large enrichments across incompatible elements, perhaps as a result of being small degree melts, as suggested by Jaramillo et al.

(2019) whilst the signatures displayed by the Combia Formation sample broadly imply a greater degree of assimilation and fractional crystallisation, reflected particularly by radiogenic isotope composition.

7 Conclusions and avenues for further work:

7.1 Conclusions:

This study uses a detailed examination of the Northern Volcanic Province (NVP) alongside a broader study of the Colombian arc to assess the role of crustal, and to a lesser extent, slab inputs on the character of magmatism in the Colombian arc. Both the NVP and the rest of the Colombian arc have a broadly similar and narrow range of isotopic compositions which are closer to DMM and MORB values than other parts of the Andes where a large role for crustal assimilation has been suggested (e.g.: Hildreth and Moorbath, 1988; Feeley and Davidson, 1994; Mamani et al. 2010). This had led to the hypothesis that Colombian arc rocks have undergone relatively little assimilation of crustal material (Vatin-Perignon et al. 1990), leading to the development of slab derived melt models to explain enriched compositions (e.g.: Errazuriz-Henao et al. 2019). Here we have shown through modelling that modern Colombian arc compositions can be successfully modelled by a limited amount of assimilation fractional crystallization (AFC), especially in the NVP where this process is enabled by well-developed magmatic plumbing systems under some edifices and supported by a greater prevalence of intermediate and evolved erupted magma compositions. This, alongside assimilation of enriched plutonic material in mid- to upper-crustal magma chambers (<10 km), is a viable mechanism for generating enriched the intermediate magma compositions observed.

Indeed, varying degrees of AFC appear to be the dominant process across the whole Colombian arc, even where evidence of assimilation of enriched material is less pronounced. The common feature across the whole arc could be magma storage

within the lower crust where amphibole and clinopyroxene fractionation, and a limited degree of wallrock assimilation, predominates. Therefore, all Colombian arc magmas analysed are part of a spectrum of compositions which have undergone varying degrees of lower crustal storage and fractional crystallisation, and in some cases further assimilation of upper crustal material (as in the case of NVP rocks which have assimilated enriched Eocene basement). At the extreme end of these compositions lies Cerro Machin which is the most evolved and radiogenic of the Colombia arc volcanoes. Such chemistry could be indicative of highest degrees of crustal assimilation and fractionation. The particular depleted HREE and Y contents of Cerro Machin also imply that these processes took place at the greatest depths observed in the arc, in the presence of amphibole and possibly garnet. The majority of melts from across the Colombian arc are likely derived from a fairly homogenous depleted mantle derived melts which ascend and stall in the lower crust, where clinopyroxene + amphibole saturate and begin to crystallise. This would be a viable process for generating the andesite compositions observed across the whole arc. Length of storage may also play a role, as less prolonged storage of magmas within plumbing systems would lead to less AFC. Our models indicate this is a reasonable suggestion for less enriched and evolved compositions in the NVP such as the early magmas of Paramillo de Santa Rosa. This short residence is facilitated by numerous crustal scale faults which provide pathways for rapid ascent. This is mirrored in the Central and Southern segments, where geochemical variability between arc segments and volcanoes can be best attributed to differing degrees of fractionation and residence time in the crust.

Assessment of so called “adakites” and high-Mg# andesites in the Colombian arc points to misapplication of the former term in this case, with adakites (sensu stricto) absent from the Colombian arc and no evidence of slab melt processes from the arc found in this study. Elevated ratios of adakite parameters (e.g.: Sr/Y, La/Yb, Dy/Yb) as well as isotopic evidence instead point to a role for AFC in the petrogenesis of these rocks in areas of the crust where amphibole and clinopyroxene are stable. HREE and Y depletions are viewed mainly as a function of amphibole control here but may also be the result of small amounts of garnet in the deepest parts of the plumbing system beneath the Colombian arc, beneath Cerro Machin for example. Assimilation of components enriched in trace elements such as the Eocene plutonic bodies situated beneath the NVP has also driven the composition of these unusual rocks.

Some aspects of the arc lava geochemistry observed, especially incompatible trace element enrichment, are derived from components of the subducting slab. It is obvious from isotopic and trace element data that the arc lavas are derived from a fluxed, mantle source, but the input from Colombian subducting sediment components varies across the arc. Geophysical studies of shear wave splitting (SKS) show a change in splitting pattern at ~2.8°N, between the Central and Southern Colombian arcs segments, interpreted as a shallowing in the dip of the slab south of this latitude (Idarraga-Garcia et al. 2016), attributed to subduction of the buoyant Carnegie Ridge shallowing the slab further south beneath Ecuador (Bourdon et al. 2003). This is in contradiction of slab depth data based on the Slab2 modelling of Hayes et al. (2018) presented here, however such shallowing would place the slab at lower pressure, lowering the slab thermal parameter beneath the Southern

Colombian arc segment. This could partially account for the lower ratios of slab derived components (e.g.: Ba/Th and Ba/La) due to breakdown of fewer hydrous minerals within slab sediments at these lower pressures (e.g.: Tatsumi and Eggins, 1995). The exception to this is Azufral, projected to be the Southern Colombian edifice with the shortest mantle melting column, but with the highest Ba/Th and Ba/La ratios of Southern Colombian edifices (Figures 6.45 and 6.47). This discrepancy could be due to a local influence beneath the volcano, such as a crustal scale fracture in the upper plate (i.e.: the Cauca-Patia fault) providing a vector subduction derived fluids, or a fracture zone or ridge on the subducting plate beneath the volcano, which has been suggested based on subduction of the Malpelo Ridge beneath this area (Idarraga-Garcia et al. 2016). However, given Azufral is represented by only two data points, further speculation on the influences on this by factors such as ridge subduction or subduction angle which may influence slab thermal parameter beneath the volcano are not possible here. The view taken here overall, based on incompatible element enrichments and Ba ratios is that aqueous fluids play a primary role in delivering the chemical components from the subducting slab to the source of arc magmas beneath the Colombian arc. This contrasts with the view taken by other recent studies which have invoked sediment melts of carbonate and hemipelagic sediment as the primary mechanism for delivering slab components through the mantle wedge (Errazuriz-Henao et al. 2019). This is due to the lack of evidence for high degrees of slab melting (i.e.: lack of adakites sensu stricto), but primarily the evidence of fractionation of Th, LREE and of isotopic systematics by processes within the crust rather than at the slab or within the mantle, as shown above. Rather, either supercritical fluids or low degree melts of subducting sediments at greater slab depths may play a role in liberating larger amounts of Th and

conservative elements from the slab, though which of these two processes is dominant is not clear, but the starting material for almost all Colombian lavas is a variable amount of slab-derived aqueous fluid which ultimately leads to partial melting of the mantle wedge. Differentiating whether more conservative trace element components such as Th were delivered by a supercritical fluid or a low degree slab melt is beyond the scope of this study with the data available. Slab derived enrichments in these more conservative elements are secondary to those imparted by later fractionation and assimilation within the crust.

Unfortunately, the Miocene dataset presented here is too limited to draw firm conclusions from, and a possible future study could focus on assembling a larger dataset of major, trace and isotopic data for Miocene to recent volcanism to better assess the above processes over time. Recent efforts by the Servicio Geologico Colombiano (SGC) to systematically map, sample and geochemically analyse the modern edifices of the Colombian arc, along with and the upcoming MUSICA (Modeling, Uplift, Seismology, and Igneous geochemistry in the Colombian Andes) project, which aims to recover a larger sample set of Miocene arc remnant data in the coming years, may help in this regard. Overall, this study improves our understanding of Colombian arc petrogenesis and processes such as magma mixing and assimilation which may act as eruption triggers and will therefore hopefully feed into the wider assessment of the hazards posed by the volcanic centres of the arc being conducted by the Servicio Geologico Colombiano (SGC). Additionally, further research on the link between reported adakite signatures and the metalliferous bearing parts Miocene arc remnants (Leal-Mejia et al. 2018) may shed light the occurrence of magmatic ore deposits in western Colombia.

7.2 Avenues for Further Work:

7.2.1 Pb isotope studies and the Mecaderes xenoliths:

In this study we have analysed Sr, Nd and Hf isotopic trends, with reference to previous Pb isotope studies (e.g.: Marín-Cerón et al. 2010) which point to a Pb radiogenic lower crustal source similar to the Mercaderes xenoliths (Weber et al. 2002; Rodriguez-Vargas et al. 2005). Obtaining and scrutinising the Pb isotope compositions of the samples in this study (or material from a similar range of edifices across the Colombian arc) represents a next obvious step in assessing the petrogenesis of the arc and the processes driving it, and would especially help to further constrain the role of the Pb radiogenic lower continental crust.

Linked to this is further study of the lower crustal xenolith suite in Colombia. Despite their usefulness in assessing the origin of Colombian arc magmatism (e.g: Marín-Cerón et al. 2010; 2019; Errazuriz-Henao et al. 2019) the Mercaderes xenoliths have only been subject to a small handful of studies (Weber, 1998; Weber et al. 2002; Rodriguez-Vargas et al. 2005; Bloch et al. 2017). Further study and sample collection of a large number of xenoliths from the Granatifera Tuff could resolve arguments between lithosphere delamination (Bloch et al. 2017) and slab diapirism and relamination at the lithosphere-asthenosphere boundary (Errazuriz-Henao et al. 2019). As outlined in this study, the first possibility appears most compelling based on the evidence. Furthermore, garnet clinopyroxene xenoliths show rim compositions formed at higher P-T conditions than their cores, indicative of material foundering from the crustal root into the mantle (Bloch et al. 2017). However, the small number of garnet clinopyroxene xenoliths (and xenoliths in general) collected and analysed

mean it is uncertain whether such features are representative or statistically significant. In summary, the xenoliths of the Granatifera Tuff represent a valuable resource for study of the Colombian arc and continental arc magmatism generally, and future studies should seek to marry geochemical studies of the arc with geochemical study of the xenolith suite. A role for lower crustal foundering as a mechanism for generating Colombian arc magmas could be explored in this way.

7.2.2 Radiometric Dating of Cerro Bravo and the VMTVF:

K-Ar analyses have recently been performed on some of the edifices of the VMTVF, revealing ages for these edifices between 10 ka and 1.9 Ma (H. Murcia, personal communication). However, further Ar-Ar analyses of this material, as stated above, has not been forthcoming and future work should look to gaining more high precision geochronology for the edifices and formations sampled here. In particular, further research on Cerro Bravo, beyond the scope of this project, is clearly needed. One of the most intriguing findings of this work is a compositional and isotopic similarity between parts of the VMTVF and Cerro Bravo, particularly its Ancestral/Quebrada Seca stage (Chapter 5). One possible explanation for this is a link between the plumbing systems at depth linking post-glacial VMTVF edifices and Cerro Bravo at some point in time, similar to that proposed between Nevado del Ruiz and Ancestral VMTVF edifices. However, to properly establish this, further field mapping and sampling of the area west of Cerro Bravo and north of the VMTVF is needed to establish the bounds of the Ancestral/Quebrada Seca stage of Cerro Bravo. Chemical and isotopic analysis of the samples, in conjunction with further work on the VMTVF, may shed light on this.

7.2.3 Mineral Chemistry Studies of the Colombian Arc:

To date, only two volcanoes (Cerro Bravo and Cerro Machin) in the Colombian arc have been the subject of mineral chemistry studies (e.g.: analysis of individual mineral chemistries), in particular for geothermobarometry. Such analyses can shed light on P-T-t conditions during the ascent of magmas through the crust, their storage and residence times as well as oxygen fugacity and water contents (Laeger et al. 2013; Pinzon et al. 2017). Further studies of this nature across the Colombian arc would allow for the hypothesised complexity of magma storage beneath some edifices to be better quantified, and to verify that fractionation at certain levels in the crust (for example, the hypothesised shallow fractionation and assimilation of Eocene plutonic material beneath the NVP) is consistent with geothermobarometry findings.

7.2.4: Large Scale Zircon Studies to Constrain Crystallisation History:

Recent advances in the high-precision dating of minerals (e.g.: high-resolution ion probe dating) have demonstrated a diversity of ages within granitic bodies and major differences in compositional histories and ages between crystals even within a single sample. These findings illustrate that magmatic systems can remain episodically active over thousands to millions of years (Miles and Woodcock, 2018 and references therein). One mineral in particular which can survive and record both a protracted crystallisation history and successive magmatic pulses within a magmatic plumbing system is zircon (e.g.: Miller et al. 2007; Claiborne et al. 2010).

Zircon and other accessory mineral phases as described in samples of this study may be of particular importance for recording the ages of crystallisation within deep crustal hot zones where silicic melts could be generated by crystallisation of mafic magmas and assimilation or partial melting of crustal rocks (Collins et al. 2016). Therefore, a detailed study and high-precision dating of these accessory minerals could provide a reliable record of magmatic processes in the lower crust of Colombia.

Such a zircon-based timescale could chart the journey and residence time of magma within crystal plumbing systems from the lower crustal hosted MASH zones to storage areas in the shallow crust and final emplacement (Miles and Woodcock, 2018; Woodcock et al. 2019). This method could be applied to the rocks of the modern Colombian arc where zircon could be identified as an accessory mineral and extracted, and more broadly to the Eocene to Miocene plutonic and hypabyssal rocks of the preceding arc segments (Bustamante et al. 2017; Leal-Mejia et al. 2018) to better constrain their emplacement and origin.

Bibliography

Abers, G. A. *et al.* (2006) 'The thermal structure of subduction zones constrained by seismic imaging: Implications for slab dehydration and wedge flow', *Earth and Planetary Science Letters*. doi: 10.1016/j.epsl.2005.11.055.

Annen, C., Blundy, J. D. and Sparks, R. S. J. (2006) 'The genesis of intermediate and silicic magmas in deep crustal hot zones', *Journal of Petrology*, 47(3), pp. 505–539. doi: 10.1093/petrology/egi084.

Annen, C. and Sparks, R. S. J. (2002) 'Effects of repetitive emplacement of basaltic intrusions on thermal evolution and melt generation in the crust', *Earth and Planetary Science Letters*. doi: 10.1016/S0012-821X(02)00929-9.

Arai, S., Shimizu, Y. and Gervilla, F. (2003) 'Quartz diorite veins in a peridotite xenolith from Tallante, Spain: Implications for reaction and survival of slab-derived SiO2- oversaturated melt in the upper mantle', *Proceedings of the Japan Academy Series B: Physical and Biological Sciences*. doi: 10.2183/pjab.79B.145.

Aspden, J. A., McCourt, W. J. and Brook, M. (1987) 'Geometrical control of subduction-related magmatism: the Mesozoic and Cenozoic plutonic history of western Colombia.', *Journal of the Geological Society*. doi: 10.1144/gsjgs.144.6.0893.

Atherton, M. P. and Petford, N. (1993) 'Generation of sodium-rich magmas from newly underplated basaltic crust', *Nature*, 362(6416), pp. 144–146. doi: 10.1038/362144a0.

Bas, M. J. L. *et al.* (1986) 'A chemical classification of volcanic rocks based on the total alkali-silica diagram', *Journal of Petrology*. doi: 10.1093/petrology/27.3.745.

Bayona, G. *et al.* (2011) 'Intraplate subsidence and basin filling adjacent to an oceanic arc-continent collision: A case from the southern Caribbean-South America

plate margin', *Basin Research*. doi: 10.1111/j.1365-2117.2010.00495.x.

Bea, F., Pereira, M. D. and Stroh, A. (1994) 'Mineral/leucosome trace-element partitioning in a peraluminous migmatite (a laser ablation-ICP-MS study)', *Chemical Geology*. doi: 10.1016/0009-2541(94)90133-3.

Bebout, G. E. (2007) 'Metamorphic chemical geodynamics of subduction zones', *Earth and Planetary Science Letters*. doi: 10.1016/j.epsl.2007.05.050.

Bebout, G. E. (2013) 'Chemical and Isotopic Cycling in Subduction Zones', in *Treatise on Geochemistry: Second Edition*. doi: 10.1016/B978-0-08-095975-7.00322-3.

Bechon, F. and Monsalve, M. L. (1991) 'Activite recente prehistorique du volcan Azufral (SW de la Colombie)', *Comptes Rendus - Academie des Sciences, Serie II*.

Bédard, J. H. (2006) 'A catalytic delamination-driven model for coupled genesis of Archaean crust and sub-continental lithospheric mantle', *Geochimica et Cosmochimica Acta*, 70(5), pp. 1188–1214. doi: 10.1016/j.gca.2005.11.008.

Behn, M. D. *et al.* (2011) 'Diapirs as the source of the sediment signature in arc lavas', *Nature Geoscience*. doi: 10.1038/ngeo1214.

Berly, T. J. *et al.* (2006) 'Supra-subduction zone pyroxenites from San Jorge and Santa Isabel (Solomon Islands)', *Journal of Petrology*. doi: 10.1093/petrology/egl019.

Best, M. G. (2002) *Igneous and Metamorphic Petrology*. 2nd Editio, *Blackwell Publishing*. 2nd Editio. Blackwell Publishing. doi: 10.1180/minmag.1983.047.344.33.

Bezard, R. *et al.* (2014) 'Seeing through the effects of crustal assimilation to assess the source composition beneath the southern lesser antilles arc', *Journal of Petrology*. doi: 10.1093/petrology/egv018.

Bissig, T. *et al.* (2017) 'High Sr/Y magma petrogenesis and the link to porphyry mineralization as revealed by garnet-bearing I-type granodiorite porphyries of the

middle Cauca Au-Cu belt, Colombia', *Economic Geology*, 112(3), pp. 551–568. doi: 10.2113/econgeo.112.3.551.

Blanco, J. F., Vargas, C. A. and Monsalve, G. (2017) 'Lithospheric thickness estimation beneath Northwestern South America from an S-wave receiver function analysis', *Geochemistry, Geophysics, Geosystems*, 18(4), pp. 1376–1387. doi: 10.1002/2016GC006785.

Bloch, E. *et al.* (2017) 'Recent crustal foundering in the Northern Volcanic Zone of the Andean arc: Petrological insights from the roots of a modern subduction zone', *Earth and Planetary Science Letters*. doi: 10.1016/j.epsl.2017.07.041.

Borrero, C. *et al.* (2009) 'Geochemistry and tectonic controls of the effusive activity related with the ancestral Nevado del Ruiz volcano, Colombia', *Geofisica Internacional*. doi: 10.22201/igeof.00167169p.2009.48.1.105.

Borrero, C. and Toro-toro, L. M. (2016) 'MIEMBRO INFERIOR DE LA FORMACIÓN COMBIA (MIOCENO TARDÍO) AL SUR DE LA SUBCUENCA DE', *BOLETÍN DE GEOLOGÍA*, 38(1), pp. 87–100.

Borrero, C. and Toro, L. M. T. (2016) 'Adakite-like signature in the lower member of the Combia Formation (Late Miocene) at the southern of Amagá Sub-Basin, Northwest Colombia', *Boletin de Geologia*. doi: 10.18273/revbol.v38n1-2016005.

Boschman, L. M. *et al.* (2014) 'Kinematic reconstruction of the caribbean region since the early jurassic', *Earth-Science Reviews*. Elsevier B.V., 138(November), pp. 102–136. doi: 10.1016/j.earscirev.2014.08.007.

Botero-Gómez, L. A. *et al.* (2018) 'Campo Volcánico Monogenético Villamaría-Termales, Cordillera Central, Andes colombianos (Parte I): Características morfológicas y relaciones temporales ', *Boletin de Geología* . scieloco , pp. 85–102.

Bourdon, E. *et al.* (2003) 'Magmatic response to early aseismic ridge subduction: The

Ecuadorian margin case (South America)', *Earth and Planetary Science Letters*. doi: 10.1016/S0012-821X(02)01024-5.

Brophy, J. G. and Marsh, B. D. (1986) 'On the origin of high-alumina arc basalt and the mechanics of melt extraction', *Journal of Petrology*. doi: 10.1093/petrology/27.4.763.

Browne, B. L. *et al.* (2006) 'Magma mingling as indicated by texture and Sr / Ba ratios of plagioclase phenocrysts from Unzen volcano, SW Japan', *Journal of Volcanology and Geothermal Research*. doi: 10.1016/j.jvolgeores.2005.09.022.

Bucholz, C. E. *et al.* (2014) 'Fractional crystallization of high-K arc magmas: biotite- versus amphibole-dominated fractionation series in the Dariv Igneous Complex, Western Mongolia', *Contributions to Mineralogy and Petrology*. doi: 10.1007/s00410-014-1072-9.

Buchs, D. M. *et al.* (2010) 'Late Cretaceous arc development on the SW margin of the Caribbean Plate: Insights from the Golfito, Costa Rica, and Azuero, Panama, complexes', *Geochemistry, Geophysics, Geosystems*, 11(7), pp. 1–35. doi: 10.1029/2009GC002901.

Buchs, D. M. *et al.* (2018) 'Evidence for subaerial development of the Caribbean oceanic plateau in the Late Cretaceous and palaeo-environmental implications', *Earth and Planetary Science Letters*. Elsevier B.V., 499(July), pp. 62–73. doi: 10.1016/j.epsl.2018.07.020.

Burke, K. (1988) 'Tectonic evolution of the Caribbean', *Annual Review of Earth and Planetary Sciences*, 16, pp. 201–230. doi: 10.1146/annurev.earth.16.1.201.

Bustamante, C. *et al.* (2017) 'Geochemistry and isotopic signatures of Paleogene plutonic and detrital rocks of the Northern Andes of Colombia: A record of post-collisional arc magmatism', *Lithos*. Elsevier B.V., 277, pp. 199–209. doi:

10.1016/j.lithos.2016.11.025.

Calvache, M. L. and Duque-Trujillo, J. F. (2015) ‘Geomorphological Features of the Galeras Volcanic Complex’, in Hermelin, M. (ed.) *Landscapes and Landforms of Colombia*, pp. 1–210. doi: 10.1007/978-3-319-11800-0.

Calvache V, M. L., Cortés J, G. P. and Williams, S. N. (1997) ‘Stratigraphy and chronology of the Galeras volcanic complex, Colombia’, *Journal of Volcanology and Geothermal Research*, 77(1–4), pp. 5–19. doi: 10.1016/S0377-0273(96)00083-2.

Calvache V, M. L. and Williams, S. N. (1997) ‘Geochemistry and petrology of the Galeras Volcanic Complex, Colombia’, *Journal of Volcanology and Geothermal Research*, 77, pp. 21–38. doi: 10.1016/S0377-0273(96)00084-4.

Cardona, A. *et al.* (2014) ‘Geochronology and geochemistry of the Parashi granitoid, NE Colombia: Tectonic implication of short-lived Early Eocene plutonism along the SE Caribbean margin’, *Journal of South American Earth Sciences*. Elsevier Ltd, 50, pp. 75–92. doi: 10.1016/j.jsames.2013.12.006.

Carlos, A., Borrero, P. and Naranjo, J. L. H. (1990) ‘Casabianca formation: a Colombian example of volcanism-induced aggradation in a fluvial basin’, *Journal of Volcanology and Geothermal Research*, 41(1–4), pp. 253–267. doi: 10.1016/0377-0273(90)90091-S.

Castillo, P. R. (2012a) ‘Adakite petrogenesis’, *Lithos*. Elsevier B.V., 134–135, pp. 304–316. doi: 10.1016/j.lithos.2011.09.013.

Castillo, P. R. (2012b) ‘Adakite petrogenesis’, *Lithos*, 134–135, pp. 304–316. doi: 10.1016/j.lithos.2011.09.013.

Castro, A. *et al.* (2010) ‘Melting relations of MORB-sediment mélanges in underplated mantle wedge plumes; Implications for the origin of Cordilleran-type batholiths’, *Journal of Petrology*. doi: 10.1093/petrology/egq019.

Cediel, F. and Cáceres, C. (2000) *Geological Map of Colombia, 3rd Edition*.

Cediel, F. and Shaw, R. P. (2019) *Geology and Tectonics of Northwestern South America*. doi: 10.1007/978-3-319-76132-9.

Cediel, F., Shaw, R. P. and Cáceres, C. (2003) 'Tectonic Assembly of the Northern Andean Block', *AAPG Memoir*, 79, pp. 815–848.

Chiarabba, C. *et al.* (2016) 'Subduction system and flat slab beneath the Eastern Cordillera of Colombia', *Geochemistry, Geophysics, Geosystems*. doi: 10.1002/2015GC006048.

Chiaradia, M. *et al.* (2009) 'Adakite-like volcanism of Ecuador: Lower crust magmatic evolution and recycling', *Contributions to Mineralogy and Petrology*, 158(5), pp. 563–588. doi: 10.1007/s00410-009-0397-2.

Chiaradia, M. (2015a) 'Crustal thickness control on Sr/Y signatures of recent arc magmas: an Earth scale perspective.', *Scientific reports*, 5, p. 8115. doi: 10.1038/srep08115.

Chiaradia, M. (2015b) 'Crustal thickness control on Sr/Y signatures of recent arc magmas: An Earth scale perspective', *Scientific Reports*, 5, p. 8115. doi: 10.1038/srep08115.

Claiborne, L. L., Miller, C. F., Flanagan, D. M., Clynne, M. A., & Wooden, J. L. (2010). Zircon reveals protracted magma storage and recycling beneath Mount St. Helens. *Geology*. https://doi.org/10.1130/G31285.1

Clarke, A. P. (2015) *Geological History of the Osa Melange by*.

Clarke, G. L., Daczko, N. R. and Miescher, D. (2013) 'Identifying relic igneous garnet and clinopyroxene in eclogite and granulite, Breaksea orthogneiss, New Zealand', *Journal of Petrology*. doi: 10.1093/petrology/egt036.

Clift, P. D., Schouten, H. and Vannucchi, P. (2009) 'Arc-continent collisions, sediment

recycling and the maintenance of the continental crust', *Geological Society Special Publication*. doi: 10.1144/SP318.3.

Coats, R. R. (1962) 'Magma Type and Crustal Structure in the Aleutian Arc', in. doi: 10.1029/gm006p0092.

Cochrane, R. *et al.* (2014) 'Distinguishing between in-situ and accretionary growth of continents along active margins', *Lithos*. doi: 10.1016/j.lithos.2014.05.031.

Collins, W. J., Huang, H. Q., & Jiang, X. (2016). Water-fluxed crustal melting produces Cordilleran batholiths. *Geology*. https://doi.org/10.1130/G37398.1

Condie, K. C. (2014) 'Thirty-five years of TTG research', in *Modern Approaches to Solid Earth Sciences*. doi: 10.1007/978-94-007-7615-9.

Cuadros, F. A. *et al.* (2014) 'Mesoproterozoic crust in the San Lucas Range (Colombia): An insight into the crustal evolution of the northern Andes', *Precambrian Research*. doi: 10.1016/j.precamres.2014.02.010.

Davidson, J. *et al.* (2007) 'Amphibole "sponge" in arc crust?', *Geology*, 35(9), pp. 787–790. doi: 10.1130/G23637A.1.

Decelles, P. G. *et al.* (2009) 'Cyclicity in Cordilleran orogenic systems', *Nature Geoscience*. doi: 10.1038/ngeo469.

Defant, M. J. (1992) 'The geochemistry of young volcanism throughout western Panama and southeastern Costa Rica: an overview', *Journal - Geological Society (London)*. doi: 10.1144/gsjgs.149.4.0569.

Defant, M. J. and Drummond, M. S. (1990) 'Derivation of some modern arc magmas by melting of young subducted lithosphere', *Nature*, 347(6294), pp. 662–665. doi: 10.1038/347662a0.

Delacour, A. *et al.* (2007) 'Magma evolution of Quaternary minor volcanic centres in southern Peru, Central Andes', *Bulletin of Volcanology*. doi: 10.1007/s00445-006-

0096-z.

DePaolo, D. J. (1981) ‘Trace element and isotopic effects of combined wallrock assimilation and fractional crystallization’, *Earth and Planetary Science Letters*. doi: 10.1016/0012-821X(81)90153-9.

Dickinson, W. R. (1975) ‘Potash-Depth (K-h) relations in continental margin and intra-oceanic magmatic arcs’, *Geology*. doi: 10.1130/0091-7613(1975)3<53:PKRICM>2.0.CO;2.

Droux, A. and Delaloye, M. (1996) ‘Petrography and geochemistry of Plio-Quaternary calc-alkaline volcanoes of Southwestern Colombia’, *Journal of South American Earth Sciences*, 9(1–2), pp. 27–41. doi: 10.1016/0895-9811(96)00025-9.

Ducea, M. (2001) ‘The California arc: Thick granitic batholiths, eclogitic residues, lithospheric-scale thrusting, and magmatic flare-ups’, *GSA Today*. doi: 10.1130/1052-5173(2001)011<0004:TCATGB>2.0.CO;2.

Ducea, M. N., Saleeby, J. B. and Bergantz, G. (2015) ‘The Architecture, Chemistry, and Evolution of Continental Magmatic Arcs’, *Annual Review of Earth and Planetary Sciences*, 43(1), pp. 299–331. doi: 10.1146/annurev-earth-060614-105049.

Ducea, M. and Saleeby, J. (1998) ‘Crustal recycling beneath continental arcs: Silica-rich glass inclusions in ultramafic xenoliths from the Sierra Nevada, California’, *Earth and Planetary Science Letters*. doi: 10.1016/s0012-821x(98)00021-1.

Dufek, J. and Bergantz, G. W. (2005) ‘Lower crustal magma genesis and preservation: A stochastic framework for the evaluation of basalt-crust interaction’, *Journal of Petrology*. doi: 10.1093/petrology/egi049.

Duncan, R. A. and Hargraves, R. B. (1984) ‘Plate tectonic evolution of the Caribbean region in the mantle reference frame’, *Memoir of the Geological Society of America*. doi: 10.1130/MEM162-p81.

Duque-Caro, H. (1990) ‘The Choco Block in the northwestern corner of South America: structural, tectonostratigraphic, and paleogeographic implications’, *Journal of South American Earth Sciences*, 3(1), pp. 71–84. doi: 10.1016/0895-9811(90)90019-W.

Duque T, J. F. *et al.* (2010) ‘Geología, geocronología y geoquímica del Volcán Morasurco, Pasto, Colombia’, *Boletín de Ciencias de la Tierra*, (27), pp. 25–36. Available at: http://www.scielo.org.co/pdf/bcdt/n27/n27a03.pdf.

Echeverri, S. *et al.* (2015) ‘Regional provenance from southwestern Colombia fore-arc and intra-arc basins: implications for Middle to Late Miocene orogeny in the Northern Andes’, *Terra Nova*, 27(5), pp. 356–363. doi: 10.1111/ter.12167.

Eichelberger, J. C. (1978) ‘Andesitic volcanism and crustal evolution’, *Nature*. doi: 10.1038/275021a0.

Elderfield, H. and Greaves, M. J. (1982) ‘The rare earth elements in seawater’, *Nature*. doi: 10.1038/296214a0.

Elliott, T. *et al.* (1997) ‘Element transport from slab to volcanic front at the Mariana arc’, *Journal of Geophysical Research: Solid Earth*. doi: 10.1029/97jb00788.

Elliott, T. (2004) ‘Tracers of the slab’, in *Geophysical Monograph Series*. doi: 10.1029/138GM03.

Errázuriz-Henao, C. *et al.* (2019a) ‘The role of subducted sediments in the formation of intermediate mantle-derived magmas from the Northern Colombian Andes’, *Lithos*. Elsevier B.V., 336–337(April), pp. 151–168. doi: 10.1016/j.lithos.2019.04.007.

Errázuriz-Henao, C. *et al.* (2019b) ‘The role of subducted sediments in the formation of intermediate mantle-derived magmas from the Northern Colombian Andes’, *Lithos*. doi: 10.1016/j.lithos.2019.04.007.

Estrada, J. J. (1995) *Paleomagnetism and Accretion Events in the Northern Andes*.

State University of New York.

Ewart, A. (1982) ‘The mineralogy and petrology of Tertiary-Recent orogenic volcanic rocks: with special reference to the andesitic-basaltic compositional range’, in Thorpe, R. S. (ed.) *Orogenic Andesites and Related Rocks*. New York: John Wiley, pp. 25–95.

Farner, M. J. and Lee, C. T. A. (2017) ‘Effects of crustal thickness on magmatic differentiation in subduction zone volcanism: A global study’, *Earth and Planetary Science Letters*. doi: 10.1016/j.epsl.2017.04.025.

Farris, D. W. *et al.* (2011) ‘Fracturing of the Panamanian Isthmus during initial collision with: South America’, *Geology*, 39(11), pp. 1007–1010. doi: 10.1130/G32237.1.

Feeley, T. C., Davidson, J. P. and Armendia, A. (1993) ‘The volcanic and magmatic evolution of Volcán Ollagüe, a high-K, late quaternary stratovolcano in the Andean Central Volcanic Zone’, *Journal of Volcanology and Geothermal Research*. doi: 10.1016/0377-0273(93)90065-Y.

Forero, J., Zuluaga, C. and Mojica, J. (2011) ‘Alteration Related To Hydrothermal Activity of the Nevado Del Ruiz Volcano (Nrv), Colombia’, *Boletin de Geología*, 33, pp. 59–67.

Fuck, R. A., Brito Neves, B. B. and Schobbenhaus, C. (2008) ‘Rodinia descendants in South America’, *Precambrian Research*. doi: 10.1016/j.precamres.2007.04.018.

Fumagalli, P. and Poli, S. (2005) ‘Experimentally determined phase relations in hydrous peridotites to 6.5 GPa and their consequences on the dynamics of subduction zones’, *Journal of Petrology*. doi: 10.1093/petrology/egh088.

Gale, A. *et al.* (2013) ‘The mean composition of ocean ridge basalts’, *Geochemistry, Geophysics, Geosystems*. doi: 10.1029/2012GC004334.

Garc, G. Z. and Rodr, G. (2013) ‘PETROGRÁFIA , GEOQUÍMICA Y EDAD DE LA GRANODIORITA de Farallones y las rocas volcánicas asociadas .’, *Boletin de Geologia*, 35.

Gertisser, R. and Keller, J. (2003) ‘Temporal variations in magma composition at Merapi Volcano (Central Java, Indonesia): Magmatic cycles during the past 2000 years of explosive activity’, *Journal of Volcanology and Geothermal Research*. doi: 10.1016/S0377-0273(03)00025-8.

Gerya, T. V., Stöckhert, B. and Perchuk, A. L. (2002) ‘Exhumation of high-pressure metamorphic rocks in a subduction channel: A numerical simulation’, *Tectonics*. doi: 10.1029/2002tc001406.

Gerya, T. V. and Yuen, D. A. (2003) ‘Rayleigh - Taylor instabilities from hydration and melting propel “cold plumes” at subduction zones’, *Earth and Planetary Science Letters*. doi: 10.1016/S0012-821X(03)00265-6.

Gerya, T. V., Yuen, D. A. and Maresch, W. V. (2004) ‘Thermomechanical modelling of slab detachment’, *Earth and Planetary Science Letters*. doi: 10.1016/j.epsl.2004.07.022.

Gil-Rodriguez, J. (2014) ‘Petrology of the Betulia Igneous Complex, Cauca, Colombia’, *Journal of South American Earth Sciences*. doi: 10.1016/j.jsames.2014.09.016.

Gill, J. B. (1981) ‘Orogenic Andesites and Plate Tectonics.’, *Orogenic Andesites and Plate Tectonics.* doi: 10.1016/0377-0273(82)90060-9.

Gómez-Tuena, A., Straub, S. M. and Zellmer, G. F. (2014) ‘An introduction to orogenic andesites and crustal growth’, *Geological Society Special Publication*, 385(1), pp. 1–13. doi: 10.1144/SP385.16.

Gómez, J. T. *et al.* (2017) ‘Geological map of Colombia 2015’, *Episodes*. doi:

10.18814/epiiugs/2017/v40i3/017023.

González-garcia, J. *et al.* (2015) 'Nevado Del Ruiz Volcano (Colombia): A 3D Model Combining Geological and Geophysical Information', *World Geothermal Congress 2015*, (April), pp. 19–25.

González, H. (2001) 'Mapa Geológico del Departamento de Antioquia (Memoria explicativa)', *Boletin Geológico. Ingeominas*.

Goss, A. R. and Kay, S. M. (2006) 'Steep REE patterns and enriched Pb isotopes in southern Central American arc magmas: Evidence for forearc subduction erosion?', *Geochemistry, Geophysics, Geosystems*. doi: 10.1029/2005GC001163.

Goss, A. R., Kay, S. M. and Mpodozis, C. (2013) 'Andean Adakite-like high-Mg Andesites on the Northern Margin of the Chilean-Pampean Flat-slab (27-28.58°S) Associated with Frontal Arc Migration and Fore-arc Subduction Erosion', *Journal of Petrology*. doi: 10.1093/petrology/egt044.

Gourgaud, A. and Thouret, J.-C. (1990) 'Magma mixing and petrogenesis of the 13 November 1985 eruptive products at Nevado del Ruiz (Colombia)', *Journal of Volcanology and Geothermal Research*, 41(1–4), pp. 79–96. doi: 10.1016/0377-0273(90)90084-S.

GOVINDARAJU, K. (1989) '1989 COMPILATION OF WORKING VALUES AND SAMPLE DESCRIPTION FOR 272 GEOSTANDARDS', *Geostandards Newsletter*. doi: 10.1111/j.1751-908X.1989.tb00476.x.

Grove, T. L. *et al.* (2003) 'Fractional crystallization and mantle-melting controls on calc-alkaline differentiation trends', *Contributions to Mineralogy and Petrology*, 145(5), pp. 515–533. doi: 10.1007/s00410-003-0448-z.

Grove, T. L., Till, C. B. and Krawczynski, M. J. (2012) ' The Role of H 2 O in Subduction Zone Magmatism ', *Annual Review of Earth and Planetary Sciences*. doi:

10.1146/annurev-earth-042711-105310.

Gutscher, M. A. *et al.* (2000) 'Can slab melting be caused by flat subduction?', *Geology*, 28(6), pp. 535–538. doi: 10.1130/0091-7613(2000)28<535:CSMBCB>2.0.CO;2.

Hack, A. C. and Thompson, A. B. (2011) 'Density and viscosity of hydrous magmas and related fluids and their role in subduction zone processes', *Journal of Petrology*. doi: 10.1093/petrology/egq048.

Hacker, B. R. (2008) 'H2O subduction beyond arcs', *Geochemistry, Geophysics, Geosystems*. doi: 10.1029/2007GC001707.

Hacker, B. R., Abers, G. A. and Peacock, S. M. (2003) ' Subduction factory 1. Theoretical mineralogy, densities, seismic wave speeds, and H 2 O contents ', *Journal of Geophysical Research: Solid Earth*. doi: 10.1029/2001jb001127.

Hacker, B. R., Kelemen, P. B. and Behn, M. D. (2011) 'Differentiation of the continental crust by relamination', *Earth and Planetary Science Letters*. Elsevier B.V., 307(3–4), pp. 501–516. doi: 10.1016/j.epsl.2011.05.024.

Hall, M. L. and Wood, C. A. (1985) 'Volcano-tectonic segmentation of the northern Andes.', *Geology*. doi: 10.1130/0091-7613(1985)13<203:VSOTNA>2.0.CO;2.

Hardy, N. C. (1991) 'Tectonic evolution of the easternmost Panama basin: Some new data and inferences', *Journal of South American Earth Sciences*, 4(3), pp. 261–269. doi: 10.1016/0895-9811(91)90035-J.

Hastie, A. R. *et al.* (2013) 'Geochemical components in a Cretaceous island arc: The Th/La-(Ce/Ce*)Nd diagram and implications for subduction initiation in the inter-American region', *Lithos*. Elsevier B.V., 162–163, pp. 57–69. doi: 10.1016/j.lithos.2012.12.001.

Hastie, A. R. *et al.* (2015) 'Can Fractional Crystallization, Mixing and Assimilation

Processes be Responsible for Jamaican-type Adakites? Implications for Generating Eoarchaean Continental Crust', *Journal of Petrology*, 56(7), pp. 1251–1284. doi: 10.1093/petrology/egv029.

Hastie, A. R. and Kerr, A. C. (2010) 'Mantle plume or slab window?: Physical and geochemical constraints on the origin of the Caribbean oceanic plateau', *Earth-Science Reviews*. Elsevier B.V., 98(3–4), pp. 283–293. doi: 10.1016/j.earscirev.2009.11.001.

Hawkesworth, C. J. *et al.* (1993) 'Mantle and Slab Contributions in Arc Magmas', *Annual Review of Earth and Planetary Sciences*, 21(1), pp. 175–204. doi: 10.1146/annurev.ea.21.050193.001135.

Hayes, G. P. *et al.* (2018) 'Slab2, a comprehensive subduction zone geometry model', *Science*. doi: 10.1126/science.aat4723.

Hermann, J. *et al.* (2006) 'Aqueous fluids and hydrous melts in high-pressure and ultra-high pressure rocks: Implications for element transfer in subduction zones', *Lithos*. doi: 10.1016/j.lithos.2006.03.055.

Hermann, J. and Spandler, C. J. (2008) 'Sediment melts at sub-arc depths: An experimental study', *Journal of Petrology*. doi: 10.1093/petrology/egm073.

Hickey-Vargas, R. *et al.* (2016) 'Basaltic rocks from the Andean Southern Volcanic Zone: Insights from the comparison of along-strike and small-scale geochemical variations and their sources', *Lithos*. doi: 10.1016/j.lithos.2016.04.014.

Hildreth, W. and Moorbath, S. (1988) 'Crustal contributions to arc magmatism in the Andes of Central Chile', *Contributions to Mineralogy and Petrology*. doi: 10.1007/BF00372365.

Van Der Hilst, R. and Mann, P. (1994) 'Tectonic implications of tomographic images of subducted lithosphere beneath northwestern South America', *Geology*, pp. 451–

454. doi: 10.1130/0091-7613(1994)022<0451:TIOTIO>2.3.CO;2.

Holm, P. M. *et al.* (2014) 'Enrichments of the mantle sources beneath the Southern Volcanic Zone (Andes) by fluids and melts derived from abraded upper continental crust', *Contributions to Mineralogy and Petrology*, 167(5), pp. 1–27. doi: 10.1007/s00410-014-1004-8.

Holm, P. M. *et al.* (2016) 'Subduction zone mantle enrichment by fluids and Zr–Hf-depleted crustal melts as indicated by backarc basalts of the Southern Volcanic Zone, Argentina', *Lithos*. doi: 10.1016/j.lithos.2016.06.029.

Hora, J. M., Singer, B. S. and Wörner, G. (2007) 'Volcano evolution and eruptive flux on the thick crust of the Andean Central Volcanic Zone: 40Ar/39Ar constraints from Volcán Parinacota, Chile', *Bulletin of the Geological Society of America*. doi: 10.1130/B25954.1.

Horton, B. K. *et al.* (2015) 'Application of detrital zircon U-Pb geochronology to surface and subsurface correlations of provenance, paleodrainage, and tectonics of the Middle Magdalena Valley Basin of Colombia', *Geosphere*, 11(6), pp. 1790–1811. doi: 10.1130/GES01251.1.

Hou, X. *et al.* (2016) 'Inductively Coupled Plasma Optical Emission Spectrometry', *Encyclopedia of Analytical Chemistry*. (Major Reference Works), pp. 1–25. doi: doi:10.1002/9780470027318.a5110.pub3.

Idárraga-García, J., Kendall, J. M. and Vargas, C. A. (2016) 'Shear wave anisotropy in northwestern South America and its link to the Caribbean and Nazca subduction geodynamics', *Geochemistry, Geophysics, Geosystems*. doi: 10.1002/2016GC006323.

Irvine, T. N. and Baragar, W. R. A. (1971) 'A Guide to the Chemical Classification of the Common Volcanic Rocks', *Canadian Journal of Earth Sciences*. doi:

10.1139/e71-055.

Jacques, G. *et al.* (2013) ‘Across-arc geochemical variations in the Southern Volcanic Zone, Chile (34.5-38.0°S): Constraints on mantle wedge and slab input compositions’, *Geochimica et Cosmochimica Acta*. doi: 10.1016/j.gca.2013.05.016.

Jagoutz, O. and Schmidt, M. W. (2013) ‘The composition of the foundered complement to the continental crust and a re-evaluation of fluxes in arcs’, *Earth and Planetary Science Letters*. doi: 10.1016/j.epsl.2013.03.051.

James, D. E. and Murcia, L. A. (1984) ‘Crustal contamination in northern Andean volcanics.’, *Journal of the Geological Society*. doi: 10.1144/gsjgs.141.5.0823.

Jaramillo, J. S. *et al.* (2019a) ‘Petrogenesis of the late Miocene Combia volcanic complex, northwestern Colombian Andes: Tectonic implication of short term and compositionally heterogeneous arc magmatism’, *Lithos*. Elsevier B.V., 330–331(March), pp. 194–210. doi: 10.1016/j.lithos.2019.02.017.

Jaramillo, J. S. *et al.* (2019b) ‘Petrogenesis of the late Miocene Combia volcanic complex, northwestern Colombian Andes: Tectonic implication of short term and compositionally heterogeneous arc magmatism’, *Lithos*, 330–331, pp. 194–210. doi: 10.1016/j.lithos.2019.02.017.

Jarvis, K. E. (2014) ‘Inductively coupled plasma-mass spectrometry (ICP-MS)’, in *Modern Analytical Geochemistry: An Introduction to Quantitative Chemical Analysis Techniques for Earth, Environmental and Materials Scientists*. doi: 10.4135/9781446247501.n2037.

Jerez H., E.K. (2010). ‘CARACTERIZACIÓN PETROGRÁFICA, GEOQUÍMICA y GEOCRONOLÓGICA EN ROCAS ÍGNEAS INTRUSIVAS DE LA CUENCA CAUCA-PATÍA (CCP), DEPARTAMENTO DEL CAUCA, COLOMBIA’, Maestría en Ciencias de la Tierra Departamento de Geología Universidad EAFIT.

Jiménez Mejía, D. M., Juliani, C. and Cordani, U. G. (2006) 'P-T-t conditions of high-grade metamorphic rocks of the Garzon Massif, Andean basement, SE Colombia', *Journal of South American Earth Sciences*. doi: 10.1016/j.jsames.2006.07.001.

Johnson, M. C. and Plank, T. (2000) 'Dehydration and melting experiments constrain the fate of subducted sediments', *Geochemistry, Geophysics, Geosystems*. doi: 10.1029/1999GC000014.

Kay, R. W. (1978) 'Aleutian magnesian andesites: Melts from subducted Pacific ocean crust', *Journal of Volcanology and Geothermal Research*. doi: 10.1016/0377-0273(78)90032-X.

Kay, R. W. (1980) 'Volcanic Arc Magmas: Implications of a Melting-Mixing Model for Element Recycling in the Crust-Upper Mantle System', *The Journal of Geology*. doi: 10.1086/628541.

Kay, R. W. and Mahlburg Kay, S. (1993) 'Delamination and delamination magmatism', *Tectonophysics*. doi: 10.1016/0040-1951(93)90295-U.

Van Keken, P. E. *et al.* (2011) 'Subduction factory: 4. Depth-dependent flux of H2O from subducting slabs worldwide', *Journal of Geophysical Research: Solid Earth*. doi: 10.1029/2010JB007922.

Kelemen, P. B., Hanghøj, K. and Greene, A. R. (2013) 'One View of the Geochemistry of Subduction-Related Magmatic Arcs, with an Emphasis on Primitive Andesite and Lower Crust', in *Treatise on Geochemistry: Second Edition*. doi: 10.1016/B978-0-08-095975-7.00323-5.

Kennan, L. and Pindell, J. L. (2009) 'Dextral shear, terrane accretion and basin formation in the Northern Andes: best explained by interaction with a Pacific-derived Caribbean Plate?', *Geological Society, London, Special Publications*, 328(1), pp. 487–531. doi: 10.1144/SP328.20.

Kepezhinskas, A. (1995) ‘Na Metasomatism in the Island-Arc Mantle by Slab Melt—Peridotite Interaction: Evidence from Mantle Xenoliths in the North Kamchatka Arc’, *Journal of Petrology*. doi: 10.1093/oxfordjournals.petrology.a037263.

Kerr, A. C. *et al.* (1997) ‘Cretaceous basaltic terranes in western Colombia: Elemental, chronological and Sr-Nd isotopic constraints on petrogenesis’, *Journal of Petrology*, 38(6), pp. 677–702. doi: 10.1093/petrology/38.6.677.

Kerr, A. C. *et al.* (1999) ‘A new plate tectonic model of the Caribbean: Implications from a geochemical reconnaissance of Cuban Mesozoic volcanic rocks’, *Bulletin of the Geological Society of America*, 111(11), pp. 1581–1599. doi: 10.1130/0016-7606(1999)111<1581:ANPTMO>2.3.CO;2.

Kerr, A. C. *et al.* (2003) ‘No Oceanic Plateau — No Caribbean Plate? The Seminal Role of an Oceanic Plateau in Caribbean Plate Evolution’, *AAPG Memoir*, pp. 126–168.

Kerr, A. C. and Tarney, J. (2005) ‘Tectonic evolution of the Caribbean and northwestern South America: The case for accretion of two Late Cretaceous oceanic plateaus’, *Geology*, 33(4), pp. 269–272. doi: 10.1130/G21109.1.

Kerrick, D. M. and Connolly, J. A. D. (2001) ‘Metamorphic devolatilization of subducted oceanic metabasalts: Implications for seismicity, arc magmatism and volatile recycling’, *Earth and Planetary Science Letters*. doi: 10.1016/S0012-821X(01)00347-8.

Kessel, R. *et al.* (2005) ‘Trace element signature of subduction-zone fluids, melts and supercritical liquids at 120-180 km depth’, *Nature*. doi: 10.1038/nature03971.

Klemetti, E. W. and Grunder, A. L. (2008) ‘Volcanic evolution of Volcán Aucanquilcha: A long-lived dacite volcano in the Central Andes of northern Chile’, *Bulletin of Volcanology*. doi: 10.1007/s00445-007-0158-x.

Klimm, K., Blundy, J. D. and Green, T. H. (2008) ‘Trace element partitioning and accessory phase saturation during H2O-saturated melting of basalt with implications for subduction zone chemical fluxes’, *Journal of Petrology*. doi: 10.1093/petrology/egn001.

Kushiro, I. (1973) ‘Origin of some magmas in oceanic and circum-oceanic regions’, *Tectonophysics*. doi: 10.1016/0040-1951(73)90003-6.

Laeger, K. *et al.* (2013) ‘Crystallization conditions and petrogenesis of the lava dome from the ~900 years BP eruption of Cerro Machín Volcano, Colombia’, *Journal of South American Earth Sciences*, 48, pp. 193–208. doi: 10.1016/j.jsames.2013.09.009.

Lapierre, H. *et al.* (2000) ‘Multiple plume events in the genesis of the peri-Caribbean Cretaceous oceanic plateau province’, *Journal of Geophysical Research: Solid Earth*. doi: 10.1029/1998jb900091.

Leal-Mejía, H. (2011) ‘Phanerozoic Gold Metallogeny in the Colombian Andes: A Tectono-Magmatic Approach’, *Tesis de Doctorado*.

Lee, C. T. A., Cheng, X. and Horodyskyj, U. (2006) ‘The development and refinement of continental arcs by primary basaltic magmatism, garnet pyroxenite accumulation, basaltic recharge and delamination: Insights from the Sierra Nevada, California’, *Contributions to Mineralogy and Petrology*. doi: 10.1007/s00410-005-0056-1.

Leeman, W. P. (1983) ‘The influence of crustal structure on compositions of subduction-related magmas’, *Journal of Volcanology and Geothermal Research*. doi: 10.1016/0377-0273(83)90026-4.

Lescinsky, D. (1990) *Geology, volcanology and petrology of Cerro Bravo, a young dacitic stratovolcano in west–central Colombia.* Lousiana State University, Baton Rouge, USA.

Lieu, W. K. and Stern, R. J. (2019) ‘The robustness of Sr / Y and La / Yb as proxies for crust thickness in modern arcs’, 15(3), pp. 621–641.

Londono, J. M. (2016) ‘Evidence of recent deep magmatic activity at Cerro Bravo-Cerro Machín volcanic complex, central Colombia. Implications for future volcanic activity at Nevado del Ruiz, Cerro Machín and other volcanoes’, *Journal of Volcanology and Geothermal Research*. doi: 10.1016/j.jvolgeores.2016.06.003.

Lonsdale, P. (2005) ‘Creation of the Cocos and Nazca plates by fission of the Farallon plate’, *Tectonophysics*. doi: 10.1016/j.tecto.2005.05.011.

Lopez C, S.M. (2009) ‘ESTRATIGRAFÍA, PETROLOGÍA Y GEOQUÍMICA DE LAS ROCAS VOLCÁNICAS DEL FLANCO OCCIDENTAL DEL VOLCÁN PURACÉ, ALREDEDORES DE COCONUCO’, Maestría en Ciencias de la Tierra Departamento de Geología Universidad EAFIT.

Lopez-Escobar, L. *et al.* (1993) ‘Petrography and geochemistry of Quaternary rocks from the Southern Volcanic Zone of the Andes between 41°30′ and 46°00′S, Chile’, *Revista Geologica de Chile*. doi: 10.5027/andgeoV20n1-a04.

Macpherson, C. G., Dreher, S. T. and Thirlwall, M. F. (2006a) ‘Adakites without slab melting: High pressure differentiation of island arc magma, Mindanao, the Philippines’, *Earth and Planetary Science Letters*, 243(3–4), pp. 581–593. doi: 10.1016/j.epsl.2005.12.034.

Macpherson, C. G., Dreher, S. T. and Thirlwall, M. F. (2006b) ‘Adakites without slab melting: High pressure differentiation of island arc magma, Mindanao, the Philippines’, *Earth and Planetary Science Letters*. doi: 10.1016/j.epsl.2005.12.034.

Mamani, M., Tassara, A. and Wörner, G. (2008) ‘Composition and structural control of crustal domains in the central Andes’, *Geochemistry, Geophysics, Geosystems*. doi: 10.1029/2007GC001925.

Mamani, M., Wörner, G. and Sempere, T. (2010) ‘Geochemical variations in igneous rocks of the Central Andean orocline (13°S to 18°S): Tracing crustal thickening and magma generation through time and space’, *Bulletin of the Geological Society of America*. doi: 10.1130/B26538.1.

Manning, C. E. (2004) ‘The chemistry of subduction-zone fluids’, *Earth and Planetary Science Letters*. doi: 10.1016/j.epsl.2004.04.030.

Mantilla Figueroa, L. C. *et al.* (2013) ‘The magmatic history of the Vetas-California mining district, Santander Massif, Eastern Cordillera, Colombia’, *Journal of South American Earth Sciences*, 45, pp. 235–249. doi: 10.1016/j.jsames.2013.03.006.

Marín-Cerón, M. I. *et al.* (2010) ‘Slab decarbonation and CO2 recycling in the Southwestern Colombian volcanic arc’, *Geochimica et Cosmochimica Acta*, 74(3), pp. 1104–1121. doi: 10.1016/j.gca.2009.10.031.

Marín-Cerón, M. I. *et al.* (2019) ‘Late Cenozoic to modern-day volcanism in the Northern Andes: A geochronological, petrographical, and geochemical review’, in *Frontiers in Earth Sciences*. doi: 10.1007/978-3-319-76132-9_8.

Marschall, H. R. and Schumacher, J. C. (2012) ‘Arc magmas sourced from mélange diapirs in subduction zones’, *Nature Geoscience*. Nature Publishing Group, 5(12), pp. 862–867. doi: 10.1038/ngeo1634.

Martin, H., Smithies, R. H., *et al.* (2005) ‘An overview of adakite, tonalite-trondhjemiten-granodiorite (TTG), and sanukitoid: Relationships and some implications for crustal evolution’, *Lithos*, 79(1-2 SPEC. ISS.), pp. 1–24. doi: 10.1016/j.lithos.2004.04.048.

Martin, H., Smithies, R. H. H., *et al.* (2005) ‘An overview of adakite, tonalite–trondhjemite–granodiorite (TTG), and sanukitoid: relationships and some implications for crustal evolution’, *Lithos*, 79(1–2), pp. 1–24. doi: 10.1016/j.lithos.2004.04.048.

Martin, H. *et al.* (2014) ‘Why Archaean TTG cannot be generated by MORB melting in subduction zones’, *Lithos*. Elsevier B.V., 198–199, pp. 1–13. doi: 10.1016/j.lithos.2014.02.017.

Martínez, L. *et al.* (2014) ‘Geología y estratigrafía del complejo volcánico Nevado del Ruiz.’, p. 853.

McDonald, I. and Viljoen, K. S. (2006) ‘Platinum-group element geochemistry of mantle eclogites: A reconnaissance study of xenoliths from the Orapa kimberlite, Botswana’, *Transactions of the Institutions of Mining and Metallurgy, Section B: Applied Earth Science*, 115(3), pp. 81–93. doi: 10.1179/174327506X138904.

McDonough, W. F. and Sun, S.-S. (1995) ‘The composition of the Earth’, *Chemical Geology*, 120, pp. 223–253.

McGeary, S., Nur, A. and Ben-Avraham, Z. (1985) ‘Spatial gaps in arc volcanism: The effect of collision or subduction of oceanic plateaus’, *Tectonophysics*, 119(1–4), pp. 195–221. doi: 10.1016/0040-1951(85)90039-3.

McKenzie, D. and O’Nions, R. K. (1991) ‘Partial melt coefficients from inversion of rare earth element concentrations’, *J. Petrol.*

Melson, W. G. *et al.* (1990) ‘Water contents, temperatures and diversity of the magmas of the catastrophic eruption of Nevado del Ruiz, Colombia, November 13, 1985’, *Journal of Volcanology and Geothermal Research*, 41(1–4), pp. 97–126. doi: 10.1016/0377-0273(90)90085-T.

Miles, A. J., & Woodcock, N. H. (2018). A combined geochronological approach to investigating long lived granite magmatism, the Shap granite, UK. *Lithos*. https://doi.org/10.1016/j.lithos.2018.02.012

Miller, J. S., Matzel, J. E. P., Miller, C. F., Burgess, S. D., & Miller, R. B. (2007). Zircon growth and recycling during the assembly of large, composite arc plutons.

Journal of Volcanology and Geothermal Research.

https://doi.org/10.1016/j.jvolgeores.2007.04.019

Monsalve, M.L., Pulgarín, B., (1995) 'Cadena volcánica de los Coconucos (Colombia): Centros eruptivos y productos recientes', Boletín Geológico, v 37 (1-3), p 17 – 51.

Monsalve, M.L., (2000) 'Catalogo de las volcánicas Neógenas de Colombia, Fascículo Formación Coconucos', INGEOMINAS, 32 p.

Monsalve, M. L. *et al.* (2015) 'Firma Adakítica en los productos recientes de los volcanes Nevado del Huila y Puracé, Colombia', *Boletín Geológico*. doi: 10.32685/0120-1425/boletingeo.43.2015.27.

Monsalve, M. L., Ortiz, I. D. and Norini, G. (2019) 'El Escondido, a newly identified silicic Quaternary volcano in the NE region of the northern volcanic segment (Central Cordillera of Colombia)', *Journal of Volcanology and Geothermal Research*. Elsevier B.V., 383, pp. 47–62. doi: 10.1016/j.jvolgeores.2017.12.010.

Montes, C. *et al.* (2012) 'Evidence for middle Eocene and younger land emergence in central Panama: Implications for Isthmus closure', *Bulletin of the Geological Society of America*, 124(5–6), pp. 780–799. doi: 10.1130/B30528.1.

Montes, C. *et al.* (2015) 'Middle Miocene closure of the Central American Seaway', *Science*. doi: 10.1126/science.aaa2815.

Mori, Y., Shigeno, M. and Nishiyama, T. (2014) 'Fluid-metapelite interaction in an ultramafic mélange: Implications for mass transfer along the slab-mantle interface in subduction zones', *Earth, Planets and Space*. doi: 10.1186/1880-5981-66-47.

Moyen, J.-F. F. and Martin, H. (2012) 'Forty years of TTG research', *Lithos*. Elsevier B.V., 148, pp. 312–336. doi: 10.1016/j.lithos.2012.06.010.

Moyen, J. F. (2009) 'High Sr/Y and La/Yb ratios: The meaning of the "adakitic

signature"', *Lithos*, 112(3–4), pp. 556–574. doi: 10.1016/j.lithos.2009.04.001.

Münker, C. *et al.* (2001) 'Separation of high field strength elements (Nb, Ta, Zr, Hf) and Lu from rock samples for MC-ICPMS measurements', *Geochemistry, Geophysics, Geosystems*. doi: 10.1029/2001GC000183.

Müntener, O., Kelemen, P. B. and Grove, T. L. (2001) 'The role of H2O during crystallization of primitive arc magmas under uppermost mantle conditions and genesis of igneous pyroxenites: An experimental study', *Contributions to Mineralogy and Petrology*. doi: 10.1007/s004100100266.

Murcia, H., Borrero, C. and Németh, K. (2019) 'Overview and plumbing system implications of monogenetic volcanism in the northernmost Andes' volcanic province', *Journal of Volcanology and Geothermal Research*. Elsevier B.V., 383, pp. 77–87. doi: 10.1016/j.jvolgeores.2018.06.013.

Murcia, H. F. *et al.* (2010) 'TITAN2D simulations of pyroclastic flows at Cerro Machín Volcano, Colombia: Hazard implications', *Journal of South American Earth Sciences*, 29(2), pp. 161–170. doi: 10.1016/j.jsames.2009.09.005.

Naranjo, A. *et al.* (2018) 'La Colosa Au porphyry deposit, Colombia: Mineralization styles, structural controls, and age constraints', *Economic Geology*. doi: 10.5382/econgeo.2018.4562.

Neill, I. *et al.* (2011) 'Origin of the Aves ridge and Dutch-Venezuelan Antilles: Interaction of the cretaceous "Great Arc" and Caribbean-Colombian oceanic plateau?', *Journal of the Geological Society*, 168(2), pp. 333–347. doi: 10.1144/0016-76492010-067.

Neill, I., Kerr, A. C., Hastie, A. R., Pindell, J. L., & Millar, I. L. (2013). The Albian-Turonian island arc rocks of Tobago, West Indies: Geochemistry, petrogenesis, and Caribbean plate tectonics. *Journal of Petrology*.

https://doi.org/10.1093/petrology/egt025

Neill, I., Kerr, A. C., Hastie, A. R., Pindell, J. L., Millar, I. L., & Atkinson, N. (2012). Age and petrogenesis of the lower Cretaceous North Coast Schist of Tobago, a fragment of the proto-Greater antilles inter-American arc system. *Journal of Geology*. https://doi.org/10.1086/665798

Nerlich, R., Clark, S. R. and Bunge, H. P. (2014) 'Reconstructing the link between the Galapagos hotspot and the Caribbean Plateau', *GeoResJ*. doi: 10.1016/j.grj.2014.02.001.

Nivia, A. *et al.* (2006) 'The Quebradagrande Complex: A Lower Cretaceous ensialic marginal basin in the Central Cordillera of the Colombian Andes', *Journal of South American Earth Sciences*, 21(4), pp. 423–436. doi: 10.1016/j.jsames.2006.07.002.

Nowell, G. and Parrish, R. R. (2007) 'Simultaneous acquisition of isotope compositions and parent/daughter ratios by non-isotope dilution-mode plasma ionisation muti-colector mass spectrometry (PIMMS)', in *Plasma Source Mass Spectrometry*. doi: 10.1039/9781847551696-00298.

Oneill, C. *et al.* (2006) 'The nature of subduction on the early Earth', *Geochimica et Cosmochimica Acta*, 70(18), p. A458. doi: 10.1016/j.gca.2006.06.922.

Osorio, P. *et al.* (2018a) 'Campo Volcánico Monogenético Villamaría-Termales, Cordillera Central, Andes colombianos (Parte II): Características composicionales', *Revista Boletín de Geología*, 40(3), pp. 103–123. doi: 10.18273/revbol.v40n3-2018006.

Osorio, P. *et al.* (2018b) 'Campo Volcánico Monogenético Villamaría-Termales, Cordillera Central, Andes colombianos (Parte II): Características composicionales ', *Boletin de Geología* . scieloco , pp. 103–123.

de Paoli, M. C. *et al.* (2009) 'The eclogite-granulite transition: Mafic and intermediate

assemblages at Breaksea sound, New Zealand', *Journal of Petrology*. doi: 10.1093/petrology/egp078.

Pardo, N. *et al.* (2019) 'Facing geological mapping at low-latitude volcanoes: The Doña Juana Volcanic Complex study-case, SW-Colombia', *Journal of Volcanology and Geothermal Research*. Elsevier B.V., 385, pp. 46–67. doi: 10.1016/j.jvolgeores.2018.04.016.

Peacock, S. M., Rushmer, T. and Thompson, A. B. (1994) 'Partial melting of subducting oceanic crust', *Earth and Planetary Science Letters*. doi: 10.1016/0012-821X(94)90042-6.

Pearce, J. A. (1983). Role of the sub-continental lithosphere in magma genesis at active continental margins. *Continental Basalts and Mantle Xenoliths*.

Pennington, W. D. (1981) 'Subduction of the eastern Panama basin and seismotectonics of northwestern South America.', *Journal of Geophysical Research*. doi: 10.1029/JB086iB11p10753.

Perfit, M. R. *et al.* (1980) 'Chemical characteristics of island-arc basalts: Implications for mantle sources', *Chemical Geology*, 30(3), pp. 227–256. doi: 10.1016/0009-2541(80)90107-2.

Petford, N. and Atherton, M. (1996) 'Na-rich Partial Melts from Newly Underplated Basaltic Crust: the Cordillera Blanca Batholith, Peru', *Journal of Petrology*, 37(6), pp. 1491–1521. doi: 10.1093/petrology/37.6.1491.

Petterson, M. G. *et al.* (1999) 'Geological-tectonic framework of Solomon Islands, SW Pacific: Crustal accretion and growth within an intra-oceanic setting', *Tectonophysics*, 301(1–2), pp. 35–60. doi: 10.1016/S0040-1951(98)00214-5.

Pindell, J. *et al.* (2005) 'Plate-kinematics and crustal dynamics of circum-Caribbean arc-continent interactions: Tectonic controls on basin development in Proto-

Caribbean margins', *Special Paper of the Geological Society of America*. doi: 10.1130/0-8137-2394-9.7.

Pindell, J. *et al.* (2006) 'Foundations of Gulf of Mexico and Caribbean evolution: Eight controversies resolved', *Geologica Acta*, 4(1–2), pp. 303–341. doi: 10.1144/SP328.1.

Pindell, J. *et al.* (2012) 'The Greater Antillean Arc: Early Cretaceous origin and proposed relationship to Central American subduction mélanges: Implications for models of Caribbean evolution', *International Geology Review*. doi: 10.1080/00206814.2010.510008.

Pindell, J. and Kennan, L. (2001) 'Processes and Events in the Terrane Assembly of Trinidad and Eastern Venezuela', in *Petroleum Systems of Deep-Water Basins: Global and Gulf of Mexico Experience: 21st Annual*. doi: 10.5724/gcs.01.21.0159.

Pinzón, C. *et al.* (2018) 'Petrogénesis y condiciones de cristalización del domo intracratérico del volcán Cerro Bravo, Colombia', *Revista Boletín de Geología*, 40(3), pp. 67–84. doi: 10.18273/revbol.v40n3-2018004.

Pirard, C., Hermann, J. and O'neill, H. S. C. (2013) 'Petrology and geochemistry of the crust-mantle boundary in a Nascent Arc, Massif du Sud Ophiolite, New Caledonia, SW Pacific', *Journal of Petrology*. doi: 10.1093/petrology/egt030.

Plank, T. (2005) 'Constraints from Thorium/Lanthanum on sediment recycling at subduction zones and the evolution of the continents', *Journal of Petrology*. doi: 10.1093/petrology/egi005.

Plank, T., Cooper, L. B. and Manning, C. E. (2009) 'Emerging geothermometers for estimating slab surface temperatures', *Nature Geoscience*. doi: 10.1038/ngeo614.

Plank, T. and Langmuir, C. H. (1988) 'An evaluation of the global variations in the major element chemistry of arc basalts', *Earth and Planetary Science Letters*. doi: 10.1016/0012-821X(88)90135-5.

Plank, T. and Langmuir, C. H. (1993) ‘Tracing trace elements from sediment input to volcanic output at subduction zones’, *Nature*. doi: 10.1038/362739a0.

Plank, T. and Langmuir, C. H. (1998) ‘The chemical composition of subducting sediment and its consequences for the crust and mantle’, *Chemical Geology*. doi: 10.1016/S0009-2541(97)00150-2.

Poveda, E., Monsalve, G. and Vargas, C. A. (2015) ‘Receiver functions and crustal structure of the northwestern Andean region, Colombia’, *Journal of Geophysical Research: Solid Earth*. doi: 10.1002/2014JB011304.

Profeta, L. *et al.* (2015) ‘Quantifying crustal thickness over time in magmatic arcs’, *Scientific Reports*, 5(1), p. 17786. doi: 10.1038/srep17786.

Pulgarín, A. B. A. *et al.* (2017) *GEOLOGÍA Y ESTRATIGRAFÍA DEL COMPLEJO VOLCÁNICO PARAMILLO DE SANTA ROSA*.

Pulgarín, B. *et al.* (2009) *INFORME DE AVANCE GEOLOGÍA Y ESTRATIGRAFÍA DEL COMPLEJO VOLCÁNICO SOTARÁ, COLOMBIA*.

Ramírez, C. 1982. ‘El vulcanismo Neogénico y Cuaternario de Colombia: cronología y caracterización químico-petrográfica’, Tesis de grado. Universidad Nacional de Colombia, Bogotá, 207p.

Ramos, V. A. (2009) ‘Anatomy and global context of the Andes: Main geologic features and the Andean orogenic cycle’, in *Memoir of the Geological Society of America*. doi: 10.1130/2009.1204(02).

Rapp, R. P. and Watson, E. B. (1995) ‘Dehydration melting of metabasalt at 8-32 kbar: Implications for continental growth and crust-mantle recycling’, *Journal of Petrology*. doi: 10.1093/petrology/36.4.891.

Restrepo-Pace, P. a. *et al.* (1997) ‘Geochronology and Nd isotopic data of Grenville-age rocks in the Colombian Andes: new constraints for Late Proterozoic-Early

Paleozoic paleocontinental reconstructions of the Americas', *Earth and Planetary Science Letters*, 150(3–4), pp. 427–441. doi: 10.1016/S0012-821X(97)00091-5.

Restrepo-Pace, P. A. and Cediel, F. (2010) 'Northern South America basement tectonics and implications for paleocontinental reconstructions of the Americas', *Journal of South American Earth Sciences*, 29(4), pp. 764–771. doi: 10.1016/j.jsames.2010.06.002.

Reubi, O. *et al.* (2011) 'Assimilation of the plutonic roots of the Andean arc controls variations in U-series disequilibria at Volcan Llaima, Chile', *Earth and Planetary Science Letters*. doi: 10.1016/j.epsl.2010.12.018.

Reubi, O. and Blundy, J. (2009) 'A dearth of intermediate melts at subduction zone volcanoes and the petrogenesis of arc andesites', *Nature*. doi: 10.1038/nature08510.

Ribeiro, J. M., Maury, R. C. and Grégoire, M. (2016) 'Are adakites slab melts or high-pressure fractionated mantle melts?', *Journal of Petrology*. doi: 10.1093/petrology/egw023.

Richards, J. P., & Kerrich, R. (2007). Special paper: Adakite-like rocks: Their diverse origins and questionable role in metallogenesis. *Economic Geology*, *102*(4), 537–576. https://doi.org/10.2113/gsecongeo.102.4.537

Ringwood, A. E. (1974) 'The petrological evolution of island arc systems', *Journal of the Geological Society*. doi: 10.1144/gsjgs.130.3.0183.

Ringwood, A. E. and Green, D. H. (1966) 'An experimental investigation of the Gabbro-Eclogite transformation and some geophysical implications', *Tectonophysics*. doi: 10.1016/0040-1951(66)90009-6.

Roberts, N. M. W. *et al.* (2015) 'Continent formation through time', *Geological Society Special Publication*, 389(1), pp. 1–16. doi: 10.1144/SP389.13.

Rodriguez-Vargas, A. *et al.* (2005) 'Mantle diversity beneath the Colombian Andes,

Northern Volcanic Zone: Constraints from Sr and Nd isotopes', *Lithos*, 82(3–4), pp. 471–484. doi: 10.1016/j.lithos.2004.09.027.

Rodríguez García, G. and Zapata García, G. (2012) 'Características del plutonismo Mioceno Superior en el segmento norte de la Cordillera Occidental e implicaciones tectónicas en el modelo geológico del Noroccidente colombiano', *Boletín de Ciencias de la Tierra*, (31), pp. 5–22.

Rollinson, H. R. (1993) *Using Geochemical Data: Evaluation, Presentation, Interpretation*. 1st Editio. Longman.

Rudnick, R. L. (1995) 'Making continental crust', *Nature*. doi: 10.1038/378571a0.

Rudnick, R. L. and Fountain, D. M. (1995) 'Nature and composition of the continental crust: A lower crustal perspective', *Reviews of Geophysics*. doi: 10.1029/95RG01302.

Rudnick, R. L. and Gao, S. (2013) *Composition of the Continental Crust*. 2nd edn, *Treatise on Geochemistry: Second Edition*. 2nd edn. Elsevier Ltd. doi: 10.1016/B978-0-08-095975-7.00301-6.

Rudnick, R. L. and Presper, T. (1990) 'Geochemistry of intermediate/- to high-pressure granulites', *Granulites and crustal evolution*. doi: 10.1007/978-94-009-2055-2_27.

Rüpke, L. H. *et al.* (2004) 'Serpentine and the subduction zone water cycle', *Earth and Planetary Science Letters*. doi: 10.1016/j.epsl.2004.04.018.

Saleeby, J., Ducea, M. and Clemens-Knott, D. (2003) 'Production and loss of high-density batholithic root, southern Sierra Nevada, California', *Tectonics*. doi: 10.1029/2002tc001374.

Sawka, W. N. and Chappell, B. W. (1988) 'Fractionation of uranium, thorium and rare earth elements in a vertically zoned granodiorite: Implications for heat production

distributions in the Sierra Nevada batholith, California, U.S.A.', *Geochimica et Cosmochimica Acta*. doi: 10.1016/0016-7037(88)90267-0.

Schiano, P. *et al.* (2010) 'Simple mixing as the major control of the evolution of volcanic suites in the Ecuadorian Andes', *Contributions to Mineralogy and Petrology*. doi: 10.1007/s00410-009-0478-2.

Schmidt, M. W. and Poli, S. (1998) 'Experimentally based water budgets for dehydrating slabs and consequences for arc magma generation', *Earth and Planetary Science Letters*. doi: 10.1016/S0012-821X(98)00142-3.

Schmitz, M. (1994) 'A balanced model of the southern Central Andes', *Tectonics*. doi: 10.1029/93TC02232.

Sertek, J. P., Andrade, S. and Ulbrich, H. H. (2015) 'An Evaluation of the Effects of Primary and Cross-Contamination during the Preparation of Rock Powders for Chemical Determinations', *Geostandards and Geoanalytical Research*, 39(3), pp. 381–397. doi: 10.1111/j.1751-908X.2014.00324.x.

Sigurdsson, H. *et al.* (1990) 'Pre-eruption compositional gradients and mixing of andesite and dacite magma erupted from Nevado del Ruiz Volcano, Colombia in 1985', *Journal of Volcanology and Geothermal Research*, 41(1–4), pp. 127–151. doi: http://dx.doi.org/10.1016/0377-0273(90)90086-U.

Sinton, C. W. *et al.* (1998) 'An oceanic flood basalt province within the Caribbean plate', *Earth and Planetary Science Letters*. doi: 10.1016/s0012-821x(97)00214-8.

Skora, S. and Blundy, J. (2010) 'High-pressure hydrous phase relations of radiolarian clay and implications for the involvement of subducted sediment in arc magmatism', *Journal of Petrology*. doi: 10.1093/petrology/egq054.

Smith, D. J. *et al.* (2009) 'The petrogenesis of sodic island arc magmas at Savo volcano, Solomon Islands', *Contributions to Mineralogy and Petrology*, 158(6), pp.

785–801. doi: 10.1007/s00410-009-0410-9.

Smith, D. J. (2014) ‘Clinopyroxene precursors to amphibole sponge in arc crust’, *Nature Communications*. doi: 10.1038/ncomms5329.

Solano, J. M. S., Jackson, M. D., Sparks, R. S. J., Blundy, J. D., & Annen, C. (2012). Melt segregation in deep crustal hot zones: A mechanism for chemical differentiation, crustal assimilation and the formation of evolved magmas. *Journal of Petrology*. https://doi.org/10.1093/petrology/egs041

Sørensen, E. V. and Holm, P. M. (2008) ‘Petrological inferences on the evolution of magmas erupted in the Andagua Valley, Peru (Central Volcanic Zone)’, *Journal of Volcanology and Geothermal Research*. doi: 10.1016/j.jvolgeores.2008.05.021.

Spandler, C. and Pirard, C. (2013) ‘Element recycling from subducting slabs to arc crust: A review’, *Lithos*. doi: 10.1016/j.lithos.2013.02.016.

Spikings, R. *et al.* (2015) ‘The geological history of northwestern South America: From Pangaea to the early collision of the Caribbean Large Igneous Province (290-75 Ma)’, *Gondwana Research*. doi: 10.1016/j.gr.2014.06.004.

Stern, C. R. (2004) ‘Active Andean volcanism: Its geologic and tectonic setting’, *Revista Geologica de Chile*. doi: 10.4067/S0716-02082004000200001.

Stern, R. J. (2002) ‘Subduction zones’, *Reviews of Geophysics*. doi: 10.1029/2001RG000108.

Stolper, E. and Newman, S. (1994) ‘The role of water in the petrogenesis of Mariana trough magmas’, *Earth and Planetary Science Letters*. doi: 10.1016/0012-821X(94)90074-4.

Streck, M. J., Leeman, W. P. and Chesley, J. (2007) ‘High-magnesian andesite from Mount Shasta: A product of magma mixing and contamination, not a primitive mantle melt’, *Geology*. doi: 10.1130/G23286A.1.

Summerfield, M. A. (2014) *Global geomorphology*, *Global Geomorphology*. doi: 10.4324/9781315841182.

Sun, S.-S. and McDonough, W. F. (1989) 'Chemical and isotopic systematics of oceanic basalts: implications for mantle composition and processes', *Geological Society, London, Special Publications*, 42, pp. 313–345.

Syracuse, E. M. *et al.* (2010) 'The global range of subduction zone thermal models', *Physics of the Earth and Planetary Interiors*. doi: 10.1016/j.pepi.2010.02.004.

Syracuse, E. M. and Abers, G. A. (2006) 'Global compilation of variations in slab depth beneath arc volcanoes and implications', *Geochemistry, Geophysics, Geosystems*. doi: 10.1029/2005GC001045.

Taboada, A. *et al.* (2000) 'Geodynamics of the northern Andes', *Tectonics*.

Taira, A. *et al.* (1998) 'Nature and growth rate of the Northern Izu–Bonin (Ogasawara) arc crust and their implications for continental crust formation', *Island Arc*. John Wiley & Sons, Ltd, 7(3), pp. 395–407. doi: 10.1111/j.1440-1738.1998.00198.x.

Takahashi, N. *et al.* (2007) 'Crustal structure and evolution of the Mariana intra-oceanic island arc', *Geology*. doi: 10.1130/G23212A.1.

Tang, M. *et al.* (2019) 'Nb/Ta systematics in arc magma differentiation and the role of arclogites in continent formation', *Nature Communications*. Springer US, 10(1). doi: 10.1038/s41467-018-08198-3.

Tatsumi, Y. *et al.* (1983) 'Generation of arc basalt magmas and thermal structure of the mantle wedge in subduction zones (Japan arc).', *Journal of Geophysical Research*. doi: 10.1029/JB088iB07p05815.

Tatsumi, Y. (1989) 'Migration of fluid phases and genesis of basalt magmas in subduction zones', *Journal of Geophysical Research*. doi:

10.1029/JB094iB04p04697.

Tatsumi, Y. (2012) ‘The andesite problem: Why is this planet to be the Earth?’, in *American Geophysical Union, Fall Meeting 2012, abstract id. V22A-01*. doi: 2012AGUFM.V22A..01T.

Tatsumi, Y. and Eggins, S. (1995) ‘Subduction zone magmatism’, *Subduction zone magmatism*.

Tatsumi, Y. and Kogiso, T. (1997) ‘Trace element transport during dehydration processes in the subducted oceanic crust: 2. Origin of chemical and physical characteristics in arc magmatism’, *Earth and Planetary Science Letters*. doi: 10.1016/s0012-821x(97)00019-8.

Tatsumi, Y. and Kogiso, T. (2003) ‘The subduction factory: its role in the evolution of the Earth’s crust and mantle’, *Geological Society, London, Special Publications*, 219(1), pp. 55–80. doi: 10.1144/GSL.SP.2003.219.01.03.

Taylor, S. . and McLennan, S. . (1995) ‘The geochemical evolution of the continental crust’, *Reviews of Geophysics*, 33(2), pp. 241–265. doi: 10.1029/95RG00262.

Thorkelson, D. J. (1996) ‘Subduction of diverging plates and the principles of slab window formation’, *Tectonophysics*. doi: 10.1016/0040-1951(95)00106-9.

Thorpe, R. S. (1982) ‘Andesites: Orogenic Andesites and Related Rocks.’ doi: 10.1016/0377-0273(83)90135-x.

Thouret, J. C. (1990) ‘Effects of the November 13, 1985 eruption on the snow pack and ice cap of Nevado del Ruiz volcano, Colombia’, *Journal of Volcanology and Geothermal Research*, 41(1–4), pp. 177–201. doi: 10.1016/0377-0273(90)90088-W.

Thouret, J. C. *et al.* (1990) ‘Quaternary eruptive history of Nevado del Ruiz (Colombia)’, *Journal of Volcanology and Geothermal Research*, 41(1–4), pp. 225–251. doi: 10.1016/0377-0273(90)90090-3.

Tistl, M. *et al.* (1994) ‘Origin and emplacement of Tertiary ultramafic complexes in northwest Colombia: Evidence from geochemistry and KAr, SmNd and RbSr isotopes’, *Earth and Planetary Science Letters*, 126(1–3), pp. 41–59. doi: 10.1016/0012-821X(94)90241-0.

Tonarini, S., Leeman, W. P. and Leat, P. T. (2011) ‘Subduction erosion of forearc mantle wedge implicated in the genesis of the South Sandwich Island (SSI) arc: Evidence from boron isotope systematics’, *Earth and Planetary Science Letters*. Elsevier B.V., 301(1–2), pp. 275–284. doi: 10.1016/j.epsl.2010.11.008.

Torres, M. P., Ibáñez, D., Vásquez, E., (1992) ‘Geología y estratigrafía de la Formación Popayán’, Informe interno INGEOMINAS, 85 p.

Torres, M. P., Monsalve. M.L., Pulgarín, B., Cepeda, H., (1999) ‘Caldera de Paletará: Aproximación a la fuente de las ignimbritas del Cauca y Huila’, Boletín Geológico de INGEOMINAS, v 37, p 1 – 15.

Torres, M.P., Monsalve, M.L., Pulgarín, B. y Toro, G. (2011) ‘Caldera de Paletará: Fuente de un voluminoso vulcanismo riolítico en la Cordillera Central de Colombia’, Memorias XIV Congreso Latinoamericano de Geología XIII Congreso Colombiano de Geología, 29 de Agosto al 2 de Septiembre, Medellín, Colombia, pp.188.

Toro-Toro, L. M., Fernando, L. and Carmona, A. (2010) ‘PETROGRAFÍA Y GEOQUÍMICA DE LAS ROCAS ANCESTRALES DEL VOLCÁN NEVADO DEL RUIZ’, *Boletin de Geologia*, 32, pp. 95–105.

Toro, L., Alvarán, M. and Borrero, C. (2008) ‘Rocas con afinidad adakítica al sur-este de Manizales: rasgos petrogenéticos y geoquímicos’, *Boletín de*, 30. Available at: http://www.scielo.org.co/scielo.php?pid=S0120-02832008000200004&script=sci_abstract.

Toussaint, J. F. and Restrepo, J. J. (1982) ‘Magmatic evolution of the northwestern

Andes of Colombia', *Earth Science Reviews*. doi: 10.1016/0012-8252(82)90037-X.

Turner, S. J. and Langmuir, C. H. (2015a) 'The global chemical systematics of arc front stratovolcanoes: Evaluating the role of crustal processes', *Earth and Planetary Science Letters*, 422(October), pp. 182–193. doi: 10.1016/j.epsl.2015.03.056.

Turner, S. J. and Langmuir, C. H. (2015b) 'What processes control the chemical compositions of arc front stratovolcanoes?', *Geochemistry, Geophysics, Geosystems*, 16(October), pp. 1865–1893. doi: 10.1002/2014GC005633.

Ulmer, P. and Trommsdorff, V. (1995) 'Serpentine stability to mantle depths and subduction-related magmatism', *Science*. doi: 10.1126/science.268.5212.858.

Vallejo, C. *et al.* (2006) 'The early interaction between the Caribbean Plateau and the NW South American Plate', *Terra Nova*, 18(4), pp. 264–269. doi: 10.1111/j.1365-3121.2006.00688.x.

Vargas, C. A. *et al.* (2017) 'Breathing of the Nevado del Ruiz volcano reservoir, Colombia, inferred from repeated seismic tomography', *Scientific Reports*. doi: 10.1038/srep46094.

Vargas, C. A. and Mann, P. (2013) 'Tearing and breaking off of subducted slabs as the result of collision of the panama arc-indenter with Northwestern South America', *Bulletin of the Seismological Society of America*. doi: 10.1785/0120120328.

Vatin-Pérignon, N. *et al.* (1988) 'Magmatic evolution of the Nevado del Ruiz volcano, Central Cordillera, Colombia: Mineral chemistry and geochemistry', *Géodynamique, ORSTOM*, 3(1–2), pp. 163–194.

Vatin-Pérignon, N., Goemans, P., Oliver, R. A., & Palacio, E. P. (1990). Evaluation of magmatic processes for the products of the Nevado del Ruiz Volcano, Colombia from geochemical and petrological data. *Journal of Volcanology and Geothermal Research*. https://doi.org/10.1016/0377-0273(90)90087-V

Villagómez, D. *et al.* (2011) ‘Geochronology, geochemistry and tectonic evolution of the Western and Central cordilleras of Colombia’, *Lithos*. Elsevier B.V., 125(3–4), pp. 875–896. doi: 10.1016/j.lithos.2011.05.003.

Villagómez, D. and Spikings, R. (2013) ‘Thermochronology and tectonics of the Central and Western Cordilleras of Colombia: Early Cretaceous-Tertiary evolution of the Northern Andes’, *Lithos*. Elsevier B.V., 160–161(1), pp. 228–249. doi: 10.1016/j.lithos.2012.12.008.

Vogel, T. A. *et al.* (2006) ‘Origin of silicic magmas along the Central American volcanic front: Genetic relationship to mafic melts’, *Journal of Volcanology and Geothermal Research*, 156(3–4), pp. 217–228. doi: 10.1016/j.jvolgeores.2006.03.002.

Wagner, L. S. *et al.* (2017) ‘Transient slab flattening beneath Colombia’, *Geophysical Research Letters*. doi: 10.1002/2017GL073981.

Weber, M. *et al.* (2015) ‘Geochemistry of the Santa Fé Batholith and Buriticá Tonalite in NW Colombia – Evidence of subduction initiation beneath the Colombian Caribbean Plateau’, *Journal of South American Earth Sciences*, 62, pp. 257–274. doi: 10.1016/j.jsames.2015.04.002.

Weber, M. B. I. *et al.* (2002) ‘Crustal make-up of the northern Andes : evidence based on deep’, 345, pp. 49–82.

Wegner, W. *et al.* (2011) ‘Magmatic history and evolution of the Central American Land Bridge in Panama since Cretaceous times’, *Bulletin of the Geological Society of America*, 123(3–4), pp. 703–724. doi: 10.1130/B30109.1.

Wendlandt, E., DePaolo, D. J. and Scott Baldridge, W. (1993) ‘Nd and Sr isotope chronostratigraphy of Colorado Plateau lithosphere: implications for magmatic and tectonic underplating of the continental crust’, *Earth and Planetary Science Letters*.

doi: 10.1016/0012-821X(93)90043-9.

Williams, M. *et al.* (2017) 'Correlation of eruptive products, Volcán Azufral, Colombia: Implications for rapid emplacement of domes and pyroclastic flow units', *Journal of Volcanology and Geothermal Research*. Elsevier B.V., 341, pp. 21–32. doi: 10.1016/j.jvolgeores.2017.05.001.

Wolf, M. B. and Wyllie, P. J. (1994) 'Dehydration-melting of amphibolite at 10 kbar: the effects of temperature and time', *Contributions to Mineralogy and Petrology*. doi: 10.1007/BF00320972.

Woodcock, N. H., Soper, N. J., & Miles, A. J. (2019). Age of the acadian deformation and devonian granites in northern england: A review. In *Proceedings of the Yorkshire Geological Society*. https://doi.org/10.1144/pygs2018-009

Woodhead, J. D. (1988) 'The origin of geochemical variations in mariana lavas: A general model for petrogenesis in intra-oceanic island arcs?', *Journal of Petrology*. doi: 10.1093/petrology/29.4.805.

Workman, R. K. and Hart, S. R. (2005) 'Major and trace element composition of the depleted MORB mantle (DMM)', *Earth and Planetary Science Letters*. doi: 10.1016/j.epsl.2004.12.005.

Wright, J. E. and Wyld, S. J. (2011) 'Late cretaceous subduction initiation on the eastern margin of the caribbean-colombian oceanic plateau: One great arc of the caribbean(?)', *Geosphere*. doi: 10.1130/GES00577.1.

Wyllie, P. J. (1973) 'Experimental petrology and global tectonics -A preview', *Tectonophysics*. doi: 10.1016/0040-1951(73)90002-4.

Wyllie, P. J. and Sekine, T. (1982) 'The formation of mantle phlogopite in subduction zone hybridization', *Contributions to Mineralogy and Petrology*. doi: 10.1007/BF01132067.

Yogodzinski, G. M. *et al.* (2001) ‘Geochemical evidence for the melting of subducting oceanic lithosphere at plate edges’, *Nature*. doi: 10.1038/35054039.

Yogodzinski, G. M. and Kelemen, P. B. (1998) ‘Slab melting in the Aleutians: implications of an ion probe study of clinopyroxene in primitive adakite and basalt’, *Earth and Planetary Science Letters*. doi: 10.1016/S0012-821X(98)00041-7.

Zandt, G. *et al.* (2004) ‘Active foundering of a continental arc root beneath the southern Sierra Nevada in California’, *Nature*. doi: 10.1038/nature02847.

Zapata, G. and Rodríguez, G. (2011) ‘Basalto de El Botón, Miocene volcanic arc of shoshonitic affinity to the north of Cordillera Occidental of Colombia’, *Boletín de Ciencias de la Tierra*.

Zarifi, Z., Havskov, J. and Hanyga, A. (2007) ‘An insight into the Bucaramanga nest’, *Tectonophysics*, 443(1–2), pp. 93–105. doi: 10.1016/j.tecto.2007.06.004.

Appendix A: Extended Thin Section Descriptions

Northern Volcanic Province:

Cerro Bravo Samples:

UB-03 (Letras):

Phenocryst phases composed of plagioclase, hornblende and clinopyroxene with pyroxene most predominant (and preferentially altered). Phenocryst phases are typically general far smaller and more poorly formed than in younger Cerro Bravo samples (c.f.: DC16-006). Texturally, the sample is dominated by a trachytic groundmass defined by small laths of feldspar. The pyroxene phenocrysts appear to have been preferentially removed and appear as voids in section.

DC16-006 (Basal):

Phenocryst phases consist of euhedral plagioclase, euhedral to subhedral amphibole euhedral biotite and orthopyroxene. Microphenocrysts phases consist of subhedral pyroxenes and opaque minerals. Groundmass is glassy with microcrystalline phases, predominantly amphibole, plagioclase and pyroxene. Sample itself is highly vesicular, with vesicles making up the majority of the section (>50%).

VMTVF Samples:

DC16-009 (VMTVF Group 1):

Groundmass dominated sample, with this composed of microcrystals and microliths of olivine, pyroxene and plagioclase. These mafic minerals and groundmass as a whole make up >80% of the sample. Olivine is the only major phenocryst phase, with sparse crystals up to 3 mm. A tracytic texture is observed in the groundmass, similar to sample UB-03, defined by plagioclase and to a lesser extent pyroxene microliths.

UB-16 (VMTVF Group 3):

Porphyritic sample with phenocrysts of euhedral plagioclase, euhedral quartz and pyroxene (orthopyroxene and clinopyroxene) along with microphenocrysts of amphibole with opaque reaction rims. Plagioclase phenocrysts display abundant disequilibrium textures, especially sieve and honeycomb textures. Groundmass is devitrified where glass is present but largely cryptocrystalline to microcrystalline. The modal abundance of quartz in this sample of Gallinazo dome appears to accord with previous reports of higher modal proportions compared to other domes and areas of the VMTVF sampled (i.e.: UB-17, see also Osorio et al. 2018b).

UB-17 (VMTVF Group 3):

Porphyritic sample with phenocrysts of euhedral pyroxene, which varies in size from <1 – 3 mm but is most numerous, subhedral plagioclase (up to >500 μm) and subhedral amphibole microphenocrysts (<1 mm). The groundmass is is micro- to cryptocrystalline and composed of microliths of plagioclase and pyroxene. Disequilibrium sieve textures are observed in plagioclase. Reaction rims are

observed on both pyroxene and especially amphibole crystals and phenocrysts. Clinopyroxene also appears as anhedral inclusions within large plagioclase phenocrysts.

Nevado del Ruiz Samples:

UB-06 (Ruiz Ancestral):

Porphyritic rock with phenocrysts of clinopyroxene, plagioclase and orthopyroxene. Skeletal biotite is also observed, and microphenocrysts of biotite and amphibole are observed as accessory phases. Pyroxene glomerocrysts are also observed. Matrix is crypto- to microcrystalline, and composed of plagioclase and pyroxene microliths. These plagioclase microliths do in some instances define a subtle trachytic texture.

DC16-012 (Ruiz Ancestral):

Porphyritic rock in which plagioclase is the dominant phenocryst phase, with lesser proportions of smaller pyroxene, amphibole and biotite phenocrysts. Groundmass is glassier than other Ruiz Ancestral samples (i.e.: UB-06) with a lower proportion of crystalline groundmass observed. Plagioclase phenocrysts show abundant sieve textures. Alteration of microphenocrysts makes determining proportions of pyroxene, amphibole and biotite difficult in groundmass, though it is clear this is microcrystalline where these are present, but otherwise glassy and aphanitic.

DC16-021 (Ruiz Ancestral):

Altered sample with phenocryst phases of plagioclase, which where not altered to sericite show oscillatory zoning and inclusions similar to groundmass and in some cases pyroxene phenocrysts. Pyroxene (predominantly clinopyroxene) phenocrysts are also present in section, though these are commonly altered along with amphibole to chlorite and to epidote. Biotite and amphibole are also present in section as phenocryst and microphenocryst phases, along with opaques. Groundmass largely altered to clays and a secondary minerals.

Paramillo de Santa Rosa Samples:

DC16-019 (Pre-Paramillo de Santa Rosa/Tarapaca Formation):

Porphyritic sample composed of phenocrysts of plagioclase, orthopyroxene, amphibole. Pyroxenes and amphiboles display reaction rims (and some pseudomorphs) and microphenocrysts of clinopyroxene and plagioclase are also observed. Groundmass is microcrystalline and dominated by plagioclase microliths which form a minor trachytic flow texture in some parts of section. Microcrystalline matrix with skeletal plagioclase; and a higher content of amphibole microphenocrysts compared to other phases. A greater proportion of vitreous inclusions in plagioclase compared to the rest of the Tarapaca Formation is also recorded (c.f.: Pulgarin et al. 2017).

S.W. Colombian Arc Segments:

Purace Samples:

PKSW-16A:

Porphyritic rock dominated by euhedral to subhedral tabular laths of plagioclase phenocrysts between 1 – 4 mm. These make up ~60% of the crystalline proportion of the rock. Remaining phenocryst phases are orthopyroxene and clinopyroxene, in euhedral to subhedral laths and rounded crystals of 0.5 – 3 mm. Small phenocrysts of opaque minerals, Fe-Ti oxides are also observed <0.5 – 2 mm. Plagioclase shows albite and Carlsbad twinning, with disequilibrium textures of sieving and oscillatory zoning observed in the plagioclase phenocrysts. Orthopyroxene phenocrysts contain inclusions of oxides (<0.5 mm), and pyroxene opaque joint glomerocrysts are observed in section in PKSW-16A. Groundmass is crypto- to microcrystalline, plagioclase microliths being the only visibly identifiable phases, with no defined flow textures.

PKSW-16B:

Similar to PKSW-16A with a glassy to cryptocrystalline groundmass and large plagioclase phenocrysts phase in similar proportions making up the bulk of the rock. Euhedral to subhedral orthopyroxene and clinopyroxene are the only other major phenocryst phases (0.5 – 3 mm), along with smaller amounts of microphenocrystic and phenocrystic (<1 – 2 mm) Fe-Ti oxides and opaque minerals. Plagioclase exhibits albite and Carlsbad twinning, as well as oscillatory zoning and sieve textures

in phenocrysts. Groundmass is crypto- to microcrystalline, with plagioclase microliths being the only visibly identifiable phases, with no defined flow textures. One minor occurrence of olivine (<1 mm) observed.

SESW-55B:

Porphyritic rock with primary phenocryst phases of euhedral to subhedral laths of plagioclase (1 – 3 mm) and subhedral orthopyroxene and clinopyroxene (<2 mm). Larger plagioclase crystals (>1 mm) show prominent disequilibrium textures such as oscillatory zoning and sieve textures, especially near their rims. This is distinct from smaller plagioclase phenocrysts and microliths which do not show these features. Small inclusions of opaques (<0.5 mm) are entrained within plagioclase and pyroxene phenocrysts. Groundmass is a smaller proportion of the sample than phenocryst and crystalline phases and is composed of microcrystalline laths of plagioclase with some small pyroxenes, all at random orientations with no discernable flow textures.

SESW-106A:

Porphyritic rock with phenocrysts of plagioclase, orthopyroxene and clinopyroxene very similar to SESW-55B, though in this sample there is a greater proportion of groundmass compared to crystalline phases. Additionally, pyroxene glomerocrysts are observed in section. Groundmass is glassy, within which there are are oikilitic

crystals <0.5 mm. Groundmass is composed of microcrystalline laths of plagioclase and pyroxene, with no flow textures.

Sotara Samples:

JLSW-032B:

Porphyritic and hypocrystalline, and have a large or dominant groundmass component, which is altered to amorphous silica. Main phases are euhedral to anhedral plagioclase crystals 2 – 5 mm, alongside phenocrysts of minor pyroxene and opaque minerals. Plagioclase phenocrysts exhibit Carlsbad twinning and oscillatory zoning textures.

LHSW-17B:

Porphyritic and hypocrystalline rock dominanted by groundmass. Major phenocryst phases are euhedral to anhedral plagioclase crystals (2 – 5 mm) and euhedral crystals of biotite (up to 3 mm) and amphibole and pyroxene (<1 – 3 mm). Plagioclase phenocrysts Carlsbad twinning and oscillatory zoning textures are observed in plagioclase phenocrysts. Microphenocrysts (<1 mm) of subhedral amphibole and pyroxene, which both commonly show opaque altered rims, indicative of disequilibrium and alteration to oxides are observed in the groundmass, which is otherwise glassy to aphanitic.

LHSW-18F:

Porphyritic rock composed of euhedral to subhedral plagioclase crystals (2 – 5 mm) and subhedral biotite, amphibole and pyroxene (<1 – 3 mm). Plagioclase phenocrysts exhibit Carlsbad twinning and oscillatory zoning textures. Orthopyroxene occurs as microphenocrysts of ~1 – 1.5 mm. Similar in respect of phenocryst type and proportion to LHSW-17B, suggesting they are related. Subhedral plagioclase is also seen as inclusions and poikilitic to amphibole phenocrysts, possibly suggesting two generations of plagioclase crystallisation. However, plagioclase phenocrysts lack the lack sieve textures which are present in other Purace samples. Microliths of plagioclase, amphibole and pyroxene visible in the groundmass which is otherwise aphanitic.

Morasurco Sample:

DC16-024:

Holocrystalline porphyritic rock with principle phenocryst phases of plagioclase and lesser proportions of smaller crystals of clinopyroxene, orthopyroxene (all of which are 1 – 3 mm). Opaque oxide phases also occur as small, anhedral crystals (<1 mm). Plagioclase phenocrysts show both albite and Carlsbad twinning and strongly developed oscillatory zoning textures, especially in the largest phenocryst phases. Pyroxenes are found clumped together with minor anhedral opaques into glomoerocrysts. Groundmass is crypto- to microcrystalline, and largely composed of

plagioclase microliths which define a trachytic flow texture, which is otherwise aphanitic.

Galeras Samples:

DC16-034:

Porporphyritic rock in which plagioclase is present as large euhedral laths (1 – 3 mm) and is the dominant phenocryst phase. Remaining phenocrysts are subhedral to anhedral clinopyroxene and orthopyroxene (1 – 2 mm). Orthopyroxenes are less abundance than clinopyroxenes, though occur in similar proportions in the sample. Small anhedral opaques (<1 mm) are common in groundmass, and also as attachments to the edges of or inclusions within pyroxenes. The groundmass is microcrystalline and plagioclase microlith and opaque dominated.

DC16-037:

Porphyritic rock in which euhedral to subhedral plagioclase albite twinned phenocrysts and microphenocrysts (<1 – 3 mm) are almost the sole phenocryst phase observed. Only other phenocryst and microphenocryst phases are small opaque minerals and minor occurrences of pyroxene with distinct reaction rims. Disequilibrium textures area lso observed as sieve textures and some oscillatory zoning, abundant in plagioclase crystals >2 mm in both samples. Groundmass is microcrystalline and largely composed of plagioclase microliths which define a minor trachytic texture.

Bordoncillo Sample:

DC16-028:

Porphyritic rock with phenocryst phases of euhedral to subhedral plagioclase (<4 mm) and euhedral crystals of pyroxene and opaque minerals (1 – 3 mm). An overprint of clay and sericite alteration throughout the sample is observed, though crystal forms and some original textures are preserved. These include twinning and oscillatory zoning textures in plagioclase, as well as relict pyroxene phenocrysts with minor oikilitic inclusions of oxides. Groundmass consists of plagioclase microliths along with microphenocrysts of opaques and pyroxene, otherwise aphanitic.

Azufral Sample:

DC16-039:

Porphyritic rock, made up of phenocrysts of plagioclase (1 – 3 mm), orthopyroxene and clinopyroxene (<1 – 2 mm) and generally smaller opaque accessory minerals. However, in one case (possibly as a xenocryst of an Fe-Ti phase) these opaque minerals can be much larger, up to 3 mm, but far more commonly are present as <1 mm phases. The majority of the groundmass is made up of plagioclase microliths, with minor pyroxenes, but is otherwise aphanitic and these minerals do not define any flow texture or cumulate.

Miocene Arc and Basement:

El Boton Basalt Sample:

DB15-082:

Phaneritic rock, dominated by interlocked phenocrysts of plagioclase, euhedral clinopyroxene (augite) and, in rare cases in section, <0.1 mm crystals of amphibole. Plagioclase occurs as large euhedral megaphenocrysts of up to 0.5 cm in places, but varies greatly in size in section, down to microphenocryst scale. Euhedral to subhedral clinopyroxenes are <1 mm - 2 mm, whilst opaque phases are anhedral and of <0.1 to 1 mm. Plagioclase commonly displays albite twinning, and Carlsbad twinning less frequently. Clinopyroxene is identified as augite, and is euhedral, with green brown pleochroism and eroded edges. The groundmass is microcrystalline and consists of euhedral to subhedral clinopyroxene and plagioclase, reflective of the general mineralogy. This is altered to chlorite and to palagonite in interstitial areas.

Barroso Formation/Cañas Gordas Basement Sample:

DB15-087:

Holocrystalline porphyritic rock with plagioclase as the overwhelmingly dominant phenocryst phase, with interlocking phenocrysts and microphenocrysts >1 mm. Groundmass is predominantly interstitial microcrysts of plagioclase, clinopyroxene and minor opaque phases (all <1 mm). Groundmass is altered in places to chlorite, and plagioclase shows sausserite alteration in many parts of the section. Anhedral

calcite also seen, possibly as infill of vesicles or as a replacement/later precipitation texture.

Combia Formation Sample:

DC16-001:

Porphyritic sample with 1 – 2 mm phenocrysts of plagioclase, though heavily altered crystals up to ~5 mm are also observed. Remaining phenocryst phases consist of euhedral to subhedral amphibole (~1 mm) and small amounts of euhedral biotite (0.5 – 1 mm). Opaques vary in size from phenocrysts to groundmass component, though the larger examples may be pseudomorphs of other phenocryst phases. Garnet is also observed in a single occurrence in section. A pervasive overprint of sericite and secondary mineral alteration is seen throughout section, leaving relict crystals and pseudomorphs in some cases. Groundmass is composed of <1 mm plagioclase laths but is otherwise cryptocrystalline and largely altered to sericite and chlorite.

Central Colombian Intrusions Samples:

PKSW-098:

Porphyritic rock with very large, anhedral phenocrysts of quartz >5 mm, along with smaller crystals of plagioclase of 5 – 7 mm and biotite of 2 – 3 mm. One occurrence of garnet, subhedral is also observed in the section, with a strong reaction corona at its rim. Quartz phenocrysts are largely unaltered and anhedral. In contrast,

plagioclase exhibits zoning and twinning where preserved but is altered to sericite throughout much of the section and almost all biotite is altered to chlorite. Apatite and zircon are also (rarely) observed as minor phases of <0.5 mm. Voids in section are also observed, most likely due to removal of phases by alteration and secondary hydrothermal processes as with the alteration of phenocryst phases. The groundmass is made up of equigranular plagioclase laths along with alteration products of calcite and sericite, all of which are <0.2 mm.

JLSW-008A:

Porphyritic rock with euhedral to subhedral plagioclase (>7 mm), euhedral amphibole crystals of ~3 mm, euhedral to subhedral biotite of ~1 – 2 mm and rare small quartz microphenocrysts of <1 mm. Plagioclase phenocrysts exhibit both Carlsbad and albite twinning, and significant oscillatory zoning. Biotite commonly shows an oxide reaction rim. Plagioclase phenocrysts also commonly contain inclusions of amphibole and melt. Amphibole phenocrysts themselves also include minor inclusions of opaque minerals. Groundmass of sample is crypto- to microcrystalline, and dominantly composed of plagioclase and minor quartz.

Appendix B: Extended Methods

Full methods for preparation of samples for geochemical analysis (ICP-MS/OES and Sr-Nd-Hf radiogenic isotope analysis) are outlined below. All samples in this study were prepared from primary hard rock material sampled either directly by the author (DC16 samples) or collected by external project partners (DB15; UB; PKSW; JLSW; LHSW; SESW samples). Preparation of samples, as outlined below, was undertaken at Cardiff University between 2016 and 2019. Efforts were made at all stages to minimise the risk of contamination.

B.1.: Preparation of rock powders:

Rock saws:

All samples were cut into smaller pieces with rock saws for further processing, and to leave an archive of excess material. Any altered edges of samples were also removed. The majority of sawing was done on a 10” diameter (0.04” thickness) saw with a continuous 1/2 - 5/8” bore diamond impregnated blade. Samples too large to be cut on the 10” saw were first cut on a Norton Clipper CHW saw with 350 mm x 25.4 mm Norton Silencio diamond impregnated blade. Additionally, approximately 76 x 26 x 10 mm slices of unaltered material from which thin sections could be prepared were cut from each sample using a 6” diameter (0.032” thickness) saw with a continuous 1/2 - 5/8” bore diamond impregnated blade, which was also used to trim away any minor alteration surfaces.

Jaw crusher:

Cut pieces of each were sample were then inserted into a metal jaw crusher, which was cleaned thoroughly with clean tissue and deionised water between crushing of each sample. Samples were run through crusher multiple times. As the jaw crusher width was variable, initial runs of each sample were performed at its widest setting and then narrower settings until samples were adequately crushed. An extractor was used during runs to minimise the amount of rock dust contamination, and a vacuum cleaner was used to clean up the workspace and crusher between runs to further minimise contamination risk. Despite this, the jaw crusher may have introduced limited metal contamination to the analyses. Jaw crushed samples were collected in labelled polythene bags at the end of each run cycle.

Agate planetary ball mill:

Jaw crushed samples were milled using a Model RETSCH PM 400 agate planetary ball mill to produce the final powders. This was done in place of a tungsten carbide mill to avoid Nb and Ta contamination of the samples. Excess jaw crushed material was archived for some samples. As the vast majority of samples were lavas or shallow intrusions, a standard running time and revolutions per minute (rpm) of 30 minutes at 275 rpm was adopted. Samples were inspected for coarse fragments and/or crystals following each run and any samples deemed too coarse were run in the same pots for an additional 10 - 15 minutes at 275 rpm. This ensured that very fine powders were produced and any large fragments or acid resistant crystal phases such as zircon were broken down prior to solution inductively coupled plasma (ICP)

analysis. Between runs, agate pots and balls were thoroughly cleaned and dried. A vacuum cleaner was also used to clean up any excess dust or possible build up of rock dust within the mill between runs. A few samples adhered more than others (e.g.: UB-02) to the pot walls and agate balls, possibly as a result of the samples containing more water from hydrous phases or by condensation within polythene sample bags during transport and storage. However, this was not significant enough to warrant further drying or processing prior to loss on ignition.

Loss on ignition (LOI):

Most silicate rocks contain a measurable proportion of volatiles, dominantly H_2O (water) but also elements such as carbon, sulfur, chlorine and fluorine in chemical compounds (e.g.: CO_2, SO_2, H_2S, HCl and HF). These may be liberated from hydrous mineral phases such as amphibole or mica or water trapped on grain surfaces or pore spaces. They may also be present in alteration products, such as water in clay minerals or CO_2 in secondary carbonate minerals. As inductively coupled plasma optical emission spectrometry (ICP-OES) and ICP-mass spectrometry (MS) cannot analyse for volatiles such as water and carbon dioxide within samples, we can use a calculated loss on ignition (LOI) to account for these. This can be done by baking a portion of each sample at high temperature to burn off volatiles and calculating the mass loss of the sample. In some instances, a mass gain (recorded as a negative LOI) can be recorded. This is likely due to oxidation of iron in a sample from Fe^{2+} to denser Fe^{3+}.

At Cardiff University the LOI procedure was as follows. Clean crucibles were placed in a Vecstar furnace at ~150°C for 1 hour in order to drive off any volatiles accumulated to the crucibles during storage. Crucibles were then removed and left to cool for ~15 minutes. Once cooled, the empty crucibles were weighed on a Sartorius research scale (accuracy ±0.0001g) and empty mass recorded. Scales were then zeroed and ~2 - 3g of “wet” sample powder was added, and mass of “wet” sample recorded. Crucibles containing “wet” sample powders were then placed in batches in a Vecstar furnace at 900°C for ~2 hours to “burn off” the volatiles. Crucibles were then removed and allowed to cool for 15 minutes. The crucibles were then reweighed to give an ignited total (crucible + “dry” sample mass), and “dry” sample masses were calculated by deducting the recorded empty mass for the crucible from the ignited total in each case. LOI of each sample was calculated by subtracting the “wet” mass from the “dry” mass to give a mass loss figure, which was then divided by the “wet” mass of sample and the final figure multiplied by 100 to give a percentage.

To prevent contamination by addition of volatiles at each stage, a tongs was used to transfer crucibles to and from the furnace during drying and igniting phases, and gloves were used at all times, though contact with gloves was minimised as much as possible. It is possible that some contamination could have come from debris such as sample material and the refractory lining itself on the roof of the furnace falling into sample crucibles, though this was not observed. To prevent any additional moisture being added to samples during and after the procedure, dry powders were stored in airtight sample bags and housed in desiccators until the next stage of preparation for ICP-MS/OES.

Additionally, five samples from the submerged seamounts and subaerial volcanoes of the Scotia arc, available as preexisting archive from the author's Masters project at the University of Leicester were also processed and analysed from LOI stage onwards for comparison with between ICP data obtained at Cardiff University and from previous analyses by XRF and ICP-MS at the University of Leicester.

B.2.: Preparation of sample solutions and analysis by ICP-OES and ICP-MS:

Fusion of powders:

Sample powders for this study were prepared for sample solution analysis by ICP-OES and ICP-MS by rock powder fusion, alongside a subset of International Standard Reference Materials (ISRM) powders available at Cardiff University. The ISRM are prepared in line with other samples and used to provide an assessment of the accuracy of the data compared to known reference ISRM values. As ICP-OES and ICP-MS for Colombian samples was conducted in two separate runs in September 2017 and June 2019, two respective sets of reference materials were analysed. The ISRMs in the September 2017 run were JB1a, JG1a and JA2 and the June 2019 run reference materials were JB1a, MRG1, JA2 and SDO1. All powders (samples for this study, Scotia rocks and ISRMs) were prepared by the following procedure.

To enable fusion, sample and a flux were first mixed, with 0.1 ± 0.001g of sample and 0.6 ± 0.001g of flux (50:50 lithium borate) were weighed out on a Sartorius Mettler Toledo research scales (accuracy ±0.0001g) and placed into clean platinum

crucibles. A clean plastic spatula was then used to thoroughly mix sample and flux and 5 - 6 drops of lithium iodide wetting agent were added to the mixture. Three crucibles at a time were then placed in mounts on a Claisse Fluxy fusion machine. Positioned below each crucible to catch the sample at the end of the fusion run was a labelled Teflon beaker containing 30 ml of deionised water, 20 ml of 10% nitric acid and a magnetic stirring bar. The Claisse Fluxy was then set to run for ~9 minutes heating the sample and then emptying the resulting glass into the teflon beakers for dissolution. Crucibles were briefly allowed to cool and checked for any remaining glass, which was carefully removed by adding the crucible to the respective teflon beaker. Teflon beakers were then placed on to ~80°C hotplates for 10 - 15 minutes until glass is completely dissolved. Crucibles were then removed and rinsed in deionised water, which was then poured into the teflon beakers to add any remaining sample. These solutions were transferred to prepared and labelled 100 ml Nalgene flasks and a A 1 ml Rhenium spike of 100 ppm Rh stock solution added to each sample solution. Deionised water was added to each solution to make each 100 ml and the complete solutions were transferred to labelled storage beakers ready for ICP-OES and ICP-MS analysis.

As with each previous stage, efforts were made to minimise potential sources of contamination. All equipment used at the fusion stage was thoroughly cleaned prior to use. Separate spatulas were used to weigh out sample and flux, and both were cleaned between each sample weighing. Some loose debris was observed on the Claisse Fluxy fusion machine during the September 2017 run, and this was removed where observed to prevent being added to the sample mixtures. Despite this, some small debris was observed falling into samples which was removed. This however

means that some debris could have been added to samples whilst the Claisse Fluxy fusion machine was left unobserved. Additionally, the June 2019 sample run was performed using a newer Claisse Fluxy fusion machine had less chance of imparting debris to the samples. The previous Claisse Fluxy fusion machine had heating elements which had to be lit manually, increasing the risk of contamination when doing this, whereas the newer Claisse Fluxy fusion machine used in the second run lit automatically. Lastly, small quantities of dust from the laboratory atmosphere were observed in some sample solutions once the liquid have settled in the storage beakers, presenting another possible contamination vector.

Analysis of major and trace elements by ICP-MS and ICP-OES:

Sample solutions were analysed for their major and trace elements (excluding Ge, As, Tl, Se, Ag, Bi, W, Mo, S, Ru, Sn and Sb) via solution ICP-OES for major element oxides and selected trace elements, and by ICP-MS for trace elements. ICP-MS is used for a wider number of trace elements due to its low detection limits (down to the parts per billion or trillion range) compare to ICP-OES techniques.

Inductively coupled plasma (ICP) is produced by a stream of argon atoms inductively heated a radio-frequency controlled coil and ignited to produce a plasma at ~10,000 K. Sample solutions are introduced to the plasma via a nebuliser, which produces the solution as an aerosol. The sample volitalises and disassociates in the high temperature argon plasma, producing a mixture of atoms, ions, dissociated molecular fragments and unvolatilised particles (Rollinson, 1993; Hou et al. 2016).

In optical emission spectrometry (OES), also sometimes known as atomic emission spectrometry (AES), the excited atomic and ionic species emit a photon to relax to their ground state. The wavelength of these photons can be used to identify the elements from which they originated, and the number of photons is proportional to the element concentration of the sample (Hou et al. 2016). A portion of these photons emitted from the ICP are collected by a lens or concave mirror, which focuses an image onto the aperture of a wavelength selection device (a monochromator). A photo detector will then convert these wavelengths to an electric signal, which is processed, amplified and input into a computer, where calibrations, correlations and corrections can be performed (Hou et al. 2016).

Mass spectrometry (MS) techniques also use an ICP, but instead to produce a beam of ions which are directed toward a mass spectrometer. The mass spectrometer needs to kept at high vacuum, and is cut off from the chamber housing the ICP by two conical apertures, the sample cone and skimmer, which allow the passage of ions to the spectrometer but deflect away uncharged particles (Jarvis, 1997). An electrostatic lens focuses the ions into a beam beyond the skimmer, and a physical barrier (the photon stop) is placed in the path of the ion beam to stop light from reaching the ion detector and adding to the background signal. The ion beam is deflected around the photon stop by a lens and continues to a mass analyser, the most common type being a quadrupole mass filter (Jarvis, 1997). In principle this is an electromagnet which splits up the ions according to their mass-to-charge ratio (m/z), producing a mass spectrum of lighter and heavier ions dependent on radius of curvature (Rollinson, 1993). 100s or 1000s of these analyses are combined to create an aggregate peak for each atomic mass number, with the quadrupole of sufficient

resolution to distinguish separate elemental mass number peaks, whilst elemental proportions are accounted for by sensitive ion detectors counting individual ions with specific m/z values (Rollinson, 1993; Jarvis, 1997). This information from the detectors is then amplified and transferred digitally to a computer for correction and correlation.

Analysis of sample solutions was undertaken by Iain McDonald at Cardiff University following the methods of McDonald and Viljoen (2006) and results provided to the author.

B.3.: Preparation of sample powders for Sr, Nd, Hf radiogenic isotope analyses:

Selection of samples:

Archive of sample powders prepared at Cardiff University (see procedures outlined above) was utilised for radiogenic isotope analyses. This material was then prepared for Sr, Nd and Hf isotope analysis at the NERC Isotope Geosciences Laboratory (NIGL) laboratories at the British Geological Survey in Keyworth, Nottingham. This work was supervised by the project's CASE supervisor, Dr Ian Millar. Full results of isotopic analyses of Colombian samples are presented in **Appendix E**.

Sample dissolution and column chemistry:

0.2 ± 0.0200g of each sample were weighed into 15 ml Savillex teflon beakers and leached in 5 mls of 6M HCl at 60°C for 2 hours. Leachate was discarded and samples were washed in MilliQ H_2O and centrifuged twice, then dried and reweighed. 1 - 2 mls of 2x quartz-distilled 16M HNO_3 and 5-6 mls of 29M HF were then added. Sample beakers were then left over night on 140°C hotplate to evaporate to dryness. 1-2 mls of HNO_3 was then added to each sample, which were left overnight on the hotplate. Samples were converted to chloride form using 20 mls of 2x quartz-distilled HCl. The samples were then left to dissolve in ~2 ml of 1M HCl + 0.1M HF and finally transferred to microcentrifuge tubes and centrifuged in preparation for column chemistry.

Chemical separation by columns:

Prior to use, columns were washed through with 20 ml of 6M HCl followed by 10 ml of H_2O and another 20 ml of 6M HCl, prior to conditioning with 10 ml of 1M HCl + 0.1M HF. Primary columns consist of 2 ml of Eichrom AG50 x 8 cation exchange resin in 10 ml Biorad Poly-Prep columns. These are used to separate bulk high field strength elements (HFSE: Ti, Hf, Zr), a bulk rare-earth element (REE) fraction and a fraction containing Sr, Ca and Rb. Beakers below columns were used to collect each fraction of each sample. Samples were carefully pipetted from centrifuge tubes and loaded onto columns in ~1.5 mls of 1M HCl + 0.1M HF. HFSEs were immediately eluted from samples in 5 - 10 mls of 1M HCl + 0.1M HF and collected. This fraction was then evaporated to dryness in preparation for separation of Hf (see method below). Next, Sr and other matrix elements (Ca, Rb) were eluted in 25 mls of 1.5M HCl and collected. Lastly, the original sample beaker was rinsed thoroughly and used

to collect the REE (Nd, Sm, Lu) fraction, which was eluted in 10 mls of 6M HCl. Both the Sr and Nd eluted products were evaporated to dryness in preparation for separation of Sr and Nd, respectively.

Separation of Sr and Nd:

Primary column separated samples of Sr and matrix elements were dried down and taken up in ~2 mls of 2.5M HCl and pipetted onto quartz-glass columns containing 4 mls of AG50x8 cation exchange resin. Columns were washed with 48 mls of calibrated 2.5M HCl to remove matrix elements and was then discarded. Sr was collected in 12 mls of 2.5M HCl and then evaporated to dryness.

Bulk REE fractions of samples were dissolved in 200 microlitres of 0.2M HCl and loaded on to 10ml Biorad Poly-Prep columns packed with 2 mls of EICHROM LN-SPEC ion exchange resin, which removed Sm and Nd. La, Ce and Pr were then eluted using 14 mls of 0.2 HCl. The Nd was collected in 3 mls of 0.3M HCl.

Separation of Hf:

Hf separation follows the procedure of Münker et al. (2001), adapted by NIGL. Firstly, the HFSE concentrates derived from the primary columns were dissolved in ~2 mls of 6M HCl. These were then loaded on to 10 ml Biorad Poly-Prep columns packed with 1 ml of EICHROM LN-SPEC ion exchange resin. Matrix elements were eluted in 10 - 20 mls of 6M HCl. Following this, HCl was removed from the columns by passing 2 mls of milliQ water through them. This was done as subsequent elution stages

involve peroxide, and mixing of HCl and column to remove HCl and peroxide would cause immediate elution of all HFSE from the columns. Columns were then washed several times with 10 ml solutions of citric acid, nitric acid and peroxide. In this medium, titanium citrate complexes display a distinct orange colour, allowing Ti could to be quantitatively removed from the columns by repeated washes with this solution, until all traces of Ti have been removed from the columns. To avoid mixing of peroxide with HCl solutions, 5 mls of peroxide-free citric and nitric acid solution were eluted. Columns were washed with 50-80 ml of 6M HCl + 0.06M HF. Lastly, Hf was collected in 10 mls of 6M HCL + 0.2M HCl.

B.4.: Analysis of Sr, Nd, Hf radiogenic isotope analyses:

Overview:

Two runs of Sr, Nd and Hf analyses were performed for samples from Colombia due to failure of some analyses during the first run. The first of these was run N833, performed in September 2019, followed by run N836, performed in January 2020.

Sr analysis:

Sr fractions were loaded onto outgassed single Re filaments using a TaO activator solution. Analysis was performed in a Thermo-Electron Triton mass spectrometer in multi-dynamic mode. Data is normalised to 86Sr/88Sr = 0.1194. The standard NBS987 was analysed five times, giving a mean value of 0.710267 ± 0.000008. Sample data is normalised using a preferred value of 0.710250 for this standard.

Nd analysis:

Nd fractions were loaded onto one side of an outgassed Re filament assembly using dilute HCl, and analysed in a Thermo Scientific Triton mass spectrometer in multi-dynamic mode. Data are normalised to 146Nd/144Nd = 0.7219. Six analyses of the JND-i standard gave a value of 0.512095 ± 0.000009. Results are quoted relative to a value of 0.512115 for this standard.

Hf analysis:

Hf fractions were dissolved in 1 ml of 2% HNO_3 + 0.1M HF, then analysed in a Nu Plasma HR mass spectrometer in static multi-collection mode. Correction for 176Yb on the 176Hf peak was made using reverse-mass-bias correction of the 176Yb/173Yb ratio empirically derived using Hf mass-bias corrected Yb-doped JMC475 solutions (Nowell and Parrish, 2001). Corrections are minimal as the column procedures described above effectively removes the majority of Yb and Lu, however 176Lu interference on the 176Hf peak was corrected using the measured 175Lu and assuming 176Lu/175Lu = 0.02653. Data is reported relative to 179Hf/177Hf = 0.7325. The Hf standard solution JMC475 was analysed during each analytical session, with sample 176Hf/177Hf ratios reported relative to a value of 0.282160 for this standard (Nowell and Parrish, 2001). JMC475 total of eight times during run N833 (excluding two Yb doped analyses) with these analyses giving a mean of 0.282145 ± 0.000008. Results are quoted relative to a value of 0.282160 for this standard.

References for Appendix B:

McDonald, I. and Viljoen, K.S. (2006), 'Platinum-group element geochemistry of mantle eclogites: a reconnaissance study of xenoliths from the Orapa kimberlite, Botswana'. Applied Earth Science, 115: 81–93.

Nowell, G.M. & Parrish, R.R. (2001), 'Simultaneous acquisition of isotope compositions and parent/daughter ratios by non-isotope dilution-mode plasma ionisation multi-collector mass spectrometry (PIMMS)'. In Plasma Source Mass Spectrometry: The New Millenium (Holland, G. & Tanner, S.D. eds) Royal Soc. Chem.,Spec. Publ. 267, 298-310.

Münker, C., Weyer, S., Scherer, E., Mezger, K., (2001), 'Separation of high field strength elements (Nb, Ta, Zr, Hf) and Lu from rock samples for MC-ICPMS measurements'. Geochem. Geophys. Geosyst. 2. doi:10.1029/2001GC000183.

Appendix C: Raw analyses of Colombian and Scotia samples analysed at Cardiff and Leicester and ISRM standards

Cardiff 2017 ICP-OES Data:

ISRM Samples:

Sample		JA2	JB1a	JG1a
SiO2	wt%	56.4816391	52.6833521	72.453418
TiO2	wt%	0.70468442	1.33653629	0.26848667
Al2O3	wt%	15.5456982	14.6081422	14.1260036
Fe2O3	wt%	7.02928905	9.4767671	2.10992364
MnO	wt%	0.09257102	0.14409878	0.04139573
MgO	wt%	7.80926953	7.52520617	0.65414956
CaO	wt%	6.56656498	9.6738216	2.23815978
Na2O	wt%	3.00082734	2.76202381	3.21417757
K2O	wt%	1.7968383	1.49173435	3.96162989
P2O5	wt%	0.15928645	0.2509045	0.07197859
LOI	wt%	0.55	0.78	0.5
Total	wt%	99.1866683	99.9525869	99.139323
CR2O3	wt%			
Sc	ppm	19.7752955	29.4325532	6.12969023
V	ppm	128.953206	211.731791	18.9340603
Cr	ppm	441.317581	407.831526	28.1628593
Co	ppm	30.990695	42.3243926	10.6632405
Ni	ppm	148.592736	134.104301	8.68756029
Cu	ppm	27.153	52.5885016	5.098523
Zn	ppm	70.9133156	86.5711248	33.3503792
Sr	ppm	244.141445	450.474555	176.998688
Y	ppm	18.142274	24.6042968	32.679331
Zr	ppm	114.991733	145.658403	122.674353
Ba	ppm	324.815333	506.590086	464.057146

DC16 Samples:

Sample		DC16-001	DC16-002	DC16-003	DC16-004
SiO2	wt%	63.4675973	54.7267531	64.6811438	63.2672996
TiO2	wt%	0.76900374	0.86262635	0.61898018	0.70348962
Al2O3	wt%	16.5596347	14.7128728	16.1923821	16.6676088
Fe2O3	wt%	9.26316568	8.49529874	5.22169852	6.26360451
MnO	wt%	0.01056424	0.10322174	0.06450667	0.07238097
MgO	wt%	0.73085604	9.73275378	1.35114567	2.01196752
CaO	wt%	4.59186423	8.77572449	5.42423212	6.75625424
Na2O	wt%	3.22053308	2.91659782	3.67521234	3.64361184
K2O	wt%	1.303449	0.94106519	1.70196094	1.3678265
P2O5	wt%	0.23120682	0.18523816	0.18460175	0.19186433
LOI	wt%	2.03773893	0.14584155	2.70773179	4.11060411
Total	wt%	100.147875	101.452152	99.1158642	100.945908
CR2O3	wt%				
Sc	ppm	16.3263538	22.7279294	11.7803351	13.8776449
V	ppm	171.477749	162.968679	106.850398	112.042279
Cr	ppm	124.506592	545.681337	57.3424014	83.7211048
Co	ppm	13.527742	18.2642765	12.209796	12.237056
Ni	ppm	351.108839	219.053985	12.9982184	85.2907408
Cu	ppm	806.188315	45.4172621	18.3525707	15.6860438
Zn	ppm	32.0995229	68.7653346	77.9575335	58.1950914
Sr	ppm	545.62002	446.779894	522.780929	479.086633
Y	ppm	22.9726209	13.0217089	12.7531289	11.7046802
Zr	ppm	135.895695	84.628082	130.642737	93.2224642
Ba	ppm	181.519821	642.147835	1061.69507	865.475017

Sample		DC16-005	DC16-006	DC16-007	DC16-008
SiO2	wt%	58.0579365	64.0895675	64.4307941	58.0831135
TiO2	wt%	0.87940457	0.71805435	0.81347273	0.85896209
Al2O3	wt%	15.1331729	16.4143599	18.2381659	16.2244665
Fe2O3	wt%	7.5465936	6.7542503	6.4611107	7.20584443
MnO	wt%	0.0853914	0.08006756	0.04340759	0.07756813
MgO	wt%	4.29313555	2.96234064	2.13046093	4.26720671
CaO	wt%	8.06054831	5.67475401	4.50065793	7.20318038
Na2O	wt%	3.23246928	3.35878362	3.11715322	3.44739927
K2O	wt%	1.05441722	1.19223744	1.36971743	1.05667184
P2O5	wt%	0.20684696	0.19854167	0.21450564	0.23836496
LOI	wt%	1.0240565	0.35378415	0.42460269	0.16293469
Total	wt%	98.5499163	101.442957	101.319446	98.6627778
CR2O3	wt%				
Sc	ppm	16.1254736	17.0165966	17.4240392	20.5413517
V	ppm	122.438032	122.340515	133.075535	171.707382
Cr	ppm	222.251557	205.876219	505.264498	200.62171
Co	ppm	12.7573314	13.5559833	14.3258228	17.1455763
Ni	ppm	104.544427	80.6018312	139.739059	90.2227838
Cu	ppm	34.2151419	17.5865711	31.781405	28.6435727
Zn	ppm	60.8764195	58.814061	76.8830302	71.1761236
Sr	ppm	395.816897	457.351844	507.525848	664.06453
Y	ppm	11.0956809	12.8073188	15.1121194	14.8451018
Zr	ppm	78.8565955	104.333969	122.500248	113.835573
Ba	ppm	604.419743	1197.96766	1472.66842	1036.31898

Sample		DC16-009	DC16-010	DC16-011	DC16-012
SiO2	wt%	53.3612514	62.2201916	59.3629292	69.6367511
TiO2	wt%	0.86248763	0.77033191	0.83855281	0.5667716
Al2O3	wt%	14.4452862	16.6653802	16.1937507	16.878028
Fe2O3	wt%	8.57945909	5.8725768	7.18649193	2.28568226
MnO	wt%	0.10143946	0.07131479	0.09151224	0.0103752
MgO	wt%	9.60648889	1.82926333	2.83550615	0.02611851
CaO	wt%	8.81671251	8.39179153	8.28954631	3.16307324
Na2O	wt%	2.5046537	3.10170766	3.13375056	3.69039704
K2O	wt%	0.77470724	1.28213261	0.9871678	2.79752218
P2O5	wt%	0.19141624	0.26275499	0.22319244	0.07081907
LOI	wt%	0.11550356	8.8565326	0.56466681	2.09522257
Total	wt%	99.2439023	100.467445	99.1424002	99.1255382
CR2O3	wt%				
Sc	ppm	19.0401706	12.4550424	21.8514662	8.60872777
V	ppm	147.430529	96.7065239	172.862975	54.0615898
Cr	ppm	459.747683	60.9531057	71.3678327	60.547355
Co	ppm	15.8581356	11.3570102	15.4510988	4.76865266
Ni	ppm	308.955451	60.1018665	5.67709832	39.8204084
Cu	ppm	33.9592787	32.8695629	21.0181397	9.03876749
Zn	ppm	67.0666722	67.2418085	72.8250337	31.9570215
Sr	ppm	369.205449	612.821739	563.174434	445.211688
Y	ppm	11.546549	13.1912329	14.3755847	7.44769041
Zr	ppm	65.739305	124.228485	94.7574031	149.043308
Ba	ppm	523.964654	1086.26274	651.3251	1185.56345

Sample		DC16-013	DC16-014	DC16-015	DC16-016
SiO2	wt%	65.1716433	62.56552	65.4371482	63.5933221
TiO2	wt%	0.85884827	0.76376103	0.69082037	0.89848273
Al2O3	wt%	16.4248242	15.6709359	15.5959282	17.0089023
Fe2O3	wt%	6.04170387	6.26512819	5.34955531	5.23091034
MnO	wt%	0.05896142	0.06299231	0.05268797	0.04156541
MgO	wt%	1.68907239	2.40871512	2.13140442	1.18384471
CaO	wt%	5.79535101	6.51043007	5.84850787	5.84528978
Na2O	wt%	3.03747615	3.32519503	3.68440837	3.94460734
K2O	wt%	2.03210018	1.45696311	1.88552986	1.76446042
P2O5	wt%	0.19415436	0.19681647	0.20815436	0.29629569
LOI	wt%	3.03040738	0.59106473	0.15370165	1.77049662
Total	wt%	101.304135	99.2264572	100.884145	99.8076808
CR2O3	wt%				
Sc	ppm	17.9832177	14.5890675	11.6247267	13.5955022
V	ppm	149.248442	118.558223	110.101338	141.197127
Cr	ppm	84.1279103	90.4362873	88.0439895	63.6538981
Co	ppm	14.1773969	12.5178413	11.2538744	10.9724958
Ni	ppm	150.223448	56.5954405	58.9662342	212.146298
Cu	ppm	34.0464229	23.79005	28.4892965	44.5465627
Zn	ppm	75.2159789	46.4295568	51.448717	70.9577915
Sr	ppm	593.926401	432.945237	561.132824	674.92481
Y	ppm	19.1465493	11.8508587	11.7891982	18.6320586
Zr	ppm	163.142476	106.231154	121.191127	141.595832
Ba	ppm	1138.51271	887.01979	1044.67367	1139.92769

Sample		DC16-017	DC16-018	DC16-019	DC16-020
SiO2	wt%	62.2696009	63.4115299	62.7041866	62.375274
TiO2	wt%	0.84169465	0.87622684	0.88975341	0.85895385
Al2O3	wt%	16.7678032	17.2683703	17.2949947	17.0864305
Fe2O3	wt%	6.22263106	6.479156	6.81916732	6.36537718
MnO	wt%	0.06247534	0.06413734	0.05839322	0.06349793
MgO	wt%	1.09807931	1.03585719	1.04728241	1.38882744
CaO	wt%	6.14005791	5.29318851	5.09087055	6.40228773
Na2O	wt%	3.89015959	3.87355049	3.78482729	3.92510665
K2O	wt%	1.46794537	1.47308679	1.48258697	1.44648002
P2O5	wt%	0.23535553	0.24099486	0.24124322	0.23956906
LOI	wt%	0.91208017	2.54796827	2.49543518	1.36422494
Total	wt%	98.9958029	100.016098	99.4133057	100.151804
CR2O3	wt%				
Sc	ppm	11.871352	13.3182882	11.7127478	12.6587399
V	ppm	122.908209	133.729032	122.208429	136.51144
Cr	ppm	50.3418096	58.5980657	43.9437914	50.5948183
Co	ppm	12.5248087	13.2388842	9.56350099	12.9146415
Ni	ppm	60.5524342	32.8604738	19.249223	33.5386613
Cu	ppm	18.4253095	11.6693329	17.0633274	17.5679341
Zn	ppm	59.6990209	71.2438996	55.1926898	63.987723
Sr	ppm	465.153279	440.540654	354.774222	473.867584
Y	ppm	15.5533356	32.07694	14.4215133	16.1729963
Zr	ppm	122.016137	136.673202	115.445816	128.727471
Ba	ppm	904.957777	1090.57098	969.884165	1003.03608

Sample		DC16-021	DC16-022	DC16-023	DC16-024
SiO2	wt%	68.6908811	71.4623372	61.2845286	59.7451794
TiO2	wt%	0.65184706	0.33032401	0.68009201	0.86789091
Al2O3	wt%	16.3842799	15.0253139	16.3472986	17.5541097
Fe2O3	wt%	6.05456554	3.6303473	7.11965531	8.18217618
MnO	wt%	0.05351771	0.03903286	0.08351912	0.09185569
MgO	wt%	1.31155239	0.27248426	2.09228229	3.05684923
CaO	wt%	1.749822	2.01276714	5.94755977	7.10599775
Na2O	wt%	3.13783643	3.50656855	3.33938353	3.44522581
K2O	wt%	2.12766125	2.60863467	1.636717	1.03487726
P2O5	wt%	0.23844744	0.14638934	0.28897046	0.29838187
LOI	wt%	3.09136904	2.03851002	0.70217636	1.23090186
Total	wt%	100.400411	99.0341993	98.8200067	101.382544
CR2O3	wt%				
Sc	ppm	14.6685372	8.19797164	13.7060287	17.6560046
V	ppm	126.926017	45.7304614	145.469686	196.717207
Cr	ppm	59.1777755	3.62468532	60.1820498	77.0169099
Co	ppm	12.213705	3.31455883	15.1251895	18.8134563
Ni	ppm	118.637084	36.2108297	44.0115722	30.5814956
Cu	ppm	26.2441731	7.79629268	16.7943348	26.0800057
Zn	ppm	57.451406	93.8721848	83.3982042	537.703875
Sr	ppm	370.60884	328.298999	396.88698	461.945931
Y	ppm	15.483871	14.3178348	12.6321	20.4776203
Zr	ppm	127.287981	74.3467251	109.666383	100.642109
Ba	ppm	1016.22459	1618.9423	812.668347	733.774788

Sample		DC16-025	DC16-026	DC16-027	DC16-028
SiO2	wt%	63.1016662	61.5546305	61.0093583	58.6574446
TiO2	wt%	0.81054592	0.68376525	0.78638238	0.86755439
Al2O3	wt%	16.5648024	16.8898082	17.5471285	19.4655715
Fe2O3	wt%	7.12159443	6.85015559	8.23018717	7.31941
MnO	wt%	0.07454061	0.08501604	0.10826378	0.08693106
MgO	wt%	1.96543334	2.59437197	2.17736006	1.57064289
CaO	wt%	5.35666021	6.95128683	6.10576061	6.5015394
Na2O	wt%	3.24452513	3.21611237	3.26972802	3.3134992
K2O	wt%	1.87855233	1.1049891	1.21212274	2.22465081
P2O5	wt%	0.35435151	0.29525231	0.39583126	0.40235233
LOI	wt%	1.94575472	0.56577697	1.62084406	6.51981637
Total	wt%	100.472672	100.225388	100.842123	100.409596
CR2O3	wt%				
Sc	ppm	14.2103159	17.4955503	17.6521202	14.6997219
V	ppm	124.101271	141.444803	161.072883	143.337621
Cr	ppm	77.0421508	49.7650711	19.1446615	11.5935579
Co	ppm	13.8999738	14.2469074	19.9340625	16.6395442
Ni	ppm	21.8874359	81.398751	26.1682661	18.5342802
Cu	ppm	33.0101796	24.9621499	16.8507701	37.0464809
Zn	ppm	52.7426839	63.9804065	68.6547059	62.7521427
Sr	ppm	328.211261	409.352775	449.211158	547.81502
Y	ppm	22.7445216	12.3701927	17.7895232	17.714002
Zr	ppm	134.86358	101.056831	138.652121	140.495781
Ba	ppm	879.69439	553.022294	950.173766	703.58079

Sample		DC16-029	DC16-030	DC16-031	DC16-032
SiO2	wt%	57.6438633	57.190513	56.2159949	59.2081327
TiO2	wt%	0.7865122	0.81351643	0.82512358	0.86168
Al2O3	wt%	18.1553407	17.2146976	18.2723037	17.2513075
Fe2O3	wt%	8.19838719	8.40152051	8.98893101	8.16297476
MnO	wt%	0.10632244	0.1094333	0.12790386	0.09087446
MgO	wt%	3.09140442	2.72592184	3.70130542	2.98794997
CaO	wt%	7.67195265	7.75569073	8.76970284	7.01266063
Na2O	wt%	3.11278752	2.92223593	2.97516145	3.50167698
K2O	wt%	1.55591777	1.46909577	1.15684862	1.58054132
P2O5	wt%	0.29503054	0.27579956	0.28452947	0.51842045
LOI	wt%	0.30490129	-0.0870133	0.24849772	0.14695645
Total	wt%	100.617519	98.8784247	101.317805	101.176219
CR2O3	wt%				
Sc	ppm	16.6000606	19.7486885	25.7759876	16.7422963
V	ppm	132.725409	170.504325	202.819786	164.004783
Cr	ppm	51.7046884	31.9747498	42.9193819	131.787616
Co	ppm	16.1897578	17.964494	21.627705	19.2191072
Ni	ppm	62.8178877	9.17200057	692.215851	327.625143
Cu	ppm	43.2185806	30.5535957	53.0050799	37.1331029
Zn	ppm	69.2731856	55.1085252	82.1721706	84.919775
Sr	ppm	405.373496	418.857891	481.96637	604.224032
Y	ppm	14.6009508	14.8791723	17.3971442	15.6336814
Zr	ppm	105.341443	109.915986	105.871414	152.783632
Ba	ppm	642.35437	599.594792	607.172476	815.528005

Sample		DC16-033	DC16-034	DC16-035	DC16-036
SiO2	wt%	60.5181038	60.3730967	56.3173626	53.9577782
TiO2	wt%	0.72091301	0.79239838	0.90864084	1.03602182
Al2O3	wt%	16.1335711	18.6857393	17.3661832	17.0742692
Fe2O3	wt%	7.13154079	7.30603837	9.74084865	9.13211295
MnO	wt%	0.08656218	0.08963453	0.14113515	0.10507977
MgO	wt%	2.96898846	1.97783382	3.45704044	4.17286052
CaO	wt%	6.56536577	5.9025452	7.99776365	7.91324338
Na2O	wt%	3.11438744	3.42868818	2.77281523	3.57519698
K2O	wt%	1.37511138	1.27431185	1.24881175	1.51380244
P2O5	wt%	0.29439772	0.40209557	0.2750851	0.59767452
LOI	wt%	0.47908442	2.22063037	1.52372109	0.21621145
Total	wt%	98.9089416	100.232382	100.225687	99.0780397
CR2O3	wt%				
Sc	ppm	18.2457763	14.4244406	23.9264964	16.8574697
V	ppm	150.918841	133.715072	235.254257	166.678823
Cr	ppm	277.79963	25.5524187	79.1509703	177.214653
Co	ppm	16.3693193	17.1029337	21.2097382	20.7248304
Ni	ppm	144.218374	23.4636828	45.4978061	108.643194
Cu	ppm	20.1548027	36.5767556	76.3217991	58.2313525
Zn	ppm	77.4463807	61.2865661	53.4925558	70.5814719
Sr	ppm	421.437557	466.92344	404.976234	936.309309
Y	ppm	16.0296648	20.7346235	19.0153724	13.0946111
Zr	ppm	112.129541	155.157681	111.901878	135.240488
Ba	ppm	750.862552	864.848708	613.42951	820.020243

Sample		DC16-037	DC16-038	DC16-039
SiO2	wt%	59.7089394	60.8746004	60.1240399
TiO2	wt%	0.79533	0.70797299	0.6413017
Al2O3	wt%	20.1083496	17.0659852	16.1423653
Fe2O3	wt%	6.00282881	7.79739552	8.09909218
MnO	wt%	0.06558723	0.09838269	0.13358722
MgO	wt%	0.87190889	2.20757961	2.5085379
CaO	wt%	7.74399939	6.86167285	7.17638386
Na2O	wt%	3.59292078	3.03705345	2.7795548
K2O	wt%	1.99346041	1.40797287	1.04907854
P2O5	wt%	0.38166164	0.22555192	0.25577013
LOI	wt%	0.59322034	0.65720294	0.86168694
Total	wt%	101.264986	100.284167	98.9097115
CR2O3	wt%			
Sc	ppm	11.2089346	18.7303077	17.0282119
V	ppm	77.4587478	170.256415	148.108884
Cr	ppm	3.69954938	33.482687	159.073079
Co	ppm	8.80220049	17.8532246	18.8077735
Ni	ppm	2.14666439	9.33899154	34.4283768
Cu	ppm	31.3388102	20.5971926	23.3395599
Zn	ppm	54.3641231	74.085927	80.5771642
Sr	ppm	562.046653	445.919613	416.123135
Y	ppm	19.7724787	15.859905	16.1451786
Zr	ppm	163.338526	98.0614018	94.1931673
Ba	ppm	805.366125	863.469958	702.810654

DB15 Samples:

Sample		DB15-081	DB13-082	DB15-083	DB15-087
SiO2	wt%	55.0004141	54.7624	56.8906566	60.2385808
TiO2	wt%	0.62136645	0.61653691	0.62990089	0.71926745
Al2O3	wt%	18.8606576	19.0839295	19.8447795	15.4478587
Fe2O3	wt%	7.20513717	7.10961347	7.21139882	12.1943564
MnO	wt%	0.11237153	0.11678672	0.12843672	0.13795287
MgO	wt%	1.50144362	1.50392442	1.29129488	2.68908824
CaO	wt%	4.48027632	4.56370855	6.36092094	2.92685432
Na2O	wt%	2.29076042	3.84829937	4.45864791	4.11110414
K2O	wt%	7.74630277	6.89610254	1.89365342	1.57884053
P2O5	wt%	0.66230239	0.6161791	0.64246632	0.29560462
LOI	wt%	4.58126241	1.56004275	9.47513317	3.76908354
Total	wt%	98.4810323	99.1174806	99.352156	100.339508
CR2O3	wt%				
Sc	ppm	8.26852859	7.98696178	7.63936914	24.8152413
V	ppm	158.727015	160.75417	167.940782	243.652509
Cr	ppm	25.361697	16.9178171	19.185145	19.2507154
Co	ppm	14.6046332	14.2331623	14.9581559	22.0078404
Ni	ppm	11.2553883	7.32428215	4.19628906	16.2985109
Cu	ppm	188.454205	207.330214	184.02965	96.1761328
Zn	ppm	75.5826989	78.2538673	64.4470809	85.6425384
Sr	ppm	1268.07569	1215.50334	1678.59384	88.1262527
Y	ppm	12.2705872	11.9523695	12.2297838	12.9657924
Zr	ppm	88.2484434	79.279966	93.136417	37.0651175
Ba	ppm	1647.22916	1577.45945	1715.55222	430.234251

EAFIT Samples:

Sample		PKSW-16A	PKSW-16B	PKSW-098	JLSW-008A
SiO2	wt%	61.1441281	62.4175272	68.3790071	62.3431728
TiO2	wt%	0.87906748	0.89016149	0.35745358	0.68897293
Al2O3	wt%	16.4328042	16.2287758	16.3050101	16.7131931
Fe2O3	wt%	6.59423018	6.4997469	4.17356255	6.2566729
MnO	wt%	0.0770628	0.06822338	0.06352675	0.07240907
MgO	wt%	1.43964522	0.95435213	1.00374841	2.2368173
CaO	wt%	6.56216997	6.49371838	2.24501146	5.48716836
Na2O	wt%	3.35031996	3.59647283	4.45675861	3.68659848
K2O	wt%	2.2009103	1.9795147	1.55244137	2.04538967
P2O5	wt%	0.24451015	0.2784977	0.2529644	0.413932
LOI	wt%	1.26270017	0.52433716	2.40013789	1.33154302
Total	wt%	98.9248483	99.4069905	98.7894844	99.9443267
CR2O3	wt%				
Sc	ppm	15.0172634	12.7332638	7.29806638	8.94357531
V	ppm	148.133533	128.628481	64.9870536	89.4321003
Cr	ppm	33.3118862	21.9197693	9.73010097	25.1296072
Co	ppm	14.1608115	11.7188468	8.02809659	13.266048
Ni	ppm	39.5438222	19.6627283	4.4858314	11.5963011
Cu	ppm	39.2010012	43.2771344	8.16401433	17.9374899
Zn	ppm	59.0384098	42.7447858	20.8977418	29.8967039
Sr	ppm	636.808236	556.927995	1119.27758	490.082401
Y	ppm	16.72885	14.1504693	6.59763875	11.868293
Zr	ppm	184.660311	148.652255	86.8966648	86.7597805
Ba	ppm	1086.68662	918.061783	2377.83401	835.586097

Sample		JLSW-032B	LHSW-17B	LHSW-018F	SESW-55B
SiO2	wt%	70.918055	62.022863	62.3853266	58.4247352
TiO2	wt%	0.48624324	0.73834444	0.6575892	0.8227629
Al2O3	wt%	15.9854027	15.9036666	17.9536565	17.4677424
Fe2O3	wt%	2.99315153	7.14702673	6.14847914	6.91716371
MnO	wt%	0.01139814	0.09945572	0.06761544	0.13168594
MgO	wt%	0.13080687	1.86117457	1.85543674	2.30876962
CaO	wt%	3.03564699	5.52833442	6.30930096	6.28740248
Na2O	wt%	3.2467229	3.25216148	2.73574683	3.88226411
K2O	wt%	2.98026023	1.81780609	1.43521056	2.31177152
P2O5	wt%	0.18419588	0.41867385	0.28057758	0.44315275
LOI	wt%	1.25887828	0.40747029	3.6032276	0.63872749
Total	wt%	99.9718835	98.7895069	99.8289395	98.9974506
CR2O3	wt%				
Sc	ppm	6.44419897	9.43398401	13.1311519	13.8896527
V	ppm	26.9676358	85.8279244	93.2695041	134.228565
Cr	ppm	15.4349995	12.4860263	22.7321494	42.2078322
Co	ppm	5.62370169	12.2352232	9.24969654	14.7809181
Ni	ppm	4.02754251	21.7894738	20.2734514	30.3164688
Cu	ppm	5.46462216	18.00857	11.2428428	42.5007762
Zn	ppm	38.1414729	47.2554047	71.5514759	57.8263967
Sr	ppm	319.591282	343.164089	373.401639	738.250285
Y	ppm	12.9317058	11.3471576	12.9987452	13.5472748
Zr	ppm	209.8817	116.283539	114.049311	129.435256
Ba	ppm	1404.04757	789.276785	911.789491	1205.20633

Sample		SESW-106A
SiO2	wt%	60.7461995
TiO2	wt%	0.86098122
Al2O3	wt%	17.0489222
Fe2O3	wt%	7.31328612
MnO	wt%	0.08243474
MgO	wt%	2.19897498
CaO	wt%	6.17637101
Na2O	wt%	3.46023778
K2O	wt%	2.54269282
P2O5	wt%	0.39396705
LOI	wt%	0.63555722
Total	wt%	100.824067
CR2O3	wt%	
Sc	ppm	15.0960151
V	ppm	158.735646
Cr	ppm	17.3065893
Co	ppm	15.2352332
Ni	ppm	25.0045666
Cu	ppm	44.6023571
Zn	ppm	42.408384
Sr	ppm	616.684462
Y	ppm	13.8695475
Zr	ppm	146.627174
Ba	ppm	1007.83857

Scotia Samples:

Sample		DR166.4	DR166.7	DR167.1	DR167.4
SiO2	wt%	55.0878808	65.5615772	72.7308599	61.3209882
TiO2	wt%	0.7536831	0.54661326	0.35234592	1.00207876
Al2O3	wt%	18.4701819	14.5314429	14.6500619	14.0036357
Fe2O3	wt%	9.87271198	4.9982205	3.03376299	11.8182721
MnO	wt%	0.17315909	0.13307391	0.06732982	0.21227276
MgO	wt%	3.48629845	0.8944999	0.38498087	0.95775197
CaO	wt%	10.3758922	2.04150605	1.53766409	6.06910952
Na2O	wt%	2.04154499	3.64401273	3.6770618	3.15847555
K2O	wt%	0.34979554	6.23941124	4.78653597	0.77458363
P2O5	wt%	0.18652594	0.25055942	0.12779296	0.3062732
LOI	wt%	0.00783822	3.77916849	1.04658059	-0.0628394
Total	wt%	100.797674	98.8409171	101.348396	99.6234414
CR2O3	wt%				
Sc	ppm	33.4031699	21.5332761	9.4049906	36.7214913
V	ppm	276.208964	41.358958	3.21945189	60.7329207
Cr	ppm	49.7790726	23.1672998	9.14037581	2.89922539
Co	ppm	23.1294216	7.9989056	4.75482602	13.1453055
Ni	ppm	25.9626607	3.86300789	23.8639325	8.87066221
Cu	ppm	56.7647925	8.48869898	5.27219727	102.780457
Zn	ppm	56.0499443	35.890344	15.9152422	94.7202442
Sr	ppm	190.408366	246.214364	180.30544	130.560745
Y	ppm	19.1913271	31.3442427	36.2347573	39.9835491
Zr	ppm	60.1118994	175.580496	248.20864	99.4013509
Ba	ppm	140.404487	922.535466	768.138228	163.944012

Sample		SS18.15
SiO2	wt%	50.8783654
TiO2	wt%	0.91872814
Al2O3	wt%	17.7554323
Fe2O3	wt%	11.97496
MnO	wt%	0.15865104
MgO	wt%	4.95185388
CaO	wt%	11.8660487
Na2O	wt%	1.57469796
K2O	wt%	0.17461454
P2O5	wt%	0.13842175
LOI	wt%	0.3762813
Total	wt%	100.391774
CR2O3	wt%	
Sc	ppm	41.7527553
V	ppm	679.492315
Cr	ppm	121.932421
Co	ppm	27.4829824
Ni	ppm	48.9437741
Cu	ppm	135.891599
Zn	ppm	56.9941647
Sr	ppm	123.54986
Y	ppm	17.0902367
Zr	ppm	41.0725699
Ba	ppm	62.0215988

Cardiff 2017 ICP-MS Data:

ISRM Samples:

Sample		JA2	JB1a	JG1a
49TiO2	%	0.6716475	1.32482794	0.26389212
51V	ppm	125.635163	224.122097	20.7425783
52Cr	ppm	436.316267	416.008147	29.8250667
55MnO	%	0.10867778	0.14292101	0.05400633
57Fe2O3	%	6.8261	9.12542	1.969035
59Co	ppm	26.1916	36.39894	4.914985
60Ni	ppm	150.509833	139.340633	12.9096833
65Cu	ppm	24.3889033	58.4449413	4.09308333
66Zn	ppm	68.6224867	83.0722067	27.3997667
71Ga	ppm	15.5627567	17.1738827	15.8541667
85Rb	ppm	77.29432	40.523136	189.5095
88Sr	ppm	242.700933	452.484293	174.367333
89Y	ppm	16.9613383	23.5796933	31.6162833
90Zr	ppm	119.8504	145.21922	121.1485
93Nb	ppm	7.1227895	26.532258	10.36915
95Mo	ppm	0.49022133	1.16812571	0.58842833
118Sn	ppm	1.89167767	2.78921547	4.93845167
133Cs	ppm	4.97603467	1.19411947	10.9914717
137Ba	ppm	312.83545	507.9641	450.5035
139La	ppm	16.060175	38.585658	20.80445
140Ce	ppm	32.4136195	66.353229	43.54312
141Pr	ppm	4.08317865	7.4513908	5.8200845
146Nd	ppm	13.7687183	25.6926893	19.2133833
147Sm	ppm	3.07753967	5.02302707	4.63019517
153Eu	ppm	0.90565617	1.48697447	0.69251667
157Gd	ppm	3.1584275	4.638284	4.0340095
159Tb	ppm	0.42581587	0.70605876	0.74110998
163Dy	ppm	2.7971307	4.08486756	4.27994422
165Ho	ppm	0.50613413	0.75356913	0.79377233
166Er	ppm	1.42013	2.1690818	2.4794045
169Tm	ppm	0.24929717	0.33306147	0.42666667
172Yb	ppm	1.75809667	2.13013847	3.02773367
175Lu	ppm	0.27480983	0.32675933	0.47878333
178Hf	ppm	2.7807155	3.5611384	3.6524375
181Ta	ppm	0.617579	1.6549818	1.59697
208Pb	ppm	35.6783917	56.8041127	26.1653167
232Th	ppm	4.37712	8.8304676	11.6415
238U	ppm	2.28323883	1.60766613	4.08677833

DC16 Samples:

Sample		DC16-001	DC16-002	DC16-003	DC16-004
49TiO2	%	0.76047031	0.87514891	0.59583475	0.65914211
51V	ppm	161.066812	154.649168	106.803819	105.789418
52Cr	ppm	119.251417	503.462293	59.5122405	84.5211965
55MnO	%	0.00282457	0.10700343	0.07402447	0.07266151
57Fe2O3	%	7.82341162	6.47136138	4.32626186	4.45839406
59Co	ppm	12.0758844	36.3693626	10.4900034	11.4621008
60Ni	ppm	367.953377	218.961865	16.7253386	82.6971765
65Cu	ppm	732.176211	38.4957195	14.5220512	22.4037854
66Zn	ppm	32.6419526	73.7436024	72.75971	58.266633
71Ga	ppm	18.8181234	15.0609555	16.9573329	15.4659825
85Rb	ppm	72.1534741	21.9981224	54.3476349	39.5826888
88Sr	ppm	533.106717	437.760139	510.756931	475.328443
89Y	ppm	21.251996	12.926101	12.7084726	11.9688197
90Zr	ppm	130.391547	78.061118	130.555315	87.4663845
93Nb	ppm	6.0973157	3.57983528	5.31305605	3.86173349
95Mo	ppm	0.34964336	0.41624585	0.85926005	0.7241589
118Sn	ppm	2.39923133	1.80801369	1.36158105	1.73951153
133Cs	ppm	1.0109261	0.48766592	1.73976931	1.2543804
137Ba	ppm	181.519821	655.657215	1087.29158	872.372439
139La	ppm	18.7473842	10.5785777	17.4131627	14.3442485
140Ce	ppm	37.4992901	21.3197906	33.1109494	27.1615019
141Pr	ppm	5.04164017	2.96073389	4.06506658	3.41563486
146Nd	ppm	20.0994476	12.4972846	15.1524505	12.8274027
147Sm	ppm	4.28182998	2.92699526	3.00422209	2.74531591
153Eu	ppm	1.05682987	0.92703195	0.90628834	0.85314616
157Gd	ppm	3.94079664	2.62489787	2.59235374	2.2349199
159Tb	ppm	0.57717179	0.36772091	0.34820663	0.333266
163Dy	ppm	3.47524229	2.258429	2.12902896	1.90538026
165Ho	ppm	0.65231926	0.42475366	0.40936444	0.36916794
166Er	ppm	1.88244515	1.15686883	1.16319558	1.07849876
169Tm	ppm	0.29913056	0.18524198	0.18756615	0.16309743
172Yb	ppm	2.14818856	1.25059196	1.32246275	1.15738621
175Lu	ppm	0.31429086	0.18111435	0.2116668	0.18002166
178Hf	ppm	3.33112596	2.18622367	3.45921355	2.27640858
181Ta	ppm	0.59000067	0.24189177	0.39934124	0.28054118
208Pb	ppm	4.1977015	5.90684706	11.1954611	8.05385123
232Th	ppm	7.21767669	3.1738635	7.4858665	5.98552823
238U	ppm	1.4295551	1.09628341	1.99911609	1.41747147

Sample		DC16-005	DC16-006	DC16-007	DC16-008
49TiO2	%	0.86592473	0.69637089	0.78666775	0.83003477
51V	ppm	112.129511	117.088903	120.635122	166.692608
52Cr	ppm	221.432077	203.119001	433.751422	186.492451
55MnO	%	0.07428653	0.08322656	0.04721985	0.0889679
57Fe2O3	%	4.96787205	5.19451772	5.08500153	6.06268771
59Co	ppm	16.9910189	17.0104345	13.9931364	20.5844604
60Ni	ppm	101.28677	77.8350845	131.772218	87.9995959
65Cu	ppm	31.95772	21.6077022	27.7562686	20.6636912
66Zn	ppm	68.5623011	68.5849875	75.4667452	75.0615587
71Ga	ppm	13.3247723	17.1756846	17.7367825	17.4533441
85Rb	ppm	23.9779437	37.7830658	39.921645	31.7912594
88Sr	ppm	409.491671	491.214422	502.985107	661.43436
89Y	ppm	11.8557755	13.8298292	14.5576071	14.0493147
90Zr	ppm	75.4577128	100.656011	110.229477	105.122447
93Nb	ppm	3.43773448	4.15939467	4.76174939	4.9253114
95Mo	ppm	0.50321168	0.60611103	0.37735186	0.61541781
118Sn	ppm	1.18567656	2.6577549	2.496696	2.11710856
133Cs	ppm	0.41653914	1.13602986	0.82465629	1.33478908
137Ba	ppm	650.386726	1245.24311	1486.08416	1040.45631
139La	ppm	11.6436497	14.5974828	17.2259484	15.9803358
140Ce	ppm	22.6185334	27.1554137	26.7782785	30.3490119
141Pr	ppm	3.00437826	3.85237081	4.42541189	4.19773652
146Nd	ppm	11.840673	15.1007852	17.2331847	16.5444218
147Sm	ppm	2.73518523	3.18872288	3.71234138	3.58638079
153Eu	ppm	0.82478352	1.11039576	1.11688806	1.15215623
157Gd	ppm	2.36730256	2.85632527	3.15425079	2.97750818
159Tb	ppm	0.33075265	0.38135559	0.41912234	0.4243504
163Dy	ppm	2.05533834	2.24570553	2.44848377	2.40469462
165Ho	ppm	0.37019635	0.44136905	0.45543643	0.44423321
166Er	ppm	1.02119383	1.2192635	1.26998469	1.26111
169Tm	ppm	0.16318241	0.19000556	0.20118458	0.20274003
172Yb	ppm	1.11122419	1.3322093	1.37764731	1.34119441
175Lu	ppm	0.16476382	0.20725662	0.20604877	0.20127766
178Hf	ppm	1.98924464	2.75299118	3.02980016	2.85208088
181Ta	ppm	0.26096748	0.29157159	0.31163705	0.29320177
208Pb	ppm	5.14210086	7.64319881	11.827092	7.97599817
232Th	ppm	4.12062343	5.73559753	6.16158169	5.60892532
238U	ppm	1.21842168	1.92624239	1.79415461	1.52821223

Sample		DC16-009	DC16-010	DC16-011	DC16-012
49TiO2	%	0.86964068	0.68157528	0.8320772	0.55437449
51V	ppm	140.301821	94.8417003	157.298016	49.4017137
52Cr	ppm	415.096005	60.5402927	70.0332619	62.8060547
55MnO	%	0.09179256	0.06754459	0.09738511	0.00330436
57Fe2O3	%	5.85328873	4.16397865	5.54317961	1.82683487
59Co	ppm	23.6526707	10.2146427	14.0201326	8.41909314
60Ni	ppm	288.841565	56.7179436	11.3887651	41.7584375
65Cu	ppm	35.3346897	26.8722455	24.1139089	8.56240571
66Zn	ppm	70.5071594	70.0615207	69.922722	33.6225127
71Ga	ppm	12.5842285	15.7126119	16.3257353	16.2504915
85Rb	ppm	15.466875	17.3545856	24.8297846	115.68396
88Sr	ppm	364.09248	620.895042	557.501815	459.41147
89Y	ppm	11.2571736	12.3535272	13.9454522	7.38073995
90Zr	ppm	63.3906477	110.238167	84.3496912	141.344829
93Nb	ppm	2.83932488	4.7285664	3.63957903	8.14064442
95Mo	ppm	0.46424502	0.3328272	0.44610662	0.65729797
118Sn	ppm	1.27690898	3.61416818	1.47812617	1.17926047
133Cs	ppm	0.4515975	0.22217942	0.80523033	4.04070488
137Ba	ppm	531.427518	1072.3197	658.020503	1221.64091
139La	ppm	9.02132383	17.1868175	13.0104669	16.7804634
140Ce	ppm	18.9215464	32.0851829	25.9714384	26.5875923
141Pr	ppm	2.56363702	4.14541199	3.46299453	2.86329139
146Nd	ppm	10.7056089	15.3352363	13.4301119	9.34577113
147Sm	ppm	2.4477425	3.09405131	2.92056094	1.64922103
153Eu	ppm	0.79687964	0.92735166	0.89054128	0.73461293
157Gd	ppm	2.22215276	2.67360912	2.64368734	1.4635341
159Tb	ppm	0.3183323	0.34812634	0.35516268	0.16538158
163Dy	ppm	1.90637966	2.00356475	2.1742655	1.04570488
165Ho	ppm	0.37237856	0.3855317	0.43427894	0.22513925
166Er	ppm	0.99795022	1.07560355	1.22264356	0.63209062
169Tm	ppm	0.15228542	0.16557606	0.1927499	0.11334453
172Yb	ppm	1.09629379	1.13452742	1.31702421	0.77165456
175Lu	ppm	0.15990218	0.16686905	0.20522056	0.12861785
178Hf	ppm	1.7349528	2.74799516	2.17183463	4.03512797
181Ta	ppm	0.20129291	0.33783575	0.24261657	0.8114181
208Pb	ppm	5.54326766	10.8976492	4.4877679	15.5441222
232Th	ppm	2.85771389	5.60814068	3.84488615	18.4742359
238U	ppm	0.90183498	1.24544708	1.05157043	9.0268453

Sample		DC16-013	DC16-014	DC16-015	DC16-016
49TiO2	%	0.82280078	0.76232938	0.68816373	0.86036801
51V	ppm	144.087616	109.10093	111.060012	133.148035
52Cr	ppm	81.2668384	85.9827342	88.0863213	66.7216396
55MnO	%	0.06607622	0.06097918	0.05549211	0.04707297
57Fe2O3	%	4.86408138	4.42199253	3.99673092	4.05339505
59Co	ppm	12.3517838	14.2686656	12.6742778	11.4187054
60Ni	ppm	145.638988	52.8678343	58.6895729	222.242701
65Cu	ppm	37.7221993	30.1029524	26.7329558	44.3463362
66Zn	ppm	75.9258565	50.2816956	53.1020999	77.3911959
71Ga	ppm	18.2153247	14.4603364	15.8558185	18.022156
85Rb	ppm	97.0514899	48.2469253	62.5579403	57.0787273
88Sr	ppm	599.999144	434.576831	559.035582	704.665022
89Y	ppm	18.0892914	11.451882	11.691369	18.1279477
90Zr	ppm	143.897	100.446646	117.306673	137.321247
93Nb	ppm	8.12200513	4.30878348	5.54438367	6.41995228
95Mo	ppm	1.59138855	0.81159588	0.60152727	1.06276388
118Sn	ppm	1.40047698	1.33282933	5.77471279	1.29802671
133Cs	ppm	5.81015867	2.13083051	1.83163368	2.37101333
137Ba	ppm	1127.105	883.701981	1084.65988	1185.38431
139La	ppm	21.9707432	14.6041014	18.8722471	25.2383594
140Ce	ppm	42.1492391	27.7274428	35.0228142	48.8340117
141Pr	ppm	5.3967126	3.51082992	4.40231755	6.52571257
146Nd	ppm	19.6848036	13.1871954	15.802373	25.1766752
147Sm	ppm	4.07534624	2.7392349	2.95063462	5.14088385
153Eu	ppm	1.11371861	0.82264859	0.8790097	1.3706619
157Gd	ppm	3.83797966	2.37432141	2.6660214	4.35824089
159Tb	ppm	0.48539457	0.30457406	0.31586439	0.53770045
163Dy	ppm	2.90113454	1.82072914	1.84036303	3.08843815
165Ho	ppm	0.56833005	0.36795533	0.35493677	0.59385175
166Er	ppm	1.614735	1.00651887	0.99888599	1.59618643
169Tm	ppm	0.26972424	0.16205224	0.15967971	0.25099931
172Yb	ppm	1.83447177	1.08054985	1.05027388	1.79431172
175Lu	ppm	0.27899364	0.18101208	0.17653747	0.25668456
178Hf	ppm	4.08088115	2.69378156	3.18303189	3.56682109
181Ta	ppm	0.67763959	0.38338842	0.4382586	0.44056297
208Pb	ppm	15.6603048	7.97737806	28.0380997	12.0093505
232Th	ppm	16.1562424	9.25743408	10.3215029	9.1391658
238U	ppm	6.04135415	3.03751341	3.89803204	3.21930775

Sample		DC16-017	DC16-018	DC16-019	DC16-020
49TiO2	%	0.79084745	0.84002794	0.85721932	0.79951634
51V	ppm	119.118297	130.44334	111.35434	127.845293
52Cr	ppm	52.9757089	59.798496	48.5179695	51.916105
55MnO	%	0.06216635	0.06935963	0.05799117	0.06467648
57Fe2O3	%	4.57305576	5.07901553	4.56334708	4.82469663
59Co	ppm	10.8833235	11.4708758	9.69049985	37.0556547
60Ni	ppm	59.1045693	33.4075598	57.7967656	50.7338143
65Cu	ppm	17.6018314	16.5141082	76.6868511	17.8832402
66Zn	ppm	64.7931877	73.078792	63.6950976	65.9520508
71Ga	ppm	16.0021998	17.890665	14.5773735	17.0240012
85Rb	ppm	42.2078444	47.8942363	39.9199417	44.4029796
88Sr	ppm	471.551967	450.489002	351.133642	489.045499
89Y	ppm	15.650426	31.3600238	14.2492602	15.8862931
90Zr	ppm	116.756454	131.465749	95.112663	123.923934
93Nb	ppm	4.74425387	5.56052325	4.11384337	5.10704651
95Mo	ppm	0.57469697	0.67186227	1.91367722	0.97630479
118Sn	ppm	1.15513316	1.30954992	3.90459873	2.37894384
133Cs	ppm	1.37121988	1.89266526	1.53844911	1.97906412
137Ba	ppm	934.37074	1110.02673	976.389118	1010.84606
139La	ppm	16.2915943	35.4690583	15.7179514	17.3756965
140Ce	ppm	30.8722396	59.2153752	27.7450864	32.3464383
141Pr	ppm	4.2478943	9.09962525	4.08537248	4.4037237
146Nd	ppm	15.7576078	35.1932561	15.4617787	16.9158306
147Sm	ppm	3.31729764	7.33918918	3.24235957	3.48537981
153Eu	ppm	0.98908851	2.04186251	0.92177488	1.07374637
157Gd	ppm	2.99212099	6.40542802	2.85147434	3.14931112
159Tb	ppm	0.39635291	0.82461021	0.37348885	0.42302706
163Dy	ppm	2.42044025	4.6248247	2.25974289	2.46680775
165Ho	ppm	0.48542634	0.88647977	0.44450708	0.50383494
166Er	ppm	1.35324527	2.42308869	1.2850719	1.41720762
169Tm	ppm	0.21448412	0.37520912	0.21108344	0.23378539
172Yb	ppm	1.47758371	2.49782826	1.43335974	1.55210895
175Lu	ppm	0.2557932	0.39259976	0.21976365	0.24628696
178Hf	ppm	2.99903612	3.38633301	2.53724643	3.11379876
181Ta	ppm	0.32515004	0.37685966	0.29501114	0.35097962
208Pb	ppm	8.67350236	10.6833437	25.4841485	9.89133775
232Th	ppm	5.67111182	5.85751979	4.27507381	5.58496882
238U	ppm	1.71258484	1.90479558	1.58230103	1.78657265

Sample		DC16-021	DC16-022	DC16-023	DC16-024
49TiO2	%	0.60468677	0.32560802	0.67983119	0.90095253
51V	ppm	121.468596	48.2216398	143.56499	185.361536
52Cr	ppm	60.8362929	9.59731651	65.1924845	82.0480357
55MnO	%	0.05892984	0.05137149	0.08538759	0.09876369
57Fe2O3	%	4.64784661	2.87038359	4.23723772	5.27220294
59Co	ppm	13.0706349	2.20959284	14.8879489	18.1878042
60Ni	ppm	108.723481	39.4694736	48.9702977	34.5894287
65Cu	ppm	32.5625021	9.03102461	21.4728614	29.2255306
66Zn	ppm	60.5781871	96.4492378	87.7976256	495.514287
71Ga	ppm	17.0088676	18.809903	14.8272482	17.0603982
85Rb	ppm	67.7969906	87.1222729	39.7595706	24.188977
88Sr	ppm	375.473213	337.811944	420.37472	465.961927
89Y	ppm	15.2838807	14.1474653	13.7816874	20.677759
90Zr	ppm	122.747867	72.4749833	113.001008	99.7821153
93Nb	ppm	5.60018691	10.9423972	4.55041434	3.07812143
95Mo	ppm	0.45142332	0.08059869	0.69046215	0.88338187
118Sn	ppm	4.25374398	2.08364238	2.24610198	5.03297504
133Cs	ppm	10.1996166	2.63265954	1.5064212	0.76229145
137Ba	ppm	1041.24787	1615.17179	787.59597	722.625367
139La	ppm	18.3169604	13.0608896	15.533298	13.7962874
140Ce	ppm	35.3578055	24.4842042	27.5038894	25.9807914
141Pr	ppm	4.55891083	3.13284986	3.84474311	3.74947268
146Nd	ppm	16.9787151	10.9274808	14.9506463	15.7577648
147Sm	ppm	3.65220308	2.57336586	3.11774827	3.84505706
153Eu	ppm	1.06970483	0.77746481	0.94734143	1.20930148
157Gd	ppm	3.25177376	2.31385468	2.9625003	3.80597595
159Tb	ppm	0.43296907	0.34401536	0.38175939	0.52628842
163Dy	ppm	2.49694202	2.09727007	2.27210247	3.08908201
165Ho	ppm	0.47418876	0.40048632	0.41794664	0.61149602
166Er	ppm	1.34615458	1.17264916	1.1977531	1.68408353
169Tm	ppm	0.22075809	0.19621407	0.18228405	0.26543856
172Yb	ppm	1.37295003	1.38114012	1.26914005	1.64939149
175Lu	ppm	0.22967769	0.21512019	0.19024995	0.26957572
178Hf	ppm	3.12996654	2.30658749	2.7914164	2.64632159
181Ta	ppm	0.43359308	0.87902072	0.31740595	0.19590229
208Pb	ppm	7.82689653	10.7019666	14.594461	10.8438685
232Th	ppm	5.57299471	4.56710781	5.96865667	4.72724063
238U	ppm	1.83735902	4.2391319	1.70870535	1.20147466

Sample		DC16-025	DC16-026	DC16-027	DC16-028
49TiO2	%	0.76208418	0.66451271	0.8043431	0.83343201
51V	ppm	119.7815	137.187476	153.870334	140.762306
52Cr	ppm	83.9992995	53.5458163	22.1095537	13.9020684
55MnO	%	0.06868479	0.08085511	0.11217771	0.08358169
57Fe2O3	%	3.7620467	3.8824159	5.25313057	4.39128765
59Co	ppm	12.7436265	13.0612134	20.4663694	16.5253845
60Ni	ppm	26.4012648	78.5688748	27.178351	17.2325505
65Cu	ppm	38.1596177	26.3936333	18.2186259	44.9888767
66Zn	ppm	48.0879093	63.6652338	76.9806816	67.9495258
71Ga	ppm	14.2151665	14.3914297	16.4955625	16.9180782
85Rb	ppm	44.5071268	25.0922709	33.5559214	35.9601595
88Sr	ppm	340.483885	414.30757	444.970756	533.69908
89Y	ppm	23.6145229	12.7534163	17.5681614	16.7353533
90Zr	ppm	131.298698	102.116014	133.578743	127.757943
93Nb	ppm	4.29291538	3.70069234	5.0446349	7.26574977
95Mo	ppm	0.65234808	0.60407882	0.98155992	0.98824824
118Sn	ppm	3.34233571	1.27432873	2.27453459	1.2723988
133Cs	ppm	1.58538491	0.4289345	0.81338207	0.49028831
137Ba	ppm	846.591443	569.556855	909.700023	702.263925
139La	ppm	24.6338413	11.957757	16.5453041	16.6346818
140Ce	ppm	44.4327129	23.7062788	29.2802228	32.8876904
141Pr	ppm	6.94771503	3.12418385	4.37386926	4.28368388
146Nd	ppm	27.1386734	12.5702324	16.9346568	16.3270536
147Sm	ppm	5.55980528	2.78189972	3.67935653	3.432698
153Eu	ppm	1.3990835	0.85178665	1.18191452	1.09234898
157Gd	ppm	4.97867816	2.73726901	3.38547752	3.21901059
159Tb	ppm	0.66382033	0.35909828	0.47102306	0.43759126
163Dy	ppm	3.90199529	2.16393541	2.90356927	2.70279356
165Ho	ppm	0.69607662	0.41534946	0.55421857	0.51581219
166Er	ppm	2.02119493	1.14760729	1.64062458	1.46925085
169Tm	ppm	0.31404632	0.17521389	0.27163779	0.23657107
172Yb	ppm	2.10160081	1.26149818	1.67381565	1.60063011
175Lu	ppm	0.33184282	0.19156263	0.28825526	0.26300498
178Hf	ppm	3.25937125	2.57489218	3.36028675	3.18532761
181Ta	ppm	0.3496178	0.2381325	0.33210104	0.42693435
208Pb	ppm	11.1980026	4.38554859	8.12333118	9.84082662
232Th	ppm	8.39021766	4.60702497	5.97408957	5.13751415
238U	ppm	2.44713557	1.16458678	1.61744159	1.24141802

Sample		DC16-029	DC16-030	DC16-031	DC16-032
49TiO2	%	0.76939184	0.78749094	0.84876918	0.84878305
51V	ppm	138.487203	167.865194	216.778243	166.838567
52Cr	ppm	57.4475004	36.857051	47.8845221	138.435487
55MnO	%	0.09362823	0.10349416	0.13279992	0.09537492
57Fe2O3	%	4.42002108	4.84711705	5.84608337	5.20979382
59Co	ppm	15.3412535	17.1674927	20.8271913	19.6333257
60Ni	ppm	60.1059475	6.96492159	687.047841	320.750678
65Cu	ppm	39.5493151	30.5247558	47.3231951	38.8548408
66Zn	ppm	63.6476016	59.5284191	72.7161295	82.7853246
71Ga	ppm	14.6050131	15.4275496	17.3354043	18.2456663
85Rb	ppm	33.4950962	35.3148215	30.5672404	40.4698639
88Sr	ppm	406.161751	410.225848	485.458262	617.201037
89Y	ppm	14.6769623	15.1564457	17.510209	16.0090031
90Zr	ppm	104.102248	107.269614	103.668272	149.63742
93Nb	ppm	3.60627599	3.72831704	3.66597386	7.10075175
95Mo	ppm	0.85718674	1.01201625	0.8001054	1.10643813
118Sn	ppm	1.14110879	2.25111815	1.30119977	1.3922976
133Cs	ppm	1.43297302	1.22157686	1.28804605	0.9639141
137Ba	ppm	603.90637	573.549693	581.727442	808.928569
139La	ppm	12.8472265	12.7696786	12.5644347	20.3471544
140Ce	ppm	25.945925	25.9532727	25.2621423	39.4739925
141Pr	ppm	3.4478243	3.40710666	3.37651008	5.34212254
146Nd	ppm	13.5803361	13.5173	13.7858855	20.9403604
147Sm	ppm	2.9721965	3.16422202	3.11287213	4.23923735
153Eu	ppm	0.82456173	0.93296486	0.98551543	1.17339798
157Gd	ppm	2.89814924	3.02120413	3.03936123	3.76282139
159Tb	ppm	0.37061135	0.41981371	0.43743388	0.4812754
163Dy	ppm	2.43616513	2.59613752	2.80038385	2.86428684
165Ho	ppm	0.45525569	0.4770041	0.55641038	0.50013719
166Er	ppm	1.35507354	1.43536862	1.64561624	1.39462319
169Tm	ppm	0.21969395	0.23107433	0.27855017	0.22528871
172Yb	ppm	1.42509601	1.47972314	1.76137605	1.46694215
175Lu	ppm	0.23419454	0.23934712	0.29123181	0.22823747
178Hf	ppm	2.69105558	2.84370961	2.69256846	3.75534453
181Ta	ppm	0.26294619	0.28087519	0.2399477	0.56459226
208Pb	ppm	5.5698936	5.57741194	6.40007406	7.35452133
232Th	ppm	5.78600309	6.67146551	5.39117664	6.77392747
238U	ppm	1.71463544	1.99225938	1.48987222	2.03463122

Sample		DC16-033	DC16-034	DC16-035	DC16-036
49TiO2	%	0.73972423	0.75422065	0.90324985	1.05991209
51V	ppm	156.766441	134.920533	228.406157	168.074759
52Cr	ppm	280.531797	30.5293666	87.211277	188.912968
55MnO	%	0.08874682	0.09756859	0.14473872	0.11211868
57Fe2O3	%	4.36226489	4.6975167	6.11126036	5.87162869
59Co	ppm	14.8719544	15.9427175	20.0374422	23.5656528
60Ni	ppm	139.154272	26.5857256	52.8145115	108.175157
65Cu	ppm	22.1468835	42.7128945	77.9136394	62.0540224
66Zn	ppm	81.594885	67.5786247	49.7116972	77.0587737
71Ga	ppm	15.808703	18.8564702	16.7666535	19.2911666
85Rb	ppm	38.0548796	47.9531595	32.8560709	21.5732215
88Sr	ppm	421.437557	475.616351	406.152099	946.12118
89Y	ppm	16.3050267	21.3398338	19.6252886	13.8792679
90Zr	ppm	108.65746	152.413981	111.393903	133.852355
93Nb	ppm	4.29955617	5.39074999	4.33870842	10.5328618
95Mo	ppm	0.58116883	0.91083608	0.76672801	0.54045363
118Sn	ppm	1.23473736	1.08437262	1.04052669	2.16869644
133Cs	ppm	1.21567111	1.84244134	1.0178591	0.23462036
137Ba	ppm	758.763004	870.115376	603.854094	816.836912
139La	ppm	14.248579	22.8482804	16.0805666	27.3628163
140Ce	ppm	27.376911	39.6309414	32.9248899	52.7865461
141Pr	ppm	3.60598225	5.89845997	4.19458314	6.8857896
146Nd	ppm	13.9976211	23.1499928	16.9399712	26.1527293
147Sm	ppm	3.17890829	4.71789214	3.71089547	5.2582397
153Eu	ppm	0.97125506	1.37803789	1.06775799	1.5326113
157Gd	ppm	3.08994512	4.41211478	3.6783864	4.23744933
159Tb	ppm	0.42376087	0.54898468	0.51115448	0.48391129
163Dy	ppm	2.6443656	3.40670131	3.13605236	2.6144452
165Ho	ppm	0.5079796	0.6241185	0.5775749	0.43829003
166Er	ppm	1.44599888	1.74271945	1.67811578	1.21275279
169Tm	ppm	0.24337969	0.26073926	0.26465656	0.17612027
172Yb	ppm	1.51932651	1.77816453	1.73509802	1.10228804
175Lu	ppm	0.26111927	0.27513133	0.28854049	0.15903741
178Hf	ppm	2.7856209	3.92786276	2.92815408	3.21959927
181Ta	ppm	0.29817623	0.35482314	0.29191972	0.55274689
208Pb	ppm	11.2692638	13.1623832	8.48581391	7.06366318
232Th	ppm	5.97372017	7.69565949	5.83518069	4.95568488
238U	ppm	1.7024409	2.33820895	1.62722831	0.96443233

Sample		DC16-037	DC16-038	DC16-039
49TiO2	%	0.81084329	0.73517127	0.65725487
51V	ppm	87.8061571	160.974478	138.04442
52Cr	ppm	5.82104741	36.8802835	167.11653
55MnO	%	0.06972666	0.10670212	0.14450044
57Fe2O3	%	3.70272092	4.94435327	5.31534741
59Co	ppm	9.33293297	14.7716155	17.9034553
60Ni	ppm	4.31836986	13.99865	35.9905762
65Cu	ppm	27.5149422	20.6303289	24.8811875
66Zn	ppm	51.0084846	76.9788344	80.1305786
71Ga	ppm	18.437127	17.132148	16.5734507
85Rb	ppm	46.5213074	34.1664642	27.794026
88Sr	ppm	549.590761	433.333083	418.518025
89Y	ppm	19.2486989	16.0129083	16.4987062
90Zr	ppm	154.068413	97.9304186	93.6572317
93Nb	ppm	6.23953999	3.53283721	3.43420716
95Mo	ppm	1.22107181	0.71239712	0.73253924
118Sn	ppm	1.46001243	1.23802856	2.35339459
133Cs	ppm	0.9956283	0.62929152	0.69450044
137Ba	ppm	799.119145	849.162874	715.401396
139La	ppm	18.7760855	11.805409	12.0241564
140Ce	ppm	37.5289891	22.1958353	23.3214925
141Pr	ppm	5.01465943	3.0583906	3.41584416
146Nd	ppm	19.0317176	11.7856085	13.5801144
147Sm	ppm	4.25773217	2.84130057	3.24879508
153Eu	ppm	1.21234228	0.94033834	0.97814261
157Gd	ppm	3.87892494	2.82545647	3.1305512
159Tb	ppm	0.53602366	0.38845893	0.43111051
163Dy	ppm	3.26923105	2.60496972	2.77492047
165Ho	ppm	0.60452048	0.48675336	0.50671285
166Er	ppm	1.71401646	1.43995719	1.43184942
169Tm	ppm	0.26604492	0.24692756	0.23486772
172Yb	ppm	1.88528072	1.5975877	1.51734051
175Lu	ppm	0.28468809	0.23936943	0.23989903
178Hf	ppm	3.8733423	2.53904057	2.45677263
181Ta	ppm	0.43968967	0.26303238	0.25721913
208Pb	ppm	9.06303107	11.2519496	8.46012864
232Th	ppm	8.69276396	4.70076891	3.99927929
238U	ppm	2.33828788	1.32295043	1.23038786

DB15 Samples:

Sample		DB15-081	DB15-082	DB15-083	DB15-087
49TiO2	%	0.55315959	0.59031617	0.5501904	0.65624218
51V	ppm	156.187473	158.064855	158.314184	259.278283
52Cr	ppm	26.1058184	15.2972604	15.5921374	14.5034122
55MnO	%	0.11871293	0.12067538	0.13242288	0.13025592
57Fe2O3	%	6.27791156	6.22830532	6.18152189	10.0104496
59Co	ppm	12.8785395	13.3617275	12.8914179	20.1691196
60Ni	ppm	14.4016101	9.64780653	4.89651976	14.0235534
65Cu	ppm	193.676114	204.243555	184.480437	94.6411005
66Zn	ppm	76.5736177	75.9399095	72.8431171	81.2776388
71Ga	ppm	14.9903247	14.6865172	14.6303277	12.1581521
85Rb	ppm	141.467988	92.7278598	88.35048	10.6323326
88Sr	ppm	1262.59142	1113.70473	1638.65267	86.3056501
89Y	ppm	12.312518	12.069819	12.3310301	12.8974115
90Zr	ppm	84.0649224	82.4691229	87.4487782	37.2636234
93Nb	ppm	5.50937695	5.45788391	5.91626083	1.52621175
95Mo	ppm	0.20985654	0.92008019	1.24991186	0.20311506
118Sn	ppm	0.72480593	0.83740975	1.22857701	1.12107512
133Cs	ppm	1.33938368	1.87357231	2.23011486	-0.0030743
137Ba	ppm	1647.22916	1577.45945	1705.55222	439.505544
139La	ppm	21.010206	20.7522894	21.2089763	3.49634144
140Ce	ppm	35.3294889	34.8174777	35.7562419	8.09519366
141Pr	ppm	4.36394905	4.31677663	4.38211843	1.29402009
146Nd	ppm	15.7166763	15.2067256	15.5942403	5.9170683
147Sm	ppm	3.08845495	3.10613893	3.03859667	1.64642878
153Eu	ppm	1.14373733	1.13140248	1.15114297	0.63541716
157Gd	ppm	2.69184633	2.72442744	2.69221976	1.95532233
159Tb	ppm	0.35388396	0.34426578	0.35874792	0.30566085
163Dy	ppm	2.0357206	1.8889525	1.91711752	2.16015749
165Ho	ppm	0.38483291	0.36302178	0.3842433	0.4180515
166Er	ppm	1.13244504	1.08730147	1.15037133	1.25930395
169Tm	ppm	0.19059577	0.17541067	0.17366391	0.20141077
172Yb	ppm	1.28242307	1.22179673	1.27419408	1.43696727
175Lu	ppm	0.19971268	0.18555619	0.19667754	0.23278856
178Hf	ppm	1.87289445	1.75156031	2.01941005	1.0465729
181Ta	ppm	0.30243159	0.27353473	0.27872184	0.113131
208Pb	ppm	10.0703488	11.2476321	9.73263417	5.13976636
232Th	ppm	3.92411746	3.78783338	4.01760269	1.48585124
238U	ppm	1.57455925	1.74817206	1.7516105	0.24176934

EAFIT Samples:

Sample		PKSW-16A	PKSW-16B	PKSW-098	JLSW-008A
49TiO2	%	0.81600173	0.85471022	0.33191772	0.64884868
51V	ppm	146.976149	127.426732	56.4449186	82.8830592
52Cr	ppm	35.3944353	28.2898351	10.0142843	28.7753437
55MnO	%	0.08514266	0.0661666	0.06005695	0.0533983
57Fe2O3	%	4.71192621	4.10032733	2.58741171	3.02885241
59Co	ppm	14.3285304	12.2550695	5.44975866	15.8948291
60Ni	ppm	37.1314676	21.8697678	8.64017376	13.4835472
65Cu	ppm	39.0399249	46.9966878	7.54220125	15.1076162
66Zn	ppm	65.3389529	53.3315739	22.3377984	19.4582162
71Ga	ppm	17.3706716	14.5308594	13.9411994	12.0271773
85Rb	ppm	81.2445931	63.6696892	34.3388281	38.8693847
88Sr	ppm	662.67446	571.144933	1173.43733	503.262733
89Y	ppm	16.3227812	13.9464474	6.87755841	12.3797643
90Zr	ppm	178.097197	144.172511	84.4051777	82.2480531
93Nb	ppm	9.9237596	8.52248042	8.6979788	4.13353668
95Mo	ppm	1.24217015	0.48165238	0.09484394	0.25434752
118Sn	ppm	1.50404007	2.91163785	1.38675043	1.58961234
133Cs	ppm	2.45717776	1.29008665	2.19429608	0.796035
137Ba	ppm	1082.62113	923.770786	2272.92753	784.178524
139La	ppm	26.363224	22.2781017	17.6785755	14.2841023
140Ce	ppm	50.4790667	42.5482902	32.8413903	28.0294985
141Pr	ppm	6.41073151	5.41590226	4.14552056	3.68562699
146Nd	ppm	22.3515178	19.1902059	14.4864186	13.7280882
147Sm	ppm	4.26349407	3.66172562	2.60144976	2.82483057
153Eu	ppm	1.13598869	0.99429425	1.04458137	0.86329433
157Gd	ppm	3.73038959	3.14516113	2.06683253	2.47572013
159Tb	ppm	0.4760197	0.38832196	0.21999113	0.31599313
163Dy	ppm	2.74873446	2.30177308	1.14772763	1.947636
165Ho	ppm	0.49253498	0.43055208	0.22108053	0.36923899
166Er	ppm	1.53373333	1.27000103	0.61424147	1.13430517
169Tm	ppm	0.25605127	0.20028902	0.10329605	0.18067093
172Yb	ppm	1.57821836	1.36197842	0.70863206	1.25385137
175Lu	ppm	0.23696762	0.20120983	0.11479107	0.19655302
178Hf	ppm	4.45003936	3.50954221	2.24932509	2.11767574
181Ta	ppm	0.66552434	0.5589349	0.64264194	0.31153566
208Pb	ppm	12.5496704	12.926484	16.7623377	6.58618568
232Th	ppm	11.115453	8.29645605	5.02461589	4.70062146
238U	ppm	3.20802537	2.62047938	2.6118087	1.7213264

Sample		JLSW-032B	LHSW-17B	LHSW-018F	SESW-55B
49TiO2	%	0.46450126	0.72020079	0.61632683	0.79752605
51V	ppm	26.2495405	87.5405276	96.7863057	134.469049
52Cr	ppm	18.0216219	15.0230057	25.6069976	47.129035
55MnO	%	0.00691685	0.08149094	0.06495757	0.12681566
57Fe2O3	%	1.76437594	3.95472749	4.00331864	4.78348186
59Co	ppm	2.10197547	9.64970475	8.00953745	18.5426916
60Ni	ppm	6.76941896	22.0947457	21.8067885	32.6518462
65Cu	ppm	4.64637347	21.2575138	11.4741028	45.5750163
66Zn	ppm	11.8390784	23.3841686	33.4764709	30.8431331
71Ga	ppm	14.4351981	12.4852445	15.3869516	16.9169392
85Rb	ppm	130.762753	46.790403	51.5020393	53.6879152
88Sr	ppm	326.630439	358.354902	395.51118	758.592338
89Y	ppm	13.6966515	12.0980504	14.295141	14.3728042
90Zr	ppm	204.626355	113.844274	118.704288	131.62906
93Nb	ppm	7.93358777	8.4999448	5.00548046	8.52650108
95Mo	ppm	0.96621025	0.67770613	0.80489478	0.83347681
118Sn	ppm	2.26266732	1.2002434	2.1688026	2.43952699
133Cs	ppm	4.07839754	1.47043181	2.53294203	0.84582754
137Ba	ppm	1393.36874	726.772082	822.718566	1167.11251
139La	ppm	19.1940613	16.7646246	14.2391397	22.6351925
140Ce	ppm	34.0087566	30.474128	29.2797656	44.895322
141Pr	ppm	4.66361664	3.83517178	3.69545195	5.57777963
146Nd	ppm	16.6283054	13.3942198	13.3991356	20.2839767
147Sm	ppm	3.48869387	2.80975021	2.85391901	3.80206847
153Eu	ppm	1.00988562	0.86086731	0.93501136	1.16415141
157Gd	ppm	2.85553887	2.52751934	2.74345812	3.44517649
159Tb	ppm	0.40580263	0.34463237	0.38520449	0.41348134
163Dy	ppm	2.33611978	1.94097934	2.30957259	2.41040628
165Ho	ppm	0.4295239	0.35737025	0.4481334	0.44618834
166Er	ppm	1.28774159	1.0861294	1.35284378	1.29572257
169Tm	ppm	0.2200219	0.16951798	0.22001168	0.20646042
172Yb	ppm	1.39609982	1.13333123	1.53328601	1.35201542
175Lu	ppm	0.21180272	0.16691502	0.22248709	0.20705742
178Hf	ppm	5.13348375	2.67912621	3.10530502	3.10901042
181Ta	ppm	0.6932376	0.57097007	0.38843367	0.49844068
208Pb	ppm	13.8939882	4.91508751	8.4473293	10.1652772
232Th	ppm	12.043522	6.47415035	5.93371739	5.94224002
238U	ppm	5.87968512	2.0068502	2.45520945	1.85896998

Sample		SESW-106A
49TiO2	%	0.83083032
51V	ppm	152.11908
52Cr	ppm	21.4551963
55MnO	%	0.0823422
57Fe2O3	%	4.29274401
59Co	ppm	14.0036555
60Ni	ppm	29.3882924
65Cu	ppm	45.5962728
66Zn	ppm	48.6568932
71Ga	ppm	16.239719
85Rb	ppm	66.147026
88Sr	ppm	627.575702
89Y	ppm	14.5002613
90Zr	ppm	143.425142
93Nb	ppm	9.05265084
95Mo	ppm	1.2349311
118Sn	ppm	3.07085467
133Cs	ppm	1.92289413
137Ba	ppm	991.073632
139La	ppm	21.7384931
140Ce	ppm	40.1294809
141Pr	ppm	5.05547091
146Nd	ppm	18.8437914
147Sm	ppm	3.66912613
153Eu	ppm	1.10892902
157Gd	ppm	3.32508385
159Tb	ppm	0.41993278
163Dy	ppm	2.44867962
165Ho	ppm	0.45067204
166Er	ppm	1.28959254
169Tm	ppm	0.20538932
172Yb	ppm	1.42772614
175Lu	ppm	0.22186892
178Hf	ppm	3.67800362
181Ta	ppm	0.64776814
208Pb	ppm	11.8604063
232Th	ppm	12.4777963
238U	ppm	3.68769963

Scotia Samples:

Sample		DR166.4	DR166.7	DR167.1	DR167.4
49TiO2	%	0.74490361	0.55790383	0.35316233	1.03860302
51V	ppm	273.662306	44.1560738	3.00238172	73.1864748
52Cr	ppm	55.8155577	28.8037704	11.951847	4.98843056
55MnO	%	0.17934295	0.14169345	0.0741267	0.22926088
57Fe2O3	%	6.51093754	3.19552729	1.81588384	7.92286929
59Co	ppm	21.5749795	8.26083684	2.31409596	16.6270165
60Ni	ppm	30.5500206	5.47941737	25.7839864	9.44105516
65Cu	ppm	51.2543376	10.0133409	6.12679965	92.8436544
66Zn	ppm	62.1701501	46.2887018	18.5012782	97.2276697
71Ga	ppm	16.5317596	16.488307	16.7127159	15.8184463
85Rb	ppm	12.2138473	227.116555	136.173442	15.6866622
88Sr	ppm	186.817736	256.423096	176.879248	125.475541
89Y	ppm	19.2459654	32.8311052	35.4791634	38.6004022
90Zr	ppm	60.1271909	184.432562	244.203487	95.8779881
93Nb	ppm	1.14470345	8.88851799	11.244676	1.1514338
95Mo	ppm	0.34390943	0.7492734	0.42369112	0.62197304
118Sn	ppm	0.95456566	1.19357222	1.57227494	1.36473409
133Cs	ppm	0.11390512	6.83742646	4.48671926	0.23533335
137Ba	ppm	135.94656	919.20385	773.062789	153.633851
139La	ppm	4.48511088	41.0787439	36.3075452	4.34342858
140Ce	ppm	11.495577	84.5968036	74.1863331	12.8737653
141Pr	ppm	1.63236345	10.0820387	9.10554062	2.10265509
146Nd	ppm	7.43721475	37.088264	32.6405663	10.5176673
147Sm	ppm	2.27558611	8.08837322	6.95049122	3.93575737
153Eu	ppm	0.7460732	1.79269768	1.29043274	1.22359789
157Gd	ppm	2.55381097	6.98375791	6.16104024	4.68980588
159Tb	ppm	0.41396467	0.94557353	0.86506597	0.81107966
163Dy	ppm	3.03841995	5.71675688	5.68859075	5.9889968
165Ho	ppm	0.60585064	1.00811905	1.06958016	1.21225458
166Er	ppm	1.82325453	2.90818568	3.19705868	3.71987777
169Tm	ppm	0.31316038	0.46963643	0.54793312	0.63145596
172Yb	ppm	2.08137251	3.0514281	3.74806478	4.33497856
175Lu	ppm	0.32147349	0.46928649	0.57663601	0.6729995
178Hf	ppm	1.66151047	4.45467349	6.14993361	2.74682219
181Ta	ppm	0.09360994	0.76825044	0.86583976	0.08516654
208Pb	ppm	2.64102123	17.8824873	18.7276482	3.49536256
232Th	ppm	1.98689663	15.511232	14.8214157	2.89701313
238U	ppm	0.36882305	1.57452965	2.74785217	0.26742642

Sample		SS18.15
49TiO2	%	0.90983232
51V	ppm	683.850986
52Cr	ppm	125.041314
55MnO	%	0.15388831
57Fe2O3	%	7.17716433
59Co	ppm	27.5680256
60Ni	ppm	51.9414043
65Cu	ppm	126.493013
66Zn	ppm	55.9528149
71Ga	ppm	13.7061021
85Rb	ppm	8.82333631
88Sr	ppm	115.070505
89Y	ppm	16.5680717
90Zr	ppm	41.0725699
93Nb	ppm	0.56546328
95Mo	ppm	0.39706422
118Sn	ppm	1.51807261
133Cs	ppm	0.36903377
137Ba	ppm	64.1619069
139La	ppm	1.89243679
140Ce	ppm	5.65088336
141Pr	ppm	0.88397623
146Nd	ppm	4.62089236
147Sm	ppm	1.66530797
153Eu	ppm	0.5911378
157Gd	ppm	2.01471706
159Tb	ppm	0.33861673
163Dy	ppm	2.60608146
165Ho	ppm	0.53852505
166Er	ppm	1.5751259
169Tm	ppm	0.26451069
172Yb	ppm	1.77907642
175Lu	ppm	0.27296648
178Hf	ppm	1.14107662
181Ta	ppm	0.04136464
208Pb	ppm	0.91004959
232Th	ppm	1.27868112
238U	ppm	0.12125485

Cardiff 2019 ICP-OES Data:

ISRM Samples:

Sample		DC-JB1A	DC-MRG1	DC-JA2
SiO2	wt%	52.6340626	40.1267066	57.9743513
TiO2	wt%	1.33151442	3.83026085	0.69708008
Al2O3	wt%	14.6030191	8.43820963	15.8762206
Fe2O3	wt%	9.3390992	18.2683469	6.44061637
MnO	wt%	0.1548211	0.17631048	0.10972117
MgO	wt%	7.9374964	13.4087491	7.49696289
CaO	wt%	9.45510697	14.7728167	6.12142653
Na2O	wt%	2.76347923	0.72396694	3.17035358
K2O	wt%	1.46895573	0.21005465	1.83444726
P2O5	wt%	0.26166829	0.07621731	0.15968221
LOI	wt%	0.78	1.02	0.8
Total	wt%	100.00902	100.100451	99.9412454
CR2O3	wt%			
Sc	ppm	28.6460602	52.9934853	18.8707803
V	ppm	206.493344	543.724112	115.002799
Cr	ppm	406.374263	466.512918	410.274371
Co	ppm	38.0724295	94.0560106	23.8276266
Ni	ppm	146.373025	185.813137	126.837011
Cu	ppm	54.9493345	138.940251	29.9738461
Zn	ppm	80.3365807	176.208336	80.7269832
Sr	ppm	445.452213	268.706329	243.417514
Y	ppm	24.0122376	14.4904549	16.9814914
Zr	ppm	139.462453	106.746412	107.091119
Ba	ppm	503.562415	58.2123628	318.626554

UB Samples:

Sample		UB01	UB02	UB03	UB04L
SiO2	wt%	61.2444648	61.6808164	58.910553	61.6052941
TiO2	wt%	1.05896876	0.62317741	0.77304538	0.71281588
Al2O3	wt%	21.2988618	15.9677508	15.2792868	16.0082115
Fe2O3	wt%	7.71405632	5.76706227	6.65363815	5.68049039
MnO	wt%	0.08163158	0.09732477	0.11256631	0.09038422
MgO	wt%	1.95148881	3.48889127	5.35007439	3.71903117
CaO	wt%	0.28620176	5.57554965	6.2850951	5.35217333
Na2O	wt%	1.78057438	3.88472146	3.69009674	4.06740507
K2O	wt%	3.4801287	1.73071669	1.4652891	2.25407583
P2O5	wt%	0.16160058	0.18832062	0.2009991	0.20373182
LOI	wt%	0.48576343	0.04130342	0.03286391	0.02861488
Total	wt%	99.0724803	99.0161795	98.7576187	99.7022821
CR2O3	wt%				
Sc	ppm	15.1551484	15.9230576	19.8051842	15.8034309
V	ppm	173.23693	139.597736	162.379429	142.733617
Cr	ppm	98.8470911	81.1173308	253.166794	59.3583621
Co	ppm	14.2974698	18.2578363	24.0569829	60.9937436
Ni	ppm	47.4598074	21.9456691	69.7168746	71.9785455
Cu	ppm	20.3765184	24.4477961	40.9692629	37.3109628
Zn	ppm	113.019162	80.3798454	93.2149491	68.2001004
Sr	ppm	113.107722	524.025913	546.54362	573.116916
Y	ppm	37.1520336	13.2104496	14.5476774	13.7081048
Zr	ppm	225.54203	114.308705	111.979413	110.708289
Ba	ppm	704.139035	1011.57235	871.837158	1107.81698

Sample		UB04P	UB05	UB06	UB07
SiO2	wt%	62.8225675	62.2295938	61.3400829	62.3859704
TiO2	wt%	0.69970762	0.67842233	0.74645865	0.75217287
Al2O3	wt%	15.6550163	15.4856452	16.4561388	16.7014066
Fe2O3	wt%	5.64806398	5.45757654	6.53155579	5.29236735
MnO	wt%	0.08574561	0.09065631	0.32306435	0.09331429
MgO	wt%	3.29715127	3.97623955	2.42997255	2.71763988
CaO	wt%	4.91661205	5.34985158	4.20717403	4.12919748
Na2O	wt%	3.94506576	3.88039707	4.23551875	4.21565608
K2O	wt%	2.41623143	2.1964676	2.36088185	2.46570355
P2O5	wt%	0.2185561	0.19379813	0.25182498	0.25820851
LOI	wt%	0.19835234	0.06750248	0.32391363	0.29884963
Total	wt%	99.7127596	99.5524769	98.8864052	99.0164553
CR2O3	wt%				
Sc	ppm	14.3803548	15.7687973	12.480757	13.5203639
V	ppm	149.71987	129.201432	146.819496	140.12049
Cr	ppm	54.9721018	94.6537158	25.482065	32.9023725
Co	ppm	17.8923645	18.8479078	17.2933578	16.6529052
Ni	ppm	30.8562723	43.5905147	34.094465	40.7191386
Cu	ppm	139.158618	31.8132346	21.8527511	31.4438291
Zn	ppm	71.5606743	58.0978184	88.7012872	75.0965377
Sr	ppm	541.38311	551.966844	820.351321	819.578724
Y	ppm	12.986495	13.8773675	18.5276544	18.7831526
Zr	ppm	164.430147	132.256254	111.136891	129.576853
Ba	ppm	1125.76951	1095.74947	1330.04306	1348.11048

Sample		UB8	UB9	UB10	UB11
SiO2	wt%	69.6338329	91.3092559	61.2296759	62.7430602
TiO2	wt%	0.32767732	0.24871175	0.84843278	0.79273228
Al2O3	wt%	16.2748163	5.4130815	16.330321	16.2234037
Fe2O3	wt%	2.65356025	0.71606019	5.97036337	5.71967865
MnO	wt%	0.05179908	0.0083017	0.09852205	0.09693734
MgO	wt%	1.11784366	0.76162751	3.52799276	3.31423882
CaO	wt%	3.33707867	0.00921673	5.68527969	5.3542206
Na2O	wt%	3.75587635	0.01341067	4.17451019	4.17299019
K2O	wt%	2.17792106	0.79463737	1.64464875	1.69570803
P2O5	wt%	0.09658457	0.02115933	0.27212204	0.18295921
LOI	wt%	0.08036862	0.42364053	-1.8444587	0.03710024
Total	wt%	99.4289062	99.3344295	99.7872752	100.301858
CR2O3	wt%				
Sc	ppm	7.20561397	7.89518498	16.7638726	14.693586
V	ppm	50.4571583	3715.64113	153.233176	141.665257
Cr	ppm	13.1129474	265.757895	37.7159955	40.5950314
Co	ppm	3.7369264	2.71820885	17.9347824	17.1718792
Ni	ppm	4.93993115	71.3813483	8.57307153	14.1446422
Cu	ppm	13.6453514	53.4672062	29.4515563	24.5317113
Zn	ppm	50.2865728	64.9214096	65.8488202	65.4239089
Sr	ppm	679.719433	4.05995416	635.709607	600.960054
Y	ppm	8.65590492	6.0952056	16.2652553	14.74048
Zr	ppm	116.765159	48.4586126	147.400235	139.756989
Ba	ppm	1242.92665	1273.66039	984.954183	1004.82564

Sample		UB12	UB13	UB14	UB15
SiO2	wt%	64.0173097	61.8425286	59.549799	63.0501988
TiO2	wt%	0.62613416	0.59887149	0.78653689	0.66596249
Al2O3	wt%	16.0001029	15.3491065	16.7997822	15.802733
Fe2O3	wt%	5.16036865	5.67514144	6.84651965	5.04399765
MnO	wt%	0.0944203	0.09558276	0.11339924	0.08323091
MgO	wt%	2.9042687	4.76153877	3.95670021	3.05410524
CaO	wt%	4.89528915	5.62232255	6.29228395	4.84089137
Na2O	wt%	4.10523264	3.98214409	4.10272045	4.20383303
K2O	wt%	1.77246948	1.55157935	1.289661	2.64392125
P2O5	wt%	0.09228106	0.18508108	0.19129568	0.24500035
LOI	wt%	0.02980139	0.03987497	0.06099333	0.12301228
Total	wt%	99.6741991	99.6954935	99.9400655	99.6440728
CR2O3	wt%				
Sc	ppm	13.708727	16.7012766	21.5773464	12.5792481
V	ppm	117.697939	135.007918	166.639412	112.917321
Cr	ppm	43.290505	216.329939	77.8103473	69.768568
Co	ppm	13.5928614	19.0331095	19.0446182	212.413557
Ni	ppm	10.9146774	70.4776027	23.5121313	74.6558964
Cu	ppm	18.166464	23.7087606	24.2210791	276.275537
Zn	ppm	76.5339318	84.0303133	91.2191878	97.414762
Sr	ppm	572.232094	576.663576	535.699102	697.377792
Y	ppm	12.0129359	13.606955	18.7084805	14.9634223
Zr	ppm	127.496138	99.9957337	118.387748	132.627798
Ba	ppm	1056.74773	1046.58172	741.675354	1328.52609

Sample		UB16	UB17	UB18
SiO2	wt%	63.2123895	61.0527504	63.1449646
TiO2	wt%	0.66647013	0.76203634	0.77851539
Al2O3	wt%	15.6625608	15.3209105	16.7654775
Fe2O3	wt%	4.97055768	5.87590923	5.85621688
MnO	wt%	0.08224409	0.09430341	0.07555136
MgO	wt%	3.01549937	4.6227936	2.9878446
CaO	wt%	4.72203879	5.81668918	3.30401985
Na2O	wt%	4.11171142	3.72955145	3.37862388
K2O	wt%	2.63216938	2.34209911	3.05982605
P2O5	wt%	0.23993834	0.2607747	0.23420362
LOI	wt%	0.11640638	0.1261924	0.42162973
Total	wt%	99.3257363	99.9001609	99.5969215
CR2O3	wt%			
Sc	ppm	12.4567664	17.2214114	12.8342947
V	ppm	115.443564	144.787041	133.164335
Cr	ppm	69.4851576	152.841239	79.6457321
Co	ppm	14.3510493	20.4917233	18.5630335
Ni	ppm	27.1841156	59.1632298	38.2666979
Cu	ppm	29.1552864	19.724031	48.3711391
Zn	ppm	64.1516092	57.642331	59.3039138
Sr	ppm	689.38436	707.606442	443.123621
Y	ppm	13.4624944	15.7560548	23.9153154
Zr	ppm	143.569024	149.181812	179.254366
Ba	ppm	1318.94631	1204.93164	1601.74072

Duplicate Analyses:

Sample		UB05-D	UB13-D
SiO2	wt%	62.3237883	61.1572659
TiO2	wt%	0.69408576	0.60323605
Al2O3	wt%	15.8075436	15.3640843
Fe2O3	wt%	5.4819547	5.69949932
MnO	wt%	0.0884629	0.094496
MgO	wt%	3.95478105	4.80937742
CaO	wt%	5.42107345	5.64230059
Na2O	wt%	3.93262263	3.98181776
K2O	wt%	2.26643022	1.56037012
P2O5	wt%	0.1945364	0.18539458
LOI	wt%	0.06750248	0.03987497
Total	wt%	100.179326	99.1290038
CR2O3	wt%		
Sc	ppm	16.2013182	18.1654819
V	ppm	133.148514	134.726829
Cr	ppm	96.1499497	213.350215
Co	ppm	18.8043633	21.1043726
Ni	ppm	47.3815124	71.8805163
Cu	ppm	24.5961194	21.8419893
Zn	ppm	55.9966763	67.165585
Sr	ppm	558.601598	574.209954
Y	ppm	13.9173333	14.1285851
Zr	ppm	136.66667	97.5809161
Ba	ppm	1114.68564	1041.39256

Cardiff 2019 ICP-MS Data:

ISRM Samples:

Sample		DC-JB1A	DC-MRG1	DC-JA2
49TiO2	%	1.33005932	3.68552869	0.695108
51V	ppm	207.915366	537.297105	118.234424
52Cr	ppm	417.077467	467.93379	419.011074
55MnO	%	0.14630626	0.16561794	0.10443206
57Fe2O3	%	9.10858102	17.7221519	6.27418495
59Co	ppm	40.7258571	89.9119535	29.1974622
60Ni	ppm	151.000796	177.511218	124.871731
65Cu	ppm	58.584625	131.436112	27.4272737
66Zn	ppm	78.7777789	178.517369	84.0764693
71Ga	ppm	18.3996621	15.7731504	15.2486234
85Rb	ppm	38.5520015	6.93187125	69.4731597
88Sr	ppm	439.536739	255.619921	235.108746
89Y	ppm	23.7432599	12.8433027	17.0414989
90Zr	ppm	144.313174	112.483534	122.585883
93Nb	ppm	28.1263656	20.8474354	8.73602504
95Mo	ppm			
118Sn	ppm			
133Cs	ppm	1.26549957	0.54638582	3.94199142
137Ba	ppm	500.847805	57.1021022	320.029608
139La	ppm	38.5506581	8.8241421	16.3930918
140Ce	ppm	66.7382123	24.7671009	33.6750601
141Pr	ppm	7.29878182	3.62614075	3.85339733
146Nd	ppm	26.0232763	18.3339639	14.332728
147Sm	ppm	5.349126	4.36228266	3.16048963
153Eu	ppm	1.5037168	1.43730432	0.90624328
157Gd	ppm	4.48022535	3.66238561	2.82877643
159Tb	ppm	0.70312502	0.55165656	0.47441659
163Dy	ppm	4.1063566	2.84059426	2.83600912
165Ho	ppm	0.67544806	0.42310746	0.50625236
166Er	ppm	2.0786616	1.03564461	1.45517999
169Tm	ppm	0.31726248	0.14172652	0.24791031
172Yb	ppm	2.07018718	0.77641873	1.62986762
175Lu	ppm	0.30754699	0.11222706	0.26493286
178Hf	ppm	3.46225644	3.69978062	2.85310736
181Ta	ppm	1.8169307	0.7693268	0.74236098
208Pb	ppm	6.93988298	6.3764343	21.5965927
232Th	ppm	8.66578141	0.84301656	5.00742669
238U	ppm	1.61299868	0.20508571	2.26457378

UB Samples:

Sample		UB01	UB02	UB03	UB04L
49TiO2	%	1.01862869	0.59936122	0.76624982	0.73756227
51V	ppm	166.520641	139.768576	157.720117	143.563633
52Cr	ppm	99.1976493	84.5838699	246.274152	63.9584492
55MnO	%	0.07754494	0.09130447	0.10036779	0.08508815
57Fe2O3	%	7.25104255	5.32440032	6.32157212	5.58255591
59Co	ppm	8.06589651	14.7723385	23.2196134	78.7427035
60Ni	ppm	44.9922875	22.0381107	65.2611418	74.1813969
65Cu	ppm	18.8407575	21.0586232	29.4334512	36.2003474
66Zn	ppm	115.548315	82.5134376	96.2858592	72.7459193
71Ga	ppm	30.105317	16.7636608	16.4157337	18.110796
85Rb	ppm	168.695915	42.4417811	29.7919453	64.9227113
88Sr	ppm	108.194006	515.871098	548.818219	569.770389
89Y	ppm	38.7188484	14.7204033	15.0546333	15.1877587
90Zr	ppm	227.572866	117.339547	113.233124	111.619649
93Nb	ppm	21.754136	4.6370164	5.3365232	4.18512306
95Mo	ppm				
118Sn	ppm				
133Cs	ppm	9.23429163	1.16010819	0.48031979	2.63158546
137Ba	ppm	683.188211	981.1509	815.97048	1129.06666
139La	ppm	59.8269502	16.4775955	14.7672563	20.5240888
140Ce	ppm	123.938764	31.7850283	29.135608	39.2912479
141Pr	ppm	14.0593515	3.71539673	3.51169167	4.64667649
146Nd	ppm	54.3520199	14.9869409	15.0026574	18.4019522
147Sm	ppm	10.9476205	3.22106148	3.47505649	4.03165336
153Eu	ppm	1.99499044	0.89011099	1.00237711	1.02132896
157Gd	ppm	7.65824298	2.6693392	2.87469782	3.05865631
159Tb	ppm	1.24742182	0.43887766	0.463405	0.47689902
163Dy	ppm	6.98578462	2.36317013	2.55933249	2.69952674
165Ho	ppm	1.13865345	0.40936082	0.44092117	0.44002269
166Er	ppm	3.48281552	1.1974917	1.30904164	1.3343907
169Tm	ppm	0.554471	0.19793555	0.20588698	0.20950916
172Yb	ppm	3.68120658	1.29682242	1.27412997	1.40049083
175Lu	ppm	0.54827256	0.20380075	0.20253427	0.21299068
178Hf	ppm	5.81156542	2.95731157	2.77958447	3.16370545
181Ta	ppm	1.73218546	0.34886331	0.37493336	0.36059924
208Pb	ppm	23.0814025	13.0941138	9.83251912	14.312159
232Th	ppm	16.0637598	11.9375622	5.90315534	7.53779126
238U	ppm	3.46842688	1.68732705	1.54524123	4.43972711

Sample		UB04P	UB05	UB06	UB07
49TiO2	%	0.73300176	0.6710158	0.75851886	0.75350208
51V	ppm	152.001519	127.748614	142.991575	138.518807
52Cr	ppm	57.5996503	95.1227593	31.5825544	33.0436367
55MnO	%	0.08141758	0.08343003	0.30664666	0.0879033
57Fe2O3	%	5.52990106	5.15659351	6.3582603	5.10353777
59Co	ppm	17.3400398	18.7023224	16.8208235	16.206682
60Ni	ppm	36.6663878	46.4731876	33.9045843	43.3677981
65Cu	ppm	142.215031	24.3921083	17.0026936	26.4663984
66Zn	ppm	70.7203758	64.7316311	90.6493975	65.75285
71Ga	ppm	17.7390203	16.8242284	18.7233042	21.1393046
85Rb	ppm	71.0749862	61.9524031	56.0318569	62.340153
88Sr	ppm	537.581152	539.282426	799.692708	804.960604
89Y	ppm	14.8343544	14.626415	19.9947447	20.3839528
90Zr	ppm	160.977841	135.61156	118.944604	131.336177
93Nb	ppm	7.36058131	6.31274235	5.45202572	6.08379806
95Mo	ppm				
118Sn	ppm				
133Cs	ppm	3.06781574	2.51035567	1.18927462	1.24952339
137Ba	ppm	1138.35429	1059.72288	1330.42078	1345.76784
139La	ppm	19.3883879	19.2809325	23.6492449	24.375971
140Ce	ppm	36.9494827	37.1455906	43.3532716	44.7296676
141Pr	ppm	4.19965285	4.30953308	5.18606982	5.29538689
146Nd	ppm	16.6554618	17.5088468	21.1991637	21.724641
147Sm	ppm	3.56272654	3.75663818	4.65227966	4.64007658
153Eu	ppm	0.92790759	0.94419301	1.19741997	1.1981629
157Gd	ppm	2.65300323	3.04139304	3.70422553	3.62748816
159Tb	ppm	0.4299816	0.45819936	0.56157681	0.54737318
163Dy	ppm	2.49573364	2.55791055	3.08728817	3.02221409
165Ho	ppm	0.4191502	0.42149613	0.52133069	0.51500304
166Er	ppm	1.33120582	1.3476884	1.6630267	1.53001158
169Tm	ppm	0.20275261	0.19216356	0.23141586	0.21764468
172Yb	ppm	1.38442188	1.35180823	1.57823449	1.46540681
175Lu	ppm	0.21143846	0.21201703	0.25166359	0.21831742
178Hf	ppm	4.45035256	3.71090719	3.26687837	3.59560827
181Ta	ppm	0.61767164	0.52288635	0.52541516	0.54024642
208Pb	ppm	15.7354339	13.7908791	17.6044504	16.4759517
232Th	ppm	10.4003935	9.79375038	9.4899389	9.16453456
238U	ppm	4.97745245	4.24264193	4.08250963	3.97865359

Sample		UB8	UB9	UB10	UB11
49TiO2	%	0.34014894	0.26364529	0.8728316	0.79859892
51V	ppm	52.3957477	3594.92877	155.251682	141.968691
52Cr	ppm	15.8443586	273.507793	41.5023914	43.5302913
55MnO	%	0.05084753	0.00129422	0.09788062	0.09351801
57Fe2O3	%	2.6338653	0.70562076	5.99975923	5.57490442
59Co	ppm	3.43042535	2.40727457	16.4630568	14.8165546
60Ni	ppm	5.92350856	71.7563016	13.4024895	13.7146811
65Cu	ppm	9.57554819	23.042906	24.9395743	20.7375311
66Zn	ppm	40.1553029	63.9563958	53.5534283	62.4272908
71Ga	ppm	16.9926441	9.2140755	20.1338415	18.606985
85Rb	ppm	72.643273	36.2744973	43.4182938	43.451477
88Sr	ppm	686.319372	4.5017928	652.421823	605.900417
89Y	ppm	9.41651515	5.97853527	16.5535081	15.2258092
90Zr	ppm	118.082602	52.1501565	158.810472	137.796134
93Nb	ppm	4.94410407	3.84528569	7.29277161	6.42488543
95Mo	ppm				
118Sn	ppm				
133Cs	ppm	2.10422272	1.8347333	1.15422828	1.0451088
137Ba	ppm	1268.08295	1300.49366	1016.04443	1020.33668
139La	ppm	17.9998251	10.8718548	23.0723187	19.5535886
140Ce	ppm	33.9018673	10.7442365	44.8194327	37.3613443
141Pr	ppm	3.71212494	1.49592443	5.20305969	4.30322568
146Nd	ppm	14.4622421	5.02034577	21.2715973	17.6412949
147Sm	ppm	2.91298431	0.72671139	4.54949555	3.69655032
153Eu	ppm	0.79260098	0.17616791	1.17748577	1.02058605
157Gd	ppm	2.1430354	0.55135802	3.37172003	2.87296178
159Tb	ppm	0.31818599	0.09688226	0.51703009	0.45464125
163Dy	ppm	1.65817552	0.73640686	2.87510838	2.56764133
165Ho	ppm	0.28138437	0.16775689	0.45555784	0.41977789
166Er	ppm	0.80166808	0.58909516	1.44055691	1.28557354
169Tm	ppm	0.11770711	0.10098173	0.21425582	0.18770539
172Yb	ppm	0.8270424	0.75502662	1.41641325	1.30121409
175Lu	ppm	0.12250813	0.11439689	0.21720549	0.19918808
178Hf	ppm	3.0515021	1.26458993	3.91715164	3.27799154
181Ta	ppm	0.36647582	0.3686655	0.47390854	0.43272247
208Pb	ppm	16.6814247	19.6824167	9.89455464	9.43699073
232Th	ppm	7.00755787	4.47644844	4.62589494	4.81070726
238U	ppm	1.78961073	5.09094206	1.68914085	1.66073661

Sample		UB12	UB13	UB14	UB15
49TiO2	%	0.64065496	0.6173179	0.77585537	0.69133029
51V	ppm	127.187603	131.980339	169.870346	119.547549
52Cr	ppm	49.4592388	226.694854	89.3438642	73.7090106
55MnO	%	0.09293213	0.08948351	0.10851689	0.07853032
57Fe2O3	%	5.16732822	5.63594238	6.85835612	4.96519628
59Co	ppm	13.6109169	20.6868656	19.0374739	215.44867
60Ni	ppm	13.5948579	75.3347403	30.1324789	78.2065745
65Cu	ppm	12.7774387	19.1526279	21.1917519	291.325687
66Zn	ppm	81.3552673	89.6375341	83.7532595	88.5920633
71Ga	ppm	18.8359161	17.2745468	18.1483218	19.344662
85Rb	ppm	46.4934271	33.6347856	23.6407107	67.2686784
88Sr	ppm	582.819482	553.721541	531.000727	676.814287
89Y	ppm	13.3371504	14.2393905	20.7746313	15.3281085
90Zr	ppm	124.385537	104.173228	115.724639	132.319965
93Nb	ppm	5.50365886	3.88089356	3.29554678	6.22802807
95Mo	ppm				
118Sn	ppm				
133Cs	ppm	1.20083767	0.7970843	0.49367514	2.60651067
137Ba	ppm	1080.9852	1043.65664	760.005059	1303.00875
139La	ppm	15.6735668	13.0772994	13.5950505	24.1663579
140Ce	ppm	29.1535064	25.6713951	26.5949661	43.689433
141Pr	ppm	3.35571711	3.2582514	3.51229402	5.25794819
146Nd	ppm	13.5844443	14.079209	15.5383098	20.9880124
147Sm	ppm	3.04832503	3.35473793	3.91119859	4.35698431
153Eu	ppm	0.84468772	0.95687607	1.10787315	1.11850228
157Gd	ppm	2.44683115	2.81663098	3.34388477	3.17683019
159Tb	ppm	0.38574123	0.43881373	0.57139542	0.47831703
163Dy	ppm	2.20270043	2.47705204	3.41152378	2.51223832
165Ho	ppm	0.3689521	0.42123741	0.60530029	0.42471853
166Er	ppm	1.16645023	1.26451684	1.83968982	1.21886241
169Tm	ppm	0.18296504	0.20014378	0.29393259	0.18971839
172Yb	ppm	1.23951907	1.29107614	1.97529762	1.23831711
175Lu	ppm	0.18452836	0.1981466	0.28803851	0.19111107
178Hf	ppm	3.15099984	2.76452944	3.02227327	3.49168025
181Ta	ppm	0.38731527	0.33373583	0.23651336	0.61971736
208Pb	ppm	10.811912	9.54806722	8.47893072	17.2353494
232Th	ppm	4.41385981	3.26972977	2.6342423	6.73230234
238U	ppm	1.66280631	1.9230636	1.06624194	4.37154248

Sample		UB16	UB17	UB18
49TiO2	%	0.71965969	0.79571109	0.79474043
51V	ppm	123.710798	147.42389	136.264072
52Cr	ppm	76.8290608	164.763488	85.3621122
55MnO	%	0.07966581	0.09202486	0.07131594
57Fe2O3	%	5.1413685	5.8447791	5.6590973
59Co	ppm	15.8249941	20.5606414	16.4675074
60Ni	ppm	36.0281526	63.749118	38.4207066
65Cu	ppm	29.6606391	22.1780511	46.4652927
66Zn	ppm	70.5678189	66.3011116	66.6525982
71Ga	ppm	20.6974623	19.9909597	22.1531769
85Rb	ppm	70.0227636	56.6293423	92.6520683
88Sr	ppm	695.506191	694.732662	430.080565
89Y	ppm	15.2642204	16.5817625	24.4270017
90Zr	ppm	144.79152	148.166613	178.958605
93Nb	ppm	6.91330465	7.95017941	8.82717194
95Mo	ppm			
118Sn	ppm			
133Cs	ppm	2.79956605	2.20442472	1.43067174
137Ba	ppm	1345.93252	1203.40742	1561.89548
139La	ppm	24.8199396	24.6318277	37.5317974
140Ce	ppm	45.0491349	44.6124027	50.7285821
141Pr	ppm	5.42524109	5.52496468	7.95914543
146Nd	ppm	21.4394136	22.489013	31.9312296
147Sm	ppm	4.37938703	4.63191051	6.47991183
153Eu	ppm	1.14259557	1.23990228	1.52648045
157Gd	ppm	3.25729234	3.47145431	4.98553745
159Tb	ppm	0.49640494	0.53325881	0.74423832
163Dy	ppm	2.62266407	2.85984301	3.98056229
165Ho	ppm	0.43487157	0.47472358	0.67710596
166Er	ppm	1.27231103	1.39190734	1.98082131
169Tm	ppm	0.19577209	0.20915985	0.31137076
172Yb	ppm	1.31131246	1.37529155	2.00640492
175Lu	ppm	0.20486015	0.21633478	0.27924416
178Hf	ppm	3.92772362	3.87875324	4.7747428
181Ta	ppm	0.67192513	0.57698696	0.85541589
208Pb	ppm	18.5398383	15.0874506	16.7355851
232Th	ppm	9.64293008	9.22351801	12.9828335
238U	ppm	4.51449536	3.60490539	6.36021985

Duplicate Analyses:

Sample		UB05-D	UB13-D
49TiO2	%	0.73402544	0.60975364
51V	ppm	136.799644	131.298686
52Cr	ppm	102.339076	218.909497
55MnO	%	0.08581875	0.08823729
57Fe2O3	%	5.49271057	5.49612848
59Co	ppm	19.291932	20.5497385
60Ni	ppm	48.7591574	69.9873424
65Cu	ppm	25.3704422	18.7770028
66Zn	ppm	54.6590862	70.1975082
71Ga	ppm	18.7656786	17.0155381
85Rb	ppm	63.6613812	32.4158782
88Sr	ppm	562.525358	560.957108
89Y	ppm	15.6892664	14.1268684
90Zr	ppm	137.312027	104.16439
93Nb	ppm	6.13142036	3.6246767
95Mo	ppm		
118Sn	ppm		
133Cs	ppm	2.63391513	0.83067838
137Ba	ppm	1134.22904	1023.97162
139La	ppm	20.3427381	12.8421527
140Ce	ppm	38.9585002	25.1251112
141Pr	ppm	4.65434628	3.24087551
146Nd	ppm	19.0964895	13.7991862
147Sm	ppm	4.11975667	3.31239027
153Eu	ppm	1.06427675	0.90200874
157Gd	ppm	3.12806672	2.71749613
159Tb	ppm	0.48602739	0.42614407
163Dy	ppm	2.70941283	2.39796835
165Ho	ppm	0.45997717	0.41636154
166Er	ppm	1.37711443	1.21961672
169Tm	ppm	0.22219854	0.18490345
172Yb	ppm	1.40361426	1.23131202
175Lu	ppm	0.21990025	0.18723917
178Hf	ppm	3.61600649	2.595568
181Ta	ppm	0.54375554	0.31359954
208Pb	ppm	14.1802719	9.28864462
232Th	ppm	12.538288	6.0704409
238U	ppm	4.45589065	1.87211105

Scotia analyses performed at the University of Leicester (2015):

Sample		166.4	166.7	167.1	167.4
SiO2	wt%	54.87	64.05	71.52	61.98
TiO2	wt%	0.74	0.52	0.31	0.99
Al2O3	wt%	18.53	14.17	14.47	13.97
Fe2O3	wt%	8.59	4.37	2.53	10.78
MnO	wt%	0.172	0.143	0.083	0.217
MgO	wt%	4.57	1.45	0.71	1.63
CaO	wt%	9.29	1.73	1.30	5.64
Na2O	wt%	2.76	4.27	4.19	3.93
K2O	wt%	0.605	5.399	3.826	0.714
P2O5	wt%	0.109	0.146	0.072	0.175
SO3	wt%	<0.003	0.008	<0.003	<0.003
LOI	wt%	-0.11	3.47	0.81	-0.22
Total	wt%	100.13	99.74	99.83	99.81
As	ppm	4.0	12.4	0.7	2.5
Ba	ppm	159.5	879.6	753.6	153.5
Ce	ppm	14.4	89.6	67.9	13.2
Co	ppm	22.4	10.4	2.5	20.2
Cr	ppm	40.3	24.8	15.9	171.2
Cs	ppm	<1.6	8.3	3.7	1.7
Cu	ppm	52.9	4.2	2.4	89.5
Ga	ppm	18.6	17.9	16.0	16.9
La	ppm	6.5	44.9	34.4	3.6
Mo	ppm	1.7	1.9	1.0	1.9
Nb	ppm	1.4	10.2	11.5	1.2
Nd	ppm	11.0	41.1	35.3	11.1
Ni	ppm	16.0	6.4	1.5	<0.7
Pb	ppm	2.4	19.0	17.0	3.8
Rb	ppm	13.8	214.8	131.0	16.4
Sb	ppm	<1.1	<1.0	<0.9	<1.1
Sc	ppm	33.1	21.0	10.7	30.3
Se	ppm	<0.7	<0.6	<0.5	<0.6
Sn	ppm	<1.0	<1.0	<0.8	<1.0
Sr	ppm	196.6	264.7	180.5	129.2
Th	ppm	1.1	12.3	13.0	<0.6
U	ppm	<0.5	1.4	3.1	<0.5
V	ppm	252.9	83.8	33.8	85.6
W	ppm	<1.2	<1.0	<0.9	4.0
Y	ppm	21.9	34.1	39.1	42.3
Zn	ppm	68.1	55.9	26.5	97.3
Zr	ppm	60.2	182.9	223.9	95.0

Sample		SS 18.15
SiO2	wt%	52.32
TiO2	wt%	1.01
Al2O3	wt%	15.30
Fe2O3	wt%	11.84
MnO	wt%	0.191
MgO	wt%	5.82
CaO	wt%	10.32
Na2O	wt%	2.39
K2O	wt%	0.373
P2O5	wt%	0.186
SO3	wt%	<0.003
LOI	wt%	0.25
Total	wt%	100.01
As	ppm	3.9
Ba	ppm	74.8
Ce	ppm	11.7
Co	ppm	32.8
Cr	ppm	320.2
Cs	ppm	<1.6
Cu	ppm	137.5
Ga	ppm	17.0
La	ppm	<2.0
Mo	ppm	2.0
Nb	ppm	0.9
Nd	ppm	6.3
Ni	ppm	40.3
Pb	ppm	2.7
Rb	ppm	10.4
Sb	ppm	<1.1
Sc	ppm	42.7
Se	ppm	1.4
Sn	ppm	<1.1
Sr	ppm	125.9
Th	ppm	<0.6
U	ppm	0.8
V	ppm	413.3
W	ppm	<1.3
Y	ppm	19.8
Zn	ppm	71.3
Zr	ppm	47.7

Appendix D: Raw analyses of Sr, Nd and Hf isotopes for Colombian and ISRM samples

Sr Analyses:

BATCH	N	Sample	87Sr/86Sr (n)	± 2SE
ISRM Samples:				
N836	24	BCR-2	0.705038	0.000008
DC16 Samples:				
N836	20	DC16-001	0.704606	0.000008
N833	27	DC16-006	0.704748	0.000009
N833	28	DC16-009	0.704400	0.000014
N833	5	DC16-010	0.704525	0.000012
N833	20	DC16-011	0.704286	0.000011
N833	29	DC16-017	0.704583	0.000020
N833	30	DC16-019	0.704597	0.000011
N833	6	DC16-026	0.704423	0.000015
N833	7	DC16-028	0.704243	0.000015
N833	8	DC16-035	0.704103	0.000013
N833	9	DC16-036	0.704352	0.000008
N833	10	DC16-038	0.704264	0.000011
DB15 Samples:				
N836	1	DB15-081	0.703974	0.000003
N836	2	DB15-082	0.703797	0.000007
EAFIT Samples:				
N833	3	PKSW-016B	0.704321	0.000011
N833	1	PKSW-098	0.703783	0.000013
N833	2	JLSW-008A	0.704238	0.000016
N833	22	JLSW-32B	0.704493	0.000007
N833	21	LHSW-017B	0.704182	0.000008
N833	4	SESW-106a	0.704184	0.000014

BATCH	N	Sample	87Sr/86Sr (n)	± 2SE
UB Samples:				
N833	11	UB-01	0.738221	0.000010
N833	23	UB-02	0.704648	0.000008
N833	12	UB-03	0.704522	0.000011
N833	13	UB-04-L	0.704390	0.000013
N833	24	UB-05	0.704381	0.000009
N833	14	UB-06	0.704449	0.000024
N836	22	UB-08	0.705303	0.000009
N833	16	UB-09	0.737375	0.000010
N833	25	UB-10	0.704572	0.000014
N833	17	UB-13	0.704418	0.000013
N833	26	UB-15	0.704458	0.000011
N833	18	UB-16	0.704441	0.000017
N836	23	UB-16	0.704451	0.000010
N833	19	UB-17	0.704445	0.000013

Nd Analyses:

BATCH	N	Sample	176Hf/177Hf (n)	± 2SE	Eps_Hf
ISRM Samples:					
N836	24	BCR-2	0.282867	0.000007	2.9
DC16 Samples:					
N836	20	DC16-001	0.282796	0.000011	0.4
N833	27	DC16-006	0.282903	0.000007	4.2
N833	28	DC16-009	0.282994	0.000008	7.4
N833	5	DC16-010	0.282926	0.000008	5.0
N833	20	DC16-011	0.282963	0.000009	6.3
N833	29	DC16-017	0.282948	0.000006	5.8
N833	30	DC16-019	0.282942	0.000006	5.5
N833	6	DC16-026	0.282999	0.000008	7.6
N833	7	DC16-028	0.282951	0.000007	5.9
N833	8	DC16-035	0.283031	0.000007	8.7
N833	9	DC16-036	0.282956	0.000008	6.0
N833	10	DC16-038	0.283052	0.000007	9.4
DB15 Samples:					
N836	1	DB15-081	0.283144	0.000007	12.7
N836	2	DB15-082	0.283153	0.000007	13.0
EAFIT Samples:					
N833	3	PKSW-016B	0.282959	0.000008	6.2
N833	1	PKSW-098	0.282990	0.000010	7.2
N833	2	JLSW-008A	0.283029	0.000007	8.6
N833	22	JLSW-32B	0.282985	0.000007	7.1
N833	21	LHSW-017B	0.282975	0.000007	6.7
N833	4	SESW-106a	0.282983	0.000008	7.0

BATCH	N	Sample	176Hf/177Hf (n)	± 2SE	Eps_Hf
UB Samples:					
N833	11	UB-01	0.282881	0.000006	3.4
N833	23	UB-02	0.282930	0.000007	5.1
N833	12	UB-03	0.282962	0.000007	6.3
N833	13	UB-04-L	0.282968	0.000008	6.5
N833	24	UB-05	0.283083	0.000007	10.5
N833	14	UB-06	0.282961	0.000008	6.2
N836	22	UB-08	0.282897	0.000012	4.0
N833	16	UB-09	0.282794	0.000008	0.3
N833	25	UB-10	0.282926	0.000006	5.0
N833	17	UB-13	0.282996	0.000008	7.5
N833	26	UB-15	0.283129	0.000007	12.2
N833	18	UB-16	0.282968	0.000007	6.5
N836	23	UB-16	0.282964	0.000008	6.3
N833	19	UB-17	0.282939	0.000008	5.4

Hf Analyses:

BATCH	N	Sample	143Nd/144Nd (n)	± 2SE	Eps_Nd
ISRM Samples:					
N836	24	BCR-2	0.512639	0.000005	0.0
DC16 Samples:					
N836	20	DC16-001	0.512672	0.000009	0.7
N833	27	DC16-006	0.512723	0.000016	1.7
N833	28	DC16-009	0.512848	0.000014	4.1
N833	5	DC16-010	0.512742	0.000012	2.0
N833	20	DC16-011	0.512780	0.000012	2.8
N833	29	DC16-017	0.512741	0.000012	2.0
N833	30	DC16-019	0.512741	0.000015	2.0
N833	6	DC16-026	0.512817	0.000020	3.5
N833	7	DC16-028	0.512787	0.000015	2.9
N833	8	DC16-035	0.512880	0.000012	4.7
N833	9	DC16-036	0.512806	0.000010	3.3
N833	10	DC16-038	0.512858	0.000010	4.3
DB15 Samples:					
N836	1	DB15-081	0.512970	0.000004	6.5
N836	2	DB15-082	0.512971	0.000004	6.5
EAFIT Samples:					
N833	3	PKSW-016B	0.512783	0.000010	2.8
N833	1	PKSW-098	0.512790	0.000014	3.0
N833	2	JLSW-008A	0.512778	0.000012	2.7
N833	22	JLSW-32B	0.512786	0.000015	2.9
N833	21	LHSW-017B	0.512819	0.000011	3.5
N833	4	SESW-106a	0.512810	0.000013	3.4

BATCH	N	Sample	143Nd/144Nd (n)	± 2SE	Eps_Nd
UB Samples:					
N833	11	UB-01	0.512036	0.000011	-11.7
N833	23	UB-02	0.512755	0.000011	2.3
N833	12	UB-03	0.512813	0.000011	3.4
N833	13	UB-04-L	0.512800	0.000012	3.2
N833	24	UB-05	0.512796	0.000013	3.1
N833	14	UB-06	0.512768	0.000013	2.5
N836	22	UB-08	0.512514	0.000005	-2.4
N833	16	UB-09	0.512142	0.000023	-9.7
N833	25	UB-10	0.512774	0.000010	2.7
N833	17	UB-13	0.512824	0.000014	3.6
N833	26	UB-15	0.512785	0.000010	2.9
N833	18	UB-16	0.512790	0.000007	3.0
N836	23	UB-16	0.512790	0.000007	3.0
N833	19	UB-17	0.512787	0.000013	2.9

Appendix E: Sample report for UB samples provided by Dr Hugo Fernando Murcia

Sampling report.

Samples for isotopic analysis as part of the PhD project of David Cavell at the University of Birmingham (England).

Field camp in San Diego – Cerro Machín Volcano-Tectonic Province (Colombia)

By: Hugo Murcia, Camilo Pinzón, Pablo Osorio, Alvaro Botero

Universidad de Caldas (Colombia) – December 2018

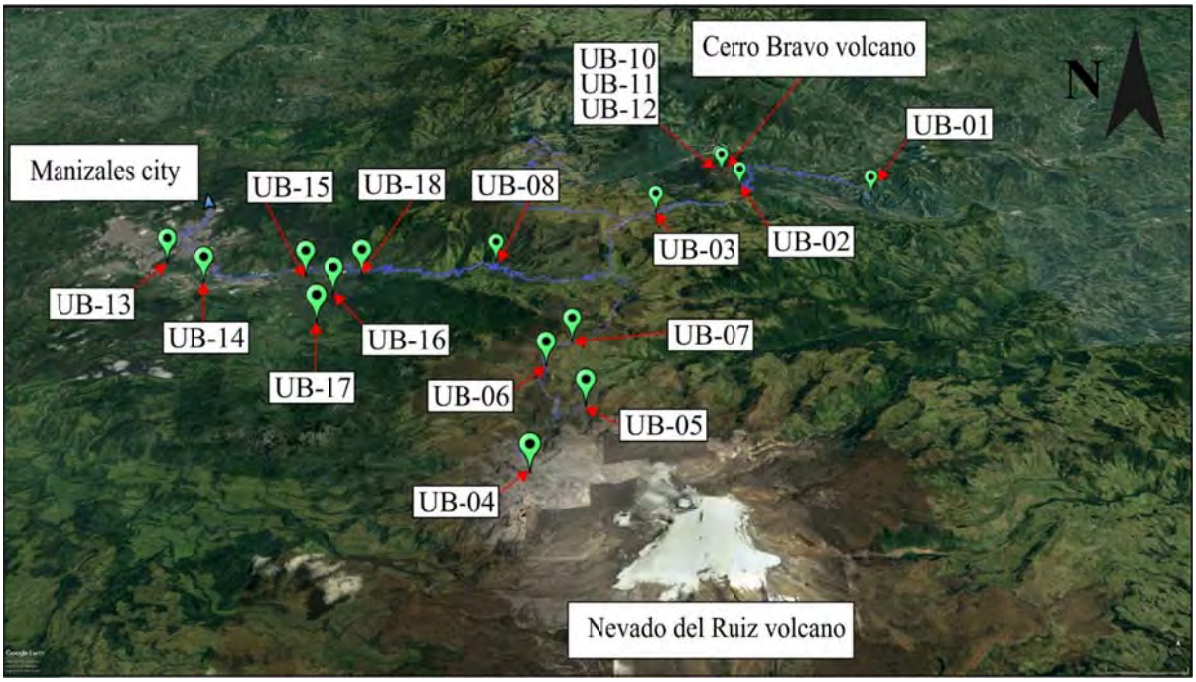

Sample list.

UB01: 5°5’33,9” N; 75°13’47,4” W; 2462,3 masl.

Place: Delgaditas-Herveo road.

Sample from: Cajamarca Complex; schists.

Fig. 1. Black to gray schist from the Cajamarca Complex.

UB02: 5°5’1” N; 75°17’1,2” W; 3304,9 masl.

Place: La Virgen sector. Letras – Delgaditas road.

Sample from: Lava flow from old Cerro Bravo volcano.

Fig. 2. Lava flows from old Cerro Bravo volcano.

UB03: 5°3’32,3” N; 75°19’2,5” W; 3504,3 masl.

Place: La Cantera sector. Letras – Delgaditas road.

Sample from: Lava flow from the Letras Volcano-Tectonic Depresion. Altered plagioclase.

Fig. 3. Lava flow from the Letras Volcano-Tectonic Depresion. Red circle represents the sampling point.

UB04 (P-L): 4°54’34,3” N; 75°21’17,4” W; 4419,4 masl

Place: Valle de Las Tumbas. Nevado del Ruiz National Park.

Sample from: 1985 eruption: pumice (**UB04-P**) and lithic (**UB04-L**)

Fig. 4. Sample place from the 1985 eruption of the Nevado del Ruiz. The black arrows represent fragments from the last (1985) eruption.

UB05: 4°56’24,4” N; 75°20’30,7” W; 4001,6 masl

Place: Gualí river. La Esperanza – Murillo road.

Sample from: Lava flow. Antique Ruiz

Fig. 5. Lava flows from Antique Ruiz.

UB06: 4°57’27,1” N; 75°21’11,1” W; 4030,5 masl

Place: Cerro Gualí. La Esperanza – National Park road.

Sample from: Lava flow. Ancestral Ruiz

Fig. 6. Lava flows from Ancestral Ruiz.

UB07: 4°58’15,6” N; 75°20’46,2” W; 3917,2 masl

Place: El Arbolito sector. La Esperanza – National Park road.

Sample from: Lava flow. Ancestral Ruiz

Fig. 7. Lava flows from Ancestral Ruiz. The red circle shows the sampling point.

UB08: 5°1’55,7” N; 75°22’24,9” W; 2938,9 masl

Place: La Mula creek. Manizales stock. Manizales – Mariquita road.

Sample from: Manizales stock

Fig. 8. Manizales Stock. The red circle shows the sampling point.

UB09: 5°02’43” N; 75°28’23” W; 0000 masl

Place: El Perro creek. Expoferias sector, Manizales.

Sample from: Quebradagrande Complex.

Fig. 9. Quebradagrande Complex.

UB10: 5° 5'12.80"N; 75°17'27.80"O (sample **CH4** in Pinzón et al., 2018 BG: 40(3):67-84)

Place: Cerro Bravo volcano

Sample from: Intracrater dome. Last eruption

Fig. 10. Cerro Bravo dome. The black arrow shows the sampling point.

UB11: 5° 5'15.70"N; 75°17'30.50"O (sample **CH5** in Pinzón et al., 2018 BG: 40(3):67-84)

Place: Cerro Bravo volcano

Sample from: Intracrater dome. Last eruption

Fig. 11. Cerro Bravo dome. The black arrow shows the sampling point.

UB12: 5° 5'20.60"N; 75°17'27.00"O (sample **CH6** in Pinzón et al., 2018 BG: 40(3):67-84)

Place: Cerro Bravo volcano

Sample from: Intracrater dome. Last eruption

Fig. 12. Cerro Bravo dome. The black arrow shows the sampling point

UB13: 5°02’45’’N; 75°29’40’’ W; 2200 masl

Place: Panamericana road, Manizales.

Sample from: Lava from the Sancancio Dome

Fig.13. Sancancio volcano; Villamaria – Termales Monogenetic Volcanic Field. Red circle represent the sampling point.

UB14: 5°01’57’’ N; 75°28’36’’ W; 2030 masl

Place: Panamericana road, Villamaria

Sample from: Lava from the Lava flow of Lusitania

Fig.14. Lusitania lava flow; Villamaria – Termales Monogenetic Volcanic Field. Red circle represent the sampling point.

UB15: 5°01’57’’ N; 75°26’27’’ W; 2400 masl

Place: Manizales- Nevado del Ruiz volcano road.

Sample from: Lava flow from the Tesorito Dome

Fig.15. Panoramic view from Tesorito volcano; Villamaria – Termales Monogenetic Volcanic Field.

UB16: 5°01’07’’ N; 75°25’40’’ W; 2700 masl

Place: Manizales- Nevado del Ruiz volcano road.

Sample from: Lava flow from the Gallinazo Dome

Fig.16. Panoramic view from Gallinazo volcano; Villamaria – Termales Monogenetic Volcanic Field.

UB17: 5°00’01’’ N; 75°25’46’’ W; 2650 masl

Place: Manizales- Nevado del Ruiz volcano road.

Sample from: Lava flow from the Victoria Dome

Fig. 17. Victoria volcano; Villamaria – Termales Monogenetic Volcanic Field. Red circle represents the sampling point.

UB18: 5°01’45’’ N; 75°25’12’’W; 2750 masl

Place: Manizales- Nevado del Ruiz volcano road.

Sample from: Lava from the Amazonas Dome

Fig. 18. Panoramic view from Amazonas volcano; Villamaria – Termales Monogenetic Volcanic Field.

Work team in the field


No ingresar por este sector